2022 Cosmology

edited by
Etienne Augé
Jacques Dumarchez
and
Jean Trân Thanh Vân

Proceedings of the 56th Rencontres de Moriond

Published by ARISF

2022

Cosmology

Sponsored by

- CNRS (Centre National de la Recherche Scientifique)
- CEA (Commissariat à l'Énergie Atomique et aux Énergies Alternatives)
- FNRS (Fond National de la Recherche Scientifique)

56th Rencontres de Moriond

La Thuile, Aosta Valley, Italy - January 23 - 30, 2022

2022 Cosmology

DOI: https://doi.org/10.58027/3q8k-ew90

ISBN: 979-10-96879-16-8

Proceedings of the 56th RENCONTRES DE MORIOND
Cosmology
La Thuile, Aosta Valley, Italy *January 23-30, 2022*

2022

Cosmology

edited by

Étienne Augé
Jacques Dumarchez
and
Jean Trân Thanh Vân

The 56^{th} Rencontres de Moriond

2022 Cosmology

was organized by

Étienne Augé (LAL, Orsay)
Jacques Dumarchez (LPNHE, Paris)

with the active collaboration of:

- Pierre Astier (Paris)
- Cliff Burgess (Toronto)
- Ken Ganga (Paris)
- Jean-Marc Le Goff (Saclay)
- Olivier Perdereau (Orsay)
- Filippo Vernizzi (Saclay)

2022 RENCONTRES DE MORIOND

The 56^{th} Rencontres de Moriond were held in La Thuile, Valle d'Aosta, Italy.

The first meeting took place at Moriond in the French Alps in 1966. There, experimental as well as theoretical physicists not only shared their scientific preoccupations, but also the household chores. The participants in the first meeting were mainly french physicists interested in electromagnetic interactions. In subsequent years, a session on high energy strong interactions was added.

The main purpose of these meetings is to discuss recent developments in contemporary physics and also to promote effective collaboration between experimentalists and theorists in the field of elementary particle physics. By bringing together a relatively small number of participants, the meeting helps develop better human relations as well as more thorough and detailed discussion of the contributions.

Our wish to develop and to experiment with new channels of communication and dialogue, which was the driving force behind the original Moriond meetings, led us to organize a parallel meeting of biologists on Cell Differentiation (1980) and to create the Moriond Astrophysics Meeting (1981). In the same spirit, we started a new series on Condensed Matter physics in January 1994. Meetings between biologists, astrophysicists, condensed matter physicists and high energy physicists are organized to study how the progress in one field can lead to new developments in the others. We trust that these conferences and lively discussions will lead to new analytical methods and new mathematical languages.

The 56^{th} Rencontres de Moriond in 2022 comprised five physics sessions:

- January 23 - 30: "Cosmology"
- January 30 - February 6: "Gravitation"
- March 12 - 19: "Electroweak Interactions and Unified Theories"
- March 19 - 26: "QCD and High Energy Hadronic Interactions"
- March 19 - 26: "Very High Energy Phenomena in the Universe"

We thank the organizers of the 56^{th} Rencontres de Moriond:

- P. Astier, C. Burgess, K. Ganga, J.-M. Le Goff, O. Perdereau and F. Vernizzi for the "Cosmology" session,
- B. Barish, M. A. Bizouard, L. Blanchet, F. Combes, P. Delva, J.-M. Le Goff, E. Rasel, S. Reynaud, F. Ricci, T. Sumner, J.-Y. Vinet and P. Wolf for the "Gravitation" session,
- A. Abada, E. Armengaud, J. Conrad, F. Déliot, P. Fayet, J.-M. Frère, P. Hernandez, L. Iconomidou-Fayard, P. Janot, M. Knecht, J. P. Lees, S. Loucatos, F. Montanet, J. Orloff, A. Pich, S. Pokorski, V. Tisserand, M. Tytgat and D. Wood for the "Electroweak Interactions and Unified Theories" session,
- E. Augé, E. Berger, S. Bethke, A. Capella, A. Czarnecki, D. Denegri, N. Glover, B. Klima, N. Mahmoudi, B. Malaescu, L. McLerran, B. Pietrzyk, L. Schoeffel, Chung-I Tan, J. Trân Thanh Vân and U. Wiedemann for the "QCD and High Energy Hadronic Interactions" session
- F. Cavalier, A. de Angelis, M. de Naurois, O. Martineau, E. Moulin, G. Sigl and V. Van Elewyck for the "Very High Energy Phenomena in the Universe" session

and the conference secretariat and technical staff:

V. de Sá-Varanda and C. Bareille, I. Cossin, G. Dreneau, F. Legrand, S. Vydelingum

The Rencontres were sponsored by the Centre National de la Recherche Scientifique. the Commissariat à l'Energie Atomique (CEA-Irfu), the Programme National GRAM du CNRS, the European Gravitational Observatory and the Fonds de la Recherche Scientifique (FRS-FNRS). We would like to express our thanks for their encouraging support.

It is our sincere hope that a fruitful exchange and an efficient collaboration between the physicists and the astrophysicists will arise from these Rencontres as from previous ones.

E. Augé, J. Dumarchez and J. Trân Thanh Vân

Table of Contents

1. Dark Energy

2. CMB and Gravitational Waves

3. Dark Matter

4. 21 cm

5. CMB and Large Scale Structures

6. Posters


La Ratrak
food & drink
ALY SKI

1.
Dark Energy

Cosmology with Xray galaxy cluster surveys ?

Marguerite Pierre
AIM, CEA, CNRS, Université Paris-Saclay,
Université Paris Diderot, Sorbonne Paris Cité, F-91191 Gif-sur-Yvette, France

This talk reviews the scientific motivations, the potential difficulty and recent advances in cosmology using cluster number-counts in the X-ray band. Our forward modelling approach shows that many of the practical and conceptual shortcomings can now be overcome. We present recent results from the XMM-XXL survey. The next step is to apply artificial intelligence techniques on simulations. This allows us to bypass the unnecessarily complicated scaling relation formalism. The net gain is to significantly reduce the number of free parameters and to provide direct access both to the cosmological parameters and to truly physical ingredients, such as AGN feedback. **In this way, we achieve cluster cosmology without explicit cluster mass calculation.**

1 A few historical landmarks

The Uhuru mission undertook the first survey of the X-ray sky in 1970. After 429 days of observations, 339 sources were discovered. Out of these sources, 45 were associated with galaxy clusters [1,2]; the angular resolution of the Uhuru collector was 30 arcmin. Subsequently, the Einstein observatory, the first imaging X-ray telescope (1978, 1 arcmin and 2 arcsec resolution) enabled the first study of X-ray emitting gas in clusters. Furthermore, the Einstein Medium Sensitivity Survey detected 733 serendipitous sources in the field of pointed targets, including 98 clusters; this allowed for the attempt to track back cluster evolution in terms of physical properties or number density [3,4].

The 1980s have been an exciting period in many respects for cosmology and we may highlight a few cornerstones, that nowadays belong to our obvious working landscape. Our view of the distant universe suddenly became much more structured with the publication of the CfA 'Slice of the Universe', revealing that the universe is 'bubbly' on very large scales [5]. This motivated the development of topological tools beyond the 2-pt correlation function, like the *genus curve* to decide whether the matter distribution is of cellular-, meatball- or sponge-like type [6]. Numerical simulations, in the new CDM paradigm, were ramping up : [7] (using 32768 particles, it collected 2850 citations!) while, in parallel, analytical calculations based on the model equation of non-linear diffusion (Burgers equation) achieved remarkable results [8]. Importantly, it was also realised that, under the hypothesis that only gravitation is at work, one can analytically predict the properties of

the local cluster population and how this population evolves [9]. There is only one physical scale in the problem : the mass-scale which is becoming non-linear at a given redshift. This yields simple scaling relations, a concept that subsequently constituted the skeleton of all cluster cosmological studies. Interestingly, C. Sarazin's book (*X-ray emission from clusters of galaxies*, 1988) which was *the* reference cluster review by the ROSAT launch (1990), did not mention possible cosmological applications of clusters in his concluding remarks and future outlook.
The 1990s truly opened the era of cluster cosmological analyses. It was realised that cluster counts are degenerate with cluster evolution: at least, the knowledge of both dn/dz and of the evolution of the luminosity function is required [10]. An analysis based on 70 ROSAT serendipitous clusters showed that their luminosity function does not evolve[a] out to $z \sim 0.8$ [11]. Amazingly, this study that assumed a flux limited sample along with a cosmological model with $H_0 = 50$ and $q_0 = 1/2$, was corroborated 20 years later by the XMM-XXL cluster survey, in the framework of the WMAP9 cosmology [12]! This is an interesting example of a 'cosmological conspiracy' between cluster evolution and cosmology... An attempt to derive σ_8 and Ω_m using the evolution of the temperature function of a sample of 39 EMSS clusters, yielded constraints that are almost compatible with the Planck2018 CMB result at 1-sigma [13]. A long term project aiming at inventorying and characterising the clusters present in the Rosat All-Sky-Survey was undertaken by the REFLEX and NORAS teams: Constraints from the luminosity function involving some 900 southern clusters ($0 < z < 0.4$) showed a very good agreement with the then Planck cluster constraints [14]. The combination of the northern and southern samples (1653 clusters) revealed a local under-density in the universe, which would have a $\sim 5\%$ effect on the measurement of H_o [15]. In the same direction, a 2021 study handling five scaling relations for a sample of 570 clusters over the entire sky (also including XMM serendipitous clusters) revealed a $> 5\sigma$ anisotropy, hence suggesting a 9% spatial variation of H_o [16].
The first XMM and Chandra observations confirmed that clusters are not simple objects; many physical processes are intricate and questioned the use of clusters as cosmological probes. Over the past 20 years, considerable X-ray observing time has been devoted to deeply study single clusters in order to elucidate the processes at work in the intra-cluster medium. In the following, we focus on the complementary approach, based on blind cluster surveys.

1.1 The XMM-XXL survey

The XMM-XXL survey consists of two 25 deg^2 regions covered at a mean point source sensitivity of $\sim 5 \times 10^{-15}$ $\mathrm{erg\,s^{-1}\,cm^{-2}}$ in the [0.5-2] keV band [17]. With 6.9 Ms total exposure time, XXL is currently the largest XMM programme and detected some 400 clusters out to a redshift of 2. It is also the only XMM 'serendipitous' cluster survey (along with XCLASS, its companion project) that provided results on $\sigma_8 - \Omega_m$ so far. This fact underlines the difficulty of the task. Indeed, given the coverage and depth of the survey, several approximations used in the past needed to be revisited. Consequently the number of degrees of freedom in the analysis significantly increased. In all that follows, we shall restrict the discussion to the cosmological analysis of cluster number counts. Comprehensive reviews of cluster cosmology can be found in e.g. [18,19].

1.2 Where do we stand now ?

During the analysis of the XXL survey data, we unveiled and addressed a few important issues. Some 20 years later, most of them are taken for granted:
- Because clusters are extended objects, the cluster selection cannot be a simple flux limit, unless the limit is set well above the survey sensitivity (but then, at the cost of the sample size). Moreover, the function must ideally depend solely on observable parameters; for XXL it is the count rate and angular size of the sources. Subsequently, the function can be translated into the [M, z] space, for any cluster and cosmological model. The selection function is not only critical

[a] which does not mean that clusters do not evolve

for the cosmological analysis, but also for the determination of the scaling relations [20,21].
- The selection function is tuned such as to favour 'purity' against 'completeness'. Indeed, the population of missed objects can be modelled for any cosmological+cluster physics model, while there is no model to a posteriori discard non-cluster or spurious detections.
- Scatter in the mass-observable relations has a critical effect on cluster counts. While increasing the scatter in the mass-temperature ($M-T$) or luminosity-temperature ($L-T$) relation increases the number of detected objects (similarly to σ_8), increasing the scatter in the masse-core_radius relation ($M-R_c$) generally decreases the number of detected objects [22].
- Consequently, scaling relations, scatters, selection function and cosmology must be fitted together: many free parameters!

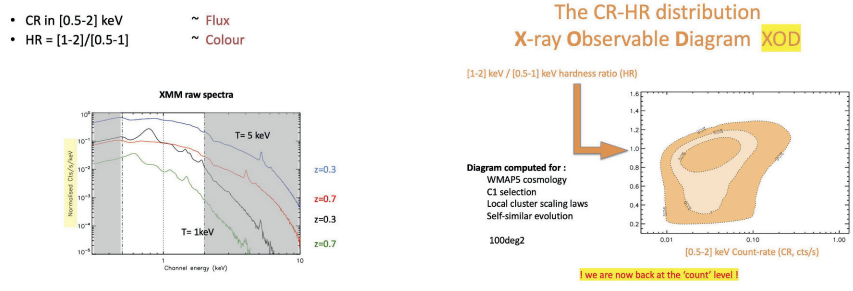

Figure 1 – The left panel shows different cluster spectra (for a heavy-element abundance of 0.3 solar) as seen by XMM. The 3 bands used to compute the count-rate (CR) and hardness ratio (HR) are indicated in white. The Y-axis is in units of XMM counts.
The right panel shows the fiducial distribution of the CR and HR values for the cluster population detected assuming the C1 XXL selection function and for the cosmology+physics set up indicated on the left. We note that the presented plot is integrated in the redshift dimension; for the cosmological analysis, the full 3-D X-ray Observable Diagram (XOD) is used.

2 Forward cosmological modelling

The implementation of the 'traditional' method that maps cluster number counts into a mass distribution as a function of redshift requires heavy machinery. When running a MCMC analysis to iterate toward the most likely set of cosmological parameters, the scaling relations must be recomputed for any considered cosmology - and this implies recomputing as well the R_{500} radius (and any other scaling parameter) in which fluxes and temperatures are integrated. Taking the problem the other way round, we developed a forward modelling approach that considers the simplest possible observed quantities, namely the XMM count-rates in three different bands [?] ASpiX method]clerc12a,pierre17a. Practically, a count-rate (CR) is analogous to a flux. The ratio of two CRs (hardness ratio, HR) is equivalent to a colour and carries information about the cluster temperature and redshift. From this, we construct 'color-magnitude-redshift' diagrams of the detected X-ray cluster populations (XOD, see. Fig.1 & 2). Fisher analyses demonstrated that the information contained in the XOD is at least as constraining for cosmology as the recovered cluster mass distribution as a function of redshift [23]. Because the HR determination requires much less photons than measuring cluster temperatures, the ASpiX method allows the inclusion of all detected clusters down to 80-100 photons; this represents a considerable advantage compared to the 'traditional' approach.

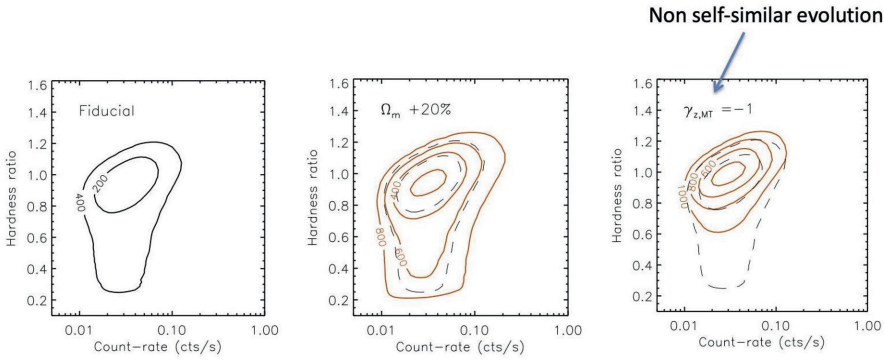

Figure 2 – Principle of the cosmological inference using XOD: effects of changing either the cosmological (middle) or the physics (right) parameters in the fiducial model (left)

2.1 Cosmological results

In Fig. 3 we show recent results from the XXL cosmological analysis: constraints on σ_8 and Ω_m from cluster counts as a function of redshift are compared to the outcome of the XOD analysis from the same population (178 clusters) and with the same degrees of freedom and priors. We obtain a factor of ~ 2 improvement on the cosmological constraints, assuming flat ΛCDM [25]. In the same paper, the impact of relaxing all scaling relation coefficients along with the implementation of priors dynamically adapted to the cosmological model is also discussed. At the time of writing, calculations related to the dark energy equation of state are being finalised (Garrel et al 2022b in prep).

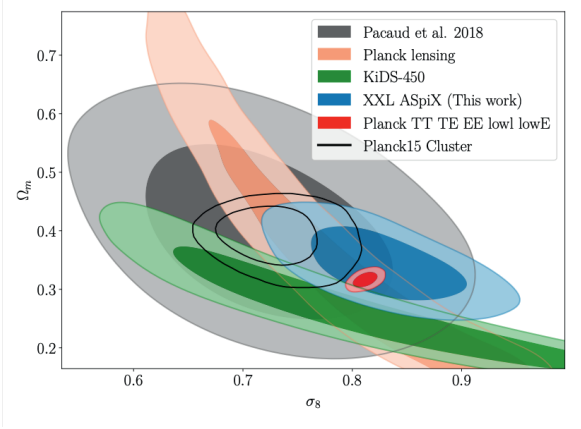

Figure 3 – Comparison of the cosmological constraints from the 178 C1 XXL clusters, derived using either the dn/dz quantity (grey) or the CR-HR-z XOD (blue); both use the same priors. Other surveys are indicated: Planck CMB (red); Planck S-Z clusters (black contours, 439 clusters); Planck lensing (orange); KIDS lensing (green). More details in [25]

2.2 A projection into the Athena era

While the XMM, eRosita and Euclid surveys essentially map the $0 < z < 1$ range, the $1 < z < 2$ cluster universe will be systematically explored by Athena, the up-coming ESA X-ray mission (launch by the mid-2030s, https://sci.esa.int/web/athena). The predicted redshift distribution of clusters to be detected by the Athena Wide Field Imager is at least one order of magnitude beyond the current surveys (Fig. 4): for the first time, we shall be in the position to accurately determine the X-ray cluster density above $z > 1.2$. We anticipate that a number of cosmological questions will remain open or emerge after Euclid-eRosita. Hence, Athena surveys will provide deep insight into both cosmology and cluster evolutionary physics, including the impact of AGN on the ICM, which is expected to be particularly efficient above $z > 1$. A paper investigating these issues will be presented in the up-coming Athena 'Red Book' (Cerardi et al in prep).

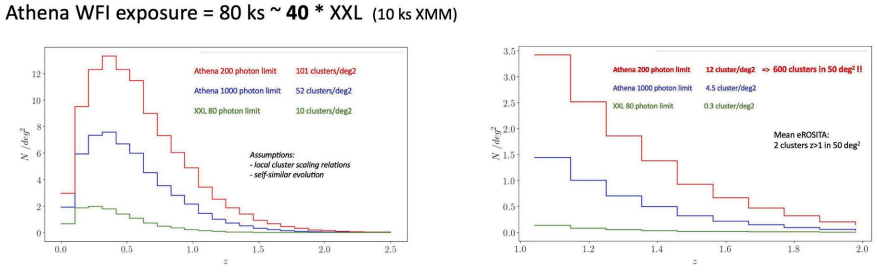

Figure 4 – Predicted cluster number density to be detected by the Athena Wide Field Imager, assuming an exposure time of 80ks. This sensitivity is roughly 40 times deeper than the XMM-XXL survey. Two detection limits are considered (blue and red); for comparison, the XXL survey is shown in green. Athena will allow in-depth cluster studies in the, so far poorly explored, $1 < z < 2$ range. [NB these estimates were performed assuming the current provisional Athena instrumental response - more detailed calculations will be presented in the Athena Red Book.]

3 The next future: combing artificial intelligence, numerical simulations and forward modelling

While the ASpiX method marked a significant improvement in the cosmological analysis of X-ray clusters, the current implementation is still burdened by two main factors: (1) the CR, HR translation to the mass function is implemented via scaling relations (even though cluster masses are not individually computed); (2) the MCMC analysis of the XOD is time-consuming (some 3 weeks with 5×20 CPUs for the analysis presented in Fig.3). We are currently implementing Artificial Intelligence techniques to radically overcome these two hurdles.

3.1 Replacing the MCMC by a likelihood free inference method

In this approach [e.g. 26], a neural network compresses the information contained in the XOD. The network is trained for a given cosmology over a set of simulated XODs (10^5) covering a large range of random scaling relation coefficients. The dimension of the output vector is the number of free cosmological parameters, while the training considers all scaling relation realisations as nuisance parameters. This is rendered possible thanks to the 3-dimensional XOD representation that alleviates the degeneracy between cluster evolution and cosmology. The final cosmological inference corresponding to the observed XOD can subsequently be performed by e.g. an Approximate Bayesian Computation approach (Kosiba et al in prep).

3.2 Overcoming the scaling relation formalism

Each scaling relation ($M-T,\ L-T,\ M-R_c$) involves 4 parameters, i.e. slope, normalisation, evolution, scatter plus possibly scatter evolution as well. This adds up to at least 12 free coefficients in addition to the cosmological parameters. However, numerical simulations suggest that very few physical ingredients are actually needed to reproduce the bulk properties of the X-ray cluster population [27]. It thus appears that the scaling relation formalism complicates the problem by unphysically increasing the number of degrees of freedom and handling complex covariance matrices: many coefficient combinations are clearly degenerate over the mass range considered and for a given level of shot noise in the XOD (determined by the size of the surveyed area). It thus appears much more sensible to draw the XODs needed for step [3.1] directly from hydrodynamic simulations that have been transformed into XMM images. However, the computing time to produce a training sample of lightcones for a wide range of cosmological and AGN feedback models would be prohibitive. We thus implemented a Larangian Deep Learning approach [28] LDL to produce the required simulations. The model uses layers of Lagrangian displacements of particles describing the observables to learn the effective physical laws; we train it on the CAMELS sample [29].

3.3 Summary

The final net outcome of the [3.2]+[3.1] procedure, when applied to an observed XOD, returns the constraints on the cosmological parameters plus one or two physics parameters (Cerardi et al in prep). The methodology totally bypasses any mass determination and derives quantities that have a direct physical interpretation. Clearly, a few more parameters remain more or less hidden in the course of the procedure, in particular in the simulations (like the prescription for the black hole seeds and the resolution of the hydrodynamic solver). Next step will be to examine how these contribute to the final systematic error budget.
An obvious extension of the current work, would be to apply the ASpiX method to Sunyaev-Zel'dovich cluster samples, since the detection also relies on the intra-cluster medium properties. A significant difference, however, resides in the fact that the X-ray spectral information (the energy of the individual X-ray photons) is a key ingredient of the XOD, while the S-Z spectral bands can only be used to assess the significance of the cluster detections; consequently, in addition to the S-Z decrement, other direct observable quantities should be investigated like, for instance, apparent cluster sizes [22], but this measure is usually very noisy.

Acknowledgments

We thank S. Madden, N. Cerardi, N. Clerc, C. Garrel, M. Kosiba, J. B. Melin, F. Pacaud and P. Valageas for useful comments on the manuscript.

References

1. R. Giacconi, S. Murray, H. Gursky, E. Kellogg, E. Schreier, T. Matilsky, D. Koch, and H. Tananbaum. The Third UHURU Catalog of X-Ray Sources. *ApJS*, 27:37, February 1974.
2. W. Forman, C. Jones, L. Cominsky, P. Julien, S. Murray, G. Peters, H. Tananbaum, and R. Giacconi. The fourth Uhuru catalog of X-ray sources. *ApJS*, 38:357–412, December 1978.
3. I. M. Gioia, T. Maccacaro, R. E. Schild, A. Wolter, J. T. Stocke, S. L. Morris, and J. P. Henry. The Einstein Observatory Extended Medium-Sensitivity Survey. I. X-Ray Data and Analysis. *ApJS*, 72:567, March 1990.

4. I. M. Gioia, J. P. Henry, T. Maccacaro, S. L. Morris, J. T. Stocke, and A. Wolter. The Extended Medium-Sensitivity Survey Distant Cluster Sample: X-Ray Cosmological Evolution. *ApJ*, 356:L35, June 1990.
5. V. de Lapparent, M. J. Geller, and J. P. Huchra. A Slice of the Universe. *ApJ*, 302:L1, March 1986.
6. III Gott, J. Richard. I. Measuring the Topology of Large-Scale Structure in the Universe. *PASP*, 100:1307, November 1988.
7. M. Davis, G. Efstathiou, C. S. Frenk, and S. D. M. White. The evolution of large-scale structure in a universe dominated by cold dark matter. *ApJ*, 292:371–394, May 1985.
8. S. N. Gurbatov, A. I. Saichev, and S. F. Shandarin. The large-scale structure of the universe in the frame of the model equation of non-linear diffusion. *MNRAS*, 236:385–402, January 1989.
9. N. Kaiser. Evolution and clustering of rich clusters. *MNRAS*, 222:323–345, September 1986.
10. J. Oukbir and A. Blanchard. X-ray clusters: towards a new determination of the density parameter of the universe. *A&A*, 317:1–13, January 1997.
11. Piero Rosati, Roberto Della Ceca, Colin Norman, and Riccardo Giacconi. The ROSAT Deep Cluster Survey: The X-Ray Luminosity Function out to z = 0.8. *ApJ*, 492(1):L21–L24, January 1998.
12. F. Pacaud, N. Clerc, P. A. Giles, C. Adami, T. Sadibekova, M. Pierre, B. J. Maughan, M. Lieu, J. P. Le Fèvre, S. Alis, B. Altieri, F. Ardila, I. Baldry, C. Benoist, M. Birkinshaw, L. Chiappetti, J. Démoclès, D. Eckert, A. E. Evrard, L. Faccioli, F. Gastaldello, L. Guennou, C. Horellou, A. Iovino, E. Koulouridis, V. Le Brun, C. Lidman, J. Liske, S. Maurogordato, F. Menanteau, M. Owers, B. Poggianti, D. Pomarède, E. Pompei, T. J. Ponman, D. Rapetti, T. H. Reiprich, G. P. Smith, R. Tuffs, P. Valageas, I. Valtchanov, J. P. Willis, and F. Ziparo. The XXL Survey. II. The bright cluster sample: catalogue and luminosity function. *A&A*, 592:A2, June 2016.
13. J. Patrick Henry. Measuring Cosmological Parameters from the Evolution of Cluster X-Ray Temperatures. *ApJ*, 534(2):565–580, May 2000.
14. Hans Böhringer, Gayoung Chon, and Chris A. Collins. The extended ROSAT-ESO Flux Limited X-ray Galaxy Cluster Survey (REFLEX II). IV. X-ray luminosity function and first constraints on cosmological parameters. *A&A*, 570:A31, October 2014.
15. Hans Böhringer, Gayoung Chon, and Chris A. Collins. Observational evidence for a local underdensity in the Universe and its effect on the measurement of the Hubble constant. *A&A*, 633:A19, January 2020.
16. K. Migkas, F. Pacaud, G. Schellenberger, J. Erler, N. T. Nguyen-Dang, T. H. Reiprich, M. E. Ramos-Ceja, and L. Lovisari. Cosmological implications of the anisotropy of ten galaxy cluster scaling relations. *A&A*, 649:A151, May 2021.
17. M. Pierre, F. Pacaud, C. Adami, S. Alis, B. Altieri, N. Baran, C. Benoist, M. Birkinshaw, A. Bongiorno, M. N. Bremer, M. Brusa, A. Butler, P. Ciliegi, L. Chiappetti, N. Clerc, P. S. Corasaniti, J. Coupon, C. De Breuck, J. Democles, S. Desai, J. Delhaize, J. Devriendt, Y. Dubois, D. Eckert, A. Elyiv, S. Ettori, A. Evrard, L. Faccioli, A. Farahi, C. Ferrari, F. Finet, S. Fotopoulou, N. Fourmanoit, P. Gandhi, F. Gastaldello, R. Gastaud, I. Georgantopoulos, P. Giles, L. Guennou, V. Guglielmo, C. Horellou, K. Husband, M. Huynh, A. Iovino, M. Kilbinger, E. Koulouridis, S. Lavoie, A. M. C. Le Brun, J. P. Le Fevre, C. Lidman, M. Lieu, C. A. Lin, A. Mantz, B. J. Maughan, S. Maurogordato, I. G. McCarthy, S. McGee, J. B. Melin, O. Melnyk, F. Menanteau, M. Novak, S. Paltani, M. Plionis, B. M. Poggianti, D. Pomarede, E. Pompei, T. J. Ponman, M. E. Ramos-Ceja, P. Ranalli, D. Rapetti, S. Raychaudury, T. H. Reiprich, H. Rottgering, E. Rozo, E. Rykoff, T. Sadibekova, J. Santos, J. L. Sauvageot, C. Schimd, M. Sereno, G. P. Smith, V. Smolčić, S. Snowden, D. Spergel, S. Stanford, J. Surdej, P. Valageas, A. Valotti, I. Valtchanov,

C. Vignali, J. Willis, and F. Ziparo. The XXL Survey. I. Scientific motivations - XMM-Newton observing plan - Follow-up observations and simulation programme. *A&A*, 592:A1, June 2016.
18. S. W. Allen, A. E. Evrard, and A. B. Mantz. Cosmological Parameters from Observations of Galaxy Clusters. *ARA&A*, 49:409–470, September 2011.
19. Nicolas Clerc and Alexis Finoguenov. X-ray cluster cosmology. *arXiv e-prints*, page arXiv:2203.11906, March 2022.
20. F. Pacaud, M. Pierre, C. Adami, B. Altieri, S. Andreon, L. Chiappetti, A. Detal, P.-A. Duc, G. Galaz, A. Gueguen, J.-P. Le Fèvre, G. Hertling, C. Libbrecht, J.-B. Melin, T. J. Ponman, H. Quintana, A. Refregier, P.-G. Sprimont, J. Surdej, I. Valtchanov, J. P. Willis, D. Alloin, M. Birkinshaw, M. N. Bremer, O. Garcet, C. Jean, L. R. Jones, O. Le Fèvre, D. Maccagni, A. Mazure, D. Proust, H. J. A. Röttgering, and G. Trinchieri. The XMM-LSS survey: the Class 1 cluster sample over the initial 5 deg^2 and its cosmological modelling. *MNRAS*, 382:1289–1308, December 2007.
21. P. A. Giles, B. J. Maughan, F. Pacaud, M. Lieu, N. Clerc, M. Pierre, C. Adami, L. Chiappetti, J. Démoclés, S. Ettori, J. P. Le Févre, T. Ponman, T. Sadibekova, G. P. Smith, J. P. Willis, and F. Ziparo. The XXL Survey. III. Luminosity-temperature relation of the bright cluster sample. *A&A*, 592:A3, June 2016.
22. A. Valotti, M. Pierre, A. Farahi, A. Evrard, L. Faccioli, J. L. Sauvageot, N. Clerc, and F. Pacaud. The cosmological analysis of X-ray cluster surveys. IV. Testing ASpiX with template-based cosmological simulations. *A&A*, 614:A72, June 2018.
23. N. Clerc, M. Pierre, F. Pacaud, and T. Sadibekova. The cosmological analysis of X-ray cluster surveys - I. A new method for interpreting number counts. *MNRAS*, 423:3545–3560, July 2012.
24. M. Pierre, A. Valotti, L. Faccioli, N. Clerc, R. Gastaud, E. Koulouridis, and F. Pacaud. The cosmological analysis of X-ray cluster surveys. III. 4D X-ray observable diagrams. *A&A*, 607:A123, November 2017.
25. Christian Garrel, Marguerite Pierre, Patrick Valageas, Dominique Eckert, Federico Marulli, Alfonso Veropalumbo, Florian Pacaud, Nicolas Clerc, Mauro Sereno, Keiichi Umetsu, Lauro Moscardini, Sunayana Bhargava, Christophe Adami, Lucio Chiappetti, Fabio Gastaldello, Elias Koulouridis, Jean-Paul Le Fevre, and Manolis Plionis. The XXL survey: XLVI. Forward cosmological analysis of the C1 cluster sample. *arXiv e-prints*, page arXiv:2109.13171, September 2021.
26. Tom Charnock, Guilhem Lavaux, and Benjamin D. Wandelt. Automatic physical inference with information maximizing neural networks. *Phys. Rev. D*, 97(8):083004, April 2018.
27. A. M. C. Le Brun, I. G. McCarthy, J. Schaye, and T. J. Ponman. Towards a realistic population of simulated galaxy groups and clusters. *MNRAS*, 441:1270–1290, June 2014.
28. Biwei Dai and Uroš Seljak. Learning effective physical laws for generating cosmological hydrodynamics with Lagrangian deep learning. *Proceedings of the National Academy of Science*, 118(16):2020324118, April 2021.
29. Francisco Villaescusa-Navarro, Shy Genel, Daniel Angles-Alcazar, Leander Thiele, Romeel Dave, Desika Narayanan, Andrina Nicola, Yin Li, Pablo Villanueva-Domingo, Benjamin Wandelt, David N. Spergel, Rachel S. Somerville, Jose Manuel Zorrilla Matilla, Faizan G. Mohammad, Sultan Hassan, Helen Shao, Digvijay Wadekar, Michael Eickenberg, Kaze W. K. Wong, Gabriella Contardo, Yongseok Jo, Emily Moser, Erwin T. Lau, Luis Fernando Machado Poletti Valle, Lucia A. Perez, Daisuke Nagai, Nicholas Battaglia, and Mark Vogelsberger. The CAMELS Multifield Dataset: Learning the Universe's Fundamental Parameters with Artificial Intelligence. *arXiv e-prints*, page arXiv:2109.10915, September 2021.

Weak lensing mass estimation of galaxy clusters with magnification

C. Murray
Université Grenoble Alpes, CNRS, LPSC-IN2P3, 38000 Grenoble, France

Weak lensing is a powerful tool to estimate the matter distribution around massive galaxy clusters. In this work we present a new method to perform stacked mass estimation for galaxy clusters using weak lensing magnification. In general such effects are measured by counting the number of galaxies in circular annuli from the lens centre. In this work we present a new method which improves on the standard approach by using the full galaxy magnitude distribution, rather than a single faint-end magnitude cut. This allows us to differentiate between the two opposing effects of magnification, whereby faint galaxies are introduced into an annulus as they are magnified above the faint-end magnitude limit and removed from an annulus as they are deflected away from the lens centre. Magnification of a galaxy image will shift the galaxy magnitude distribution and the deflection effects will change the normalisation of the distribution, therefore the effects are separable and we can increase the signal-to-noise ratio of such measurements. We investigate this new method using HSC weak lensing data and the Redmapper SDSS galaxy cluster catalogue.

1 Introduction

Galaxy clusters have been essential in construction of the standard model of cosmology, providing some of the first evidence of dark matter [2] through the motions of galaxies within galaxy clusters and their spatial distribution provided evidence for the primordial origin of density fluctuations [1]. Since their formation is sensitively dependent on the properties of both dark energy and dark matter, future measurements of the masses of galaxy clusters and their abundance will hopefully deliver deep insights on the nature of dark energy and dark matter.

In order to make precision measurements of cosmological parameters with clusters it is important to have robust estimates for cluster masses. Gravitational lensing is a particular useful tool for mass estimation as such estimates should be largely insensitive to the dynamical state of the observed clusters.

In general, weak lensing shear is used to measure cluster masses. In this work we develop a method based on weak lensing magnification. Gravitational lensing describes the effects arising from the deflection of the passage of light due to the gravitational field of a massive object which are illustrated in Figure 1. In the strong regime this leads to dramatic Einstein rings and multiple images of individual objects, in the weak regime the effects are more subtle. There are

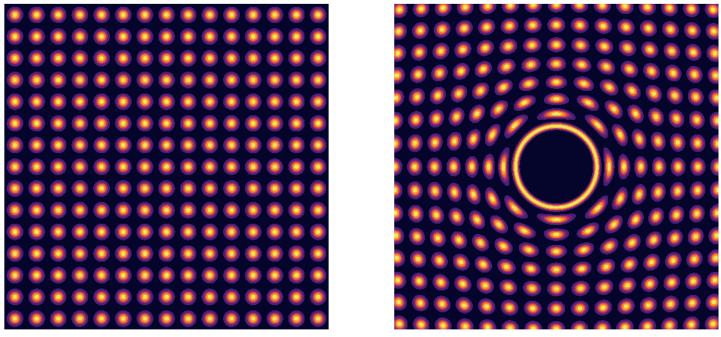

Figure 1 – Illustration of the effects of gravitational lensing of a massive object on a field of galaxies. The left image shows a field of uniformly spaced circular galaxies, the right shows the same field in the presence of a gravitational lens.

essentially two effects in the weak regime, the shearing of galaxy images and the magnification of solid angles on the sky. The second of these effects leads to two different observable properties. Firstly it will increase a galaxies apparent size, whilst conserving surface brightness. Which leads to an increase in the observed magnitude of a galaxy. Secondly on larger scales the magnification of solid angles on the sky will appear to decrease the on-sky number density of galaxies.

Shear has in general the largest signal-to-noise ratio for a given sample of galaxies because relatively the dispersion of the intrinsic distribution of galaxy shapes is smaller than that of magnitudes or the clustering of galaxies. However an important difference is that for the magnification signals we need only the background galaxy magnitudes, positions and redshifts. Opposed to the shear analysis which requires the more difficult measurement of galaxy shapes. We can therefore go deeper in magnitude and keep more galaxies in our sample and increase our signal-to-noise ratio.

In this work we use both the effects of amplification and dilution to estimate the mass of a stack of galaxy clusters. By combining both effects and going deeper in magnitude we can approach a similar signal-to-noise ratio as shear only analyses. This is particularly interesting as we will have completely different systematics from shear.

2 Method

Weak lensing effects are measured from how they distort or deform the unlensed distribution of galaxies in the universe. We call the unlensed number density distribution of galaxies n_o. All galaxies in the Universe will be to some extent lensed however the difference between this distribution and the unlensed distribution will be small. This means we can measure the approximately unlensed distribution by taking the average distribution across the survey volume $n_o(m+\delta m, z)$ where m is the galaxy magnitude and z the galaxy redshift. We can then calculate the lensed distribution by deforming it as follows,

$$n_{\rm obs} = n_o(m + \delta m, z)/\mu \tag{1}$$

where μ is the magnification $\mu \approx 1/[(1-\kappa)^2 - \gamma^2]$ which can be calculated from the weak lensing covergence κ and shear γ, and Δm is the shift in the magnitude of a galaxy from lensing

$\Delta m \approx -5\log_{10}(\mu)/2$. Note we could add both galaxy ellipticities and sizes to these distributions which would provide us with a concise manner to constrain both shear and magnification at the same time but we leave this to future work. A potential advantage of this relative to traditional shear analysis would be from the non-Gaussian distribution of tangential shears but we do not expect that this would gain much information.

We see clearly in Equation 1 how the effects of amplification and dilution are separated. The amplification changes the observed galaxy magnitude therefore shifts the distribution and the dilution changes the observed solid angle on the sky and therefore the normalisation of the distribution. There are closely related approaches (Ménard and Bartelmann 2002 [3]) although we should be able to deal with the larger magnification signal around clusters as our approach is non-perturbative.

In order to constrain cluster masses we then use a Gaussian likelihood with radial, redshift and magnitude bins. In more detail we have,

$$ln\mathcal{L} = -\frac{1}{2}\sum_{ijk}\left(n_{obs}(\theta_i, m_j, z_k) - n(\theta, m, z|M_{lens})\right)^2/\sigma^2_{ijk} \tag{2}$$

where i are radial bins, j are magnitude bins and k are redshift bins. Finally in order to estimate the mass we stack the signal around many clusters and run an MCMC to obtain the cluster mass according to our model for the lensing signal as detailed in Equation 1.

3 Results

In this work we used the redmapper SDSS galaxy cluster catalog and used the Hyper Suprime Cam data as our background galaxies.

To verify our method we use mock catalogs. We generate random positions within the HSC survey and inject a fake cluster signal. We choose random positions within the survey area and then move the galaxies to the lensed galaxy positions using the lens equation: $\theta_{\rm obs} = \theta_o + \alpha(M_{\rm lens})$ where θ_o is the unlensed angle between the source and lens centre, α is the deflection angle and $\theta_{\rm obs}$ is the observed source-lens separation . Subsequently we magnify the galaxy magnitudes: $\Delta m \approx -5\log_{10}(\mu(\mathrm{M_{lens}}))/2$.. This provides a non-trivial test of our model as we inject the artificial lensing signal at the galaxy catalog level.

By applying our method to the stacked signal around 250 mock clusters we can verify it's effectiveness. We find consistent results with the input cluster mass and additional find a factor of 2 improvement on our method versus the mass estimation from a single magnitude cut.

We then apply this method to redMaPPer clusters in the HSC field. We select 200 clusters with redshift $z > 0.3$ and a richness $\lambda > 40$. With the magnification-only analysis we obtain $\log_{10}\mathrm{M_{mag}/M_\odot} = 14.37 \pm 0.04$.

We additionally estimate the cluster mass using weak lensing shear using the stacked excess surface mass density profile, see Murray et al. 2022 [4] for more details on the shear measurements. With the shear-only analysis we obtain $\log_{10}\mathrm{M_{shear}/M_\odot} = 14.28 \pm 0.03$.

The stacked magnification profiles, for both the amplification and dilution, and the stacked shear profile are presented in Figure 2. As with the estimated masses we see excellent agreement between both methods.

4 Conclusions

We have introduced a new magnification method which we can use the full magnitude distribution and accurate model the magnification signal induced in the background field of galaxies by a cluster even in the regime of large magnification. This method was then validated using mock catalogs created by injecting artificial cluster signals into the HSC galaxy catalog. We showed that our method in general gives a factor of 2 improvement compared to a single magnitude

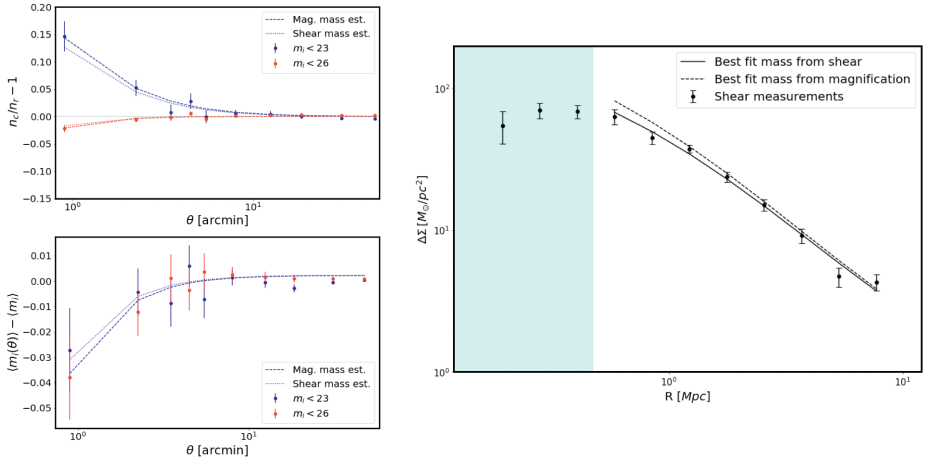

Figure 2 – The lensing signals around a stack of 200 redMaPPer galaxy clusters with redshift $z > 0.3$ and richness $\lambda > 40$ using HSC galaxies. Top left: the change in galaxy number counts n_c compared to the random field value n_r for two different magnitude cuts. Bottom left: average galaxy magnitude compared to the random field value. Right: the excess surface mass density profile estimated from HSC galaxy shapes.

cut. Finally estimating the masses of a stack of SDSS redmapper clusters with both the new magnification method presented here and a stacked shear based method we obtain consistent and competitive constraints on the mass with magnification.

References

1. N. Kaiser in *On the spatial correlations of Abell clusters*, (Astrophys. J. Lett. Ed. 284, L9 1984).
2. F. Zwicky in *Die rotverschiebung von extragalaktischen nebeln*, (Helvetica physica acta, 1933).
3. B. Ménard and M. Bartelmann in *Cosmological information from quasar-galaxy correlations induced by weak lensing*, (Astronomy & Astrophysics, 2002).
4. C. Murray, J.G. Bartlett, E. Artis and J.B. Melin in *Measuring weak lensing masses on individual clusters*, (Submitted to MNRAS, 2022).
5. C. Murray, C. Combet, C. Payerne, M. Ricci in *Measuring the masses and dust contents of galaxy clusters using stacked distributions of background galaxies*, (In prep.).

Towards *EUCLID* cluster likelihood definition: covariance calibration

A. Fumagalli
on behalf of the Euclid Consortium
Dipartimento di Fisica, Sezione di Astronomia, Università di Trieste, Via Tiepolo 11, I-34143 Trieste, Italy

We present the validation of models of covariance for number counts and clustering of galaxy clusters, which account for the effects of sample variance, lightcone geometry, and high-order terms, at the level of accuracy expected for the future *Euclid* survey. The resulting models allow us to study the response of the likelihood analysis to variations of the covariance and to provide forecasts to predict the impact of such uncertainties in the recovered cosmological parameters for the upcoming *Euclid* cluster survey.

1 Introduction

Galaxy clusters are the most massive gravitationally bound systems in the Universe, formed by the gravitational collapse of initial matter perturbations. Galaxy clusters properties are sensitive to the geometry and the evolution of the large-scale structure of the Universe; in particular, their abundance and spatial distribution are powerful tools to constrain the RMS matter fluctuations on $8\,h^{-1}\,\mathrm{Mpc}$ scales (σ_8) and the matter content of the Universe (Ω_m).

A crucial aspect for such observables to be turned into stringent cosmological constraints concerns the accurate calibration of covariance matrices. Among the different methods for estimating such covariances, analytical models can provide noise-free, cosmology-dependent matrices without requiring large computational resources. The limitation of this method lies in the difficulty of describing analytically all the contributions that compose the covariance (e.g. non-linearities, non-Gaussianities, ...). As a consequence, such models have to be validated against simulations, to determine which contributions are or are not negligible at the desired level of statistics and to calibrate eventual nuisance parameters.

We present the validation of covariance models for number counts and clustering of galaxy clusters. The resulting models allow us to study the response of the likelihood analysis to variations of the covariance, at the level of accuracy expected for the future *Euclid* survey.

2 Covariance models

Number counts covariance: Number counts describe the abundance of clusters as a function of mass and redshift. They are affected by two sources of statistical errors: the uncertainty due to the discrete nature of the data, i.e. shot-noise, and the uncertainty due to the finite size of the survey, named sample variance. The two contributions are described by the [1] model:

$$C^{NC}_{\alpha\beta ij} = \langle n \rangle_{\alpha i}\, \delta^D_{\alpha\beta}\, \delta^D_{ij} + \langle nb \rangle_{\alpha i}\, \langle nb \rangle_{\beta j}\, S_{\alpha\beta}\,, \tag{1}$$

where n and b are, respectively, the mass function and the halo bias, and $\langle - \rangle_{\alpha i}$ indicates the integration over the α-th redshift bin and the i-th mass bin. $S_{\alpha\beta}$ is the covariance of the linear

density field between two redshift bins

$$S_{\alpha\beta} = \int \frac{\mathrm{d}^3 k}{(2\pi)^3} \sqrt{P(k, z_\alpha)\, P(k, z_\beta)}\, W_\alpha(\mathbf{k})\, W_\beta(\mathbf{k})\,, \tag{2}$$

where $W_\alpha(\mathbf{k})$ is the lightcone window function [2].

Clustering covariance: We quantify the clustering of clusters with the real-space 2-point correlation function, describing the excess of correlation as a function of radial separation and redshift. The 2-point correlation covariance can be described by the Fourier transform of the power spectrum covariance [3]:

$$\begin{aligned} C^{CL}_{\alpha ij} = & \frac{2}{V_\alpha} \int \frac{\mathrm{d}k\, k^2}{2\pi^2} \left[\left\langle b^2_{\mathrm{eff}}\, P_{\mathrm{m}}(k) \right\rangle_\alpha + \left\langle \frac{1}{\bar{n}} \right\rangle_\alpha \right]^2 W^{\mathrm{s}}_i(k)\, W^{\mathrm{s}}_j(k) \\ & + \frac{2}{V_\alpha\, V_i} \int \frac{\mathrm{d}k\, k^2}{2\pi^2} \left\langle b^2_{\mathrm{eff}}\, P_{\mathrm{m}}(k) \right\rangle_\alpha \left\langle \frac{1}{\bar{n}} \right\rangle^2_\alpha W^{\mathrm{s}}_j(k)\, \delta^D_{ij}\,, \end{aligned} \tag{3}$$

where b_{eff} and $\bar{n}$ are the effective bias and the average number density of halos above a mass threshold, $P_{\mathrm{m}}(k)$ is the linear matter power spectrum, $W^{\mathrm{s}}_i(k)$ is the spherical shell window function of the i-th radial bin and $\langle - \rangle_\alpha$ indicates the average over the redshift bin. V_α and V_i are the redshift and radial shell volumes. We assume independent redshift bins. The model includes the Gaussian covariance and a shot-noise component of the non-Gaussian matrix, while neglects the high-order non-Gaussian terms, due to the complexity of their modelling.

3 Methods and results

We validate the covariance models through the comparison with numerical matrices computed from a set of 1000 *Euclid*-like lightcones. Such catalogs are produced via approximate methods by the Pinocchio algorithm [4]. Masses have been rescaled to match, on average, the [5] halo mass function. We use the [6] model for the bias, which reproduces our simulations within the 10 %.

Once the covariance models have been validated, we test their effect on cosmological posteriors by constraining Ω_{m} and σ_8 through Bayesian inference, by maximizing a likelihood function computed with different covariance configurations. The aim is to figure out which terms are or are not significant at this level of statistics, so as to find the simplest possible models that accurately reproduces the results of the numerical matrix. We estimate the accuracy of the results by computing the figure of merit [7] (FoM) from the sampled posteriors.

Number counts results: We present here the results described in [8]. We consider redshift bins of width $\Delta z = 0.1$ in range $z = 0$–2 and 5 log-spaced mass bins in range $M = 10^{14} - 10^{16}\,\mathrm{M}_\odot$. The left panel of Fig. 1 shows that the sample variance effect is higher than shot-noise, in the low-mass/low-redshift regime, and that there is a small anti-correlation between redshift bins. From the comparison of the analytical and numerical matrices, it can be seen that the analytical model reproduces the numerical matrix within 10 %. Such results are confirmed by the likelihood analysis, as shown by the right panel of Fig. 1: the posteriors obtained with the numerical and analytical matrix present the same FoM, ensuring that the model is accurate enough. Moreover, neglecting the sample variance effect or the cross-correlation between redshift bins, the analysis produces a wrong estimation of the posteriors amplitude with respect to the full covariance case. Finally, evaluating the matrix at a wrong fixed cosmology can over/underestimate the error on the posteriors; since for real data the true cosmology is unknown, this result suggests that a cosmology-dependent covariance is required.

Clustering results: We present here the preliminary results concerning the validation of clustering covariance. We compute the 2-point correlation function in redshift bins of width

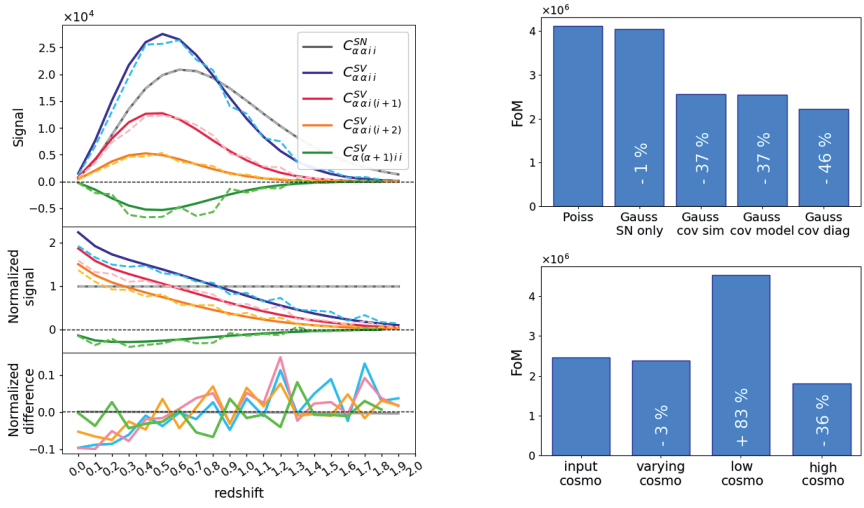

Figure 1 – *Left panel*: components of the numerical (dashed lines) and analytical (solid lines) number counts covariance as a function of redshift, in the lowest mass bin. *Right panel:* figure of merit for different covariance and likelihood configurations.

$\Delta z = 0.4$ in range $z = 0$–2, and 25 radial bins in range $r = 20$–$130\ h^{-1}\,\mathrm{Mpc}$, for halos more massive than $M_{\rm th} = 10^{14}\,\mathrm{M}_\odot$. We measure the observed correlation with the [9] estimator.

The left panel of Fig. 2 shows that our model correctly describes the numerical matrix only at low redshift, while it underestimates all the terms at high redshift. To solve this inaccuracy, we add three nuisance parameters to the model, to correct for shot-noise, that is not purely Poissonian, for the bias prediction, and for the lack of non-Gaussian terms. We fit such parameters from simulations, following the method described in [10]. The model with these additional parameters (dashed lines) correctly describes the numerical matrix at all redshifts, with deviations below the 10 % level at almost all the scales. Moving to the likelihood analysis, the left panel of Fig. 2 confirms that, while the simple model underestimates the error on parameters, the model with fitted parameters reaches an agreement within 5 % with the numerical matrix case. We also find that the secondary term in the covariance is non-negligible at small scales ($r \lesssim 40\,h^{-1}$Mpc), especially at high redshift. The study of the impact of a cosmology-dependent matrix is still under investigation.

Finally, cluster clustering is expected to be less constraining than number counts (as confirmed by the lower figure of merit shown in the right panel of Fig. 2), but it can be useful if combined with number counts, due to the different degeneracy directions of parameters. We perform the joint analysis, by considering the two observables as independent, as suggested by the zero cross-covariance computed from simulations. The resulting posteriors present an increment of the figure of merit of about the 25 %, indicating an improvement in the constraining power of clusters.

4 Conclusions

We validated covariance models for cluster number counts and cluster clustering. On the number counts side, we found that the [1] model correctly reproduces the numerical matrix. We also demonstrated that a Gaussian likelihood with full cosmology-dependent covariance is required to correctly estimate the error on cosmological parameters, at this level of accuracy. For the cluster clustering, we proposed a simple model that takes into account the Gaussian and partly

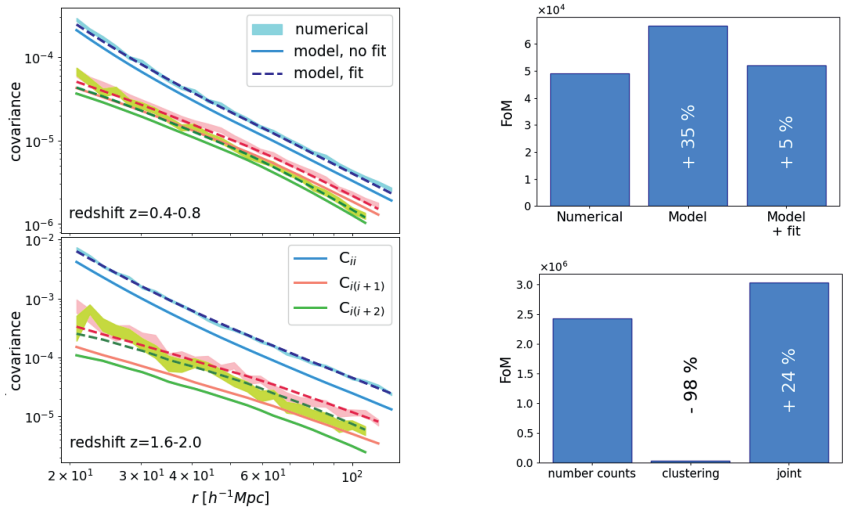

Figure 2 – *Left panel*: components of the numerical (shaded areas) and analytical (solid lines) clustering covariance as a function of the radial separation, in two redshift bins. The dashed lines represent the model corrected for the nuisance parameters. *Right panel:* FoM for different covariance configurations and for the joint constraints.

of the non-Gaussian terms of the total covariance, neglecting the higher-order terms. We showed that, with the addition of some nuisance parameters fitted from simulations, such model correctly describes the numerical matrix. Finally, we combine the two observables, finding that cluster clustering is a powerful tool to break the parameter degeneracies and improve the constraining power of number counts. The next step of this analysis will concern the validation of the covariance models in observable space, in order to provide more complete and realistic forecasts.

Acknowledgments

The *Euclid* Consortium acknowledges the European Space Agency and a number of agencies and institutes that have supported the development of *Euclid*, in particular the Academy of Finland, the Agenzia Spaziale Italiana, the Belgian Science Policy, the Canadian *Euclid* Consortium, the French Centre National d'Etudes Spatiales, the Deutsches Zentrum für Luft- und Raumfahrt, the Danish Space Research Institute, the Fundação para a Ciência e a Tecnologia, the Ministerio de Ciencia e Innovación, the National Aeronautics and Space Administration, the National Astronomical Observatory of Japan, the Netherlandse Onderzoekschool Voor Astronomie, the Norwegian Space Agency, the Romanian Space Agency, the State Secretariat for Education, Research and Innovation (SERI) at the Swiss Space Office (SSO), and the United Kingdom Space Agency. A complete and detailed list is available on the *Euclid* web site (`http://www.euclid-ec.org`).

References

1. W. Hu and A. V. Kravtsov, Astrophys. J. **584** (2003), 702-715
2. M. Costanzi *et al.* [DES], Mon. Not. Roy. Astron. Soc. **488** (2019) no.4, 4779-4800
3. A. Meiksin and M. J. White, Mon. Not. Roy. Astron. Soc. **308** (1999), 1179
4. P. Monaco, T. Theuns and G. Taffoni, Mon. Not. Roy. Astron. Soc. **331** (2002), 587
5. G. Despali *et al.* Mon. Not. Roy. Astron. Soc. **456** (2016) no.3, 2486-2504
6. J. L. Tinker *et al.* Astrophys. J. **724** (2010), 878-886
7. A. Albrecht *et al.* [arXiv:astro-ph/0609591 [astro-ph]]
8. A. Fumagalli *et al.* [Euclid], Astron. Astrophys. **652** (2021), A21
9. S. D. Landy and A. S. Szalay, Astrophys. J. **412** (1993), 64
10. A. Fumagalli *et al.* in preparation

Halo (assembly) bias from forward modeling

T. Lazeyras on behalf of A. Barreira and F. Schmidt
Dipartimento di Fisica G. Occhialini, Università degli studi di Milano Bicocca, Piazza della Scienza 3, 20126 Milano, Italy

To extract cosmological information from the observed distribution of galaxies, one needs to link it to that of the underlying dark matter field. This is done through the bias formalism. In addition, some progress was made recently to use forward modeling approaches combined with the likelihood from effective field theory of large-scale structure to analyze galaxy clustering. Here, we present new results for halo assembly bias (i.e. the dependence of halo bias on properties beyond the total mass) in the linear and second order bias parameters obtained from this approach. We show the first measurements of assembly bias in the tidal bias parameter, as well as the impact of assembly bias on known relations between the second order parameters and the linear one.

1 Bias formalism and assembly bias

The statistics of discrete tracers of the large-scale structure (LSS), δ_h, can be written in terms of bias parameters $b_{\mathcal{O}}$ multiplying operators $\mathcal{O}$ constructed out of the large-scale matter density contrast field δ_m and tidal field K_{ij} (see Desjacques *et al.*[?] for a recent review)

$$\delta_h(\mathbf{x}, z) = \sum_{\mathcal{O}} b_{\mathcal{O}}(z)\mathcal{O}(\mathbf{x}, z)\,. \tag{1}$$

This bias expansion formalism can be applied to any LSS tracer. Here we focus on dark matter halos identified in N-body simulations. Physically, the halo bias parameters describe the response of the halo number density to the long-wavelength perturbations $\mathcal{O}$. Studying them can thus give us important insights on structure formation. A robust knowledge of halo bias also helps guide the design of priors on bias parameters that enter theoretical models in LSS analyses, or even reduce the number of free parameters if useful relations between them can be found (e.g. Lazeyras *et al.*[?]), thereby leading to improved constraints on cosmological parameters.

The bias parameters were commonly thought to depend only on the redshift and mass of the considered halo population. It was however shown two decades ago that halo bias depends on properties beyond those, such as formation time or concentration. This phenomenon was naturally named halo *assembly bias*. The characterization of assembly bias is an important step to understand galaxy clustering since, at fixed halo mass, it is plausible that certain galaxy populations may preferentially inhabit halo populations with specific values for properties like concentration or formation time.

In our recent work Lazeyras *et al.*[?], we measured assembly bias with respect to halo *concentration*, *spin*, and sphericity using the *forward modeling* approach. Our companion paper Barreira *et al.*[?] brings further insight on this topic by focusing on *galaxy* bias in hydrodynamical simulations.

2 Bias parameters from forward modeling

The goal is to derive the *likelihood* function $\mathcal{P}(\delta_h|\{\theta\},\{b_\mathcal{O}\},\delta_{m,\rm in})$ that describes the probability to observe a halo density field, given a realization $\delta_{m,\rm in}$ of the initial matter field, a set of cosmological parameters $\{\theta\}$ and a set of bias parameters $\{b_\mathcal{O}\}$. This requires four ingredients: (i) A prior (usually gaussian) for the initial matter density field $\delta_{m,\rm in}$; (ii) the evolution of $\delta_{m,\rm in}$ under the action of gravity in a given cosmology, $\delta_{m,\rm fwd}[\{\theta\},\delta_{m,\rm in}]$. We do so using third-order Lagrangian perturbation theory (3LPT); (iii) A forward-evolved halo distribution using the final matter distribution and a *deterministic* bias expansion, $\delta_{h,\rm det}[\delta_{m,\rm fwd},\{b_\mathcal{O}\}]$; (iv) A likelihood $\mathcal{P}(\delta_h|\delta_{h,\rm det}) \equiv \mathcal{P}(\delta_h|\{\theta\},\{b_\mathcal{O}\},\delta_{m,\rm in})$ to sample in the combined parameter space $\{\delta_{m,\rm in},\{\theta\},\{b_\mathcal{O}\}\}$. Here we consider dark matter halos from numerical gravity-only N-body simulations, which allows us to keep the cosmological parameters $\{\theta\}$ and initial conditions field $\delta_{m,\rm in}$ fixed to those used to run the simulations. This drastically reduces the parameter space that would otherwise have to be explored.

We work with the following likelihood function in Fourier space

$$-2\ln\mathcal{P}(\delta_h|\delta_{h,\rm det}) = \int_{|\mathbf{k}|<\Lambda}\frac{\mathrm{d}^3\mathbf{k}}{(2\pi)^3}\left[\frac{|\delta_h(\mathbf{k})-\delta_{h,\rm det}(\mathbf{k})|^2}{P_\epsilon(k)}+\ln(2\pi P_\epsilon(k))\right], \tag{2}$$

which has been derived using EFT in Schmidt *et al.*[?]. The variance $P_\epsilon(k)$ in this equation takes into account the stochasticity of halo formation. For our purpose here, it is sufficient to consider only the leading order, constant contribution $P_\epsilon(k)\approx P_\epsilon^{\{0\}}$, where $P_\epsilon^{\{0\}}$ is a parameter that is also sampled (Elsner *et al.*[?]). Importantly, the integral in Eq. (**??**) is performed only up to a maximum *cutoff* wavenumber Λ. This cutoff is needed to ensure that only perturbative modes enter in the inference analyses, and it must be applied also to the initial conditions field before evolving it to the final time in order to regularize loop integrals involving non-perturbative modes (Schmidt *et al.*[?]).

The forward-evolved halo density field is constructed out of the forward-evolved matter density contrast using the deterministic bias expansion Eq. (**??**). We consider the following set of 8 operators

$$\mathcal{O}\in\{\delta_m,\delta_m^2,K^2,\delta_m^3,\delta_m K^2,K^3,O_{\rm td},\nabla^2\delta_m\}, \tag{3}$$

where $K_{ij}=(\partial_i\partial_j/\nabla^2-\delta_{ij}/3)\delta_m$, $K^2=K_{ij}K^{ij}$, $K^3=K_{ij}K^{jk}K^i_k$ and $O_{\rm td}=(8/21)K_{ij}(\partial_i\partial_j/\nabla^2)(\delta_m^2-(3/2)K^2)$. The first 7 represent all terms that exist up to third order in δ_m and K_{ij}. Additionally, we also include the first higher-derivative operators $\nabla^2\delta_m$.

To fit for a bias parameter $b_\mathcal{O}$, we first marginalize over all others in Eq. (**??**) (which can be done analytically Elsner *et al.*[?]), and then find the maximum of the likelihood in the $\{b_\mathcal{O},P_\epsilon^{\{0\}}\}$-space (using the MINUIT routine from the ROOT package). Notice that, even though the code also returns estimates of the remaining, higher-order bias parameters, we will show results only for the bias parameters b_1, b_2 and b_{K^2}. Indeed we expect results for third order bias parameters to be less accurate.

3 Results

We first present results for b_1 as a function of halo mass, as well as b_2 and b_{K^2} as a function of b_1 in Fig. **??**. The forward modeling results are the blue symbols. The results for b_1 and b_2 are in very good agreement with those from separate universe simulations (green markers, Lazeyras *et al.*[?]). We do note, however, a small trend for higher b_2 values compared to the separate universe ones at $b_1\gtrsim 2.5$. This is likely due to the fact that we neglect higher-than-third order bias parameters (which can become important for these more biased objects). Finally, the results for b_{K^2} as a function of b_1 are also in broad agreement with previous results from Lazeyras *et al.*[?] (purple markers). We further compare our results for b_{K^2} with the Lagrangian local-in-matter-density (LLIMD) prediction given by $b_{K^2}^{\rm LLIMD}=-\frac{2}{7}(b_1-1)$, and observe the same slightly

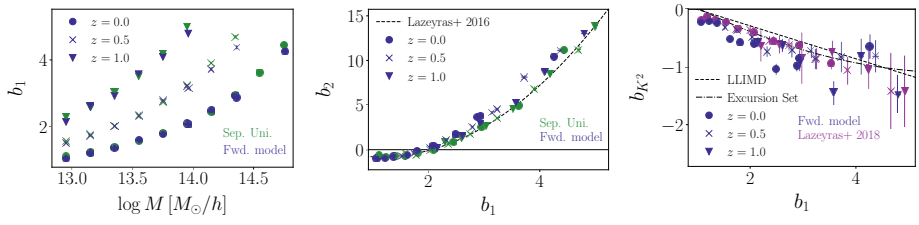

Figure 1 – Results for $b_1(M)$, $b_2(b_1)$, and $b_{K^2}(b_1)$ as a function of redshift from forward modeling, and comparison with previous results.

negative offset in our results as already pointed out in e.g. Lazeyras *et al.*[?]. The good agreement we found here validates the forward modeling approach to measure bias parameters.

We then turn to results for assembly bias in the three bias parameters considered in this work as a function of concentration c, spin λ, and sphericity s, and for different halo mass bins at $z = 0$ (Fig. **??**). The dashed lines show the value of the bias parameter in the corresponding total mass bin. On each panel, from left to right, the halos become more concentrated, have higher spin, and become more spherical. Focusing first on b_1 and b_2 for which previous results exist, we get a very clean detection of assembly bias, and our results are in qualitative agreement with previous ones. We also obtain a clear detection of assembly bias in b_{K^2}, and the effect seems more important at higher masses for all three properties. However, the trends observed in this parameter are *consistently opposite to those of* b_1: for example halos with a higher concentration

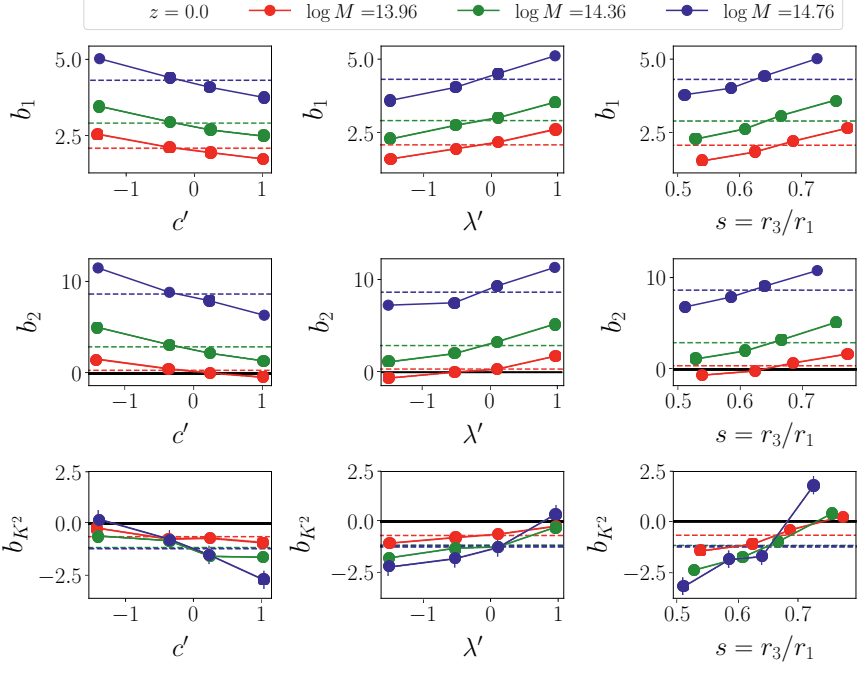

Figure 2 – Assembly bias as a function of concentration, spin and sphericity in b_1, b_2, and b_{K^2} at $z = 0$.

are *more negatively biased* in b_{K^2}, which is the opposite to the trend in b_1 in the sense that the halos are *less positively biased*.

Finally, we investigate the impact of assembly bias on the $b_2(b_1)$ and $b_{K^2}(b_1)$ relations in Figs. **??** – **??**. Each panel of these figures presents these relations when binning in mass (color coding) as well as when binning in a secondary property (four markers of the same color), at different z. Perhaps the most noteworthy feature is the fact that, although assembly bias impacts the values of b_2 strongly, it only impacts the $b_2(b_1)$ relation weakly, which is in strong contrast with the results for $b_{K^2}(b_1)$, where we see that, at fixed mass and for all redshift, the relation varies almost *orthogonally* to the LLIMD prediction as the secondary halo properties vary. This surprisingly strong difference can be understood by the fact that assembly bias impacts b_1 and b_2 in the same way but impacts b_{K^2} in a consistently opposite way.

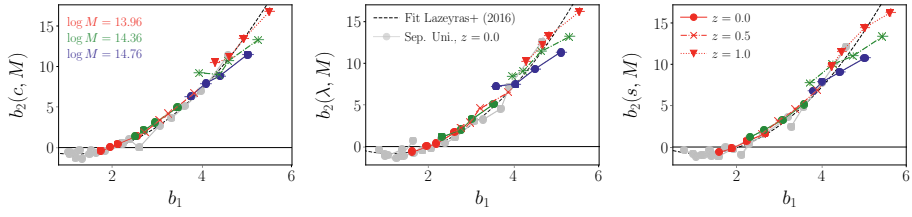

Figure 3 – Impact of assembly bias on the relation $b_2(b_1)$.

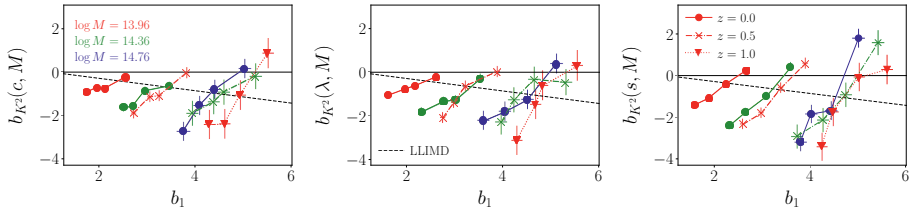

Figure 4 – Impact of assembly bias on the relation $b_{K^2}(b_1)$.

Acknowledgments

AB acknowledges support from the Excellence Cluster ORIGINS funded by the DFG (German Research Foundation) under Germany's Excellence Strategy - EXC-2094-390783311. FS acknowledges support from the Starting Grant (ERC-2015-STG 678652) "GrInflaGal" of the European Research Council.

References

1. V. Desjacques *et al*, Phys. Rep. **733**, 1 (2018).
2. T. Lazeyras *et al*, JCAP **02**, 018 (2016).
3. T. Lazeyras *et al*, JCAP **10**, 063 (2021).
4. A. Barreira *et al*, JCAP **08**, 029 (2021).
5. F. Schmidt *et al*, JCAP **01**, 042 (2019).
6. F. Elsner *et al*, JCAP **01**, 029 (2020).
7. F. Schmidt *et al*, JCAP **11**, 008 (2020).
8. T.Lazeyras & F. Schmidt, JCAP **09**, 008 (2018).

Massive Neutrinos, Dark Sector, and Hydrodynamics: The *Sejong* Suite

Graziano Rossi
Department of Physics and Astronomy, Sejong University, Seoul, 143-747, Korea

Improving the understanding of the processes governing small-scale nonlinear clustering is a necessary task for interpreting upcoming high-quality cosmological data, as it will allow one to break degeneracies and obtain tight neutrino mass and warm dark matter constraints from large-scale structure probes. The *Sejong Suite*, an extensive collection of state-of-the-art high-resolution cosmological hydrodynamical simulations, has been intended with this primary goal in mind. Spanning a large number of cosmological and astrophysical parameters (especially suitable for the *dark sector*), and organized into three main categories (*Grid Suite*, *Supporting Suite*, and *Systematics Suite*), the release may be useful for a broader variety of cosmological and astrophysical purposes – while primarily developed for Lyman-α (Lyα) forest studies. In particular, the overall architecture of the *Grid Suite* has been designed to achieve an equivalent resolution up to $3 \times 3328^3 = 110$ billion particles in a $(100h^{-1}\mathrm{Mpc})$ box, corresponding to a $30h^{-1}$kpc mean grid resolution, which ensures a convergence on Lyα flux statistics closer to the desired $\sim 1.0\%$ level that data from surveys such as the Dark Energy Spectroscopic Instrument (DESI) will provide. Here, we briefly highlight the main characteristics, improvements, and novelties of the *Sejong Suite*, as well as ongoing and future applications.

1 Scientific Rationale: Dark Sector Cosmology at Small Scales

The ability to reach small nonlinear scales will be crucial in the next few years, as it will allow one to break degeneracies and contribute to tightening neutrino mass, dark radiation, and warm dark matter (WDM) constraints derived from large-scale structure (LSS) tracers. Small nonlinear scales are in fact the key for competitive massive neutrinos and *dark sector* (i.e., dark radiation, WDM) bounds, and in this regards the remarkable potential of the Lyman-α (Lyα) forest is indeed the ability to reach such regime, still inaccessible to other probes. The Lyα forest is highly sensitive to the summed neutrino mass (M_ν) and additional dark radiation components such as sterile neutrinos (i.e., when the effective number of neutrino species $N_{\rm eff}$ departs from its canonical value), via significant attenuation effects on the matter and flux power spectra at small scales. [1,2,3,4] Currently, neutrino mass upper bounds from cosmology are closer to the minimum value allowed by the inverted hierarchy (IH), and the Lyα forest in synergy with cosmic microwave background (CMB) data provides among the strongest reported constraints in the literature on M_ν and $N_{\rm eff}$.[1,3,5,6] State-of-the-art surveys such as the Extended Baryon Oscillation Spectroscopic Survey (eBOSS) are already highly competitive in this regards [6], but ongoing

	Number of Runs	Box Sizes [h^{-1} Mpc]	Resolutions [$N_p^{1/3}$]	Softening [h^{-1} kpc]	Science Target
Grid Suite	228	25 ÷ 100	208 ÷ 832	1.00 ÷ 4.01	Parameter Constraints
Supporting Suite	114	25 ÷ 100	208 ÷ 832	1.00 ÷ 6.51	Dark Sector at Small-Scales
Systematic Suite	35	10 ÷ 100	128 ÷ 1024	0.65 ÷ 6.51	Impact of Systematics

Figure 1 – *Sejong* Suite: selected technical details.

experiments like the Dark Energy Spectroscopic Instrument (DESI) [7] are expected to greatly improve on current *dark sector* bounds/limits in terms of statistical precision and accuracy. Note also that conclusions regarding the minimal six-parameter ΛCDM concordance cosmological scenario dominated by cold dark matter (CDM) and a dark energy (DE) component in the form of a cosmological constant Λ are mainly drawn from LSS observations – while small scales remain poorly explored to date. In addition, while the role of the Lyα forest is critical in sharpening *dark sector* constraints, current results are heavily based on numerics and on details related to statistical analysis techniques. Advancement in the modeling and a careful understanding of small neutrino mass effects on key Lyα observables (particularly on the flux power spectrum) and of possible systematics (i.e., impact of complex small-scale baryonic physics) is needed to improve the robustness of all Lyα-based studies. Moreover, progress in the characterization of systematics, progress in the small-scale modeling, and a deeper theoretical understanding of neutrino mass and dark radiation effects on cosmological observables are necessary for a reliable use of LSS data to robustly constrain M_ν and $N_{\rm eff}$. All these considerations represent the primary motivations and scientific rationale of our work.

2 The *Sejong* Hydrodynamical Simulation Suite: Highlights

The *Sejong Suite* [8] is organized into three main categories, addressing different scientific and technical aspects. The *Grid Suite* ($76 \times 3 = 228$ simulations) is targeted primarily for cosmological parameter constraints especially regarding massive and sterile neutrinos and the *dark sector*, exploiting the small-scale flux power spectrum; it represents our leading effort and major deliverable. The *Supporting Suite* (114 simulations) is aimed at studying the detailed physical effects of exotic particles and dark radiation models, as well as their impact on the high-z cosmic web. The *Systematics Suite* (35 realizations) is meant to address several systematic effects, ranging from numerical challenges until parameter degeneracies. Table 1 summarizes some key characteristics of the three groups. The simulations have been produced at the Korea Institute of Science and Technology Information (KISTI) supercomputing infrastructure with a modified version of `Gadget-3` used for evolving Euler hydrodynamical equations and primordial chemistry, and interfaced with `CAMB` and a modified version of second-order Lagrangian perturbation theory (2LPT). Primarily, the suite is targeted to explore the high-z cosmic web as seen in the Lyα forest ($5.0 \leq z \leq 2.0$), although of much broader usage. The release contains a number of improvements: namely, efficiency of the pipeline, resolution, grid and stepsize accuracy, cosmology, and reionization history. Full details are provided in Rossi (2020). The most interesting novelty is the presence of mixed models, such as combined effects of WDM, neutrinos, and dark radiation. An example is provided in Figure 2: the left panel show a small $4 \times 4h^{-1}$Mpc patch at $z = 2$ in a massive neutrino cosmology with $M_\nu = 0.3$eV, as well as in a mixed scenario where also a massless sterile neutrino is added (i.e., $N_{\rm eff} = 4.046$). Differences in the cosmic web morphology, albeit small, are clearly visible. The right panel shows the relative halo abundances

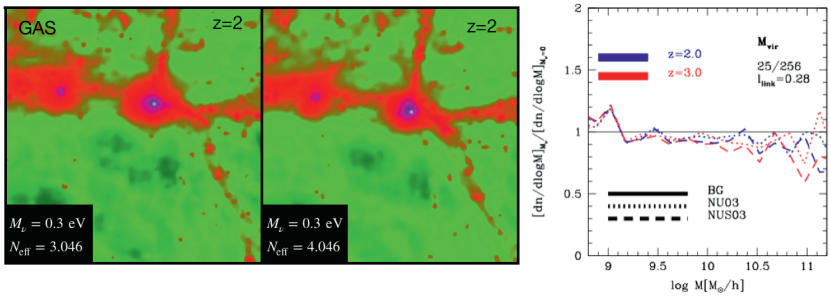

Figure 2 – [Left] $4 \times 4h^{-1}$Mpc patch at $z = 2$ in a massive neutrino cosmology with $M_\nu = 0.3$eV, and in a mixed scenario where also a massless sterile neutrino is added (i.e., $N_{\rm eff} = 4.046$). [Right] Relative halo abundances at $z = 2, 3$ in the corresponding models, normalized by the baseline massless neutrino cosmology.

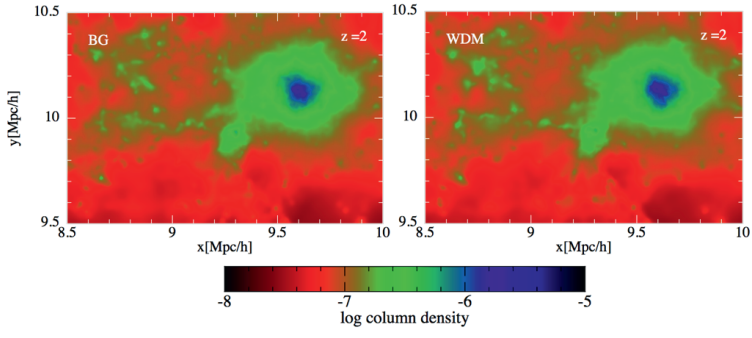

Figure 3 – Small projected patch at $z = 2$ from $25h^{-1}$Mpc simulations with 256^3 particles/type. A complex structure is displayed, as seen in the gas column density of the reference cosmology (left panel), and in a WDM cosmology when $m_{\rm WDM} = 2.00$ keV (right panel). Although differences are hardly perceptible, the impact of a $m_{\rm WDM} = 2.00$ keV relic on the high-z cosmic web is significant.

at $z = 2, 3$ in the corresponding models, normalized by the baseline massless neutrino cosmology. Halos are extracted with the `Rockstar` algorithm, assuming a linking length $l_{\rm link} = 0.28$. In essence, the presence of massive neutrinos and dark radiation delays structure formation: this primarily affects the higher end of the mass function, which is modified depending on redshift and neutrino mass and/or $N_{\rm eff}$ – because of free-streaming effects at small scales. As in our previous releases, we adopt a particle-based implementation of massive neutrinos. Regarding dark radiation, we consider models with four neutrinos, where three are massive and active while the fourth one is massless, sterile, and thermalized with the active ones – so that $N_{\rm eff} = 4.046$. As far as WDM, we focus on two implementations, following different methodologies. In both cases, we only consider early decoupled thermal relics, and assume that all DM is warm when massive neutrinos are not present (i.e., pure WDM models); suitable candidates are keV right-handed neutrinos or sterile neutrinos. As an example, Figure 3 shows a small projected patch from simulations having a box size of $25h^{-1}$Mpc and 256^3 particles/type, describing the gas column density at $z = 2.0$. The left panel displays a complex structure as seen in the BG reference model, while the right panel highlights the same structure as seen in a WDM cosmology when $m_{\rm WDM} = 2.00$ keV. Once again, differences are tiny and therefore hard to be detected visually, although the impact of a $m_{\rm WDM} = 2.00$ keV relic on the high-z LSS is significant.

3 Contributions, Applications, Outlook

Reaching a very high sensitivity on small scales and resolving baryonic physics are essential aspects for improving M_ν, $N_{\rm eff}$, and dark sector bounds, as well as for breaking degeneracies – as demanded by upcoming high-quality data. The addition of accurate small-scale observations, soon available, will in fact allow one to break degeneracies, and contribute to tighten neutrino mass and dark sector constraints from LSS probes. Motivated by these goals, we have carried out an extensive set of high-resolution cosmological hydrodynamical simulations (over 300 runs) termed the *Sejong Suite*, primarily developed for modeling the Lyα forest in the redshift interval $5.0 \leq z \leq 2.0$ – but of much broader usage. In particular, the overall design has been targeted to meet the demanding resolution of DESI (i.e., $30h^{-1}$kpc mean grid resolution). The *Sejong Suite* features a number of improvements and novelties at all levels with respect to our previous releases, related to technical, modeling, and innovative aspects. Noticeably, we have expanded the parameter space for the *Grid Suite* and tighten their variation range. We have also addressed a series of nontrivial systematics, and produced more than 288 million Lyα forest skewers mapping an extended parameter space. On the innovative side, the most significant novelty is the inclusion, for the first time, of extended mixed scenarios describing the combined effects of WDM, neutrinos, and dark radiation. These non-canonical models are quite interesting, particularly for constraining $N_{\rm eff}$ and WDM relic masses directly from Lyα forest data. Our work is thus useful for interpreting upcoming high-quality data from eBOSS and DESI (with ongoing data applications), and synergetic to particle physics experiments. In future releases of the *Sejong Suite*, we plan to expand around this framework and provide more refined realizations. In particular, the *Grid Suite* represents probably the ultimate word on splicing, as running larger-volume high-resolution hydrodynamical simulations able to meet the requirements of upcoming surveys is becoming progressively less prohibitive, in terms of computational costs. Therefore, abandoning splicing and interpolation techniques and adopting emulator-based strategies will be feasible, and we aim at extending the *Sejong Suite* in this direction.

Acknowledgments

G.R. is supported by the National Research Foundation of Korea (NRF) through Grant No. 2020R1A2C1005655 funded by the Korean Ministry of Education, Science and Technology (MoEST). The numerical simulations presented in this work were performed using the Korea Institute of Science and Technology Information (KISTI) supercomputing infrastructure (Tachyon 2) under allocations KSC-2017-G2-0008 and KSC-2018-G3-0008, and post-processed with the KISTI KAT System (KISTI/TESLA 'Skylake' and 'Bigmem' architectures) under allocations KSC-2018-T1-0017, KSC-2018-T1-0033, and KSC-2018-T1-0061. We also acknowledge extensive usage of our new computing resources (Xeon Silver 4114 master node and Xeon Gold 6126 computing node architecture) at Sejong University.

Selected References

1. Seljak, U., Makarov, A., McDonald, P., et al. 2005, Phys. Rev. D, 71, 103515
2. Rossi, G. 2015, Publication of Korean Astronomical Society, 30, 321
3. Rossi, G., et al. 2015, Phys. Rev. D, 92, 063505
4. Rossi, G. 2017, ApJS, 233, 12
5. Planck Collaboration 2020, A&A, 641, A6
6. SDSS-IV eBOSS Collaboration 2021, PhRvD, 103, 083533
7. DESI Collaboration 2016, arXiv:1611.00037
8. Rossi, G. 2020, ApJS, 249, 19
9. Abazajian, K. N., Arnold, K., Austermann, J., et al. 2015, Astroparticle Physics, 63, 66
10. LSST Dark Energy Science Collaboration 2012, arXiv:1211.0310

Higher order statistics for cosmology: likelihood development for future surveys like Euclid

Virginia Ajani[1,2], Valeria Pettorino[2], Jean-Luc Starck[2]
[1] *Institute for Particle Physics and Astrophysics, Department of Physics, ETH Zürich, Wolfgang Pauli Strasse 27 ,CH- 8093 Zürich, Switzerland*
[2] *Université Paris-Saclay, Université Paris Cité, CEA, CNRS, Astrophysique, Instrumentation et Modélisation Paris-Saclay, 91191 Gif-sur-Yvette, France*

Next generation cosmological surveys like *Euclid* will measure the matter distribution with unprecedented precision and a crucial, challenge of modern cosmology is to master this unprecedented precision and to optimise the huge amount of information we will receive, with high accuracy. We present a new summary statistics for weak lensing observables, higher than second order, suitable to extract non-Gaussian cosmological information and infer cosmological parameters: the *starlet ℓ_1-norm*. In comparison to the state of the art higher-order statistics as weak lensing peak counts, minimum counts, or combination of the two, the ℓ_1-norm provides a fast multiscale calculation of the full voids and peaks distribution, avoiding the problem of the definition of what is a peak and what is a void and carrying the information encoded in all pixels of the map and not just the one in local maxima and local minima.

1 Introduction

Second-order statistics as the two-point correlation function or its Fourier transform (the power spectrum) do not capture the non-Gaussian information encoded in the non-linear features of weak lensing data [?]. This has motivated the introduction of several higher-order statistics, such as Minkowski functionals, higher-order moments, the bispectrum, peak counts, the scattering transform, wavelet phase harmonic statistics, and machine learning-based methods, to account for non-Gaussian information in cosmological analysis, see references for such statistics in [1] and in [2]. Focusing on peak counts, it has been shown that this statistics is particularly powerful in breaking degeneracy between the standard model and fifth forces in the dark sector [3] as well as in constraining cosmological parameters when employed in a multi-scale setting [4]. In particular, in [1] we have shown that multi-scale peak counts significantly outperform the weak lensing power spectrum, improving the constraints on the sum of neutrino masses $\sum m_\nu \equiv M_\nu$ by 63% when using a starlet filter. In the same study, we have also found that multi-scale peak counts are so constraining that the addition of the power spectrum does not further improve constraints. A very interesting feature that we have found for multi-scale peaks, when they are obtained

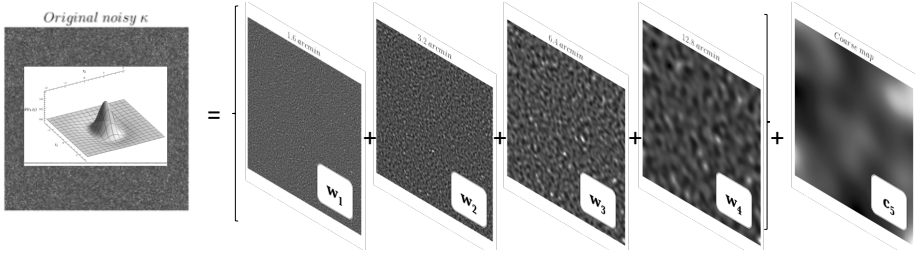

Figure 1 – Illustration of the starlet decomposition with $j_{\max} = 4$ scales. As the j index increases, larger scales are considered and the resolution decreases.

using the starlet transform [5], is the behaviour of the covariance matrix that tends to encode all information in its diagonal elements. Another weak lensing probe of large-scale structure is represented by cosmic voids, namely under-dense regions of the large-scale matter field. Local minima of weak lensing convergence maps, namely pixels with values smaller than their eight neighbouring pixels, have been proposed as tracers of the matter distribution voids to infer cosmological parameters, both in a mono-scale setting [6,7], and in a multi-scale setting [8]. More specifically, [6] found that lensing minima alone are slightly less constraining than the peaks alone and, in agreement with [7] and [8], that the combination of the two statistics produces significantly tighter constraints than the power spectrum. From the results of these studies, it becomes clearer and clearer that the information encoded in lensing minima is complementary to what we can extract through peak counts and that their combination, namely the full distribution, is more powerful than considering the two statistics alone in terms of constraining power. Motivated by this general context and by our previous findings on the potential of multi-scale wavelet based framework for high order statistics, we have then proposed a new summary statistics called starlet ℓ_1-norm that allows to perform very naturally a joint multi-scale peaks and voids analysis, accounting for the information present in all pixels in the weak lensing convergence map.

2 Toward the starlet ℓ_1-norm

2.1 Starlet peaks

Multi-scale peaks counts (peak counts are computed as pixels with values larger than their eight neighbours) can be derived either using a set of Gaussian kernels of different sizes or a wavelet decomposition such as the starlet transform [1]. The starlet transform [5] decomposes a convergence map κ of size $N \times N$ into a set $\mathcal{W} = \{w_1, ..., w_{j_{max}}, c_J\}$ of $J = j_{max} + 1$ bands of same size, where j_{max} is the number of wavelet scales considered, c_J is the coarse scale, namely a very smoothed version of the original image κ, and w_j are the wavelet bands at scale 2^j pixels. An illustration of this decomposition is shown in Fig. 1. Starlet peaks are then derived by considering n bins with bin edges given by the minimum and the maximum values of each band in $\mathcal{W}$. An interesting advantage of such an approach is that each wavelet band covers a different frequencies range which leads to an almost diagonal peaks counts covariance matrix [1]. This is not the case when a standard multiscale Gaussian analysis is applied on the convergence map.

2.2 Starlet extrema

As mentioned in the introduction, cosmic voids analysis is an alternative to peaks to study convergence maps, and the combination of both improves the constraints on cosmological parameters. It is interesting to notice how a starlet decomposition can naturally include a multiscale voids analysis. Instead of extracting maxima (peaks) in each band, we can also extract minima

(pixels with values smaller than their eight neighbours), and a joint peaks-voids multiscale is therefore obtained extracting wavelet coefficients extrema (minima+maxima). The starlet decomposition provides therefore a very natural framework for a joint multiscale peaks and voids analysis.

2.3 Starlet ℓ_1 norm

A particularity of peaks and voids statistics is that only few pixels are considered, while other high order statistics such as bispectrum or Minkowski functionals use all pixels. In a starlet framework, starlet peaks have mainly positive values and starlet voids negative value, due to the property of the wavelet function. So instead of counting the number of peaks or voids in a given bin i defined by two values B_i and B_{i+1}, we could take the sum of all wavelet coefficients with an amplitude between B_i and B_{i+1}. If B_i and B_{i+1} are positive, this corresponds to define the set of coefficients $\mathcal{S}_{j,i}$ at scale j and in bin i such that $\mathcal{S}_{j,i} = \{w_{j,k}/B_i < w_{j,k} < B_{i+1}\}$, where k is the pixel index, and compute the sum $\sum_{u=1}^{\#coef(\mathcal{S}_{j,i})} \mathcal{S}_{j,i}[u]$. This can be generalised to positive and negative bins using:

$$l_1^{j,i} = \sum_{u=1}^{\#coef(\mathcal{S}_{j,i})} \mid \mathcal{S}_{j,i}[u] \mid = ||\mathcal{S}_{j,i}||_1 \tag{1}$$

where $||.||_1$ is the standard ℓ_1 norm (i.e. $||x||_1 = \sum_k |x_k|$), the index u runs from 1 to the number of pixels in a given bin i at scale j (i.e. $\#coef(\mathcal{S}_{j,i})$). The quantity $l_1^{j,i}$ defined in Equation 1 is nothing else than the ℓ_1-norm of binned pixel values of the starlet coefficients of the original image κ map. We call S_{ℓ_1}, the starlet ℓ_1-norm, as the set S_{ℓ_1} of all $l_1^{j,i}$ numbers obtained from the different scales j and bins i. This approach enables to extract the information encoded in the absolute value of all pixels in the map instead of characterising it only by selecting local minima or maxima. An interesting advantage is that it avoids the open issue of how to define a void.

2.4 Results

We provide constraints on the sum of neutrino masses M_ν, on the matter density parameter Ω_m and on the power spectrum amplitude A_s by employing the power spectrum, mono-scale peaks + minima, starlet peak counts, starlet extrema and the starlet ℓ_1-norm computed on noisy convergence maps from the `MassiveNus` [9] simulations as summary statistics. We perform a tomographic analysis using four source redshifts $z_s = \{0.5, 1.0, 1.5, 2.0\}$. We compute the covariance matrix from simulations at a fixed cosmology, assume a Gaussian likelihood and explore parameter space through MCMC. The theoretical prediction for the observables is retrieved through a Gaussian process regression trained on the simulations. In Fig. 2 we show the comparison between the constraints obtained using different summary statistics. As expected, we see that all higher-order statistics are more constraining than the power spectrum. The new result is represented by the starlet ℓ_1-norm: the inclusion of all pixels enables to retrieve tighter constraints than the combination of local minima and maxima. To compare the improvement obtained by employing the different statistics we compute the 1σ marginalised error for each parameter. We find that the starlet ℓ_1-norm outperforms the power spectrum by 72% on M_ν, 60% on Ω_m and 75% on A_s, and the state of the art peaks + voids for a single smoothing scale respectively by 24% on M_ν, 50% on Ω_m and 24% on A_s. Starlet extrema outperform the power spectrum by 72% on M_ν, 20% on Ω_m and 70% on A_s. We also quantify the improvement provided by the ℓ_1-norm with respect of our previous study [1], finding that the ℓ_1-norm starlet outperforms starlet peaks by 28% on M_ν, 33% on Ω_m and 20% on A_s.

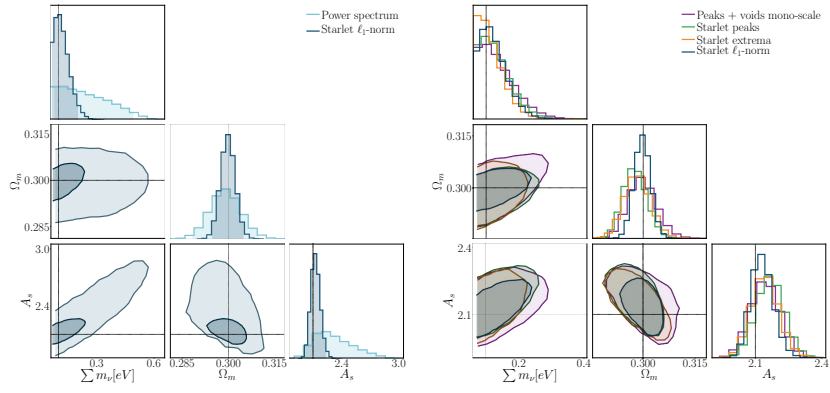

Figure 2 – 95 % confidence contours from: left-the power spectrum (light blue) computed on noisy maps smoothed with a Gaussian filter, compared to constraints from starlet ℓ_1-norm (dark blue)and right: from the combination of peaks and minima (magenta) computed on noisy maps smoothed with a Gaussian filter against constraints from starlet peak counts (green), *starlet extrema* (orange) and ℓ_1-norm (dark blue).

3 Conclusions

We conclude that the new statistics first proposed here presents several advantages in the context of cosmological parameter inference: it provides a fast calculation of the full voids and peaks distribution; it does not rely on a specific definition of peaks and voids, and on some arbitrary threshold; it rather encodes information of the entire pixel distribution, without excluding pixels that are not local minima or local maxima; it leads to tighter constraints, at least within an ideal setting. The starlet decomposition therefore provides a very powerful framework for a joint multiscale peaks and voids analysis. These results show that the multi-scale higher order statistics approach we developed represents a very promising tool to reach high levels of precision in constraining cosmological parameters. However, to serve as a robust probe for precision cosmology, the statistical power alone is not sufficient and it is very important to guarantee robustness with respect to systematic errors.

Acknowledgements

VA acknowledges support by the CNES and IdEx of Université de Paris (ANR-18-IDEX-0001).

References

1. V. Ajani et al. *Phys. Rev. D*, 102:103531, Nov 2020.
2. V. Ajani et al. *A&A*, 645:L11, 2021.
3. A. Peel et al. *A&A*, 619:A38, 2018.
4. J. Liu et al. *Phys. Rev. D*, 91(6):063507, 2015.
5. J-L. Starck et al. *IEEE transactions on image processing*, 16:297–309, 03 2007.
6. W. R. Coulton et al. *MNRAS*, 495(3):2531–2542, 04 2020.
7. Martinet, N. et al. *A&A*, 646:A62, 2021.
8. Dominik Zürcher et al. 2021(01):028–028, 2021.
9. J. Liu et al. *Journal of Cosmology and Astroparticle Physics*, 2018(3):049, March 2018.

Lyman-alpha forest tomography and cross-correlation with cosmic voids

Corentin Ravoux
IRFU, CEA, Université Paris-Saclay, F-91191 Gif-sur-Yvette, France

The Lyman-alpha (Lyα) forest is a unique probe of large-scale matter density fluctuations at high redshift $z > 2$. It is possible to obtain 3D maps of the matter distribution from Lyα data, using tomographic reconstruction methods. Here, we present the largest tomographic map of matter fluctuations at $z > 2$, over the Gpc^3 volume covered by Lyα forest from SDSS-IV quasar spectra in the Stripe 82 field [1]. We present a catalog of high-redshift voids constructed from this map. The measurement of the cross-correlation between these voids and the Lyα forest provides the first observation of the matter velocity flow around voids, through the RSD effect, at such high redshift. The data is in good agreement with simulations and is well adjusted with a linear, Kaiser velocity model [2]

1 Lyman-α tomography

The Lyα forest is a tracer of neutral hydrogen in the cosmic web. It is most easily observed in quasar spectra. When observed from ground-based telescopes at a redshift $z > 2$, quasar spectra show a broad peak of Lyα emission at $\lambda_{\rm rest} = 1215$Å. Bluewards of this peak, a forest of lines corresponds to the absorption of light by the intergalactic medium (IGM) located between the quasar and the observer. These absorption features constitute the Lyα forest and on large scale they trace the neutral hydrogen in the IGM. The measurement of the Lyα forest is complicated when using noisy spectra. As a first step, the product of the continuous emission of the quasar C_q by the average fraction of transmitted flux $\overline{F}$ is measured. From a quasar flux $f(\lambda)$, it is then possible to define the Lyα absorption contrast [3]:

$$\delta_F(\lambda) = \frac{f(\lambda)}{C_q(\lambda_{\rm rf})\overline{F}(\lambda)} - 1 \tag{1}$$

Standard Lyα BAO analysis, e.g.[3], use δ_F to calculate correlations. In this study, we interpolate between different quasar lines-of-sight to create a 3D map of Lyα absorption. This is called Lyα tomography [4]. It was achieved for the first time from observations by the CLAMATO collaboration [5] on a portion of the COSMOS field. This measurement was on a small, dense field of quasars and Lyman-break galaxies. The ultimate goal in that case, by improving the map resolution down to a ~ 1 Mpc.h^{-1} scale, is to trace the filaments of the cosmic web. This is expected to be achievable with future telescopes of the ELT class.

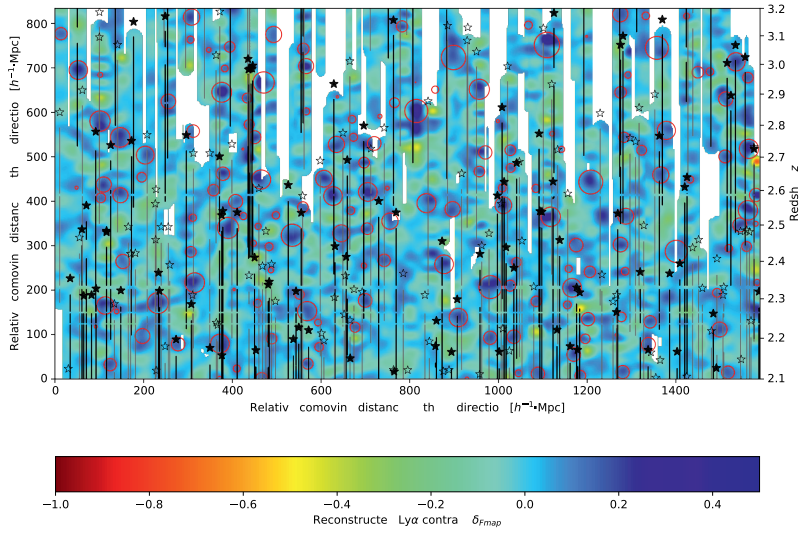

Figure 1 – Slice of the tomographic map computed from the observed eBOSS Lyα forest in the Stripe 82. The slice is at constant declination $\delta_{J2000} = 0°$, and covers right ascension $1 \leq \alpha \leq 23°$, roughly a quarter of the Stripe 82 field. The reconstruction length is 13 Mpc.h^{-1}. Circles are the intersection between the represented slice and identified voids. Filled (empty) stars represent quasars whose distance along the y axis is less than 5 (10) Mpc.h^{-1} from the slice. Lines-of-sight used for the tomographic reconstruction are pictured as full (dotted) lines if they are 5 (10) Mpc.h^{-1} from the slice.

Our study focused on building a tomographic map on a much larger volume, at the price of degraded resolution. We used the Lyα forest region from quasar spectra available in the 16^{th} Data Release of the SDSS-IV eBOSS survey. In particular, we focused on the densest and most homogeneous part of this survey: a narrow band called Stripe 82, of 220 deg^2 area, located in the equatorial plane. We used the spectra from 8200 quasars, corresponding to a surface density of 37 quasars per deg^2. To build a tomographic map, we applied a Wiener filter as implemented by CLAMATO [5]. This algorithm performs an interpolation with a Gaussian kernel taking into account the Lyα forest noise in individual pixels. We included a series of useful tools for large-volume tomography in a python package `lelantos` [6]. Fig. 1 represents a slice of the tomographic map computed from eBOSS data. The main parameter of the tomographic algorithm is the correlation length of the Gaussian kernel. We chose it to be 13 Mpc.h^{-1}, which corresponds to the average separation between lines-of-sight. This tomographic reconstruction constitutes the first large-volume, high-redshift 3D map of matter density fluctuations.

In parallel, we used synthetic data called mocks to test the tomographic reconstruction algorithms. These log-normal mocks are computed using the fluctuating Gunn-Peterson approximation [7]. They also provide the underlying matter density field associated with the Lyα absorption contrast: we could therefore use them to quantify by how much the Lyα tomographic map traces the matter density. We find that the correlation between these two fields is 34%.

The tomographic map obtained from the eBOSS data can be used for several applications. First, a stack of the tomographic map around quasars reveals a clear signal centered on the quasar position: this is a recast view of the cross-correlation between quasars and the Lyα forest as studied in [3]. Then, we identified eight proto-cluster candidates by selecting overdensities in the map, and requiring they are crossed by a large number of lines-of-sight. Finally, the application

we focused most is the search for voids. Indeed, since our tomographic map traces matter fluctuations on large scales $\geq$ 13Mpc.h^{-1}, it is well adapted to search for voids, the largest structures in the cosmic web. With a spherical void finder, that we have developed in the `lelantos` [6] package, we created the largest catalog of large voids at high redshift. To build this catalog, we selected only voids crossed by several lines-of-sight, and whose radius is larger than 7 Mpc.h^{-1}.

2 Lyα-void cross-correlation

We used the void catalog presented in our paper [1] to extend galaxy-void correlation studies [8] to high redshift $z > 2$. To do so, we measured the cross-correlation between the void centers and the Lyα forest pixels used for the tomographic mapping. Our estimator is similar to the one used for the cross-correlation with quasars [3]:

$$\xi(A \equiv (r, \mu)) = \frac{\sum\limits_{(i,j)\in A} w_i \delta_{F,i}}{\sum\limits_{(i,j)\in A} w_i}, \tag{2}$$

Here j corresponds to void index and i Lyα forest pixel index. The separation between two pairs is characterized by a length r and the angle cosine μ. The weights w_i of the associated $\delta_{F,i}$ pixels depend on noise and redshift (no weights are associated to voids).

This study aims to use the angular shape of ξ to observe the effect of redshift space distortions (RSD) around voids at redshift $z > 2$. The function ξ as computed from Stripe 82 data is illustrated in Fig. 2 (left0, and a multipole decomposition onto the Legendre polynomial basis, $\xi_\ell(r)$ for $\ell = 0, 2, 4$, is shown on Fig. 2 (right). To interpret the measurement, we have also applied this method on a set of mocks similar to the one described above, with the same geometry as Stripe 82. First, we used a series of mocks to evaluate the impact of some instrumental and astrophysical systematics on our measurement (eg. quasar continuum fitting, metals in the IGM). The main conclusion is that for this data set, the impact of the considered systematics is small with respect to statistical fluctuations.

Then, we computed the multipoles of ξ for a set of 10 mocks, as well as for an additional set of companion mocks, labelled "noRSD", for which the effect of velocity flow is not taken into account in the computation of the Lyα absorption. They are shown in Fig 2 (right). The data clearly demonstrates the existence of the velocity flow, with a statistical significance of $10\,\sigma$.

To interpret this result, we used a simple void model. It is based on the mean velocity profile around voids in the linear regime:

$$\mathbf{v} = -\frac{1}{3}\frac{fH}{1+z}\overline{\delta}(r)\mathbf{r} \tag{3}$$

This relation links the average velocity $\mathbf{v}$ to the radial position $\mathbf{r}$ around void centers, involving the logarithmic growth rate of linear perturbations f and the average isotropic matter density contrast $\overline{\delta}$ inside the sphere of radius r. Within this linear model, the monopole and the quadrupole of the Lyα-void cross-correlation are connected by a simple relation involving the void RSD parameter β. This relation is very similar to the case of the galaxy-void correlation [9]:

$$\xi_2(r) = \frac{2\beta}{3+\beta}\left[(\xi_0(r) - \overline{\xi_0(r)})\right] \tag{4}$$

As can be seen in Fig 2 (right), the cross-correlation exhibits a non-zero quadrupole even in the absence of RSD. This feature comes from the particular geometry of the Lyα forest survey, which affects the reconstructed void positions. The average flux contrast of the tomographic map built with the Wiener filter is smaller at locations further away from lines-of-sight. This reduces the efficiency of the void finder, and at the same time, displaces the reconstructed positions

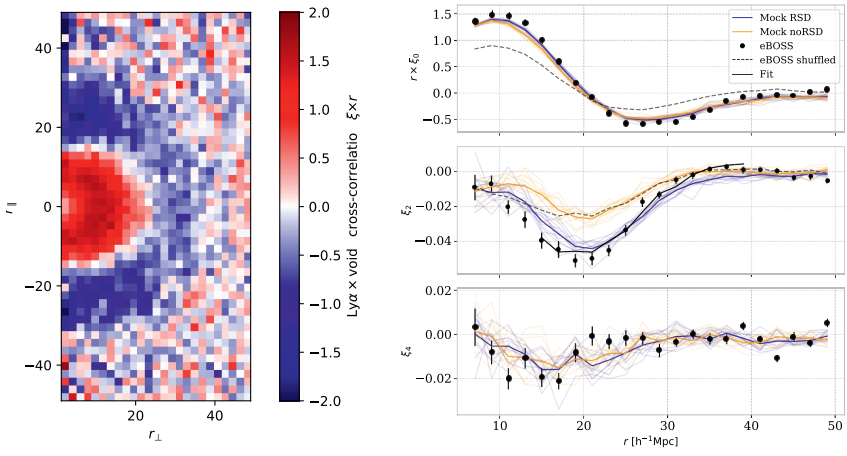

Figure 2 – (left) Measurement of $r \times \xi(r_\perp, r_\parallel)$ from eBOSS Stripe 82 data. (right) Associated Legendre multipoles for $\ell = 0, 2, 4$, for Stripe 82 data (black points) and for mock realizations including RSD (blue) or not (orange). Thin curves represent individual mock realizations, and their average is shown with thick curves. Black dashed curves show the average monopole and quadrupole measured from shuffled data. The black continuous curve shows the fit of the eBOSS quadrupole with Eqn 4.

of void centers on average, closer towards the nearest line-of-sight with respect to their true positions. We included this effect in a simple way to the model of equation 4. We also shuffled the data to confirm the geometric origin of this effect.

By fitting this corrected model to the Lyα-void cross-correlation on data, we obtained an RSD parameter $\beta = 0.52 \pm 0.05$. This value is smaller than that of a similar parameter inferred from the large-scale eBOSS Lyα auto-correlation [3]. A full study of the velocity bias from hydrodynamical simulations is probably required to interpret our measurement.

This exploratory work, applied to a statistically limited data set, opens new possibilities for observational cosmology. Upcoming large-field surveys such as WEAVE-QSO [10] and DESI [11] will extend this measurement to much larger volumes. With an expected line-of-sight density of ~ 60 deg^{-2} over a 14,000 deg^2 DESI footprint, the tomographic effect will be reduced, and statistical fluctuations will drastically shrink.

References

1. C. Ravoux, E. Armengaud, M. Walther, T. Etourneau, D. Pomarède, N. Palanque-Delabrouille, C. Yèche, J. Bautista, H. du Mas des Bourboux, S. Chabanier, K. Dawson, J.-M. Le Goff, B. Lyke, A. D. Myers, P. Petitjean, M. M. Pieri, J. Rich, G. Rossi, D. P. Schneider, J. Cosmology Astropart. Phys. **07**, 010 (2020).
2. C. Ravoux, E. Armengaud, J. Bautista, J.-M. Le Goff, N. Palanque-Delabrouille, J. Rich, M. Walther, and C. Yèche, submitted.
3. H. d. M. d. Bourboux et al., The Astrophysical Journal **901**, 153 (2020).
4. C. Pichon et al., Monthly Notices of the Royal Astronomical Society **326**, 597 (2001).
5. K.-G. Lee et al., The Astrophysical Journal Supplement Series **237**, 31 (2018).
6. LELANTOS https://github.com/corentinravoux/lelantos/
7. D. H. Weinberg et al., The Astrophysical Journal **490**, 564 (1997).
8. Y.-C. Cai et al., Monthly Notices of the Royal Astronomical Society **462**, 2455 (2016).
9. N. Hamaus et al., J. Cosmology Astropart. Phys. **07**, 014 (2017).
10. M. Pieri et al., arXiv preprint 1611.09388.
11. DESI Collaboration, arXiv preprint 1611.00036.

Cosmological implications of the full shape of anisotropic clustering measurements in BOSS and eBOSS

Agne Semenaite
Max-Planck-Institut für extraterrestrische Physik, Postfach 1312, Giessenbachstr., 85741 Garching, Germany

We perform the full shape analysis of anisotropic clustering measurement from the extended Baryon Oscillation Spectroscopic Survey (eBOSS) quasar sample together with the combined galaxy sample from the Baryon Oscillation Spectroscopic Survey (BOSS). We focus on the cosmological parameters that are not defined through the Hubble parameter h and obtain constraints for flat ΛCDM cosmologies. We find our measurements to be consistent with the latest CMB data from *Planck* within $0.64 \pm 0.03\sigma$. This agreement slightly degrades to $1.54 \pm 0.08\sigma$ when the 3×2pt data sample from the Dark Energy Survey (DES) Year 1 release is added. We furthermore study the effect of imposing a *Planck* - like prior on the parameters that define the shape of the linear matter power spectrum, and find that, in this case, the combination of low-redshift data sets prefers a value of the physical dark energy density $\omega_{\rm DE} = 0.335 \pm 0.011$, which is 1.7σ higher than the one preferred by *Planck*.

1 Introduction

Galaxy clustering has become one of the most mature and powerful probes of the low-redshift Universe, providing information about the growth of structure through Redshift Space Distortions (RSD) as well as allowing to measure the background expansion through the imprint of Baryon Acoustic Oscillations (BAO). The two effects set distinct features of the two point correlation function which can be fit with the help of summary statistics, allowing to extract cosmological parameter constraints with little dependence on the assumed cosmological model. BAO set the angular scale of the acoustic peak which can be used as a 'standard ruler' to probe the distance-redshift relation, whereas RSD distort the clustering amplitude, introducing anisotropies, as a result of galaxy peculiar velocities.

The analyses based on BAO and RSD information alone have provided consistent results, confirming ΛCDM as the preferred cosmological model [1]. Nevertheless, these summary statistics based techniques have been shown to lose additional constraining power available from the shape of the full clustering measurement. The alternative is, therefore, to fit the full measurement, in this way preserving the cosmological information, though introducing additional dependence on the particular cosmological model considered.

While ΛCDM remains the best-fit cosmological model for the current observations, the associated tensions [2] motivate to further improve the constraints on the model parameters and test the consistency among different probes. The full shape clustering analyses provide some of the most precise low-redshift measurements on a number of cosmological parameters. Furthermore, such analyses can be complimented by the inclusion of weak lensing data sets that provide information on the full matter distribution without suffering from the effects of tracer bias.

In these proceedings we summarise our work where we perform full shape analysis of the anisotropic two point correlation function measurements from eBOSS quasar sample [3]. We

combine these with clustering measurements of BOSS galaxies, which are reanalysed with an updated bias model as well as an updated model for non-linear power spectrum. We compare our constraints for ΛCDM model with the predictions by Planck for clustering alone, as well as its combination with weak lensing '3×2pt' measurements from Dark Energy Survey Year 1 (DES Y1) release. Throughout the work we define our parameter space such as to avoid dependence on the Hubble parameter h.

2 Methodology

2.1 Data

The clustering measurements used in this work come from Sloan Digital Sky Survey Data Release 12 (SDSS DR12). We use BOSS galaxy clustering wedges measurements from [4], which correspond to two redshift bins with $0.2 < z < 0.5$ (the LOWZ sample) and $0.5 < z < 0.75$ (CMASS) with the effective redshifts of $z_{\rm eff} = 0.38$ and 0.61, respectively. For eBOSS quasar clustering we use the clustering multipole measurements from [5]. The corresponding quasar sample covers the redshift range of $0.8 < z < 2.2$, with an effective redshift $z_{\rm eff} = 1.48$. The covariance matrices of these measurements were obtained using sets of mock catalogues [6,7].

Complimentary to our clustering measurements, we use weak lensing 3×2pt measurements from DES Y1, which are analysed using the publicly provided likelihood, as implemented in our chosen Markov-Chain Monte-Carlo sampler CosmoMC [8]. We compare our results with the constraints obtained using latest CMB temperature and polarization power spectra from the Planck satellite. We use the public nuisance parameter-marginalised likelihood `plik_lite_TTTEEE+lowl+lowE`.

2.2 Modelling anisotropic measurements

We model the full shape of Legendre multipoles and clustering wedges following [4] with updated bias and non-linear power spectrum modelling.

The predictions for the non-linear matter power spectrum, $P_{\rm mm}(k)$, are obtained using the Rapid and Efficient SPectrum calculation based on RESponSe functiOn approach [9] (RESPRESSO), whose key ingredient is the response function $K(k, q)$, which quantifies the variation of the non-linear matter power spectrum at scale k, induced by a change of the linear power at scale q, $P_{\rm L}(q)$. This approach allows to obtain $P_{\rm mm}(k)$ for arbitrary cosmological parameters $\boldsymbol{\theta}$ based on a measurement from N-body simulations of a fiducial cosmology $\boldsymbol{\theta}_{\rm fid}$ and a response function which can be modelled phenomenologically:

$$P_{\rm mm}(k|\boldsymbol{\theta}) = P_{\rm mm}(k|\boldsymbol{\theta}_{\rm fid}) \int {\rm d}\ln q\, K(k,q) \times [P_{\rm L}(q|\boldsymbol{\theta}) - P_{\rm L}(q|\boldsymbol{\theta}_{\rm fid})]. \quad (1)$$

The choice of $\boldsymbol{\theta}_{\rm fid}$ in RESPRESSO corresponds to the best-fitting ΛCDM model to the *Planck* 2015 data [10].

Our bias model follows [11] who relate the galaxy density fluctuations δ to the matter density fluctuations $\delta_{\rm m}$ at one loop using a four-parameter model:

$$\delta = b_1\delta_m + \frac{b_2}{2}\delta_m^2 + \gamma_2\mathcal{G}_2(\Phi_v) + \gamma_{21}\mathcal{G}_2(\varphi_1,\varphi_2) + ..., \quad (2)$$

Here the first two terms represent contributions from linear and quadratic local bias, while the remaining ones correspond to non-local terms: $\mathcal{G}_2$ is the Galileon operator of the normalized velocity potential Φ_ν, and φ_1 is the linear Lagrangian perturbation potential with φ_2 as a second-order potential that accounts for the non-locality of the gravitational evolution.

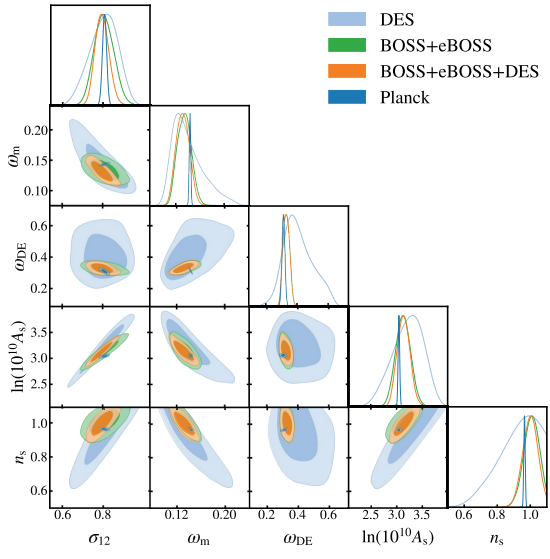

Figure 1 – In orange - 'low-redshift' constraints for flat ΛCDM obtained from combining BOSS + eBOSS clustering (green) with DES 3×2pt (light blue) and compared with Planck (dark blue). While we obtain a good consistency overall, we note the slight discrepancy between the low redshift probes and Planck contours in $\log(10^{10}A_s) - \sigma_{12}$ and ω_m–σ_{12} projections, reminiscent of the tension seen in σ_8–Ω_m plane.

We use a quadratic relation based on excursion set theory from [12] to set the value of γ_2 in terms of the linear bias b_1:

$$\gamma_2(b_1) = 0.524 - 0.547b_1 + 0.046b_1^2, \tag{3}$$

Similarly, we also relate γ_{21} and b_1 through a co-evolution relation which is derived assuming conserved evolution of galaxies after their formation:

$$\gamma_{21} = -\frac{2}{21}(b_1 - 1) + \frac{6}{7}\gamma_2. \tag{4}$$

Our model of RSD effects matches that of [4] and follows [13] and [14] with a fingers-of-god correction factor due to non-gaussian large scale limit of the generating function of the pairwise velocity distribution. In addition to the non-linear power spectrum, we also require velocity-velocity and matter-velocity power spectra. We compute these using the empirical relations based on N-body simulations [15]. We furthermore account for the non-negligible redshift errors of the QSO sample by including an additional damping factor to the power spectrum, as per [5]. Finally, we account for Alcock-Paczynski distortions by introducing geometric distortion factors.

2.3 Parameter space

As pointed out by [16], using h^{-1}Mpc units is equivalent to marginalising over the posterior of h that is recovered by a particular probe. This may not only complicate the physical parameter interpretation but also introduce artificial discrepancies when comparing constraints from probes with significantly different h posteriors.

In order to avoid such effects we focus on 'h-free' definitions of cosmological parameters: instead of σ_8, we use its equivalent defined on a scale of 12 Mpc, σ_{12}, as introduced by [16], and instead of expressing contributions of various energy components i through their relative

density Ω_i, we use the physical quantities $\omega_i = \Omega_i h^2$. Our final parameter space of interest is then $(\omega_\mathrm{b}, \omega_\mathrm{c}, \omega_\mathrm{DE}, A_\mathrm{s}, n_\mathrm{s})$.

3 Results

The posterior constraints from our analysis are presented in Figure 1. Overall, we find consistency between the clustering measurements and Planck within $\sim 0.6\sigma$ ($\sim 1.5\sigma$ when DES is added), as measured by the suspiciousness statistic.

We also find that the slight tension between DES and Planck seen in the Ω_m-σ_8 plane is no longer present in its h-independent equivalent ω_m-σ_{12} plane. Nevertheless, we do see differences of a similar significance ($\sim 2.5\sigma$) in the $\log(10^{10} A_\mathrm{s})$ – σ_{12} plane between DES and Planck, which are inherited by the full combination of low-redshift data sets. This can be straightforwardly interpreted as DES and large scale structure probes preferring slightly less structure growth than predicted by Planck.

In addition to our wide-prior analysis, we also perform a consistency check by imposing Gaussian priors on cosmological parameters that control the shape of the linear power spectrum - ω_b, ω_c and n_s [17]. The covariance matrix and mean values for this are derived from Planck-only posterior distributions. The resulting values of σ_{12} and $\ln(10^{10} A_\mathrm{s})$ preferred by our low-redshift probes are, respectively, 1.89σ and 1.22σ lower than the corresponding Planck values. We also recover a 1.73σ higher value for ω_DE.

The high value of ω_DE preferred by the low redshift probes is consistent with suppressed growth, which is hinted at our wide-prior analysis. This parameter, however, cannot be well constrained by our datasets without the additional information on the power spectrum shape from Planck. Nevertheless, this discrepancy is intriguing in the context of the high value of H_0 obtained by some of the direct measurements (the "H_0 tension").

References

1. S. Alam et al. *Phys. Rev. D*, 103(8):083533, April 2021.
2. L. Perivolaropoulos and F. Skara. *arXiv e-prints*, page arXiv:2105.05208, May 2021.
3. A. Semenaite. *arXiv e-prints*, page arXiv:2111.03156, November 2021.
4. A. G. Sánchez et al. *MNRAS*, 464(2):1640–1658, January 2017.
5. J. Hou et al. *MNRAS*, 500(1):1201–1221, January 2021.
6. F.S. Kitaura et al. *MNRAS*, 456(4):4156–4173, March 2016.
7. C. Zhao et al. *MNRAS*, 503(1):1149–1173, May 2021.
8. A. Lewis and S. Bridle. *Phys. Rev. D*, 66:103511, Nov 2002.
9. T. Nishimichi, F. Bernardeau, and A. Taruya. *Phys. Rev. D*, 96:123515, Dec 2017.
10. Planck Collaboration et al. *A&A*, 594:A13, September 2016.
11. A. Eggemeier, R. Scoccimarro, and R. E. Smith. *Phys. Rev. D*, 99(12):123514, June 2019.
12. R. K. Sheth, K. C. Chan, and R. Scoccimarro. *Phys. Rev. D*, 87:083002, Apr 2013.
13. R. Scoccimarro. *Phys. Rev. D*, 70:083007, Oct 2004.
14. A. Taruya, T. Nishimichi, and S. Saito. *Phys. Rev. D*, 82(6), Sep 2010.
15. J. Bel, A. Pezzotta, C. Carbone, E. Sefusatti, and L. Guzzo. *A&A*, 622:A109, February 2019.
16. A. G. Sánchez. *Phys. Rev. D*, 102(12):123511, December 2020.
17. A. G. Sánchez, A. N. Ruiz, J. Gonzalez Jara, and N. D. Padilla. *arXiv e-prints*, page arXiv:2108.12710, August 2021.

Dark Energy Survey year 3 results: cosmology with peaks using an emulator approach

Dominik Zürcher on behalf of the DES Collaboration
Institute for Particle Physics and Astrophysics, Department of Physics, ETH Zürich, Wolfgang Pauli Strasse 27, 8093 Zürich, Switzerland

We constrain the matter density $\Omega_{\rm m}$ and the amplitude of density fluctuations σ_8 within the ΛCDM cosmological model with shear peak statistics and angular convergence power spectra using mass maps constructed from the first three years of data of the Dark Energy Survey (DES Y3). Our analysis follows a forward-modelling scheme to create a likelihood of these statistics using N-body simulations, using a Gaussian process emulator. We include the following lensing systematics: multiplicative shear bias, photometric redshift uncertainty, and galaxy intrinsic alignment. We find that the additional non-Gaussian information leads to a tightening of the constraints on the structure growth parameter yielding $S_8 \equiv \sigma_8\sqrt{\Omega_{\rm m}/0.3} = 0.797^{+0.015}_{-0.013}$ (68% confidence limits), with a precision of 1.8%, an improvement of 38% compared to the angular power spectra only case. We find a mild tension of $1.5\,\sigma$ between our study and the results from Planck 2018, with our analysis yielding a lower S_8. Furthermore, we observe that the combination of angular power spectra and tomographic peak counts breaks the degeneracy between galaxy intrinsic alignment $A_{\rm IA}$ and S_8, improving cosmological constraints.

1 Introduction

Recent measurements from observational programs that map the large scale structure (LSS) of the Universe have delivered cosmological constraints on the matter density $\Omega_{\rm m}$ and amplitude of density fluctuations σ_8 with better than 5% precision. Weak gravitational lensing is one of the probes able to map the distribution of structures in the LSS directly [1]. The information contained in weak lensing mass maps is typically extracted using 2-point statistics such as the angular power spectrum. However, 2-point statistics do not capture all the information available in the highly non-Gaussian mass maps [2,3]. Multiple approaches have been proposed to extract this information. We utilize the peak count function, which counts local maxima of the mass maps and thus probes their highly non-linear parts [4]. The inclusion of peak counts increases the cosmological constraining power, but faces a major difficulty in its application: the prediction from theory is more challenging than that of 2-point statistics. We circumvent this problem by relying on a forward modelling approach, training an emulator on numerical simulations to predict the peak counts for different cosmologies.

The goal of this work is to infer cosmological parameter constraints using peak counts and the angular power spectra of the tomographic weak lensing mass maps from the first three years of data from the Dark Energy Survey (DES Y3) [5]. We measure the cosmological parameters σ_8 and $\Omega_{\rm m}$ in the ΛCDM model, as well as the galaxy intrinsic alignment amplitude $A_{\rm IA}$. We do not infer the values of the remaining ΛCDM parameters as they are mostly unconstrained by weak lensing measurements, but we take into account their contribution to the measurement uncertainty by marginalising them out over a prior. Further, we incorporate the effects of pho-

tometric redshift uncertainty, shear calibration biases and the redshift dependence of galaxy intrinsic alignment into the analysis. Stringent scale cuts are applied to ensure that the results are not sensitive to baryon modelling.

We refer the reader to Zürcher et al. 2022 [6] for a detailed discussion of this work.

2 Data

Dark Energy Survey Year 3 shape catalogue The Dark Energy Survey (DES) is a photometric imaging survey that observed the southern hemisphere in five optical-NIR broadbands ($grizY$) over six years (2013-2019). We use the fiducial DES Y3 weak lensing shape catalogue presented in [7]. The final sample comprises about a hundred million objects, for an effective number density of $n_{\rm eff} = 5.59$ galaxies/arcmin^2, spanning an effective area of 4143 square degrees. The galaxies of the DES Y3 shape catalogue are further divided into four tomographic bins.

N-Body simulation suite The simulations used to train the emulator sample the $\Omega_{\rm m} - \sigma_8$ plane at 58 different cosmologies. Fifty independent full-sky simulations were run for the fiducial cosmology and five simulations for every other cosmology. The simulations at the fiducial cosmology are used to estimate the covariance matrix while the remaining simulations are used to train the emulator. All simulations were produced using the publicly available code PkdGrav3 [8]. Apart from the varying $\Omega_{\rm m}$ and σ_8 parameters, all remaining cosmological parameters are fixed to the (ΛCDM,TT,TE,EE+lowE+lensing) results of Planck 2018 [9]. The dark energy density Ω_Λ is adapted for each cosmology to achieve a flat geometry. All simulations include three massive neutrino species with a mass of $m_\nu = 0.02$ eV per species. A degenerate mass hierarchy was adopted.

3 Method

The `UFalcon` [10] software is used to produce full sky mass maps from the particle shells of the PkdGrav3 simulations, utilizing the Born-Approximation. An area equal to the area observed by the DES Y3 survey is cut out from the full sky maps. Subsequently, a shape noise signal that is statistically equivalent to the shape noise in the actual DES Y3 data is added to the mass maps.

We train a Gaussian Process Regression (GPR) emulator to predict the values of the summary statistics for different inputs of $\Omega_{\rm m}$, σ_8, and $A_{\rm IA}$. The training of the GPR emulator is based on simulations at 58 different locations in the $\Omega_{\rm m} - \sigma_8$ space. At each parameter point 9 different setups are used with $A_{\rm IA}$ varying from -6 to 6 (linearly spaced). This results in the full parameter space $\Omega_{\rm m} - \sigma_8 - A_{\rm IA}$ being sampled in 522 different parameter locations. The effect of galaxy intrinsic alignment is modelled using the non-linear intrinsic alignment model (NLA).

While the amplitude of the galaxy intrinsic alignment signal $A_{\rm IA}$ is included in the emulator, the remaining systematics (photometric redshift uncertainty, multiplicative shear bias and the redshift dependence of the galaxy intrinsic alignment signal) are modelled in a cosmology independent way by fitting a set of scaling functions at the fiducial cosmology.

In the inference process we compress the data vectors using the MOPED data compression algorithm [11]. A Gaussian noise model is assumed and the parameter space is efficiently sampled using the Markov Chain Monte Carlo (MCMC) sampler `emcee` [12].

While we measured the angular power spectra in 32 square-root-spaced bins between $\ell = 8$ and $\ell = 2048$ we do not use all scales in the analysis; instead, we decided to only use the scales

$\ell \in [30, 578]$. The lower scale cut $\ell \geq 30$ is driven primarily by the decision to exclude scales that might be affected by mixing with super-survey modes. The upper scale cut $\ell \leq 578$ is imposed to stay unbiased to baryonic physics.
In order to be sensitive to peaks of different spatial extent, the mass maps are smoothed with a set of Gaussian kernels prior to identifying the peaks. Initially 12 such kernels were used, with FWHM $= [31.6, 29.0, 26.4, 23.7, 21.1, 18.5, 15.8, 13.2, 10.5, 7.9, 5.3, 2.6]$ arcmin. Again, a scale cut is applied in order to avoid biases from baryonic physics. Hence, we restrict ourselves to using peaks identified on maps that were smoothed with a Gaussian kernel with a FWHM ≥ 7.9 arcmin.

4 Cosmological Constraints

We present our fiducial constraints on the cosmological parameters Ω_m, σ_8 and S_8 in the left-hand plot in Figure 1. We observe a mild breaking of the $\Omega_\mathrm{m} - \sigma_8$ degeneracy due to the non-Gaussian information extracted using the peak counts. The combination of angular power spectra and peak counts yields

$$\begin{aligned} \Omega_\mathrm{m} &= 0.276^{+0.034}_{-0.086} \\ \sigma_8 &= 0.850^{+0.13}_{-0.068} \\ S_8 &= 0.797^{+0.015}_{-0.013}\,(\text{precision } 1.8\%). \end{aligned} \tag{1}$$

While both summary statistics find an A_IA constraint consistent with zero, the angular power spectra analysis prefers values lower than the peaks analysis ($A_\mathrm{IA} = -0.72^{+0.72}_{-0.39}$ for angular power spectra and $A_\mathrm{IA} = 0.11^{+0.22}_{-0.49}$ for peaks). In the combined analysis, we find a tight constraint of $A_\mathrm{IA} = -0.03 \pm 0.23$ and we observe the hoped-for breaking of the $S_8 - A_\mathrm{IA}$ degeneracy. As can be seen from the right-hand plot in Figure 1 this also leads to a shift of $\sim 1\,\sigma$ of the S_8 constraint towards larger values when compared to the peaks-only case.

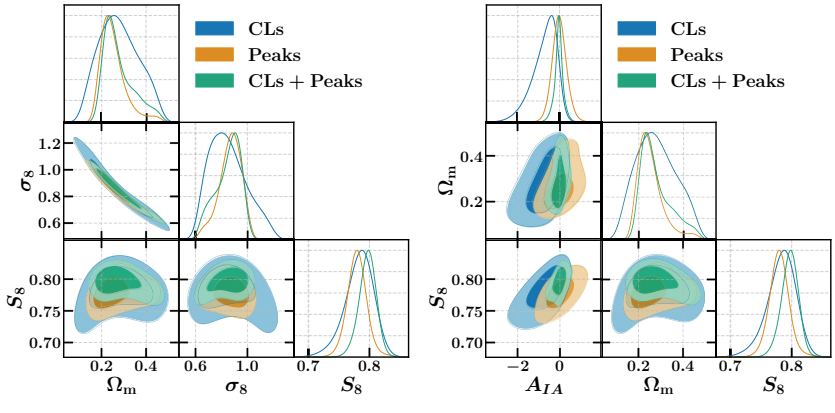

Figure 1 – **Left:** Fiducial constraints on the matter density Ω_m, the amplitude of density fluctuations σ_8, and the structure growth parameter $S_8 \equiv \sigma_8 \sqrt{\Omega_\mathrm{m}/0.3}$ inferred using the angular power spectra (CLs), peak counts (Peaks), and both summary statistics (CLs + Peaks). **Right:** Constraints on the galaxy intrinsic alignment amplitude A_IA as well as the degeneracy parameter S_8 and Ω_m as inferred using angular power spectra (CLs), peak counts (Peaks), and both (CLs + Peaks). The contour levels in both plots indicate the 68% and 95% confidence regions of the constraints.

When comparing our constraints to the (ΛCDM,TT,TE,EE+lowE+lensing) results of Planck 2018 [9] we find a mild tension of $1.5\,\sigma$. The measured tension is slightly lower than that recorded in other weak lensing studies. This can be attributed to the near zero value of $A_{\rm IA}$ and the breaking of the $S_8 - A_{\rm IA}$ degeneracy achieved by the combination of angular power spectra and peak counts.

Acknowledgments

The ETH Zurich Cosmology group acknowledges support by grants 200021_192243 and 200021_16 9130 of the Swiss National Science Foundation.

References

1. Martin Kilbinger. Cosmology with cosmic shear observations: a review. *Reports on Progress in Physics*, 78(8):086901, July 2015.
2. Volker Springel, Carlos S. Frenk, and Simon D. M. White. The large-scale structure of the Universe. *Nature*, 440(7088):1137–1144, April 2006.
3. Xiuyuan Yang, Jan M. Kratochvil, Sheng Wang, Eugene A. Lim, Zoltán Haiman, and Morgan May. Cosmological information in weak lensing peaks. *Physical Review D*, 84(4):043529, August 2011.
4. Tomasz Kacprzak, D Kirk, O Friedrich, A Amara, A Refregier, L Marian, JP Dietrich, E Suchyta, J Aleksić, D Bacon, et al. Cosmology constraints from shear peak statistics in dark energy survey science verification data. *Monthly Notices of the Royal Astronomical Society*, 463(4):3653–3673, 2016.
5. I Sevilla-Noarbe et al. Dark Energy Survey Year 3 Results: Photometric Data Set for Cosmology. *arXiv e-prints*, page arXiv:2011.03407, November 2020.
6. D Zürcher, J Fluri, R Sgier, T Kacprzak, M Gatti, C Doux, L Whiteway, A Réfrégier, C Chang, N Jeffrey, et al. Dark energy survey year 3 results: Cosmology with peaks using an emulator approach. *Monthly Notices of the Royal Astronomical Society*, 511(2):2075–2104, 2022.
7. M Gatti, E Sheldon, A Amon, M Becker, M Troxel, A Choi, C Doux, N Maccrann, A Navarro Alsina, I Harrison, et al. Dark energy survey year 3 results: Weak lensing shape catalogue. *arXiv preprint arXiv:2011.03408*, 2020.
8. Douglas Potter, Joachim Stadel, and Romain Teyssier. Pkdgrav3: beyond trillion particle cosmological simulations for the next era of galaxy surveys. *Computational Astrophysics and Cosmology*, 4(1):2, 2017.
9. Nabila Aghanim, Yashar Akrami, M Ashdown, J Aumont, C Baccigalupi, M Ballardini, AJ Banday, RB Barreiro, N Bartolo, S Basak, et al. Planck 2018 results-vi. cosmological parameters. *Astronomy & Astrophysics*, 641:A6, 2020.
10. Raphaël J Sgier, Alexandre Réfrégier, Adam Amara, and Andrina Nicola. Fast generation of covariance matrices for weak lensing. *Journal of Cosmology and Astroparticle Physics*, 2019(01):044, 2019.
11. Alan F Heavens, Raul Jimenez, and Ofer Lahav. Massive lossless data compression and multiple parameter estimation from galaxy spectra. *Monthly Notices of the Royal Astronomical Society*, 317(4):965–972, 2000.
12. Foreman-Mackey Daniel, David W Hogg, Dustin Lang, and Jonathan Goodman. emcee: The mcmc hammer. *Publications of the Astronomical Society of the Pacific*, 125(925):306, 2013.

HSC 3×2pt analysis in harmonic space as a precursor of the LSST-DESC

D. S. Cid on behalf of the LSST Dark Energy Science Collaboration (DESC)
Departamento de Investigación Básica, CIEMAT
Madrid, Spain

We perform the first harmonic space joint analysis of galaxy clustering, cosmic shear and galaxy-galaxy lensing, the so-called 3×2pt analysis, considering Hyper Suprime-Cam Subaru Strategic Program (HSC-SSP) public data. HSC is the deepest Stage III survey and uses a prototype version of the Rubin Science Pipelines, making this dataset ideal to use as a precursor to the Vera C. Rubin Observatory Legacy Survey of Space and Time (LSST). These characteristics allow us to put to the test software and tools developed by the LSST-DESC collaboration as well as setting precise constraints on ΛCDM cosmological parameters. In this analysis we explore the advantages of having the same lens and source sample and the applicability of mode deprojection as a method to correct the impact of observing conditions in spin-2 fields. As our main result, we present preliminary results in the plane $\Omega_m - S_8$ that are competitive with the current state of the art.

1 Introduction

There are two main elements which intrigue the cosmological community. One of them is the so-called *dark energy* which causes the accelerated expansion of the Universe. The other one is *dark matter*, proposed by F. Zwicky and discovered by Vera C. Rubin in the middle of the last century, to account for the matter for which we sense their gravitational influence but not their electromagnetic counterpart.

One of the primary avenues to explore the nature of dark matter and dark energy has been the observation of large areas of the sky. Photometric surveys have been one of the main ways of observing the sky, measuring the position and shapes of million of galaxies. Currently, we are living the endgame of Stage III surveys. Among these Stage III projects we can highlight *the Dark Energy Survey* (DES) which stands out for its large area covered (approximately one octant of the sky, $\sim 5000\,\mathrm{deg}^2$) and *the Hyper-Suprime Cam Subaru Strategic Program* (HSC-SSP or HSC) which aims to map a smaller area ($\sim 1400\,\mathrm{deg}^2$ of the northern sky) but being sensitive to objects approximately 3.3 times dimmer ($i < 25.9$ vs. DES $i < 24.5$)

Stage IV surveys will overcome the need for trade-offs between survey area and depth. *The Rubin Observatory Legacy Survey of Space and Time*[a] (LSST), flagship of this near-future phase,

[a] http://www.lsst.org

carried out in the Vera C. Rubin Observatory will cover the whole southern hemisphere sky to an extraordinary depth every few nights. The LSST is a multi-propose project covering a wide range of physical scales. On the largest scales, the main goal is the study of observable signatures of dark sector physics. *The Rubin Observatory LSST Dark Energy Science Collaboration*[b] (DESC) was created with the purpose of probing this dark world, to measure with precision fundamental cosmological parameters using LSST data combining different cosmological probes.

The aim of the project presented in this dissertation is twofold. On the technical and software side, we validate the DESC developed two-point correlations measurement pipeline called `TXPipe` and the collaboration statistical inference tool, `Firecrown`. On the cosmological science side, we analyse the HSC dataset as a precursor of LSST data and combine large-scale structure and weak lensing probes in the so-called 3×2pt analysis. This combined methodology enhances our statistical power to set constraints on abundance of matter, the sum of dark and baryonic matter, and the clumpsiness of the structure in the late universe.

This document is structured as follows: the introductory section ends with a brief summary of 3×2pt technique. This is followed in Sec. 2 by a description of the HSC data. In Sec. 3 the methodology is presented, this encloses the presentation of LSST-DESC two-point correlations measurement and statistical inference tools. Finally, in Sec. 4 our reproduction of HSC cosmic shear analysis results is presented as a first step to the final combination with galaxy clustering and galaxy-galaxy lensing.

1.1 Cosmology from Clustering & Weak Lensing: a 3×2pt analysis

The statistical combination of these three cosmological probes: *cosmic shear*, *galaxy-galaxy lensing* and *galaxy clustering*, has shown to be a suitable method to constrain the ΛCDM model and its different extensions. The success of this methodology applied to state-of-art photometric datasets is collected in recent papers, such as: the main results with the Year 3 data of the DES Collaboration and the joint analysis developed by *the Kilo Degree Survey* (KiDS) and *Galaxies And Mass Assembly* (GAMA).

Photometric surveys measure the *angular position*, *color* and *shapes* of galaxies contained in a large volume of our universe enabling the reconstruction of the history of the late universe. These quantities can be correlated in real space yielding the two-point correlation functions or its counterpart in harmonic space, the power spectra. The *galaxy clustering* correlation function is obtained by correlating positions with positions, *cosmic shear* is obtained by correlating shapes with shapes and the cross-correlation of shapes and positions is called *galaxy-galaxy lensing*.

To estimate these two-point correlation functions, the whole dataset of galaxies observed has to be divided in two different samples: the *lenses* and the *sources*. The lens sample contains foreground galaxies for which positions are measured and are used to compute the galaxy clustering and the galaxy-galaxy lensing. The source sample contains galaxies in the background for which shapes are measured and used in cosmic shear and galaxy-galaxy lensing.

2 Data

We analyse the Hyper Suprime-Cam Subaru Strategic Program first public data release (HSC-SSP PDR1 [1]). HSC-SSP PDR1 is a suitable dataset for the LSST preparation as it uses a prototype version of the Rubin Science Pipelines for data processing and it is the deepest Stage III wide-catalog available to date. This dataset collects positions and shapes of $\sim$ 11 million galaxies covering an area of $136.9\,\mathrm{deg}^2$ of 6 non-contiguous field of the northern hemisphere in 5 broad photometric bands, *grizy*. Observations are optimized to obtain a seeing in the i-band better than $\sim$ 0.8", suitable for shape measurements and cosmic shear cosmology. We consider the same redshift distributions as the ones in the official HSC shear analysis [2].

[b] `http://lsstdesc.org`

Two properties stand out from the catalog to consider it as a precursor of LSST: the limiting magnitude in the i-band is 25.6, similar to what is expected for the first year of data of LSST, and its high number density, 21.8 arcmin^{-2} after additional cuts.

3 Method

3.1 `TXPipe`: 2pt measurements, deprojection & covariance

Measuring 2pt statistics - To obtain two-point statistics we use the LSST-DESC official two-point pipeline, `TXPipe` (Zuntz et al. in prep.). Several tests are developed to validate the code and the data consistency. An important check consists on comparing the two-point measurements when performed over the 6 non-contiguous individual fields versus the *all-fields* calibration measurement. These different measurements are consistent for all cosmological probes and redshift bins. As a result, the *all-field* calibration becomes our fiducial measurement and it is used in cosmological inference.

Deprojection method - Photometric surveys imaging process is affected by observing conditions inducing spurious signal, contaminating the cosmological signal. In order to separate these two components we apply the so-called *deprojection method* presented in Alonso et al [3]. For the cleaning process we consider a set of 60 observing condition maps. In this scenario we perform several robustness, for instance: *a)* check the correlation between observing conditions and our overdensity and shape maps; *b)* deproject considering 22 maps condensed via principal component analysis (PCA) and as a null-test to certify we are not removing cosmological signal in the cleaning process, *c)* we look for correlations between our maps and thermal Sunyaev-Zeldovich and Cosmic Microwave Background lensing maps. We find HSC sample to be robust under observing conditions systematics. See Fig. 1 for a summary of the aforementioned tests.

Gaussian covariance - The statistical combination of galaxy clustering and weak lensing has the advantage of enhancing the constraining power. As a counterpart, we need to calculate a covariance matrix accounting for the correlation between probes due to all them been different manifestations of the same matter density field. We limit our covariance estimation to the Gaussian term [4], unlike HSC official shear analysis which also considers a non-Gaussian and a super-sample covariance term. We need to consider this difference when comparing cosmological constraints.

3.2 `Firecrown`: modeling and cosmological inference

Previous works have developed the analysis over individual probes, such as: the galaxy clustering analysis presented in Nicola et al.[5] and the cosmic shear analysis presented in Nicola et al. [4] and Hikage et al.[2]. Our study is based on Hikage et al.[2] cosmic shear modeling choices, we aim to reproduce their results to validate our tools, and extend them to join galaxy clustering and galaxy-galaxy lensing. Cosmic shear is modelled following the official HSC analysis choices [2]. We restrict our scales to multipoles in the range $300 < \ell < 1900$, consider the non-linear matter power spectrum, the Non-Linear Alignment (NLA) model to account for the intrinsic alignment. To account for uncertainties in the measurement process, a shear multiplicative bias and a shift parameter on the redshift distributions are introduced.

On the clustering side, we design the scale cuts and the choice between linear and non-linear galaxy bias in an two-steps process which proceeds as: first, generate a theoretical prediction for the different combinations of galaxy bias model and maximum scale, $k_{max} \in \{0.125, 0.5, 0.7, 1.0\}$ Mpc^{-1}; second, we compare the theoretical prediction and our measurement via its $\Delta\chi^2$ and keep the configuration which yields the greatest similarity.

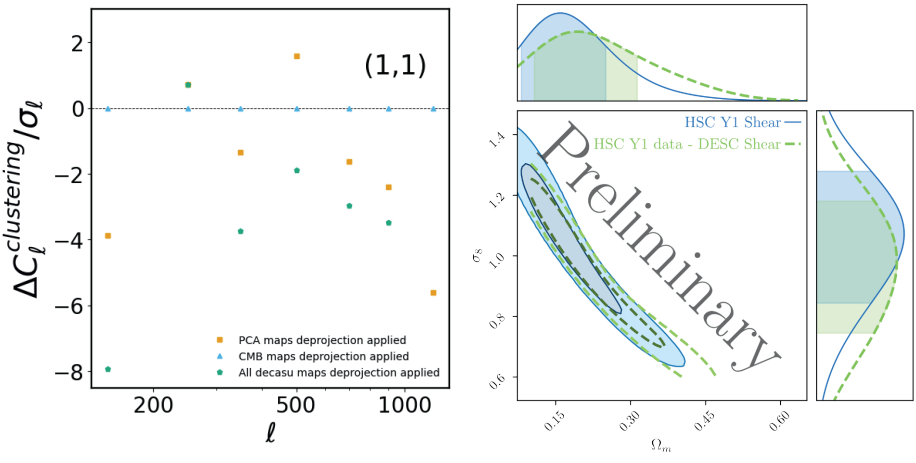

Figure 1 – (Left) Impact of different deprojection configurations with respect to raw galaxy clustering signal for the first redshift bin; (right) a comparison of the marginalized parameter constraints in the ΛCDM model between HSC official shear analysis and the shear analysis developed in our work. Discrepancies may arise from the different terms considered in the covariance computation and the fact that we do not model certain effects such as the PSF leakage

4 Results & Conclusions

In this project, `Firecrown` is also used as a statistical inference pipeline to run MCMC processes. Our main preliminary result is shown in Fig.1. We are able to reproduce Hikage et al. [2] cosmic shear analysis with our independent data reduction and pipelines. HSC obtains $\Omega_m = 0.162^{+0.086}_{-0.044}$ and $\sigma_8 = 1.029^{+0.053}_{-0.078}$. Our results yield $\Omega_m = 0.193^{+0.120}_{-0.086}$ and $\sigma_8 = 0.98^{+0.20}_{-0.24}$.

We conclude that `TXPipe` and `Firecrown` tools are highly advanced in their development and we have shown its validity and applicability in a wide range of cases. HSC sample seems to be robust to observing condition maps, we tested in-depth the effects of deprojection. Using these new measurements and inference tools we are able to replicate HSC cosmic shear results and we are ready to join galaxy clustering and galaxy-galaxy lensing statistics to conform the first 3×2pt result with HSC data in harmonic space.

Acknowledgments

This work was supported by the LSST Corporation grant 2021-02 “Bridging the Gap: Analysis of Clustering and Weak Lensing using Precursor Data Sets”.

References

1. Aihara et al., *First data release of the Hyper Suprime-Cam Subaru Strategic Program* PASJ **70**, 2053-051X (2019).
2. Hikage et al., *Cosmology from cosmic shear power spectra with Subaru Hyper Suprime-Cam first-year data* PASJ **71**, 2053-051X (2020).
3. Alonso et al., *A unified pseudo-C_ℓ framework* MNRAS **484**, 1365-2966 (2019).
4. Nicola et al., *Cosmic shear power spectra in practice* JCAP , 1475-7516 (2021).
5. Nicola et al., *Tomographic galaxy clustering with the Subaru Hyper Suprime-Cam first year public data release* JCAP , 1475-7516 (2020).

Weak lensing analysis of the 3 600 deg^2 of the CFIS-UNIONS data

Axel Guinot
On behalf of the UNIONS Collaboration
Université Paris Cité, CNRS, Astroparticule et Cosmologie, F-75013 Paris, France

The Ultraviolet Near-Infrared Optical Northern Survey (UNIONS) is a survey that aims at covering 5 000 deg^2 in the Northern sky in 5 optical bands. It is the result of the collaboration of 3 Hawaiian telescopes: CFHT, HSC, and Pan-STARRS. Due to the location of this survey, the r-band data reach an excellent sky quality (seeing ≈ 0.65 arcsec) and a depth of 24.5 mag in the r-band. The combination of a large coverage, excellent image quality, and multi-band data make UNIONS perfectly suited for weak lensing analysis. We will present the processing carried on the 3 600 deg^2 that has been observed so far. We will focus on validation tests as systematics are critical for upcoming surveys. Finally, we will show preliminary science results obtain with our shape catalogue.

1 Introduction

Euclid and the Vera C. Rubin Observatory will soon observe over a billion galaxies which will take galaxy surveys to a new era. For this generation of surveys, the control of systematics is critical to achieve the expected precision on the measurement of cosmological parameters, in particular on the dark energy equation of state. To prepare those missions we can rely on existing surveys such as Dark Energy Survey (DES), Kilo-Degree Survey (KiDS) or Ultraviolet Near-Infrared Optical Northern Survey (UNIONS) that we will discuss here.

One of the main cosmological probes of these surveys is weak lensing. Weak lensing or gravitational lensing in general, is a physical phenomenon which consists of observing background galaxies whose images have been distorted by the presence of matter along the line-of-sight, whether a massive galaxy or the large scale structure (LSS) of the universe. The study of weakly lensed objects allows to determine how the matter, including dark matter, is distributed. Studied as a function of redshift, it can also allow to measure the growth of structures at different epochs, which makes it sensitive to dark energy. In the following, we will present the ongoing effort among the UNIONS collaboration toward weak lensing analyses with a focus on the quantification and minimisation of the systematics.

The UNIONS collaboration is the reunion of three observatories:

- Canada France Hawaiian Telescope (CFHT): CFIS in r- and u-band.
- Subaru Hyper Suprime-Cam (Subaru-HSC): WISHES in z-band and WHIGS in g-band
- Pan-STARRS: PS in i-band

We will focus on the Canada France Imaging Survey (CFIS) and more specifically on the r-band data. Thanks to great atmospheric conditions at Mauna Kea summit, CFIS has an average seeing of ≈ 0.65 arcsec and reaches completness at 24.5 r-mag. These characteristics make CFIS perfectly suited for weak lensing analyses. In our group, we have developed a shape

measurement pipeline, `ShapePipe`[a], which uses state-of-the-art algorithms to infer the shapes of galaxies. It can produce calibrated shape catalogue for large surveys. The calibration is handled through the METACALIBRATION technique as introduced in Huff & Mandelbaum (2017). The pipeline is presented in Farrens et al. (*in prep*) and a first analysis of the CFIS data has been presented in Guinot et al. (*submitted*).

In the following section, we will show validation tests we performed on our processed catalogue to assess its quality and present preliminary science results to demonstrate the scientific potential of UNIONS.

2 Validation tests

As stated in the introduction, weak lensing analyses consist at precisely measuring the distortion in the shape of galaxies. It is then important to be aware of all external effects that could have an impact on the shape measurement. The main contributor is the optical system, which includes the atmosphere for ground based surveys like CFIS. To take this effect into account, we measure the response of the optical system: the Point Spread Function (PSF). The PSF can be measured with stars, as they are unresolved objects for our telescope. That means, their observed shapes come from the atmospheric turbulence and the small imperfections in the optics of the telescope. To model the PSF we make use of our newly developed software package MCCD (Liaudat et al. (2020)). We divide our star sample to keep 20% of our stars for the validation. This allows us to test the interpolation of the model and avoid to be sensitive to over-fitting. We have measured residuals between the ellipticity of the stars and our model around 10 times smaller than the ellipticity of the model. They present large circular patterns due to our second degree polynomial which do not fully capture the mirror optical aberrations. To quantify the impact of our PSF residuals on cosmology, we measure the ρ-statistics as described in Jarvis et al. (2016). In Fig 1 we can see that most of our ρ-statistics are within our requirements represented by the *grey* area. At the moment these requirements correspond to a 3% error on the estimation of σ_8 which is the most important cosmological parameter for weak lensing studies. The effects at large scales are currently under investigation.

Once the PSF model has been validated, it is important to verify that the PSF is not propagated to the shape measurement, this is called PSF leakage. PSF leakage generally creates an additive bias which we have measured in our catalogue to be less than 1×10^{-4}. More thorough measurements have shown a leakage below 1% of the PSF ellipticity which is compatible with our additive bias and again falls within our requirements.

Among all the science that weak lensing enables, the measure of cosmic shear, also known as the shear-shear 2-point correlation function, is one of the most important ones. At this stage we chose not to measure it to avoid a bias on a future parameter inference. However, we measured the Complete Orthogonal Sets of E-/B-mode Integrals (COSEBIs) which are a good indicator of level of systematics remaining that could affect such analysis. Our results are presented in Fig 2 where we can verify that B-modes are compatible with 0 as it would be expected without systematics. For a more in-depth look at those validations, we redirect the reader to our first analysis of the CFIS data presented in Guinot et al. (*submitted*).

3 Preliminary results

To date, we have produced a catalogue containing 80 million galaxies covering and effective area of 3 000 deg^2 with a galaxy density of 7.4 gal.arcmin^{-2}. In this section we present further tests focused on example science analyses where the goal is to show the potential of our shape catalogue.

[a] https://github.com/CosmoStat/shapepipe

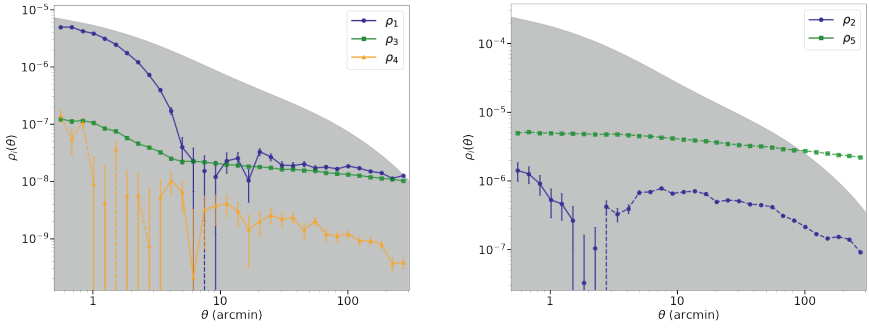

Figure 1 – The PSF residuals ρ-statistics. The *grey* area are the requirements (3% error on the estimation of σ_8). We see that our PSF model respect those requirements except for ρ_5 at large scales which more investigation at this stage.

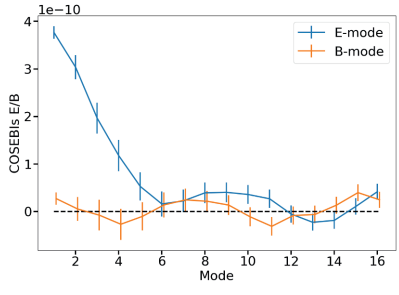

Figure 2 – We show here the COSEBIs for modes between 1 and 16. This test was performed to quantify the impact of potential systematics on the B-mode, which are consistent with 0 for our study.

We present first a cluster lensing analysis using the SDSS DR8 redMaPPER cluster catalogue. On the *left* plot of Fig 3 we compare the tangential shear, γ_t, measured around cluster positions to what is obtained around random positions illustrated by a box plot. In this figure we can see a significant detection $\approx 8\sigma$. This result confirms that our catalogue can be used for cluster lensing science and has indeed been exploited in a first analysis presented in Spitzer et al. (*submitted*).

As discussed in the introduction, weak lensing can be used to trace the distribution of matter in the universe. This can be illustrated by computing convergence map, that we produce as a second test on our data. On the *right* plot of Fig 3 we show the convergence, κ_E, for one of our fields ($\approx$ 600 deg^2). The white circles represent the position of the redMaPPER clusters previously introduced. Their positions match with high intensity regions which trace over-densities. We can then deduce that this map, as reconstructed here properly captures the dark matter distribution. We have also observed no correlation with B-modes (see Guinot et al. (*submitted*)) which confirm the low level of systematics. Mass mapping will play an important role in upcoming analysis since they enable parameter inference using higher order statistics. A first study using peak counts has been done using our catalogue by Ayçoberry et al. (*in prep*).

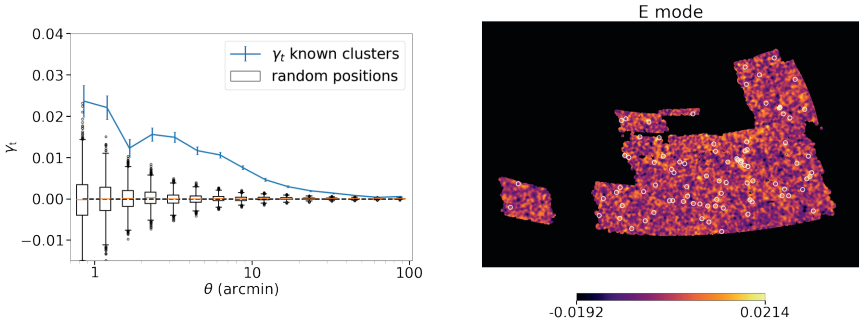

Figure 3 – *Left*: Stacked tangential shear around 85 clusters in the CFIS footprint. The box plot represents the result around 5000 × 36 random points. *Right*: Mass map for the patch P4. The *white circles* represent the positions of redMaPPER clusters.

4 Conclusion

We have presented a brief introduction to the ongoing effort among the UNIONS collaboration to enter the current weak lensing scene and prepare future missions. We have presented our second (internal) release of a shape catalogue which went through a meticulous validation process. Our preliminary results shown here and in more detail in Guinot et al. (*submitted*) the potential of this survey and the multi-band aspect of UNIONS discussed in the introduction will be integrated in a future processing, bringing forth even greater potential. High quality shape measurement combined with precise redshifts estimate will allow UNIONS to infer competitive constraints on cosmological parameters and hopefully a step towards understanding the nature of dark matter and dark energy.

Acknowledgments

I am grateful to the UNIONS weak lensing working group for their support and contributions.

References

1. Huff, E. & Mandelbaum, R. Metacalibration: Direct Self-Calibration of Biases in Shear Measurement. *ArXiv*. **1702.026** (2017,2)
2. Farrens, S., Guinot, A., Kilbinger, M., Liaudat, T., Schmitz, M. & Vitorelli, A. ShapePipe: A modular weak-lensing processing and analysis pipeline. (*in prep*)
3. Guinot, A., Kilbinger, M., Farrens, S., Peel, A., Pujol, A., Schmitz, M., Starck, J., Erben, T., Gavazzi, R., Gwyn, S., Hudson, M., Hildebrandt, H., Liaudat, T., Miller, L., Spitzer, I., Van Waerbeke, L., Cuillandre, J., Fabbro, S., A., M. & Mellier, Y. ShapePipe: a new shape measurement pipeline and weak-lensing application to UNIONS/CFIS data. (*submitted*)
4. Liaudat, T., Bonnin, J., Starck, J., Schmitz, M., Guinot, A., Kilbinger, M. & Gwyn, S. Multi-CCD Point Spread Function Modelling. *ArXiv E-prints*. pp. earXiv:2011.09835 (2020,11)
5. Jarvis, M., Sheldon, E., Zuntz, J., et al. The DES Science Verification weak lensing shear catalogues. *MNRAS*. **460** pp. 2245-2281 (2016,8)
6. Spitzer, I., Hudson, M., Cuillandre, J., Erben, T., Fabbro, S., Gavazzi, R., Guinot, A., Gwyn, S., Hildebrandt, H., Kilbinger, M., McConnachie, A., Miller, L. & Van Waerbeke, L. Galaxy group and cluster masses from weak lensing in UNIONS. (*submitted*)
7. Ayçoberry, E., Ajani, V., Guinot, A., Kilbinger, M., Pettorino, V. & UNIONS Collaboration UNIONS: The impact of systematic errors on weak-lensing peak counts. (*in prep*)

Probabilistic mass-mapping with neural score estimation

Benjamin Remy[1], François Lanusse, Niall Jeffrey, Jia Liu,
Jean-Luc Starck, Ken Osato & Tim Schrabback
1. AIM, CEA, CNRS, Université Paris-Saclay, Université Paris Diderot, Sorbonne Paris Cité, F-91191 Gif-sur-Yvette, France

In weak lensing, by measuring the lensing effect on a large number of galaxies, it is possible to reconstruct maps of the Dark Matter distribution on the sky. However, because of missing data and noise dominated measurements, the recovery of dark matter maps constitutes a challenging ill-posed inverse problem. We propose to reformulate the problem in a Bayesian framework, where the target becomes the posterior distribution of mass conditioned by the shear field. Our approach combines Neural Score Matching for learning the prior distribution from physical simulations, and a novel posterior sampling method based on Hamiltonian Monte Carlo and an annealing strategy to sample the high-dimensional posterior. After validating our method over simulated corrupted observations, we eventually applied it to the reconstruction of the HST/ACS COSMOS field based on the shape catalog from Schrabback et al. (2010), and produced the highest quality convergence map of this field to date.

1 Introduction

Massive structures along the line of sight generate deformations of apparent shapes of distant galaxies, known as gravitational lensing. In the weak regime, these deformations reduce to a small *shear* of galaxy shapes, which can be measured and used to probe the large scale structures of the Universe.

This shear can be related to the so-called *convergence* field, which directly represents the projected mass distribution on the sky, through the following equation:

$$\gamma = \mathbf{MP}\kappa + n, \tag{1}$$

where $\gamma = \gamma_1 + i\gamma_2$ is the two component shear field and $\kappa = \kappa_{\rm E} + i\kappa_{\rm B}$ the complex representation of the convergence E and B modes. $\mathbf{P}$ is a unitary linear operator derived from the lensing potential (Kaiser & Squires 1993) [1]. $\mathbf{M}$ is a binary survey mask operator describing where there is measurement in the binned map. n is the shape noise, resulting from the finite average of shapes into bins to form the shear map. Solving this equation, also called mass-mapping, aims to recover an estimate of a convergence map, for a given shear maps. However, because of the mask operator and the presence of shape noise, inverting equation 1 is an ill-posed problem, i.e.

there is no unique solution that fits to the measurements. Therefore, one needs to rely on prior assumptions to regularize this problem.

We propose to reformulate the problem in a Bayesian framework, where the target becomes the posterior distribution $p(\kappa|\gamma)$ of mass conditioned by the measured shear field. On the one hand, the likelihood factor, describing how light-rays are bent by gravity, how measurements are affected by noise, and accounting for missing observational data, is fully described by the forward physical model of Equation 1. On the other hand, the prior term encodes all the prior knowledge we have about the convergence field.

Many methods have been proposed to perform mass-mapping, assuming different priors. The Wiener filter approach assumes that the convergence follows a Gaussian Random Field, allowing to describe a prior density function (p.d.f.) from the power spectrum of the field, which can be predicted from cosmological models. While being physically motivated, this prior is only accurate at large scale. `GLIMPSE` [2] and `MCAlens` [3] have proposed *ad hoc* priors based on the sparcity of the convergence in its wavelet representation. `DeepMass` [4] was the first deep learning based method applied on real data. It was designed to provide the posterior mean given a neural prior trained on cosmological simulations. It is today the state of the art mass mapping method but suffers from two main limitations: 1) it does not have an explicit likelihood, involving no data fidelity guarantee at inference time, and 2) it does not provide uncertainty quantification. We therefore introduce `Deep Lensing Posterior` [5] to address these points. First, we keep all the physical information of the forward process in an explicit likelihood, resorting to machine learning for the prior only. Then, we sample the full posterior distribution, describing all the possible solutions fitting to the data, which can be summarized into a point estimate, such as the posterior mean, or used to compute higher moments.

2 Learning a prior from an N-body simulation

There is no closed form expression for a convergence field taking into account the non-linear gravitational collapse and baryonic effects. However, we do have access to an *implicit* prior through hydrodynamical N-body simulations such as κTNG [6], generated from the IllustrisTNG simulations. The TNG simulations are a set of cosmological, large-scale gravity and magneto-hydrodynamical simulations, where baryonic processes such as stellar evolution, chemical enrichment, gas cooling, supernovae and black hole feedback are incorporated as subgrid models.

In our paper [5], we propose to learn this implicit prior with a recent class of generative model called *neural score estimation*. A generative model is a class of neural network whose purpose is to model the prior distribution of some data. In particular, neural score estimation, first proposed by Hyvärinen (2005) [7], provide an evaluation of the gradient of the log p.d.f., i.e. $\nabla_\kappa \log p(\kappa)$, also known as the *score function*. This quantity is much more tractable to estimate than the normalised p.d.f. $p(\kappa)$, because it avoids computing the normalisation factor $\int p(\kappa) d\kappa$. As it will be presented in the next section, being able to evaluate the prior score is sufficient to run efficient gradient-based MCMC algorithms in order to sample the posterior distribution.

One way to train a generative model to learn an implicit distribution, is to artificially corrupt the data with white Gaussian noise, and train a neural netwrok to denoise them. This technique has been demonstrated to be tractable for high-dimensional data and guaranteed to approximate the score function under the following theorem [8,9]:

$$\nabla_\kappa \log p_\sigma(\kappa) = \frac{r^*(\kappa', \sigma) - \kappa'}{\sigma^2} + o(1), \quad \text{as} \quad \sigma^2 \to 0, \tag{2}$$

where r^* is an optimal gaussian denoiser, trained under an ℓ_2 loss, taking as input a noisy convergence map $\kappa' = \kappa + u$, $u \sim \mathcal{N}(0, \sigma^2 \mathrm{I}_d)$ and the noise level σ. Note that equation 2 computes the score of the prior convolved with a Gaussian of variance σ^2. The data score can be evaluated using a very small sigma, but the Gaussian convolved feature turns out to be very useful for our sampling scheme.

3 Sampling mass-maps with annealing HMC

Markov Chain Monte Carlo are widely used in the cosmological community to probe posterior distributions. However, when the parameter space dimension becomes to high (here $d > 10^5$ for a 360×360 pixels map), standard MCMCs are computationaly intractable because of the curse of dimensionality. This curse can be dimmed if one has access to the gradients of the posterior, which can be used to make smarter proposals such as in the Hamiltonian Monte Carlo algorithm[10,11]. As shown by Song and Ermon (2019) [12], when the posterior distribution is multi-modal, even gradient-based MCMCs struggle to sample the whole posterior space, and to recover the relative mode weights. Therefore, they introduce the annealing strategy, increasing the *temperature* of the posterior distribution, merging the different modes into a wide distribution, much easier to sample. Annealing consists of convolving the target distribution with a Gaussian distribution at a given variance, also called temperature, as in $p_\sigma(\kappa|\gamma) = p(\kappa|\gamma) * \mathcal{N}(0, \sigma^2 \mathrm{I}_d)$. The posterior score can be decomposed as the sum of the analytical likelihood score and the neural score prior:

$$\nabla_\kappa \log p_\sigma(\kappa|\gamma) = \nabla_\kappa \log p_\sigma(\gamma|\kappa) + \nabla_\kappa \log p_\sigma(\kappa) \tag{3}$$

Therefore, to sample a convergence map $\hat{\kappa} \sim p(\kappa|\gamma)$, one need to initialize an MCMC with a Multivariate Normal realization of sufficiently high variance T to be associated with the convolved posterior at high temperature $p_T(\kappa|\gamma)$. Then, running the MCMC while decreasing the temperature with a geometric schedule, the chain converges towards a sample of the posterior distribution. We show these posterior samples, in Remy et al 2022, Fig. 7. One can observe that these highly resolved maps look very similar to the κTNG simulation, both at large and small scales. Furthermore, we show that the samples and the target convergence power spectra are in very good agreement. Among the samples, more variations can be observed outside the survey region, since there was no data to constrain the reconstruction, and some cluster inside the survey region also show variation because of the shape noise. We report in Table 1 of Remy et al. (2022) [5] the evaluation metrics of mass-mapping and show that it achieves state-of-the-art reconstruction level.

4 Reconstruction of the HST/ACS COSMOS convergence field

Eventually, we applied this method, using the shape catalog from Schrabback et al. (2010) [13], to the reconstruction of the highest quality HST/ACS COSMOS mass-map to date. See Figure 1 for a comparison between the Massey et al. (2007) [14] mass-map and the `DLPosterior` mean. We do not only provide the posterior mean, but also a set of posterior samples which can be used for uncertainty quantification and the computation of higher moments, see the variance map in Remy et al. (2022) for instance.

References

1. Nick Kaiser and Gordon Squires. Mapping the dark matter with weak gravitational lensing. *The Astrophysical Journal*, 404:441, 2 1993.
2. F. Lanusse, J. L. Starck, A. Leonard, and S. Pires. High resolution weak lensing mass mapping combining shear and flexion. *Astronomy and Astrophysics*, 591, 2016.
3. J. L. Starck, K. E. Themelis, N. Jeffrey, A. Peel, and F. Lanusse. Weak-lensing mass reconstruction using sparsity and a gaussian random field. *A&A*, 649:A99, May 2021.
4. Niall Jeffrey, François Lanusse, Ofer Lahav, and Jean-Luc Starck. Deep learning dark matter map reconstructions from DES SV weak lensing data. *Monthly Notices of the Royal Astronomical Society*, 492(4):5023–5029, March 2020.

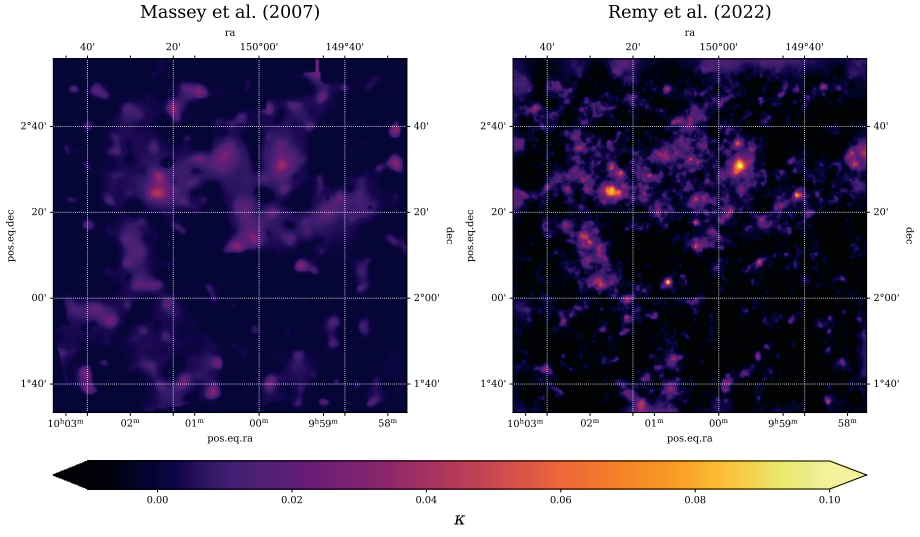

Figure 1 – Reconstructions of the HST/ACS COSMOS field. The *left panel* is the mass map presented in Massey et al. (2007) computed using a variant of the Kaiser & Squires (1993) method. The *right panel* is the mean of the full posterior distribution, with a prior learned on the κTNG suite of simulations.

5. Benjamin Remy, Francois Lanusse, Niall Jeffrey, Jean-Luc Starck, Ken Osato, and Tim Schrabback. Probabilistic mass mapping with neural score estimation. 2022.
6. Ken Osato, Jia Liu, and Zoltán Haiman. κTNG: effect of baryonic processes on weak lensing with IllustrisTNG simulations. *Monthly Notices of the Royal Astronomical Society*, 502(4):5593–5602, April 2021.
7. Aapo Hyvärinen. Estimation of Non-Normalized Statistical Models by Score Matching. *Journal of Machine Learning Research*, 6:695–708, 2005.
8. Pascal Vincent. A connection between scorematching and denoising autoencoders. *Neural Computation*, 23(7):1661–1674, 2011.
9. Guillaume Alain and Yoshua Bengio. What regularized auto-encoders learn from the data generating distribution. In *ICLR 2013 - Conference Track Proceedings*, volume 15, pages 3743–3773, 2013.
10. Radford M. Neal. MCMC using hamiltonian dynamics. *Handbook of Markov Chain Monte Carlo*, pages 113–162, 2011.
11. Michael Betancourt. A Conceptual Introduction to Hamiltonian Monte Carlo. Technical report, 2017.
12. Yang Song and Stefano Ermon. Generative Modeling by Estimating Gradients of the Data Distribution. In *NeurIPS*, 2019.
13. T. Schrabback, T. Erben, P. Simon, J.-M. Miralles, P. Schneider, C. Heymans, T. Eifler, R. A. E. Fosbury, W. Freudling, M. Hetterscheidt, H. Hildebrandt, and N. Pirzkal. Cosmic shear analysis of archival HST/ACS data. *Astronomy & Astrophysics*, 468(3):823–847, 6 2007.
14. Richard Massey, Jason Rhodes, Richard Ellis, N. Scoville, Alexie Leauthaud, A. Finoguenov, Peter Capak, David Bacon, Herve Aussel, Jean-Paul Kneib, Anton Koekemoer, Henry McCracken, Bahram Mobasher, S. Pires, Alexandre Refregier, Shunji Sasaki, Jean-Luc Starck, Yoshi Taniguchi, Andy Taylor, and James Taylor. Dark matter maps reveal cosmic scaffolding. *Nature*, 445:286–90, 02 2007.

Is there a tension on the amplitude of matter fluctuations (S_8) in the ΛCDM model ?

A. Blanchard [1], S. Ilić [2,3,1]
[1] *IRAP, Université de Toulouse, CNRS, CNES, UPS, Toulouse, France*
[2] *Université Paris-Saclay, CNRS/IN2P3, IJCLab, 91405 Orsay, France*
[3] *Centre National d'Etudes Spatiales, Toulouse, France*

The amplitude of matter fluctuations at low-redshift inferred from the abundance of clusters of galaxies appeared lower than predicted from CMB data within the ΛCDM model. The eBOSS survey results provide the best current measurements of galaxy distribution properties, constituting the summary of a long-term SDSS effort. Among these, the amplitude of the matter fluctuations, expressed in terms of the S_8 parameter, is measured at several redshifts thanks to redshift-space distortions (RSD). These data by themselves do not provide strong constraints but are powerful when used in combination with others. In this work, we discuss the impact for the standard model of the eBOSS measurements when combined with the Planck data and the consequence on the S_8 amplitude on the calibration of galaxy cluster masses.

1 Introduction

1.1 Successes of ΛCDM

After the discovery of fluctuations in the cosmological background radiation by COBE [1], progress has been rapid in the field of observational cosmology: small scales fluctuations were convincingly indicative of a flat universe [2,3,4] and after the indication of the accelerated expansion from the Hubble diagram of type Ia SN [5,6], the ΛCDM has emerged as the standard model of cosmology. A further impressive success was obtained with the measurements of the correlation function of galaxies from the Sloan Digital Sky Survey (SDSS), including the detection of the BAO peak [7].

Since that time, the accuracy of data has remarkably improved: CMB measurements with Planck have achieved sub-percent accuracy, reaching a precision of the order of one percent for ΛCDM parameters, making it the reference for the standard model. Thanks to larger and larger galaxy surveys, the properties of the 3D matter distribution in the late universe (roughly at redshifts $z < 3$) have been sampled in detail, the final eBOSS survey providing the result of more than twenty years of efforts[8]. Moreover, large-area deep photometric surveys are now

providing additional direct information on the total matter distribution.

While these data were supporting the ΛCDM model during the 2000−2015 period, several observations were claimed to challenge the validity of this standard paradigm. These tensions appear from the confrontation between cosmological parameters inferred from low-redshift data with values inferred from data based on early physics (CMB and BAO). Many of these potential tensions occur on small scales, but those scales are non-linear and subject to complications due to the possibly complex baryonic physics [9]. Nevertheless, two problems are regarded as the most problematic: the local value of the Hubble constant [10] and the amplitude of the matter fluctuations in the late universe. These tensions are the topic of numerous recent reviews [11,12]. In the following, we only address the second issue.

The abundance of clusters, the weak lensing field (obtained from wide field photometric surveys) and redshift-space distortions (RSD, that are obtained from redshift survey are techniques) are often referred to for the measurements of the amplitude of matter fluctuations. This amplitude is traditionally expressed in term of σ_8, the r.m.s. fluctuations of matter in a sphere of $8h^{-1}$Mpc. However, for several probes this quantity significantly varies with the density parameter Ω_m therefore an alternative parameter has been introduced, S_8, defined as:

$$S_8 = \sigma_8 \left(\frac{\Omega_m}{0.3}\right)^{1/2} \tag{1}$$

This quantity is well-adapted for constraints obtained from clusters abundance. A picture illustrative of the tension on S_8 is provided in Figure 6 of a recent article [13]. From this, it seems that the values among different probes are consistent with an average value around 0.75. For instance, in the recent "H_0 Olympics" work [14], $S_8 \sim 0.76 \pm 0.022$ was used as one of the constraints to distinguish between models. This value is in tension with the latest value from Planck CMB $S_8 = 0.834 \pm 0.016$ [15]. However, recent DES 3yr 3×2 pt measurements provided $S_8 \sim 0.776 \pm 0.017$, a value that is claimed to be consistent with Planck for ΛCDM [17].

2 Clusters for cosmology

The Press and Schechter formalism [18] and its extensions provide a framework in which the non-linear mass function of halos can be computed theoretically once the cosmological model and the fluctuations are set. This has been tested extensively in the past by numerical simulations, and fitting formula are now provided with an accuracy better than 20% for dark matter only simulations [19]. Inclusion of neutrinos has been studied and the role of baryons although still uncertain is believed to be understood sufficiently. This allows one to use cluster abundances as an useful tool to constrain cosmological models.

2.1 Principles

The basic idea is that once a cosmological model is specified (through the cosmological parameters and the properties of the fluctuations) the abundance of clusters can be predicted. A specific interest of this test is that the evolution of the abundance is much sensitive to the growth rate of fluctuations [20]. The drawback of this approach is that ones need the knowledge of the relation between halos and observed objects in the sky. Scaling arguments are a powerful way to identify the dependence on mass and redshift. For instance the relation between x-ray temperature and their mass of clusters is expected to follow the relation:

$$T_X = A_{T-M} (h\, M_\Delta)^{2/3} \left(\frac{\Omega_m \Delta(z)}{178}\right)^{1/3} (1+z) \tag{2}$$

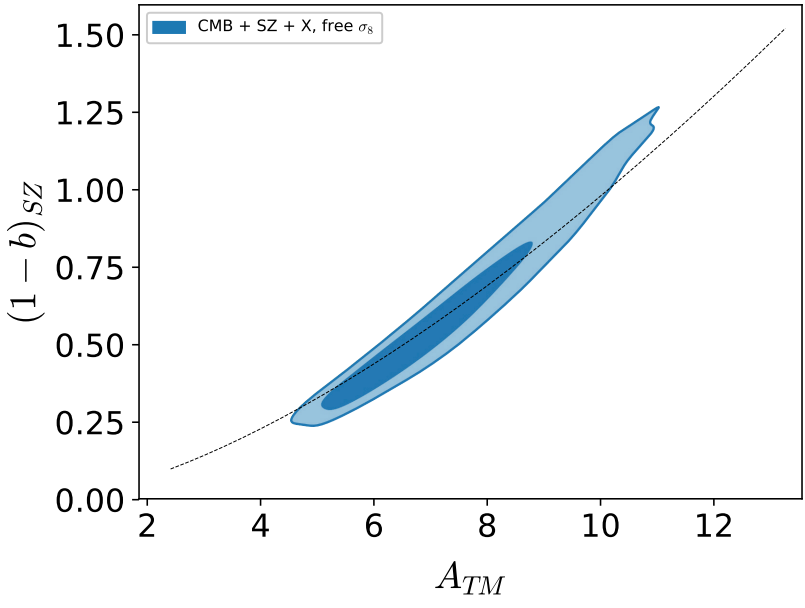

Figure 1 – Cluster mass calibrations ($1-b$ for SZ and A_{TM} for x-ray) for the ΛCDM combining cluster data with Planck CMB but low redshift σ_8 being let free i.e. not fixed from Planck CMB. Blue contours are 1 and 2 σ regions.

in which the calibration A_{T-M} is unknown. A similar scaling relation can be established for the Sunyaev-Zeldovich signal:

$$1.2\,h^{8/3}A_{T-M}f_\nu(x)f_B M_{15}^{5/3}\left(\frac{\Omega\Delta(z)}{178}\right)^{1/3}(1+z)/D^2(z)\mathrm{mJy} \tag{3}$$

which can be reformulated in term of the so-called hydrostatic bias parameter $1-b$:

$$\propto((1-b)M_{15})^{5/3}\left(\frac{\Delta(z)}{178}\right)^{1/3} \tag{4}$$

2.2 Application to clusters counts

The above tools allows us to fit clusters temperature distribution or luminosity function, as well as clusters number counts for cosmological purpose. At this point, there are two approaches: either the calibration is taken as a nuisance parameter which is left free in the fitting procedure, an approach dubbed self-calibration [21,22] or the calibration is taken from some independent data. This latter approach is the one which has been followed in the Planck collaboration for the first adjustment of SZ number counts, using a fiducial calibration of $1-b=0.8$ [23] leading to $S_8\sim 0.74$. Although caution about the role of calibration in this conclusion was emphasized, this work certainly had a strong influence in highlighting a possible tension between the value inferred from low-redshift data and that derived from the Planck CMB: the observed number counts of SZ clusters were 3 or 4 times less than predicted (see figure 7 in Planck2013. XX. [23]). Of course this tension disappears if the calibration is left free. This is illustrated by figure 1: its shows the contours in the calibration plane (A_{TM},$1-b$) for ΛCDM models matching cluster counts and Planck CMB, but leaving the present day amplitude of matter fluctuations σ_8 free.

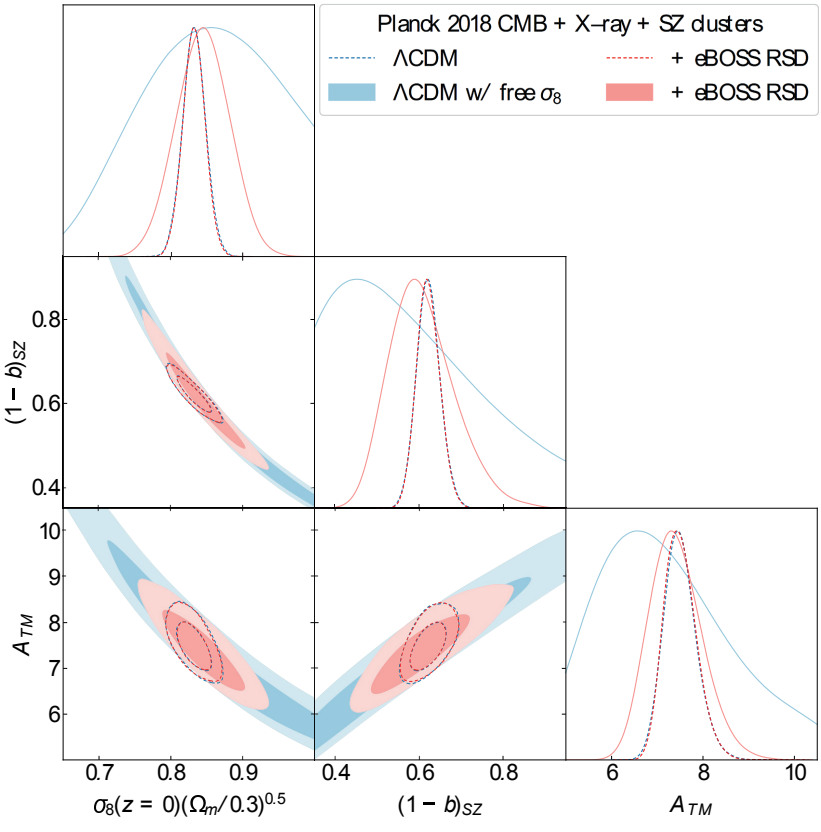

Figure 2 – Usual triplot for S_8 and cluster mass calibrations ($1-b$ for SZ and A_{TM} for x-ray). Lines show the ΛCDM calibration assuming the σ_8 from Planck. Blue contours show the (weak) constraints when this amplitude is left as a free parameter. The corresponding likelihoods shrink down when the eBOSS RSD data are added (red contours), in very good agreement with those derived from the full Planck CMB (lines).

The line correspond to the relation between A_{TM} and $1-b$ leading to the same mass for a sample of clusters for which both x-ray and SZ data are available [16].

The tension appears when the calibration is estimated while keeping the present day amplitude of matter fluctuations σ_8 determined by Planck CMB. On figure 2, the dashed lines show the contours on calibrations for ΛCDM models normalized from Planck CMB: for SZ the preferred calibration is $1-b \sim 0.6$ and for x-ray clusters $A_{TM} \sim 7.5$ keV. The likelihoods on calibrations are shown in figure 3: the fiducial value $1-b=0.8$ is almost 6 σ away from the value normalized from Planck CMB (green lines).

3 Combining with RSD from eBOSS

3.1 Implication for the cluster calibrations

Using Planck CMB and clusters samples together, the amplitude of matter fluctuations at low-redshift is treated as a free parameter, following the self-calibration method, the constraints

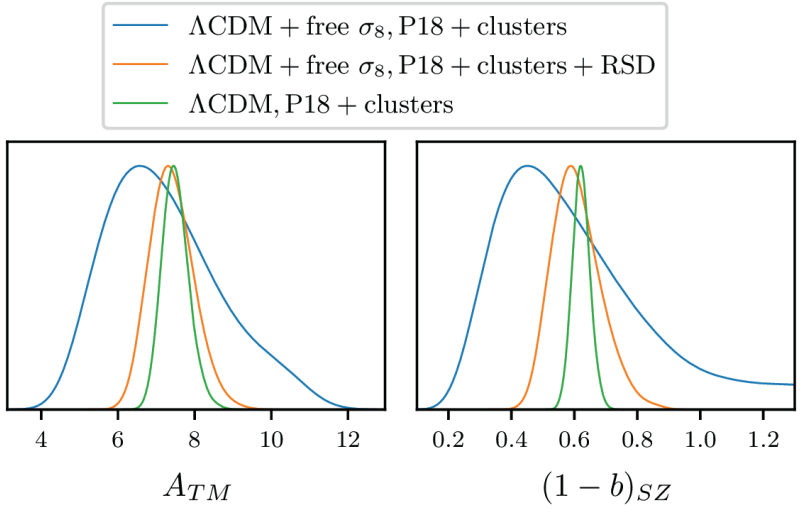

Figure 3 – Normalized likelihood on clusters mass calibration in ΛCDM. Green line: data used are the Planck CMB plus x-ray and SZ clusters samples, the amplitude of matter σ_8 is constrained by Planck. Blue line: same data but the amplitude σ_8 being left free. Orange line: the amplitude σ_8 being left free, same data with the addition of the $f\sigma_8$ amplitude from eBOSS.

we obtained on the calibration (and thereby on σ_8) are weak: this can be seen from figures 2 and 3 (blue contours and blue lines), even if the likelihood on the calibration is not flat, as low calibration ($1-b \sim 0.5$) is preferred but not at a statistically significant level (slightly above 1σ). We have therefore used an additional low-redshift data set recently provided by the eBOSS summary [17], that is the data on $f\sigma_8$ measured by RSD (see their table 3). By its own this data set does not provide strong constraint on ΛCDM (blue contours in their Figure 9 left). However, using this data in combination with Planck but still leaving the amplitude of matter at low-redshift as a parameter which is not determined by Planck CMB, we obtained the red contours and lines figures 2 and 3. The calibrations for clusters are then completely consistent with what was derived when the amplitude of σ_8 from Planck is kept.

3.2 Implication for the amplitude of matter fluctuations.

A direct look at the amplitude of matter fluctuations, though the S_8 parameter is illuminating. This parameter is the first variable in abscissa in figure 2. This also summarized in figure 4: again with Planck CMB and clusters samples together, the amplitude of matter at low-redshift is treated as a free parameter, the constraint on S_8 is weak (blue contours). However, with the addition eBOSS RSD data we obtain tight contours (orange contours). This is an important result : these low-redshift data restricted by the priors provided by Planck on all parameters but σ_8 lead to a rather high value of the amplitude [24]:

$$S_8 \equiv \sigma_8 \left(\frac{\Omega_m}{0.3}\right)^{0.5} = 0.841 \pm 0.038 \tag{5}$$

This value is still not statistically very discriminant, as it is only 2.4 σ away from $S_8 \sim 0.75$, but certainly indicative that RSD data are subject to significant possible biases, as for instance Benisty (2021) obtained $S_8 \sim 0.70 \pm 0.38$ [25] (and $\Omega_M \sim 0.201 \pm 0.035$), while using a larger set of data, with possible unidentified correlations. The eBOSS data have been extensively tested

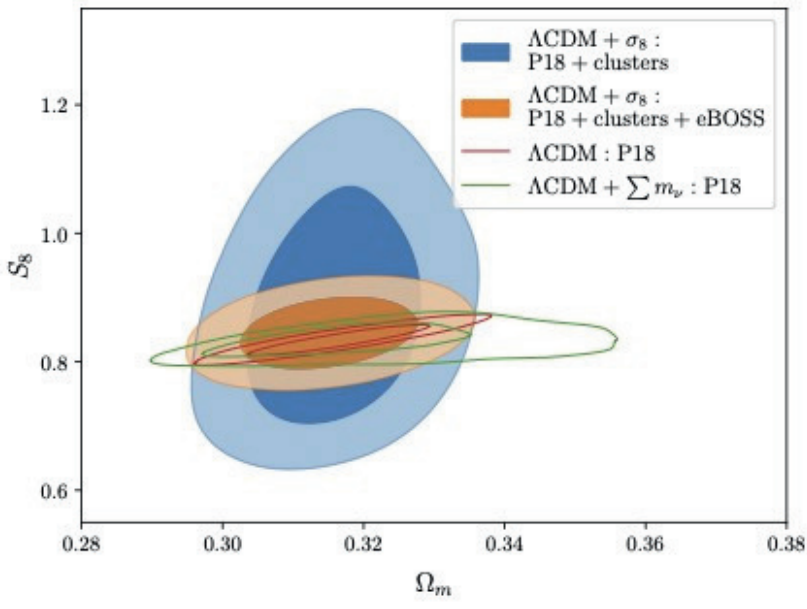

Figure 4 – The amplitude of matter fluctuations S_8: red contours are 1 and 2 σ from Planck CMB (green lines with massive neutrinos, showing that S_8 is essentially the same). The blue areas correspond to the 1 and 2 σ derived from Planck + (x-ray and SZ) clusters counts, with the amplitude of matter at $z = 0$ being left as a free parameter *i.e.* not derived from Planck CMB (contrary to red contours) and free cluster calibration. The orange contours are obtained by adding the RSD data from eBOSS. This illustrates the fact that eBOSS RSD lead to an amplitude of matter fluctuations which is entirely consistent with Planck CMB.

against mock samples to ensure that there derived values are not biased [17]. This provides an important check on their reliability.

4 Conclusions

The (spatially flat) ΛCDM model is a remarkably simple model, based on standard physics, that has been very successful in accounting for the main cosmological probes on large scales CMB, LSS and the Hubble diagram of type Ia supernovae [a]. Over the last ten years the emergence of tensions has gained importance. The SZ cluster number counts from Planck has played an important role for promoting a possible low amplitude of matter fluctuations at low-redshift σ_8, a concern which was existing before. During the last ten years, this low amplitude has been obtained from other probes like the weak lensing surveys and redshift spectral distortion, comforting its relevance.

However, the recent DES3yr data concluded to a higher final value, consistent with Planck when clustering data are taken into account [17]. It has also been pointed out that weak lensing data are sensitive to non-linear scale, that may be affected by baryonic physics [26]. An indication statistically significant of a low matter amplitude would be critical as this would be a clear indication of physics beyond the standard ΛCDM.

[a] Of course this model implies the existence of two new components in the universe: non-baryonic dark matter and a cosmological constant. However, these components remain "simple", as the cosmological constant dates back to 1917 and the CDM is the simplest form of matter one could think of.

In our recent work [24], we have examined the eBOSS RSD data with priors on cosmological parameters from Planck, leaving the amplitude of matter fluctuations at low-redshift σ_8 as a free parameter. The motivation for that is that CMB data provide stringent constraints on the universe at $z \sim 1100$ but does not directly constrain the present day amplitude. We combined this data with clusters counts leaving their mass calibration free. This has allowed us to show that the amplitude of matter fluctuations at low-redshift could actually be consistent with Planck CMB. The consequence for clusters is that the calibration of their mass is away from the fiducial value used by Planck2013. XX. [23]. Indeed clusters mass estimation from their observed properties is a long-standing subject of debates. Removing uncertainties on cluster mass is critical for cluster cosmology. This is certainly connected to the physics of baryons as it is clear than non-gravitational process like heating and cooling are critical for the shaping of their internal physical properties [27].

Acknowledgments

SI thanks the Centre national d'études spatiales which supports his postdoctoral research contract.

References

1. Bennett C. L., Banday A. J., Gorski K. M., Hinshaw G., Jackson P., Keegstra P., Kogut A., et al., 1996, ApJL, 464, L1. doi:10.1086/310075
2. Lineweaver C. H., Barbosa D., Blanchard A., Bartlett J. G., 1997, A&A, 322, 365
3. Lineweaver C. H., Barbosa D., 1998, ApJ, 496, 624. doi:10.1086/305408
4. de Bernardis P., Ade P. A. R., Bock J. J., Bond J. R., Borrill J., Boscaleri A., Coble K., et al., 2000, Natur, 404, 955. doi:10.1038/35010035
5. Riess A. G., Filippenko A. V., Challis P., Clocchiatti A., Diercks A., Garnavich P. M., Gilliland R. L., et al., 1998, AJ, 116, 1009. doi:10.1086/300499
6. Perlmutter S., Aldering G., Goldhaber G., Knop R. A., Nugent P., Castro P. G., Deustua S., et al., 1999, ApJ, 517, 565. doi:10.1086/307221
7. Eisenstein D. J., Zehavi I., Hogg D. W., Scoccimarro R., Blanton M. R., Nichol R. C., Scranton R., et al., 2005, ApJ, 633, 560. doi:10.1086/466512
8. Alam S., Aubert M., Avila S., Balland C., Bautista J. E., Bershady M. A., Bizyaev D., et al., 2021, PhRvD, 103, 083533. doi:10.1103/PhysRevD.103.083533
9. Bull P., Akrami Y., Adamek J., Baker T., Bellini E., Beltrán Jiménez J., Bentivegna E., et al., 2016, PDU, 12, 56. doi:10.1016/j.dark.2016.02.001
10. Riess A. G., Yuan W., Macri L. M., Scolnic D., Brout D., Casertano S., Jones D. O., et al., 2021, arXiv, arXiv:2112.04510
11. Abdalla E., Abellán G. F., Aboubrahim A., Agnello A., Akarsu O., Akrami Y., Alestas G., et al., 2022, arXiv, arXiv:2203.06142
12. Di Valentino E., Mena O., Pan S., Visinelli L., Yang W., Melchiorri A., Mota D. F., et al., 2021, CQGra, 38, 153001. doi:10.1088/1361-6382/ac086d
13. Stahl B. E., de Jaeger T., Boruah S. S., Zheng W., Filippenko A. V., Hudson M. J., 2021, MNRAS, 505, 2349. doi:10.1093/mnras/stab1446
14. Schöneberg N., Abellán G. F., Pérez Sánchez A., Witte S. J., Poulin V., Lesgourgues J., 2021, arXiv, arXiv:2107.10291
15. Planck Collaboration, Aghanim N., Akrami Y., Ashdown M., Aumont J., Baccigalupi C., Ballardini M., et al., 2020, A&A, 641, A6. doi:10.1051/0004-6361/201833910
16. Ilić S., Sakr Z., Blanchard A., 2019, A&A, 631, A96. doi:10.1051/0004-6361/201936423
17. Abbott T. M. C., Aguena M., Alarcon A., Allam S., Alves O., Amon A., Andrade-Oliveira F., et al., 2022, PhRvD, 105, 023520. doi:10.1103/PhysRevD.105.023520

18. Press W. H., Schechter P., 1974, ApJ, 187, 425. doi:10.1086/152650
19. Despali G., Giocoli C., Angulo R. E., Tormen G., Sheth R. K., Baso G., Moscardini L., 2016, MNRAS, 456, 2486. doi:10.1093/mnras/stv2842
20. Blanchard A., Bartlett J. G., 1998, A&A, 332, L49
21. Hu W., 2003, PhRvD, 67, 081304. doi:10.1103/PhysRevD.67.081304
22. Lima M., Hu W., 2004, PhRvD, 70, 043504. doi:10.1103/PhysRevD.70.043504
23. Planck Collaboration, Ade P. A. R., Aghanim N., Armitage-Caplan C., Arnaud M., Ashdown M., Atrio-Barandela F., et al., 2014, A&A, 571, A20. doi:10.1051/0004-6361/201321521
24. Blanchard A., Ilić S., 2021, A&A, 656, A75. doi:10.1051/0004-6361/202140974
25. Benisty D., 2021, PDU, 31, 100766. doi:10.1016/j.dark.2020.100766
26. Amon A., Robertson N. C., Miyatake H., Heymans C., White M., DeRose J., Yuan S., et al., 2022, arXiv, arXiv:2202.07440
27. Voit G. M., 2005, RvMP, 77, 207. doi:10.1103/RevModPhys.77.207

The H_0 olympics: a fair ranking of proposed models

N. Schöneberg, A. P. Sánchez, J. Lesgourgues
Institute for Theoretical Particle Physics and Cosmology (TTK), RWTH Aachen University, D-52056 Aachen, Germany.

G.F. Abellán, V. Poulin
Laboratoire Univers & Particules de Montpellier (LUPM), CNRS & Université de Montpellier, Place Eugène Bataillon, F-34095 Montpellier Cedex 05, France

S. J. Witte
GRAPPA Institute, Institute for Theoretical Physics Amsterdam and Delta Institute for Theoretical Physics, University of Amsterdam, Science Park 904, 1098 XH Amsterdam, The Netherlands

Despite the remarkable success of the Λ Cold Dark Matter (ΛCDM) cosmological model, a growing discrepancy has emerged between the value of the Hubble constant H_0 measured using the local distance ladder and the value inferred using the cosmic microwave background and galaxy surveys. While a vast array of ΛCDM extensions have been proposed to explain these discordant observations, understanding the (relative) success of these models in resolving the tension has proven difficult – this is a direct consequence of the fact that each model has been subjected to differing, and typically incomplete, compilations of cosmological data. In this talk, I discuss a systematic comparison of seventeen different models which have been proposed to resolve the H_0 tension, and explain how to quantify the relative success of each using a series of metrics and a vast array of data combinations.

1 Introduction

The "Hubble tension" refers to the 5σ mismatch between the value of the Hubble constant measured by the SH0ES collaboration using the Cepheid-calibrated cosmic distance ladder ($H_0 = 73.04 \pm 1.04$ km/s/Mpc [1]) and the value inferred by Planck's observations of the cosmic microwave background (CMB) assuming the ΛCDM model ($H_0 = 67.27 \pm 0.60$ km/s/Mpc [2]) .

The problem, however, is more severe than the naïve comparison between Planck and SH0ES may suggest. On the one hand, one can consider several high-redshift calibrations of ΛCDM which are Planck-independent or even CMB-independent, and they all result in values of H_0 in strong agreement with the value inferred by Planck. On the other hand, alternative methods for directly measuring the local expansion rate tend to yield values of H_0 systematically larger than the Planck inferred value. While an unknown systematic effect at the origin of this discrepancy is not excluded, the existence of several independent observations disfavoring the ΛCDM predictions strengthen the case for new physics.

The primary goal of this work is to create a comprehensive and systematic comparison of the relative success of various proposed solutions to the H_0 tension – the broader intent being to better understand the successes and drawbacks of each approach, and to generate a meaningful set of benchmarks for future proposals.

2 Brief overview of models entering the contest

We have considered seventeen different models which are intended to be representative of the wide variety of models presented in the literature, such as those listed in Ref. [3] First, our analysis includes six early-universe models featuring extra relativistic relics: Free-streaming Dark Radiation [$\Delta N_{\rm ur}$], Self-Interacting Dark Radiation [SIDR], Self-interacting Dark Radiation scattering on Dark Matter [DR-DM], Free-streaming plus self-interacting Dark Radiation [mixed DR], Self-interacting neutrinos plus free-streaming Dark Radiation [SIν+DR], and one model featuring a Majoron [Majoron].
Second, we consider six early-universe models that don't involve dark radiation: a primordial magnetic field [primordial B], a varying effective electron mass [varying m_e], a varying effective electron mass in a curved universe [varying m_e+Ω_k], two models of Early Dark Energy [EDE] (a phenomenological EDE model and the theoretically better motivated New Early Dark Energy [NEDE] model), and an Early Modified Gravity model [EMG].
Finally, we compare four models with a modification of the late-time cosmological evolution, either due to Dark Energy (Late Dark Energy with Chevallier-Linder-Polarski parametrization [CPL], Phenomenological Emergent Dark Energy [PEDE]) or late decaying Dark Matter (fraction of CDM decaying into DR [DM $\rightarrow$ DR], CDM decaying into DR and WDM [DM $\rightarrow$ DR+WDM]). We implement PEDE in two ways: with a parametrisation of the DE density such that ΛCDM is recovered for a particular value of the additional parameter (Generalized Phenomenological Emergent Dark Energy [GPEDE]), or with another fixed value of this parameter assumed in many previous works [PEDE].

3 Statistical tests to quantify model success

For each model $\mathcal{M}$ and compilation of data sets $\mathcal{D}$, we discuss three ways to quantify the tension between the cosmological inferred value and the SH0ES experiment [a], each one related to a different question:

- Criterion 1: *When considering a dataset $\mathcal{D}$ not including SH0ES, what is the residual level of tension between the posterior on M_b inferred using $\mathcal{D}$ and the SH0ES measurement?* The tension on $x = M_b$ can be quantified through the Gaussian Tension (GT), defined as

$$\frac{\bar{x}_{\mathcal{D}} - \bar{x}_{\rm SH0ES}}{(\sigma^2_{\mathcal{D}} + \sigma^2_{\rm SH0ES})^{1/2}}\,, \tag{1}$$

  where $\overline{x}_i$ and σ_i are the mean and standard deviation of observation i. A problem of this metric is that it is only strictly valid if the parameter's posteriors are Gaussian. In addition, this criterion does not quantify how good (or bad) the χ^2 of the new model is. In order to avoid such problems, we instead use the two additional tests listed below.

- Criterion 2: *How does the addition of the SH0ES measurement to the data set $\mathcal{D}$ impact the fit within a particular model $\mathcal{M}$?* We compute the change in the effective best-fit chi-square $\chi^2 = -2\ln\mathcal{L}$ between the combined data set and the dataset $\mathcal{D}$ as

$$\Delta\chi^2 = \chi^2_{\rm min,\mathcal{D}+SH0ES} - \chi^2_{\rm min,\mathcal{D}}. \tag{2}$$

  The tension can simply be expressed as Tension=$\sqrt{\Delta\chi^2}$ in units of σ, which is identical to the $Q_{\rm DMAP}$ metric discussed in Ref. [5]. This criterion naturally generalizes the commonly used criterion discussed in point 1 to the case of non-Gaussian posteriors. However, it is

[a] We treat SH0ES not as a model-dependent measurement of H_0, but as a direct measurement of the intrinsic magnitude of supernovae Ia (SNIa), $M_b = -19.2435 \pm 0.0373$ [4]. This allows to take into account the correlation between the information contained in SH0ES and Pantheon catalog of remote SNIa.

sensitive to the effect of over-fitting, which usually requires Bayesian methods to compute Occam's razor factors. For this reason, we also consider a third criterion, which attempts to penalize overly complex models.

- Criterion 3: *When the dataset $\mathcal{D}$ includes the SH0ES likelihood, does the fit within a particular model $\mathcal{M}$ significantly improve upon that of ΛCDM?* We compute the Akaike Information Criterium (AIC) of the extended model $\mathcal{M}$ relative to that of ΛCDM , defined as

$$\Delta\text{AIC} = \chi^2_{\text{min},\mathcal{M}} - \chi^2_{\text{min},\Lambda\text{CDM}} + 2(N_{\mathcal{M}} - N_{\Lambda\text{CDM}}) \ , \tag{3}$$

  where $N_{\mathcal{M}}$ stands for the number of free parameters of the model. This metric attempts to penalize models which introduce new parameters that do not subsequently improve the fit. The ΔAIC criterion offers the advantage of being numerically cheap and prior independent, as opposed to several Bayesian estimators.

In the case of Tests 1 and 2 , we require models to reduce the tension below the 3σ level. For Test 3, we demand that the preference for the extended cosmology $\mathcal{M}$ over ΛCDM is larger than a "weak preference" on Jeffrey's scale, which leads to the criterion $\Delta\text{AIC} \leq -6.91$. As long as the $\Delta\chi^2$ computed for the AIC test is negative , we will conservatively consider that a model is successful when one of criterion 2 or 3 is fulfilled. To summarize the success of each suggested solution we attribute "medals" to models passing our tests: A model passing either criterion 2 or 3 receives a bronze medal. A model passing both criteria receives a silver medal. We reserve the gold medal for models that additionally pass criterion 1.

4 Results

For our baseline dataset, $\mathcal{D}_{\text{baseline}}$ = Planck 2018 (including TTTEEE and lensing)+ BAO (including BOSS DR12 + MGS + 6dFGS)+ Pantheon, the result of our main tests are summarized in Table 1. Firstly, none of the late-universe models are able to pass to the final. This was to be expected, since it was shown that for a wide range of smooth expansion histories at late-times – assuming the ΛCDM value of the sound horizon – the "inverse distance ladder" calibration [b] of Pantheon SNIa data cannot be made compatible with the direct calibration from SH0ES [6]. This is the main reason why late-time solutions are typically more constrained than early-time solutions, since the former cannot modify the sound horizon by definition. Secondly, the early-universe models involving dark radiation perform significantly better than late-universe models, but a majority are not successful enough to pass our pre-determined criteria. Thirdly, all the early-universe models that shift the sound horizon using an ingredient that is not dark radiation are successful in passing at least one of the tests.
In summary, the finalist models are, in order of increasing ΔAIC: EDE, varying m_e+Ω_k, NEDE, EMG, primordial B, varying m_e, Majoron and SIDR. Unfortunately, none of these models are able to relieve the S_8 tension, as illustrated in Fig. 1. We remark that this analysis corresponds to an extended dataset $\mathcal{D}_{\text{extended}} = \mathcal{D}_{\text{baseline}}$ + Redshift-Space-Distortions (from BOSS DR12, 6dFGS, MGS and eBOSS DR 14 quasars), Cosmic Chronometers and Lyman-α based high-z BAO.

5 Conclusions

We conclude that some of the models presented in this work can reduce the Hubble tension in a significant way, but there are still many difficulties to be overcome in the model building and

[b] The inverse distance ladder calibration of SNIa consists in making use of the determination of $D_A(z) \equiv D_L(z)/(1+z)^2$ as extracted from the BAO data that have been calibrated onto the CMB (or other determination of the sound horizon). The knowledge of the luminosity distance $D_L(0.1 \lesssim z \lesssim 1)$, together with the (uncalibrated) SNIa magnitude from the Pantheon survey, allows for a determination of the intrinsic SNIa magnitude. This determination depends on the assumed cosmological model in the pre-recombination era.

Table 1: Test of the models based on dataset $\mathcal{D}_{\rm baseline}$, using the direct measurement of M_b by SH0ES as the GT for the quantification of the tension (4^{th} column), the $Q_{\rm DMAP}$ criterion (5^{th} column), or the computation of the Δ AIC (7^{th} column).

Model	$\Delta N_{\rm param}$	M_B	Gaussian Tension	$Q_{\rm DMAP}$ Tension		$\Delta\chi^2$	ΔAIC		Finalist
ΛCDM	0	-19.416 ± 0.012	4.4σ	4.5σ	X	0.00	0.00	X	X
$\Delta N_{\rm ur}$	1	-19.395 ± 0.019	3.6σ	3.8σ	X	-6.10	-4.10	X	X
SIDR	1	-19.385 ± 0.024	3.2σ	3.3σ	X	-9.57	-7.57	✓	✓
mixed DR	2	-19.413 ± 0.036	3.3σ	3.4σ	X	-8.83	-4.83	X	X
DR-DM	2	-19.388 ± 0.026	3.2σ	3.1σ	X	-8.92	-4.92	X	X
SIν+DR	3	$-19.440^{+0.037}_{-0.039}$	3.8σ	3.9σ	X	-4.98	1.02	X	X
Majoron	3	$-19.380^{+0.027}_{-0.021}$	3.0σ	2.9σ	✓	-15.49	-9.49	✓	✓
primordial B	1	$-19.390^{+0.018}_{-0.024}$	3.5σ	3.5σ	X	-11.42	-9.42	✓	✓
varying m_e	1	-19.391 ± 0.034	2.9σ	2.9σ	✓	-12.27	-10.27	✓	✓
varying m_e+Ω_k	2	-19.368 ± 0.048	2.0σ	1.9σ	✓	-17.26	-13.26	✓	✓
EDE	3	$-19.390^{+0.016}_{-0.035}$	3.6σ	1.6σ	✓	-21.98	-15.98	✓	✓
NEDE	3	$-19.380^{+0.023}_{-0.040}$	3.1σ	1.9σ	✓	-18.93	-12.93	✓	✓
EMG	3	$-19.397^{+0.017}_{-0.023}$	3.7σ	2.3σ	✓	-18.56	-12.56	✓	✓
CPL	2	-19.400 ± 0.020	3.7σ	4.1σ	X	-4.94	-0.94	X	X
PEDE	0	-19.349 ± 0.013	2.7σ	2.8σ	✓	2.24	2.24	X	X
GPEDE	1	-19.400 ± 0.022	3.6σ	4.6σ	X	-0.45	1.55	X	X
DM $\rightarrow$ DR+WDM	2	-19.420 ± 0.012	4.5σ	4.5σ	X	-0.19	3.81	X	X
DM $\rightarrow$ DR	2	-19.410 ± 0.011	4.3σ	4.5σ	X	-0.53	3.47	X	X

in explaining the growing S_8-tension. Further work must be done to establish whether these remaining theoretical and observational issues can be overcome in a new concordant cosmology, one that may either build upon the models studied here, or perhaps lie in a yet unexplored direction.

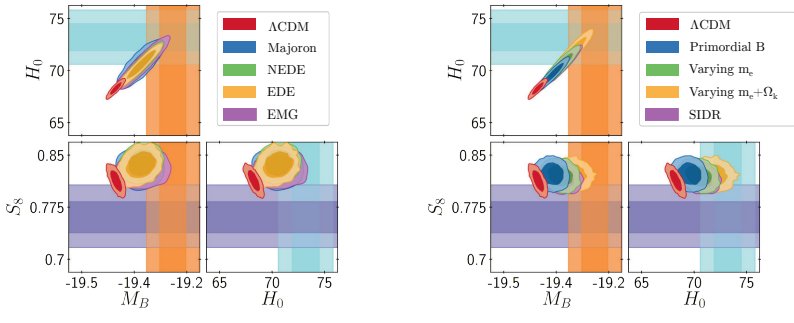

Figure 1 – Contours of $\{H_0, M_b, S_8\}$ obtained when considering the $\mathcal{D}_{\rm extended}$ dataset for the "finalists" models compared to ΛCDM. The purple band represents the S_8 measurement from KiDS-1000 [7].

References

1. Adam G. Riess et al. *arXiv:2112.04510*, December 2021.
2. N. Aghanim et al. *Astron. Astrophys.*, 641:A6, 2020.
3. Eleonora Di Valentino et al. *arXiv:2103.01183*, March 2021.
4. Adam G. Riess et al. *Astrophys. J. Lett.*, 908(1):L6, 2021.
5. Marco Raveri et al. *Phys. Rev. D*, 99(4):043506, 2019.
6. George Efstathiou. *arXiv:2103.08723*, March 2021.
7. Marika Asgari et al. *Astron. Astrophys.*, 645:A104, 2021.

An estimator for lensing potential from galaxy number counts

Viraj Nistane [a]
Université de Genève, Département de Physique Théorique and Centre for Astroparticle Physics, 24 quai Ernest-Ansermet, CH-1211 Genève 4, Switzerland

We derive an estimator for the lensing potential from galaxy number counts which contains a linear and a quadratic term. We show that this estimator has a much larger signal-to-noise ratio than the corresponding estimator from intensity mapping. This is due to the additional lensing term in the number count angular power spectrum which is present already at linear order. We estimate the signal-to-noise ratio for future photometric surveys. Particularly at high redshifts, $z \gtrsim 1.5$, the signal to noise ratio can become of order 30. Therefore, the number counts in photometric surveys would be an excellent means to measure tomographic lensing spectra.

1 Introduction

Light coming to us from far away sources is deflected by the intervening gravitational field due to cosmic structure which, in the regime of weak lensing and to first order in the cosmological perturbations, can be described by the lensing potential ϕ.

This work focuses on the measurement of the lensing potential at different redshifts using a new estimator similar to a *quadratic estimator* [1,2].

2 Galaxy number counts and lensing

Neglecting large scale relativistic effects which are relevant only at very large scales, the number counts at first order in perturbation theory are given by [3,4]

$$\Delta_g(z,\mathbf{n}) = b_g(z)\delta - \mathcal{H}^{-1}\mathbf{n}\boldsymbol{\nabla}(\mathbf{n}\cdot\mathbf{V}) - (2-5s(z))\,\kappa(z,\mathbf{n}) = \tilde{\Delta}_g(z,\mathbf{n}) - (2-5s(z))\,\kappa(z,\mathbf{n})\,. \quad (1)$$

The first two terms are the density fluctuation and the redshift space distortion (RSD) which we collect as $\tilde{\Delta}_g$ or $\Delta_g^{\rm std}$ as they are also called the 'standard terms'. The third term is proportional to the convergence, $\kappa(z,\mathbf{n}) = -\Delta_2\phi(z,\mathbf{n})/2$, where Δ_2 denotes the 2D Laplacian on the sphere. The term 2 in the pre-factor $(2-5s)$ of convergence in Eq. (1) takes into account the convergence of light rays due to lensing which lowers the number of galaxies per apparent surface area while the term $5s(z)$ accounts for the increase due to the enhancement of the flux in a flux limited

[a] arXiv:2201.04129, in collaboration with Mona Jalilvand, Julien Carron, Ruth Durrer, Martin Kunz

sample. Here $s(z)$ is the logarithmic derivative of the number density at the flux limit, F_*, of the survey, which corresponds to the luminosity $L_*(z) = 4\pi D_L(z)^2 F_*$ where $D_L(z)$ denotes the luminosity distance,

$$5s(z, F_*) = 2\,\frac{\partial \log \bar{n}(z, L)}{\partial \log L}\bigg|_{L=L_*(z)} . \tag{2}$$

While the first order expression is sufficient to compute the variance of the estimator, we want to consider number counts up to second order in perturbation theory for the signal. At second order (in $\boldsymbol{\ell}$-space and in the flat sky approximation) we obtain [5],

$$\begin{aligned}\Delta_g(\boldsymbol{\ell}, z) &= \tilde{\Delta}_g(\boldsymbol{\ell}, z) - \ell^2 \left(1 - \frac{5}{2}s(z)\right)\phi(\boldsymbol{\ell}, z) \\ &\quad - \int \frac{d^2\ell_1}{2\pi}\tilde{\Delta}_g(\boldsymbol{\ell}_1, z)\phi(\boldsymbol{\ell} - \boldsymbol{\ell}_1, z)\left[\left(1 - \frac{5}{2}s\right)(\boldsymbol{\ell} - \boldsymbol{\ell}_1)^2 + \boldsymbol{\ell}_1 \cdot (\boldsymbol{\ell} - \boldsymbol{\ell}_1)\right] . \end{aligned} \tag{3}$$

where we denote

$$g_\Delta(\ell, z) = -\ell^2\left(1 - \frac{5}{2}s(z)\right) \;\; ; \quad K_\Delta(\boldsymbol{\ell}_1, \boldsymbol{\ell}_2, z) = -\left(1 - \frac{5}{2}s(z)\right)(\boldsymbol{\ell}_2 - \boldsymbol{\ell}_1)^2 - \boldsymbol{\ell}_1 \cdot (\boldsymbol{\ell}_2 - \boldsymbol{\ell}_1) .$$

In K_Δ, the second term is the kernel of CMB lensing [6] and intensity mapping lensing [2], but the first term is new and only present for number counts. Also new is of course the entire first order term. For the ensemble average at fixed lensing potential this yields

$$\langle \Delta_g(\boldsymbol{\ell}, z)\rangle_\phi = g_\Delta(\ell, z)\phi(\boldsymbol{\ell}, z) \;;\; \langle \Delta_g(\boldsymbol{\ell}, z)\Delta_g(\boldsymbol{\ell}', z)\rangle_\phi = \delta(\boldsymbol{\ell} + \boldsymbol{\ell}')\tilde{C}_\ell(z) - \frac{1}{2\pi}\phi(\boldsymbol{\ell} + \boldsymbol{\ell}')f_\Delta(\boldsymbol{\ell}, \boldsymbol{\ell}') \tag{4}$$

where $f_X(\boldsymbol{\ell}, \boldsymbol{\ell}', z) = K_X(-\boldsymbol{\ell}, \boldsymbol{\ell}', z)\tilde{C}_\ell(z) + K_X(-\boldsymbol{\ell}', \boldsymbol{\ell}, z)\tilde{C}_{\ell'}(z)$

3 The LIN+QUAD estimator

The expectation value $\langle \cdots \rangle_\phi$ is an ensemble average only over any stochastic observable (here, Δ_g), at fixed lensing potential ϕ. This makes sense only if ϕ is (nearly) uncorrelated with Δ_g. For sufficiently high redshifts this is usually a good approximation as the lensing kernel peaks roughly in the middle between 0 and $r(z)$. We can now derive an estimator for $\phi(\mathbf{L})$ which combines the linear and the quadratic terms in X to which ϕ contributes. It is given by

$$\begin{aligned}\hat{\phi}_\Delta(\mathbf{L}, z) &= A_\Delta(L, z)N_\Delta(L, z)\int \frac{d^2\ell}{2\pi}X(\boldsymbol{\ell}, z)X(\mathbf{L} - \boldsymbol{\ell}, z)F_\Delta(\boldsymbol{\ell}, \mathbf{L} - \boldsymbol{\ell}, z) \\ &\quad + (1 - A_\Delta(L, z))\frac{X(\mathbf{L}, z)}{g_\Delta(L, z)} \end{aligned} \tag{5}$$

where

$$F_\Delta(\boldsymbol{\ell}_1, \boldsymbol{\ell}_2, z) = \frac{f_\Delta(\boldsymbol{\ell}_1, \boldsymbol{\ell}_2, z)}{2C_{\ell_1}(z)C_{\ell_2}(z)} \quad , \quad N_\Delta(L, z) = \left[\int \frac{d^2\ell}{(2\pi)^2}f_\Delta(\boldsymbol{\ell}, \mathbf{L} - \boldsymbol{\ell}, z)F_\Delta(\boldsymbol{\ell}, \mathbf{L} - \boldsymbol{\ell}, z)\right]^{-1} ,$$
$$\text{and} \qquad A_\Delta(L, z) = C_L(z)/\left(g_\Delta(L, z)^2 N_\Delta(L, z) + C_L(z)\right) .$$

By construction $\langle \hat{\phi}_\Delta(\mathbf{L}, z)\rangle_\phi = \phi(\mathbf{L}, z)$. Here, imposing that the quadratic part of the estimator is unbiased and has minimum variance allows us to choose F_Δ and N_Δ. Similar conditions for $\hat{\phi}_\Delta$ give us the factor A_Δ. We have assumed that the ϕ power spectrum, which is quadratic in ϕ, is smaller than both, C_L and N_Δ and can be neglected in these expressions. Note that while the $\tilde{C}_\ell$'s appearing in f_Δ are the theoretical spectra neglecting lensing, those appearing in F_Δ are the measured C_ℓ's, including both, lensing and (shot) noise. The total noise from the combined linear and quadratic terms then becomes

$$N_\Delta^{(\mathrm{tot})}(L, z) = \frac{C_L(z)N_\Delta(L, z)}{C_L(z) + g_\Delta^2(L, z)N_\Delta(L, z)} = \frac{1}{N_\Delta^{(\mathrm{lin})}} + \frac{1}{N_\Delta^{(\mathrm{quad})}} , \tag{6}$$

where $N_\Delta^{(\mathrm{quad})} \equiv N_\Delta$ and $N_\Delta^{(\mathrm{lin})} \equiv C_L/[L^4(1 - \frac{5}{2}s(z))^2]$.

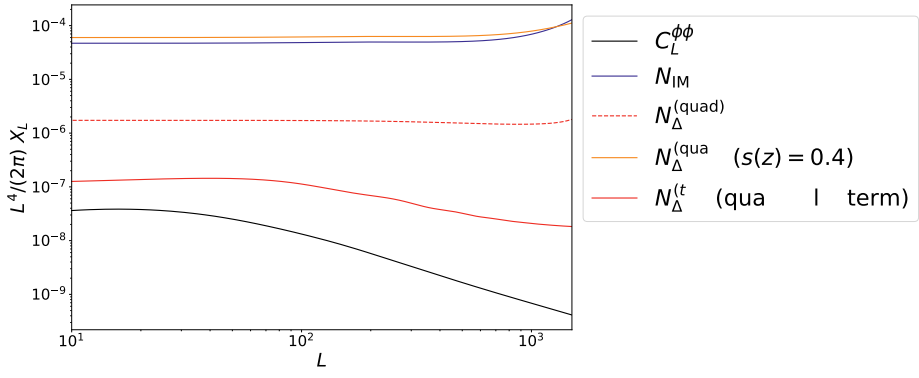

Figure 1: The lensing reconstruction noise for halofit power spectra for IM (HIRAX) and galaxy number counts (Euclid-like) for $z = 1.9$, $\Delta z = 0.5$. We also indicate the signal $C_\ell^{\phi\phi}$ for comparison. We also show the galaxy number count noise obtained when replacing $s(z)$ by 2/5. Note that the naive L^{-4} scaling of the noise holds very well for the quadratic noise, but the total noise, $N_\Delta^{\rm tot}$ decays faster for $L > 60$. This is due to the significantly smaller linear noise.

4 Signal-to-Noise (SNR)

We consider three exemplary photometric 15'000 square-degree surveys: (1) *Euclid-like* survey [7] with a limiting depth of 24, (2) *LSST-like-25* [8] with limiting magnitude $m_{\rm lim} = 25$, and (3) *LSST-like-27* with $m_{\rm lim} = 27$. Forecasts [9,10,11] for the number densities $n(z)$ and the magnification bias $s(z)$ are shown in Fig. 2. We also use the forecasts for the galaxy bias $b(z)$. The total signal-to-noise values per redshift bin evaluated using Eq. (7) for the estimator are shown in Fig. 3.

$$\left(\frac{S}{N}\right)^2(L,z) = \frac{f_{\rm sky}\,(2L+1)}{2}\left(\frac{C_L^{\phi\phi}(z)}{C_L^{\phi\phi}(z)+N_\Delta^{\rm tot}(L,z)}\right)^2;\ \left(\frac{S}{N}\right)_{\rm tot,z} = \sqrt{\sum_{L_{\rm min}=20}^{L_{\rm max}=1500}\left(\frac{S}{N}\right)^2(L,z)} \tag{7}$$

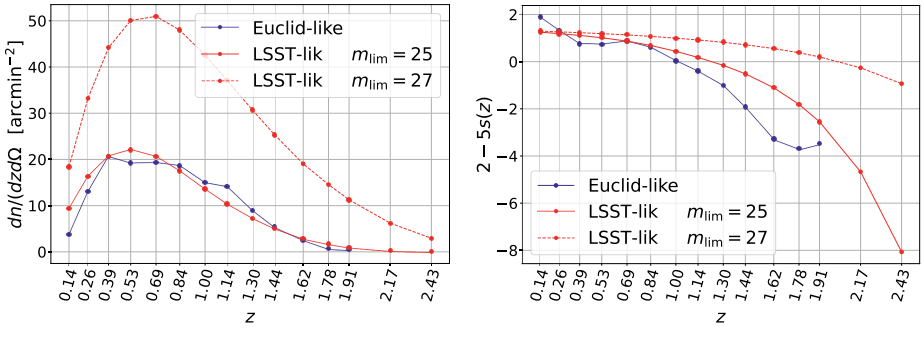

(a) (b)

Figure 2: (a) $\frac{dn}{dzd\Omega}$ [arcmin^{-2}], and (b) forecasts for the magnification bias $s(z)$, for the surveys [9,11] considered in this work.

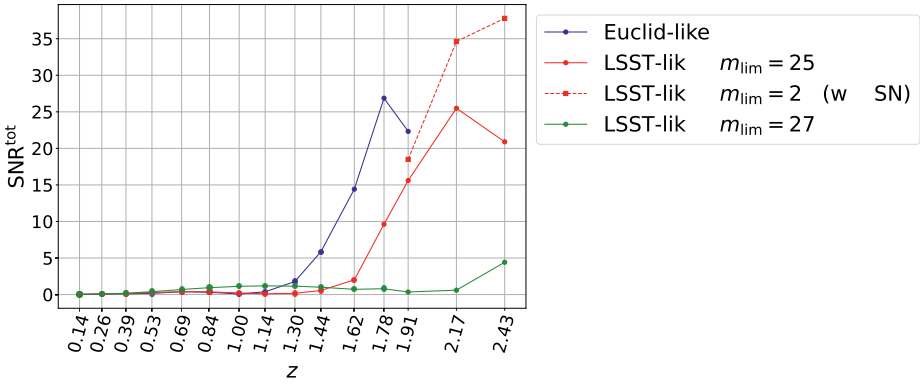

Figure 3: Total SNR per redshift bin plotted against the mean redshift of each bin for non-linear perturbation theory results for Euclid-like and LSST-like surveys. In the highest redshift bins of the LSST-like survey, shot noise starts to become important, the red-dashed curve shows the SNR that we would find without shot noise.

5 Conclusion

We have derived a new linear+quadratic estimator for the lensing potential from galaxy number count observations. Contrary to the CMB and intensity mapping, lensing contributes to number counts already at first order in perturbation theory. This leads to us connstructing an estimator for measuring ϕ with an additional linear contribution as compared to the quadratic estimator for intensity measurements. As a result, the estimator noise also has a linear contribution which is otherwise absent in CMB/IM. The kernel K_Δ of galaxy number count lensing already has an additional term (proportional to $(2-5s)$) which results in the quadratic noise of galaxy number counts estimator being more than an order lower than the quadratic noise (also the total estimator noise) of intensity mapping. In galaxy number counts, the linear noise contribution results in the total lensing reconstruction noise shifting further down by an order. For a high SNR (especially in high redshift bins where the lensing effect is more important), as maximizing $|2-5s(z)|$ is crucial for a high SNR, it may be more optimal in some cases to consider a higher flux limit F_* in order to increase this pre-factor, even though increasing F_* reduces the number density of galaxies and therefore increases the shot noise.

References

1. W. Hu and T. Okamoto, Astrophys. J. 574 (2002) 566–574
2. S. Foreman, P. D. Meerburg, A. van Engelen, and J. Meyers, JCAP 07 (2018) 046.
3. C. Bonvin and R. Durrer, Phys. Rev. D 84 (2011) 063505.
4. A. Challinor and A. Lewis, Phys. Rev. D 84 (2011) 043516.
5. J. T. Nielsen and R. Durrer, JCAP 03 (2017) 010.
6. Planck Collaboration, N. Aghanim et al., Astron. Astrophys. 641 (2020) A8.
7. EUCLID Collaboration, R. Laureijs et al., Euclid Definition Study Report.
8. LSST Project Collaboration, P. A. Abell et al., LSST Science Book, Version 2.0.
9. D. Alonso, P. Bull, P. G. Ferreira, R. Maartens, and M. Santos, Astrophys. J. 814 (2015), no. 2 145.
10. G. Jelic-Cizmek, F. Lepori, C. Bonvin, and R. Durrer, JCAP 04 (2021) 055
11. Euclid Collaboration, F. Lepori et al., arXiv:2110.05435

Dark Energy Survey Year 3 Results: Redshift Calibration of the MagLim Lens Sample from the combination of SOMPZ and clustering and its impact on Cosmology

Giulia Giannini [a]
Institut de Fisica d'Altes Energies (IFAE),
The Barcelona Institute of Science and Technology, Campus UAB, 08193 Bellaterra (Barcelona) Spain

We present an alternative calibration of the MagLim lens sample redshift distributions from the Dark Energy Survey (DES) first three years of data (Y3). The new calibration is based on a combination of a Self-Organising Maps based scheme and clustering redshifts to estimate redshift distributions and inherent uncertainties, which is expected to be more accurate than the original DES Y3 redshift calibration of the lens sample. The new calibration is found to be in fairly agreement with the fiducial DES Y3 *n(z)* calibration, with only mild differences ($< 3\sigma$) in the means and widths of the distributions. We study the impact of this new calibration on cosmological constraints, analysing DES Y3 galaxy clustering and galaxy-galaxy lensing measurements, assuming a ΛCDM cosmology. We obtain $\Omega_{\rm m} = 0,30 \pm 0.04$, $\sigma_8 = 0.81 \pm 0.07$ and $S_8 = 0.81 \pm 0.04$, which implies a $\sim 0.4\sigma$ shift in the $\Omega - S_8$ plane compared to the fiducial DES Y3 results, highlighting the importance of the redshift calibration of the lens sample in multi-probe cosmological analyses.

1 Introduction

The Dark Energy Survey (DES [1]) is currently the largest photometric galaxy survey, with hundreds millions of galaxies detected in 5000 deg^2 in the southern hemisphere. The analysis of the first three years (Y3) of DES data [2] allowed to place tight constraints on cosmological parameters combining three measurements of two-point (3x2pt) correlation functions: *cosmic shear*, [3] [4] whose DES Y3 measurements involve the angular correlation of 100,000,000 galaxy shapes from the weak lensing sample [5]; *galaxy clustering* which correlates the positions of bright galaxies (the "lens" sample) [6]; *galaxy-galaxy lensing*: the cross-correlation function of galaxy shapes and the position of the galaxies of the lens sample [7].

The modelling of these correlation functions requires knowledge of the redshift distributions (*n(z)*) of both lens and source galaxies. Unfortunately, it is not feasible to obtain spectroscopic observations other than for a small fraction of our science sample. Cosmological surveys like DES therefore have to rely only on a few, noisy, broad-band fluxes, requiring robust and unbiased redshift calibration pipelines.

For the DES Y3 3x2pt analysis, two different lens samples were used. The first sample is defined by selecting luminous red galaxies through the "RedMaGiC" algorithm [8], which retains galaxies with high quality photometric redshift. The galaxies passing the RedMaGiC selection have, however, a low number density (3,000,000 galaxies). The second sample slightly compromises on the redshift accuracy to the benefit of a larger number density. The MagLim sample [9] is a magnitude-limited sample comprising roughly 10,000,000 galaxies. In the fiducial DES 3x2pt [2] and 2x2pt analyses [10], the MagLim sample *n(z)* have been characterised using the photometric

[a] E-mail: ggiannini@ifae.es

redshift code DNF [11], which provides per-galaxy estimates, but it does not characterise the uncertainties. The *n(z)* were then further calibrated by matching them to clustering redshift estimates (hereafter WZ), which relies on cross-correlation measurements with spectroscopic samples [12]. This calibration step also allowed to place uncertainties on the *n(z)* .

This work presents an additional and more sophisticated calibration of the redshift distributions of the lens sample, and study the impact of the new estimates on the cosmological constraints using DES Y3 galaxy clustering and galaxy-galaxy lensing measurements (2x2pt). We adopt an approach similar to the one adopted to characterise the redshift distributions of the DES Y3 weak lensing (WL) sample, presented in [13], [14]. This methodology also combines photometric and clustering constraints to produce redshift estimates, but it is more powerful than the fiducial redshift calibration adopted for the lenses for a number of reasons, as the combination improve each other method's weaknesses.

2 Redshift Inference Methodology

The methodology is a combination of two key techniques:

- photometric classification with Self-Organising Maps (SOM), known as the SOMPZ method [13]. It takes advantage of the deeper photometry of the 8 bands (ugrizYJHKs) of the DES deep fields, where galaxies with high-quality redshifts can be accurately classified in the deep colour space, to ensure small selection biases and uncertainties of DES wide field galaxies; galaxies from wide and deep fields are grouped into phenotypes using SOMs; redshifts in the deep fields are validated through high precision redshift samples, and are assigned back to the wide field by mapping the two SOMs through a transfer function, computed from the *Balrog* simulated catalog [15].

- clustering-based techniques (WZ), which allows to calibrate redshift distributions based on angular correlation with a reference sample with high-quality redshift estimates. This method does not suffer from the typical biases affecting photometric methods (e.g., lack of representative spectroscopic sample for calibration), which in turns help improving the robustness of our redshift estimates.

This two techniques are combined together to provide an estimate of the *n(z)* of the lens sample. Such a combination is powerful because it exploits the complementarity of the two methods, which are affected by two very different sets of biases and uncertainties.

In order to combine SOMPZ and WZ constraints, we write the clustering likelihood by forward modelling the full clustering signal and we introduce a systematic function Sys that absorbs uncertainties in our method, mostly driven by the lack of knowledge of $b_{\rm u}$ and its redshift dependence. The Sys is function of an order-6 Legendre polynomial. parameterized by $\mathbf{s} = \{s_1, s_2, \ldots\}$, that we will marginalize over.

We importance-sample $n(z)_{\rm pz}$ SOMPZ samples by assigning each a weight through the following likelihood

$$\mathcal{L}\mathrm{WZ}|n_{\rm u}(z), b_{\rm r}(z), \alpha_{\rm r}(z), w_{\rm DM}(z) = \int d\mathbf{s}\, d\mathbf{p}\, \exp[-\frac{1}{2}(w_{\rm ur} - \hat{w}_{\rm ur})^T \Sigma_w^{-1} (w_{\rm ur} - \hat{w}_{\rm ur}) p(\mathbf{s}) p(\mathbf{p}), \quad (1)$$

were $b_r(z_i)$,$b_u(z_i)$ are the galaxy biases, $\alpha_{\rm u}(z_i)$,$\alpha_{\rm r}(z_i)$ are the magnification coefficients, $w_{\rm DM}(z_i)$ is the clustering of dark matter estimated from theory assuming fixed cosmology. Σ_w is the clustering covariance, and $\mathbf{p} = b_{\rm u}, \alpha_{\rm u}$. In this work, we set the prior $p(\mathbf{s})$ to be a simple diagonal normal distribution informed by the measured auto-correlation of the MagLim sample. Note that for efficiency reasons, instead of importance-sampling the SOMPZ realisations, we implemented a Hamiltonian Monte Carlo sampler (HMC) that simultaneously sample the SOMPZ and WZ likelihood.

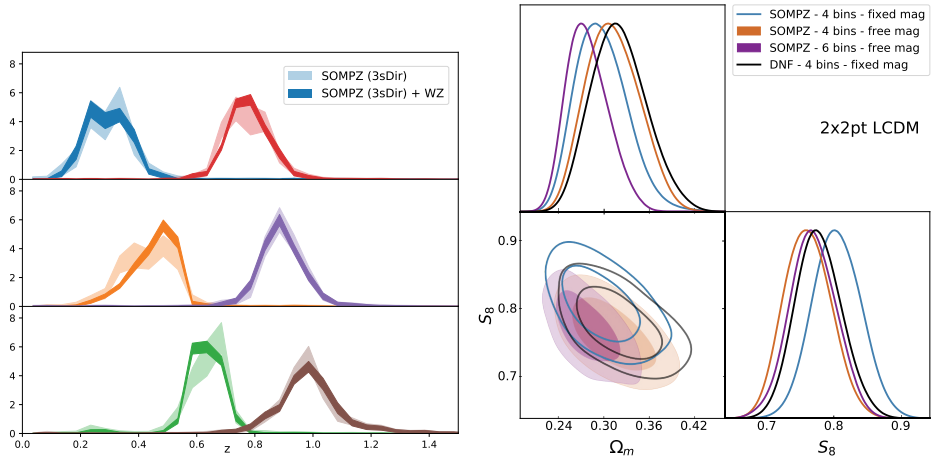

Figure 1 – *Left panel*:SOMPZ distributions before (lighter shades) and after the combination with WZ (solid shades) which produces tighter constraints on the *n(z)* shape. The bands represent the 1σ from the central value. *Right panel*: Posterior distributions of the cosmological parameters $\Omega_{\rm m}$, and S_8 for the ΛCDM analysis. The "fiducial" posteriors (black) have been obtained using the DNF+WZ *n(z)* and they are compared to the ones obtained using the SOMPZ+WZ *n(z)* for three different cases: 1) 4 bins and fixed magnification parameters; 2) 4 bins and marginalised over magnification parameters; 3) 6 bins and marginalising over magnification parameters. The 2D marginalised contours in both of these figures show the 68 per cent and 95 per cent confidence levels.

Table 1: Values of mean and width of the SOMPZ+WZ final ensemble of distributions and for the DNF estimate. The tension is computed by considering the uncertainties of both methods, summed in quadrature. We refer to these as are lower limits. Because the WZ measurement is very similar in the two cases, and the uncertainties summed in quadrature are correlated and therefore we are likely underestimating the tension.

		BIN 1	BIN 2	BIN 3	BIN 4	BIN 5	BIN 6
$\overline{z}$	SOMPZ	0.315±0.016	0.463±0.010	0.633±0.009	0.781±0.008	0.893±0.009	0.990±0.012
	DNF	0.292±0.007	0.422±0.011	0.616±0.006	0.762±0.006	0.887±0.007	0.969±0.008
	Tension (σ)	1.3	2.7	1.7	1.9	0.5	1.5
σ_z	SOMPZ	0.080±0.005	0.081±0.005	0.060±0.002	0.073±0.003	0.074±0.004	0.102 ± 0.007
	DNF	0.078±0.005	0.094±0.007	0.055±0.003	0.062±0.003	0.075±0.004	0.080±0.007
	Tension (σ)	0.2	1.6	1.3	2.2	0.3	2.3

3 Results

In Figure 1a we compare the redshift estimates obtained from the SOMPZ method alone and after including the WZ information. The combination of the two methods result in stronger constraints on the shape of the *n(z)* due to the additional information probed by WZ. The improvement on the uncertainty on the mean is more modest, but not null. This is due to the inclusion of the tight prior on the *Sys* function, estimated in data from the MagLim auto-correlation function, whereas in the case of the WL sample a much looser prior has been assumed.

We report in Table 1 the redshift means and widths of the two sets of distributions, and their agreement, computed assuming the uncertainties of the two methods to be uncorrelated. This is likely not true, therefore, the reported agreements are optimistic. Large tensions between means/widths of the two methods might indicate that either that the DNF+WZ uncertainties are under estimated, or there are some real differences between the two methods (one or both are biased). The reported values in Table 1 never exceed 3σ, with some bins showing differences at the 2σ level, which does not point to dramatic differences between the two methods.

4 Cosmological analyses results

Here we show the constraints on cosmological and nuisance parameters obtained using the DES Y3 measurements for 2x2pt measurements, and the *n(z)* from this paper. In our analysis, we vary 5 (or 6) cosmological parameters assuming a ΛCDM (or wCDM) cosmology: $\Omega_{\rm m}$, σ_8, n_s, $\Omega_{\rm b}$, h_{100}, and w for the wCDM case. Moreover, we also marginalise over "astrophysical" nuisance and calibration parameters. Our setup (parameters varied, prior ranges, etc.) is the same as the one adopted in the fiducial analysis [10], except for the redshift *n(z)* and uncertainties priors of the lens sample, where the ones obtained in this work have been assumed. We marginalise over 2 parameters for each tomographic bin, a shift on the mean and on a stretch on the width. Following [10], we required the goodness-of-fit $p-$value on unblinded data vectors was larger than 1 per cent.

The posterior on the the cosmological parameters $\Omega_{\rm m}$, and S_8 is shown in Fig. 1b for ΛCDM (wCDM), only for 4 bins case as the 6 bins did not pass our requirement. This mirrors the one presented in the fiducial 2x2pt analysis [10] and the magnification coefficients of the lens sample are fixed to the values estimated from Balrog [15]. The marginalised mean values of S_8, $\Omega_{\rm m}$, and σ_8, along with the 68% confidence intervals, are: $\Omega_{\rm m} = 0,30 \pm 0.04$, $\sigma_8 = 0.81 \pm 0.07$, $S_8 = 0.81 \pm 0.04$. The size of the posteriors is similar for the two cases, but the distance between the posteriors' peaks in the 2D $\Omega_{\rm m} - S_8$ plane is $d \sim 0.4\sigma$. This implies the large impact that a different redshift calibration of the lens sample can have on the cosmological constraints, differently from the results obtained for the source sample $n(z)$ [3], where uncertainties in the redshift calibration had a negligible impact.

We then proceed relaxing the fixed priors on the magnification parameters for the lens sample. Instead of fixing them to the values estimated from [16] (as done in the previous section), we leave them as free parameters, using wide flat priors. One of the main reasons the DES Y3 fiducial analysis did not vary the magnification parameters was merely computational, as 4 (or 6) additional parameters lengthen the parameter inference process. In principle there is no reason to doubt these estimates. We find that the $p-$value indicates a good fit of the model to the data not only for the 4 bins case, but also for 6 bins case. Adding the last 2 lens bins significantly improves the constraining power on Ω by 25% compared to the 4 bins case. For the fiducial analysis that adopted the DNF+WZ $n(z)$ they did not obtain a sufficiently good $p-$value for 6 bins, even when freeing the magnification parameters. For both the 4 and 6 bins case the posteriors prefer lower S_8 values compared to the fixed magnification case. This is a consequence of an interesting degeneracy between S_8 and the magnification parameters.

References

1. Flaugher B., et al. 2015, AJ, 150, 150
2. Dark Energy Survey Collaboration, 2021, 2022PhRvD.105b3520A
3. Amon, A., et al., 2021, Submitted to PRD, arXiv:2105.13543
4. Secco, L. F., Samuroff, S., Krause, E., et al., 2021, arXiv e-prints,arXiv:2105.13544
5. Gatti M., et al., 2020a, arXiv e-prints, p. arXiv:2011.03408
6. Rodriguez-Monroy M., 2021, 2022MNRAS.511.2665R
7. Prat J. at al., 2021, arXiv e-prints, 2021arXiv210513541P
8. Rozo e., et al. (DES), Mon. Not. Roy. Astron. Soc. (2016), arXiv:1507.05460
9. Porredon A., et al. 2021b, Phys. Rev. D, 103, 043503
10. Porredon et al. 2021, arXiv e-prints, 2021arXiv210513546P
11. De Vicente J., MNRAS 459, 3078 (2016), arXiv:1511.07623
12. Cawthon R., et al. 2020, arXiv e-prints, p. arXiv:2012.12826
13. Myles J. & Alarcon A., et al., 2020, arXiv e-prints, p. arXiv:2012.08566
14. Gatti M. & Giannini G., et al., 2020b, arXiv e-prints, p. arXiv:2012.08569
15. Everett S., et al., 2021, arXiv e-prints, arXiv:2012.12825
16. Elvin-Poole J., to be submitted to MNRAS

Spatial geometry of the large-scale universe: the role of quantum gravity, dark energy and other unknowns

M. Holman
Utrecht University,
Heidelberglaan 8, 3584 CS, Utrecht, Netherlands

It has been known for some time that the usual inference drawn from the observed near-flatness of the large-scale Universe - namely the existence of a cosmological "flatness problem", which is then taken as a partial, but key motivation for assuming the existence of an ultra-short, inflationary expansion of the very early Universe - is in itself deeply problematic. The present contribution consolidates the earlier results regarding the absence of a cosmological flatness problem of the sort that could potentially be resolved by inflation, by clearing up some common misunderstandings and by presenting some arguments in more detail.

1 Introduction

1.1 Measure of Cosmological Curvature

Within the class of *Friedmann-Lemaître-Robertson-Walker* (FLRW) solutions to Einstein's equation, proximity of the Universe's large-scale spatial geometry to flatness is conventionally captured in terms of a continuous parameter, $\Omega \equiv \Omega_m + \Omega_\Lambda$, where $\Omega_m \equiv \rho/\rho_c \equiv 8\pi\rho/3H^2$, $\Omega_\Lambda \equiv \Lambda/3H^2$, ρ and Λ respectively denote the density of matter and a cosmological constant and $H \equiv \dot{a}/a$ denotes the Hubble parameter associated with the scale factor a. FLRW dynamics is completely specified by the Friedmann equation

$$\Omega \; = \; 1 \; + \; \frac{k}{\dot{a}^2} \; = \; 1 \; + \; \frac{k}{H^2 a^2} \tag{1}$$

where k can take three possible values $k = -1$, $k = 0$, $k = +1$, depending on whether spatial geometry is respectively hyperbolic, flat or elliptic. Observations indicate that $\Omega \simeq 1$ in the present epoch and the *flatness problem* of FLRW cosmologies, broadly construed, is the alleged "improbability" of this basic empirical fact[a].

1.2 Distinguishing Issues

Closer inspection of the relevant literature however reveals that "the" cosmological flatness problem raises at least three distinct potential issues [2]. A first broad categorization of these

[a] Homogeneous cosmologies (i.e., Bianchi models) obey a *generalized* Friedmann equation

$$\Omega \; + \; \Sigma \; + \; K \; = \; 1 \tag{2}$$

with Ω defined similar as in the isotropic case, K a spatial curvature parameter (defined in terms of scalar three-curvature, ${}^{(3)}R$) and Σ a shear-parameter [1]. Proximity of Ω to 1 now does not necessarily entail near-vanishing spatial curvature and the flatness problem in the way it is conventionally characterized is therefore restricted to FLRW cosmologies (cosmological precision data of course tightly constrain Σ, justifying the FLRW approximation).

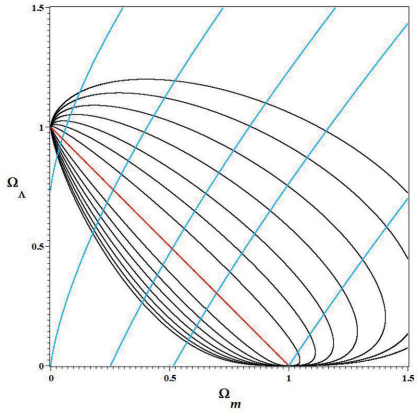

Figure 1 – Level sets of α (in black) in the $\Omega_m \geq 0, \quad \Omega_\Lambda \geq 0$ region of the phase plane, approaching the delimiter corresponding to a flat model (in red) from below ($k = -1$) and above ($k = +1$), as $|\alpha| \longrightarrow \infty$ (depicted are level sets corresponding to the specific values $|\alpha| = 6, 8, 12, 20, 40, 100, 500$). Different universe ages (in blue) progress upward from the lower right to the upper left and all models evolve from $(1, 0)$ (Big Bang) into $(0, 1)$ (asymptotic de Sitter phase). Earlier observational constraints from CMB- and SN IA-data put $|\alpha| \gtrsim 500$. Similar current constraints from Planck (in particular CMB TT/EE power spectra and BAO constraints) increase this lower bound by a factor of at least $6,000$ (the level sets corresponding to this value of $|\alpha|$ would be indistinguishable from the flat model on the scale depicted).

can be made according to whether a particular formulation of the problem depends on the dynamical nature of Ω or not. If it does, two basic varieties are found to exist (which are often conflated in practice, however). According to the *fine-tuning argument*, the observed value for Ω at the present time implies that it had to be *extremely* close to 1 at very early times and (unless $k = 0$) this is deemed highly improbable. On the other hand, if it is accepted that Ω was indeed extremely close to 1 at very early times, according to the *instability argument*, it would be highly improbable that Ω is still close to 1 today. Versions of the flatness problem in which the time-dependence of Ω plays no effective role are essentially variations on the theme of "anthropic coincidences" (i.e., why physical parameters, such as Newton's constant, G_{N}, or the fine-structure constant, α, take the particular values they do) and will be discarded in what follows.

1.3 Fine-tuning

The fine-tuning argument is often simply *identified* with the flatness problem – especially within the context of inflationary models – despite the fact that its problematic nature has been known for quite some time (see Ref. [2] and references therein). The key point here is that the "fine-tuning" is *inherent* to all cosmologically relevant FLRW solutions – in particular, it also occurs for solutions for which Ω is *not* $\simeq 1$ after some 13.8 Gyr. Put differently, the "fine-tuning" of Ω is an intrinsic part of singular FLRW models, since any such model starts with $\Omega = 1$ exactly. This contradicts the assumption of a flat, non-divergent probability distribution of initial values of Ω around $\Omega = 1$. It is this (non-warranted) assumption what creates the (fine-tuning version of the) flatness problem.

1.4 Instability

Given that Ω was extremely close to 1 at very early times and that, *at least initially*, it necessarily moves away from 1 in any non-flat representative model, it may seem plausible at first glance that one "should" not expect Ω to *still* be "close" to 1 today, i.e., after some fourteen billion odd years of cosmological evolution. Such expectations are easily shown to be incorrect through simple examples [2], which also provide a qualitative account of the following more rigorous argument due to Lake [3]. A fully equivalent specification of FLRW dynamics in the case of dust ($w = 0$) is given by

$$\Omega_m' \quad = \quad (\Omega_m - 2\Omega_\Lambda - 1)\Omega_m \tag{3}$$

$$\Omega_\Lambda' \;=\; (\Omega_m - 2\Omega_\Lambda + 2)\Omega_\Lambda \tag{4}$$

where $' \equiv d/d\eta = H^{-1}d/d\tau$, with $\eta \equiv \ln(a/a_0)$. The key feature of the argument is that

$$\alpha \;\equiv\; \mp\frac{27\Omega_m^2\Omega_\Lambda}{4\Omega_k^3} \qquad \text{for } \; k = \pm 1, \quad \Omega_k \equiv -k/\dot{a}^2 \tag{5}$$

is a constant of the motion for (3), (4) (for any FLRW solution $\Omega_k = 1 - \Omega_m - \Omega_\Lambda$) and thus can be used to label dynamical trajectories in the phase plane (cf. Figure 1). When this is done, *typical* models are found to never develop any significant curvature, a property which moreover continues to hold in the more generic case (i.e., including different components $w_i \neq 0$).

2 Flatness of the Very Early Universe

Although the foregoing conclusions seem transparent and decisive enough, doubts are sometimes expressed, although so far not really made explicit, that some subtle point or other has been overlooked in the entire discussion. For instance, it is obvious that when initial conditions are imposed at, say, the Planck scale, for the overwhelming majority of singular FLRW models, Ω will still start "very close" to 1. The fact that it is less obvious how to express such a property in a mathematically precise way should not be confused with evidence for fine-tuning. In order to appreciate this point better, momentarily consider a more general cosmological setting.

2.1 Measure and Probability in Cosmology

As is well known, general relativity has a Hamiltonian formulation, which formally gives rise to a canonical (Liouville) measure, μ, on the corresponding phase space, Γ. In practice, this picture is more involved because of (a) the necessity to "truncate" Γ, so that its dimension becomes finite (μ - which is proportional to the top exterior product of the symplectic form with itself - otherwise being ill-defined), and (b) the presence of gauge constraints. Adopting as the configuration manifold Wheeler's superspace of all Riemannian three-geometries, partially deals with the second issue, while restricting attention to homogeneous models renders superspace finite-dimensional ("*mini-superspace*") and thus addresses the first issue. Pull-back of the symplectic form to the corresponding physical phase space $\Gamma_{\rm ms}$ in this case gives rise to the so-called *GHS measure* $\mu_{\rm GHS}$ [4]. If $\mu_{\rm GHS}(\Gamma_{\rm ms}) < \infty$, it would then make sense to define probabilities as in ordinary statistical physics. If F denotes some particular observable feature (e.g., the property that $|\Omega - 1| < \epsilon$, $\epsilon \in \mathbb{R}^+$) and $X_F \subseteq \Gamma_{\rm ms}$ such that F holds, the probability to observe F would be given by

$$P(F) \;=\; \frac{\mu_{\rm GHS}(X_F)}{\mu_{\rm GHS}(\Gamma_{\rm ms})} \tag{6}$$

However, $\mu_{\rm GHS}$ is not finite and probabilities for most measurable subsets are ambiguous (in fact, expression (6) is well defined only if X_F has finite measure (yielding $P(F) = 0$) or if the complement of X_F has finite measure (yielding $P(F) = 1$)). By implementing a "regularization procedure" these ambiguities can be removed, albeit in a highly non-unique way [5] (as a result, different authors have also obtained widely different estimates for the "probability of inflation"). Attempts to go beyond the GHS framework run into further difficulties. Even if attention is restricted to near-FLRW solutions, as soon as inhomogeneous modes are included, a truncation is again necessary and this gives rise to several serious difficulties [5]. The upshot of the foregoing remarks is that, despite superficial appearances to the contrary perhaps, standard techniques do *not* provide any information on how values of Ω are probabilistically distributed, not even in the simplest FLRW-context. Furthermore, *non-standard* techniques based on an objective Bayesian approach to probability *do* give additional information in the form of divergent, improper measures around $\Omega = 1$ [6].

2.2 Quantum Gravity Effects?

It would make little sense (if at all) to argue that the absence of initial fine-tuning in Ω would somehow be overthrown by mysterious quantum gravity effects. Although it is of course impossible - given the lack of agreement about the very identity of these effects - to say anything in this regard with absolute certainty, it would seem little short of a miracle if a future theory of quantum gravity were found to somehow generically predict $\Omega(t_{\rm Pl})$ to take any value in some finite interval including 1 with more or less equal probability. Even though it is certainly true that initial conditions at the classical level can be chosen such that $\Omega(t_{\rm Pl})$ takes any prescribed value, it does not appear to widely appreciated that initial conditions for which $\Omega(t_{\rm Pl})$ is not close to 1 would lead to fine-tuning issues themselves, i.e., for the integration constants [2].

3 Flatness of the Large-Scale Late Universe

3.1 Dark Energy Effects?

It may also be wondered whether the conclusions of subsection 1.4 could somehow be affected by unknown "dark energy" effects. Even though all present cosmological data are perfectly consistent with - and perhaps even favoured by - the concordance model, i.e., Λ = constant , representation of dark energy [7], *if* Λ would turn out to be dynamical, this could only play a role at late times - with dark energy slowly decaying away and potentially giving rise to curvature effects. Since the effects of such dynamical Λ would be equivalent to those of a cosmological constant up until the present age, the conclusions presented earlier would retain their validity[b]

4 Conclusion

A cosmological flatness problem - of either the fine-tuning or instability variety - cannot be said to exist. Even though *all present evidence points against it*, one could *imagine* that fine-tuning could after all still *become* an issue within a particular approach towards quantum gravity in the future. Until then, it appears that a much more fruitful way of proceeding would consist in reshaping the evidence for both absence of fine-tuning and stability of flatness over cosmological aeons into a selectional *constraint* on a theory of quantum gravity.

References

1. J. Wainwright and G. F. R. Ellis in *Dynamical Systems in Cosmology*, (Cambridge University Press, Cambridge, 1997).
2. M. Holman Found. Phys. **48**, 1617 (2018).
3. K. Lake PRL **94**, 201102 (2005).
4. G. W. Gibbons and S. W. Hawking and J. M. Stewart *Nucl. Phys.* B **281**, 736 (1987).
5. J. Schiffrin and R. M. Wald *Phys. Rev.* D **86**, 023521 (2012).
6. P. Coles and G. F. R. Ellis in *Is the Universe Open or Closed ? The Density of Matter in the Universe*, (Cambridge University Press, Cambridge, 1997).
7. Planck Collaboration A6 (1807.06209) Astronomy & Astrophysics **641**, (2020)

[b] A strong motivation that is sometimes given to prefer dynamical (i.e., "dark energy") interpretations of Λ, is that these would avoid the so-called cosmological coincidence problem, of why ρ and Λ roughly have the same values in the present epoch. This is essentially just the instability version of the flatness problem in disguise, however, and it was seen in subsection 1.4 that this version is perfectly amenable to treatment with Λ constant!

A cautionary tale: dark energy in single-field, slow-roll inflationary models

Sveva Castello[1], Stéphane Ilić[2,3], Martin Kunz[1]
[1] *Département de Physique Théorique, Université de Genève, 1211 Geneva 4, Switzerland*
[2] *IRAP, Université de Toulouse, CNRS, CNES, UPS, Toulouse, France*
[3] *Université PSL, Observatoire de Paris, Sorbonne Université, CNRS, LERMA, F-75014 Paris, France*

The current epoch of accelerated cosmic expansion is postulated to be driven by dark energy, which in the standard model takes the form of a cosmological constant with equation of state parameter $w = -1$. We propose an innovative perspective over the nature of dark energy by drawing a parallel with inflation, which we assume to be driven by a single scalar field, the inflaton. The inflaton was not a cosmological constant, as indicated by the fact that inflation ended and by the *Planck* satellite's constraint of $n_s \neq 1$ at 8σ confidence. Therefore, it is interesting to verify whether its equation of state parameter was measurably different from -1. We analyze this question for a class of single-field slow-roll inflationary models, where the hierarchy of Hubble slow-roll parameters is truncated at different orders. Based on the latest *Planck* and BICEP2/Keck data, we obtain a 68% upper bound of $1+w < 0.0014$ for the three-parameter model, which gives the best description to the data. This provides a cautionary tale for drawing conclusions about the nature of today's dark energy based upon the non-detection of a deviation from $w = -1$ with current and upcoming cosmological surveys.

1 Introduction

The observed accelerated expansion of the Universe is postulated to be driven by a component with negative pressure, dark energy. In the standard model of cosmology, the latter takes the form of a cosmological constant, Λ, interpreted as a homogeneously-distributed vacuum energy with equation of state parameter $w \equiv \bar{p}/\bar{\rho} = -1$. Available observations constrain its abundance to approximately 68.9% of the total density, but do not allow to unveil its properties, which remain one of the key issues in modern theoretical physics.

As suggested by Ilić *et al.* [1] and Castello *et al.* [2], a precious insight about the nature of dark energy can be achieved by drawing a parallel with a previous epoch of accelerated expansion: inflation. In the simplest description, inflation is driven by a single scalar field, the inflaton, which can be interpreted as a form of dynamical dark energy. However, it cannot be identified with a pure cosmological constant, since it is thought to have rapidly decayed away at the end of inflation. Thus, it is interesting to verify whether a hypothetical observer would have been able to measure the deviation of w from -1 in the inflationary epoch. In the following, we answer this

question by characterizing the evolution of w during inflation in light of the latest data about the temperature and polarization anisotropies of the cosmic microwave background (CMB).

2 Theoretical framework

2.1 The Hubble slow-roll parameters

We assume that inflation lasts for enough e-foldings to ensure that the inflaton dominates the total energy density and adopt the Hamilton-Jacobi formalism [3], where the Hubble parameter $H \equiv \dot{a}/a$ [a] is the reference quantity. Under the standard assumption of slow-roll, we consider the hierarchy of "Hubble slow-roll" (HSR) parameters [4] ξ_n, where each parameter is proportional to the time derivative of the previous one. The first two parameters take the form

$$\xi_1(\phi) \equiv \epsilon_H(\phi) = 2M_{Pl}^2 \left(\frac{H'(\phi)}{H(\phi)}\right)^2 \tag{1}$$

$$\xi_2(\phi) \equiv \eta_H(\phi) = 2M_{Pl}^2 \frac{H''(\phi)}{H(\phi)}, \tag{2}$$

with the reduced Planck mass $M_{Pl} \equiv 1/\sqrt{8\pi}$ and $G = c = \hbar = 1$.

The first HSR parameter encodes the deviation of w from -1 according to the following exact relation,

$$1 + w = \frac{2}{3}\xi_1\,, \tag{3}$$

and, since $\xi_1 \geq 0$ by definition, this implies that values of w below -1 are nonphysical in our modelling. Moreover, the tensor-to-scalar ratio r and the scalar spectral index n_s can be expressed in terms of the first two HSR parameters at lowest order in slow roll:

$$r = 16\,\xi_1 \tag{4}$$

$$n_s - 1 = 2\xi_2 - 4\xi_1. \tag{5}$$

Since the *Planck* satellite has constrained the value of n_s away from 1 at the 8σ level [5], Eq. (5) implies that either ξ_1 or ξ_2 must be nonzero. According to Eq. (3) and the definition of the HSR parameters, we therefore must require that either $w \neq -1$ or $\frac{dw}{dt} \neq 0$, in both cases yielding a strong observational indication that the inflaton was not a cosmological constant.

2.2 Inflationary models

Our inflationary set-up requires to specify a functional form for $H(\phi)$, which we Taylor-expand around an arbitrary pivot value of the inflaton ϕ_* as in Lesgourgues *et al.* [6]:

$$H(\phi - \phi_*) = \sum_{i=0}^{n} \hat{H}_i\,(\phi - \phi_*)^n. \tag{6}$$

By inserting the series in the definitions of the HSR parameters, the n-th order Taylor coefficient can be expressed in terms of the first n parameters evaluated at ϕ_* and an additional one, $\xi_0^*(\phi) \equiv \left.\frac{H^4(\phi)}{64M_{Pl}^2 H'^2(\phi)}\right|_{\phi_*}$.

In our analysis, we truncate the Taylor series at an order varying between one and three, corresponding to models with two, three and four nonzero HSR parameters respectively, labelled HSR{2}, HSR{3} and HSR{4}. We do not consider the zero-th order approximation, since, according to Eq. (5), $\xi_1 = \xi_2 = 0$ implies $n_s = 1$ and thus contradicts the aforementioned *Planck* constraint.

[a] Dots and primes indicate derivatives with respect to cosmic time and ϕ respectively.

3 Data sets and numerical investigation

The temperature and polarization anisotropies of the CMB provide a suitable observable to constrain inflationary quantities, since they are believed to mirror the primordial curvature perturbations generated during inflation. We employ the 2018 *Planck* likelihoods [7, 8] and the joint BICEP2/Keck-WMAP-*Planck* likelihood [9] in three combinations:

(i) *Planck* low-ℓ T/E/B and high-ℓ TT/TE/EE (dubbed *P18all* here)

(ii) *Planck* low-ℓ T/E, high-ℓ TT/TE/EE, and low-ℓ BICEP2/Keck (*P18+BK15*)

(iii) *Planck* low-ℓ T/E, high-ℓ TT/TE/EE, lensing and low-ℓ BICEP2/Keck (*P18+lens+BK15*).

We perform a Markov Chain Monte Carlo (MCMC) parameter estimation for our inflationary models with the ECLAIR suite of codes [10] interfaced with the CLASS Boltzmann solver [11]. We obtain n_s, r and the primordial scalar spectral amplitude A_s as outputs of CLASS, while the MCMC chains for the nonzero ξ^* parameters are converted into allowed evolution histories $w(\phi)$. To achieve a more intuitive interpretation, the constraints on w are then translated to k-space via the "horizon-crossing condition", $k = aH(\phi(a))$, fixing the pivot scale to the standard value in CLASS, $k_* = 0.05$ Mpc^{-1}, and considering the range $[k_{\rm min}, k_{\rm max}] = [2 \times 10^{-4}, 0.1]$ Mpc^{-1}, which encloses the observable *Planck* interval [12].

4 Results

4.1 Parameter constraints

Fig. 1 shows a strong model-dependence of the MCMC constraints on the parameter ξ_1^*, with interesting cosmological implications. In the HSR{2} model, where ξ_2 is zero, Eq. (5) requires a non-trivial value of ξ_1 to satisfy the *Planck* constraint of $n_s \neq 1$. This implies the presence of primordial tensor perturbations ($r \neq 0$ from Eq. (4)) and yields a detection of $w \neq -1$ according to Eq. (3), as is clearly portrayed in Fig. 2. On the other hand, ξ_1^* is compatible with zero in models with more parameters, such that r is pushed to the trivial value and w to -1. As can be noted from Fig. 3, the bounds on w get weaker in the HSR{4} model with respect to HSR{3} and blow up at the boundaries of the chosen k-interval, in agreement with the constraints on the observable *Planck* scales [12].

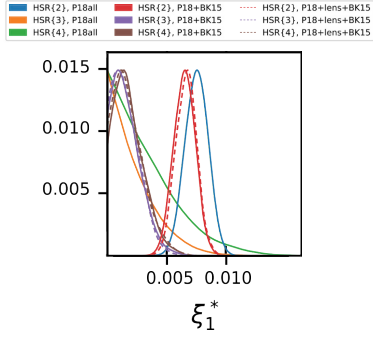

Figure 1 – The marginalized constraints on ξ_1^* for all combinations of our tested inflationary models and likelihoods.

4.2 Model comparison

We identify the model providing the best description to the data sets through the tools of Bayesian model comparison. Since the HSR{n} model is nested into HSR{n+1} at $\xi_n^* = 0$, we can compute the Bayes factor B according to the Savage-Dickey Density Ratio [13], i.e. as the ratio of the prior to the posterior at the nested point, marginalized over the common parameters. We consider two possible choices of flat priors: the "wide prior" $[-1, 1]$, since we expect the HSR parameters to be smaller than, but generally of order 1, and the "slow-roll (SR) prior" $[-0.04, 0.04]$, based on the deviation from a scale-invariant spectrum $|n_s - 1| \approx 0.04$ [5].

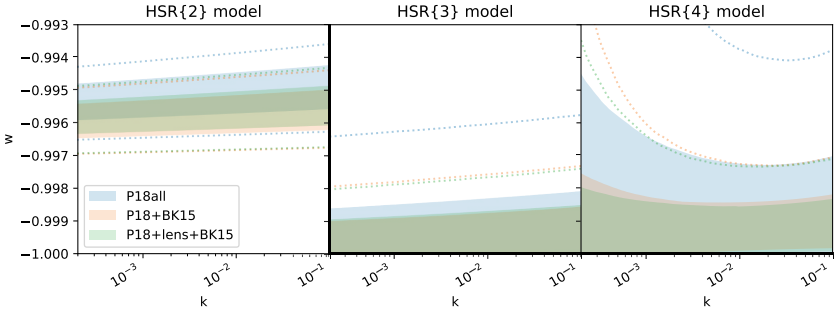

Figure 2 – The evolution of w as a function of k at horizon crossing, for each possible pairing of our three inflationary models (left, middle and right panels) and three combinations of likelihoods (in blue, orange and green). The shaded areas correspond to the 68% confidence intervals and the dotted lines indicate the 95% ones.

The fit to the *P18all* data set yields $B = 11.1$ in favour of HSR{2} over HSR{3} with the wide prior and gives an undecided outcome with the SR prior. When including the *BK15* data set, however, we obtain a preference for HSR{3} in both cases, with $B = 1.3$ for the wide prior and $B = 31$ for the SR prior. The inclusion of *P18lens* strengthens the preference for HSR{3} and the comparison with HSR{4} indicates that the additional parameter in this model is not constrained by the data.

5 The cautionary tale

Based on the analysis with the combined *Planck* and BICEP2/Keck data sets, we conclude that the model with three nonzero parameters, HSR{3}, provides the overall best description. This is a non-trivial result, since, as discussed in Sec. 4.1, the choice of model has important cosmological implications in terms of the value of the tensor-to-scalar ratio r and the equation of state parameter of the inflaton w.

We obtain a 68% upper bound of $1 + w < 0.0014$ for HSR{3}, which is around one order of magnitude below the expected precision of the next generation of cosmological surveys [14]. Thus, provided that the current epoch of accelerated expansion can be compared to inflation, our analysis suggests that the lack of an observational detection of $w \neq -1$ in the upcoming decade does not necessarily indicate that today's dark energy is a cosmological constant.

References

1. S. Ilić, M. Kunz, A. R. Liddle and J. A. Frieman, *Phys. Rev.* D **81**, 103502 (2010).
2. S. Castello, S. Ilić and M. Kunz, *Phys. Rev.* D **104**, 023522 (2021) no. 2.
3. D. S. Salopek and J. R. Bond, *Phys. Rev.* D **42**, 3936-3962 (1990).
4. A. R. Liddle, P. Parsons and J. D. Barrow, *Phys. Rev.* D **50**, 7222-7232 (1994).
5. Planck Collaboration *et al.*, *A&A* **641** (2020), A6.
6. J. Lesgourgues, A. A. Starobinsky and W. Valkenburg, *JCAP* **01** (2008), 010.
7. Planck Collaboration *et al.*, *A&A* **641** (2020), A5.
8. Planck Collaboration *et al.*, *A&A* **641** (2020), A8.
9. BICEP2 and Keck Array Collaborations *et al.*, *Phys. Rev. Lett.* **121**, 221301 (2018).
10. S. Ilić, M. Kopp, C. Skordis and D. B. Thomas, *Phys. Rev.* D **104**, 043520 (2021) no.4.
11. D. Blas, J. Lesgourgues and T. Tram, *JCAP* **07** (2011), 034.
12. Planck Collaboration *et al.*, *A&A* **641** (2020), A10.
13. R. Trotta, *Mon. Not. Roy. Astron. Soc.* **378** (2007), 72-82.
14. Planck Collaboration *et al.*, *A&A* **642** (2020), A191.

Symbolic Implementation of Extensions of the PyCosmo Boltzmann Solver

Beatrice Moser

Institute for Particle Physics and Astrophysics, ETH Zürich, Wolfgang-Pauli-Strasse 27, CH-8093 Zürich, Switzerland

PyCosmo is a Python-based framework for the fast computation of cosmological model predictions. One of its core features is the symbolic representation of the Einstein-Boltzmann system of equations. Efficient C/C++ code is generated from the SymPy symbolic expressions making use of the sympy2c package. This enables easy extensions of the equation system for the implementation of new cosmological models. We illustrate this with three extensions of the PyCosmo Boltzmann solver to include a dark energy component with a constant equation of state, massive neutrinos and a radiation streaming approximation. We compare the PyCosmo predictions for the ΛCDM model extensions with CLASS, in terms of accuracy. We find a good agreement, to better than 0.1% when using high-precision settings and a comparable computational speed. Links to the Python Package Index (PyPI) page of the code release and to the PyCosmo Hub, an online platform where the package is installed, are available at: https://cosmology.ethz.ch/research/software-lab/PyCosmo.html.

1 Introduction

One of the key theoretical predictions in cosmology is the evolution over time of the linear order perturbations of the constituents of the Universe, captured by the Einstein-Boltzmann equations (see, e.g., [1], [2]). The system of ordinary differential equations, due to its complexity and the coupling of the fields, needs to be solved numerically. For this purpose, several codes have been developed. The currently maintained Boltzmann solvers are CAMB [3], CLASS [4] and PyCosmo [5]. PyCosmo was introduced as a novel Python library that uses symbolic representation of equations for generating efficient C/C++ code. The framework includes both a Boltzmann solver as well as prediction tools for the computation of cosmological observables with several different fitting functions and approximations [6].

An important feature of PyCosmo is the possibility to easily implement model extensions in symbolic form in the code, while taking advantage of the computational speed of the generated C/C++ code. This feature has been improved by rewriting and refactoring the related code as a new sympy2c package presented in [7], which expands the idea of generating fast C/C++ code from symbolic representations of equations. Both sympy2c and PyCosmo are publicly available in the Python Package Index (PyPI). We illustrate the extensibility of PyCosmo by implementing two extensions of the Standard Model of Cosmology: a constant dark energy equation of state and massive neutrinos. We also implement a radiation streaming approximation (RSA) for photons and massless relics, which approximates the evolution of radiation at late times providing a speedup. More details on the model extensions can be found in [8].

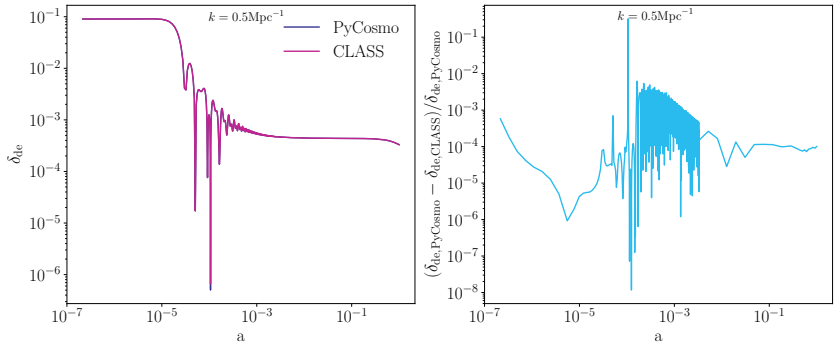

Figure 1 – The dark energy perturbation δ_{de} as a function of scale factor a for a dark energy equation of state with $w = -0.9$ and sound speed $c^2_{\mathrm{s,de}} = 1$ at $k = 0.5\mathrm{Mpc}^{-1}$. In the left plot, we show the perturbation computed with `PyCosmo` (blue) and `CLASS` (violet), in the right plot the relative difference between the two.

2 Code comparisons setup

In order to validate the newly introduced models, we carry out detailed comparisons with `CLASS`[a]. We evaluate the accuracy in terms of relative difference between observables. Since this is often a function of the wavenumber k, we compare it visually by plotting as a function of k or, when specified, we look at the maximum relative difference in a k interval.

Comparing the two codes implies carefully setting the cosmological parameters and the precision settings. In the following, we will make use of two precision settings: *speed* and *precision*. In the case of `CLASS`, we use the precision files shipped with the code: `cl_permille.pre` for fast and accurate computation and `pk_ref.pre` for high precision [9]. In the case of `PyCosmo` we tune the parameters `l_max`, `boltzmann_rtol` and `boltzmann_atol`, `l_max_mnu` and `mnu_relerr` in the massive neutrino case. See [8] for more details. The parameters we modify are Ω_m, N_ν, $N_{\nu,m}$, Σm_ν and w_{de}. Ω_Λ is computed by imposing the flatness condition $\sum_i \Omega_i = 1$. The other parameters remain fixed.

3 Dark Energy with a constant equation of state

In order to search for deviations from a cosmological constant, we consider a dark energy equation of state with $w_{\mathrm{de}} = p_{\mathrm{de}}/\rho_{\mathrm{de}} \neq -1$. We implement the background and linear order perturbation equations of this model symbolically in `PyCosmo` using `sympy2c` .

In Fig. 1 we show the dark energy perturbation δ_{de} as a function of scale factor a for $k = 0.5$ Mpc^{-1}, plotted both with `PyCosmo` as well as `CLASS`. We also display the relative difference between the evolution of the perturbations obtained by the two codes. The cosmology we consider is

- w**CDM**: $\{\Omega_\Lambda, \Omega_m, N_\nu, N_{\nu,m}, \Sigma m_\nu, w_{\mathrm{de}}\} = \{0.69992, 0.3, 3.044, 0, 0, -0.9\}$

using the *precision* settings from section 2. In general, we find good agreement between the codes. When the fields are highly oscillating, we observe a degradation of the agreement, as expected, given the impact of step-size control and numerical precision of the solver in that regime.

[a] We use `CLASS` v3.1.0, through the `Python` wrapper `classy`.

4 Massive Neutrinos

Massive neutrinos modify both the background evolution and the linear order perturbations. Qualitatively, massive neutrinos undergo a phase transition: they behave like radiation at early times, when they are fully relativistic, and shift to a matter-like behaviour at late times (see, e.g., [10,11]). The transition happens smoothly through cosmic time and the dependence on mass, scale factor and momentum in the evolution of the distribution function prevents from integrating out the momentum dependence. For this reason, the inclusion of massive neutrinos in the Boltzmann equations is highly non trivial and has a strong impact on the size of the ODE system.

In `PyCosmo` we introduce $N_{\nu,m}$ degenerate massive neutrinos. The implementation of the massive neutrino equations uses `sympy2c` similarly to the `PyCosmo` implementation of ΛCDM and wCDM. The background integral over momentum q is computed using indefinite numerical integration from `sympy2c` , whereas the integrals at perturbation level use a Gauss-Laguerre quadrature integration scheme in our symbolic representation of the ODE system, since we need to evolve a finite number of equations. This follows the approach used in [12].

In Figure 2 we show the total matter power spectrum obtained with `PyCosmo` and `CLASS` for 200 log-spaced k values between 10^{-4} and 1 Mpc^{-1}. On the left we show the two power spectra and on the right the relative difference between the two with the following cosmological parameters:

- **degenerate Σm_ν = 60 meV**: $\{\Omega_m,\ N_\nu,\ N_{\nu,m},\ \Sigma m_\nu,\ w_{\rm de}\} = \{0.29869,\ 0.00440,\ 3,\ 0.06,\ -1\}$.

We use the *precision* settings for the two codes. In general, we observe a very good agreement,

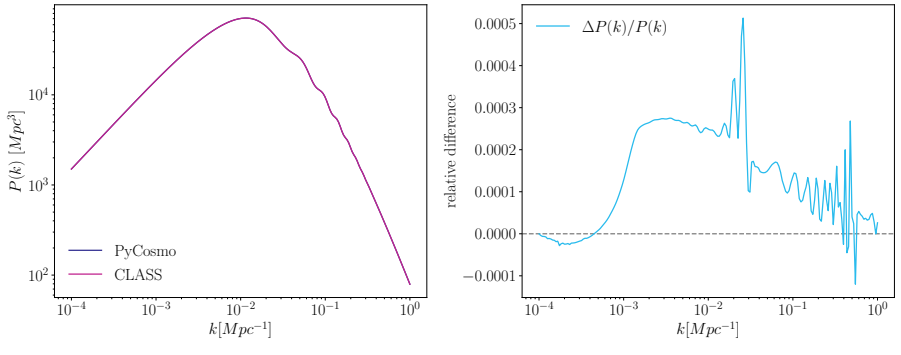

Figure 2 – Total matter power spectrum for a cosmology with three massive neutrinos with Σm_ν = 60 meV, plotted both with `PyCosmo` and `CLASS` for 200 log-spaced k values between 10^{-4} and 1 Mpc^{-1}. On the right side, we display the relative difference between the two.

with a maximum relative discrepancy of 5×10^{-4} on intermediate scales.

5 Radiation Streaming Approximation

After decoupling, photons and massless neutrinos behave approximately like test particles free-streaming in the gravitational field determined by the massive components, making it possible to derive a non-oscillatory solution of the inhomogeneous Boltzmann equations inside the Hubble radius. This approximation, called the Radiation Streaming Approximation (RSA), was introduced in the Newtonian gauge by [13] and in the synchronous gauge by [14]. This treatment allows both to avoid unphysical oscillations resulting from the hierarchy truncation and to speed up the

Table 1: Maximum relative differences in k ranges between `PyCosmo` and `CLASS` for different models and precision.

`Model`	precision	k range [Mpc^{-1}]				
		$10^{-4} - 10^{-3}$	$10^{-3} - 10^{-2}$	$10^{-2} - 10^{-1}$	$10^{-1} - 1$	$1 - 10$
ΛCDM	*speed*	0.0006	0.0007	0.0007	0.0031	0.0077
	precision	0.0001	0.0003	0.0005	0.0003	0.0008
wCDM	*speed*	0.0006	0.0007	0.0008	0.0031	0.0078
	precision	0.0002	0.0003	0.0005	0.0003	0.0008
degenerate M_ν	*speed*	0.0004	0.0010	0.0010	0.0046	0.0146
	precision	0.0001	0.0003	0.0005	0.0002	0.0001

integration, which is slowed down by fast late time oscillations of the radiation fields especially on small scales. In order to implement the Radiation Streaming Approximation within `PyCosmo` we use a functionality from `sympy2c` to switch between two different ODEs at a dynamically computed time point.

6 Agreement with `CLASS`

We present benchmarks of the `PyCosmo` Boltzmann solver for all the models described in the previous sections, in terms of relative difference to `CLASS`. We compare the numerical results of `PyCosmo` and `CLASS` in Table 1. We report the maximum relative difference between the matter power spectra in `PyCosmo` and `CLASS` in five k ranges for the different models and precision settings. The RSA is not relevant here because it leads to a 10^{-5} relative difference, when compared to the full computation with the same `l_max`. The size of the relative differences is comparable in all models when using the same k ranges, with the exception of the model with massive neutrinos for $k > 0.1$ Mpc^{-1}. The difference in precision between *speed* and *precision* settings is dominant on scales $k > 0.1$ Mpc^{-1}, where the truncation effects have the largest impact. The *precision* settings lead to a relative difference to `CLASS` that is better than 0.1% on all scales $k < 10$ Mpc^{-1}, while the *speed* settings lead to a relative difference of order $0.5 - 1\%$ beyond $k = 0.1$ Mpc^{-1}. This is acceptable, especially since `cl_permille.pre` comes with no guarantees for scales $k > 1\ h$Mpc^{-1}. The computational speed is comparable in the two codes.

Acknowledgements

This work was supported in part by grant 200021_192243 from the Swiss National Science Foundation.

References

1. C. Ma and E. Bertschinger. *Astrophys.J.*, (455):7–25, 1995.
2. S. Dodelson. *Modern Cosmology*. Academic Press, Elsevier Science, 2003.
3. A. Lewis, A. Challinor, and A. Lasenby. *The Astrophysical Journal*, 2000.
4. J. Lesgourgues. Technical report, CERN, 2011.
5. A. Refregier, L. Gamper, A. Amara, and L. Heisenberg. *Astronomy and Computing*, 2018.
6. F. Tarsitano, U. Schmitt, and et al. *Astronomy and Computing*, 36:100484, 2021.
7. U. Schmitt, A. Refregier, et al. *Astronomy and Computing*, in prep.
8. B. Moser, C. S. Lorenz, et al. *arXiv e-prints*, page arXiv:2112.08395, December 2021.
9. J. Lesgourgues. *arXiv e-prints*, page 1104.2934, 2011.
10. M. Lattanzi and M. Gerbino. *Front. in Phys.*, 5:70, 2018.
11. K. Ichikawa, M. Fukugita, and M. Kawasaki. *Phys. Rev. D*, 71:043001, 2005.
12. J. Lesgourgues and T. Tram. *JCAP*, 2011(09):032–032, Sep 2011.
13. M. Doran. *JCAP*, 06:011, 2005.
14. D. Blas, J. Lesgourgues, and T. Tram. *JCAP*, 2011(07):034–034, Jul 2011.

Constraining modified gravity with gravitational wave distance measurements

Isabela S. Matos [a]
Universidade Federal do Rio de Janeiro, Instituto de Física,
CEP 21941-972 Rio de Janeiro, RJ, Brazil
Départment de Physique Théorique and Center for Astroparticle Physics, Université de Genève,
CH-1211 Genève 4, Switzerland

It has been shown in the literature that detections of gravitational waves (GWs) emitted by binary sources can provide measurements of luminosity distance. The events followed by electromagnetic counterparts are, then, suitable for probing the distance-redshift relation and doing cosmological parameter estimation, as well as investigating modified gravity (MG) models. In the context of effective approaches to MG equivalent to Horndeski, this GW distance differs from the standard electromagnetic luminosity distance due to the presence of a modified friction in the wave propagation. Here, we investigate how precisely the future-planned interferometer Einstein Telescope will probe such deviations from General Relativity, considering phenomenological parametrizations for both the dark energy equation of state and the GW friction. Despite being an independent test of gravity, for $f(R)$ in particular, we conclude that it may provide weaker constraints than the current available ones.

1 Introduction

Since the groundbreaking discovery of LIGO-Virgo in 2015, a lot of effort has been devoted to clarify how much we can learn from gravitational wave (GW) detections in different topics of interest in spacial physics, *e.g.* the equation of state of neutron stars, the current expansion rate of the universe, tests of gravity, compact objects and so on. In particular, the so-called multimesseger events, *i.e.* those that are followed by electromagnetic signals such as γ-ray bursts, stand out as the ones which allow us to assess more information about the source, *e.g.* its redshift, and also about possible differences in the propagation of gravitons and photons.

In our work [1] [b] we performed simulations of multimessenger events emitted by binary neutron stars (BNS) for the future planned 3rd generation interferometer Einstein Telescope (ET) [2]. In an optimistic scenario, 10^3 of such signals are expected to be detected up to redshift 2, which allows us to test modified gravity (MG) theories at cosmological scales in the tensor sector. This can be achieved by parametrizing MG signatures in the evolution, from emittion to detection, of

[a] isa@if.ufrj.br
[b] in collaboration with M. O. Calvão and I. Waga.

the wave's amplitude in the inspiral phase where perturbation theory applies. Our framework is defined by a perturbed spatially flat FLRW metric,

$$ds^2 = a(\tau)^2 \left[-(1+2\Psi)d\tau^2 + (1-2\Phi)(\delta_{ij}+h_{ij})dx^i dx^j\right] , \tag{1}$$

where a is the scale factor, τ is the conformal time, Φ and Ψ are the usual scalar perturbations and h_{ij} is the transverse traceless GW, specified by the two degrees of freedom h_+ and $h_\times$.

In the context of cosmology, it has been shown [5] that several MG theories can be distinguished at background and linear perturbation levels only through the specification of a tuple

$$(\Omega_{m0}, \mathcal{H}, \alpha_M, \alpha_T, \alpha_K, \alpha_B) , \tag{2}$$

where Ω_{m0} is the matter energy density parameter today, $\mathcal{H} := a'/a$ is the conformal Hubble parameter ($' := d/d\tau$) and the α's are time-dependent functions that govern the evolution of perturbations. They all vanish in General Relativity (GR) and their physical meanings are associated with the presence of, respectively, a running Planck mass M_*^2, a tensor speed excess, kineticity and braiding. This setting encompasses the most general theories that give rise to second order field equations with a single scalar field ϕ, the Horndeski theories. Moreover, the evolution equation for the GW polarization modes is given by

$$h_P'' + (2+\alpha_M)\mathcal{H}h_P' + (1+\alpha_T)k^2 h_P = \Pi_P , \tag{3}$$

with $P = +, \times$, where Π_P is the tensor part of the anisotropic stress. This equation differs from its corresponding one in Einstein's gravity by the introduction of features such as a change in the GW speed of propagation $c_T^2 = 1 + \alpha_T$. However, this was already strongly constrained by the GW170817 event to be equal to the speed of light [3], which motivates restricting to $\alpha_T = 0$.

The particularly important deviation from GR in the propagation of tensor modes is encoded in the friction rate at which they are damped whenever $\alpha_M \neq 0$. This effect gives rise to a new cosmological distance that can be inferred by local interferometers, the GW distance $D^{\rm gw}$ [4]. It relates to the standard electromagnetic luminosity distance by

$$\Xi(z) := \frac{D^{\rm gw}(z)}{D_L^{\rm em}(z)} = \exp\left\{\frac{1}{2}\int_0^z \frac{\alpha_M(\tilde{z})}{1+\tilde{z}} d\tilde{z}\right\} = \sqrt{\frac{M_*^2(0)}{M_*^2(z)}} . \tag{4}$$

In $f(R)$ theories, where our analysis is focused on, this reduces to $\sqrt{1+f_{R0}}/\sqrt{1+f_R}$, where f_R is the derivative of the Lagrangian with respect to the Ricci scalar. For viable models that recap GR at high redshifts, this function goes asymptotically to $1 + f_{R0}/2$. Its typical behavior is shown in the right pannel of Fig. 1 for a particular model.

2 GW simulations

We now summarize the procedure to simulate the GW mock data for the ET with $N_{\rm obs} = 1000$ events. We considered the waveform emitted at redshift z by a BNS merger up to the 3rd PN correction neglecting spins, which is given by

$$\tilde{h}(f, z, D^{\rm gw}, \boldsymbol{s}) = \frac{\mathcal{A}(f, z, \boldsymbol{s})}{D^{\rm gw}} \left(\frac{c}{f^7}\right)^{1/6} e^{i\Phi(f)} , \tag{5}$$

where Φ is a phase and $\mathcal{A}$ is a function of frequency, redshift and the parameters of the source $\boldsymbol{s} = (m_1, m_2, \iota, \theta, \phi, \psi)$, which stand for, respectively: the masses of the binary components, the angle of orbital inclination, the direction of the line of sight and the GW polarization angle.

Given a gravitational and cosmological model with parameter values $\boldsymbol{\Theta}$, we draw the redshift of the i-th binary source from the distribution

$$\rho(z_i|\boldsymbol{\Theta}) = N_z(\boldsymbol{\Theta}) \frac{4\pi[\mathcal{D}_c(z_i, \boldsymbol{\Theta})]^2}{(1+z_i)H(z_i, \boldsymbol{\Theta})} r(z_i) , \tag{6}$$

where $\mathcal{D}_c(z,\mathbf{\Theta}) = \int_0^z c/H(z,\mathbf{\Theta})$ is the comoving distance, N_z is a normalization factor and $r(z)$ is the rate of evolution of the BNS mergers.

Accounting for the degeneracy between $D^{\rm gw}$ and ι and adding a contribution due to weak lensing, the error in the GW distance, in the Fisher matrix approximation, is given by

$$\sigma^2 = \left[\frac{2\mathcal{D}^{\rm gw}(z)}{\mathrm{SNR}(z,\boldsymbol{s})}\right]^2 + [\sigma_{\rm lens}(z)]^2 \quad \text{with} \quad \mathrm{SNR}^2 = 4\int_{f_{\rm low}}^{f_{\rm up}} \frac{\left|\tilde{h}\right|^2}{S_n} df\,, \tag{7}$$

where S_n is the power spectral density of the detector's noise. The GW distances are drawn from a Gaussian distribution with standard deviation σ and, therefore, our posterior results in

$$\rho(\mathbf{\Theta}|\boldsymbol{z}, \boldsymbol{D}_L^{gw}, \boldsymbol{s}) \propto \rho(\mathbf{\Theta}) \exp\left\{ -\sum_{i=1}^{N_{\rm obs}} \frac{\left[D_{L,i}^{gw} - \mathcal{D}_L^{gw}(z_i,\mathbf{\Theta})\right]^2}{2\sigma(z_i,\boldsymbol{s}_i)^2} \right\}. \tag{8}$$

3 Results

When restricting to ΛCDM, we find that a thousand GW events followed by electromagnetic counterparts, if detected by ET, would provide measurements of H_0 and Ω_{m0} with accuracies of $\Delta H_0/H_0 \sim 1\%$ and $\Delta\Omega_{m0}/\Omega_{m0} \sim 7.6\%$. Secondly, when allowing for a relative difference between GW and luminosity distances in a generic viable $f(R)$ theory, we obtain the bound $|f_{R0}| < 10^{-2}$. In fact, we estimate that 10^{10} of such multimessenger events would be needed to reduce this number to 10^{-6}, which is the current known bound from large scale structure (LSS) and local tests.

3.1 Parametrizations

In order to account for MG effects both at the background level and in the friction we propose parametrizations for the dark energy equation of state (EOS) parameter $w_{\rm DE}$ and the ratio of distances Ξ. They are:

$$w_{\rm DE}(z,A,z_t,z_f) = \quad -1 - A(z-z_f)(z_t-z)\sin\left[\tfrac{2\pi z - \pi(z_f+z_t)}{z_t-z_f}\right], \quad z_f < z < z_t \tag{9}$$

$$\Xi(z,\Xi_0,\nu) = \quad \Xi_0 + (1-\Xi_0)e^{1-(1+z)^\nu}\,. \tag{10}$$

The most relevant parameters are Ξ_0, which is the assymptotic value of Ξ, and the amplitude of the dark energy EOS deviation from -1, A. Figure 1 shows the resulting contours in the parameter space $\Theta = (\Xi_0, A, H_0, \Omega_{m0})$ when allowing for deviations of GR with the parametrizations. We also adapted existing codes for SNe and a combination of CMB and BAO data to include our MG parametrizations and used the results as priors. However, to exemplify, a particular model of the γ-gravity $f(R)$ theories [6], that is easily ruled out by other kinds of tests is represented with a green star: despite having $|f_{R0}|$ of order 10^{-2} it cannot be distinguished from ΛCDM.

4 Conclusions and next steps

In this work, we studied the evolution of the GW distance in MG with special interest in $f(R)$-like theories. By generating a mock dataset of 1000 GWs emitted by BNS mergers as could be detected by the ET in near future, we investigated the constraints that the inference of the GW distances and redshifts of the sources could provide to cosmological and phenomenological parameters. Apart from measurements of the cosmological parameters, however, regarding $f(R)$ models, first, this test was shown to provide weak bounds to f_{R0} when restricting to viable models; second, even when accounting for the modified background via $w_{\rm DE}$, we showed that it was not possible to distinguish between ΛCDM and typical $f(R)$ models that are already

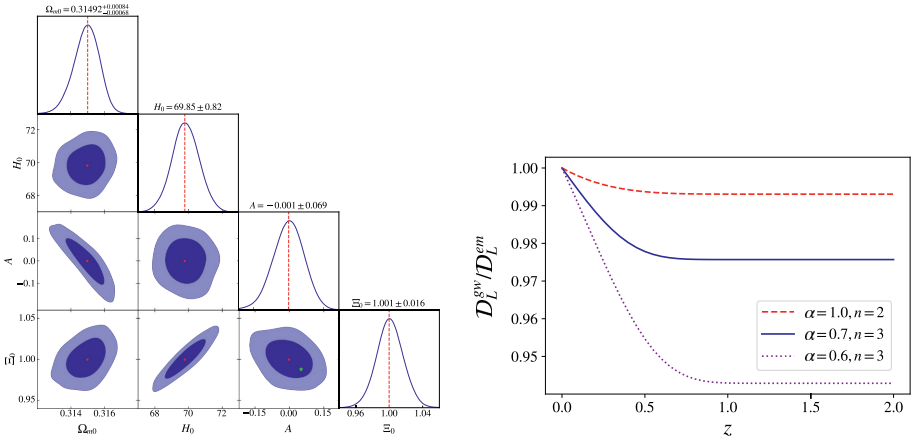

Figure 1 – On the left, 68% and 95% CLs from simulations of a thousand GW detections assuming the redshifts of the sources are known. Red dots or dashed lines correspond to ΛCDM. On the right, the theoretical prediction for the ratio of distances in γ-gravity $f(R)$ for three values of the parameters defining the Lagrangian.

discarded with other probes. We also find that the GW bounds to the amplitude of the dark energy EOS A are weaker than the ones from SNe and BAO/CMB data. Our conclusions indicate, therefore, that the test is not suitable to look for signatures of $f(R)$ modifications of gravity, neither from dark energy effects or modified friction in GW propagation, even in our optimistic scenario. Still, it constitutes an independent probe of gravity at cosmological scales that provides a measurement of deviations from GR at the percent level ($\Delta\Xi_0 \sim 10^{-2}$) and it could be quantitatively competitive for other theories within Horndeski and beyond.

Lastly, we remark that, as first highlighted in [7], in our MG context, the same functions that modify the propagation of tensor modes also affect the scalar sector. For instance,

$$\Psi - (1 + \alpha_T)\Phi + (\alpha_M - \alpha_T)\mathcal{H}(\delta\phi/\dot{\phi}) = \Pi\,. \tag{11}$$

In particular, the friction α_M makes the slip $\eta = \Phi/\Psi$ deviate from the GR value of unity, a feature usually generated whenever the matter content considered has anisotropic stress Π. Therefore, by combining slip measurements from LSS probes and GWs it might be possible to break the degeneracy between a scenario in which the gravity theory is GR with the presence of a matter sourced anisotropic stress, and a perfect fluid in MG. Studying the constraining power of the combination of future GW and LSS data on α_M is the subject of our current project.[c]

References

1. I. S. Matos, M. O. Calvão and I. Waga, *Phys. Rev.* D **103**, 104059 (2021).
2. M. Maggiore *et al.*, JCAP **03**, 2020 (050).
3. B. P. Abbott *et al.*, *Astrophys. J.* **848**, L13 (2017).
4. E. Belgacem *et al.*, JCAP **07**, 2019 (024).
5. E. Bellini and I. Sawicki, JCAP **07**, 2014 (050).
6. M. O' Dwyer, S. E. Jorás, and I. Waga, *Phys. Rev.* D **88**, 063520 (2013).
7. I. D. Saltas *et al.*, PRL **113**, 191101 (2014)

[c] in collaboration with M. Kunz and E. Bellini.

2.
CMB and Gravitational Waves

The Latest Constraints on Inflationary B-modes from the BICEP/*Keck* Telescopes

King Lau on behalf of the BICEP/*Keck* Collaboration
School of Physics and Astronomy, University of Minnesota, Minneapolis, Minnesota 55455, USA

For the past decade, the BICEP/*Keck* collaboration has been operating a series of telescopes at the Amundsen-Scott South Pole Station measuring degree-scale B-mode polarization imprinted in the Cosmic Microwave Background (CMB) by primordial gravitational waves (PGWs). These telescopes are compact refracting polarimeters mapping about 2% of the sky, observing at a broad range of frequencies to account for the polarized foreground from Galactic synchrotron and thermal dust emission. Our latest publication "BK18" utilizes the data collected up to the 2018 observing season, in conjunction with the publicly available WMAP and *Planck* data, to constrain the tensor-to-scalar ratio r. It particularly includes (1) the 3-year BICEP3 data which is the current deepest CMB polarization map at the foreground-minimum 95 GHz; and (2) the *Keck* 220 GHz map with a higher signal-to-noise ratio on the dust foreground than the *Planck* 353 GHz map. We fit the auto- and cross-spectra of these maps to a multicomponent likelihood model (ΛCDM+dust+synchrotron+noise+r) and find it to be an adequate description of the data at the current noise level. The likelihood analysis yields $\sigma(r) = 0.009$. The inference of r from our baseline model is tightened to $r_{0.05} = 0.014^{+0.010}_{-0.011}$ and $r_{0.05} < 0.036$ at 95% confidence, meaning that the BICEP/*Keck* B-mode data is the most powerful existing dataset for the constraint of PGWs. The up-coming BICEP Array telescope is projected to reach $\sigma(r) \lesssim 0.003$ using data up to 2027.

1 Introduction

The inflation paradigm is one of the leading candidates for a theory that describes the evolution of the early Universe. It suggests that at the time of $\approx 10^{-36}$ s after the Big Bang, the Universe underwent a brief period of exponential expansion in which its scale was increased by 50 to 60 e-folds. This scenario offers natural solutions to the horizon, flatness and magnetic monopole problems arising from the hot Big Bang expansion model [1]. Moreover, inflation predicts the generation of scalar perturbations in the early Universe. These perturbations are supposed to be adiabatic, nearly Gaussian and close to scale-invariant, which are consistent with high precision full-sky Cosmic Microwave Background (CMB) measurements [2].

Nevertheless, generic inflationary models make a prediction that has not yet been observed — the existence of a background of primordial gravitational waves (PGWs). The magnitude of these PGWs can be parameterized by the tensor-to-scalar ratio r, which was constrained to be at least an order of magnitude smaller than one by CMB temperature data in early 2010s [3]. PGWs would also leave potentially detectable "primordial B-modes" [4,5] which are characteristically different from and substantially weaker than the E-modes in CMB polarization. Thus, the search for B-mode polarization can serve as a probe of PGWs. The constraints on r from B-mode measurements, when combined with the constraint on spectral index n_s, can discriminate among inflation models [6].

Galactic foregrounds are one of the factors obscuring the detection of primordial B-modes. In 2014, the publication of BICEP2 analysis [7] and *Planck* 353 GHz data [8,9] revealed that polarized thermal emission from dust within our galaxy dominates the B-mode signals at high

microwave frequencies. Other studies [10] also found Galactic polarized synchrotron emission at low frequency. These facts imply that multiple-frequency measurements are necessary to account for the contribution of foregrounds.

Gravitational lensing is another major source of B-modes. While polarized CMB photons were propagating from the last-scattering surface, they were deflected by gravitational lensing, and this transforms part of the E-modes into "lensing B-modes" [11]. Therefore, in the absence of Galactic foreground, the total B-mode power spectrum is the combination of primordial B-modes and lensing B-modes. As the latter component is prominent at small scales, measuring the degree-scale B-mode polarization emerges as one of the most promising methods for a first detection.

The BICEP/*Keck* collaboration has been operating a series of small-aperture telescopes covering a broad range of frequencies for B-mode polarization measurement for the past decade. This proceeding discusses the latest constraints on PGWs by the BICEP/*Keck* data as well as the prospect of the BICEP Array system. In section 2, we provide an overview of the BICEP/*Keck* program; in section 3 we show the analysis results driven by BICEP3 and *Keck Array* data up to the 2018 observing season. This includes their maps, power spectrum and the derived constraints on r and inflation models; and in section 4 we briefly outline the r constraints offered by BICEP Array in the future.

2 The BICEP/*Keck* Telescope Series

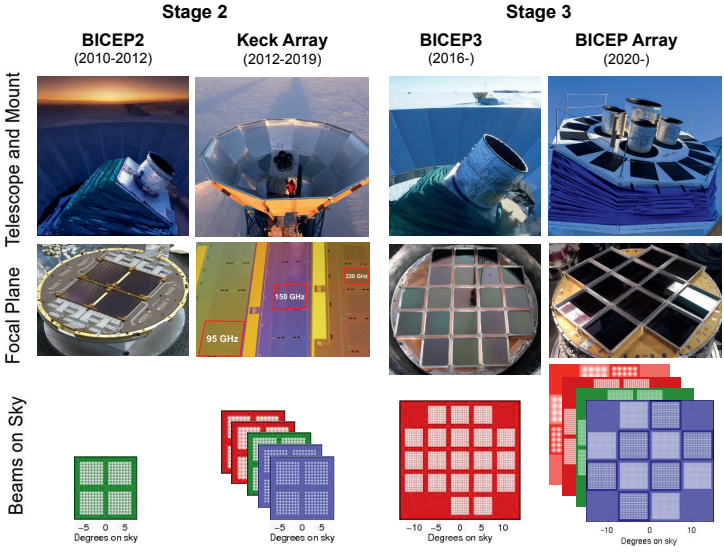

Figure 1 – The BICEP/*Keck* telescopes are Stage-2 and Stage-3 CMB ground-based experiments characterized by $\approx 10^3$ and $\approx 10^4$ detectors respectively. The top two panels show the telescopes (and their physical focal planes) operating since 2010. In the bottom panel, each plane stands for a receiver. The white dots represent the detectors and the beam size as projected on the sky, while the color of a plane denotes the observing frequency. The first receiver (30/40 GHz) of BICEP Array started running in 2020, and it will be fully upgraded to have the other three receivers shown in the figure by 2023.

As illuminated in figure 1, the BICEP/*Keck* collaboration has designed, manufactured and operated four dedicated telescopes to measure CMB B-mode polarization since 2010. BICEP2 [12], a single-receiver telescope observing at 150 GHz from 2010-2013, had the conceptual designs of

detector and optic employed by subsequent upgrades. Its aperture size was $\approx$ 250 mm and its focal plane contained four $4'' \times 4''$ wafers with a total of $\approx$ 500 bolometric detectors — the antenna-coupled transition edge sensors (TES). Each pair of co-located detectors consisted of interleaved arrays of orthogonal slot antennas so that the pair difference timestream is a measure of polarized emission from the sky. During observations, the focal plane was cooled to the temperature of $\approx$ 250 mK by a 3-stage Helium sorpotion refrigerator, and the detectors were read out by time-division multiplexing SQUID amplifiers. The telescope insert with a compact, on-axis, two-lens refractor optical design was cooled to 4 K to minimize in-band photon loading. The receiver was further coupled with a cylindrical co-moving forebaffle and surrounded by a reflective ground shield for optical shielding.

The *Keck Array* telescope [13] incorporated five BICEP2-style receivers with pulse tube cooled cryostats. All receivers, each with $\approx$ 500 detectors, initially observed at 150 GHz. As the focus of CMB experiments targeting primordial B-modes shifted from raw sensitivity improvement to multiple-frequency observation, it gradually switched to cover 95 GHz and 220 GHz from 2014 to 2019 to constrain the contribution from dust foreground emission.

BICEP3 [14] has been observing at the foreground-minimum 95 GHz since 2016. It is a single-receiver telescope with doubled aperture size $\approx$ 500 mm for a larger instantaneous field of view. BICEP3 hosts $\approx$ 2500 detectors packed into twenty $4'' \times 4''$ focal plane modules, and is equivalent to about eight of the *Keck* 95 GHz receivers in terms of map depth.

In late 2019, *Keck* was decommissioned and replaced by the BICEP Array telescope [15,16] which will eventually carry four BICEP3-style receivers. It will be discussed separately in section 4.

All four telescopes were deployed to observe at the Amundsen-Scott South Pole Station. BICEP2 and BICEP3 were installed on the same mount at the Dark Sector Laboratory (DSL), while *Keck* and BICEP Array were located at the Martin A. Pomerantz Observatory (MAPO) about 200 m away. The high altitude ($\approx$ 2800 m) and extreme cold ($\approx -70\,^{\circ}$C in winter) of the South Pole suppress precipitable water vapor. The atmosphere is hence exceptionally stable and transparent at microwave frequencies, providing one of the best observation sites for ground-based CMB telescopes. Other advantages include the 6-month nighttime, the continuous visibility of the "Southern Hole" (i.e. a low-foreground patch of the sky) and minimal light pollution.

The BICEP/*Keck* observation strategy is to concentrate on one of the cleanest patches of the sky available from the South Pole. The observing field is centered at RA 0 hr, Dec. -57.5°. With the elevation fixed, the telescope moves back and forth along the azimuth direction to scan $\approx 100^{\circ}$ on the sky. In 50 minutes of time, it conducts 100 "half-scans" in this way, and these yield a single observation unit, a "scan set". After several tens of scan sets, the telescope spins along its boresight ("deck angle" rotation) to another deck angle choice to cover 4 to 8 distinct angles for the demodulation of Q and U signals. Moreover, a total of 21 evenly divided elevation offsets between Dec. -55° to -60° expand the effective observation area to $\approx$ 400 square degrees for BICEP2/*Keck*, or $\approx$ 585 square degrees for BICEP3/BICEP Array. Over a full observation season, each telescope can accumulate $\approx$ 4500 scan sets, and around 60% of them survive data cuts. That means abundant observation time is devoted to $\approx$ 2% of the sky for deep maps. This is a typical strategy for a first detection.

3 BK18 Maps, Power spectrum and Constraints on Inflation Models

In our previous mainline publication (hereafter "BK15") [17], we utilize BICEP2 and *Keck* 95/150/220 GHz data up to the 2015 observing season, in conjunction with external data, to yield the constraint $r_{0.05} < 0.06$ (evaluated at the pivot scale $k = 0.05\,\mathrm{Mpc}^{-1}$) at 95% confidence. Our latest publication (hereafter "BK18") [18] adds three more years of data from *Keck* and BICEP3. While the BK15 dataset consists of 4/17/2 *Keck* receiver-years at 95/150/220 GHz respectively, the BK18 dataset is equivalent to about 28/18/14 *Keck* receiver-years at 95/150/220 GHz respectively.

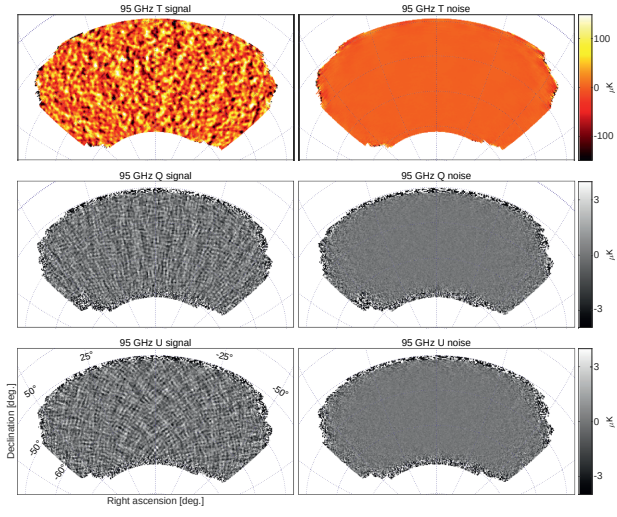

Figure 2 – The BICEP3 95 GHz T, Q, U maps from the BK18 paper are displayed in the left column. These signal maps are made using BICEP3 data from the 2016-2018 observing seasons. The right column shows maps of a noise realization produced by randomly and evenly flipping the sign of scan sets during the map coadding process. Note that the signal maps in general appear different from the full-sky measurement of the same sky patch since they are heavily filtered by beam smoothing, timestream processing and deprojection.

The analysis starts by processing the detector timestreams of scan sets. They are first relatively calibrated to eliminate the gain difference between two detectors in a pair. To remove the $1/f$ atmospheric noise, ground signals and magnetic pickup, third-order polynomial filtering and scan-synchronous subtraction are applied to the timestreams of each half-scan. They are also run through the deprojection process for the removal of $T \rightarrow P$ leakage, and two distinct rounds of data cut are further applied to remove data from bad weather periods. Pair difference timestreams from multiple deck angle measurements can then be demodulated into Q and U signals via a rotation matrix inversion. Finally, they can be binned into T, Q, U maps with the pointing trajectory information.

Figure 2 and figure 3 show the BICEP3 95 GHz and *Keck* 220 GHz T, Q, U maps published in the BK18 paper. They contain the BICEP3 and *Keck* data up to the 2018 observing season. The comparison between regular maps and noise maps indicates high S/N detection of polarization signals. With the expanded field of view, and an order of magnitude increase in detector number, the BICEP3 Q/U maps, which are the current deepest 95 GHz CMB polarization maps, achieve a map depth of 2.8 μK-arcmin. The *Keck* 220 GHz Q/U map depth of 8.8 μK-arcmin also far exceeds the sensitivity provided by *Planck* 353 GHz measurement in the same sky patch.

Apart from the modest smoothing due to the change of beam size, these two sets of maps display strong correlation over frequency and show clear "+" structure in Q and "×" structure in U, implying that they detect the dominating E-mode signals from the ΛCDM model. The exception is the small "anomalies" around the lower right corners of the *Keck* polarization maps. This pattern is contributed by the polarized thermal dust emission. It obeys the expected spectral behavior that it is strong at 220 GHz while it becomes nearly invisible at 95 GHz.

In order to handle the contribution from the ΛCDM model, the foreground emission and r, we use the same multi-component multi-spectral likelihood analysis as in BK15. In our baseline model, we first describe the BB foreground cross spectrum between maps with frequency ν_1 and

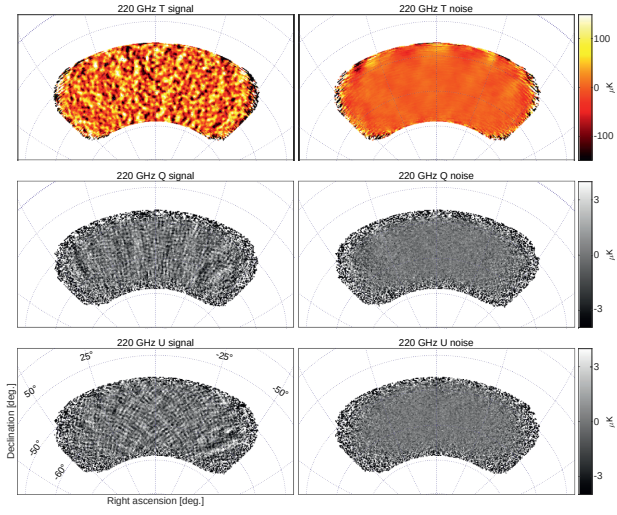

Figure 3 – *Keck* 220 GHz T, Q, U regular and noise maps from the BK18 paper. They are made using data equivalent to 14 *Keck* receiver-years. Note that the irregularities around the lower right corners of the Q and U maps are due to polarized dust emission.

ν_2 by

$$\mathcal{D}_{\ell,BB}^{\nu_1\times\nu_2} = A_{\rm d} f_{\rm d}^{\nu_1} f_{\rm d}^{\nu_2} \left(\frac{\ell}{80}\right)^{\alpha_{\rm d}} + A_{\rm s} f_{\rm s}^{\nu_1} f_{\rm s}^{\nu_2} \left(\frac{\ell}{80}\right)^{\alpha_{\rm s}} + \epsilon\sqrt{A_{\rm d}A_{\rm s}}\,(f_{\rm d}^{\nu_1} f_{\rm s}^{\nu_2} + f_{\rm s}^{\nu_1} f_{\rm d}^{\nu_2}) \left(\frac{\ell}{80}\right)^{(\alpha_{\rm d}+\alpha_{\rm s})/2}, \tag{1}$$

where $A_{\rm d}$ specifies the dust power amplitude at pivot frequency $\nu = 353$ GHz and $\ell = 80$; $A_{\rm s}$ is similarly the synchrotron power amplitude at $\nu = 23$ GHz; ϵ is the correlation parameter between dust and synchrotron; $\alpha_{\rm d}$ and $\alpha_{\rm s}$ are angular power spectrum power law indexes; and $f_{\rm d}$ and $f_{\rm s}$ are frequency scaling accounting for the spectral energy density (SED) of foreground integrated in the actual bandpasses of a given frequency. The synchrotron SED is modeled by a power law in frequency with index $\beta_{\rm s}$ while the dust SED is modeled by the modified blackbody with $T_{\rm d} = 19.6\,{\rm K}$ and frequency power law index $\beta_{\rm d}$. We also fix the scalar ΛCDM parameters to be the *Planck* 2018 best fit values. Therefore, we have the ΛCDM+dust+synchrotron+r baseline model with 8 parameters: $A_{\rm d}$, $A_{\rm s}$, $\alpha_{\rm d}$, $\alpha_{\rm s}$, $\beta_{\rm d}$, $\beta_{\rm s}$, ϵ and r.

On the data side, we have BB power spectra. Four internal maps (BICEP3 95 GHz, *Keck* 95 GHz, BICEP2/*Keck* 150 GHz and *Keck* 220 GHz) are used with multiple reprocessed WMAP (23 & 33 GHz) and *Planck* (30, 44, 143, 217 & 353 GHz) maps in our observation field to increase the total maps involved to 11. These maps are then purified and inverse noise apodized [19] to yield 66 BB auto- and cross-spectra.

Figure 4 shows a subset of BB and EE spectra as a demonstration. In particular, all BICEP3 auto- and cross-spectral bandpowers are consistent with the ΛCDM+foreground model lines which use the foreground best fit from our previous BK15 analysis with *no* BICEP3 data! This agreement is hence a validation of our foreground model at the current noise level since it correctly predicted weak foreground emission at 95 GHz. The small error bars of the BICEP3 BB bandpowers further suggest these data should provide strong constraining power on r.

We then supply our real BB power spectra, bandpower covariance matrix, bandpower window function and baseline model to `CosmoMC` [20] to evaluate the Hamimeche-Lewis (HL) likelihood [21]. Figure 5 shows the results with the BK15 comparison. The constraint of $r_{0.05}$ from the

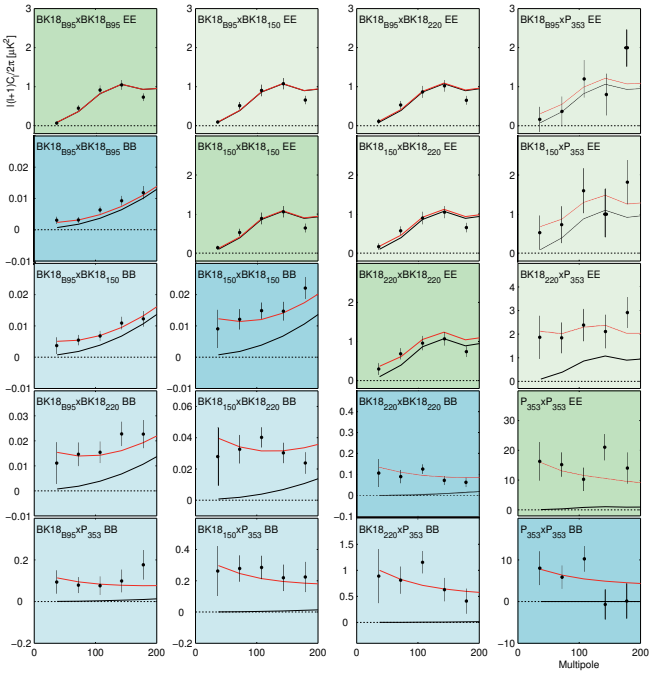

Figure 4 – *BB* (blue) and *EE* (green) auto- and cross-spectra from BICEP3 95 GHz, BICEP2/*Keck* 150 GHz, *Keck* 220 GHz and *Planck* 353 GHz maps. The black lines are the ΛCDM model expectation values, while the red lines are the ΛCDM+foreground expectation values from the foreground best fit of our previous BK15 analysis. The *EE* spectra are computed as a demonstration under the assumption $EE/BB = 2$ for dust. *EE* spectra are not included in our likelihood analysis.

baseline analysis, after marginalized over foreground parameters, evolves from $r_{0.05} = 0.020^{+0.021}_{-0.018}$ to $r_{0.05} = 0.014^{+0.010}_{-0.011}$. The confidence interval of $r_{0.05}$ is halved, dropping from $r_{0.05} < 0.07$ to $r_{0.05} < 0.036$ at 95% confidence. The constraint on dust amplitude is improved from $A_{\rm d} = 4.6^{+1.1}_{-0.9}$ μK^2 to $A_{\rm d} = 4.4^{+0.8}_{-0.7}$ μK^2 due to the additional *Keck* 220 GHz data.

Figure 5 also shows the constraints on the r vs. n_s plane as in figure 28 of Ref. [22]. Since this analysis is instead a *Planck*+BK18 joint fit, we vary those 8 parameters as well as other nuisance and scalar parameters including n_s. With the BK18 data it manifests unprecedented discrimination power on inflation models — the natural inflation and monomial inflation models now lie outside the 95% contour. Moreover, as adding *Planck* temperature and other data only gives a slightly improved upper limit $r_{0.05} < 0.035$, it implies the progress on the constraint of r is now entirely driven by B-mode measurements.

4 The Prospect of BICEP Array

The BICEP Array (BA) telescope is the successor to *Keck Array*. BA will have four BICEP3-style receivers covering six distinct bands centered at 30, 40, 95, 150, 220 and 270 GHz. It will be equipped with $\approx 30,000$ detectors, representing another order of magnitude increase in detector number relative to BICEP3. At the end of 2019, we installed a new, larger BA mount at MAPO and deployed the first BA 30/40 GHz receiver for the constraint of Galactic synchrotron emission. Since then, it has been observing with three adapted *Keck* receivers on the same mount. It will be followed by the deployments of 95 GHz and 150 GHz receivers in 2022, and

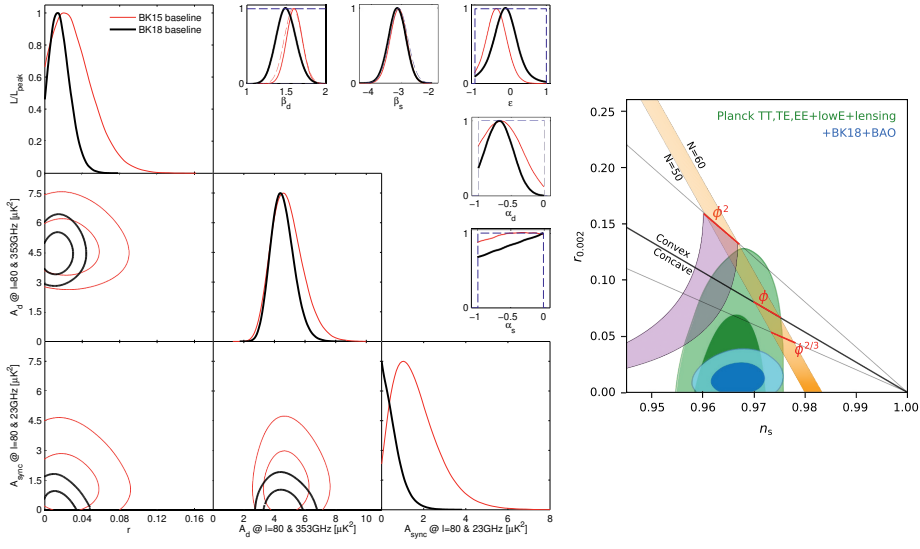

Figure 5 – *Left*: `CosmoMC` likelihood results for the BICEP/*Keck* baseline model. Selected 1D and 2D marginalized posteriors are shown. The red faint curves are the results from BK15 while the black solid curves are the results of BK18. The dashed blue and red lines show priors on foreground parameters. The analysis method is the same as in BK15, except the β_d prior based on *Planck* data from other regions of the sky is removed this time due to the improved sensitivity of BK18. *Right*: Constraints in the r vs. n_s plane. The purple and orange bands are natural inflation and monomial inflation respectively. The blue contour shows the updated constraint after adding BK18 and BAO data to the *Planck* baseline analysis. The r posterior is tightened from $r_{0.05} < 0.11$ to $r_{0.05} < 0.035$ at 95% confidence.

the 220/270 GHz receiver in 2023. Observations will continue to at least the end of 2027.

The observation plan and sensitivity forecast for BICEP Array is presented in figure 6. The post-BK18 progress on $\sigma(r)$ will soon stall as the constraint will become limited by lensing variation. We therefore have been working with the South Pole Telescope (SPT) collaboration to use the overlapping SPT-3G maps for "delensing" [23]. Following this strategy, even after 2 years of COVID delay, it is projected to give $\sigma(r) \lesssim 0.003$ using data up to 2027. This will either confirm or rule out other popular classes of inflation models.

Acknowledgments

The collaboration would like to give special thanks to our heroic winter-overs Robert Schwarz, Steffen Richter, Sam Harrison, Grantland Hall and Hans Boenish. K. Lau again expresses his gratitude to the organizers of the Rencontres de Moriond for holding a safe and successful conference during the pandemic.

References

1. A. H. Guth, *Phys. Rev.* D **23**, 347 (1981).
2. N. Aghanim *et al.* (*Planck* Collaboration), *Astron. Astrophys.* **641**, 56 (2020).
3. P. A. R. Ade *et al.* (*Planck* Collaboration), *Astron. Astrophys.* **571**, A22 (2014).
4. U. Seljak and M. Zaldarriaga, *Phys. Rev. Lett.* **78**, 2054 (1997).
5. M. Kamionkowski, A. Kosowsky and A. Stebbins, *Phys. Rev. Lett.* **78**, 2058 (1997).
6. CMB-S4 Collaboration, arXiv:1610.02743 (2016).

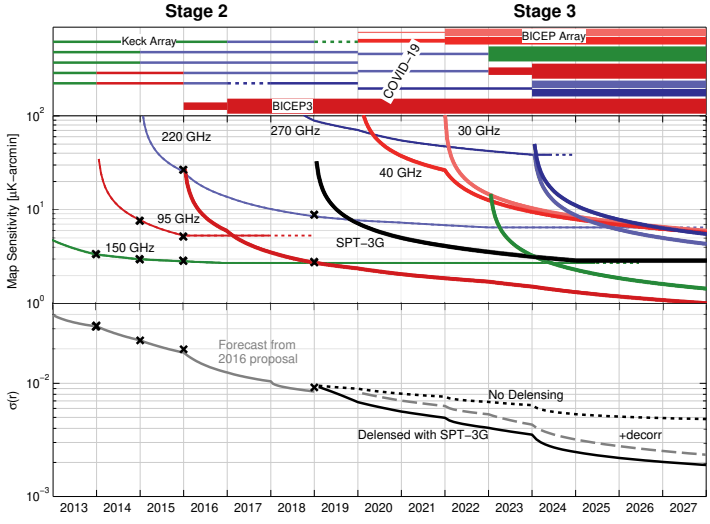

Figure 6 – The forecasts for the BICEP/*Keck* program. The top panel shows the plan of observation. The thickness of each line represents the detector number in a single receiver while its color represents the center frequency labeled in the next panel; the middle panel shows the corresponding map depth over time as lines. The cross marks are published values including those in BK15 and BK18. The sensitivity beyond 2018 is predicted by scaling based on achieved performance. The black SPT-3G line is the combined 95/150 GHz map depth projected from the achieved sensitivity in the 2019 and 2020 seasons; the bottom panel transforms map depth into $\sigma(r)$. Cross marks are again the published values. The good agreement between these cross marks and projection lines indicates that the forecasting method is realistic. Two independent forecasts (solid and dotted lines) highlight the significance of delensing. Including dust decorrelation in the delensing case (the dashed line) results in slightly higher $\sigma(r)$.

7. P. A. R. Ade *et al.* (BICEP2 Collaboration), *Phys. Rev. Lett.* **112**, 241101 (2014).
8. P. A. R. Ade *et al.* (*Planck* Collaboration), *Astron. Astrophys.* **586**, A133 (2016).
9. P. A. R. Ade *et al.* (BICEP2/*Keck* and *Planck* Collaborations), *Phys. Rev. Lett.* **114**, 101301 (2015).
10. N. Krachmalnicoff *et al.*, *Astron. Astrophys.* **618**, A166 (2018).
11. D. Hanson *et al.*, *Phys. Rev. Lett.* **111**, 141301 (2013).
12. P. A. R. Ade *et al.* (BICEP2 Collaboration), *Astrophys. J.* **792**, 62 (2014).
13. P. A. R. Ade *et al.* (BICEP2 and *Keck Array* Collaborations), *Astrophys. J.* **806**, 206 (2015).
14. P. A. R. Ade *et al.* (BICEP/*Keck* Collaboration), *Astrophys. J.* **927**, 77 (2022).
15. H. Hui *et al.*, *Proc. SPIE Int. Soc. Opt. Eng.* **10708**, 1070807 (2018).
16. L. Moncelsi *et al.*, *Proc. SPIE Int. Soc. Opt. Eng.* **11453**, 1145314 (2020).
17. P. A. R. Ade *et al.* (*Keck Array* and BICEP2 Collaborations), *Phys. Rev. Lett.* **121**, 221301 (2018).
18. P. A. R. Ade *et al.* (BICEP/*Keck* Collaboration), *Phys. Rev. Lett.* **127**, 151301 (2021).
19. P. A. R. Ade *et al.* (*Keck Array* and BICEP2 Collaborations), *Astrophys. J.* **825**, 66 (2016).
20. A. Lewis and S. Bridle, *Phys. Rev.* D **66**, 103511 (2002).
21. S. Hamimeche and A. Lewis, *Phys. Rev.* D **77**, 103013 (2008).
22. N. Aghanim *et al.* (*Planck* Collaboration), *Astron. Astrophys.* **641**, A6 (2020).
23. P. A. R. Ade *et al.* (The BICEP/*Keck* and SPTpol Collaborations), *Phys. Rev.* D **103**, 022004 (2021).

Cosmic Birefringence from *Planck* Public Release 4

P. Diego-Palazuelos[1,2], J. R. Eskilt[3], Y. Minami[4], M. Tristram[5], R. M. Sullivan[6], A. J. Banday[7,8], R. B. Barreiro[1], H. K. Eriksen[3], K. M. Górski[9,10], R. Keskitalo[11,12], E. Komatsu[13,14], E. Martínez-González[1], D. Scott[6], P. Vielva[1], and I. K. Wehus[3]

[1] *Instituto de Física de Cantabria (CSIC-Universidad de Cantabria), Santander, Spain*
[2] *Departamento de Física Moderna, Universidad de Cantabria, Santander, Spain*
[3] *Institute of Theoretical Astrophysics, University of Oslo, Oslo, Norway*
[4] *Research Center for Nuclear Physics, Osaka University, Osaka, Japan*
[5] *Université Paris-Saclay, CNRS/IN2P3, IJCLab, Orsay, France*
[6] *Department of Physics & Astronomy, University of British Columbia, Vancouver, Canada*
[7] *Université de Toulouse, UPS-OMP, IRAP, Toulouse, France*
[8] *CNRS, IRAP, Toulouse, France*
[9] *Jet Propulsion Laboratory, California Institute of Technology, Pasadena, U.S.A*
[10] *Warsaw University Observatory, Warszawa, Poland*
[11] *Computational Cosmology Center, Lawrence Berkeley National Laboratory, Berkeley, U.S.A.*
[12] *Space Sciences Laboratory, University of California, Berkeley, U.S.A*
[13] *Max Planck Institute for Astrophysics, Garching, Germany*
[14] *Kavli Institute for the Physics and Mathematics of the Universe, Todai Institutes for Advanced Study, University of Tokyo, Kashiwa, Japan*

We search for the signature of parity-violating physics in the Cosmic Microwave Background using *Planck* polarization data from the Public Release 4 (PR4 or `NPIPE`). For nearly full-sky data, we initially find a birefringence angle $\beta = 0.30^\circ \pm 0.11^\circ$ (68% C.L.). We also find that the values of β decrease as we enlarge the Galactic mask, which can be interpreted as the effect of polarized foreground emission. We use two independent approaches to model this effect and mitigate its impact on β. Although results are promising, and the good agreement between both models is encouraging, we do not assign cosmological significance to the measured value of β until we improve our knowledge of the foreground polarization. Acknowledging that the miscalibration of polarization angles is not the only instrumental systematic that can create spurious TB and EB correlations, we also perform a detailed study of `NPIPE` end-to-end simulations to prove that our measurements of β are not significantly affected by any of the known systematics.

1 Parity-violating physics in the CMB polarization

To this day, we only fully understand about 5% of the contents of the Universe, with the remainder of its energy content split into approximately 27% of Dark Matter (DM), and 68% of Dark Energy (DE). Numerous models have been proposed to explain these two dark components, *e.g.* [1,2], a wide range of new weakly interacting massive particles, exotic neutrino models, quintessence, and modified gravity models. Some of them, whether be it as a solution for DM or DE, have in common the introduction of a new pseudoscalar field, ϕ, that changes sign under the inversion of spatial coordinates, $\phi(-\vec{n}) = -\phi(\vec{n})$, thus violating parity conservation. A particularly interesting candidate that predicts this type of pseudoscalar field are axion-like particles [3], which, depending on the value of their mass, could act at the same time as a solution for early DE and then behave like DM at later times.

An interesting property that these parity-violating pseudoscalar fields have in common is that, if coupled to the electromagnetic tensor, $F_{\mu\nu}$, and its dual, $\tilde{F}^{\mu\nu}$, via a Chern-Simons term

in the Lagrangian density, $\mathcal{L} \supset \frac{1}{4} g_{\phi\gamma} \phi F_{\mu\nu} \tilde{F}^{\mu\nu}$, they can make the phase velocities of the right- and left-handed helicity states of photons differ [4,5,6]. Such offset has the effect of rotating the plane of linear polarization clockwise on the sky by an angle $\beta = -\frac{1}{2} g_{\phi\gamma} \int \frac{\partial \phi}{\partial t} dt$, where $g_{\phi\gamma}$ is the coupling constant between photons and the new pseudoscalar field. This rotation is what we call "cosmic birefringence" because it is as if space itself acted like a birefringent material (see Ref. [7] for a review).

Although we know $g_{\phi\gamma}$ must be small, in principle, we could constraint this kind of DM and DE models by measuring the rotation of the plane of polarization of a well-known source of linearly polarized light situated at a far away enough distance as to allow photons to experience a significant $\partial\phi/\partial t$ evolution. Emitted at the epoch of recombination ($z \approx 1100$), and with its polarization angular power spectra accurately predicted by the Λ Cold Dark Matter (ΛCDM) model, the Cosmic Microwave Background (CMB) is, therefore, the perfect tool for the search of cosmic birefringence [8].

CMB polarization can be decomposed into two eigenstates of parity [9,10]: the parity-even E-modes, and the parity-odd B-modes. Expressing these two modes in terms of their spherical harmonic coefficients, $E^{\rm CMB}_{\ell m}$ and $B^{\rm CMB}_{\ell m}$, we can calculate their corresponding two-point correlation functions to obtain one parity-odd and two parity-even angular power spectra:

$$\left.\begin{aligned} \langle E^{\rm CMB}_{\ell m} E^{\rm CMB*}_{\ell' m'} \rangle &= \delta_{mm'} \delta_{\ell\ell'} C^{EE,{\rm CMB}}_{\ell} \\ \langle B^{\rm CMB}_{\ell m} B^{\rm CMB*}_{\ell' m'} \rangle &= \delta_{mm'} \delta_{\ell\ell'} C^{BB,{\rm CMB}}_{\ell} \end{aligned}\right\} \quad \text{Parity-even}$$
$$\left.\begin{aligned} \langle E^{\rm CMB}_{\ell m} B^{\rm CMB*}_{\ell' m'} \rangle &= \delta_{mm'} \delta_{\ell\ell'} C^{EB,{\rm CMB}}_{\ell} \end{aligned}\right\} \quad \text{Parity-odd} \tag{1}$$

In the presence of cosmic birefringence, the intrinsic CMB polarization would then be rotated by an angle β,

$$\begin{pmatrix} E^{\rm o}_{\ell m} \\ B^{\rm o}_{\ell m} \end{pmatrix} = \begin{pmatrix} {\rm c}(2\beta) & -{\rm s}(2\beta) \\ {\rm s}(2\beta) & {\rm c}(2\beta) \end{pmatrix} \begin{pmatrix} E^{\rm CMB}_{\ell m} \\ B^{\rm CMB}_{\ell m} \end{pmatrix}, \tag{2}$$

so that the observed EB angular power spectra (denoted by the "o" superscript) becomes

$$C^{EB,{\rm o}}_{\ell} = \frac{1}{2} {\rm s}(4\beta) \Big(C^{EE,{\rm CMB}}_{\ell} - C^{BB,{\rm CMB}}_{\ell} \Big) + {\rm c}(4\beta) C^{EB,{\rm CMB}}_{\ell}. \tag{3}$$

For brevity, we refer to the sine, cosine, and tangent functions as s, c, and t. According to ΛCDM, the Universe has no preferred direction and the statistics of CMB anisotropies should be invariant under parity transformation, yielding a null EB correlation at recombination. In this way, finding $C^{EB,{\rm o}}_{\ell} \neq 0$ would be an evidence of parity-violating physics [8], something that so far has only been observed in the weak interaction. Furthermore, any signal found in the measured EB correlation that resembles that of $C^{EE,{\rm CMB}}_{\ell}$ can be attributed to being the effect of cosmic birefringence.

2 Joint estimate of birefringence and miscalibrated polarization angles

Analyses that search for cosmic birefringence in the CMB polarization face two obstacles. Firstly, any miscalibration of the polarization angle of the detector (created, *e.g.*, by a misalignment of the star tracker on the satellite with respect to the telescope mount, or a side effect of the half-wave plate that some future CMB experiments will implement) will also produce the rotation of the plane of linear polarization [11]. For an α miscalibration angle, this means that the observed EB correlation would yield $\beta + \alpha$ instead of β. And secondly, the CMB is not the only source of polarized emission in the microwave range. Our Galaxy is a bright source of polarized foreground emission, consisting of mainly synchrotron radiation at lower frequencies, and thermal dust emission at higher frequencies.

Fortunately, we can use Galactic foreground emission to break the degeneracy between the β and α angles [12]. Since Galactic foregrounds are produced locally, it is safe to assume that

the $\partial\phi/\partial t$ evolution of ϕ that they see within our Galaxy is negligible when compared to that experienced by the CMB photons that have been traveling since the epoch of recombination. In this way, Galactic foregrounds would not be significantly affected by cosmic birefringence, and they would only be rotated by the miscalibration of the detector. Updating Eq. 2 to include the foreground signal and a potential α miscalibration,

$$\begin{pmatrix} E^{\rm o}_{\ell m} \\ B^{\rm o}_{\ell m} \end{pmatrix} = \begin{pmatrix} {\rm c}(2\alpha) & -{\rm s}(2\alpha) \\ {\rm s}(2\alpha) & {\rm c}(2\alpha) \end{pmatrix} \begin{pmatrix} E^{\rm FG}_{\ell m} \\ B^{\rm FG}_{\ell m} \end{pmatrix} + \begin{pmatrix} {\rm c}(2\alpha+2\beta) & -{\rm s}(2\alpha+2\beta)) \\ {\rm s}(2\alpha+2\beta) & {\rm c}(2\alpha+2\beta) \end{pmatrix} \begin{pmatrix} E^{\rm CMB}_{\ell m} \\ B^{\rm CMB}_{\ell m} \end{pmatrix}, \quad (4)$$

it can be proven [13,14,15] that the observed EB angular power spectrum can be written like

$$C_\ell^{EB,{\rm o}} = \frac{{\rm t}(4\alpha)}{2}\left(C_\ell^{EE,{\rm o}} - C_\ell^{BB,{\rm o}}\right) + \frac{1}{{\rm c}(4\alpha)} C_\ell^{EB,{\rm FG}} + \frac{{\rm s}(4\beta)}{2{\rm c}(4\alpha)}\left(C_\ell^{EE,{\rm CMB}} - C_\ell^{BB,{\rm CMB}}\right) \quad (5)$$

when an intrinsic $C_\ell^{EB,{\rm CMB}} = 0$ is considered. As initially assumed in Refs. [12,13,16], the $C_\ell^{EB,{\rm FG}}$ term in Eq. 5 could be neglected because, according to current experimental constraints [17,18], it is still statistically compatible with being null. From Eq. 5, we can build a Gaussian likelihood to simultaneously determine both angles,

$$-2\ln\mathcal{L} = \sum_{\ell=\ell_{\rm min}}^{\ell_{\rm max}} \left(\mathbf{A}\bar{C}_\ell^{\rm o} - \mathbf{B}\bar{C}_\ell^{\rm CMB}\right)^T \mathbf{M}_\ell^{-1} \left(\mathbf{A}\bar{C}_\ell^{\rm o} - \mathbf{B}\bar{C}_\ell^{\rm CMB}\right) + \sum_{\ell=\ell_{\rm min}}^{\ell_{\rm max}} \ln|\mathbf{M}_\ell|, \quad (6)$$

using the information contained in the polarization angular power spectra from the cross-correlation of the different $i, j = 1, 2, ..., N_\nu$ frequency bands of any given CMB experiment, and the theoretical CMB angular power spectra:

$$\bar{C}_\ell^{\rm o} = \left(C_\ell^{E_iE_j,{\rm o}} \quad C_\ell^{B_iB_j,{\rm o}} \quad C_\ell^{E_iB_j,{\rm o}}\right)^T, \quad \bar{C}_\ell^{\rm CMB} = \left(C_\ell^{EE,{\rm CMB}} b_\ell^i b_\ell^j \omega_\ell^2 \quad C_\ell^{BB,{\rm CMB}} b_\ell^i b_\ell^j \omega_\ell^2\right)^T. \quad (7)$$

In this last vector, b_ℓ^i and ω_ℓ are, respectively, the instrumental beam and pixel window functions. The $\mathbf{M}_\ell$ covariance matrix in Eq. 6 is $\mathbf{M}_\ell = \mathbf{A}{\rm Cov}\left(\bar{C}_\ell^{\rm o}, \bar{C}_\ell^{{\rm o}T}\right)\mathbf{A}^T$, with $\mathbf{A}$ and $\mathbf{B}$ rotation matrices defined like

$$\mathbf{A}(\alpha_i, \alpha_j) = \begin{pmatrix} \frac{-{\rm s}(4\alpha_j)}{{\rm c}(4\alpha_i)+{\rm c}(4\alpha_j)} & \frac{{\rm s}(4\alpha_i)}{{\rm c}(4\alpha_i)+{\rm c}(4\alpha_j)} & 1 \end{pmatrix}, \quad \mathbf{B}(\alpha_i, \alpha_j, \beta) = \frac{{\rm s}(4\beta)}{2{\rm c}(2\alpha_i+2\alpha_j)} \begin{pmatrix} 1 & -1 \end{pmatrix}. \quad (8)$$

Note that, both the data vector $\bar{C}_\ell^{\rm o}$, and the covariance matrix $\mathbf{M}_\ell$, are built from the observed spectra so that the only model needed is that of the CMB angular power spectra in $\bar{C}_\ell^{\rm CMB}$. A more detailed description of this methodology is given in Refs. [13,14,15].

This technique was recently applied by Ref. [16] to polarization data from the 100, 143, 217, and 353 GHz frequency bands of the third data release (PR3) of the *Planck* satellite. Ignoring the potential contribution of the foreground EB correlation, and cross-correlating half-mission splits to reduce the effect of instrumental noise and systematics, they found a birefringence angle of $\beta = 0.35^\circ \pm 0.14^\circ$ (68% C.L.) for nearly the full-sky. Encouraged by this exciting 2.4σ hint of a signal, we wanted to update this result using data from the latest *Planck* data release [19], known as PR4 or `NPIPE` reprocessing. In the following sections, we present a summary of the main results and conclusions drawn from that analysis, emphasizing some of the aspects of the study on the impact of instrumental systematics that were not covered in Ref. [20]. All the uncertainties are given at a 68% confidence level (C.L.).

3 New measurement

The `NPIPE` release offers a new reprocessing of the raw, uncalibrated detector data from both the low-frequency (LFI) and high-frequency (HFI) instruments of the *Planck* mission. `NPIPE` achieves a scale-dependent reduction of the total uncertainty thanks to the addition of the data

acquired during repointing maneuvers and a general improvement in the modeling of instrumental noise and systematics. See Ref. [19] for a more in-depth description of the NPIPE processing pipeline and its associated data products.

Closely following the analysis done in Ref. [16], we work with polarization data from the HFI's 100, 143, 217, and 353 GHz frequency bands. To further reduce the impact of correlated noise and systematics, we work with A/B detector splits and exclude the auto-power spectra of the same maps, *e.g.*, 100A×100A. The cross-correlation of detector splits is more robust against the effects of noise and systematics because detector splits are built from independent subsets of antennas observing at the same frequency, while half-mission splits correspond to different exposure times of all the antennas observing at a common frequency. Being built from different antennas, A/B detector splits can present slightly different miscalibrations. Thus, we must fit a different polarization angle for each of them, α_i with $i = 100\mathrm{A}, 100\mathrm{B}, ..., 353\mathrm{B}$, doubling the number of free parameters with respect to the previous PR3 analysis. As done in Ref. [16], we focus on high-ℓ data, binning both angular power spectra and covariance matrix from $\ell_{\rm min} = 51$ to $\ell_{\rm max} = 1490$, with $\Delta\ell = 20$ spacing ($N_{\rm bins} = 72$), to target the cosmic birefringence angle from the epoch of recombination. We initially ignore the potential contribution of a foreground EB correlation.

For this baseline analysis we find consistent results across four independent groups (PDP, JRE, YM, MT). Each analysis pipeline uses different pseudo-C_ℓ estimators (`PolSpice`[21], `NaMaster`[22], `Xpol`[23]) and implementations: JRE, YM, and MT follow the original implementation [13,16] and obtain the posterior distribution through Markov chain Monte Carlo methods, while PDP uses an alternative approach in which the maximum likelihood solution is analytically calculated by minimizing the log-likelihood within the small-angle approximation [14].

We start by masking point-like extragalactic sources and pixels where the emission from the carbon monoxide (CO) line is bright (CO+PS mask in Figure 1). We mask regions of strong CO emission ($> 45 \mathrm{K_{RJ}kms^{-1}}$) because, although CO is not polarized, the mismatch of detector bandpasses can create a spurious polarization signal via intensity-to-polarization leakage. As our first result, we obtain a birefringence angle of $\beta = 0.30^\circ \pm 0.11^\circ$ for this nearly full-sky configuration. This measurement is compatible with and more precise than the previous result obtained from PR3 [16].

The birefringence angle that we are looking for is supposed to be an isotropic signal in the sky. Therefore, verifying that we recover compatible values of β when masking different regions of the sky would be a good consistency test. However, we found that the measured value of β decreased as we started to mask progressively larger regions of the brightest foreground emission in the Galactic plane (5%, 10%, 20%, and 30% Galactic masks in Figure 1). Although it is not shown in Figure 1, the decrease on β as we enlarge the Galactic mask is accompanied by the complementary increase on $\langle\alpha\rangle = N_\nu^{-1}\sum_i^{N_\nu}\alpha_i$ so that the $\beta + \langle\alpha\rangle$ sum maintains a constant value of $\simeq 0.3^\circ$.

As it was anticipated in Refs. [12,16,24], this behavior can be explained by the foreground EB correlation that we have ignored until now. To understand the effect that a non-zero foreground EB correlation might have on our measurements, we can rewrite the observed foreground angular power spectrum to be

$$\begin{aligned} C_\ell^{EB,\mathrm{FG,o}} &= \frac{1}{2}\mathrm{s}(4\alpha)\left(C_\ell^{EE,\mathrm{FG}} - C_\ell^{BB,\mathrm{FG}}\right) + \mathrm{c}(4\alpha)C_\ell^{EB,\mathrm{FG}} \\ &= \frac{1}{2}\sqrt{4\left(C_\ell^{EB,\mathrm{FG}}\right)^2 + \left(C_\ell^{EE,\mathrm{FG}} - C_\ell^{BB,\mathrm{FG}}\right)^2}\,\mathrm{s}(4\alpha + 4\gamma_\ell), \end{aligned} \tag{9}$$

where γ_ℓ is a new effective angle that, within the small-angle approximation, corresponds to

$$\gamma_\ell \approx \frac{C_\ell^{EB,\mathrm{FG}}}{2\left(C_\ell^{EE,\mathrm{FG}} - C_\ell^{BB,\mathrm{FG}}\right)}. \tag{10}$$

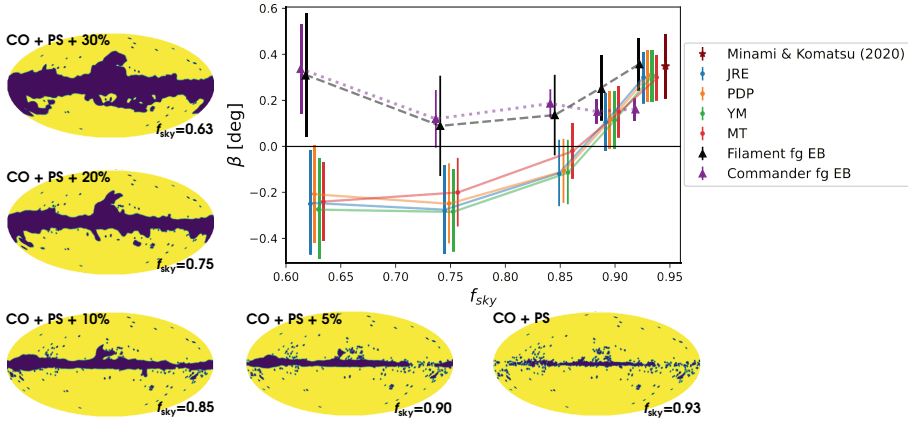

Figure 1 – Constraints on β for several sky fractions ($f_{\rm sky}$) with and without accounting for the foreground EB correlation. For the former, black and purple markers show the corrections using, respectively, the filament model in the JRE pipeline and the `Commander` sky model in the PDP pipeline. For the latter, the results of four pipelines (JRE, PDP, YM, MT) are shown. The Galactic masks corresponding to each sky fraction are displayed along the left and bottom margins. The birefringence angle obtained for the nearly full-sky analysis of PR3 polarization data is also shown for reference (brown star). However, the $f_{\rm sky}$ value at which it is plotted is merely illustrative and does not necessarily correspond to the actual effective $f_{\rm sky}$ from that analysis.

From this model, one can see that, if $C_\ell^{EB,\rm FG}$ is proportional to $C_\ell^{EE,\rm FG} - C_\ell^{BB,\rm FG}$, then the γ_ℓ angle would be independent of the multipole, $\gamma_\ell = \gamma$. In this scenario, γ becomes degenerate with α, meaning that we will effectively measure $\alpha+\gamma$ instead of α, and $\beta-\gamma$ instead of β, with the $\alpha+\beta$ sum remaining unaffected [12]. Previous analyses of *Planck* data have already reported that Galactic dust emission has a positive TB correlation [17], suggesting that dust could also have a positive EB correlation. A positive $C_\ell^{EB,\rm FG}$ would give $\gamma > 0$, producing a reduction of β and an increase of α like the ones seen in our results. In other words, the measured value of β, which is actually $\beta - \gamma$, is a lower bound for the true value of β [16].

4 Modeling the impact of the foreground EB correlation

We now need a model of $C_\ell^{EB,\rm FG}$ to correct the impact of foregrounds on our measurements and obtain an unbiased estimation of the true underlying birefringence angle. To this end, we use the model for $C_\ell^{EB,\rm FG}$ proposed in Ref. [25]. In that work, they demonstrate that the misalignment between the filamentary dust structures of the interstellar medium and the plane-of-sky orientation of the Galactic magnetic field induces a non-null EB correlation on Galactic dust emission. If the long axes of filamentary structures are, on average, perfectly aligned with the magnetic field, then null TB and EB correlations are expected. However, a small misalignment between filaments and the magnetic field will produce non-null TB and EB correlations, with their sign depending on the ψ angle of the misalignment. In particular, TB$\propto \sin(2\psi)$, EB$\propto \sin(4\psi)$, and TE$\propto \cos(2\psi)$ correlations are expected.

From their study of the misalignment between the distribution of filaments of neutral hydrogen atoms on synthetic dust simulations and Galactic magnetic field lines derived from *Planck* data, they also conclude that the dust EB correlation produced by this mechanism is strongly dependent on the analysis mask. They expect a small effect for a nearly full-sky configuration, whereas they expect a larger effect when a significant percentage of the Galactic plane is masked. This expectation agrees with the decline in β seen on the data as we enlarge the Galactic mask.

With the minor modifications discussed in Refs. [15,20], we adopt the model proposed by Ref. [25]

to predict the amplitude and sign of the dust EB angular power spectrum from the dust EE, TE, and TB correlations:

$$C_\ell^{EB,\mathrm{dust}} \approx 2A_\ell C_\ell^{EE,\mathrm{dust}} \frac{C_\ell^{TB,\mathrm{dust}}}{C_\ell^{TE,\mathrm{dust}}}, \tag{11}$$

where we leave A_ℓ to be a free amplitude parameter ($0 \leq A_\ell \ll 1$) to fit alongside β and α_i in the likelihood. We take the dust EE, TE, and TB angular power spectra from `NPIPE` data at 353GHz since dust emission dominates over the CMB at that frequency. To account for the possible dependence on ℓ, we split A_ℓ into four bins ($51 \leq \ell \leq 130$, $131 \leq \ell \leq 210$, $211 \leq \ell \leq 510$, and $511 \leq \ell \leq 1490$). With this correction, we now recover consistent positive values of β for all sky fractions (black markers in Figure 1). This result confirms our initial hypothesis that the decline in β was caused by the foreground EB correlation.

To further corroborate this idea, we also tried another completely independent approach using `NPIPE` foreground simulations of the `Commander` sky model. The `Commander` [26] sky model is built by fitting power-law synchrotron and one-component modified blackbody dust spectral energy distributions (SEDs) to *Planck* data, producing templates of the observed synchrotron and dust emissions in the sky. We used those templates to calculate the angular power spectra of Galactic dust emission and directly introduce them in our equations,

$$C_\ell^{EB,\mathrm{o}} = \frac{\mathrm{t}(4\alpha)}{2}\left(C_\ell^{EE,\mathrm{o}} - C_\ell^{BB,\mathrm{o}}\right) + \frac{1}{\mathrm{c}(4\alpha)}\mathcal{D}C_\ell^{EB,\mathrm{dust}} + \frac{\mathrm{s}(4\beta)}{2\mathrm{c}(4\alpha)}\left(C_\ell^{EE,\mathrm{CMB}} - C_\ell^{BB,\mathrm{CMB}}\right), \tag{12}$$

leaving also a free amplitude parameter $\mathcal{D}$ to be simultaneously fitted alongside β and α in the likelihood.

This approach also leads to consistent positive values of β for all sky fractions (purple markers in Figure 1). The results obtained with this model are in very good agreement with the ones from the filament model, except for the nearly full-sky measurement. That discrepancy could merely be a consequence of the difficulties faced by the `Commander` sky model in capturing the complexity of the dust emission on the center of the Galactic plane.

Another caveat to consider when interpreting the results of this approach is that the `Commander` SED model does not consider the existence of a potential α_i miscalibration across frequency bands. This might eventually yield a small spurious EB correlation on their foreground maps. In addition, the `Commander` sky model is derived from previous releases of *Planck* data, and does not yet provide a signal-dominated template for the foreground EB. Thus, `Commander` foreground maps are very well correlated with `NPIPE` data, maybe even to the point of reproducing some of its statistical fluctuations. This leads to a reduction of the covariance matrix and the smaller uncertainties seen in Figure 1.

On the other hand, the filament model might be limited in its simplicity, and not fully capture the complex interplay of dust and magnetic field lines at all angular scales. In that sense, these two approaches are complementary, and, although it is encouraging that they yield similar results, we need to improve our understanding of the foreground EB before achieving a definitive measurement of β.

5 Quantifying systematics using the end-to-end simulations

The miscalibration of the polarization angle of the detector is not the only instrumental effect that can potentially affect our analysis. Systematic effects like intensity-to-polarization leakage, beam leakage, or cross-polarization effects, can also produce spurious TB and EB correlations. To assess the impact of such systematics on our measurements, we conducted a detailed study of the official `NPIPE` end-to-end simulations. Although briefly commented in Ref. [20], further results of that study will be presented in Ref. [14].

`NPIPE` end-to-end simulations are built by passing the expected CMB and foreground signals for each frequency band through the full *Planck* instrument model and the `NPIPE` processing

pipeline. In addition to the CMB and foreground signals, the frequency maps produced in this way also capture the instrumental noise and systematics, and the non-linear response of the instrument that eventually leads to couplings between noise and signal. "Residuals" maps, which contain only instrumental noise and systematics, are then produced by subtracting the initial input CMB and foreground signals from those frequency maps. See Ref. [19] for a more technical description of `NPIPE` end-to-end simulations.

Since the effect of Galactic foregrounds was already determined, here we focus on the effect of systematics by using simulations of just CMB and Residuals. However, without foregrounds, we are no longer able to break the degeneracy between the birefringence and polarization angles. Therefore, we can either fit a different angle for each detector split, *i.e.*, α_i, or we can fit the same angle for all frequency bands, *i.e.*, β.

For this test, we built a set of 100 simulations by coadding each CMB realization with its associated Residual map, which we mask and analyze as we did with the data. Taking turns fitting angles that behave either like α_i or β, we obtain the mean systematic angles shown in Figure 2. We find the presence of some systematic α_i angles on the simulations, especially for the 100A and 100B detector splits. To understand their origin, we performed a closer study of the simulations, finding that the angular power spectra of CMB + Residuals simulations at the 100A and 100B frequency bands resemble that of $C_\ell^{EE,\mathrm{CMB}}$. In general, intensity-to-polarization leakage gives $C_\ell^{EB} \propto C_\ell^{TT}$, whereas the cross-polarization effect gives $C_\ell^{EB} \propto C_\ell^{EE}$, and a combination of the two would give $C_\ell^{EB} \propto C_\ell^{TE}$. Thus, we believe that the systematic angles found in the simulations are due to a cross-polarization effect. This kind of systematic is particularly dangerous for our analysis since our estimator relies precisely on finding a $C_\ell^{EE,\mathrm{CMB}}$-like signal in the measured EB correlation to determine both the birefringence and polarization angles.

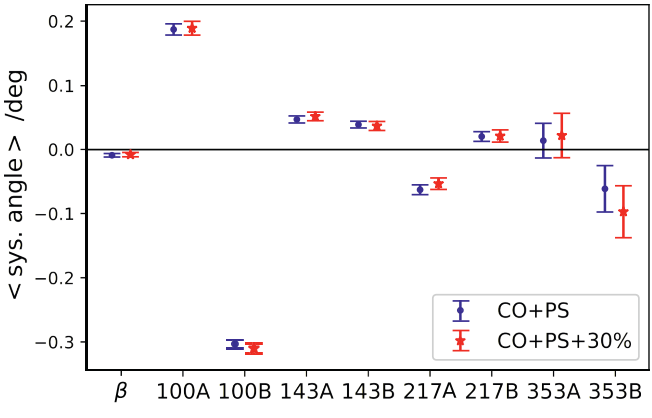

Figure 2 – Mean systematic birefringence and polarization angles found in `NPIPE` CMB + Residuals simulations. Angles are averaged over $N_{\mathrm{sim}} = 100$ simulations, with uncertainties calculated as the simulations' dispersion over $\sqrt{N_{\mathrm{sim}}}$. The blue points show the results for our smallest mask (CO+PS, $f_{\mathrm{sky}} = 0.93$), while the red points are for our largest mask (CO+PS+30%, $f_{\mathrm{sky}} = 0.63$).

Identifying the existence of this cross-polarization effect is essential to understand all the effects at play in both simulations and data. Nevertheless, note that the systematic angles found on the simulations do not need to agree with the ones found in the data because the simulations do not, and in fact cannot, include the actual unknown miscalibration angles present in the data. In this way, the main conclusion to draw from these results is that, even in the presence of such cross-polarization effect, and the rest of the known systematics, our methodology is able to correctly capture their effect within the α_i miscalibration angles, leaving the measurement of

β not significantly affected by any of them. This observation justifies our decision not to correct our β measurements for any of the known systematics.

Another conclusion to draw from the results in Figure 2 is that we find consistent mean systematic angles for our largest (CO+PS+30%) and smallest (CO+PS) masks. This means that none of the known systematics can reproduce the decline in β as we enlarge the Galactic mask, reinforcing our hypothesis that it is driven by the foreground EB correlation.

6 Conclusions

In this work, we continue the search for cosmic birefringence in the CMB polarization by updating the previous analysis of *Planck* PR3 data [16] with the latest `NPIPE` data release. We initially find a birefringence angle of $\beta = 0.30^\circ \pm 0.11^\circ$ for nearly full-sky data, which is consistent with and more precise than the previously reported value for PR3. Exploring the dependence of β on Galactic masks, we found that our measurements of birefringence decreased as we enlarged the Galactic mask, which can be interpreted as the effect of the EB correlation of polarized dust emission. We have used two independent models to account for this component, and although results are promising and the good agreement between both models is encouraging, we chose not to assign cosmological significance to our measurement of β until we have a better understanding of polarized foreground emission.

If confirmed, cosmic birefringence would be an evidence of physics beyond the standard model of cosmology and particle physics. To make progress, we need to continue the search in independent datasets, especially those with access to the full-sky, like the LiteBIRD [27] mission. A first follow-up analysis incorporating *Planck* LFI data and exploring the frequency-dependence of the birefringence signal has already been published [15]. We also need to improve our knowledge of the EB science, both in the sense of achieving a better understanding of the foreground emission, and a better control of the systematics that plague this channel. In this regard, we wanted to stress the need for high-fidelity end-to-end simulations, which have played a paramount role in this analysis by helping to understand all of the systematics affecting the EB correlation.

Last but not least, we can avoid Galactic foregrounds altogether if we do not rely on the measured EB correlation for calibration. To this end, we must improve upon the accuracy of calibrating the artificial rotation of polarization angles due to telescopes, optics, and detectors. Our result suggests that the target accuracy should be well below 0.1°, *e.g.*, 0.06° for a 5σ result for $\beta \simeq 0.3^\circ$. While challenging, the current technology should allow for such precision [28,29,30]. This line of research should be pursued to obtain the most robust measurement of cosmic birefringence.

Acknowledgments

PDP thanks the organizers for the opportunity to present this work at the Cosmology session of the 56$^{\text{th}}$ *Rencontres de Moriond* and for such a great conference. PDP thanks the Spanish Agencia Estatal de Investigación (AEI, MICIU) for the financial support provided under the project with reference PID2019-110610RB-C21, and also acknowledges funding from the Formación del Profesorado Universitario (FPU) program of the Spanish Ministerio de Ciencia, Innovación y Universidades, and the Unidad de Excelencia María de Maeztu (MDM-2017-0765). The results presented here are based on observations obtained with *Planck*, an ESA science mission with instruments and contributions directly funded by ESA Member States, NASA, and Canada. This research used resources of the National Energy Research Scientific Computing Center (NERSC), a U.S. Department of Energy Office of Science User Facility operated under Contract No. DE-AC02-05CH11231. We acknowledge the use of `HEALPix` [31], `PolSpice` [21], `NaMaster` [22], `Xpol` [23], `emcee` [32], `Matplotlib` [33], and `NumPy` [34].

References

1. J. L. Feng, Annu. Rev. Astron. Astrophys., **48** (2010).
2. J. Yoo and Y. Watanabe, Int. J. Mod. Phys. D, **21**, 1230002 (2012).
3. D. J. E. Marsh, Phys. Rep., **643** (2016).
4. S. M. Carroll *et al.*, Phys .Rev. D, **41**, 1231 (1990).
5. S. M. Carroll and G. B. Field, Phys. Rev. D, **43**, 3789 (1991).
6. D. Harari and P. Sikivie, Phys. Lett. B, **289**, 67 (1992).
7. E. Komatsu, Nat. Rev. Phys. 4, 452-469 (2022).
8. A. Lue *et al.*, Phys. Rev. Lett., **83**, 1506 (1999).
9. M. Zaldarriaga and U. Seljak, Phys. Rev. D, **55**, 1830 (1997).
10. M. Kamionkowski *et al.*, Phys. Rev. D, **55**, 7368 (1997).
11. N. Krachmalnicoff *et al.*, J. Cosmol. Astropart. Phys., **2022**, 039 (2022).
12. Y. Minami *et al.*, Prog. Theor. Exp. Phys., **2019**, 083E02, (2019).
13. Y. Minami and E. Komatsu, Prog. Theor. Exp. Phys., **2020**, 103E02 (2020).
14. P. Diego-Palazuelos *et al.*, arXiv:2210.07655 (2022).
15. J. R. Eskilt, Astron. Astrophys., 662 A10 (2022).
16. Y. Minami and E. Komatsu, Phys. Rev. Lett., **125**, 221301 (2020).
17. Planck Collaboration, Y. Akrami *et al.*, Astron. Astrophys., **641**, A11 (2020).
18. F. A. Martire *et al.*, Accept. J. Cosmol. Astropart. Phys., 2022 (04), 003 (2022).
19. Planck Collaboration, Y. Akrami *et al.*, Astron. Astrophys., **643**, A42 (2020).
20. P. Diego-Palazuelos *et al.*, Phys. Rev. Lett., **128**, 091302 (2022).
21. G. Chon *et al.*, Mon. Not. Roy. Astron. Soc., **350**, 914 (2004).
22. D. Alonso *et al.*, Mon. Not. Roy. Astron. Soc., **484**, 4127 (2019).
23. M. Tristram *et al.*, Mon. Not. Roy. Astron. Soc., **358**, 833 (2005).
24. Y. Minami, Prog. Theor. Exp. Phys., **2020**, 063E01, (2020).
25. S. E. Clark *et al.*, Astrophys. J., **919**, 53 (2021).
26. Planck Collaboration, Y. Akrami *et al.*, Astron. Astrophys., **641**, A4 (2020).
27. LiteBIRD Collaboration, E. Allys *et al.*, arXiv:2202.02773 (2022).
28. F. J. Casas *et al.*, Sensors **2021**, 21(10), 3361 (2021).
29. F. Nati *et al.*, J. Astron. Instrum., **6**, 2, 1740008 (2017).
30. M. F. Navaroli *et al.*, Proceedings of the SPIE, **10708**, 107082A (2018).
31. K. M. Górski *et al.*, Astrophys. J., **622**, 759 (2005).
32. D. Foreman-Mackey *et al.*, Publ. Astron. Soc. Pac., **125**, 925, 306 (2013).
33. J. D. Hunter, Comput. Sci. Eng., **9**, 3 (2007).
34. C. R. Harris *et al.*, Nature, **585**, 7825 (2020).

Prospects and challenges for future CMB bispectrum measurements

William R. Coulton
Center for Computational Astrophysics, Flatiron Institute, New York, NY 10010, USA

The next generation of CMB experiments will make low-noise, high resolution measurements of the temperature and polarization fluctuations. These data sets offer opportunities to improve constraints on primordial non-Gaussianity (pnG), however this impressive resolution requires a detailed understanding of all potential contaminants to ensure bias free inferences. The biggest challenge arises from signal confusion and extra-variance from non-Gaussian CMB secondary anisotropies. Here we explore how these effects will impact the upcoming Simons Observatory experiment and how they can be mitigated. These low-noise measurements also provide the chance to study novel signals in the CMB such as second-order perturbations. Second-order evolution of Gaussian initial conditions generates non-Gaussian, curl-like polarization signals (B modes). We show that the three point function between a second-order B mode and two first-order T/E modes is a powerful probe of second-order B modes and should be detectable by upcoming CMB experiments. The three point function contains a component from non-linear evolution and scattering processes before the end of recombination that can be isolated from other contributions and can provide new information on the pre-recombination era.

1 Introduction

Measurements of primordial non-Gaussianity (pnG) are one of the most powerful probes of the early universe providing constraints on the field content, strength of interactions and deviations from vacuum initial conditions. The cosmic microwave background (CMB) is an ideal place to search for pnG as the measured anisotropies are, largely, linearly related to the primordial anisotropies, thus measurements of the statistics of the primary CMB anisotropies straightforwardly maps to the statistics of the primordial fluctuations. Given the theoretical motivation, there has been extensive work developing the tools to measure pnG in the CMB and apply them to data (see e.g [1] for a recent overview). To date there is not yet a statistical significant detection of pnG and the best constraints are provided by the *Planck* satellite [2].

In the coming decade there are a range of CMB experiments that will improve upon *Planck*'s measurement of the CMB anisotropies. Experiments such as the Simons Observatory and CMB-S4 will provide low, noise and high resolution of the CMB across $\sim 30\%$ of the sky. These experiments offer the prospects of tightening bounds on deviations from Gaussianity in the primordial universe by factors of ~ 2, which can then be used to further constrain the properties of models of the primordial universe.

In this talk we will consider some of the challenges and additional opportunities that upcoming measurements will provide.

2 Challenges

The enhanced sensitivity of these upcoming experiments also brings increased sensitivity to late-time astrophysical processes that can obscure inferences of pnG. We consider two classes

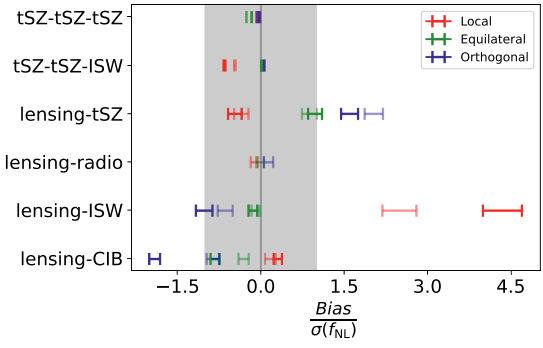

Figure 1 – The individual biases from correlations between gravitational lensing, thermal Sunyaev Zeldovich (tSZ), Integrated Sachs-Wolfe (ISW) and cosmic infrared background (CIB) anisotropies to primordial non-Gaussianity measurements for a Simons Observatory like experiment. The dark (light) points denote those from the Websky (Sehgal et al) suite of simulations. The size of the biases is normalized by the experimental error on the primordial shape.

of effects that have the potential to interfere with pnG searches: biases to measurements from extragalactic foregrounds and additional effective noise arising from gravitational lensing induced non-Gaussianity.

We focus our analysis on constraining primordial bispectra, the harmonic equivalent of real-space three point function, and on three types of pnG that are commonly considered in the literature: local, equilateral and orthogonal non-Gaussianity. Each of these types corresponds to a specific bispectrum shape that describes the strength of the correlations between three fields as a function of momentum. These bispectra are considered as they are highly informative of the physics of the early universe and are quite generically produced in models of the early universe (see e.g. [3]).

2.1 Extragalactic Foreground Biases

Observations of the primary CMB anisotropies are obscured by CMB secondary anisotropies, anisotropies as CMB photons propagate through the universe to the observer. Secondary anisotropies include a range of gravitational, scattering and emission processes and are typically highly non-Gaussian. Their non-Gaussian nature means they can have non-zero bispectra and hence bias inferences on the primordial bispectrum.

The bias arising from correlations between the integrated Sachs-Wolfe effect and lensing has been well known and recently [4] showed that a range of other CMB secondaries can lead to non-trivial biases. Building on that work, we perform an exploration of all of the key CMB secondary anisotropies. To do so we analyze two sets of non-Gaussian simulations of CMB secondary anisotropies: the Websky simulations [5] and the Sehgal et al simulations [6].

We measured the bispectra produced by all the simulated CMB secondaries and then computed how these bispectra would project onto the primordial bispectrum to bias constraints. In Fig. 1 we show the largest biases that would be present for a future survey like the Simons Observatory. These results are after a standard method, the harmonic internal linear combination method, has been used minimize the contribution of non-primary CMB anisotropies and so the biases arises from the residuals. We see that there are non-trival biases from correlations between gravitational lensing and the thermal Sunyaev Zeldovich effect and cosmic infrared background that remain.

These results indicate that a highly careful analysis of potential biases will be necessary to ensure unbiased inferences can be made about the primordial perturbations. More details of

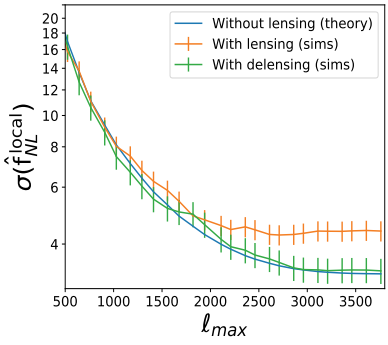

Figure 2 – The experimental error on local-type pnG for a Simons Observatory experiment. We consider three forecasts: an idealized case accounting for Gaussian noise and foregrounds (blue), a case that includes the extra variance sourced by gravitational lensing (orange) and finally a case that includes a mitigation strategy for removing the lensing induced variance (green).

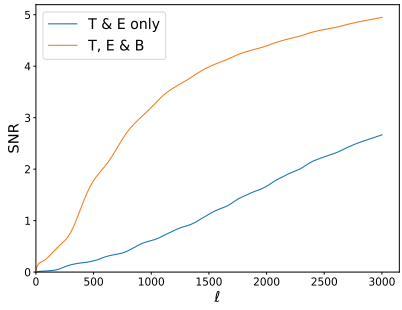

Figure 3 – The signal to noise (SNR) on the intrinsic bispectrum between second order B modes and T and E mode anisotropies for the CMB-S4 experiment. The solid (dotted) lines show the SNR as a function of scale. For reference the SNR on the intrinsic bispectrum between only T and E modes is shown in blue.

these results will be soon available in Coulton et al (in prep).

2.2 Gravitational Lensing

CMB lensing distorts the trajectories of CMB photons as they propagate through the universe resulting in remapping of the location of the unlensed CMB anisotropies, $\Delta\tilde{T}(\mathbf{n})$, by the lensing potential, $\phi(\mathbf{n})$, as

$$\Delta T(\mathbf{n}) = \Delta\tilde{T}(\mathbf{n} + \nabla\phi) \tag{1}$$

where $\Delta T(\mathbf{n})$ are the observed anisotropies. As was discussed in [7,8] gravitational lensing induces non-Gaussianity that, in addition to the biases discussed above, acts as a source of effective noise in CMB pnG measurements. This can be straightforwardly understood by expanding the effect of the lensing

$$\Delta T(\mathbf{n}) = \Delta\tilde{T}(\mathbf{n}) + \nabla\phi(\mathbf{n}) \cdot \nabla\Delta\tilde{T}(\mathbf{n}) + ... \tag{2}$$

The quadratic term here means that evaluations of the bispectrum covariance, a six-point function of the observed anisotropies, is no longer given purely by a simple Wick contraction of the observed anisotropies. The importance of these additional contributions is shown in Fig. 2 where it can be seen that this effect negates any potential gain in constraining power from measuring scales above $\ell \sim 2000$.

We explored how effective delensing is at mitigating this additional variance. The idea of delensing is that if we have an estimate of the lensing potential, $\hat{\phi}(\mathbf{n})$, we can attempt to undo the lensing effect as

$$\Delta\hat{\tilde{T}}(\mathbf{n}) = \Delta T(\mathbf{n} - \nabla\hat{\phi}). \tag{3}$$

In Fig. 2 we implement a delensing method using a consistently reconstructed lensing potential and find that this can remove all of the additional variance. This can be done without introducing any sources of bias. More details can be found in [8].

3 New signals with the B-mode intrinsic bispectrum

The increased sensitivity will not only bring increased challenges, it also brings new opportunities and one such opportunity is the potential to perform the first measurements of the CMB

intrinsic bispectrum. The CMB intrinsic bispectrum arises from the non-linear evolution of cosmological perturbations before the surface of last scattering as well as the non-linear scattering and deflections that occur. As these processes are non-linear they generate non-Gaussianity in the primary CMB anisotropies even if the primordial perturbations are purely Gaussian.

The intrinsic bispectrum present in temperature and E mode anisotropies has been studied in [9]. Here we discuss the potential of the intrinsic bispectrum that occurs between T,E and B modes. Whilst at linear of B-mode anisotropies are only sourced by primordial gravitational waves, at non-linear order they can be generated from purely scalar perturbations - the most well-known example of this is CMB lensing induced B-modes. As these B-modes are sourced by a non-linear function of the Gaussian, scalar perturbations they will be non-Gaussian and not independent from the T and E mode perturbations.

In Fig. 3 we plot the detectability of the intrinsic bispectrum arising between correlations of the second order B modes with the T and E mode anisotropies for a CMB S4 like experiment. We find that upcoming experiments will be able to provide the first measurements of this effect! Further details of this work can be found in [10].

4 Outlook

Future CMB experiments will continue to enhance our knowledge of the primordial universe by improved constraints on pnG. The high precision of these measurements will require improved techniques to ensure unbiased and optimal inferences can be made. However there will also be new opportunities including the ability to detect the CMB intrinsic bispectrum.

References

1. P. D. Meerburg et al. Primordial Non-Gaussianity. BAAS, 51(3):107, May 2019.
2. Planck Collaboration. Planck 2018 results. IX. Constraints on primordial non-Gaussianity. *A&A*, 641:A9, September 2020.
3. Xingang Chen. Primordial Non-Gaussianities from Inflation Models. *Advances in Astronomy*, 2010:638979, January 2010.
4. J. Colin Hill. Foreground biases on primordial non-Gaussianity measurements from the CMB temperature bispectrum. Phys. Rev. *D*, 98(8):083542, October 2018.
5. G. Stein et al. The websky extragalactic cmb simulations. *Journal of Cosmology and Astroparticle Physics*, 2020(10):012–012, Oct 2020.
6. Neelima Sehgal et al. Simulations of the Microwave Sky. *ApJ*, 709(2):920–936, February 2010.
7. Daniel Babich and Matias Zaldarriaga. Primordial bispectrum information from CMB polarization. Phys. Rev. *D*, 70(8):083005, October 2004.
8. William R. Coulton et al. Minimizing gravitational lensing contributions to the primordial bispectrum covariance. Phys. Rev. *D*, 101(12):123504, June 2020.
9. Guido W. Pettinari et al. The intrinsic bispectrum of the cosmic microwave background. J. Cosmology Astropart. Phys., 2013(4):003, April 2013.
10. William R. Coulton. Parity-odd intrinsic bispectrum. Phys. Rev. *D*, 104(10):103527, November 2021.

Status of QUBIC, the Q&U bolometric interferometer for cosmology

L. Mousset on behalf of the QUBIC collaboration
IRAP, Université de Toulouse, CNRS, CNES, UPS, Toulouse, France

The Q&U Bolometric Interferometer for Cosmology (QUBIC) is a novel kind of polarimeter optimized for the measurement of the B-mode polarization of the Cosmic Microwave Background (CMB), which is one of the major challenges of observational cosmology. The signal is expected to be of the order of a few tens of nK, prone to instrumental systematic effects and polluted by various astrophysical foregrounds which can only be controlled through multichroic observations. QUBIC is designed to address these observational issues with a novel approach that combines the advantages of interferometry in terms of control of instrumental systematics with those of bolometric detectors in terms of wide-band, background-limited sensitivity.

1 Introduction

The quest for B-mode polarization of the Cosmic Microwave Background (CMB) is among the major challenges of observational cosmology. Cosmic inflation predicts primordial scalar perturbations of the metric (density fluctuations), but also tensor perturbations, equivalent to primordial gravitational waves. These tensor modes should be imprinted in the CMB polarization fluctuations with a very specific signature: odd-parity patterns (curl term), known as B-modes [6]. The amplitude of the tensor modes, relative to the scalar modes, is parametrized by the so called tensor-to-scalar ratio r. The expected signal is weak, requiring high sensitivity detectors. In addition, astrophysical foregrounds produce non-primordial B-mode polarization, such as thermal emission from dust grains in the Galaxy.

The Q&U Bolometric Interferometer for Cosmology (QUBIC) was designed to address the B-mode detection challenge [1]. Characterization and calibration of a Technical Demonstrator (TD) started in 2018, at Astroparticle Physics & Cosmology (APC) laboratory. In May 2021, the instrument has been sent to Argentina. A second calibration phase is undergoing and the instrument will be installed on the observation site in the next months. In Hamilton *et al.* [1], we give forecasts for typical observations and measurements: with three years of integration on the sky and assuming perfect foreground removal as well as stable atmospheric conditions from our site in Argentina, our simulations show that we can achieve a statistical sensitivity to the effective tensor-to-scalar ratio (including primordial and foreground B-modes) $\sigma(r) = 0.015$.

2 Control of systematic effects with QUBIC

As a bolometric interferometer, QUBIC combines the advantages of interferometry in terms of control of instrumental systematic effects with those of bolometric detectors in terms of wide-band, background-limited sensitivity. A picture of the instrument with a sketch of the optical design is shown in Figure 1.

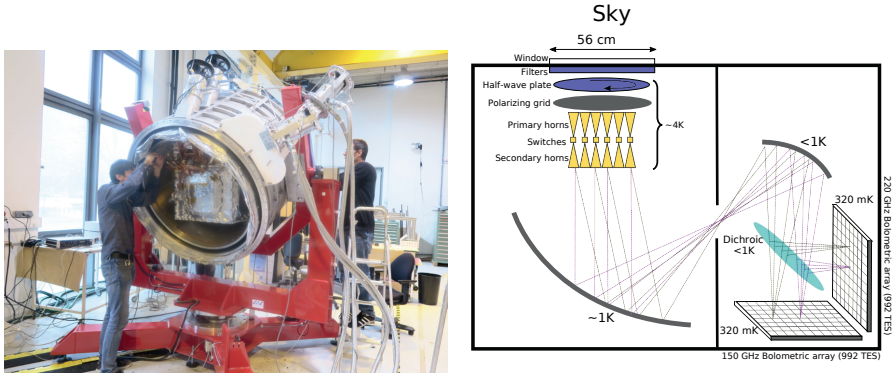

Figure 1 – *Left:* Picture of the QUBIC instrument at APC during the integration phase. *Right:* Optical sketch of the instrument.

2.1 Low cross-polarization

QUBIC bolometers are full power detectors. The measurement of the polarization is only done by modulating the signal amplitude with a rotating Half-Wave Plate (HWP) and a fixed polarizing grid. Every optical element has its own systematic effects which could induce cross-polarization. This means that the two polarization directions (x, y) of the signal can be mixed when interacting with the instrument and this is a major issue. The x-axis is defined as the transmission axis of the polarizing grid. By putting the HWP and the polarizing grid right after the window, the x polarization is selected as early as possible. In this way, any cross-polarization occurring after the polarizing grid, for example generated by the horn-array, the mirrors or any reflection in the instrument, has no impact.

The modulation of the polarization was tested during the calibration phase and a very low cross-polarization was indeed detected. Those measurements are presented in Torchinsky *et al.*[3] and D'Alessandro *et al.*[4] and the cross-polarization contamination at 150 GHz is compatible with zero to within 0.6%.

2.2 Self-calibration technique

Interferometry offers the possibility to self-calibrate the instrument systematic effects. This technique has been used for a long time in radio astronomy [8]. Self-calibration relies on the concept of equivalent baselines, one baseline b being formed with two horns. The full horn-array is shown in Figure 2 (left).

The self-calibration technique is based on the fact that, in case of an ideal instrument without any systematic effect, equivalent baselines produce the same interference pattern on the focal plane, for an observation at infinity, in the Fraunhofer regime. Thus, by measuring the differences, one can calibrate the systematics of the instrument. The demonstration of this technique for QUBIC was done in Bigot-Sazy *et al.*[7].

3 Spectral imaging capability

The instrument beam pattern, shown in Figure 2 (right), is given by the geometric distribution of the horn-array. It contains multiple peaks whose angular separation is linearly dependent on the wavelength. As a result, and after a non-trivial map-making process, a bolometric interferometer such as QUBIC can simultaneously produce sky maps at multiple frequency sub-bands with data

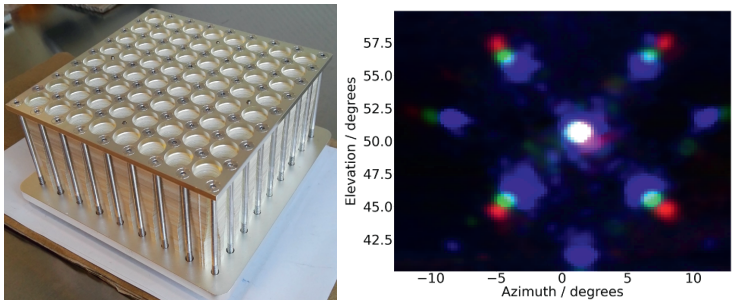

Figure 2 – *Left:* Picture of the TD horn-array (8×8 back-to-back horns), taken from Cavaliere *et al.*[5]. *Right:* Superimposition of three monochromatic beams measured in the laboratory at 130 GHz (red), 150 GHz (green) and 170 GHz (blue), taken from Torchinsky *et al.*[3].

acquired over a single wide frequency band. The demonstration of this technique, called spectral imaging, and the characterization of its performance are presented in Mousset *et al.*[2].

3.1 Tested on end-to-end simulations

We demonstrate spectral imaging capabilities by trying to recover the frequency dependence of the thermal galactic dust emission with simulated observations. We simulate an observation in a sky patch of 15 degree radius. The parameters of the pipeline are set in such a way that the simulated instrument has a single focal plane operating either at 150 GHz or at 220 GHz with a 25% bandwidth each. From these wide-band TOD, we are able to reconstruct several numbers of sub-bands using spectral imaging.

The reconstructed intensity as a function of frequency is studied in a given pixel. Figure 3 shows the intensity of the input sky convolved with the instrument beam, and the reconstructed intensity for a given pixel, considering 5 sub-bands in each wide band at 150 (red) and 220 (blue) GHz.

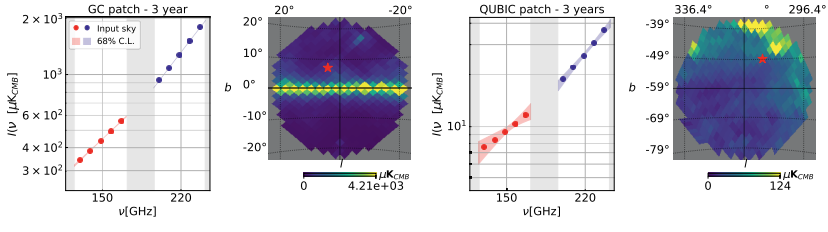

Figure 3 – Intensity as a function of the frequency for $N_{\rm rec} = 5$ sub-bands in each wide band at 150 (red) and 220 (blue) GHz for a given pixel. The grey regions correspond to the unobserved frequencies outside our physical bands. Two sky pixels are shown as red stars, one in a patch centered at the Galactic center and one in the patch that QUBIC plans to observe centered in [0, -57 deg]. Red and blue dots: Input sky convolved with the instrument beam. In both cases are shown in light color the 68% CL regions for a modified black-body spectrum reconstructed with a MCMC from our simulated measurements and sub-band covariance matrices. Maps are in μK CMB and $N_{\rm side} = 32$.

3.2 First trial on real data

Spectral imaging has been applied on real data for the first time during the calibration campaign at the APC laboratory. The QUBIC instrument was placed on an alt-azimuth mount in order to

scan a calibration source tuned at 150 GHz (with 144 Hz bandwidth) and placed in the far field. The corresponding analysis is presented in Torchinsky *et al.*[3]. We performed a scan in azimuth and elevation with the instrument, obtaining a TOD for each bolometer. We then applied our spectral imaging map-making algorithm with five sub-bands to a selection of 26 bolometers that do not exhibit saturation. The synthesized beam for each bolometer is realistically modeled in our map-making through a series of Gaussian whose amplitude, width and locations are fit from a measured map of the synthesized beam for each bolometer (see Figure 20 from Torchinsky *et al.*[3] for an example). We were able to reconstruct a map of the point-like artificial calibration source as well as its location in frequency space. In Figure 4, we show the reconstruction onto 5 sub-bands. The expected point-source shape is clearly visible in the central frequency sub-band containing the emission frequency of the source at 150 GHz, it is fainter in adjacent bands, and not visible in the furthest bands. On the right, we show the detected amplitude in the central pixel as a function of the frequency. The measurement in red is compared to the expected value spectrum in blue.

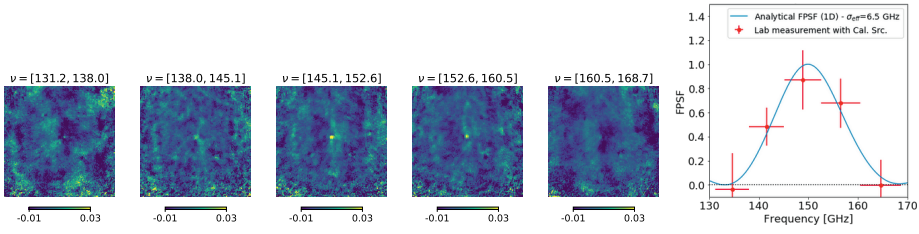

Figure 4 – *Left:* Calibration data with the source at 150 GHz projected on the sky using our map-making software to deconvolve from the multiple peaked synthesized beam and split the physical band of the instrument into 5 sub-bands. *Right:* Measurement of the flux of the source in reconstructed sub-bands. The measurement (simple aperture photometry) in red is compared to the expected value spectrum in blue.

4 Conclusion and perspectives

The QUBIC Technical Demonstrator was successfully tested at APC laboratory and sent to Argentina to be installed on the observation site in the following year. The QUBIC instrument relies on an innovative design which allows a very low cross-polarization, a high control of systematic effects thanks to self-calibration and a spectroscopic capability. Spectral imaging technique was demonstrated on end-to-end simulations and applied to calibration data successfully. Testing it on real astrophysical sources is the next determining step.

References

1. J.-Ch. Hamilton *et al.* (QUBIC Collaboration), arXiv:2011.02213, to appear on JCAP.
2. L. Mousset *et al* (QUBIC Collaboration), arXiv:2010.15119, to appear on JCAP.
3. S.A. Torchinsky *et al* (QUBIC Collaboration), arXiv:2008.10056, submitted to JCAP.
4. G. D'Alessandro *et al* (QUBIC Collaboration), arXiv:2008.10667, submitted to JCAP.
5. F. Cavaliere *et al* (QUBIC Collaboration), arXiv:2008.12721, submitted to JCAP.
6. M. Zaldarriaga and U. Seljak, *Phys. Rev.* D **55**, 1830 (1997)
7. M.-A. Bigot-Sazy *et al*, *A&A*, vol. 550, A59, Feb. 2013, arXiv:1209.4905
8. T. Cornwell and P. Wilkinson, Mon. Not. Roy. Astron. Soc., vol. 196, 1067, Sep. 1981.

Moment expansion of polarized dust SED: A new path towards capturing the CMB B-modes with *LiteBIRD*

L. Vacher, J. Aumont, L. Montier, S. Azzoni, F. Boulanger and M. Remazeilles
for the *LiteBIRD* Collaboration
IRAP, Université de Toulouse, CNRS, CNES, UPS, Toulouse, France

Characterizing accurately the polarized dust emission from our Galaxy will be decisive for the quest for the Cosmic Microwave Background (CMB) primordial B-modes. The incomplete modeling of its potentially complex spectral properties could lead to biases in the CMB polarization analyses and to a spurious detection of the tensor-to-scalar ratio r. Variations of the dust properties along and between lines of sight lead to unavoidable distortions of the spectral energy distribution (SED) that can not be easily anticipated by standard component separation methods. This issue can be tackled using a moment expansion of the dust SED, an innovative parametrization method imposing minimal assumptions on the sky complexity. In the recent work [1], we apply this formalism to the B-mode cross-angular power spectra computed from simulated *LiteBIRD* polarization data at frequencies between 100 and 402 GHz, containing CMB, dust and instrumental noise. Thanks to the moment expansion, we can measure an unbiased value of the tensor-to-scalar ratio with a dispersion compatible with the target values aimed by the instrument.

1 Introduction

Several astrophysical sources emit polarized light in the same frequency range as the cosmic microwave background (CMB) fluctuations, with an intensity that can be several orders of magnitudes greater. Two main contributions are expected to be significant: at low frequencies (≤ 70 GHz), the synchrotron emission dominates. It is due to charged light particles, often coming from ionized regions, accelerated circularly in the Galactic magnetic field. At higher frequencies, thermal dust signal is the main contribution. Dust grains are forged in the envelopes of pulsing massive stars and supernovae from which they are expelled into the interstellar medium where they will play a key role in the Galactic dynamics and chemistry. Dust grains are heated by starlight which they re-emit in microwave and infrared. At least $\sim 30\%$ of the starlight of the universe is reradiated that way [2]. Because of their elongated shape, the dust grains will have a preferred alignment in the galactic magnetic field and their signal will be strongly polarized. As such, dust grains will create strong B-modes signal over the sky, largely exceeding the predicted primordial ones.

In order to seek for the faint leftover signal from inflation in the CMB, it is thus critical to identify the dust contribution to the total B-mode emission in order to separate both signals. Doing so is highly non trivial and can lead to spurious measurement of the tenso-to-scalar ratio r, quantifying the intensity of the primordial B-modes.

The canonical way to model the frequency dependence of the dust signal – its spectral energy distribution (SED) – in a given line of sight $\vec{n}$, is given by the modified black body (MBB):

$$I(\nu, \vec{n}) = \left(\frac{\nu}{\nu_0}\right)^{\beta(\vec{n})} \frac{B_\nu(T(\vec{n}))}{B_{\nu_0}(T(\vec{n}))} A(\vec{n}) = \frac{I_\nu(\beta(\vec{n}), T(\vec{n}))}{I_{\nu_0}(\beta(\vec{n}), T(\vec{n}))} A(\vec{n}), \tag{1}$$

which is a black body function B_ν at a temperature T_0 multiplied by the frequency ν to the power of the spectral index β_0. A is the amplitude of the dust signal across the sky. The overall SED is normalized by a MBB with a reference frequency ν_0. The MBB function is an empirical model that has proven to provide a robust description of the dust signal. However, it is non linear: the sum of two different MBBs do not result in a MBB. The MBB is then not a good model to fit over mixed MBB signals. This is problematic since, in true experimental conditions, averages of SED coming from different sky regions can not be avoided: along the line of sight; between different lines of sight, inside the beam of the instrument or; when doing a spherical harmonic decomposition to calculate the angular power spectra over large regions of the sky. These averages will deform the SED away from its canonical model, these deformations are called SED distortions. Miss-modelling those distortions can easily lead to confuse dust B modes and primordial ones, leading to a spurious measurement of the tensor-to-scalar ratio.

2 The moment expansion formalism

The moment expansion, proposed in[3] aims to model these SED distortions with a Taylor inspired expansion of the SED with respect to its spectral parameters. For the MBB, the expansion is done with respect to β and T around the pivot values β_0 and T_0:

$$I(\nu,\vec{n}) = \frac{I_\nu(\beta_0,T_0)}{I_{\nu_0}(\beta_0,T_0)}\Bigg\{A(\vec{n}) + \omega_1^\beta(\vec{n})\ln\left(\frac{\nu}{\nu_0}\right) + \frac{1}{2}\omega_2^\beta(\vec{n})\ln^2\left(\frac{\nu}{\nu_0}\right) + \omega_1^T(\vec{n})\Big(\Theta(\nu,T_0)-\Theta(\nu_0,T_0)\Big) + \dots\Bigg\}, \tag{2}$$

where Θ is the derivative of B_ν with respect to T. The coefficients ω_i^p are the so called *moments* of order i with respect to the parameter p, that quantify the amplitude of the SED distortions. This expression can be generalized at the cross-frequency power spectra level[4]:

$$\begin{aligned}
\mathcal{D}_\ell(\nu_i\times\nu_j) = \frac{I_{\nu_i}(\beta_0(\ell),T_0(\ell))I_{\nu_j}(\beta_0(\ell),T_0(\ell))}{I_{\nu_0}(\beta_0(\ell),T_0(\ell))^2}\cdot\Bigg\{ \\
0^{\text{th}}\text{ order }\Bigg\{ & \mathcal{D}_\ell^{A\times A} \\
1^{\text{st}}\text{ order }\beta\Bigg\{ & +\mathcal{D}_\ell^{A\times\omega_1^\beta}\left[\ln\left(\tfrac{\nu_i}{\nu_0}\right)+\ln\left(\tfrac{\nu_j}{\nu_0}\right)\right] \\
& +\mathcal{D}_\ell^{\omega_1^\beta\times\omega_1^\beta}\left[\ln\left(\tfrac{\nu_i}{\nu_0}\right)\ln\left(\tfrac{\nu_j}{\nu_0}\right)\right] \\
1^{\text{st}}\text{ order }T\Bigg\{ & +\mathcal{D}_\ell^{A\times\omega_1^T}(\Theta_i+\Theta_j-2\Theta_0) \\
& +\mathcal{D}_\ell^{\omega_1^T\times\omega_1^T}\Big(\Theta_i-\Theta_0\Big)(\Theta_j-\Theta_0) \\
1^{\text{st}}\text{ order }T\beta\Bigg\{ & +\mathcal{D}_\ell^{\omega_1^\beta\times\omega_1^T}\left[\ln\left(\tfrac{\nu_j}{\nu_0}\right)\Big(\Theta_i-\Theta_0\Big)+\ln\left(\tfrac{\nu_i}{\nu_0}\right)(\Theta_j-\Theta_0)\right] \\
2^{\text{nd}}\text{ order }\beta\Bigg\{ & +\tfrac{1}{2}\mathcal{D}_\ell^{A\times\omega_2^\beta}\left[\ln^2\left(\tfrac{\nu_i}{\nu_0}\right)+\ln^2\left(\tfrac{\nu_j}{\nu_0}\right)\right] \\
& +\tfrac{1}{2}\mathcal{D}_\ell^{\omega_1^\beta\times\omega_2^\beta}\left[\ln\left(\tfrac{\nu_i}{\nu_0}\right)\ln^2\left(\tfrac{\nu_j}{\nu_0}\right)+\ln\left(\tfrac{\nu_j}{\nu_0}\right)\ln^2\left(\tfrac{\nu_i}{\nu_0}\right)\right] \\
& +\tfrac{1}{4}\mathcal{D}_\ell^{\omega_2^\beta\times\omega_2^\beta}\left[\ln^2\left(\tfrac{\nu_i}{\nu_0}\right)\ln^2\left(\tfrac{\nu_j}{\nu_0}\right)\right] \quad +\dots\Bigg\},
\end{aligned} \tag{3}$$

where $\mathcal{D}_\ell(\nu_i\times\nu_j) = \frac{\ell(\ell+1)}{2\pi}\mathcal{C}_\ell(\text{map}(\nu_i)\times\text{map}(\nu_j))$. This expression provides an analytical expression that can model dust SED with varying spectral parameters over the sky. The $\mathcal{D}_\ell^{A\times B}$ are the free parameters to estimate, quantifying the SED distortions. To define various fitting

schemes, we cut the above expansion at different orders: up to order 0 (MBB), up to order 1 in β (β-1), up to order 1 in both β and T (β-T) and up to order 2 for β only (β-2).

3 Application to *LiteBIRD*

In order to test this method with *LiteBIRD*, we generate (I, Q, U) simulated maps including Gaussian instrumental noise at the 9 highest frequency bands of the instrument ($\geq 100\,\mathrm{GHz}$). We mask the maps in order to keep a large sky fraction of $f_{\mathrm{sky}} = 0.7$. Three different dust models are considered, containing a MBB of increasing complexity in every pixel: `d0` in which both β and T are constant over the sky, including no SED distortions, `d1T` having T constant but a spatially varying spectral index $\beta(\vec{n})$ and `d1` where both β and T are allowed to vary spatially. The amplitude and varying spectral parameter templates are taken from the *Planck* 2015 data at 353 GHz and extrapolated to a frequency ν using the corresponding MBB. We generate $N_{\mathrm{sim}} = 500$ simulations with each dust type. For every simulation, we add a Gaussian contribution of CMB with $r_{\mathrm{sim}} = 0$.

We then calculate the cross-frequency power spectra $\mathcal{D}_\ell^{\mathrm{sim}}(\nu_i \times \nu_j)$ for every simulation. Keeping 9 bands, we end up with 45 cross-frequency spectra. Only the $B \times B$ auto spectra are consider in the analysis. For every simulation, the following model is fitted over the extracted cross-frequency power spectra:

$$\mathcal{D}_\ell^{\mathrm{model}}(\nu_i \times \nu_j) = \mathcal{D}_\ell^{\mathrm{dust}}\left(\beta_0(\ell), T_0(\ell), \mathcal{D}_\ell^{\mathcal{M}\times\mathcal{N}}(\nu_i \times \nu_j)\right) + \mathcal{D}_\ell^{\mathrm{lensing}} + r \cdot \mathcal{D}_\ell^{\mathrm{tensor}}, \tag{4}$$

where $\mathcal{D}_\ell^{\mathrm{dust}}$ is given by Eq. 3 with the various fitting schemes described above. $\mathcal{D}_\ell^{\mathrm{lensing}}$ is the CMB lensed E modes contribution to the B-modes in the simulation and $\mathcal{D}_\ell^{\mathrm{tensor}}$ is the expected theoretical primordial B mode spectra.

The following χ^2 is minimized:

$$\chi^2 = (\mathcal{D}_\ell^{\mathrm{sim}} - \mathcal{D}_\ell^{\mathrm{model}})^T \mathbb{C}^{-1} (\mathcal{D}_\ell^{\mathrm{sim}} - \mathcal{D}_\ell^{\mathrm{model}}), \tag{5}$$

where $\mathbb{C}$ is the covariance given by $\mathbb{C}_{\ell,\ell'}^{i\times j,k\times l} = \mathrm{cov}\left(\mathcal{D}_\ell^{\mathrm{sim}}(\nu_i \times \nu_j), \mathcal{D}_{\ell'}^{\mathrm{sim}}(\nu_k \times \nu_l)\right)$.

After χ^2 minimization, it can be shown that the moments are significantly detected only when the dust content is more complex than `d0`. They thus remain compatible with zero if there is no SED distortions in the signal but are used by the fit when such distortions are present. A single best-fit value of the tensor-to-scalar ratio $\hat{r}$ is obtained for each simulation. An histogram can be built with the N_{sim} values of $\hat{r}$ over which we can fit a Gaussian curve as displayed in Fig. 1. The fitted Gaussian standard deviation is noted $\sigma_{\hat{r}}$. For the simplest case `d0`, all fitting schemes allows to recover a value of $\hat{r}$ centered on $r_{\mathrm{sim}} = 0$, as desired. For `d1T` and `d1`, the

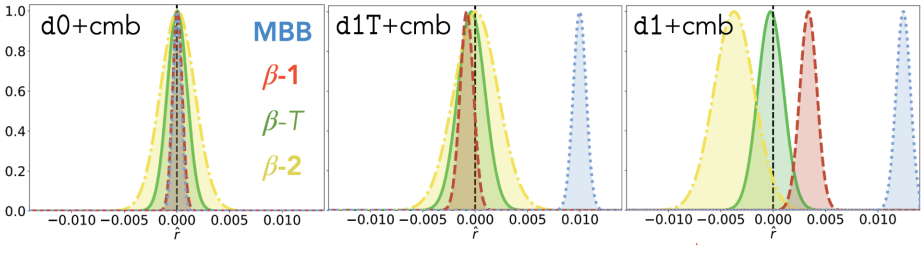

Figure 1 – Recovered posterior for the tensor to scalar ratio with the three different kind of dust models; `d0` (left), `d1T` (center) and `d1` (right) with the different fitting schemes: MBB (blue), β-1 (red), β-T (green) and β-2 (yellow). The black dashed line indicates $r_{\mathrm{sim}} = 0$.

MBB is not a good fit anymore due to the presence of the SED distortions mentioned above. The posteriors are strongly biased ($\sim 20\sigma_{\hat{r}}$). Adding some moments with the β-1 fitting scheme allows to reduce the bias of the posterior for `d1T` and `d1` but is not enough to get a posterior compatible with $r_{\rm sim}$ at $1 \cdot \sigma_{\hat{r}}$. The β-T fitting scheme centers the posteriors for both `d1T` and `d1` with a width of $\sim 1 \times 10^{-3}$, providing a good model for the SED distortions in both cases. While the β-2 fitting scheme correctly model the spectral distortions in `d1T`, an unexpected negative bias appears for `d1`. As discussed in [1], this bias is due to the failure of the β moments to model the temperature distortions and a strong degeneracy between these moments and the CMB signal.

4 Conclusion and discussion

Moment expansion in harmonic space provides a powerful tool to model the SED distortions coming from averaging effects of spatially varying spectral parameters. Such a modeling will be necessary for next generations of CMB experiments as *LiteBIRD*. Using the first order moments in both β and T allows to recover an unbiased value of the tensor-to-scalar ratio r in all the scenarios considered, even the most complex one where the dust signal is given by a MBB in every pixel, with spatially varying spectral index and temperature over the sky. In [1], it has been shown that this result is robust using different sky fractions, adding a synchrotron component and when adding a non zero value of $r_{\rm sim}$. The method can also be optimized in order to keep only the necessary coefficients in order to decrease the recovered value of $\sigma_{\hat{r}}$. However the correction provided by the moments seems to be strongly dependent of the moment frequency dependence themselves and expending around the wrong canonical model could have strong implications. Moreover, some correlations between some of these moments and the CMB could be a strong limitation in more complex scenarios than the ones considered here.

References

1. Vacher, L. and Aumont, J. and Montier, L. et al. in *Moment expansion of polarized dust SED: A new path towards capturing the CMB B-modes with LiteBIRD*, (A&A, 2022).
2. Bernstein, R. A. and Freedman, W. L. and Madore, B. F. in *The First Detections of the Extragalactic Background Light at 3000, 5500, and 8000 Å. III. Cosmological Implications*, (The American Astronomical Society, 2002).
3. Chluba, J. and Hill, J. C. and Abitbol, M. H. in *Rethinking CMB foregrounds: systematic extension of foreground parameterizations*, (MNRAS, 2017).
4. Mangilli, A. and Aumont, J. and Rotti, A. et al. in *Dust moments: towards a new modelling of the galactic dust emission for CMB B-modes analysis*, (A&A, 2021).

Bridging the Gap: Spectral Distortions meet Gravitational Waves

Thomas Kite
Jodrell Bank Centre for Astrophysics, School of Physics and Astronomy, The University of Manchester, Manchester, M13 9PL, U.K.

This talk has the goal of introducing two upcoming exciting avenues of discovery in precision Cosmology: spectral distortions (SDs) and gravitational waves (GWs). The former signals offer a clear window into the state of the primordial plasma at times prior to recombination, and thus sheds light on small-scale primordial perturbations, dark matter decay and black hole formation to just mention a few scenarios. The latter signals, which are already offering new insights into the landscape of black hole and neutron star mergers, will reveal intricate dynamics of the early universe including primordial black holes, inflationary potentials, and even reheating dynamics. An elegant link is drawn between these two future observations since primordial GW backgrounds will source SDs, a coupling which offers unique insight to over six decades of GW frequencies. More importantly the SD visibility window bridges the gap between astrophysical high- and cosmological low-frequency measurements. This means SDs will not only complement other GW observations, but will be the sole probe of physical processes at certain scales.

Disclaimer

This document has been written in such a way to mirror the talk presented at the 2022 Cosmology session of the 56th Rencontres de Moriond. In particular the focus is on qualitatively reviewing the main Physics and providing a more heuristic overview of the content. For a more complete and detailed discussion with mathematical details we point the reader to [1] and references therein.

1 Spectral Distortions

For many decades the focus of precision Cosmology, at least in the early Universe, has been the power spectrum of Cosmic Microwave Background (CMB) temperature anisotropies [2,3]. The wealth of information contained in this signal has now been exquisitely well measured, allowing for the consolidation of a concordance model of Cosmology, ΛCDM.

It is a trivial yet important statement that there is only one CMB sky to observe, and as such it is imperative we tease as much information from it as possible. It is in this vein that we introduce spectral distortions (SDs) as one way of extending the enormous success of CMB observations for decades to come. The fundamental novelty in SD measurements is to step back from thinking of *spatial* information content locked in angular distributions across the sky, and instead focus on the frequency distribution of the photon flux[a], which promises more information than a single-parameter blackbody.

A useful analogy for this is in expressing a function $f(x)$ as a Fourier series, where a continuous function thus is expressed as a countably infinite series of coefficients f_i. Only for a very special class of functions would you have a single non-zero coefficient. Similarly, the CMB photon flux spectrum across frequency is currently described using a single number: temperature. This is a natural and effective choice given that an interacting spectrum of photons will

[a] Although future missions might detect SD anisotropies.

tend towards the thermal equilibrium described by a blackbody, but this only causes other *CMB coefficients* to be small, not 0. Standard ΛCDM predicts [4] primordial SD amplitudes $\sim 10^{-8}$.

1.1 Primordial Origin of SDs

Many processes in the universe can cause a deviation from a simple background blackbody (e.g. emission lines we observe from atomic transitions, up-scattered CMB photons upon colliding with hot gas). In this talk however we care about SDs from the primordial Universe which are usually decomposed in a few main types, each caused by energy injection in different eras.

• The earliest energy injection into the photon bath ($z \geq 2 \times 10^6$) occurs in the very high temperature universe - a sufficiently energetic system to create photons (bremsstrahlung, double Compton emission) and redistribute their energies (Compton/Thompson scattering). This results in an unobservable shift to the blackbody spectrum to a higher temperature.

• At later times ($5 \times 10^4 \leq z \leq 2 \times 10^6$) the mechanisms for photon production are no longer efficient even though photons can be redistributed. This results in a spectrum containing a μ-distortion, equivalent to a chemical potential in an otherwise perfect blackbody.

• The final era which roughly lasts all the way to recombination ($1100 \leq z \leq 5 \times 10^4$) is characterised by the lack of efficient energy redistribution mechanisms within the photon gas, leaving a y-distortion in the spectrum.

1.2 Example: Dissipation of Acoustic Modes

A primary source of SDs within ΛCDM is from Silk damping of small-scale acoustic modes. Simply stated, small patches of differing temperature in the early Universe are sufficiently close to mix photons, thus erasing the temperature differences. This spatial isotropisation of the medium renders these patches invisible to CMB temperature anisotropies (hence the large k damping in the CMB power spectrum), but a SD signal persists to be seen today. The key to understanding this process is that adding two blackbodies at T_1 and T_2 respectively will not exactly produce the expected $(T_1 + T_2)/2$ blackbody, but rather an excess photon tail remains at high frequency [5] as illustrated in Fig. 1. Those excess photons constitute an energy injection, which will remain in the spectrum as a SD.

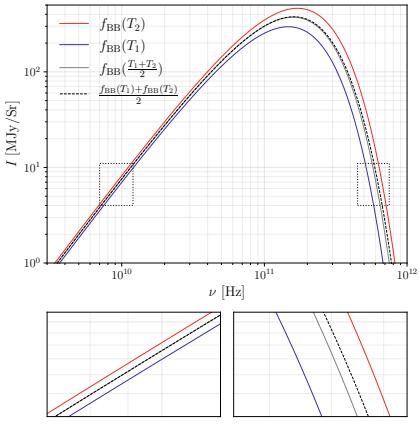

Figure 1 – A plot illustrating how the mix of two blackbodies differs from the blackbody at the average temperature, rather there is an excess of high frequency photons. Figure adapted from [5]

2 Gravitational Waves

The second upcoming cosmological probe this talk is concerned with is the gravitational wave background (GWB) [b]. The key to the excitement in GW Cosmology is the simple fact that these tensorial waves interact extremely weakly with the intervening matter. Consider for example the existence of the *CMB curtain*, which shields our view from the first 380 thousand years of the Universe. This happens because the electromagnetic waves carrying the information interact too strongly with charged particles (which incidentally makes them easy to detect too). GWs have no such interaction, and it is very possible to see a GWB arising from inflationary dynamics or

[b] In contrast to single localised GWs, which are usually associated with individual astrophysical events.

reheating mechanisms which travel to our detectors unhindered. This direct glimpse into the fundamental physics of the early-universe is the enticing proposal of GW Cosmology.

2.1 Detection Prospects

There are a diverse range of upcoming probes spanning over 20 orders of magnitude in frequency seeking to pin down the shape of the GWB [6]. On the lowest frequencies (largest scales) we have the cosmological scale probes with B-mode polarisation searches. Moving to higher frequencies (smaller scales) there is potential to glimpse GWs with astrophysical level probes like Pulsar Timing Arrays (PTA), astrometry and binary system resonances [7]. The highest of frequencies are covered by direct interferometry or even some solid state detectors. Each of these techniques are based on different physics, which links directly to the frequencies they're sensitive to.

An interesting *gap* exists between the cosmological large-scale and astrophysical small-scale. Primordial waves in this window damp too early to leave notable impacts on the CMB polarisation. However, analogously to the previously discussed Silk damping, these waves excite a quadrupole moment in the photon multipole hierarchy, which ultimately causes an energy injection to the photon bath, and thus a SD signal.

3 Bridging the Gap

In this section we will give some more mathematical detail about the calculation of SD arising from a GWB while still leaving main technical details to [1 8]. The bottom line is that for a given cosmology a lot of the calculation can be precomputed, leaving only a single integral over wavenumber k of the tensor power spectrum $\mathcal{P}_T(k)$ multiplied by a SD window function $W_\mu^{z_{\rm max}}(k)$:

$$\langle \mu_{\rm GW} \rangle = \int_0^\infty {\rm d}\ln k\ \mathcal{P}_T(k) W_\mu^{z_{\rm max}}(k)\,. \qquad (1)$$

The window function is calculated by combining three main terms:

$$\mathcal{W}_\mu = (1.401\mathcal{J}_\mu)\left(\frac{8H^2}{45\dot{\tau}}h'^2\right)\left(\mathcal{T}_\Theta e^{-\Gamma^*_\gamma \eta}\right)\,, \qquad (2)$$

which from left to right correspond to: firstly a *SD branching ratio* which dictates the resulting μ-distortion amplitude from some energy injection, secondly a term corresponding to the energy content of a GW, and thirdly the term expressing the coupling between GWs and photons. Integrating this over the relevant redshifts while keeping in mind an upper redshift cutoff for any GWB created subhorizon,

$$W_\mu^{z_{\rm max}}(k) = \int_0^{z_{\rm max}} {\rm d}z\ \mathcal{W}_\mu(k,z)\,, \qquad (3)$$

gives the full SD window function. These window functions are shown in Fig. 2.

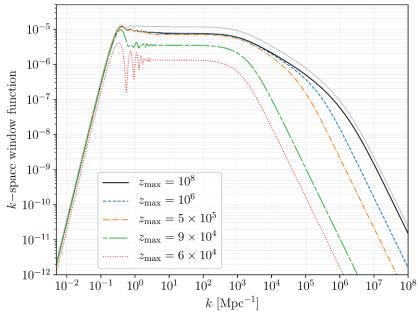

Figure 2 – A plot showing the μ-distortion window functions for GW power spectra. There is a plateau for $10^0 \lesssim k\,[{\rm Mpc}^{-1}] \lesssim 10^3$. Very late subhorizon GW injection reduces the total visibility by up to an order of magnitude, as seen by increasing $z_{\rm max}$. The gray line shows the window function if neutrino damping is neglected.

To facilitate this type of calculation we provide the precomputed window functions for standard ΛCDM using best fit *Planck18* cosmological parameters [9] via a simple python tool `GW2SD` (`https://github.com/CMBSPEC/GW2SD.git`).

Mapping these SD window functions into sensitivity curves reveal how SDs complement other probes in the GWB landscape, as shown in Fig. 3. As previously discussed SDs are able to bridge the gap between high- and low-frequency probes. This means that, despite their overall lower sensitivity (GWs and photons only interact feebly) SDs will provide a unique or complementary

probe of new physics on certain energy scales. Furthermore, with a wide sensitivity curve it is possible to integrate sufficient power over many frequency bins to produce a measurable μ-distortion signal from a GWB that would otherwise be too weak to detect. To illustrate these points we investigate a few models of interest in [1], and show which regions of parameter space can be constrained with either future data or even using the three decades old data available from *COBE/FIRAS*[10].

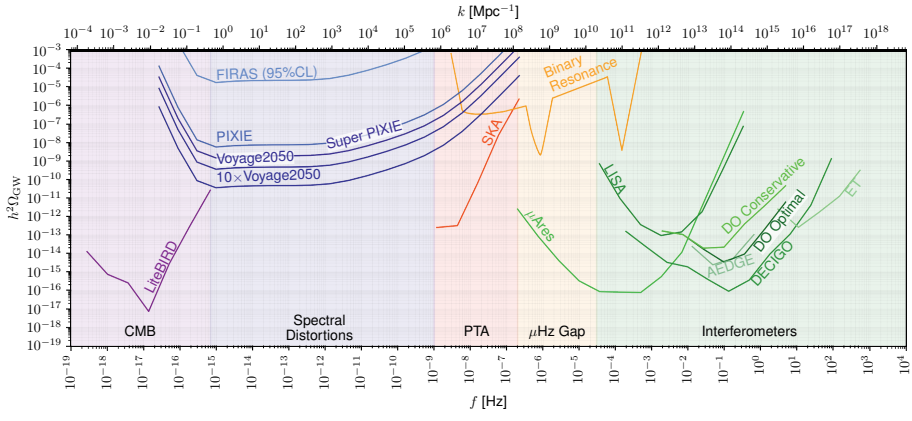

Figure 3 – A plot showing the different probes of the GWB in their respective frequency bands. From left to right (low to high frequency, large to small-scales) there are CMB B-modes, CMB spectral distortions, pulsar timing arrays, binary resonance searches and direct detection interferometry. The SD window bridges the gap between the cosmological large-scale probes and the astrophysical small-scale. Sensitivity curves are taken from [1 6 11].

References

1. Thomas Kite, Andrea Ravenni, Subodh P. Patil, and Jens Chluba. Bridging the gap: spectral distortions meet gravitational waves. MNRAS, 505(3):4396–4405, August 2021.
2. WMAP Collaboration. Nine-year Wilkinson Microwave Anisotropy Probe (WMAP) Observations: Final Maps and Results. *The Astrophysical Journal Supplement*, 208(2):20, October 2013.
3. Planck Collaboration. Planck 2018 results. I. Overview and the cosmological legacy of Planck. *arXiv e-prints*, page arXiv:1807.06205, Jul 2018.
4. Jens Chluba. Which spectral distortions does ΛCDM actually predict? MNRAS, 460(1):227–239, July 2016.
5. Jens Chluba, Jan Hamann, and Subodh P. Patil. Features and new physical scales in primordial observables: Theory and observation. *International Journal of Modern Physics D*, 24(10):1530023, Jun 2015.
6. Chiara Caprini and Daniel G. Figueroa. Cosmological Backgrounds of Gravitational Waves. *Class. Quant. Grav.*, 35(16):163001, 2018.
7. Diego Blas and Alexander C. Jenkins. Detecting stochastic gravitational waves with binary resonance. *Physical Review D*, 105(6):064021, March 2022.
8. Jens Chluba, Liang Dai, Daniel Grin, Mustafa A. Amin, and Marc Kamionkowski. Spectral distortions from the dissipation of tensor perturbations. *Monthly Notices of the Royal Astronomical Society*, 446(3):2871–2886, Jan 2015.
9. Planck Collaboration. Planck 2018 results. VI. Cosmological parameters. *arXiv e-prints*, page arXiv:1807.06209, Jul 2018.
10. D. J. Fixsen, E. S. Cheng, J. M. Gales, J. C. Mather, R. A. Shafer, and E. L. Wright. The Cosmic Microwave Background Spectrum from the Full COBE FIRAS Data Set. *Astrophysical Journal*, 473:576, Dec 1996.
11. Diego Blas and Alexander C. Jenkins. Bridging the μHz Gap in the Gravitational-Wave Landscape with Binary Resonances. *Physical Review Letters*, 128(10):101103, March 2022.

First constraints on the intrinsic CMB dipole and our velocity with Doppler and aberration

Pedro da Silveira Ferreira
Observatório do Valongo, Universidade Federal do Rio de Janeiro, 20080-090, Rio de Janeiro, RJ, Brazil

We test the usual hypothesis that the Cosmic Microwave Background (CMB) dipole, its largest anisotropy, is due to our peculiar velocity with respect to the Hubble flow by measuring independently the Doppler and aberration effects on the CMB using Planck 2018 data. We remove the spurious contributions from the conversion of intensity into temperature and arrive at measurements which are independent from the CMB dipole itself for both temperature and polarization maps and both SMICA and NILC component-separation methods. Combining these new measurements with the dipole one we get the first constraints on the intrinsic CMB dipole. Assuming a standard dipolar lensing contribution we can put an upper limit on the intrinsic amplitude: 3.7mK (95% CI). We estimate the peculiar velocity of the solar system without assuming a negligible intrinsic dipole contribution: $v = (300^{+111}_{-93})$ km/s with $(l, b) = (276\pm33,\ 51\pm19)^\circ$ [SMICA], and $v = (296^{+111}_{-88})$ km/s with $(l, b) = (280\pm33,\ 50\pm20)^\circ$ [NILC] with negligible systematic contributions. These values are consistent with the peculiar velocity hypothesis of the dipole. See the complete work at arXiv:2011.08385.

1 Introduction

The CMB temperature dipole is the largest CMB anisotropy not coming from foregrounds, and has been precisely measured since a few decades ago. After removal of the orbital contribution due to the motion of the instrument with respect to the Sun, we are left with the so-called solar dipole, with an amplitude of 3.36208 ± 0.00099 mK [1], which is ~ 100 larger than the other multipoles. It is thus fully credited to the proper motion between the solar system and the CMB rest frame. If one assumes that the whole dipole has such a kinematic origin, one infers a relative velocity of (369.82 ± 0.11) km/s. This velocity estimate is widely reported and often used in astronomy in order to convert observed redshifts into CMB-centric (cosmological) ones.

Nevertheless there exists the possibility that part of the dipolar effect could be due to primordial fluctuations in the surface of last-scattering (SLS). The degeneracy between primordial and kinematic effects in the CMB dipole can be broken by measuring the Doppler-like and aberration-like couplings in the CMB present in all scales [2]. In the case of a peculiar velocity these couplings must be present with well-determined coefficients, as discussed in our companion paper [3] (see also [4]). In other scenarios, one of both of these couplings can differ [2], and therefore

by combining the observations of the dipole, Doppler and aberration effects one can independently measure our peculiar velocity and the intrinsic CMB dipole in a more model-independent way. This is what we pursue in the present work.

2 Estimators and pipeline

The aberration and Doppler estimators and pipelines used here are discussed in detail in our companion paper [3]. The used pipeline allows for measurements of aberration ($\beta^{\rm A}$) and Doppler ($\beta^{\rm D}$) which are independent between themselves and with the dipole, both in temperature (TT) and polarization (EE) maps. We also consider the more traditional case in which one assumes *a priori* that $\beta^{\rm A} \equiv \beta^{\rm D} \equiv \beta^{\rm B}$ as in a standard boost (B) transformation (i.e. assuming no additional sources of Doppler-like or aberration-like couplings). This leads to a higher significance detection, but it only serves as a simple cross-check as all physical information is already encoded in the high-precision observation of the temperature dipole. The precision in both $\beta^{\rm A}$ and $\beta^{\rm D}$ is estimated in [3].

3 Measuring the intrinsic dipole

Besides the standard scenario of a simple Doppler effect on the monopole, a temperature dipole Δ_1 can also be due to an intrinsic dipole component $\Delta_{1,\rm int}$ in the SLS of either the temperature (τ) or gravitational potential (ϕ) perturbations. A significant contribution from the late Integrated Sachs-Wolfe effect is less likely since the integrand is non-zero only after matter-domination. On large scales both temperature or gravitational potential perturbations are proportional, but the proportionality depends on whether the perturbations are adiabatic or isocurvature (entropic). For small scales the CMB fluctuations are known to be adiabatic, but for the dipole it could be either or a combination of both. The nature of the dipole can thus only be understood by adding new observables.

Through a detailed investigation of second-order perturbations on the CMB, the effects of these different primordial scenarios on the Doppler and aberration signals in the CMB was discussed in [2]. An aberration effect could be mimicked by the dipolar component of gravitational lensing. Lensing is however an integrated quantity and depends on fluctuations along the whole past light-cone. This means that only in fine-tuned models would it produce an aberration signature in the same direction of the dipole and correct amplitude. The Doppler couplings on the other hand are produced by second-order perturbation effects on the SLS. Surprisingly, it was found in [2] that apart from the standard velocity coupling ($\beta\Theta$, where Θ represent the linear temperature fluctuations) there are also second-order contributions from $\tau\Theta$ and $\phi\Theta$ which, if Gaussian, produce a total coupling which is given exactly by $\Delta_1\Theta$ in both adiabatic and isocurvature case. I.e., these couplings are insensitive to the nature of Δ_1. If, on the other hand, the fluctuations contain non-Gaussianities (NG) this degeneracy is broken. In particular, for the much-studied local NG [5] new terms proportional to ϕ^2 appear which result in extra $\Delta_1\phi$ couplings. This changes the amplitude (but not the direction) of the intrinsic Doppler couplings. Thus a detection of conflicting Doppler, aberration and dipole measurements can hint at the presence of a non-standard large intrinsic dipole and allows one to test physics beyond the single-field slow-roll inflation model and modifications on recombination physics, see, e.g. [6,7,8,9,10].

4 Results

Figure 1a shows results for different values of $\ell_{\rm max}$ for TT up to 1800. For EE we stop at 1150. We use always $\ell_{\rm min} = 200$ [3]. For aberration we draw the 1 and 2σ (68.3% and 95.4%) confidence intervals (CI) for TT+EE. The figures use the standard Mollweide projection for galactic coordinates. Figure 1b shows the boost estimator contours. As expected, since this case

assumes the same direction for both aberration and Doppler, this results in greater precision but is only useful as a cross-check.

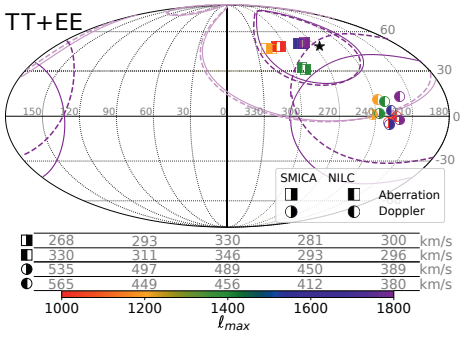

(a) Aberration and Doppler estimations as a function of $\ell_{\rm max}$ for the main pipeline for SMICA and NILC. The $\star$ represents the dipole. Solid (dashed) contours are the 1 and 2σ confidence levels for SMICA (NILC). The values below the Mollweide plot are the amplitudes of the estimated vectors.

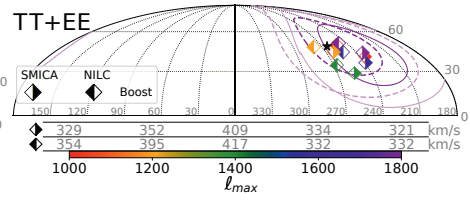

(b) Same as Figure 1a for the boost estimator.

The statistical significance of each estimator result is quoted in two complementary ways. First, we compare each estimator with the kinematic dipole hypothesis. The second estimate assumes there is no Doppler or aberration effects whatsoever in the data, which allows one to get the overall statistical significance of these $\ell, \ell+1$ correlations in the data. Table 1 summarizes the results, which are in agreement with the kinematic hypothesis.

Table 1: Statistical significance for both component separation methods. The $\beta = \Delta_1$ column assumes the dipole is completely due to our velocity; the $\beta = \mathrm{DD} = 0$ column assumes there is no Doppler or aberration effect of any kind.

		$\boldsymbol{\beta = \Delta_1}$		$\beta = \mathrm{DD} = 0$	
TT+EE		χ^2	σ-value	χ^2	σ-value
SMICA	Aberration	0.3	0.1	18	3.5
	Doppler	4.6	1.3	12	2.6
	Boost	1.3	0.3	45	6.1
	Aber. & Dopp.	4.9	0.6	30	4.1
NILC	Aberration	0.3	0.1	21	3.9
	Doppler	2.7	0.8	13	2.9
	Boost	0.4	0.1	49	6.4
	Aber. & Dopp.	3.0	0.2	34	4.6

As discussed above by measuring Doppler and aberration separately we can constrain the intrinsic dipole. The results for $\boldsymbol{\Delta}_{1,\rm int}$ are in Table 2 using 95% CI. In all cases the values are consistent with zero, so we only quote limits for $|\boldsymbol{\Delta}_{1,\rm int}|$, which turns out to be similar to the observed Δ_1 value.

We remark that these are the first direct constraints on the intrinsic CMB dipole, the largest mode in the SLS. Our results are fully consistent with the kinematic dipole interpretation and show no sign of non-Gaussianities, as expected by the standard cosmological model. These findings, however, exclude for instance the possibility of a ~ 1000 km/s value for $c\beta$, the raw result in many Cosmic Radio dipole measurements, see e.g. [11], which otherwise could be fine-tuned with a large $\boldsymbol{\Delta}_{1,\rm int}$ opposite to $\boldsymbol{\beta}$ such that the vector sum resulted in the observed $\boldsymbol{\Delta}_1$.

Table 2: Measurements and null-hypothesis test of the intrinsic dipole using the full TT+EE results. The total observed dipole is 3.362 mK.

$\boldsymbol{TT}$+$\boldsymbol{EE}$	$\boldsymbol{\Delta}_{1,\mathrm{int}}$	
	amplitude	σ-value
SMICA	< 3.6 mK [95% CI]	0.1
NILC	< 3.7 mK [95% CI]	0.1

5 Perspectives

In over half a century since the discovery of the CMB we have been able to measure temperature, polarization and lensing to very high ℓs. But only now we are finally able to put physical constraints on the largest possible scale, the temperature dipole.

The measurements of $\boldsymbol{\beta}$ and $\boldsymbol{\Delta}_{1,\mathrm{int}}$ are limited by the precision of the aberration and Doppler estimators in Planck data. Doppler in particular has high uncertainty: after removing the uninformative DD it is detected at less than 2σ. Future high-resolution CMB experiments can improve this precision by both probing higher multipoles and by measuring the E modes with higher S/N [3].

If $|\boldsymbol{\Delta}_{1,\mathrm{int}}| \sim 0.03$mK as in the higher multipoles, it will remain undetectable with this method in the foreseeable future, but ruling out exotic scenarios with $|\boldsymbol{\Delta}_{1,\mathrm{int}}| \sim 1$mK will be feasible in the near future. Although such a large intrinsic dipole would be inconsistent with our standard inflation scenario, there has been numerous claims of large scale anomalies in the CMB [12], and so it is important to also try to detect its largest possible scale.

Acknowledgments

We would like to thank the anonymous referees for helpful suggestions. Pedro da Silveira Ferreira is supported by the Brazilian research agency CAPES (Coordenação de Aperfeiçoamento de Pessoal de Nível Superior).

References

1. Planck Collaboration, arXiv:1807.06205
2. Roldan, Omar and Notari, Alessio and Quartin, Miguel, arXiv:1603.02664
3. P. da Silveira Ferreira and M. Quartin, arXiv:2107.10846
4. Notari, Alessio and Quartin, Miguel, arXiv:1112.1400
5. Wands, David, arXiv:1004.0818
6. Erickcek, Adrienne L. and Kamionkowski, Marc and Carroll, Sean M., arXiv:0806.0377
7. Lyth, David H., arXiv:1304.1270
8. Dai, Liang and Jeong, Donghui and Kamionkowski, Marc and Chluba, Jens, arXiv:1303.6949
9. Mathews, G.J. and Suh, I.S. and Lan, N.Q. and Kajino, T., arXiv:1406.3409
10. Meerburg, P. Daniel and Meyers, Joel and van Engelen, Alexander, arXiv:1704.00718
11. Siewert, Thilo M. and Schmidt-Rubart, Matthias and Schwarz, Dominik J., arXiv:2010.08366
12. Schwarz, Dominik J. and Copi, Craig J. and Huterer, Dragan and Starkman, Glenn D., arXiv:1510.07929

Diffuse polarized foregrounds from component separation with QUIJOTE-MFI

E. de la Hoz on behalf of the QUIJOTE collaboration
Instituto de Física de Cantabria (CSIC-Universidad de Cantabria), Avda. de los Castros s/n, E-39005 Santander, Spain

Polarized component maps in the Northern Sky are derived from the QUIJOTE-MFI wide survey data at 11 and 13 GHz, the WMAP K and Ka bands and all Planck polarized channels using the parametric component separation method `B-SeCRET`. The addition of QUIJOTE-MFI data significantly improves the uncertainty in the parameter estimation of the low frequency dominant foreground, in particular the estimation of the synchrotron spectral index. We find statistically significant spatial variability across the sky. A power law model of the synchrotron emission provides a good fit of the data outside the galactic plane but fails to track the complexity of this region. Moreover, when we assume a synchrotron model with uniform curvature we find, in the 95% confidence region, a non-zero c_s value. However, there is not sufficient statistical significance to determine which model is favoured.

1 Introduction

One of the major milestones of the CMB scientific community is the detection of primordial B-modes. Such a detection would constitute a compelling evidence of the existence of an inflationary phase at the beginning of the Universe. However, this signal is hidden among other B-mode sources e.g., astrophysical foregrounds, lensed E-modes, instrumental noise, etc. A comprehensive knowledge of astrophysical foregrounds is crucial to recover this faint signal from the measured sky data. Here, we have characterized diffuse polarized foregrounds performing component separation analyses with the new wide survey maps from the Q-U-I JOint TEnerife Multi-Frequency Instrument (QUIJOTE-MFI) experiment along with data from WMAP and Planck. The inclusion of QUIJOTE-MFI data in the analysis helps significantly with the characterization of the synchrotron emission [1].

2 Component Separation Methodology

The component separation analyses are performed using the Bayesian-Separation of Components and Residuals Estimate Tool (`B-SeCRET`) [2]. `B-SeCRET` is a parametric Bayesian pixel-based maximum-likelihood pipeline which uses an MCMC to sample from the posterior distribution:

$$\mathcal{P}(\theta_p|\mathbf{d}_p) \propto \mathcal{P}(\mathbf{d}_p|\theta_p)\mathcal{P}(\theta_p)\,. \tag{1}$$

where θ_p and $\mathbf{d}_p$ are the model parameters and the signal at the pixel p, $\mathcal{P}(\theta_p)$ is the prior information and, $\mathcal{P}(\mathbf{d}_p|\theta_p)$ is the likelihood:

$$\mathcal{P}(\mathbf{d}_p|\theta_p) = \frac{\exp\left(-\frac{1}{2}\left(\mathbf{d}_p - \mathbf{S}_p\right)^T \mathbf{C}^{-1}\left(\mathbf{d}_p - \mathbf{S}_p\right)\right)}{\sqrt{(2\pi)^N \det(\mathbf{C})}}\,, \tag{2}$$

Table 1: Parametric models (antenna units) and parameters priors used to fit the sky polarized components.

Component	Model	Prior
CMB	$\begin{bmatrix} c^{\mathrm{Q}} \\ c^{\mathrm{U}} \end{bmatrix} \frac{x^2 e^x}{(e^x-1)^2}$	-
Synchrotron	$\begin{bmatrix} a_s^{\mathrm{Q}} \\ a_s^{\mathrm{U}} \end{bmatrix} \left(\frac{\nu}{\nu_s}\right)^{\beta_s}$	$\beta_s \in \mathcal{N}(-3.1, 0.3)$
	$\begin{bmatrix} a_s^{\mathrm{Q}} \\ a_s^{\mathrm{U}} \end{bmatrix} \left(\frac{\nu}{\nu_s}\right)^{\beta_s + c_s(\nu/\nu_s)}$	$\begin{cases} \beta_s \in \mathcal{N}(-3.1, 0.3) \\ c_s \in \mathcal{N}(0, 0.1) \end{cases}$
Thermal dust	$\begin{bmatrix} a_d^{\mathrm{Q}} \\ a_d^{\mathrm{U}} \end{bmatrix} \left(\frac{\nu}{\nu_d}\right)^{\beta_d - 2} \frac{\mathrm{B}(\nu, \mathrm{T_d})}{\mathrm{B}(\nu_\mathrm{d}, \mathrm{T_d})}$	$\begin{cases} \beta_d \in \mathcal{N}(1.55, 0.1) \\ T_d \in \mathcal{N}(21, 3) \end{cases}$

where $\mathbf{C}$ is the noise covariance matrix, N is the number of elements in the $\mathbf{d}_p$ array, and $\mathbf{S}_p$ is the parametric model considered. The models and priors used are shown in Table 1.

3 Data

The QUIJOTE-MFI[3] instrument is a polarimetric CMB experiment in the 10-20GHz microwave range located at the Teide observatory. The instrument consists of 4 horns, each of which has 8 independent channels. Combining all the data, the QUIJOTE-MFI provides four frequency bands centred around 11, 13, 17 and 19 GHz with a bandwidth of approximately 2 GHz. The low-frequency bands (11 and 13 GHz) have an approximate angular resolution of 52 arc min while the 17 and 19 GHz channels have one of approximately 38 arc min.

In this study we have used the results from the MFI wide survey, a shallow survey where the instrument covered all the visible sky from Tenerife at elevations above 30°. After removing the Radio Frequency Interference (RFI) from the geostationary satellite band and some areas with large atmospheric air mass we are left with $\sim 51\%$ of the sky. This survey provides an average sensitivity in polarization of $\sim$ 35-40μK deg^{-1}. In the analysis we used only the 11 and 13 GHz, since they have better sensitivity and the largest signal-to-noise ratio.

We have used the low frequency WMAP's K (22.8 GHz) and Ka (33.1 GHz) bands [4] and Planck's polarization maps from Planck Release 4 (PR4) [5] i.e., the low frequency instrument (LFI) 30, 44 and 70 GHz frequency maps and the high frequency instrument (HFI) 100, 143, 217 and 353 GHz maps.

All the maps are smoothed to the common angular resolution of 2°, and downgraded to $N_{side} = 64$. We have calculated the frequency covariance $\mathbf{C}$ using noise simulations specific to each instrument. In the case of QUIJOTE [3] and Planck [5] we have used the noise simulations provided by the collaboration. For WMAP, we generated a set of white noise simulations using the rms noise per pixel provided by the WMAP collaboration [4]. To account for the unequal detectors response across their bandwidth we apply colour corrections calculated using the python code `fastcc` [6].

4 Results

Fig. 1 shows the estimated synchrotron spectral index (β_s) map and its uncertainty map obtained from the component separation analysis when the synchrotron is modeled with a power law using different combinations of the available data. The reduced χ^2 statistic map is also shown. It is

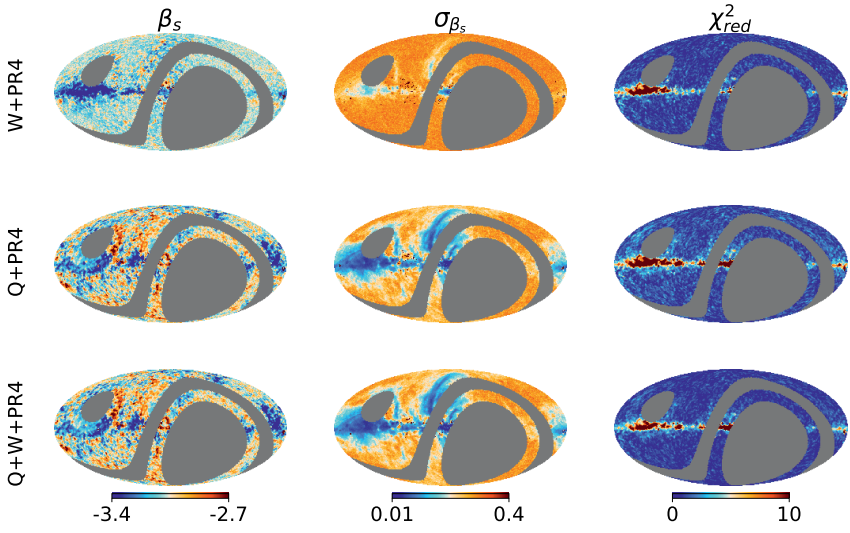

Figure 1 – β_s (left column), β_s uncertainty (center column) and reduced χ^2 statistic obtained from the fit using a power law model using different data. WMAP and Planck data (top row), QUIJOTE and Planck data (center row), QUIJOTE, WMAP and Planck (bottom row).

Table 2: Estimated curvature and its uncertainty values obtained assuming that the curvature is uniform within the region.

Region	c_s^R	$\sigma_{c_s^R}$	$\lvert c_s^R \rvert / \sigma_{c_s^R}$
RC1	-0.1095	0.0013	82
RC2	-0.3107	0.0019	161
Haze	-0.046	0.010	4.78
North bubble	-0.044	0.007	6.29

clear that the inclusion of QUIJOTE-MFI channels improves the characterization of β_s, specially in the regions where the synchrotron has the largest signal-to-noise-ratio. Besides, the power law model represents well the data except along the galactic disk where the physics might be more complex.

We have also modeled the synchrotron emission as a power law with spatially varying curvature. The pixel-based analysis of the curvature shows that c_s is only detected in some regions at the galactic disk where the fit is bad, see Fig. 2.

Moreover, we considered the case where the synchrotron's curvature is uniform in a given region. We have studied four regions (Table 2): i) RC1 composed of the pixels whose χ^2_{red} is within 95% confidence region [a], ii) RC2 is a subset of the RC1 pixels that satisfy that the synchrotron's polarized intensity signal-to-noise ratio is larger than 5 and, iii) the Haze and iv) North bubble which are two physically-defined regions studied in more detailed in a companion QUIJOTE paper [7]. In all cases we detect a non-zero negative curvature. We found that both models, i.e., power law and power law with uniform curvature, provide a good fit given the data available. However there is not enough statistical significance to distinguish which model is better. A more thorough study is left for further work.

[a] Pixels whose χ^2 value is lower than the critical value that satisfies that the probability of exceeding itself is less than 0.05 given a χ^2-distribution with the appropriate degrees of freedom.

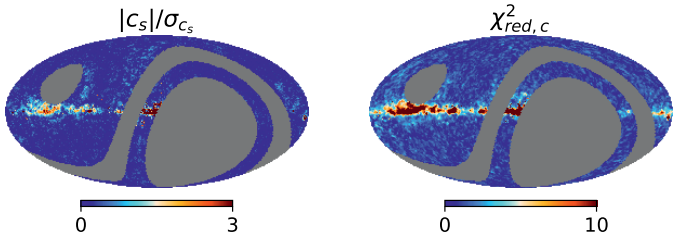

Figure 2 – Signal-to-noise map of the recovered synchrotron curvature and the reduced χ^2 statistic obtained from the fit using a power law with spatially varying curvature model.

5 Conclusions

The inclusion of the low-frequency QUIJOTE-MFI data improves significantly the characterization of the synchrotron model parameters, specially the synchrotron spectral index. We find statistically significant spatial variability of β_s across the sky. We obtain that a power law and power law with curvature model well the synchrotron emission outside the Galactic plane but fails to track the complexity of this region. Also, when we assume uniform curvature we detect a non-zero negative curvature. However, our results are not robust enough to distinguish the model, either the power law or the power law with uniform curvature, which fits better the data.

Acknowledgements

We thank the staff of the Teide Observatory for invaluable assistance in the commissioning and operation of QUIJOTE. The QUIJOTE experiment is being developed by the Instituto de Astrofisica de Canarias (IAC), the Instituto de Fisica de Cantabria (IFCA), and the Universities of Cantabria, Manchester and Cambridge. Partial financial support was provided by the Spanish Ministry of Science and Innovation under the projects AYA2007-68058-C03-01, AYA2007-68058-C03-02, AYA2010-21766-C03-01, AYA2010-21766-C03-02, AYA2014-60438-P, ESP2015-70646-C2-1-R, AYA2017-84185-P, ESP2017-83921-C2-1-R, AYA2017-90675-REDC (co-funded with EU FEDER funds), PGC2018-101814-B-I00, PID2019-110610RB-C21, PID2020-120514GB-I00, IACA13-3E-2336, IACA15-BE-3707, EQC2018-004918-P, the Severo Ochoa Programs SEV-2015-0548 and CEX2019-000920-S, the Maria de Maeztu Program MDM-2017-0765, and by the Consolider-Ingenio project CSD2010-00064 (EPI: Exploring the Physics of Inflation). We acknowledge support from the ACIISI, Consejeria de Economia, Conocimiento y Empleo del Gobierno de Canarias and the European Regional Development Fund (ERDF) under grant with reference ProID2020010108. This project has received funding from the European Union's Horizon 2020 research and innovation program under grant agreement number 687312 (RADIOFOREGROUNDS). Some of the results in this paper have been derived using the HEALPix (K.M. Górski et al., 2005, ApJ, 622, p759) package.

References

1. E. de la Hoz and QUIJOTE collaboration, *MNRAS* in prep. (2022).
2. E. de la Hoz *et al.*, *JCAP* **2020**, 006 (2020).
3. J. A. Rubiño-Martín and QUIJOTE collaboration, *MNRAS* in prep. (2022).
4. C. L. Bennett *et al.*, *ApJS* **208**, 20 (2013).
5. Planck Collaboration *A&A* **643**, A42 (2020).
6. R. T. Génova-Santos and QUIJOTE collaboration, *MNRAS* in prep. (2022).
7. F. Guidi and QUIJOTE collaboration, *MNRAS* in prep. (2022).

Combined constraints on polarized synchrotron emission from Planck and WMAP – *what do we know?*

T. L. Svalheim
on behalf of the BeyondPlanck collaboration
Institute of Theoretical Astrophysics, University of Oslo,
Sem Sælands vei 13, 0371 Oslo, Norway

Precise estimates of the low-frequency polarized microwave sky are essential for next-generation B-mode experiments. The current BeyondPlanck analysis represents the first joint polarized synchrotron analysis with both Planck LFI and WMAP observations. However, even with the combination of these two state-of-the-art data sets, we find that there is very limited constraining power for the spectral energy density of polarized synchrotron emission. For instance, is there a curvature in the synchrotron SED? What is the spectral index, and to what degree does it vary across the sky? The current data are simply unable to tell, and additional high sensitivity experiments, such as C-BASS and QUIJOTE, are desperately needed to answer such questions.

1 Introduction

The most immediate goal in current CMB analysis is the detection of primordial gravitational waves, and if not, tightening the constraints on the tensor to scalar ratio "r". For a simulated Stokes Q map of the CMB, generated from $r = 0.01$, we retrieve a map with an amplitude of approximately $0.1\mu K$. In contrast, the raw amplitude of a 30 GHz sky map in Stokes Q has an amplitude approximately 300 times greater. Furthermore, the current tightest constraints on the tensor to scalar ratio is $r < 0.032$[1]. It is therefore necessary to know the confounding signals to exhaustive detail. In the low frequency regime most commonly used for CMB observations, the dominating foregrounds are is synchrotron and thermal dust emission, in this work we look at synchrotron specifically.

1.1 Synchrotron emission

Synchrotron emission is generated when cosmic ray electrons gyrate in the galactic magnetic field. As the charged particle, typically ejected from a nearby supernovae, spiral along, they essentially light up the surrounding magnetic field. Hence, observations of it would also serve

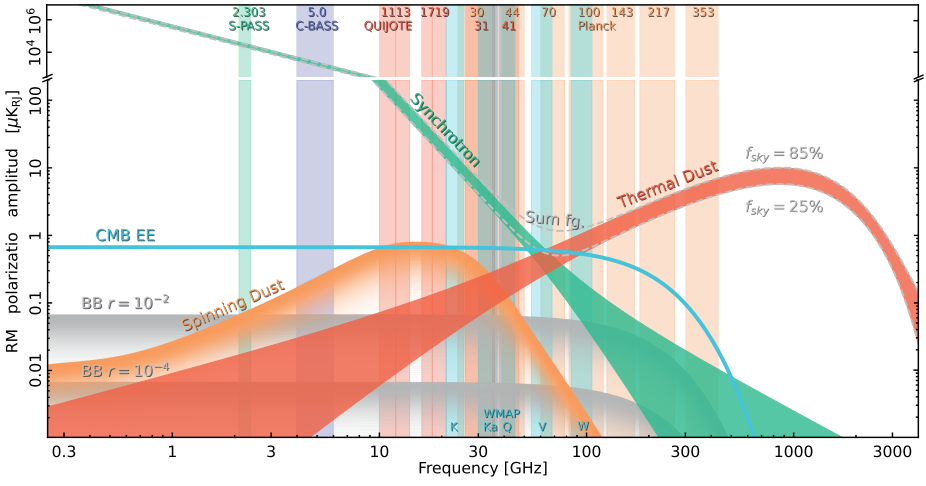

Figure 1 – Polarization amplitude root-mean-square (RMS) as a function of frequency and astrophysical component and polarized emission. The EE CMB spectrum is generated from ideal CMB simulations based on the best-fit Planck ΛCDM model, while the BB limits are derived with tensor-to-scalar ratios of $r = 10^{-2}$ and 10^{-4}, respectively. Additionally, we visualize an upper limit on the polarization fraction of spinning dust of 0.06%.

as a powerful probe to map the galactic magnetic field, which would be of great interest to cosmologists and astrophysicists alike.

Measuring this radiation and constraining models is challenging for a few important reasons. Calibrating instruments is incredibly hard, and there are a lot of moving parts in the analysis pipeline for both ground based and satellite observations. There is currently very few full sky measurements of synchrotron, especially in polarization, making it even harder to constrain models and instrument parameters. Furthermore, the signal may be heavily Faraday-rotated, which makes it hard to extract the true physical conditions due to line of sight magnetic fields.

One of the biggest challenges is creating a realistic model of its spectral behavior as a function of frequency. Figure 1 shows the microwave in polarization with the synchrotron component modeled as a power-law model,

$$S_{synch} = a_s \left(\frac{\nu}{\nu_0}\right)^{\beta_s}, \tag{1}$$

where a_s is the amplitude, ν_0 is the pivot frequency and β_s is the spectral index (values are typically found to be between -2.8 and -3.3). This is a very simple and common representation of its spectral behavior, but not necessarily correct. With this assumption, we may observe the signal over a large range of frequencies to tightly constrain its amplitude. If this is ill-defined however, the results are useless.

2 BeyondPlanck

Another great challenge when observing the microwave sky is understanding the interplay between systematics and foregrounds. Typically, each of the processing steps are carried out by separate teams, and is then passed on. One major drawback of this is that the results of a step far down the analysis pipeline, might reveal errors that were made in the first few steps. This limits the analysis to only make a few total "loops" over the course of the analysis effort. This is what BeyondPlanck intends to improve. By creating a fully integrated end-to-end machinery, as outlined in Fig. 2, we are able to produce 1000 samples in the span of approximately a month.

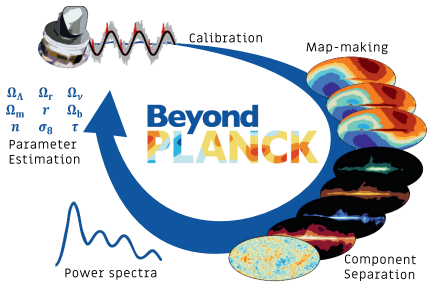

Figure 2 – The BeyondPlanck algorithm. Visualizing the idea of end-to-end analysis, where the results of one part of the signal processing is automatically fed into the next part for a fully integrated loop.

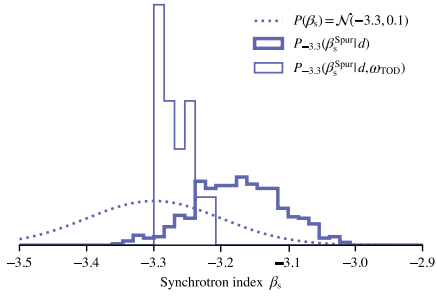

Figure 3 – Normalized histogram showing the spectral index β_s, of synchrotron being sampled for a full BeyondPlanck analysis, marginalizing over all instrumental parameters (bold), versus the result when fixing the system on one set of instrumental parameters and sampling conditionally.

From the figure, we see how each of the processing steps feeds into the next for a fluid system. This gives us a unique window into how spectral indices, cosmological parameters etc. vary with low-level systematic corrections, and a more complete view of the uncertainties.

2.1 Results

With the introduction of additional instrumental parameters one also runs the risk of degeneracies, on the other hand the amount of moving parts in integrated analysis can be used to our advantage, as it lets us explore the wider parameter space. A lot of effort has gone into limiting degeneracies, which in turn has restricted the fidelity of the spectral index sampling effort. For BeyondPlanck, this meant dividing the sky into four disjoint regions for independent sampling as opposed to a pixel-by-pixel approach. However, this is a symptom of a lack of data points, and as BeyondPlanck is a path-finder for similar efforts in the future, the addition of already available datasets will increase constraining power. Even without a pixel-by-pixel analysis, the region-based approach gives us a clear indication of variational tendencies on the sky.

For synchrotron emission, an end-to-end analysis means a better understanding of how the spectral index values are influenced by the low-level systematics such as bandpass errors. For example, one may be forced to develop more sophisticated and perhaps unrealistic models if the data one is working with gives the wrong impression of the underlying signal. Figure 3 shows the true advantage of an end-to-end analysis. Here, the thin line shows the result of the synchrotron spectral index for the case when instrumental parameters are fixed, representing the typical analysis step. The bold line, on the other hand, shows the result when marginalizing over the full parameter-space with BeyondPlanck. We note that the mean value is different between the two distributions, and that the bold line is perhaps a more realistic result.

2.2 The future of synchrotron modeling

The next big open question is whether or not a curvature parameter should be added to the power law model [2]. As already mentioned, a joint analysis could help explain whether or not this is an instrumental artefact. However, recent studies have shown that several observations [3] favor a shallower slope at low frequencies versus high frequencies, which makes a curved spectral index distribution plausible. For a definite conclusion however, we require more data points, such as the low-frequency observations of C-BASS [4] and QUIJOTE [5], or even additional *Planck* data points that have been omitted for computational efficiency among other things. For an in

depth description of this project, we refer the interested reader to the BeyondPlanck overview paper [6].

Acknowledgments

We thank the entire *Planck* and *WMAP* teams for invaluable support and discussions, and for their dedicated efforts through several decades without which this work would not be possible. The current work has received funding from the European Union's Horizon 2020 research and innovation programme under grant agreement numbers 776282 (COMPET-4; BeyondPlanck), 772253 (ERC; bits2cosmology), and 819478 (ERC; Cosmoglobe). In addition, the collaboration acknowledges support from ESA; ASI and INAF (Italy); NASA and DoE (USA); Tekes, Academy of Finland (grant no. 295113), CSC, and Magnus Ehrnrooth foundation (Finland); RCN (Norway; grant nos. 263011, 274990); and PRACE (EU).

References

1. M. Tristram, A. J. Banday, K. M. Górski, R. Keskitalo, C. R. Lawrence, K. J. Andersen, R. B. Barreiro, J. Borrill, L. P. L. Colombo, H. K. Eriksen, R. Fernandez-Cobos, T. S. Kisner, E. Martínez-González, B. Partridge, D. Scott, T. L. Svalheim, and I. K. Wehus. Improved limits on the tensor-to-scalar ratio using BICEP and Planck. *arXiv e-prints*, page arXiv:2112.07961, December 2021.
2. A. Kogut. Synchrotron Spectral Curvature from 22 MHz to 23 GHz. *ApJ*, 753(2):110, Jul 2012.
3. Melis O Irfan, Philip Bull, Mario G Santos, Jingying Wang, Keith Grainge, Yichao Li, Isabella P Carucci, Marta Spinelli, and Steven Cunnington. Measurements of the diffuse galactic synchrotron spectral index and curvature from meerklass pilot data. *Monthly Notices of the Royal Astronomical Society*, 509(4):4923–4939, Nov 2021.
4. Luke Jew, Angela C Taylor, Michael E Jones, A Barr, H C Chiang, C Dickinson, R D P Grumitt, S E Harper, H M Heilgendorff, J Hill-Valler, J L Jonas, J P Leahy, J Leech, T J Pearson, M W Peel, A C S Readhead, and J Sievers. The C-Band All-Sky Survey (C-BASS): Simulated parametric fitting in single pixels in total intensity and polarization. *Monthly Notices of the Royal Astronomical Society*, 490(2):2958–2975, 10 2019.
5. R. Génova-Santos, J. A. Rubiño-Martín, R. Rebolo, A. Peláez-Santos, C. H. López-Caraballo, S. Harper, R. A. Watson, M. Ashdown, R. B. Barreiro, B. Casaponsa, C. Dickinson, J. M. Diego, R. Fernández-Cobos, K. J. B. Grainge, C. M. Gutiérrez, D. Herranz, R. Hoyland, A. Lasenby, M. López-Caniego, E. Martínez-González, M. McCulloch, S. Melhuish, L. Piccirillo, Y. C. Perrott, F. Poidevin, N. Razavi-Ghods, P. F. Scott, D. Titterington, D. Tramonte, P. Vielva, and R. Vignaga. QUIJOTE scientific results - I. Measurements of the intensity and polarisation of the anomalous microwave emission in the Perseus molecular complex. *MNRAS*, 452(4):4169–4182, October 2015.
6. BeyondPlanck. beyondplanck i. global bayesian analysis of the *Planck* low frequency instrument data. *A&A, in preparation*, 2022.

Characterization of the polarized synchrotron emission from Planck and WMAP data

F. A. Martire, R. B. Barreiro and E. Martínez-González
Instituto de Física de Cantabria, CSIC-Universidad de Cantabria,
Avda. de los Castros s/n, E-39005 Santander, Spain

The purpose of this work is to characterize the diffuse Galactic polarized synchrotron. We present EE, BB, and EB power spectra estimated cross-correlating Planck and WMAP polarization frequency maps at 23 and 30 GHz, for a set of six sky regions covering from 30% to 94% of the sky. The EE and BB angular power spectra show a steep decay of the spectral amplitude as a function of multipole, approximated by a power law with power indices around -2.9 for both components. The B/E ratio is about 0.22. The EB cross-component is compatible with zero at 1σ, with upper constraint on the EB/EE ratio of 1.2% at the 2 σ level. The recovered SED, in the frequency range 23–30 GHz, shows E and B power-law spectral indices compatible between themselves with a value of about -3.

1 Introduction

An important challenge in cosmology is the precise measurement of the CMB polarization anisotropies. However, mixed with the cosmological signal, CMB observations also contain different astrophysical emissions, usually called *CMB foregrounds*. The accuracy of the CMB measurements thus depends critically on the foregrounds removal process.
At low frequency, roughly below 100 GHz, the dominant polarized foreground is the diffuse synchrotron emission. The synchrotron radiation is generated by relativistic cosmic ray electrons accelerating around the Galactic magnetic field, which spiral around the field lines emitting radiation. In this work, we characterize the diffuse synchrotron polarization analyzing the observations of *WMAP* K-band and *Planck* 30 GHz frequency channels focusing on the intermediate and low Galactic latitudes.

2 Data and Simulations

For our analysis, we use the *Planck* [1] 2018 data release (PR3), obtained from the full set of observations, focusing on the lowest channel at central frequency 28.4 GHz. Moreover, we use the lowest frequency channel of the *WMAP* [2] dataset, namely the K-band centered at 23 GHz, obtained from the 9-yr data release.

In order to estimate the power spectra from only *Planck* data, we cross-correlate the two half-ring maps. For the only-*WMAP* analysis, we use as splits the co-added maps from 1 to 4 years on one side, and from 5 to 9 years on the other. By cross-correlating splits we mitigate the noise and reduce the effect of systematics. Power spectra results are also obtained from the cross-correlation of *WMAP* and *Planck* maps, using in this case the full-mission *Planck* and the co-added nine-year *WMAP* maps. By cross-correlating data from independent experiments, we can use directly the full data set rather than the splits, since the instrumental noise is uncorrelated and the effect of the systematics is also reduced.
The full-mission *Planck* maps have significantly lower noise than the nine-year *WMAP* maps, however, the synchrotron brightness in the *Planck* lowest frequency, at 28 GHz, is around half that in the *WMAP* K-band, at 23 GHz, what ends up in very similar foreground signal-to-noise for both experiments.

3 Masks

Although Galactic foregrounds studies usually focus on regions at high Galactic latitudes (since these are of greater interest for CMB analyses), the sensitivity at low frequency of *WMAP* and *Planck* does not allow a good characterization of the polarized signals at intermediate and high Galactic latitudes. Therefore, in order to have a higher signal-to-noise, our analysis will instead concentrate on low and intermediate latitudes, by constructing a set of customised masks with different sky fractions.
We define a Galactic mask in order to exclude the emission of the central part of the Galactic centre which has a very complex behaviour. Moreover, we masked very bright point sources, both Galactic and extragalactic, because we found that they have a significant effect at the spectra at all scales. The combination of the Galactic and point sources masks defines a preliminary region of around 6 per cent of the sky. Once these pixels are removed, we construct a set of masks that select those areas with the largest polarization signal in the remaining 94 per cent of the sky. Thus, we mask those pixels below successively lower thresholds of P in the *Planck* 30 GHz polarization map. In this way, we obtain a set of 5 masks, from 30% to 70% sky fraction, plus the near full sky mask, 94% sky fraction.
For our main results, we pick as the reference mask the one with $f_{sky} = 50\%$, which is a good compromise between the considered sky fraction and the signal-to-noise ratio.

4 Angular Power Spectra

In order to characterize the Galactic synchrotron polarization signal, we compute EE, BB and EB cross-spectra. We estimate pseudo-spectra with `NaMaster` [3], including its purification method. We focus our main analyses in the multipole range $30 \leq \ell \leq 300$, binning with $\Delta\ell = 10$ for multipoles $30 \leq \ell \leq 200$ and with $\Delta\ell = 20$ for multipoles $\ell > 200$.
We model the EE and BB synchrotron power spectra as a power law

$$C_\ell^{XX} = A^{XX}\Big(\frac{\ell}{80}\Big)^{\alpha_{XX}} \tag{1}$$

with $XX = EE,\ BB$. The EB cross-spectra is simply modelled as a constant

$$C_\ell^{EB} = A^{EB}. \tag{2}$$

Note that before performing the fit, the CMB contribution is subtracted from the data at the spectra level. More details about the analysis can be found in Martire et al [4].

4.1 WMAP-Planck cross-spectra

For our reference mask ($f_{sky} = 50\%$), the EE and BB power spectra, shown in Figure 1 (right), of the diffuse synchrotron emission show a steep decay as a function of multipoles with consistent

	Planck-WMAP	*Planck*	*WMAP*
α_{EE}	-2.95 ± 0.04	-2.99 ± 0.13	-2.92 ± 0.07
α_{BB}	-2.85 ± 0.14	-2.24 ± 0.28	-2.84 ± 0.29
A^{BB}/A^{EE}	0.22 ± 0.02	0.27 ± 0.04	0.23 ± 0.03
A^{EB} $[10^{-3}\mu K]$	0.08 ± 0.11	-0.11 ± 0.21	0.37 ± 0.83
A^{EB}/A^{EE}	$\leq 1.2\%$	$\leq 4.2\%$	$\leq 4.4\%$

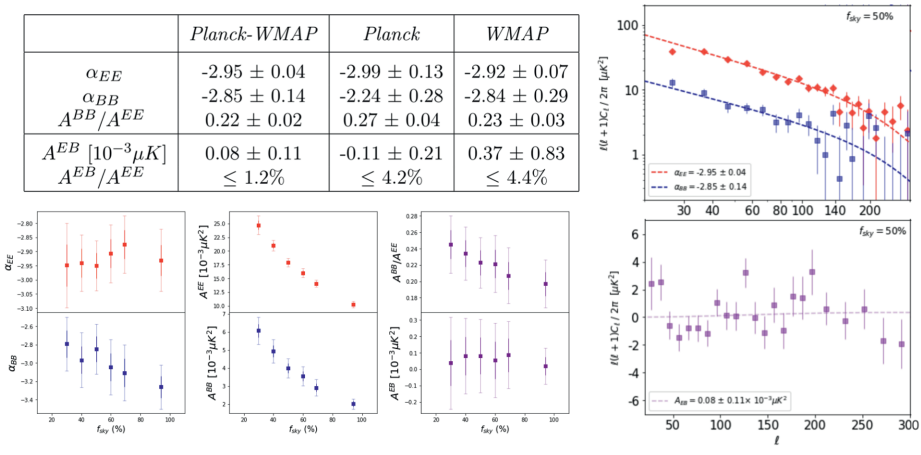

Figure 1 – Left (top): Best-fit results for the reference mask ($f_{sky} = 50\%$). Left (bottom): *Planck-WMAP* results for the whole mask set. Right: EE (red diamonds), BB (blue squares) and EB (purple squares) *Planck-WMAP* cross-spectra for the reference mask ($f_{sky} = 50\%$)

power spectrum indices $\alpha_{EE} = -2.95 \pm 0.04$ and $\alpha_{BB} = -2.85 \pm 0.14$. Considering the results for the full set of masks shown in Figure 1 (left bottom), α_{EE} is very stable and compatible with the nearly-full sky case (94%). Instead, the BB power law shows a slight tendency to steeper values when including high latitudes. The B-to-E ratio for the reference mask is found to be 0.22 ± 0.02 and it ranges from 0.20 in the 94% mask to 0.25 for the 30% mask. The EB cross-spectra is consistent with zero at 1σ for the whole mask set. We can put an upper constraint on the EB amplitude, finding it to be smaller than 1.2% (2σ) that of the EE amplitude.
In order to test the robustness of our results, we fit the model to the same data set, but to a larger multipole range $10 \leq \ell \leq 400$. The conclusions agree well with the baseline results, confirming the robustness of the fits and that the model is also valid at a larger scale range.

4.2 Planck and WMAP spectra

The model of the synchrotron polarization spectra derived independently from *Planck* and *WMAP* are consistent with the power law model with null EB already obtained in the cross-analysis, as showed in Figure 1 (left top). However, the only-*Planck* analysis suggests a less steep decay of the B-component and a slightly larger B-to-E ratio, nevertheless, the error bars overlap at 2σ and the other analyses do not show these features.
As consistency test, we also performed the same analysis with the *Planck* `NPIPE`[5] (PR4) data, cross-correlating the A/B detector splits, finding agreement with the results found with PR3.

Hemisphere analysis

We repeat the same analysis independently for the Northern and Southern hemispheres, simply separating the regions from our mask set. We find that the synchrotron polarized emission in the Northern hemisphere is brighter than in the Southern hemisphere, with a factor around 1.4 larger for the amplitude of the EE spectra (slightly lower factor for BB). We also find a steeper decay of the synchrotron amplitude in the Southern hemisphere with respect to the Northern one. Nevertheless, the B-to-E ratio is quite consistent for the two hemispheres. The EB cross-term is compatible with zero at the 2σ level for the whole mask set.

β_{EE}	-3.00 ± 0.10
β_{BB}	-3.05 ± 0.36
α_{EE}	-2.94 ± 0.07
α_{BB}	-2.65 ± 0.20
A^{BB}/A^{EE}	0.24 ± 0.04

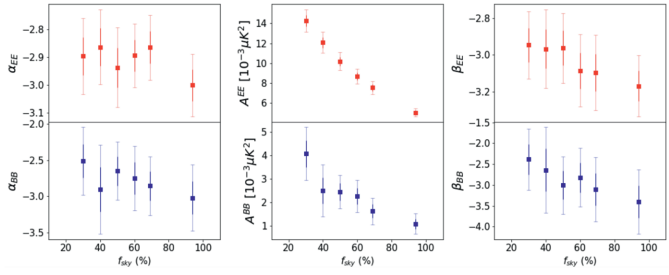

Figure 2 – Left: Best-fit results for the reference mask ($f_{sky} = 50\%$). Right: Results for the whole mask set.

5 Spectral energy distribution

Using observations at different frequencies, nominally at 23 and 30 GHz, we can get information on the behaviour of the diffuse synchrotron polarization with frequency. The synchrotron spectral energy distribution (SED) is generally described by a power law $S = S_0\ \nu^{\beta}$, where β is the energy spectral index. If we combine it with equation 1, we get a system of equations that relate the energy spectral index β and the power spectrum index α

$$\begin{cases} (C_\ell^{XX})^{Planck} = (A^{XX})^{Planck} \left(\frac{\ell}{80}\right)^{\alpha_{XX}} \\ (C_\ell^{XX})^{WMAP} = (A^{XX})^{Planck} \left(\frac{\ell}{80}\right)^{\alpha_{XX}} \left(\frac{\nu^{WMAP}}{\nu^{Planck}}\right)^{2\beta_{XX}} \end{cases} \tag{3}$$

with $XX = EE,\ BB$. We perform a χ^2 fit to the system of equations 3 for the EE and BB auto-spectra, keeping A, α and β as free parameters.
For our reference mask (50%), the spectral indices β_{EE} and β_{BB} are very consistent, with values of -3.00±0.10 and -3.05±0.36 respectively. Figure 2 shows the best-fit parameters for each of the considered masks for both the E- and B-mode components. It is interesting to point out that the power spectral indices tend to move towards steeper values when considering larger sky fractions, i.e., when including higher Galactic latitudes in the analysis.

Acknowledgments

The authors would like to thank the Spanish Agencia Estatal de Investigación (AEI, MICIU) for the financial support provided under the projects with references PID2019-110610RB-C21, as well as from the Unidad de Excelencia María de Maeztu (MDM-2017-0765). We acknowledge the Legacy Archive for Microwave Background Data Analysis (LAMBDA), supported by the NASA office of Space Science, and *Planck*, an ESA science mission with instruments and contributions directly funded by ESA Member States, NASA, and Canada. This research used resources of the National Energy Research Scientific Computing Center (NERSC).

References

1. N. Aghanim *et al.* [Planck], Astron. Astrophys. **641** (2020), A1
2. C. L. Bennett *et al.* [WMAP], Astrophys. J. Suppl. **208** (2013), 20
3. D. Alonso *et al.* [LSST Dark Energy Science], Mon. Not. Roy. Astron. Soc. **484** (2019) no.3, 4127-4151
4. F. A. Martire *et al.*, Accept. J. Cosmol. Astropart. Phys., arXiv:2110.12803 (2022)
5. Y. Akrami *et al.* [Planck], Astron. Astrophys. **643** (2020), A42

Primordial standard clocks and CMB anomalies

Matteo Braglia
Instituto de Fisica Teorica, Universidad Autonoma de Madrid, Madrid, 28049, Spain

We propose an adventurous inflationary trajectory to explain both the large and small-scale anomalies in the cosmic microwave background anisotropy spectra measured by the Planck mission. The model is currently statistically indistinguishable from the Standard Model, but we show that planned observations such as the Simons Observatory, LiteBIRD and CMB-S4 will complement each other in distinguishing the model differences due to their accurate E-mode polarization measurements, offering very optimistic prospects for a detection or exclusion.

1 Introduction

The inflation scenario is the leading candidate theory for the primordial Universe that started the Big Bang [1]. Signals of primordial features can hopefully help us access information beyond the vanilla models of inflation [2,3]. They are strongly-scale-dependent deviations from the otherwise approximately scale-invariant spectra of the primordial density perturbations predicted in the slow-roll paradigm. Several statistically marginal anomalies in both large and small scales of the CMB temperature anosotropies measured by WMAP and Planck may hint at a feature-like origin [4,5]. Such anomalies consist in a dip in the spectrum around $\ell \sim 20$ already noticed in the WMAP data [4] and an oscillatory feature near $\ell \sim 750$ in the Planck data [5]. While it is well known that step-like features in the inflationary potential and resonant features can explain large and small scale anomalies respectively, none of them can address both anomalies at the same time. One interesting possibility [6,7] is that the two anomalies may be conneceted by the classical primordial clock (CPSC) effect [8,9].

The main idea behind the CPSC effect is that sharp features along the inflationary trajectory, which are generic in inflation (see e.g. [1] for a recent review), may temporarily disturb the inflaton away from its eventual attractor trajectory, and during the recovery process from the disturbance, some massive fields may be excited temporarily, oscillating and then settling down around potential minima after a few e-folds. In this picture, the disturbance generates a characteristic sinusoidal-running signal as a candidate for the large-scale anomaly, and the high frequency oscillation of a massive field generates the resonant-running signal as a candidate for the small-scale anomaly.

In the following, we will present an explicit realization of the CPSC effect that vividly describes how, during the initial moment of the Universe, the inflaton is rolling at the top of an adventurous potential which is nonetheless quite natural from the point of view of a landscape. The emerging picture is drastically different from that of a single-field slow-roll model, but the feature signals in the CMB are all small corrections.

2 The CPSC model and its predictions

The requirement for a model to be qualified as a CPSC model is that there should be two observable stages of inflation connected by a sharp feature which classically excites a massive field [8,7]. The most

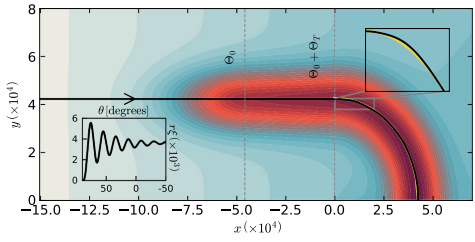

Figure 1 – A birdseye example of background trajectory in our model, plotted over equipotential surfaces (redder means lower potential). In terms of the Cartesian coordinates x and y shown here, for $x<0$ the Θ and σ are Cartesian with $x=\Theta-(\Theta_T+\Theta_0)$ and $y=\sigma+\xi^{-1}$; while for $x>0$ they become radial coordinates with $r=\sigma+\xi^{-1}$ and $\theta=\pi/2-\xi(\Theta-\Theta_0-\Theta_T)$. The insets show how the inflaton overshoots the bottom of the valley (yellow line) and climbs onto a side of the cliff [top-right], and the clock oscillation [bottom-left].

model-dependent part of the full CPSC signal is the amplitude of the sharp feature signal and its smooth connection to the clock signal. In order to fit the low-ℓ anomaly, we will use a step potential as part of the sharp feature, which is the most model-dependent part of the CPSC signal. The model is described by the following Lagrangian [a]

$$\mathcal{L}=-\frac{1}{2}\left[1+\Xi(\Theta)\sigma\right]^2(\partial\Theta)^2-\frac{1}{2}(\partial\sigma)^2-V(\Theta,\sigma)\ , \tag{1}$$

where the kinetic coupling and the potential take the following form

$$\Xi(\Theta)=\xi\ \mathrm{Heav}(\Theta-\Theta_0-\Theta_T)$$
$$V(\Theta,\sigma)=V_{\rm inf}\left\{1-\frac{1}{2}C_\Theta\Theta^2+C_\sigma\left[1-\exp\left(-\frac{(\Theta-\Theta_0)^2}{\Theta_f^2}\mathrm{Heav}(\Theta-\Theta_0)-\frac{\sigma^2}{\sigma_f^2}\right)\right]\right\}.$$

In this model, Θ is the inflationary direction and σ a field orthogonal to Θ. The evolutionary history of the inflaton is shown in Fig. 1. During the first stage of inflation, the inflaton is rolling at the top of a plateau, until it encounters a cliff, located at $\Theta=\Theta_0$ and falls into a lower valley. In the two-field space, the path at the bottom of the lower valley starts out straight and begins to curve after a distance Θ_T. At the entrance of the curved path, the inflaton overshoots the bottom of the valley and climbs onto a side of the cliff, exciting the oscillation of a massive field. Due to the Hubble friction, the oscillation gradually decays and the inflaton settles down in the second stage of inflation.

The signal in this model consists in two kinds of characteristically different running behaviors at large and small scales, respectively. At the large scales $k<k_r$, there is the sharp feature signal with its signature sinusoidal running $\sim\sin(2k/k_0+\text{phase})$, which starts near $k=k_0$. At the small scales $k>k_r$, the clock signal starts to appear with its signature resonant running $\sim(\frac{2k}{k_r})^{-3/2}\sin(\frac{m_\sigma}{H}\ln\frac{2k}{k_r}+$ phase). While the runnings are robust to model variations, the envelope of the sharp feature signal and its connection and relative amplitude to the clock signal are strongly model dependent, and play a crucial role in determining part of the model configuration. In our model, the momentary acceleration of the inflaton after the step produces a dip-like envelope for the sinusoidal running. Following the methodology of Ref. [10], we directly compare numerical results on power spectrum with data. In order to efficiently do that, we first need to build combinations of the parameters in the lagrangian that describe distinct properties of the signal, i.e. the location, width and amplitude of the dip signal and the location and amplitude of the resonant one [11,12].

[a] The mathematical expressions of the potential V and coupling Ξ may be modified as long as they model the simple geometric configuration illustrated in Fig. 1.

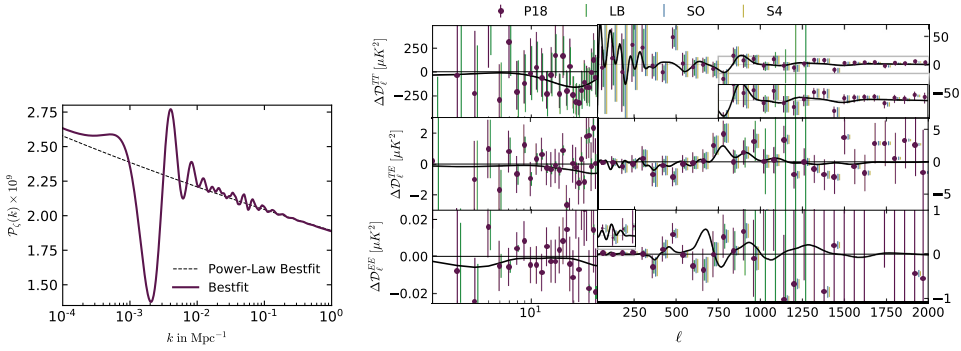

Figure 2 – [Left] The PPS of the bestfit model.for the bestfit parameters. [Right] Residual plot the candidate. P18 error bars are plotted in purple, whereas the forecast error bars for LiteBIRD, SO and CMB-S4 are plotted in green, blue and gold, respectively. Errors for $\ell > 30$ are binned with binwidth $\Delta\ell = 60$.

3 Data comparison and forecasts

Our analysis is based on publicly available latest Planck data of CMB temperature, E-mode polarization and their cross-correlation at large and small angular scales, referred to as P18 in the following. In order to deal with the multimodality of the posterior distributions typical of featuremodels, we sample the likelihood using the nested sampling algorithm implemented in `PolyChord` [b].

Although, from the model selection point of view, our model is indistinguishable from the Standard Model [c], our analysis picks up an interesting bestfit candidate with clock signal frequency of $m_\sigma/H \sim 18$. Our bestfit candidate's PPS and the corresponding residuals are presented in the left and right panels of Fig. 2 respectively. The $\Delta\chi^2 = 19.8$ improvement over the featureless model includes those from the dip feature, fitting low-ℓ data ($\Delta\chi^2_{\rm low-T} = 5.34$ and $\Delta\chi^2_{\rm low-E} = 1.11$), and those from the clock signal, fitting high-ℓ data ($\Delta\chi^2_{{\rm high}-\ell} = 13.31$). The improvement in fit is driven not only by the better fit to the dip in the TT residuals around $\ell \sim 20$, but also by the sinusoidal running of the sharp feature signal and, in particular, the clock signal. The latter starts around $\ell \gtrsim 600$ and addresses the dip followed by a bump in the TT residuals around $\ell \sim 750$ and the associated feature in the TE residuals.

Assuming the $\mathcal{D}_\ell^{\rm TT}, \mathcal{D}_\ell^{\rm EE}, \mathcal{D}_\ell^{\rm TE}$ from the best fit as the fiducial angular power spectra, using the projected noise power spectra from the upcoming Simons Observatory (SO), LiteBIRD, and CMB-S4, we forecast future constraints on our model. The fisrt two experiments are expected to take data in 2023 and 2028 respectively, whereas CMB-S4, has not been funded yet. SO and CMB-S4 are ground based observatories, so they will be sensitive mainly to high-multipoles and cover only a smaller fraction of the sky compared to LiteBIRD which is a space based experiment aiming at the characterization of polarization spectra at large scales. Their projected error bars are shown in Fig. 2. Future experiments will play complementary roles in constraining the model. SO, while impressively increasing the constraints on the clock frequency, will not be able to definitively detect neither the clock signal nor the dip feature because of residual degeneracies induced by the poor constraints on the latter. With the launch of LiteBIRD, though, the constraining power at large scales will increase drastically, being capable of detecting the dip feature amplitude at more than 4σ and a 5σ detection forecast of the resonant signal amplitude [12]. For Planck+LiteBIRD+SO, we find a projected Bayes factor of +22.7, suggesting that in less than a decade we may be able to provide decisive evidence in favor of or against our model. CMB-S4 will further increase constraints on the clock frequency.

[b] https://github.com/PolyChord/PolyChordLite.

[c] The Bayes factor is $\ln B \equiv \ln(Z_{\rm feature}/Z_{\rm featureless}) = -0.13 \pm 0.38$, which is inconclusive according to the Jeffreys' scale.

4 Conclusions

CMB anomalies may hint at primordial physics beyond the standard model of cosmology. We proposed a full classical standard clock model of inflation where a sharp feature exciting massive-field oscillations addresses the low and mid-ℓ anomalies, whereas anomalies at high-ℓ are instead fitted by the clock signal. The improvement in the χ^2 for the model best-fit candidate, characterized by a clock field with an effective mass ~ 18 times the Hubble scale of inflation, is $\Delta\chi^2 \sim 19.8$, although the model is currently indistinguishable from the Standard Model, according to model selection. Assuming such a candidate as a fiducial cosmology, we have performed a forecast for future CMB experiments and highlighted the complementarity of measurements of E-mode spectra across different scales. We find these experiments offer promising prospects within the next decade: Simons Observatory and LiteBIRD, joint with the Planck data, will be able to place significant constraints on all parameters of our model, and CMB-S4 will further improve these constraints. Our results suggest promising prospects of model-building and testing of primordial feature models such as the one presented in this work. If detected, such a model can provide vital information about the origin of the Big Bang and the detailed dynamics of the inflation model.

Besides signatures in CMB, primordial feature models also leave correlated imprints in other observables, which will be further tested in future Large-Scale Structure and 21cm observations, and correlated signals in primordial non-Gaussianities. ll these add to the exciting prospects of probing the history of the primordial Universe using data from near future observations.

Acknowledgments

The author thanks Xingang Chen and Dhiraj Kumar Hazra for collaborating on the works discussed in these proceedings. The author is supported by the Atracción de Talento contract no. 2019-T1/TIC-13177 granted by the Comunidad de Madrid in Spain.

References

1. A. Achúcarro, M. Biagetti, M. Braglia, G. Cabass, E. Castorina, R. Caldwell, X. Chen, W. Coulton, R. Flauger and J. Fumagalli, *et al.* [arXiv:2203.08128 [astro-ph.CO]].
2. X. Chen, Adv. Astron. **2010**, 638979 (2010) doi:10.1155/2010/638979 [arXiv:1002.1416 [astro-ph.CO]].
3. J. Chluba, J. Hamann and S. P. Patil, Int. J. Mod. Phys. D **24**, no.10, 1530023 (2015) doi:10.1142/S0218271815300232 [arXiv:1505.01834 [astro-ph.CO]].
4. H. V. Peiris *et al.* [WMAP], Astrophys. J. Suppl. **148**, 213-231 (2003) doi:10.1086/377228 [arXiv:astro-ph/0302225 [astro-ph]].
5. Y. Akrami *et al.* [Planck], Astron. Astrophys. **641**, A10 (2020) doi:10.1051/0004-6361/201833887 [arXiv:1807.06211 [astro-ph.CO]].
6. X. Chen and M. H. Namjoo, Phys. Lett. B **739**, 285-292 (2014) doi:10.1016/j.physletb.2014.11.002 [arXiv:1404.1536 [astro-ph.CO]].
7. X. Chen, M. H. Namjoo and Y. Wang, JCAP **02** (2015), 027 doi:10.1088/1475-7516/2015/02/027 [arXiv:1411.2349 [astro-ph.CO]].
8. X. Chen, JCAP **01**, 038 (2012) doi:10.1088/1475-7516/2012/01/038 [arXiv:1104.1323 [hep-th]].
9. X. Chen, Phys. Lett. B **706**, 111-115 (2011) doi:10.1016/j.physletb.2011.11.009 [arXiv:1106.1635 [astro-ph.CO]].
10. M. Braglia, X. Chen and D. K. Hazra, JCAP **06**, 005 (2021) doi:10.1088/1475-7516/2021/06/005 [arXiv:2103.03025 [astro-ph.CO]].
11. M. Braglia, X. Chen and D. K. Hazra, [arXiv:2106.07546 [astro-ph.CO]].
12. M. Braglia, X. Chen and D. K. Hazra, [arXiv:2108.10110 [astro-ph.CO]].

Primordial Black Holes forbid the inflaton being dominated by quantum backreaction

Ashley Wilkins & Gerasimos Rigopoulos
School of Maths, Stats & Physics, Newcastle University, Newcastle, UK

We use the Hamilton-Jacobi (H-J) formulation of stochastic inflation to describe the evolution of the inflaton during a period of Ultra-Slow Roll (USR), taking into account the field's velocity and its gravitational backreaction. We compute the mass fraction, β, of Primordial Black Holes (PBHs) formed by a plateau in the inflationary potential. By fully accounting for the inflaton velocity as it enters the plateau, we find that PBHs are generically overproduced before the inflaton's velocity reaches zero, ruling out a period of free diffusion or even stochastic noise domination on the inflaton dynamics. We surmise that the evolution of the inflaton is always predominantly classical with diffusion effects always subdominant. There is a very sharp transition between the under- and over-production regimes. This can be seen either as severe fine-tuning on the inflationary production of PBHs, or as a very strong link between the fraction β and the shape of the potential and the plateau's extent.

1 Introduction

Primordial Black Holes (PBHs) were first theorised in the 60s [1] and 70s [2] and it was soon realised that they could be a Dark Matter (DM) candidate [3]. There are numerous constraints on the abundance of PBHs from many different effects – for a comprehensive review of these see e.g. [4]. Even if PBHs are not all of DM, their abundance (be it small or large) can act as an invaluable probe of the inflationary potential outside of the narrow CMB window.

If one wants to generate an appreciable number of PBHs from single-field inflation then one generally needs to go beyond the Slow-Roll (SR) regime into a so-called period of Ultra-Slow Roll (USR) inflation. Utilising the Hamilton-Jacobi (H-J) formalism as originally described by Salopek and Bond [5] to describe the evolution of the inflaton allows the dynamics to be reduced to first order without making any assumptions about being in a SR or USR regime - the approximation only involves dropping higher order spatial gradient terms (i.e. focuses on long wavelengths) and includes the field's velocity fully. This will enable us to smoothly describe the transition between SR and USR regimes. Stochastic Inflation [6] has enjoyed much success as the leading framework to describe the evolution of non-linear perturbations and their backreaction on the dynamics of the inflaton. We merge the H-J description with stochastic inflation, as shown in [7], in order to have a full, non-linear, description of inflationary dynamics which can

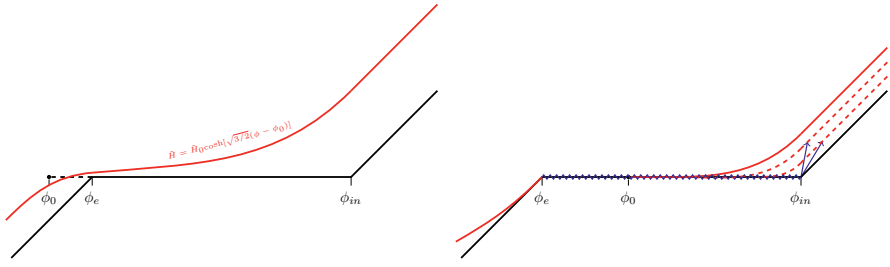

Figure 1 – Scenario A (left panel) corresponds to a plateau shorter than $\Delta\phi_{cl}$, the Hamilton-Jacobi trajectory is plotted in red. Scenario B (right panel) corresponds to a plateau longer than $\Delta\phi_{cl}$, the free diffusion is plotted in blue and the Hamilton-Jacobi trajectory in red as before. When the diffusion reaches ϕ_{in} the field jumps onto a new H-J trajectory and will follow it to a new ϕ_0 before freely diffusing again.

include large quantum-stochastic backreaction.

2 Evolution along a finite plateau using the Stochastic Hamilton-Jacobi equation

Consider a region of the inflationary plateau described by a plateau of finite width. There then exists two distinct scenarios represented in Fig. 1. Scenario A (left panel) corresponds to a plateau width $\Delta\phi_{pl}$ shorter than the distance carried by classical drift $\Delta\phi_{cl} \equiv \phi_{in} - \phi_0$ i.e. the field enters the region with sufficient velocity to carry it all the way through. The inflaton therefore stays on the Hamilton-Jacobi trajectory for all times. Scenario B (right panel) corresponds to $\Delta\phi_{pl} > \Delta\phi_{cl}$, meaning the inflaton cannot be carried all the way through by classical drift. Therefore, once the inflaton has crossed ϕ_0 by a stochastic kick it undergoes free diffusion. As we will demonstrate, realising scenario B is in general forbidden as it leads to an overproduction of PBHs so we will not examine its behaviour in detail.

Incorporating the short-wavelength quantum fluctuations results in the addition of a stochastic noise term in the inflaton's equation of motion:

$$\frac{\mathrm{d}\phi}{\mathrm{d}\alpha} = -2M_{\mathrm{p}}^2 \frac{\partial \ln H(\phi,\phi_0)}{\partial\phi} + \frac{H(\phi,\phi_0)}{2\pi}\xi(\alpha), \quad \left\langle \xi(\alpha)\xi(\alpha')\right\rangle = \delta(\alpha-\alpha') \tag{1}$$

where $H(\phi,\phi_0)$ represents a particular solution to the Hamilton-Jacobi equation which for Scenario A is given in the left panel of Fig. 1.

3 Abundance of Primordial Black Holes from a plateau in the potential

The PBH mass fraction, β, can be computed from the probability distribution function (PDF) of the coarse-grained scalar curvature perturbation $\zeta_{cg} = \mathcal{N} - \langle\mathcal{N}\rangle$:

$$\beta(M) \;=\; 2\int_{\zeta_c}^{\infty} P(\zeta_{cg})\,\mathrm{d}\zeta_{cg} \tag{2}$$

We can clearly see that the mass fraction β roughly represents the area under the curve of the PDF above some critical value, ζ_c. The precise value of ζ_c is not known *a priori* but depends on both the equation of state at horizon re-entry and the shape of perturbation itself[8]. However it is known to be very close to 1 and despite β generically being exponentially sensitive to ζ_c it does not change the qualitative nature of our results.

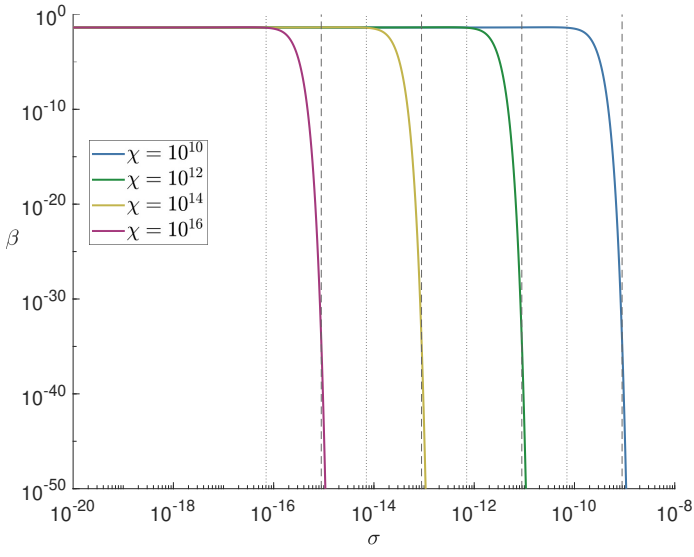

Figure 2 – The mass fraction of PBHs, β, as a function of σ for four values of χ computed using (5). The dotted lines represent the scale when the classical approximation fails, $\sigma_{cl} = 1/\sqrt{2}\chi$. The dashed lines represent the pivot scale to overproduce PBHs, σ_p, predicted by (6). It is clear that values of σ significantly smaller than σ_p overproduced PBHs whereas values of σ larger than this value correspond to negligible production.

3.1 Computing the mass fraction

If we consider the large $\Delta\mathcal{N}$ limit i.e. deep in the tail where the PBH mass fraction is calculated then the pdf for exit time simplifies to:

$$\rho(\mathcal{N}) \simeq \frac{6}{\sqrt{\pi}}\chi \; e^{-\chi^2\sigma^2} e^{-3\Delta\mathcal{N}} \tag{3}$$

where we introduced the dimensionless parameters χ and σ:

$$\chi \equiv \sqrt{\frac{3}{2v_0}}\frac{\Delta\phi_{cl}}{M_{pl}} \simeq \sqrt{\frac{\epsilon_{in}}{2v_0}}, \quad \sigma \equiv \frac{\Delta\phi_{cl} - \Delta\phi_{pl}}{\Delta\phi_{cl}} \tag{4}$$

defined in terms of the classical drift distance, $\Delta\phi_{cl}$ and the width of the plateau itself $\Delta\phi_{pl}$. Notice that $\sigma = 0$ corresponds to $\Delta\phi_{cl} = \Delta\phi_{pl}$ and that the limit $\sigma \to 1$ corresponds to $\Delta\phi_{pl} \to 0$. We have also introduced $\mathrm{erfc}(x)$ which is the standard complementary error function.
Using the mass fraction definition (2) under the large $\Delta\mathcal{N}$ limit (3) we obtain:

$$\beta(M) \simeq \frac{4}{\sqrt{\pi}}\chi \; e^{-\chi^2\sigma^2} \; e^{-3(\zeta_c + \langle\mathcal{N}\rangle - N_{in})} \underbrace{e^{\frac{9}{4}\chi^{-2}}}_{SR} \tag{5}$$

where we have also included the contribution from a previous slow-roll phase. This slow-roll contribution is only important for $\chi \ll 1$ where it very quickly forces β to unrealistically large values.

We can identify a pivot scale σ_p below which β violates constraints – strongest $\beta < 10^{-24}$, weakest $\beta < 10^{-2}$ – given by:

$$\sigma_p \equiv \frac{\sqrt{\pi}}{4\chi} \; e^{3\zeta_c} \tag{6}$$

This scale is verified in Fig. 2 where we plot, using (5), the dependence of the mass fraction, β on σ for a few values of χ. We can see that the behaviour of β almost looks like a step function with a sharp drop off as σ is increased. The dashed lines – corresponding to the scale predicted by (6) – accurately describes where this sharp dropoff takes place and marks the separation between overproduction of PBHs and negligible production.

We can also compute the value of σ for which the classicality parameter – a measure of how good the semi-classical approximation is – is violated, $\eta_{cl} = 1$. We find that the classicality parameter is violated at $\sigma_{cl} = 1/\sqrt{2}\chi$ and that decreasing the value of σ pushes you into the quantum diffusion dominated regime from classically dominated dynamics. As can be clearly shown by the dotted lines in Fig. 2 one only enters the diffusion dominated regime – given by σ_{cl} – once the mass fraction of PBHs, β, is prohibitively high. In other words the classically dominated evolution will already overproduce PBHs before the inflaton even enters the diffusion dominated regime.

4 Conclusion

Our main result can be stated as follows:

The inflaton cannot enter a period of quantum diffusion dominated dynamics without first overproducing Primordial Black Holes.

A semi-classical approximation seems to always be adequate for observationally allowed inflationary dynamics. We demonstrated this by considering the evolution of the inflaton entering a finite width plateau from a previous Slow-Roll (SR) phase utilising the Stochastic Inflationary formalism and taking into account properly the General Relativity momentum constraint. For further details and extensions to inflection points please see [9].

Acknowledgments

A.W. acknowledges support from the EPSRC under Project 2120421.

References

1. Ya. B Zel'dovich and I.˜D. Novikov. The Hypothesis of Cores Retarded during Expansion and the Hot Cosmological Model. *Soviet Astron. AJ (Engl. Transl.)*, 10:602, feb 1967.
2. S. Hawking. Gravitationally Collapsed Objects of Very Low Mass. *Monthly Notices of the Royal Astronomical Society*, 152(1):75–78, apr 1971.
3. GEORGE F. CHAPLINE. Cosmological effects of primordial black holes. *Nature*, 253(5489):251–252, jan 1975.
4. Bernard Carr, Kazunori Kohri, Yuuiti Sendouda, and Jun'ichi Yokoyama. Constraints on Primordial Black Holes. feb 2020.
5. D. S. Salopek and J. R. Bond. Nonlinear evolution of long-wavelength metric fluctuations in inflationary models. *Physical Review D*, 42(12):3936–3962, 1990.
6. Alexei A. Starobinsky and Junichi Yokoyama. Equilibrium state of a self-interacting scalar field in the de Sitter background. *Physical Review D*, 50(10):6357–6368, 1994.
7. Tomislav Prokopec and Gerasimos Rigopoulos. $\Delta\mathcal{N}$ and the stochastic conveyor belt of ultra slow-roll inflation. *Phys. Rev. D*, 104:083505, Oct 2021.
8. Ilia Musco, Valerio De Luca, Gabriele Franciolini, and Antonio Riotto. Threshold for primordial black holes. II. A simple analytic prescription. *Physical Review D*, 103(6):063538, mar 2021.
9. Gerasimos Rigopoulos and Ashley Wilkins. Inflation is always semi-classical: diffusion domination overproduces Primordial Black Holes. *JCAP*, 12(12):027, 2021.

About non-classical gravitational states

Federico Piazza
Aix Marseille Univ, Université de Toulon, CNRS, CPT, Marseille, France

Take the gravitational field, a number of macroscopic observers and put them in a "highly-quantum" state, made by a coherent superposition of different classical configurations. How would that look like? I try to study this system by introducing a spatial distance operator among the observers and looking at the properties of its expectation values.

1 Introduction

By a *classical state* here I mean a state whose wave-function is peaked around one solution of the classical equations of motion. The situation is famously illustrated by coherent states, centered around a classical trajectory and just "furbished" with the minimal uncertainty allowed by the Heisenberg principle.

The double-well potential offers an equally known example of *deviations* from classicality. Its ground state does not correspond to a classical configuration sitting on either of the minima, but is a coherent superposition of the two. As nicely explained by Coleman [1], this generalizes to periodic potentials and, most notably, to gauge theories. The ground state of a non-Abelian Yang-Mills theory *is not* just $A^\mu = 0$ "furbished" with the minimal amount of quantum indeterminacy. The *θ-vacua* of such theories are coherent superpositions of topologically inequivalent configurations. When time-dependent or transient, deviations from classicality are normally associated with tunneling.

Hovering over the latter examples are *Euclidean* path integrals. Broadly speaking, when the relevant classical saddles live in Euclidean spacetime and are non-trivial, in the sense that they interpolate different classical configurations, this often signals a departure from classicality.

Recently, gravitational Euclidean methods have played an important role in addressing aspects of the black hole information puzzle [2]. Non-trivial Euclidean saddles connecting different boundaries account for the decrease of entropy in the late-Hawking radiation, as expected if the whole system evolves unitarily. It is tempting to wonder if *gravitational* deviations from classicality at low energy are at play in this context. Perhaps related to all this, gravitational instantons/wormholes have been advocated as a non perturbative mechanism to solve the cosmological constant problem [3]. But what would it mean for the gravitational field to be in a coherent superposition of different classical metrics? What would an observer living in such a spacetime experience?

In this talk I report on recent little advances in understanding these issues [4]. I will show that, perhaps counterintuitively, a highly quantum gravitational state does not seem to imply anything exotic, *locally*. However, anomalous geometrical effects can build up at large separations.

2 A fluid (or a solid) of observers

I am interested in low energy phenomena, governed by Einstein gravity. In the standard canonical theory [5] the spatial metric h_{ij} is the relevant dynamical variable. Physical states satisfy Hamiltonian and momentum constraints. The idea is then to consider a highly quantum such state $\Psi[h_{ij}(x^k)]$ and try to understand it "operationally", i.e. in terms of the mutual observations of a bunch of observers living therein. One should thus introduce additional fields in the low energy theory to model the observers and their mutual interactions.

My choice of observers is that of a continuum "fluid" of them. The effective field theory description of a fluid or a solid [7] involves three scalar fields X^I, $I = 1, 2, 3$. Each triplet of values labels and "follows in time" an infinitesimal volume of the medium. Equivalently, each triplet is the *name* of an observer. One can arrange the Lagrangian in such a way that $X^I = const.$ is a geodesic on any classical solution. In this case we are dealing with a non-relativistic fluid. However, for the moment, I will maintain agnostic about the dynamics of the medium.

The three fields X^I effectively serve as a reference system, to which I will add a fourth "time" field T. Dynamical reference systems have a long story as a mean to define gauge invariant observables [8] and dress local operators [9] in quantum gravity. Ideally one would like to add also a light field to model signal exchanges among the observers. A more economic strategy is to focus directly on spacetime *distances* as a proxy for all such mutual relations.[a]

In the canonical theory the fields introduced above are commuting, and thus can be used as independent variables in the wave-function. It is known that $\Psi[h_{ij}(x^k),\, X^I(x^k),\, T(x^k)]$, despite depending of spatial quantities, portraits a portion of space*time*. The point is that the Hamiltonian constraint makes Ψ invariant under time-diffeomorphisms. However, my very limited task here is to define *spatial distances between the observers along a given time slice*, which can be made gauge-invariant with the aid of the reference fields X^I and T.

3 Spatial-distance operator

I will use the field T to define the *conditional probability amplitude* that all remaining fields be in some configuration *given that* the value of $T(x^k)$ is a constant, T_0,

$$\tilde{\Psi}[h_{ij}(x^k),\, X^I(x^k); T_0] \;\equiv\; \mathcal{N}(T_0)\Psi[h_{ij}(x^k),\, X^I(x^k),\, T(x^k) = T_0]. \tag{1}$$

This is a portrait of the system "at a given time". The $\tilde{\Psi}$-functionals only depend on h_{ij} and X^I and must satisfy the momentum constraint. A convenient (overcomplete) basis for the corresponding Hilbert space are the common eigenvectors of such commuting variables, $|h_{ij}(x^k),\, X^I(x^k)\rangle$. Each element of this basis represents a very classical three-dimensional geometry with the positions of the observers perfectly specified on it. On $|h_{ij}(x^k),\, X^I(x^k)\rangle$ it is thus possible to calculate the distance between any chosen pair of observers.

So I define a spatial distance operator between $\vec{X}$ and $\vec{Y}$, $\hat{d}(\vec{X}, \vec{Y})$, by declaring that it is diagonal on $|h_{ij}(x^k),\, X^I(x^k)\rangle$,

$$\hat{d}(\vec{X}, \vec{Y})\; |h_{ij}(x^k),\, X^I(x^k)\rangle \;=\; d(\vec{X}, \vec{Y})_{\{h, X^I\}}\; |h_{ij}(x^k),\, X^I(x^k)\rangle\,. \tag{2}$$

In the above equation the two triplets $\vec{X}$ and $\vec{Y}$ are the names of the two observers and the eigenvalue $d(\vec{X}, \vec{Y})_{\{h, X^I\}}$ is their distance on the corresponding eigenstate. In practice, as usual, one needs to find the geodesic between $\vec{X}$ and $\vec{Y}$ and integrate the spatial line element along it. The subscript $\{h, X^I\}$ is there to remind us that this procedure depends on the geometry and on the fields' configuration on the eigenstate $|h_{ij}(x^k),\, X^I(x^k)\rangle$.

[a] E.g. if a light ray connects events A and B then A and B are at null Lorentzian distance. See also [6] on this.

4 Expectation values

On a generic state $\tilde{\Psi}$, expectation values of $\hat{d}(\vec{X},\vec{Y})$ are calculated by expanding $\tilde{\Psi}$ on the classical eigenbasis,

$$\left\langle \hat{d}(\vec{X},\vec{Y})^2 \right\rangle = \sum_I \int \widetilde{\mathcal{D}h}\, \mathcal{D}X^I \left| \langle \tilde{\Psi} | h, X^I \rangle \right|^2 \left(d(\vec{X},\vec{Y})_{\{h,X^I\}} \right)^2 . \tag{3}$$

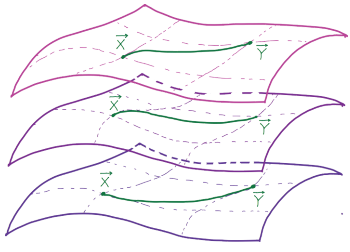

Figure 1 – Every classical configuration contributes to the distance expectation value, weighted by the amplitude probability $\tilde{\Psi}$. On each configuration the distance between $\vec{X}$ and $\vec{Y}$ is a well-defined calculable quantity.

Because of gauge redundancy, different metric configurations represent the same geometry. The tilde on $\mathcal{D}h$ means that we should pick just one representative for each gauge orbit.

In (3) I have evaluated the average of $\hat{d}^2$ because it has better analytic properties than that of $\hat{d}$ and is more naturally generalizable to the Lorentzian case: Lorentzian distances can be either positive or imaginary and averaging over them could be meaningless. The distances *squared*, instead, are always real and thus average to a positive, negative or null value.

The observers' labels $\vec{X}$ define a coordinate system on a three-dimensional manifold which is very naturally equipped with the distance

$$\overline{d(\vec{X},\vec{Y})} \equiv \sqrt{\left\langle \hat{d}(\vec{X},\vec{Y})^2 \right\rangle} . \tag{4}$$

Is (4) itself a *Riemannian* distance? In other words, is there an "average line element" on the manifold that reproduces (4) for each pair of points? It will be sufficient to show a counterexample in order to give a negative answer to this question.

5 Average distances are non-additive

Consider a superposition of two classical eigenvectors, $|\tilde{\Psi}\rangle = (|\tilde{\Psi}_1\rangle + |\tilde{\Psi}_2\rangle)/\sqrt{2}$. The system is one-dimensional and the classical states $|\tilde{\Psi}_1\rangle$ and $|\tilde{\Psi}_2\rangle$ are depicted in the figure below. Only four observers are picked out in the figure: A, B, C, and D.

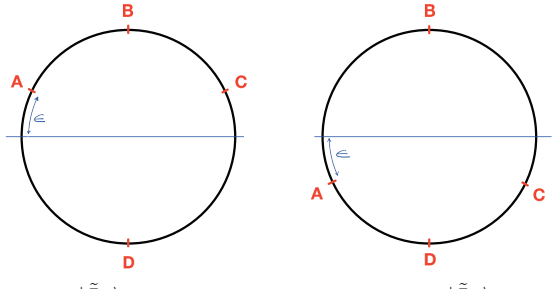

$|\tilde{\Psi}_1\rangle$ $|\tilde{\Psi}_2\rangle$

To first order in ϵ,

$$\overline{d(A,B)} = \overline{d(B,C)} = \overline{d(A,D)} = \overline{d(C,D)} = \pi/2\,, \qquad \overline{d(B,D)} = \pi\,, \qquad \overline{d(A,C)} = \pi - 2\epsilon\,. \tag{5}$$

It is clear from this example that average distances *are not* Riemannian distances. In particular, even in one dimension they fail to add up: $\overline{d(A,B)} + \overline{d(B,C)} \neq \overline{d(A,C)}$.

This anomalous behavior, in general, builds up at large separation and is reminiscent of some IR non-local effect found in double holography [10]. On the opposite, in the neighbors of each observer nothing particularly exotic happens. There is [4] an average metric $\mathcal{G}_{IJ}$ such that

$$\overline{d(0,\vec{X})} \;=\; \sqrt{\mathcal{G}_{IJ}\; X^I X^J} \;+\; \mathcal{O}(X)^3\,, \tag{6}$$

where the labels $\vec{X}$ have been used directly as coordinates and one of the two observers has been located at the origin. Overall, average distances behave like *chord distances* of embedded manifolds: they have a standard locally flat limit but fail to be additive at large separation [4].

6 Conclusions

I have tried to study departures from classicality in gravity with the aid of certain auxiliary scalar fields that serve as a reference frame of "observers". The expectation values of their mutual distances are a good diagnostic of the quantum-ness of the state. Most strikingly, average distances can grow in some non-additive way while maintaining a regular behavior at small separations. The physical implications of this effect are far from obvious—space-like distances do not have direct operational meaning anyway. However, if some of this non-additivity leaks along the time direction, this could have interesting implications e.g. on causality [4 10].

My considerations are purely kinematical in the sense that, from the onset, I consider states that already deviate from classicality. There is no firm indication, at present, about when and how a low-energy gravitational system could find itself in such a highly quantum state. However, it is not difficult to see that the non-additive effect just described is always going to be there, to some extent. Perhaps it is just negligible in most realistic situations. It would be interesting to quantify this effect, say, in a Hartle-Hawking state. It would be nice also to extend this study to four-dimensional spacetime distances, which have more direct operational meaning.

References

1. S. Coleman, "Aspects of Symmetry: Selected Erice Lectures," (1985), Chap. 7.
2. See e.g. A. Almheiri, T. Hartman, J. Maldacena, E. Shaghoulian and A. Tajdini, "The entropy of Hawking radiation," Rev. Mod. Phys. **93** (2021) no.3, 035002 [arXiv:2006.06872 [hep-th]], and references therein.
3. See e.g. A. Hebecker, T. Mikhail and P. Soler, "Euclidean wormholes, baby universes, and their impact on particle physics and cosmology," Front. Astron. Space Sci. **5** (2018), 35 [arXiv:1807.00824 [hep-th]], and references therein.
4. F. Piazza, "Glimmers of a post-geometric perspective," [arXiv:2108.12362 [hep-th]].
5. B. S. DeWitt, "Quantum Theory of Gravity. 1. The Canonical Theory," Phys. Rev. **160** (1967), 1113-1148
6. E. Witten, "Light Rays, Singularities, and All That," Rev. Mod. Phys. **92** (2020) no.4, 045004 [arXiv:1901.03928 [hep-th]].
7. S. Dubovsky, T. Gregoire, A. Nicolis and R. Rattazzi, "Null energy condition and superluminal propagation," JHEP **03** (2006), 025 [arXiv:hep-th/0512260 [hep-th]]. S. Endlich, A. Nicolis, R. Rattazzi and J. Wang, "The Quantum mechanics of perfect fluids," JHEP **04** (2011), 102 [arXiv:1011.6396 [hep-th]].
8. C. Rovelli, "Quantum Reference Systems," Class. Quant. Grav. **8** (1991), 317-332.
9. D. Marolf, "Comments on Microcausality, Chaos, and Gravitational Observables," Class. Quant. Grav. **32** (2015) no.24, 245003 [arXiv:1508.00939 [gr-qc]].
10. H. Omiya and Z. Wei, "Causal Structures and Nonlocality in Double Holography," [arXiv:2107.01219 [hep-th]].

The primordial structure from Quantum Cosmological bouncing models

Jaime de Cabo Martin
National Centre for Nuclear Research, Pasteura 7, 02-093 Warszawa, Poland

By quantizing the background as well as the perturbations in a simple one fluid cosmological model, we show that there exists an ambiguity in the choice of relevant variables, potentially leading to incompatible observational physical predictions. In a classical inflationary background, the exact same canonical transformations lead to unique predictions, so the ambiguity we put forward demands a semiclassical background with a sufficiently strong departure from classical evolution. The latter condition is clearly satisfied by bouncing models. We propose coherent states as the tool for introducing the semiclassical universe. We solve the quantum dynamics of the perturbation modes both analytically and numerically and investigate the amplitude spectra of the perturbations. We study the underlying quantum state, the Bunch-Davies vacuum, from the point of view of late-time observers by means of the Bogolyubov transformations. In particular, we study the phase space probability distributions obtained with the standard coherent states built from instantaneous vacua. We discuss the issue of the temporal phase shift with which the modes emerge from the bounce as sine waves. Finally, we find that the model may be fitted to data and shed light on the physical universe, constraining free parameters of the bouncing universe.

1 Introduction

Observational data from the Cosmic Microwave Background indicates that the Universe has emerged from its primordial phase furnished with small adiabatic density perturbations with a nearly scale-invariant amplitude spectrum, providing a direct proof on the large scale (or small mode) power suppression. The most accepted theoretical explanation to the current observations is the idea that they seem to be coming from quantum vacuum fluctuations of single scalar field added to Einstein-Hilbert action, and this is compatible with inflation scenario, that supposes a phase of exponential accelerating expansion with constant Hubble rate. Moreover, the inflationary paradigm help us to solve some issues of the Big Bang theory, for instance the horizon or the flatness problem, homogeneity, isotropy, etc. However, there exist some problems that are not addressed by inflation, specially the so-called singularity problem, and here is where the motivation for studying the bouncing cosmological solutions arises. We propose the construction a theory of the primordial universe based on the assumption that it was dominated by quantum gravity effects, which led the Universe to avoid the initial singularity when quantizing the model. This would create a physical mechanism to generate the primordial structures and started the cosmological expansion. In the future, these description will also allow us to construct a theory that will need a smaller number of primordial symmetries, with new features like anisotropic evolution. The results presented here represent a summary of the present work in d. C. Martin *et al.*[1], and an extension included in the forthcoming work *Quantum bounce models and the primordial structure*, along with P. Małkiewicz (NCBJ, Warsaw) and P. Peter (IAP, Paris).

The basis for obtaining a quantum cosmological theory is to write General Relativity in Hamiltonian formulation. It was proven[2] that, starting from the usual 3+1 foliation of the GR

ADM-metric: $ds^2 = -N^2dt^2 + q_{ab}(dx^a + N^a dt)(dx^b + N^b dt)$, the scalar physical Hamiltonian for a FLRW universe filled with one fluid, up to second order in perturbations, is found to read:

$$\mathbf{H} = \int N\mathcal{H}_0\big|^{(0)} + \sum_k N\left(\kappa_0 \frac{w(w+1)ap^2}{6}\Pi_k^2 + \frac{3}{2(w+1)}\frac{a^{-3}k^2\mathcal{V}_0}{\kappa p^2}\Phi_k^2\right) \tag{1}$$

with $\kappa_0 = 8\pi G_N/\mathcal{V}_0$, w representing the kind of fluid, and a, p, our the canonical variables. It consist in a zeroth-order background which is a first class constraint, and a second order part in terms of the Dirac observables Φ, Π that are the gauge-invariant scalar perturbation variables.

2 Obtaining the quantum theory

2.1 Classical Solution

Our background variables can be redefined into new variables q, and p in terms of the fluid Friedmann time τ in order to simplify the Hamiltonian and equations of motion. The perturbation variables can also be redefine in many (classically equivalent) different ways, each one yielding to a different parametrization of the Hamiltonian. In our work we just considered two of them: Mukhanov-Sasaki (or *Conformal*) param. with $v_k = Z\phi_k$, and Natural (or *Fluid*) param. with $\phi_k = \Phi_k/(\mathcal{V}_0\sqrt{Z})$. We can also conveniently redefine our time variable into a conformal time η, so that we can write the equations of motion in the usual way of the Mukhanov-Sasaki equation $v_k'' + (wk^2 - (q^r)''/q^r)v_k = 0$ where there are two classically equivalent choices of r: $r_1 = (3w-1)/(3-3w)$ and $r_2 = 2/(3-3w)$. The background solutions are just straight lines with constant momentum in the half-plane phase space that terminate or emerge from singularity. The solution for the perturbations is finite and physically equivalent for both parametrizations but discontinuous at the singularity $\eta = 0$

2.2 Quantization and Semiclassical portrait

We want to quantize both perturbations and background spacetime. For the perturbations we perform the usual HO quantization process in the same way that is made for inflationary models. For the background we use a formalism called *affine coherent state quantization*[4], which, when applied to the selected observables q and p, makes an extra repulsive term naturally arise, resolving the singularity and being the term responsible for the generation of bouncing trajectories in the phase space (Fig. 1 in de Cabo Martin *et al.*[1]).

After that, assuming the full state vector to be a product of background and perturbation states without backreaction, we produce a class of semiclassical (or semi-quantum) description for the background[3]. We just don't look for a generic solution of the background but in the space of coherent states, computing the expectation value of the Hamiltonian inside them, and generating the dynamics. We end up with two different semiclassical Hamiltonians for each parametrization, and we will solve the perturbations quantum dynamics within this portrait.

Thus, when we solve the Heisenberg equations of motion of perturbations for each of both parametrizations, we obtain two Mukhanov-Sasaki equations with two different potential terms $\mathcal{V} = (q^r)_{,\eta\eta}/q^r$, for natural param. being $r = r_1$ and for M-S being $r = r_2$. Both potential have different shape in time close to the bounce and coincide in the classical limit $|\eta| \to \infty$, meaning we obtain two inequivalent quantum theories with different predictions for every mode $k_{N/MS}$ (see Fig. 3 and Fig. 4 in de Cabo Martin *et al.*[1]).

3 Amplitude spectrum of curvature perturbations

We want to solve the quantum dynamics of the perturbations, and we do it both numerically and analytically, in order to compute the amplitude spectrum of the perturbations defined as: $\delta_\xi[k, \tau(\eta)] = \hbar\sqrt{\mathcal{V}_0}\frac{|v_{|k|}|}{2\pi a}k^{3/2}$. In order to do that we need some expressions for the initial

conditions coming from the minimisation of the Hamiltonian. The process is similar for both parametrizations. First we do it numerically, and we obtain its value for a wide discrete set of modes just after the moment they exit the potential, because we expect its value to get frozen during its evolution (Fig. 1 left) for a significant fraction of its period after that moment. That value is what we shall call primordial spectrum, and when we compute it in terms of the different modes (Fig. 1 right) we clearly obtain a different sets of slopes depending on w for each parametrization, representing two different values of the spectral index: $n_S = 6w/(3w+1)$ for M-S param. and $n_S = (3w+3)/(3w+1)$ for natural.

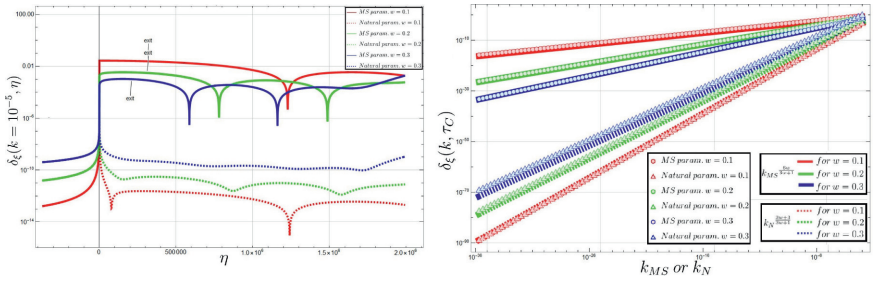

Figure 1 – *Left*: amplitude spectrum of perturbations evolution in η for a single mode with $k_{N/MS} = 10^{-5}$, for three different fluids w. *Right*: (in logarithmic scale) numerical and analytical primordial power spectrum vs. $k_{N/MS}$ for both parametrizations and different kind of fluid w.

For the analytical integration we need to take some approximation in order to solve the complex equations, the one being that we are interested only in very small modes that crossed the potential far before the bounce when it could be assumed as in its classical limit. Then, we need match those solutions with the known vacuum ones at the initial crossing potential time. We compute them at the exit crossing time to obtain the formulas for the primordial spectrum:

$$\delta_\xi^{MS} = \frac{\sqrt{\mathcal{V}_0 \mathfrak{M}_s}\omega f}{2w^{\frac{3}{2}}} \left(\frac{q_B \omega f}{\gamma}\right)^{\frac{-6w}{1+3w}} \left|\frac{2}{3-3w}C + (w+1)fD\right| k_{MS}^{\frac{6w}{3w+1}} \tag{2}$$

$$\delta_\xi^{N} = \frac{\sqrt{\mathcal{V}_0}}{2\pi w^{\frac{3}{2}}} \left(\frac{q_B \omega f}{\gamma}\right)^{\frac{-2}{1+3w}} \left|\frac{3w+1}{3-3w}C + 2(w+1)fD\right| k_{N}^{\frac{3w+3}{3w+1}} \tag{3}$$

where C, D are normalization constants, $f = \sqrt{2(1-3w)}/3(1-w^2)$ and q_B, ω, γ and $\mathfrak{M}_s$ are defined in [1][‡]. We obtain the same n_s as from the numerical calculations. It is worthy to mention that in M-S param. we found the same spectral index that for primordial gravitational waves[3].

4 Final quantum state

4.1 Particle distributions

In what follows we study further differences and similarities between the respective final states. For a fixed mode, we characterize using different approaches. We start using particle distributions. By relating different mode expansions of the perturbation fields $v(x, \eta)$ with different creation and annihilation operators $\hat{a}^\dagger$, $\hat{a}$ and $\hat{b}^\dagger$, $\hat{b}$ we can introduce the known Bogolyubov coefficients α and β. Via the Bogolyubov transformations we can express the initial Bunch Davies vacuum of a-particles with respect to the b-particles instantaneous vacuum state that an observer will see at a later time. Hence, although we start with a state of no a-particles, this same state ends up containing b-particles with quantas of left and right moving waves forming a standing wave, yielding to particle production. We can compute the occupation number of the n-particle state of that wave, as a function of n representing the probability distribution of particles at the exit crossing time.

4.2 Phase space representation and temporal phase shift

The next analysis would begin by decomposing the Fourier components of the field in real and imaginary part, since they describe two modes of the standing wave. The final state of both modes can be expressed in the standard coherent state representation by action of a this displacement operator on b-vacuum. We compute the probability distribution for the final state starting from fixed Bunch-Davies vacuum which underlies evolution in Heisenberg picture (Fig. 2). Once the system evolves through the bounce, the vacuum gets excited and particles are produced leading to final squeezed states. The most important result is that the value of the primordial amplitude is of quantum nature, different for each parametrization and has non-zero uncertainty, but there is a temporal phase of oscillation with which this amplitude emerges when exiting the potential which is classical and represented in Fig. 2 by the black arrows.

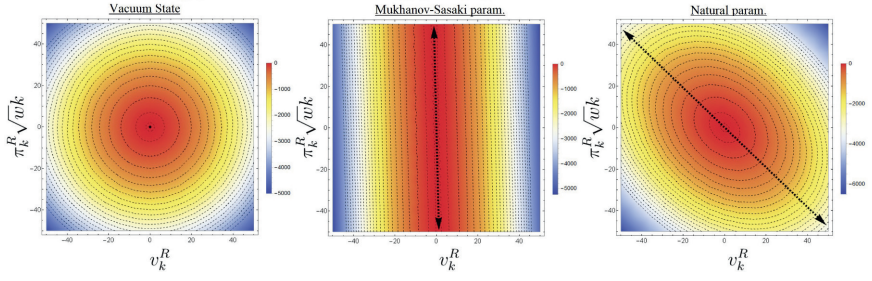

Figure 2 – Phase space probability distribution for $w = 0.28$ and $k = 10^{-5}$. *Left:* The initial vacuum state. *Center:* M-S param. squeezed state at exit crossing time η_c. *Right:* Natural param. squeezed state at η_c.

This phase shift can be obtained analytically, and it plays the role of making the perturbation fields behave as sine waves when the gravitational potential vanish and radiation era begins, what is a very important feature to ensure the constancy of primordial amplitude of the comoving curvature $\delta R_k \propto \sin(\sqrt{w}k\eta)/\eta \approx \sqrt{w}k$, as inflation does. It can be also proven that this phase shift is scale independent for large scales so that all modes emerge more or less coherently.

5 Conclusions

We are able to obtain models of the primordial universe avoiding the singularity problem. Also, we found that classically equivalent parametrizations lead to two unitarily inequivalent quantum theories. This dependence on parametrizations is a natural consequence of the non-linearity of the theory of gravity, which yields to this ambiguity when we perform quantization. Moreover, we found that these models may be fitted to data of the primordial spectrum, and are able to explain the constancy of curvature perturbations like inflationary models. Finally, writing the results (2), (3) in terms of physical parameters $\delta_\xi^{MS}(k_*) \propto r/\sqrt{\mathfrak{K}}$, the data from Planck observations allow us to set constraints on features like the strength of the bounce $\mathfrak{K}$ or size ratio between entire-observable universe r, depending on the kind of fluid w governing the dynamics.

References

1. J. de Cabo Martin, P. Małkiewicz & P. Peter, Phys. Rev. D **105**, 023522, arXiv:2111.02963.
2. P. Małkiewicz, Class. Quant. Grav. **36**, 215003 (2019), arXiv:1810.11621.
3. P. Małkiewicz & A. Miroszewski, Phys. Rev. D **103**, 083529 (2021), arXiv:2011.03487.
4. J. P. Gazeau & R. Murenzi. J. Math. Phys. **57**, 052102 (2016), arXiv:1512.08274.

Cosmology of a new class of massive vector fields

V. Pozsgay
Theoretical Physics, Blackett Laboratory, Imperial College, London, SW7 2AZ, UK

I introduce (Extended) Proca-Nuevo, a non-linear theory of a massive spin-1 field enjoying a non-linearly realized constraint. I will provide a covariantization scheme that allows for consistent, ghost-free cosmological solutions, describing the correct number of dynamical variables in the presence of perfect fluid matter. I will finally exhibit explicit hot Big Bang solutions featuring a late-time self-accelerating epoch, where all the stability and subluminality conditions are satisfied and where gravitational waves behave precisely as in General Relativity.

1 Introduction

Finding the most general theory of a massive vector field can play an important part in the ongoing search for extensions to General Relativity (GR). It was proven in the context of Generalized Proca (GP) theories [1,2] that a massive vector condensate could behave as Dark Energy (DE). Here we provide a new and non-equivalent massive vector field theory, dubbed as Proca-Nuevo (PN) [3] (and its extension, namely Extended Proca-Nuevo (EPN) [4]), that provides an interesting DE model and predicts a self-accelerating branch for a hot Big Bang scenario.

2 Proca-Nuevo and Extended Proca-Nuevo

We start with a vector field A_μ living on flat spacetime with Minkowski metric $\eta_{\mu\nu}$. The construction of PN theory follows the intuition drawn from the helicity decomposition of massive gravity [5], beginning with the definition

$$f_{\mu\nu}[A] = \eta_{\mu\nu} + 2\frac{\partial_{(\mu}A_{\nu)}}{\Lambda^2} + \frac{\partial_\mu A^\rho \partial_\nu A_\rho}{\Lambda^4}\,, \tag{1}$$

where Λ is an energy scale that will ultimately control the strength of the vector self-interactions. Next we introduce the tensor $\mathcal{K}^\mu{}_\nu$ defined as [6,7]

$$\mathcal{K}^\mu{}_\nu = \mathcal{X}^\mu{}_\nu - \delta^\mu{}_\nu\,, \tag{2}$$

$$\text{with} \quad \mathcal{X}^\mu{}_\nu[A] = \left(\sqrt{\eta^{-1}f[A]}\right)^\mu{}_\nu\,, \qquad \text{i.e.} \qquad \mathcal{X}^\mu{}_\alpha \mathcal{X}^\alpha{}_\nu = \eta^{\mu\alpha} f_{\alpha\nu}\,. \tag{3}$$

In four dimensions, the PN and EPN theories for the vector field A_μ are then expressed as [3,4]

$$\mathcal{L}_{\rm PN} = \Lambda^4 \sum_{n=0}^{4} \alpha_n(X) \mathcal{L}_n[\mathcal{K}[A]] \,, \qquad \mathcal{L}_{\rm EPN} = \Lambda^4 \sum_{n=0}^{4} \alpha_n(X) \mathcal{L}_n[\mathcal{K}[A]] + \Lambda^4 \sum_{n=1}^{4} d_n(X) \frac{\mathcal{L}_n[\partial A]}{\Lambda^{2n}} \,, \quad (4)$$

where the nth order symmetric polynomial of a matrix M is defined by

$$\mathcal{L}_n[M] = -\frac{1}{(4-n)!} \epsilon^{\mu_1 \cdots \mu_n \mu_{n+1} \cdots \mu_4} \epsilon_{\nu_1 \cdots \nu_n \mu_{n+1} \cdots \mu_n} M^{\nu_1}{}_{\mu_1} \cdots M^{\nu_n}{}_{\mu_n} \,. \quad (5)$$

In Eq. 4 the coefficients $\alpha_n(X)$ and $d_n(X)$ are arbitrary functions of

$$X = -\frac{1}{2\Lambda^2} A^\mu A_\mu \,. \quad (6)$$

Note that the product $\alpha_0(X)\mathcal{L}_0 \equiv V(A^\mu A_\mu)$ contains the standard potential of the vector field. In order for the trivial vacuum $\langle A_\mu \rangle = 0$ to be a consistent state one should demand that α_0 have a non-zero quadratic contribution, i.e. $\alpha_0 \supseteq -\frac{1}{2}(m^2/\Lambda^4) A^\mu A_\mu$.

Null Eigenvector. In PN (and EPN) theory the constraint is realized through a field-dependent null eigenvector (NEV). Indeed, it was shown that there exists a non-perturbative normalized time-like NEV $V_\mu^{\rm PN}$ of the PN operators satisfying $\eta^{\mu\nu} V_\mu^{\rm PN} V_\nu^{\rm PN} = -1$ and $\mathcal{H}^{\mu\nu} V_\mu^{\rm PN} = 0$. The NEV $V_\mu^{\rm PN}$ and the Hessian matrix of time derivatives $\mathcal{H}^{\mu\nu}$ are given by [3]

$$V_\mu^{\rm PN}(\Lambda) = (\mathcal{X}^{-1})^{0\nu} \left(\eta_{\mu\nu} + \frac{1}{\Lambda^2} \partial_\nu A_\mu \right) , \qquad \mathcal{H}^{\mu\nu} = \frac{\partial^2 \mathcal{L}_{\rm PN}}{\partial \dot{A}_\mu \partial \dot{A}_\nu} \,. \quad (7)$$

Given that the additional $d_n(X)\mathcal{L}_n[\partial A]$ operators do not affect the Hessian matrix, the NEV of EPN coincides with that of PN defined above in Eq. 7.

3 Special model without non-minimal couplings

In the present work we focus on a covariantization in which all non-minimal coupling terms are omitted. The field A_μ lives on a spacetime with metric $g_{\mu\nu}$, ∇ corresponds to covariant derivatives with respect to that metric, and $f_{\mu\nu}$ and $\mathcal{K}^\mu{}_\nu$ are promoted to covariant operators by taking $\partial \to \nabla$ and $\eta \to g$. The "special" model we consider is defined by the action

$$S = \int \mathrm{d}^4x \sqrt{-g} \left(\frac{M_{\rm Pl}^2}{2} R + \mathcal{L}_{\rm EPN}^{\rm (cov)} + \mathcal{L}_M \right) . \quad (8)$$

Here, R is the curvature scalar, and the covariant EPN Lagrangian reads

$$\mathcal{L}_{\rm EPN}^{\rm (cov)} = -\frac{1}{4} F^{\mu\nu} F_{\mu\nu} + \Lambda^4 \left(\mathcal{L}_0^{\rm (cov)} + \mathcal{L}_2^{\rm (cov)} + \mathcal{L}_2^{\rm (cov)} + \mathcal{L}_3^{\rm (cov)} \right) , \quad (9)$$

where

$$\begin{aligned} \mathcal{L}_0^{\rm (cov)} &= \alpha_0(X) \,, & \mathcal{L}_1^{\rm (cov)} &= \alpha_1(X)\mathcal{L}_1[\mathcal{K}] + d_1(X) \frac{\mathcal{L}_1[\nabla A]}{\Lambda^2} \,, \\ \mathcal{L}_2^{\rm (cov)} &= \alpha_{2,X}(X) \left(\mathcal{L}_2[\mathcal{K}] - \frac{\mathcal{L}_2[\nabla A]}{\Lambda^4} \right) , & \mathcal{L}_3^{\rm (cov)} &= -\frac{1}{6} \alpha_{3,X}(X) \left(\mathcal{L}_3[\mathcal{K}] - \frac{\mathcal{L}_3[\nabla A]}{\Lambda^6} \right) . \end{aligned} \quad (10)$$

Finally, we choose $\mathcal{L}_M$ to be the Schutz-Sorkin perfect fluid matter Lagrangian [8], given by

$$\mathcal{L}_M = -\rho_M(n) - \frac{J^\mu}{\sqrt{-g}} \left(\partial_\mu l + \mathcal{A}_i \partial_\mu \mathcal{B}^i \right) , \qquad \text{with} \qquad n = \sqrt{\frac{J^\mu J_\mu}{g}} \,. \quad (11)$$

Note that the model has no non-minimal couplings between the vector field and the metric. This special model is free of ghost on cosmological backgrounds and this holds here upon accounting for the dynamical mixing between the gravitational and vector degrees of freedom.

3.1 Background

We proceed by deriving the background cosmological equations of motion. We focus on the FLRW metric

$$\mathrm{d}s^2 = -N^2(t)\mathrm{d}t^2 + a^2(t)\delta_{ij}\mathrm{d}x^i\mathrm{d}x^j\,, \tag{12}$$

with the vector field profile

$$A_\mu \mathrm{d}x^\mu = -\phi(t)\mathrm{d}t\,. \tag{13}$$

We specify the matter perfect fluid to be a mixture of pressureless matter ($P_m = 0$) and radiation ($P_r = \frac{1}{3}\rho_r$), respectively denoted by subscripts "m" and "r", i.e. $\rho_M = \rho_m + \rho_r$ and $P_M = P_m + P_r$. This means that the equations of state translate into $\dot{\rho}_m + 3H\rho_m = 0$ and $\dot{\rho}_r + 4H\rho_r = 0$. Next, it is convenient to introduce the density parameters

$$\Omega_r \equiv \frac{\rho_r}{3M_{\rm Pl}^2H^2}\,, \qquad \Omega_m \equiv \frac{\rho_m}{3M_{\rm Pl}^2H^2}\,, \qquad \Omega_{\rm EPN} \equiv \frac{\rho_{\rm EPN}}{3M_{\rm Pl}^2H^2}\,, \tag{14}$$

where $\rho_{\rm EPN}$ is the effective energy density of the vector condensate, so that the Friedmann equation reads

$$\Omega_r + \Omega_m + \Omega_{\rm EPN} = 1\,. \tag{15}$$

We now specify the parameters of the model by making the following choice:

$$\alpha_0 = -\tfrac{m^2}{\Lambda^2}X\,, \qquad \alpha_1 = -\tfrac{\Lambda^4}{M_{\rm Pl}^4}b_1X^2 - \tfrac{\Lambda^2}{M_{\rm Pl}^2}c_1X\,, \qquad d_1 = -\tfrac{\Lambda^4}{M_{\rm Pl}^4}e_1X^2 + \tfrac{\Lambda^2}{M_{\rm Pl}^2}c_1X\,, \tag{16}$$

$$\alpha_{2,X} = \tfrac{\Lambda^4}{M_{\rm Pl}^4}b_2X^2 + \tfrac{\Lambda^2}{M_{\rm Pl}^2}c_2X\,, \quad \text{and} \quad \alpha_{3,X} = \tfrac{\Lambda^4}{M_{\rm Pl}^4}b_3X^2 + \tfrac{\Lambda^2}{M_{\rm Pl}^2}c_3X\,, \tag{17}$$

$$b_1 + e_1 = \tfrac{1}{12\sqrt{6}}\,, \qquad m^2M_{\rm Pl}^2 = \Lambda^4\,. \tag{18}$$

We are interested in the time evolution of the density parameters $\Omega_{\rm EPN}$ and Ω_r (Ω_m being trivially determined from these). Primes denote derivatives with respect to the e-folding number $N = \log(a)$. The autonomous system determining the evolution of $\Omega_{\rm EPN}$ and Ω_r reads

$$\begin{aligned}\Omega'_{\rm EPN} &= \frac{4\Omega_{\rm EPN}(3(1-\Omega_{\rm EPN})+\Omega_r)}{3+\Omega_{\rm EPN}}\,,\\ \Omega'_r &= -\frac{\Omega_r\,(3(1-\Omega_r)+13\Omega_{\rm EPN})}{3+\Omega_{\rm EPN}}\,.\end{aligned} \tag{19}$$

A straightforward analysis shows that this system admits three fixed points corresponding to radiation domination, matter domination and dark energy domination (de Sitter (dS) fixed point). There exists a particular solution that qualitatively mimics our universe's hot Big Bang phase, starting very close to the radiation point, flowing toward the matter point, and then asymptotically approaching the dS point, as seen in Fig. 1.

3.2 Perturbations

One can now add perturbations to the metric, the vector field A_μ and the matter content. The perturbations include tensor, vector and scalar sectors, decoupling from each other at the quadratic level in the action. It is possible to prove that the tensor sector is identical to the one of GR. This means that EPN predicts the same gravitational waves as GR.

Turning then to the vector and scalar sector, it is also possible to show that there is one helicity-1 and one helicity-0 mode that physically propagate. This amounts to the expected 3 degrees of freedom of a healthy non-ghostly massive vector field. Note that there is also a physical scalar and vector mode in the matter sector.

It is possible to show that for some given choice of coefficients b_I, c_I and e_1, one can get stable and subluminal perturbations. Explicitly, the kinetic terms are positive (avoiding Ostrogradski -instabilities), the square velocities are positive (avoiding gradient stabilities) and subluminal, and the mass terms are positive (avoiding tachyonic instabilities).

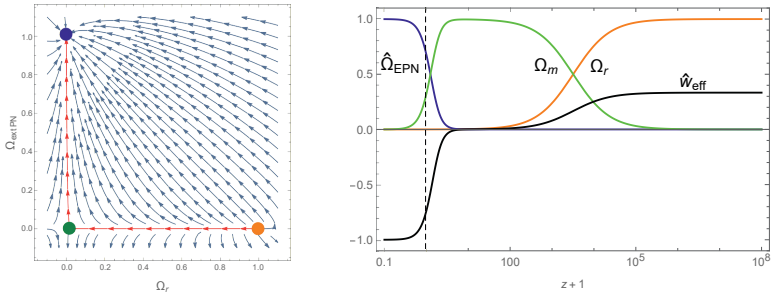

Figure 1 – (left) Phase portrait of the autonomous system Eq. 19. The red trajectory is a particular solution resembling the hot Big Bang phase of our universe with epochs of radiation (orange dot), matter (green) and dark energy (blue) domination. (right) Evolution of the density parameters as functions of redshift, with initial conditions chosen such that $\Omega_{\rm EPN} = 0.68$ and $\Omega_r = 10^{-4}$ at $z = 0$. Taken from [4].

4 Conclusions

We have proven that EPN is ghost-free on a flat background. We have then provided a consistent covariantization scheme for cosmological backgrounds. The background equations of motion can be solved to find that EPN dynamically coupled to gravity predicts a universe with three distinct domination era : radiation, matter, and finally dark energy. This is qualitatively in agreement with the observations. Furthermore, EPN provides a hot big-bang scenario with a self-accelerating branch, i.e. the acceleration is driven by the vector condensate and not a cosmological constant. Finally, all perturbations can be made stable and subluminal, giving a well-behaved and ghost-free theory on cosmological backgrounds, even at the level of perturbations. In particular, we predict gravitational waves to be exactly luminal, as in GR, which is in agreement with tight experimental bounds placed on their speed of propagation.

Acknowledgments

V.P. would like to thank Claudia de Rham, Sebastian Garcia-Saenz and Lavinia Heisenberg.

References

1. Antonio De Felice, Lavinia Heisenberg, Ryotaro Kase, Shinji Mukohyama, Shinji Tsujikawa, and Ying-li Zhang. Cosmology in generalized Proca theories. *JCAP*, 1606(06):048, 2016.
2. Antonio De Felice, Lavinia Heisenberg, Ryotaro Kase, Shinji Mukohyama, Shinji Tsujikawa, and Ying-li Zhang. Effective gravitational couplings for cosmological perturbations in generalized Proca theories. *Phys. Rev.*, D94(4):044024, 2016.
3. Claudia de Rham and Victor Pozsgay. New class of Proca interactions. *Phys. Rev. D*, 102(8):083508, 2020.
4. Claudia de Rham, Sebastian Garcia-Saenz, Lavinia Heisenberg, and Victor Pozsgay. Cosmology of Extended Proca-Nuevo. *arXiv:2110.14327 [hep-th]*, 2021.
5. Claudia de Rham, Gregory Gabadadze, and Andrew J. Tolley. Helicity Decomposition of Ghost-free Massive Gravity. *JHEP*, 11:093, 2011.
6. Claudia de Rham, Gregory Gabadadze, and Andrew J. Tolley. Resummation of Massive Gravity. *Phys. Rev. Lett.*, 106:231101, 2011.
7. Claudia de Rham. Massive Gravity. *Living Rev. Rel.*, 17:7, 2014.
8. Bernard F Schutz and Rafael Sorkin. Variational aspects of relativistic field theories, with application to perfect fluids. *Annals of Physics*, 107(1):1–43, 1977.

3.
Dark Matter

Searching for axion dark matter with the south pole telescope

K. R. Ferguson, On Behalf Of The SPT-3G Collaboration
Department of Physics and Astronomy, University of California, Los Angeles, 475 Portola Plaza, Los Angeles, CA, 90095-1547, USA

Axion-photon coupling induces a polarization rotation in linearly polarized photons traveling through an axion field; thus, as the local axion dark matter field oscillates in time, distant static polarized sources will appear to oscillate with a frequency proportional to the axion mass m_ϕ. We use observations of the cosmic microwave background from SPT-3G, the current receiver on the South Pole Telescope, to set upper limits on the value of the axion-photon coupling constant $g_{\phi\gamma}$ over the approximate mass range $10^{-22}-10^{-19}$ eV. For periods between 1 and 100 days (4.7×10^{-22} eV $\leq m_\phi \leq 4.7\times10^{-20}$ eV), where the limit is approximately constant, we set a median 95% C.L. upper limit on the amplitude of on-sky polarization rotation of 0.071 deg. Assuming that dark matter comprises a single ALP species with a local dark matter density of 0.3 GeV/cm^3, this corresponds to $g_{\phi\gamma} < 1.18\times10^{-12}$ GeV$^{-1}\times\left(\frac{m_\phi}{1.0\times10^{-21}\text{ eV}}\right)$. These new limits represent an improvement over the previous strongest limits set using the same effect by a factor of $\sim$3.8.

1 Introduction

Astrophysical and laboratory observations have provided strong evidence for the existence of non-baryonic dark matter [1]. In particular, axions and axion-like particles make promising dark matter candidates [2]; ultralight axions are especially interesting due to their potential to resolve long-standing discrepancies between observations and predictions of the standard cosmological model ΛCDM on small scales [3].

Fedderke *et al.* [4][hereafter F19] proposed using the cosmic microwave background (CMB) as a source with which to carry out an axion search. The effect relevant to this work is the *AC oscillation effect*, in which the oscillation of the local axion dark matter field induces a time-dependent birefringence effect, causing the polarization angle of CMB photons to oscillate in time with a frequency proportional to the axion mass m_ϕ. Because the coherence length of the local axion field is so large at the masses under consideration, this oscillation is coherent over long periods of time. Additionally, because the measured rotation is set by the local value of the axion field, the oscillation appears in-phase across the entire sky. CMB experiments can measure the amount of polarization rotation as a function of time, directly measuring the effect of the dark matter. The BICEP/Keck collaboration has recently published results of searches for this AC oscillation effect, demonstrating its viability as a search technique [5][hereafter BK22]. We perform a similar search using SPT-3G, the current camera installed on the South Pole Telescope (SPT).

2 Instrument and Dataset

The SPT is a 10-meter millimeter-wavelength telescope located at the Amundsen-Scott South Pole Station in Antarctica [6]. The current camera installed on the telescope is SPT-3G. It is

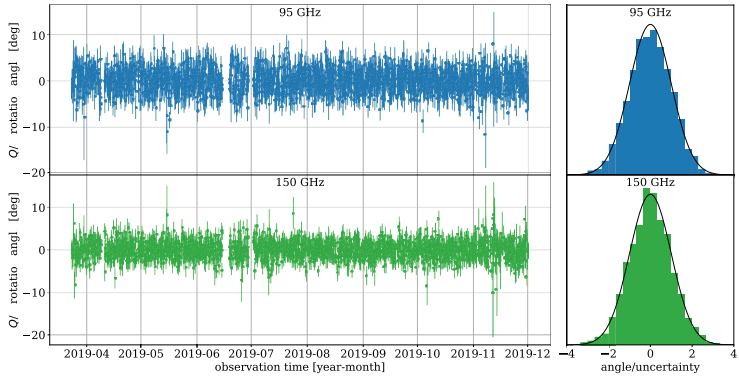

Figure 1 – (left) Timeseries of polarization rotation angles measured for both the 95 and 150 GHz bands. The gaps where there are no angles for a short period correspond with telescope downtime due to unscheduled drive maintenance. (right) Histograms of $x = \hat{\rho}/\sigma_{\hat{\rho}}$ for both observing bands. In both cases, this quantity is consistent with a unit Gaussian, plotted as a solid black line.

designed to observe the CMB in three bands, centered at approximately 95, 150, and 220 GHz, with an angular resolution of approximately 1.2 arcminutes at 150 GHz. SPT-3G observes a $\sim$1500 deg^2 patch of the southern sky many times a day over an ongoing multi-year survey. For the work presented here, we use data from SPT-3G's 2019 observing season. Specifically, we use only the 95 and 150 GHz bands, as they have the highest CMB sensitivity.

3 Methods and Results

The analysis proceeds in three main steps. First, maps of each observation are created by filtering the time-ordered data and binning the samples into map pixels.

Second, for each map, we calculate a polarization rotation angle and uncertainty. This is done by assuming a small-angle rotation and taking as our model

$$\begin{aligned} Q_i^{\mathrm{m}}(\rho) &= Q_{0,i} - \rho U_{0,i} \\ U_i^{\mathrm{m}}(\rho) &= U_{0,i} + \rho Q_{0,i}, \end{aligned} \tag{1}$$

where Q and U are the Stokes parameters, the "m" superscript denotes *model*, the 0 subscript denotes the Q and U fields that would be measured in the limit where the axion-photon coupling constant $g_{\phi\gamma} = 0$ (we do not know the true CMB fields Q_0 and U_0, so we use the full-season coadded and filtered Q and U maps as estimates), i represents the index of an individual map pixel (since the rotation is the same across the entire map), and ρ is the polarization rotation angle induced by the axion[a]. By assuming this model, we can construct the map-space quantity

$$\chi^2(\rho) = \sum_{pq,ij} \left(P_{pi} - P_{pi}^{\mathrm{m}}(\rho)\right) \left(\mathbf{C}^{-1}\right)_{pq,ij} \left(P_{qj} - P_{qj}^{\mathrm{m}}(\rho)\right), \tag{2}$$

where P_{pi} represents the observed Q and U maps at pixel i (i.e. $p \in \{Q, U\}$ with $P_{Qi} = Q_i$ and $P_{Ui} = U_i$), P_{pi}^{m} represents the model expectation for Stokes parameter p at pixel i (given by Eqn. 1), and $\mathbf{C}_{pq,ij}$ is the map-domain covariance between all pixels and Q and U maps. The best-fit rotation angle $\hat{\rho}$ is determined by minimizing the χ^2 with respect to ρ. Uncertainties are determined by calculating $\hat{\rho}$ for 1000 noise maps per observation and taking the standard deviation of the resulting distribution. The timeseries for our data are shown in Fig. 1.

[a] The true on-sky rotation angle ρ_{sky} is related to the Q/U rotation angle by a factor of 2: $\rho_{\mathrm{sky}} = \rho/2$.

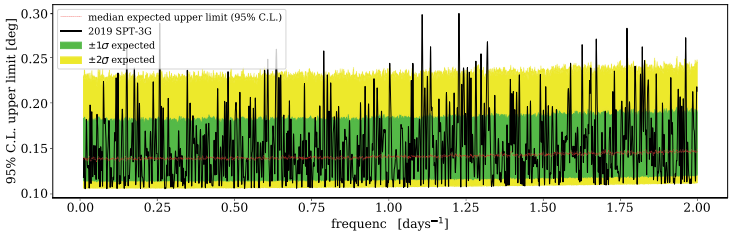

Figure 2 – 95% C.L. upper limits on Q/U rotation angle as a function of oscillation frequency (solid black line), along with simulated background-only median behavior (red) and 1σ (green) and 2σ (yellow) regions. Due to the large number of frequency bins, we expect some limits in excess of the 2σ background contour; this does not necessarily constitute evidence for a sinusoidal polarization rotation.

Lastly, we search for a periodic signal in this timeseries. We consider frequencies spaced 5×10^{-4} inverse-days apart between 0.01 and 2.00 inverse-days (or, in terms of oscillation period, between 12 hours and 100 days). In each frequency bin, we calculate a Bayesian 95% C.L. upper limit on the amplitude of rotation. These limits, along with expected background-only contours, are shown in Fig. 2. The median expected limit is nearly constant as a function of frequency, but degrades slightly at higher frequencies due to a changing rotation angle over the course of the ∼2-hour observation. Below 1.00 inverse-days, where the effect of averaging is negligible (that is, $\lesssim 1\%$), we set a median limit of $\tilde{A} < 0.142$ deg, corresponding to $A_{\rm sky} < 0.071$ deg.

Although the 95% C.L. data limit in Fig. 2 exceeds the 2σ background contour in a number of frequency bins, this is not necessarily evidence of a time-varying birefringence signal due to the large number of frequency bins under consideration. In fact, when we test for detection of such a signal, we find that the data are consistent with the background-only model with a p-value of 0.48.

Following the method in F19, we can convert the upper limit on rotation amplitude into an upper limit on the axion-photon coupling constant $g_{\phi\gamma}$. If we assume that the local dark matter density is 0.3 GeV/cm^3 and that axions comprise the full fraction of the dark matter, this translates to

$$g_{\phi\gamma} < 1.18\times10^{-12}\ \text{GeV}^{-1} \times \left(\frac{m_\phi}{1.0\times10^{-21}\ \text{eV}}\right), \tag{3}$$

where we have used our approximately-constant limit for frequencies below 1.00 inverse-days.

This limit on $g_{\phi\gamma}$ is shown for our results, along with other relevant limits in this region of parameter space, in Fig. 3. With a single year of data, SPT-3G sets the strongest limit yet using the AC oscillation effect, approximately 3.8 (3.4) times stronger than BK22 for the flat (complete) region. At some masses this work sets the strongest limit of any CMB analysis yet, surpassing the washout limit set with *Planck* polarization power spectra [4].

Acknowledgments

The South Pole Telescope program is supported by the National Science Foundation (NSF) through grants PLR-1248097 and OPP-1852617. Partial support also comes from NSF AST-1716965 and CSSI-1835865. This research was done using resources provided by the Open Science Grid, which is supported by the NSF award 1148698, and the U.S. Department of Energy's Office of Science. The data analysis pipeline also uses the scientific python stack.

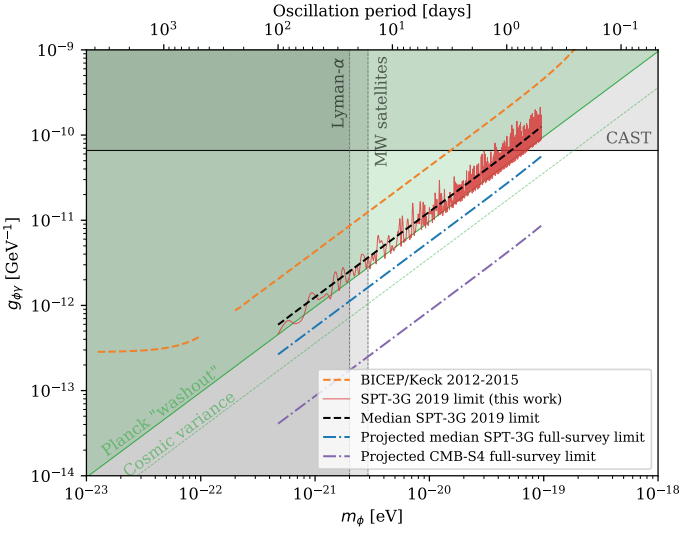

Figure 3 – The parameter space for axion-photon coupling $g_{\phi\gamma}$ as a function of axion mass m_ϕ. The SPT-3G 95% C.L. upper limit is given by the solid red line, and the smoothed fit to this (Eqn. 3) by the dashed black line. The dashed orange lines represent the most recent limits set by the BICEP/Keck collaboration [5] using the AC oscillation effect, and the dot-dashed lines represent projections with future datasets. Other relevant limits in this region of parameter space taken from [4,7,8,9].

References

1. Katherine Garrett and Gintaras Dūda. Dark Matter: A Primer. *Advances in Astronomy*, 2011:968283, January 2011.
2. John Preskill, Mark B. Wise, and Frank Wilczek. Cosmology of the invisible axion. *Physics Letters B*, 120(1-3):127–132, January 1983.
3. Wayne Hu, Rennan Barkana, and Andrei Gruzinov. Fuzzy Cold Dark Matter: The Wave Properties of Ultralight Particles. *Phys. Rev. Lett.* , 85(6):1158–1161, August 2000.
4. Michael A. Fedderke, Peter W. Graham, and Surjeet Rajendran. Axion dark matter detection with cmb polarization. *Physical Review D*, 100(1), Jul 2019.
5. Bicep/Keck Collaboration. BICEP/Keck XIV: Improved constraints on axionlike polarization oscillations in the cosmic microwave background. *Phys. Rev. D* , 105(2):022006, January 2022.
6. J. E. Carlstrom et al. The 10 Meter South Pole Telescope. *PASP*, 123:568–581, May 2011.
7. CAST Collaboration. New CAST limit on the axion-photon interaction. *Nature Physics*, 13(6):584–590, June 2017.
8. Vid Iršič, Matteo Viel, Martin G. Haehnelt, James S. Bolton, and George D. Becker. First Constraints on Fuzzy Dark Matter from Lyman-α Forest Data and Hydrodynamical Simulations. *Phys. Rev. Lett.* , 119(3):031302, July 2017.
9. DES Collaboration. Constraints on Dark Matter Properties from Observations of Milky Way Satellite Galaxies. *Phys. Rev. Lett.* , 126(9):091101, March 2021.

Search for Black Holes in the Galactic Halo by Gravitational Microlensing [a]

T. Blaineau, M. Moniez, presented by M. Moniez
Laboratoire de physique des 2 infinis Irène Joliot-Curie, CNRS Université Paris-Saclay, Bât. 100, Faculté des sciences, F-91405 Orsay Cedex, France

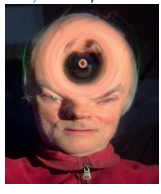

We combined light curves from the EROS-2 and MACHO surveys to the Large Magellanic Cloud (LMC) to create a joint database for 14.1 million stars, covering a total duration of 10.6 years, with fluxes measured through 4 wide band filters. We searched for multi-year microlensing events in this catalog of extended light curves, complemented by 24.1 million light curves observed by only one of the surveys. Our analysis shows that compact objects with mass between 10^{-6} and $200M_\odot$ can not constitute more than $\sim 20\%$ of the total mass of a standard halo (at 95% CL). We also exclude that $\sim 50\%$ of the halo is made of Black Holes (BH) lighter than $1000M_\odot$.

1 Introduction: microlensing toward LMC

When a point object (lens) of mass M_L located at distance D_L from an observer passes close enough to the line of sight of a point source at distance $D_{LMC} = 49.5$ kpc, the luminosity of the source appears to be temporarily magnified by a time-dependent factor $A(t)$ according to[1]:

$$A(t) = \frac{u(t)^2+2}{u(t)\sqrt{u(t)^2+4}}\ , \quad \text{where } u(t) = \sqrt{u_0^2 + (t-t_0)^2/t_{\rm E}^2} \tag{1}$$

is the distance of the lens to the line of sight divided by the Einstein radius $r_{\rm E}$,

$$r_{\rm E} = \sqrt{\frac{4GM_L}{c^2} D_{LMC} x(1-x)} \simeq 10.0\text{AU} \times \left[\frac{M_L}{M_\odot}\right]^{\frac{1}{2}} \frac{[x(1-x)]^{\frac{1}{2}}}{0.5}. \tag{2}$$

G is the Newtonian gravitational constant, $M_\odot$ is the mass of the Sun, and $x = D_L/D_{LMC}$. t_0 is the instant of the minimal approach u_0. If the lens has a constant relative transverse velocity v_T, $t_{\rm E} = r_{\rm E}/v_T$ is the Einstein radius crossing time. Assuming that the Milky Way dark matter halo is isotropic and isothermal[2] (S-model), and using its most recents parameters[3], the optical depth

[a] This paper uses public domain data obtained by the MACHO Project, jointly funded by the US Department of Energy through the University of California, Lawrence Livermore National Laboratory under contract No. W-7405-Eng-48, by the National Science Foundation through the Center for Particle Astrophysics of the University of California under cooperative agreement AST-8809616, and by the Mount Stromlo and Siding Spring Observatory, part of the Australian National University.

to the LMC is $\tau \sim 4.7 \times 10^{-7}$. If all lenses have the same mass M_L, then the mean duration of the events is $\langle t_E \rangle \sim 63\,\mathrm{days} \times \sqrt{M_L/M_\odot}$. Past microlensing searches to the LMC have shown that objects with masses $10^{-6} < M_L < 10 M_\odot$ do not contribute significantly to the hidden mass of the Milky Way's spherical halo[4,5,6], but the analysis of these surveys was insensitive to heavier objects such as those responsible for gravitational wave emissions. To explore the dark matter halo beyond $10 M_\odot$ by searching for longer duration events[7] (several years), we combined the EROS-2 and MACHO databases[8,3], which were acquired during different periods.

2 Combining EROS-2 and MACHO data

The EROS-2 (MACHO) survey setup, consisting of a $1.0m$ ($1.27m$) telescope and two cameras with 8 (4) CCD of 2Kx2K pixels each, monitored 88 (82) fields of $1.\,(^\circ)^2$ ($0.5\,(^\circ)^2$) towards the LMC (see Table 1). The MACHO light-curves and images are publicly available[b] [9], and the EROS-2 catalog for LMC was produced for the final EROS LMC publication[4]. After astrometric corrections using the GAIA EDR3 catalog[10], we could associate the objects of the two surveys, with a precision of better than 0.1 arcsec.

Table 1: Statistics of the MACHO and EROS-2 surveys. Survey durations, number of monitored objects, median stellar densities, approximate limiting magnitudes, median numbers of flux measurements per object after cleaning.

	EROS-2 only	MACHO only	common
Dates (month/yr)	7/96-2/03	7/92-1/00	7/92-2/03
T_{obs} (year)	6.7	7.7	10.6
$N_{objects}(\times 10^6)$	15.8	6.9	14.1
central fields $(^\circ)^2$	~ 10	~ 10	~ 10
stars/arcmin^2	~ 70	~ 100	~ 70
mag. lim. $V_{Cousins}$	~ 20.5	~ 20.5	~ 20.5
# measurements B	500	1400	1900
# measurements R	600	1550	2150
outer fields $(^\circ)^2$	~ 77	~ 39	~ 39
stars/arcmin^2	~ 30	~ 20	~ 20
mag. lim. $V_{Cousins}$	~ 22.5	~ 21.5	~ 21.5
# measurements B	250	200	450
# measurements R	300	250	550

3 Event selection

14.1×10^6 objects benefit from 10.6 years of luminosity measurements, of which 3.8 years overlap, with photometric series corresponding to the 4 passbands (2 per survey). 22.7×10^6 objects, monitored by only one survey, were also included in our search, although they are monitored for shorter times. We first eliminated measurements associated with the remaining problematic images (blurred or with a guiding or readout defect), and poor measurements due to instrumental effects. We then renormalized the photometric uncertainties of EROS-2 and MACHO for each light curve so that the time-averaged normalized uncertainties correspond to the point-to-point flux dispersions along the curve. We performed a discriminant analysis on the 36.8×10^6 light curves, based on comparing the fit of a microlensing event with that of a constant light curve. We then require that light curves with a good microlensing fit have their maximum brightness between $[t_{start} + 200\,\mathrm{days}, t_{end}]$, where t_{start} and t_{end} are the instants of the start and end of the measurements, and that $100\,\mathrm{days} < t_E < (t_{end} - t_{start})/2$. These latter criteria reject most short-lived eruptive events and in particular supernovae. We eliminate so-called "blue bumpers", Be

[b] https://macho.nci.org.au/

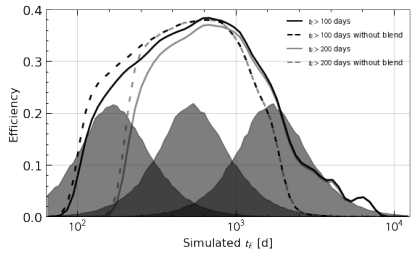

Figure 1 – Detection efficiency: Full (dotted) lines show efficiencies taking (on not) into account blending effects. Grey lines show efficiencies of the analysis adding the constraint $t_E > 200$ days. Grey histograms (not normalized) are the expected t_E distributions for a halo made of 10, 100, and $1000 M_\odot$ compact objects (from left to right).

class stars that sometimes show asymmetric bumps, by making a stricter selection in their color-magnitude diagram (CMD) region. After this preselection, we reject three types of objects that show variabilities that can be confused with long-lasting microlensing effects: Objects outside the region of the CMD containing 99% of the stars, more likely to show variability; echoes from SN1987A; and variable objects identified in external catalogs. Only two microlensing candidates satisfy the whole selection process. Following a detailed examination, one of them is probably a type II-L or II-P supernovae, and the other shows hints of variability outside the main event. However, we cannot formally exclude these candidates without external data or stricter selection, so we conservatively keep them in our calculation of limits on the macho content of the Halo.

4 Detection efficiency, expected rate, and limits on heavy objects in the halo

The efficiency, $\epsilon(t_E)$ (Fig. 1), defined as the ratio of the number of events that satisfy our selection to the number of events with $u_0 < 1$ and t_0 within the observation period, was computed by subjecting simulated events to our selection procedure. To be realistic, the simulations were produced by superimposing simulated microlensing events on the light curves of a representative random subsample of the observed objects. We took into account "blending" by assigning a set of stars to each object in a way that is consistent with the observed density of LMC stars in Hubble Space Telescope (HST) images. We also estimated that blending from undetected binarity on HST images has a negligible impact on the evaluation of the efficiency. We finally subtract from our catalog the contamination by Galactic stars, estimated to be less than 5% by counting stars in the GAIA catalog[10] in adjacent fields, and we consider that 10% of microlensing events may escape detection due to lens binarity[4,6]. The top panel of Figure 2 shows, as a function of M, the expected number of detected microlensing events for the halo S-model, assuming it consists entirely of M mass deflectors, using the efficiency shown in Fig. 1 for the simulation with blending. For any lens mass distribution, the expected number of events is simply calculated by integrating the $N_{exp}(M_L)$ curve, weighted by the mass distribution in question. We perform a Bayesian analysis taking into account the expected $N_s \sim 0.64$ disk and self-lensing events with $t_E > 100$ days. The excluded halo fraction with 95% CL, $f(M_L)$, as a function of the deflector mass is shown in the lower panel of Fig. 2 by the red curve. We tested the robustness of this result by restricting ourselves to events with $t_E > 200$ days. By doing so, N_s becomes negligible (< 0.05 event) and no candidates are retained. The resulting exclusion limit, shown as the black curve, is weaker at the lower mass end, but unchanged on the high mass side.

5 Conclusions and perspectives

We conclude that BHs with masses up to a thousand solar masses, similar to the ones observed by LIGO and VIRGO as binary BH mergers, do not make up a major fraction of the Milky

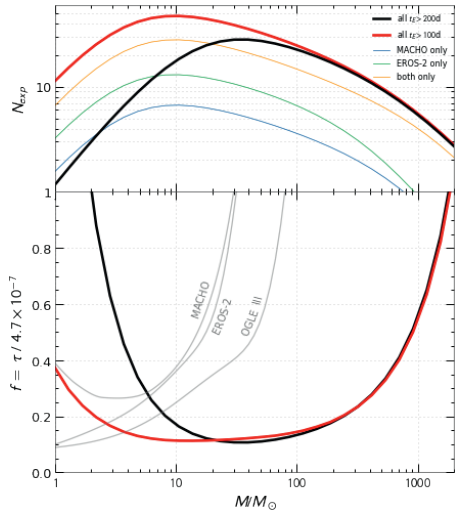

Figure 2 – Top : Number of expected events from the halo S-model as a function of the mass M of the lensing objects : blue (green) line, from objects monitored only by MACHO (EROS-2); orange line, from objects monitored by both surveys; full red line shows the total; black line shows the total adding the constraint $t_E > 200$ days in the analysis. Bottom: 95% CL upper limits on the fraction $f = \tau_{LMC}/4.7 \times 10^{-7}$ of the halo mass in the form of compact objects. Limits obtained in this analysis are shown in red, and in black if we require $t_E > 200$ days. The grey curves correspond to the latest limits published by MACHO, EROS-2 and OGLE-III.

Way dark matter, at least if assumed to be distributed as a standard spherical halo. Such BHs are more likely to be found in structures following the visible mass distribution, and could be searched for through microlensing toward the Galactic bulge and spiral arms, in the long t_E tail of event duration distribution, extending the previous searches and analysis[11,12,13].

Acknowledgments

We thank Łucasz Wyrzykowski and Christopher Stubbs for providing useful information. This work was supported by the Paris Ile-de-France Region.

References

1. B. Paczynski. ApJ, 304:1, 1986.
2. Alcock, C., et al. (MACHO Coll.). ApJ, 542(1):281–307, 2000.
3. Blaineau, T. et al. (EROS Coll.). *arXiv:2202.13819*, 2022.
4. Tisserand, P., et al., (EROS-2 Coll.). A&A, 469(2):387–404, 2007.
5. Alcock, C., et al. (MACHO Coll.). ApJ, 550(2):L169–L172, 2001.
6. Wyrzykowski, Ł., et al. (OGLE Coll.). MNRAS, 416(4):2949–2961, 2011.
7. A. Mirhosseini and M. Moniez. *A&A*, 618:L4, 2018.
8. Tristan Blaineau. PhD thesis, October 2021.
9. Alcock, et al. (MACHO Coll.). PASP, 111(766):1539–1558, 1999.
10. Brown, A. G. A., et al. (Gaia Coll.). *arXiv:2012.01533*, 2020.
11. Hamadache, C., et al. (EROS Coll.). A&A, 454(1):185–199, 2006.
12. Moniez, M. et al. A&A, 604:A124, 2017.
13. Mróz, P. et al., (OGLE Coll.). *The Astrophysical Journal Sup. Series*, 249(1):16, 2020.

Statistics of the subhalo population in the Milky Way for the detection of dark matter point sources

G. Facchinetti[†,⋆], J. Lavalle[⋆], and M. Stref[⋆]
[†] *Service de Physique Théorique, Université Libre de Bruxelles, C.P. 225, B-1050 Brussels, Belgium*
[⋆] *Laboratoire Univers & Particules de Montpellier (LUPM), CNRS & Université de Montpellier (UMR-5299), Place Eugène Bataillon, F-34095 Montpellier Cedex 05, France*
[⋆] *LAPTh, Université Savoie Mont Blanc & CNRS, Chemin de Bellevue, 74941 Annecy Cedex, France*

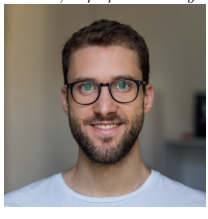

Analyzing Fermi-LAT data and/or using numerical simulations, several studies have investigated the possibility that among the 1525 unassociated point sources identified by the collaboration (4FGL catalog), some of them be DM subhalos of the Milky Way. I present a new statistical analysis for the detectability of DM substructures as point-like sources with a semi-analytical and dynamically constrained subhalo population model. This approach not only allows to consistently and analytically compute the detection probability of point-like subhalos but also gives valuable information on the most visible ones (*e.g.,* on their position) and can be used to make predictions for the next generation of telescopes, like CTA.

1 Introduction

Cold dark matter (DM) forms structures on scales much smaller than the size of typical galaxies and this clustering translates into a very large population of subhalos in the Milky Way (MW). Interestingly, the Fermi-LAT collaboration has found a total of 1525 unidentified γ-ray point sources in their 4FGL catalog [1]. Even though most of these sources are expected to be of extragalactic origin, in a scenario of self-annihilating DM, some may also correspond to subhalos. One can then search for specific DM signatures in the data or predict the number of detectable subhalos from the extrapolation of cosmological simulation results. However, this latter approach relies on simulated MW-like objects, with features that can differ from the real MW. In addition, the cosmological simulations do not probe the smallest DM clumps (with a mass that can reach 10^{-12} $M_\odot$). To avoid these shortcomings, we use a semi-analytical model for the subhalo population [2] – hereafter referred to as SL17 [a], built on mass distributions for DM and baryons constrained by observation [5]. We use the same mass distribution of baryons to model the diffuse γ-ray foreground/background – hereafter indistinguishably called background – and to evaluate

[a] Complementary works have also used analytical models with Monte Carlo simulations [3,4]

the impact of baryonic tidal stripping on the subhalo population. Hence, we account for implicit spatial correlations between subhalo properties and the background. The goal is to determine an order of magnitude for the number of detectable point-like subhalos in that model. We further check if we could detect these subhalos before the diffuse DM emission around the Galactic center (GC). We perform our analysis for Fermi-LAT-like [6] and CTA-like instruments.

In Sect. 2, we introduce the subhalo model and evaluate the subsequent γ-ray emission from DM point-like subhalos. In Sect. 3, we detail our model for the γ-ray background and our statistical analysis. Eventually, in Sect. 4, we present our main results and conclusions.

2 Subhalo population and γ rays from DM annihilation

In the SL17 model, subhalos populating the host DM halo of the MW are fully characterized by three quantities, their cosmological virial mass m, their concentration c (or, equivalently, their scale density $\rho_{\rm s}$ and scale radius $r_{\rm s}$) and their position $\vec{R}$ from the GC. We start from a cosmological distribution of their number density,

$$\left.\frac{\partial^2 n}{\partial m \partial c}\right|_{\rm cosmo} = N_{\rm cosmo}\, p_m(m) p_c(c\,|\,m) p_{\vec{R}}(\vec{R})\,, \tag{1}$$

where we have introduced cosmological distribution functions for m, c and $\vec{R}$ on the right hand side. The total cosmological number of subhalos, $N_{\rm init}$, is calibrated on DM-only simulations. See the SL17 paper [2] for more details.

Subhalos are further impacted by dynamical stripping in the MW, in particular, due to the presence of baryons. They lose mass and shrink over time. We call $r_{\rm t}(m,c,\vec{R})$ and $m_{\rm t}^\star(m,c,\vec{R})$ the current *tidal*/physical extension and mass of a halo with original mass m and concentration c. They are computed by combining the effect of smooth tidal stripping and shocking from the baryonic disc. In the end, we can evaluate the current distribution as

$$\left.\frac{\partial^2 n}{\partial m_{\rm t} \partial c}\right|_{\rm final} = \int \left.\frac{\partial^2 n}{\partial m \partial c}\right|_{\rm cosmo} \Theta\left(\frac{r_{\rm t}(m,c,\vec{R})}{r_{\rm s}(m,c,\vec{R})} - \epsilon_{\rm t}\right) \delta\left(m_{\rm t} - m_{\rm t}^\star(m,c,\vec{R})\right) {\rm d}m\,. \tag{2}$$

The constant $\epsilon_{\rm t}$ encodes the capacity of subhalos to resist tidal disruption (which can happen if they become too small). For our analysis we choose $\epsilon_{\rm t} = 10^{-2}$, *i.e.* highly resilient subhalos which must be pruned to their very center to be disrupted, in agreement with recent results [7].

The γ-ray flux from Majorana DM annihilation can be written under the form

$$\left\langle \frac{{\rm d}^2\phi_{\gamma,\chi}(E)}{{\rm d}E{\rm d}\Omega} \right\rangle_{\mathcal{P}} = \frac{\langle\sigma v\rangle}{2m_\chi^2}\frac{{\rm d}N_\gamma}{{\rm d}E} \left\{ J(\mathcal{P}) \equiv \frac{1}{4\pi}\int_{\hat{q}\in\mathcal{P}} {\rm d}^2\Omega_{\hat{q}} \int {\rm d}s\, \rho_\chi^2(s,\hat{q}) \right\}\,, \tag{3}$$

where $\langle\sigma v\rangle$ is the velocity averaged cross-section, m_χ the DM mass and ${\rm d}N_\gamma/{\rm d}E$ the emitted photon spectrum. In the bracket, we introduce the J-factor. It is the integral over every line-of-sight in the sky patch $\mathcal{P}$ – with solid angle element ${\rm d}^2\Omega_{\hat{q}}$ in direction $\hat{q}$. We write $\rho_\chi(s,\hat{q})$ the DM density at a distance s from Earth along $\hat{q}$. We denote by $J_{\rm sub}$ the J-factor for a single subhalo and by $J_{\rm diff.}$ that for the diffuse emission of the smooth DM distribution and unresolved subhalos. The latter provides a source of background for the detection of point sources. The average number of point-like subhalos with a J-factor above the threshold J in the patch $\mathcal{P}$ is

$$N_>^{\rm pt}(J,\mathcal{P}) = \int_{\hat{q}\in\mathcal{P}} {\rm d}^2\Omega_{\hat{q}} \int_{\rm pt} \left.\frac{\partial^2 n}{\partial m_{\rm t}\partial c}\right|_{\rm final.} \Theta(J_{\rm sub}(m_{\rm t},c,s) - J) s^2 {\rm d}m_{\rm t}{\rm d}c{\rm d}s\,, \tag{4}$$

where the second integral only includes point-like structures – *i.e.*, those with an apparent angular size smaller than the angular resolution of the instrument $\theta_{\rm r}$. If we know $J_{\rm min}$, the sensitivity of a telescope to point sources in terms of J-factor, the average number of detectable point-like subhalos in the patch $\mathcal{P}$ is then simply $N_>^{\rm pt}(J_{\rm min},\mathcal{P})$. Therefore, the goal of the next section is to determine the value of $J_{\rm min}$ for Fermi-LAT-like and CTA-like instruments.

3 Background and Likelihood analysis

In this section, we first detail our treatment of the baryonic γ-ray background. Instead of performing a full data analysis, we build a simple but sufficiently accurate model for our needs. We include *(i)* an isotropic extragalactic component which we calibrate on Fermi-LAT data, *(ii)* a galactic diffuse emission background from π meson decay, with a spectrum also calibrated on Fermi-LAT data but with a spatial dependence relying on a model for the hydrogen distribution in the MW (the same one used to compute tidal stripping of subhalos by disc shocking), *(iii)* an isotropic cosmic-ray component [8]. The latter matters for CTA-like instruments that are not able to perfectly distinguish some cosmic-ray events from γ-ray ones.

We can then evaluate a constraint on $\langle\sigma v\rangle$ from the diffuse emission and the sensitivity to point sources, $J_{\rm min}$. Consider patches/bins of the sky, $\mathcal{P}_i$, observed over a time $\mathcal{T}(\mathcal{P}_i)$. We divide the energy range into bins of width ΔE_j. From the background model, we can evaluate a mock number of photon counts in each bin:

$$\mu_{ij}[\langle\sigma v\rangle, \eta_k, J_i] = \Delta E_j \mathcal{T}(\mathcal{P}_i) \left\{ \langle\sigma v\rangle \, M_j (J_{\rm diff}(\Delta E_j, \mathcal{P}_i) + J_i) + \sum_k \eta_k R^k_{\rm diff}(\Delta E_j, \mathcal{P}_i) \right\} . \qquad (5)$$

Here, J_i is the contribution of a possible point source in $\mathcal{P}_i$ and M_j encodes the photon spectrum produced by DM as well as the collection area of the instrument in ΔE_j. The parameters η_k modulate the levels of the different baryonic emission rates $R^k_{\rm diff}$. The index k runs over the diffuse cosmic-ray, galactic, and isotropic background. Afterwards, we perform a Monte Carlo analysis. In each bin, we draw a mock number of photons from a Poisson distribution with mean μ_{ij} (making sure that it is compatible with photon counts obtained in Fermi-LAT analyses). We process the mock data using the Likelihood-ratio method and the Likelihood [8]

$$\mathcal{L}[\langle\sigma v\rangle, \eta_k, J_i, \alpha_{ij}] = \prod_{ij} \left[\frac{(\alpha_{ij}\mu_{ij})^{n_{ij}}}{\sqrt{2\pi\sigma^2_\alpha} n_{ij}!} e^{-\alpha_{ij}\mu_{ij} - \frac{(\alpha_{ij}-1)^2}{2\sigma^2_\alpha}} \prod_k \left(\frac{1}{\sqrt{2\pi\sigma^2_{\eta_k}}} e^{-\frac{(\eta_k - \bar{\eta}_k)^2}{2\sigma^2_{\eta_k}}} \right) \right] . \qquad (6)$$

This form accounts for systematic uncertainties with the parameters α_{ij}. The values of σ_α and σ_{η_k} are adjusted to match with results from real data analyses. Conveniently, the maximization of the Likelihood can be achieved with a Newton-Raphson algorithm. The $\langle\sigma v\rangle$ constraint is set at 3σ with sky patches around the GC. To determine $J_{\rm min}$ in a given direction of the sky we assume a point source in a central bin and the usual background in surrounding patches. The value is then set with a test statistic of 25.

4 Discussion and conclusion

In the left panel of Fig. 1, we show the value of $J_{\rm min}$ obtained for Fermi-LAT-like instruments after T years of observation, at 20° above the GC. We assume an NFW profile for the MW host halo and a 100 GeV DM particle that annihilates through the $\tau^+\tau^-$ channel. The green (resp. red) curves assume a detection of the DM diffuse emission at $T = 10$ (resp. 20) years, which fixes the value of $\langle\sigma v\rangle$. For the blue curves we assume that the DM diffuse emission is never detected and we set, for all T, the annihilation cross-section to its upper limit $\langle\sigma v\rangle = \langle\sigma v\rangle_{\rm max}(T)$. At large observation time $J_{\rm min} \propto 1/(\langle\sigma v\rangle \sqrt{T})$ and $\langle\sigma v\rangle_{\rm max} \propto 1/\sqrt{T}$ (neglecting systematic uncertainties). Therefore, both time factors cancel out in the blue curve, which translates into an asymptote. The solid lines correspond to the true likelihood analysis and the dashed lines to a simple model that we have derived to better understand the aforementioned scaling relations. Plugging the value of $J_{\rm min}$ in Eq. (4), assuming no detection of the DM diffuse emission, we find at most $\mathcal{O}(1)$ point-like subhalos detectable in the entire sky, after 20 years of observation, with Fermi-LAT-like instruments. The numbers are slightly higher for a cored DM profile of the MW host halo because of a weaker constraint on $\langle\sigma v\rangle$.

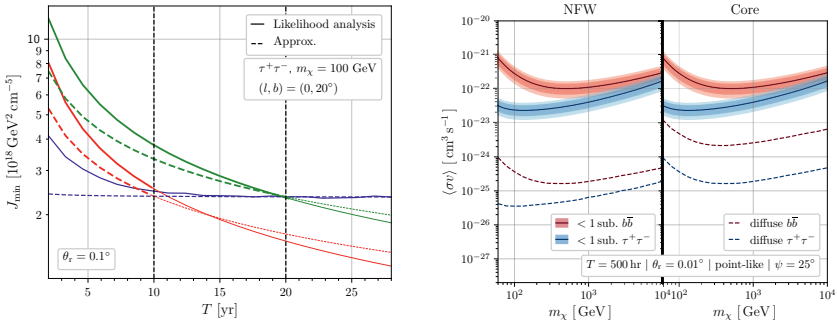

Figure 1 – Left panel: Sensitivity to point sources in terms of the J-factor vs. observation time, for a Fermi-LAT-like telescope. Right panel: Constraints on the DM annihilation cross-section, set with a CTA-like telescope, from the DM diffuse emission around the GC compared to that from the non detection of subhalos as point-like sources at 25° from the GC. We consider a NFW and a cored host DM halo. The resolution angles are assumed constants and fixed to $\theta_{\rm r} = 0.1^\circ$ for Fermi-LAT-like instruments and to $\theta_{\rm r} = 0.01^\circ$ for CTA-like instruments.

In the right panel of Fig. 1, we present the CTA-like constraint on $\langle\sigma v\rangle$, after 500 hr of observation, obtained from the DM diffuse emission (dashed curve) and assuming no subhalos are detected (solid). We consider two annihilation channels, $\tau^+\tau^-$ (blue) and $b\bar{b}$ (red). For the diffuse search, we point around the GC. For the subhalo search, we point at 25° from the GC, in a patch with the size of the field of view of the instrument (~ 0.024 sr). The shaded region shows the statistical uncertainty on the subhalo count. The constraint from the subhalos is always weaker by several orders of magnitude. Therefore, in this configuration, we would need to have detected the diffuse emission to also detect point-like subhalos.

Nonetheless, we have put in evidence that the best sources for a detection (both with Fermi-LAT-like and CTA-like instruments) are within 40° around the GC. They are originally large subhalos (from 10^3 to 10^8 $M_\odot$ depending on the resolution angle), which have been tidally stripped, sufficiently to become point-like but not enough to be disrupted.

Acknowledgments

This work has been supported by funding from the ANR project ANR-18-CE31-0006 (*GaDaMa*), from the national CNRS-INSU programs PNHE and PNCG, and from European Union's Horizon 2020 research and innovation program under the Marie Skłodowska-Curie grant agreement N° 860881-HIDDeN — in addition to recurrent funding by CNRS-IN2P3 and the University of Montpellier. GF also acknowledges support of the ARC program of the Federation Wallonie-Bruxelles and of the Excellence of Science (EoS) project No. 30820817 - be.h "The H boson gateway to physics beyond the Standard Model"

References

1. The Fermi LAT Collaboration. *Astrophysical Journal*, 247(1):33, 2020.
2. M. Stref and J. Lavalle. *Phys. Rev.*, D95(6):063003, 2017.
3. M. Hütten, C. Combet, G. Maier, and D. Maurin. *JCAP*, 2016(09):047–047, 2016.
4. F. Calore, M. Hütten, and M. Stref. *Galaxies*, 7(4), 2019.
5. P. J. McMillan. *MNRAS*, 465:76–94, 2017.
6. G. Facchinetti, J. Lavalle, and M. Stref. 2020. arXiv: 2007.10392.
7. F. C. v. d. Bosch, G. Ogiya, O. Hahn, and A. Burkert. *MNRAS*, 474(3):3043–3066, 2018.
8. H. Silverwood, C. Weniger, P. Scott, and G. Bertone. *JCAP*, 2015(03):055–055, 2015.

Breit-Wigner enhancement in the interactions of a light scalar dark matter

S. Chakraborti[1] (speaker), T. Binder[2], S. Matsumoto[2] and Y. Watanabe[2]
[1]*LAPTh, Univ. Grenoble Alpes, USMB, CNRS, F-74940 Annecy, France*
[2]*Kavli IPMU (WPI), UTIAS, University of Tokyo, Kashiwa, Chiba 277-8583, Japan*

We study a minimal model for light scalar dark matter (DM) which requires a light scalar mediator to address the core-cusp problem as well as interact with the standard model. We focus on the Breit-Wigner resonance for the DM annihilation and self-scattering channels. The parameter space can be constraned by astrophysical observations such as CMB and indirect searches, as well as from terrestrial experiments probing rare decay of mesons and low-mass direct detection of dark matter. A systematic analysis of the model is done involving the relevant latest and future constraints.

1 Context

Singlet scalar is the simplest of the Beyond the Standard Model extensions. When it behaves as a dark matter (DM) candidate, there is only Higgs portal for it to interact with the Standard Model. In such a DM model, all other mass region is excluded by direct detection except for the Higgs resonance at $m_S \sim 62.5$ GeV[1]. In this study, we consider a much lighter scalar DM and shed light on the Breit-Wigner resonance region facilitated by a lighter Higgs-like scalar mediator interacting with the scalar DM.

2 Features

Model: We have two new scalars in our theory apart from the SM: (1) a $\mathbf{Z}_2$ odd real singlet scalar DM, χ which acts as DM; and (2) another charge neutral scalar which mixes with the SM Higgs boson to give rise to the physical mass eigenstates, h and ϕ. [a]

Decay of the mediator particle: The mediator particle behaves like a light SM Higgs boson, as it interacts with SM particles through the mixing between H and the new scalar. Its partial

[a] Only the interaction terms significant for phenomenology are discussed here. For complete Lagrangian, one may refer to the full text of the paper [2].

decay width into SM particles is given by

$$\Gamma\left(\phi \to \text{SMs}\right) = \sin^2\theta \; \Gamma(h_{\text{SM}} \to \text{SMs})|_{m^2_{h_{\text{SM}}} \to m^2_\phi} \,,$$

with h_{SM} being the SM Higgs boson and $\sin\theta$ the mixing angle.

Dark matter annihilation into SM particles: When we focus on the so-called resonance parameter region, i.e., the region satisfying $m_\chi \sim m_\phi/2$, the annihilation cross-section of the DM into the SM final state 'f_{SM}' is given by[3]

$$\sigma v\left(\chi\chi \to f_{\text{SM}}\right) \simeq \frac{2C^2_{\phi\chi\chi}}{\sqrt{s}} \frac{\left[\Gamma\left(\phi \to f_{\text{SM}}\right)\right]_{m^2_\phi \to s}}{(s-m^2_\phi)^2 + s\,\Gamma^2_\phi(s)} \simeq \frac{32C^2_{\phi\chi\chi}}{m^5_\phi} \frac{\left[\Gamma\left(\phi \to f_{\text{SM}}\right)\right]_{m^2_\phi \to s}}{(v^2-v^2_R)^2 + 16\Gamma^2_\phi(s)/m^2_\phi},$$
$$\Gamma_\phi(s) \equiv \left[\Gamma\left(\phi \to \chi\chi\right) + \sum_{f_{\text{SM}}} \Gamma\left(\phi \to f_{\text{SM}}\right)\right]_{m^2_\phi \to s},$$

where $C_{\phi\chi\chi}$ is the trilinear $\phi\chi\chi$ coupling, $v^2_R \equiv 4(m_\phi/m_\chi - 2)$, i.e. $m_\chi = (m_\phi/2)/(1+v^2_R/8)$, and the center of mass energy is $s \simeq m^2_\chi\,(4+v^2) = m^2_\phi(1+v^2/4)/(1+v^2_R/8)^2$ in the non-relativistic limit of DM. Also, the velocity average of the annihilation cross-section (times the relative velocity 'v') is

$$\langle \sigma v\left(\chi\chi \to f_{\text{SM}}\right)\rangle_{v_0} \simeq \int_0^\infty dv\, \sigma v\left(\chi\chi \to f_{\text{SM}}\right) f(v, v_0), \qquad f(v, v_0) \simeq \frac{4v^2 e^{-v^2/v^2_0}}{\sqrt{\pi} v^3_0},$$

where the velocity distribution function for the DM particle $f(v, v_0)$ is normalized to be one, i.e. $\int_0^\infty dv f(v, v_0) = 1$, so that the averaged velocity and the velocity dispersion of the DM particle are given by $\langle v\rangle = 2v_0/\sqrt{\pi}$ and $\langle v^2\rangle = 3v^2_0/2$, respectively.

Dark matter self-scattering In this model, apart from the χ quartic self-interaction, we also have the s-channel self-interaction diagram mediated by ϕ and the SM Higgs. DM self-scattering cross-section around the resonance region, i.e, $m_\chi \simeq m_\phi/2$ can introduce the velocity dependence, which can explain the small-scale structure problem. More specifically, we address the core-cusp problem, which denotes the mismatch between the result of N-body simulations with a collision-less DM which predicts a cuspy DM profile at the galactic center, and that of astrophysical observations which indicate shallower profiles. The cross-section of the scattering in the N.R limit of the DM particles is then estimated as[4]

$$\sigma(\chi\chi\to\chi\chi) = \frac{1}{32\pi s}\left|\lambda_\chi + \frac{C^2_{\phi\chi\chi}}{s-m^2_\phi+i\sqrt{s}\Gamma_\phi} + \frac{C^2_{h\chi\chi}}{s-m^2_h} + \frac{2C^2_{\phi\chi\chi}}{t-m^2_\phi} + \frac{2C^2_{h\chi\chi}}{t-m^2_h}\right|^2 \simeq \sigma_0 + \frac{1}{2\pi m^6_\phi}\frac{C^4_{\phi\chi\chi}}{(v^2-v^2_R)^2 + 16\frac{\Gamma^2_\phi}{m^2_\phi}}.$$

Here, we assume $m_\phi \ll m_h$, $v \ll 1$, to obtain the last equation with $\sigma_0 \equiv (\lambda_\chi - 2C^2_{\phi\chi\chi}/m^2_\phi - 3C^2_{h\chi\chi}/m^2_h)^2/(32\pi m^2_\phi)$. λ_χ and $C_{h\chi\chi}$ are the quartic term denoting χ self-interaction and the $h\chi\chi$ trilinear coupling respectively.

3 Analysis

Parameters: To define the model, it is convenient to use the following set of model parameters: v_R, $C_{h\chi\chi}$, σ_0, γ_ϕ, $C_{\phi\phi\chi\chi}$, $\sin\theta$, $C_{\phi\phi h}$, m_ϕ, $C_{\phi\phi\phi}$, $C_{\phi\phi\phi\phi}$. We use $v_R \equiv 2\,(m_\phi/m_\chi - 2)^{1/2}$ as an input parameter instead of m_χ, because we focus on the resonance parameter region, $m_\chi \sim m_\phi/2$. On the other hand, the coupling between χ and ϕ plays the most important role in the phenomenology of the light scalar DM, and we use the parameter $\gamma_\phi = (C_{\phi\chi\chi}/m_\phi)^2/(64\pi)$ as an input parameter. Moreover, we take the mass of the mediator particle and the mixing, m_ϕ

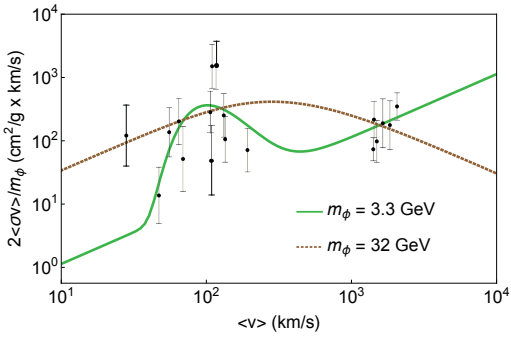

Figure 1 – *The velocity-dependence of the self-scattering cross-section (times the relative velocity) predicted by the scalar dark matter: The prediction using the parameter set,* $(v_R,\ \sigma_0/m_\phi,\ \gamma_\phi,\ m_\phi) = (110\,\mathrm{km/s},\ 0.06\,\mathrm{cm^2/g},\ 10^{-7.9},\ 3.3\,\mathrm{GeV})$ *is shown by a green solid line, while that using the set,* $(5035\,\mathrm{km/s},\ 0,\ 10^{-1.1},\ 32\,\mathrm{GeV})$*, is shown by a brown dashed line. The data obtained by kinematical observation is given by black dots with error bars*[5].

and $\sin\theta$ as input parameters. Finally, we use σ_0, $C_{h\chi\chi}$, and $C_{\phi\phi h}$ as input parameters for their important roles in the DM self-scattering, the direct DM detection, and the Higgs decay into a mediator pair. Physical quantities relevant to our discussion depend on these seven parameters discussed here.

Condition from the core-cusp problem: We impose the condition that the model parameter set should give the self-scattering cross-section that is consistent with the data. In our likelihood analysis, this condition favors the following two model parameter regions of the scalar DM when the total decay width of the mediator particle is governed by the invisible decay into a DM pair. The first one is the parameter region with the mediator mass of $m_\phi \approx \mathcal{O}(10)$ GeV. On the other hand, when $m_\phi \lesssim 10$ GeV, the self-scattering condition requires a narrow resonance, i.e., a small γ_ϕ. In Fig. 1, the velocity dependence of the self-scattering cross-section is shown in comparison with the data.

Condition from the thermal relic abundance: We assume that the DM abundance observed today is obtained by the freeze-out mechanism of the scalar DM in the standard thermal history. Since the annihilation cross-section of DM is enhanced by the s-channel resonance, the mixing angle $\sin\theta$ is generally required to be very much suppressed to explain the observed relic.

By imposing the condition of the thermal relic abundance (and the condition of the self-scattering), our likelihood analysis implies that the parameter region with the mediator mass below twice the muon mass, $2m_\mu$, is excluded.

Constraint from CMB: The CMB observation gives a severe constraint on the annihilation cross section of light thermal DM candidates because such annihilations could inject electromagnetically interacting particles into the primordial plasma in the early universe, which would increase the residual ionization fraction and modify the anisotropies of CMB. Here, DM annihilations can be considered as s-wave. Imposing this constraint on top of other existing ones indicates that the region above the bottom quark threshold is excluded, and consequently the resonance is restricted in the tiny region $v_R \sim 10^{-3}$.

Constraint from Indirect Detection: Since $v_R \sim 10^{-3}$ and this is close to the velocity of DM in the Milky Way $v_{MW} \sim 240\,\mathrm{km/s}$, the annihilation of DM is enhanced through the s-channel resonance. Therefore DM in our model can be searched for by observing energetic particles produced by their annihilation in the galaxy. We used the data of $e^\pm$ flux from *Voyager I* and *AMS-02* satellites. Since the injection spectra in the hadron channel have large uncertainties around $m_\phi \sim 2$ GeV, we consider only the lepton channel contribution in our analysis. Morover, there are some uncertainties in the local DM density, which we assume to be

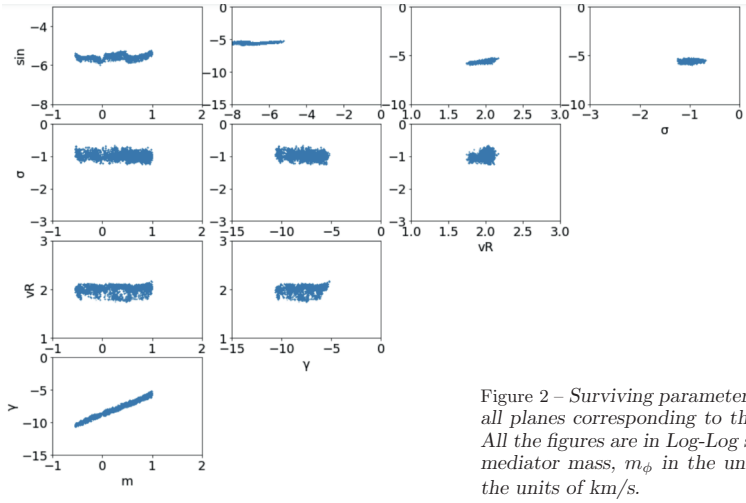

Figure 2 – *Surviving parameter region projected on all planes corresponding to the input parameters. All the figures are in Log-Log scale. m denotes the mediator mass, m_ϕ in the units of GeV. v_R is in the units of km/s.*

$0.25 \pm 0.11\,\mathrm{GeV\,cm^{-3}}$. We find that the injection spectra for the lepton channel favors the tiny region $1 \lesssim m_\phi \lesssim 2$ GeV.

4 Conclusion

We have done a systematic analysis of a minimal light scalar thermal DM model which interacts with the SM through s-channel resonance mediated by a Higgs-like light scalar. While the major constraints come from DM self-interaction, relic abundance, indirect searches and CMB data, we also consider some other minor constraints, namely $\Delta N_{\rm eff}$ and the rare decay of mesons. To sum up, for such a toy model, we conclude that the parameter region which survives all the relevant constraints considered correspond to mediator mass, $1 \lesssim m_\phi \lesssim 2$ GeV with $v_R \sim 10^{-3}$ and the mixing angle $\sin\theta \sim 10^{-5}$.

Acknowledgments

SC thanks the organizers of the 2022 Cosmology session, 56th Rencontres de Moriond for the opportunity and partial financial support to present this work. SC also acknowledges support from CEFIPRA (Grant no. 6304-2).

References

1. James M. Cline, Kimmo Kainulainen, Pat Scott, and Christoph Weniger. Update on scalar singlet dark matter. *Phys. Rev. D*, 88:055025, 2013.
2. Tobias Binder, Sreemanti Chakraborti, Shigeki Matsumoto, and Yu Watanabe. Manuscript in preparation.
3. Masahiro Ibe, Hitoshi Murayama, and T. T. Yanagida. Breit-Wigner Enhancement of Dark Matter Annihilation. *Phys. Rev. D*, 79:095009, 2009.
4. Xiaoyong Chu, Camilo Garcia-Cely, and Hitoshi Murayama. Velocity Dependence from Resonant Self-Interacting Dark Matter. *Phys. Rev. Lett.*, 122(7):071103, 2019.
5. Manoj Kaplinghat, Sean Tulin, and Hai-Bo Yu. Dark Matter Halos as Particle Colliders: Unified Solution to Small-Scale Structure Puzzles from Dwarfs to Clusters. *Phys. Rev. Lett.*, 116(4):041302, 2016.

To detect dark matter with gravitational wave interferometers

Federico R. Urban
CEICO, Institute of Physics of the Czech Academy of Sciences
Na Slovance 1999/2, 182 21 Praha 8, Czech Republic

I review how dark matter, if it has spin-2 and is ultra-light, looks like a continuous gravitational wave, and how current and planned gravitational wave interferometers can place the most stringent limits on this model.

1 Introduction

The recent detection of gravitational waves has consecrated gravitational wave interferometers (GWIs) as a vital experimental tool for astronomy, cosmology, and fundamental physics. The GWs detected thus far are a product of cataclysmic transient events, such as binary black hole mergers. These signals are strong, with gravitational strain of the order of $h \sim 10^{-21}$, but very short, from a fraction of a second to several seconds. Much weaker signals can be detected if they are coherent over a longer time, such as the continuous waves (CWs) emitted by rapidly spinning neutron stars or ultra-compact Galactic binaries. Having detected no CWs thus far, this set the upper limit $h \sim 10^{-25}$ on the maximum strain for this type of signal at frequencies of about $f \sim 10^2$ Hz.

Here we show that, if dark matter is ultra-light (ULDM) and has spin-2, it interacts with GWIs in a way that, owing to its quasi-monochromaticity and persistence, closely resembles CWs and can be detected by existing and future Earth-based facilities as well as space-based ones [1].

2 The shape and strength of the signal

The behaviour of the spin-2 ULDM in sufficiently small regions inside the local dark matter halo is described by the oscillating tensor field [2]

$$M_{ij}(t) = \frac{\sqrt{2\rho_{\rm DM}}}{m} \cos\left(mt + \Upsilon\right)\varepsilon_{ij}(\mathbf{r})\,, \tag{1}$$

where $\rho_{\rm DM}$ is the observed local dark matter energy density, for which we assume $\rho_{\rm DM} = 0.3\ {\rm GeV/cm^3}$, and Υ is a random phase. The five polarisations of the spin-2 field are encoded in

the $\varepsilon_{ij}(\mathbf{r})$ tensor, which has unit norm and zero trace, is symmetric and is direction-dependent via the unit vector $\mathbf{r}$.

In the ULDM reference frame $(\mathbf{p}, \mathbf{q}, \mathbf{r})$ the polarisations of the spin-2 field can be described as $\varepsilon_{ij}(\mathbf{r}) \equiv \sum_\kappa \varepsilon_\kappa \mathcal{Y}^\kappa_{ij}(\mathbf{r})$ [3,4], where the summation runs over the five amplitudes $\{\varepsilon_\times, \varepsilon_+, \varepsilon_\mathrm{L}, \varepsilon_\mathrm{R}, \varepsilon_\mathrm{S}\}$ that obey $\sum_\kappa \varepsilon_\kappa^2 = 1$—the overall amplitude is fixed by the requirement that M_{ij} makes up all of the dark matter. The five polarisation matrices are given by

$$\mathcal{Y}^\times_{ij} \equiv \frac{1}{\sqrt{2}}\left(p_i q_j + q_i p_j\right), \qquad \mathcal{Y}^+_{ij} \equiv \frac{1}{\sqrt{2}}\left(p_i p_j - q_i q_j\right), \qquad \mathcal{Y}^S_{ij} \equiv \frac{1}{\sqrt{6}}\left(3 r_i r_j - \delta_{ij}\right)$$
$$\mathcal{Y}^L_{ij} \equiv \frac{1}{\sqrt{2}}\left(q_i r_j + r_i q_j\right), \qquad \mathcal{Y}^R_{ij} \equiv \frac{1}{\sqrt{2}}\left(p_i r_j + r_i p_j\right),$$

Notice that, unlike for CWs, there is no propagation along the $\mathbf{r}$ direction, which in our case serves merely as reference for the decomposition in tensor, vector, and scalar helicities according to their behaviour under a rotation about $\mathbf{r}$.

The effect of spin-2 ULDM on the detector can be equivalently described by the gravitational effect of an oscillating metric perturbation h_{ij} given by

$$h_{ij}(t) = \frac{\alpha}{M_\mathrm{P}} M_{ij}(t) = \frac{\alpha\sqrt{2\rho_\mathrm{DM}}}{m M_\mathrm{P}} \cos\left(mt + \Upsilon\right)\varepsilon_{ij}(\mathbf{x})\,. \tag{2}$$

The parameter α is idiosyncratic for spin-2 ULDM because it is required by the self-consistency of the model, such as in bigravity [5]. This parameter defines the inverse ULDM self-interaction strength: there is no ULDM at all with $\alpha \to 0$ because the ULDM field becomes infinitely strongly coupled in this limit. Furthermore, spin-2 ULDM is ineluctably coupled universally to standard matter fields, so that ULDM will appear as a Yukawa-like fifth force modification of the gravitational potential Φ in the weak field regime, for which α quantifies the strength: $\Phi \to \Phi\left[1 + \alpha^2 \exp(-mr)\right]$. The strength of this fifth force for different values of the mass m is constrained by tests of gravity: we call this maximal coupling $\alpha = \alpha_Y$.

In the reference frame of the detector, $(\mathbf{x}, \mathbf{y}, \mathbf{z})$, the response function D^{ij} is given by the differential change in the length of the detector arms directed along the unit vectors $\mathbf{n}$ and $\mathbf{m}$ as $D^{ij} = (n^i n^j - m^i m^j)/2$. The signal is the combination of the variation of the metric perturbation and the response function:

$$h(t) \equiv D^{ij} h_{ij}(t) = \frac{\alpha\sqrt{\rho_\mathrm{DM}}}{\sqrt{2} m M_\mathrm{P}} \cos\left(mt + \Upsilon\right)\Delta\varepsilon \equiv h_s \sin\left(mt\right) + h_c \cos\left(mt\right), \tag{3}$$

where we defined $\Delta\varepsilon \equiv \varepsilon_{ij}(n^i n^j - m^i m^j)$, and introduced the sine h_s and cosine h_c amplitudes. This is the central equation of the paper.

The spin-2 ULDM signal has a unique geometric structure that sets it apart from other CWs. Explicitly we have

$$\Delta\varepsilon = \frac{\cos 2\phi}{\sqrt{2}}\left[\varepsilon_+\left(\cos^2\theta + 1\right) + \varepsilon_\mathrm{R}\,\sin 2\theta + \sqrt{3}\,\varepsilon_\mathrm{S}\,\sin^2\theta\right] - \sqrt{2}\sin 2\phi\left(\varepsilon_\times\,\cos\theta + \varepsilon_\mathrm{L}\,\sin\theta\right), \tag{4}$$

where we have set $\mathbf{n} = \mathbf{x}$ and $\mathbf{m} = \mathbf{y}$, which we can always do for a single L-shaped detector, and we have defined the ULDM reference frame in terms of the detector's frame as $\mathbf{r} = (\sin\theta\cos\phi, \sin\theta\sin\phi, \cos\theta)$, $\mathbf{p} = (\cos\theta\cos\phi, \cos\theta\sin\phi, -\sin\theta)$, $\mathbf{q} = (-\sin\phi, \cos\phi, 0)$; the origins of the two frames are connected by the vector $r\mathbf{r}$.

All-sky searches for CWs with Earth-bound GWIs resort to semi-coherent methods because it is not computationally feasible to analyse the data from the entire observation campaign in a fully coherent way. In semi-coherent methods the whole data set is broken into shorter time chunks of length T_chunk, each of which is then analysed coherently but separately. One of the advantages of this approach is that, by choosing $T_\mathrm{chunk} < T_\mathrm{Doppler} \equiv 1/\Delta f_\mathrm{Doppler}$ the Doppler

frequency shift can be neglected. Moreover, one should ensure that $T_{\rm chunk} < t_{\rm coh}$ in order to have a stable ULDM configuration within a given chunk. The sensitivity for a coherent analysis over the whole observation campaign time $T_{\rm obs}$ scales as $T_{\rm obs}^{-1/2}$. In semi-coherent methods, assuming that all N chunks last the same time $T_{\rm chunk}$ and all together they cover the whole observation run such that $T_{\rm obs} = NT_{\rm chunk}$, the sensitivity scales instead as $N^{-1/4}T_{\rm chunk}^{-1/2} = T_{\rm obs}^{-1/4}T_{\rm chunk}^{-1/4}$. Thanks to the coherence of the signal, even within the limitation of the semi-coherent methods, the actual sensitivity attained by current facilities for CW searches is more than a factor 10^{-3} smaller than the design sensitivity h_0 for transient events.

The semi-coherent techniques have been adapted and optimised, taking into account the coherence time and the geometry of the signal, for dark photon dark matter searches [6]. They can therefore be tailored for spin-2 ULDM-CW searches by replacing the average over the different polarisations of ULDM waves (which for the spin 1 dark photon case amounts to a factor $\sqrt{2}/3$) with $\sqrt{\langle \Delta\varepsilon^2 \rangle} = \sqrt{2/5}$.

3 Results

In order to estimate the values of α accessible with GWIs, we compare the expected theoretical signal $h \equiv \langle h_s^2 + h_c^2 \rangle^{1/2} = \frac{\alpha\sqrt{\rho_{\rm DM}}}{\sqrt{5}mM_{\rm P}}$ with the design sensitivities of a number of current and planned GWIs. We find that the HLV detectors can nominally detect spin-2 ULDM for $\alpha \gtrsim 10^{-4}$ depending on the frequency. We expect that a dedicated semi-coherent search for the spin-2 ULDM signal will improve the range of detectable α by a few orders of magnitude, potentially down to $\alpha \sim 10^{-7}$ or less for frequencies of tens of Hz, corresponding to masses around the 10^{-13} eV mark; this is shown as the dotted line "HLV opt". In this frequency range, from $f \sim 10$ Hz ($m \sim 4 \times 10^{-14}$ eV) to $f \sim 10^3$ Hz ($m \sim 4 \times 10^{-12}$ eV) and beyond the planned experiments Einstein Telescope (ET) and Cosmic Explorer (CE) should reach sensitivities of order $h_0 \sim 10^{-22}$—10^{-23}, further improving the chances to detect spin-2 ULDM.

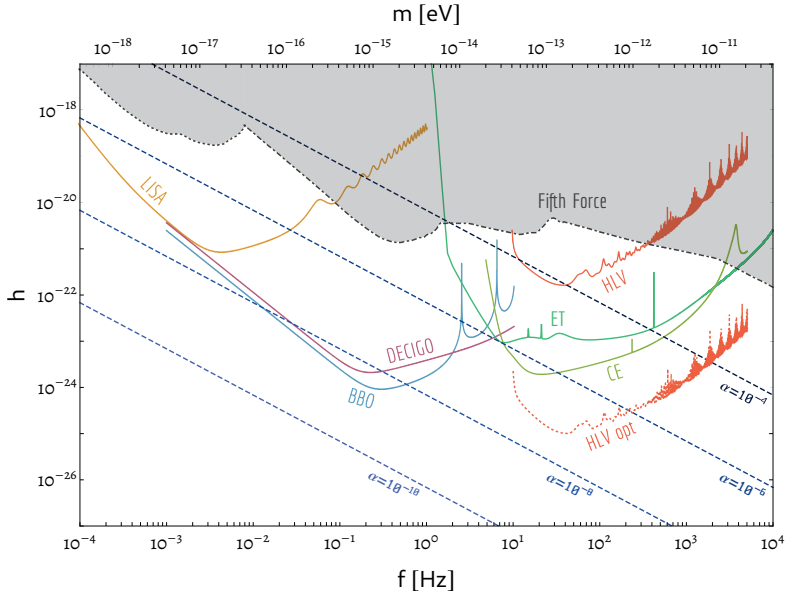

Figure 1 – Strain sensitivities, see text for details.

Future facilities will also be able to probe much lower values of the ULDM mass. In the intermediate frequency range 0.1 Hz $\lesssim f \lesssim$ 1 Hz, corresponding to 4×10^{-16} eV $\lesssim m \lesssim 4 \times 10^{-15}$ eV, the BBO and DECIGO detectors are expected to attain sensitivities of order of $h_0 \sim 10^{-23}$—10^{-24}. This means these GWIs could detect a spin-2 ULDM-CW signal for $\alpha \lesssim 10^{-8}$ at those frequencies. In the low frequency range the planned space-based interferometer LISA will reach a sensitivity of $h_0 \sim 10^{-21}$ for $f \sim 10^{-2}$ Hz ($m \sim 4 \times 10^{-17}$ eV), which means that it could detect spin-2 ULDM with $\alpha \sim 10^{-7}$ and below. These limits would be much improved with a dedicated pipeline for these interferometers, as is the case for HLV. We collect all the sensitivities and compare them to the theoretical signal in Fig. 1.

Acknowledgments

I would like to thank immensely the organisers of this very successful Moriond session despite all the challenges of the times. My work is supported by the European Regional Development Fund (ESIF/ERDF) and the Czech Ministry of Education, Youth and Sports (MEYS) through Project CoGraDS - `CZ.02.1.01/0.0/0.0/15_003/0000437`.

References

1. J. M. Armaleo, D. López Nacir and F. R. Urban, JCAP **04** (2021), 053 doi:10.1088/1475-7516/2021/04/053 [arXiv:2012.13997 [astro-ph.CO]].
2. L. Marzola, M. Raidal and F. R. Urban, Phys. Rev. D **97** (2018) no.2, 024010 doi:10.1103/PhysRevD.97.024010 [arXiv:1708.04253 [hep-ph]].
3. J. M. Armaleo, D. López Nacir and F. R. Urban, JCAP **01** (2020), 053 doi:10.1088/1475-7516/2020/01/053 [arXiv:1909.13814 [astro-ph.HE]].
4. J. M. Armaleo, D. López Nacir and F. R. Urban, JCAP **09** (2020), 031 doi:10.1088/1475-7516/2020/09/031 [arXiv:2005.03731 [astro-ph.CO]].
5. E. Babichev, L. Marzola, M. Raidal, A. Schmidt-May, F. Urban, H. Veermäe and M. von Strauss, JCAP **09** (2016), 016 doi:10.1088/1475-7516/2016/09/016 [arXiv:1607.03497 [hep-th]].
6. A. L. Miller, P. Astone, G. Bruno, S. Clesse, S. D'Antonio, A. Depasse, F. De Lillo, S. Frasca, I. La Rosa and P. Leaci, *et al.* Phys. Rev. D **103** (2021) no.10, 103002 doi:10.1103/PhysRevD.103.103002 [arXiv:2010.01925 [astro-ph.IM]].

Quintessential cosmological tensions: a study of the Albrecht-Skordis model

A. Adil, A. Albrecht, L. Knox
Department of Physics & Astronomy, University of California, Davis
One Shields Avenue, Davis, CA, USA

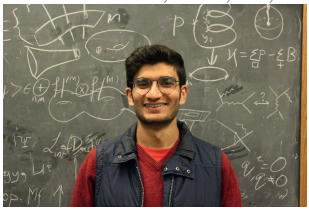

Several cosmological tensions have emerged in light of recent data, most notably in the inferences of the parameters H_0 and σ_8. We explore the possibility of alleviating both these tensions *simultaneously* by means of the Albrecht-Skordis "quintessence" potential. The field can reduce the size of the sound horizon r_s^* while concurrently suppressing the power in matter density fluctuations before it comes to dominate the energy density budget today. Interestingly, this rich set of dynamics is governed entirely by one free parameter that is of $O(10)$ (Planck units). We find that the inferred value of H_0 can be increased, while that of σ_8 can be decreased, both by $\approx 1\sigma$. However, ultimately the model is disfavored by Planck and BAO data alone, compared to the standard ΛCDM model, with a $\Delta\chi^2 \approx +6$. There is, however, an important lesson for model building: historically much attention has been focused on preserving the three angular scales θ_D, θ_{EQ}, and θ_s^* to their ΛCDM values. This work shows that, while doing so indeed maintains a good fit to the CMB data for an increased number of ultra-relativistic species, it is a-priori insufficient in maintaining such a fit when this intuition is extrapolated to other species.

1 Introduction

Much attention in cosmology today is devoted to tensions that exist between modern cosmological data and the standard "Λ-Cold Dark Matter" (ΛCDM) cosmological model, notably in inference of the H_0 and σ_8 parameters. Extensions to ΛCDM which modify the matter content around the time of last scattering have been explored in the hopes of addressing these tensions. The Albrecht-Skordis (AS) model is a quintessence model in which the dark energy takes the form of an evolving scalar field with a number of special properties. One of these is that the scalar field contributes a significant fraction of the total energy density of the Universe starting at extremely early times, suggesting that it might offer relief from the cosmological tensions.

Several authors have previously studied quintessence models of dark energy and have dismissed them as a remedy for the H_0 tension However, the models studied till now have focused on "tracking" quintessence fields which are *a-priori* unfit to alleviate the value of H_0 using Planck data. Instead, this letter offers a systematic analysis of the AS model, which *a-priori* is approximately the best-case scenario for a single-field massive quintessence component to resolve the H_0 tension. However, ultimately these features are unable to resolve the H_0 tension, though

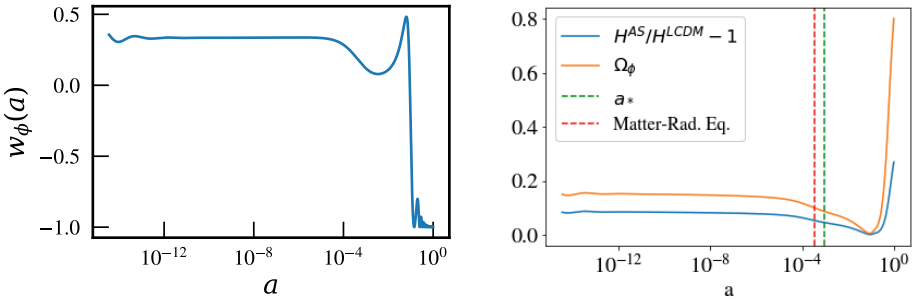

Figure 1 – The left panel shows the evolution of the equation of state parameter for the AS field over several decades of scale factor. The right panel shows the corresponding contribution from the energy density in the scalar field, along with the change in the expansion rate for $\lambda = 5$ (at fixed θ_s^*). Notice that the field tracks the background component during radiation domination but breaks from away the tracker solution during matter domination.

the model can provide concordance with the late-time measurements of σ_8.

We find that the best fit AS model fits the data overall about as well as ΛCDM when considering a hollistic dataset which includes Large-Scale Structure (LSS) and supernovae (SNe) data, but that the model is disfavored compared to the standard cosmological model when using only Planck and BAO data. This allows us to extract some interesting lessons about attempts to resolve the tensions.

2 The Albrecht-Skordis (AS) Model

The Albrecht-Skordis (AS) model, first introduced in [1] is a particular quintessence model with a scalar field evolving in a potential of the form

$$V(\phi) = \left((\phi - B)^2 + A\right) e^{-\lambda\phi}. \tag{1}$$

This potential admits a local minimum due to the polynomial pre-factor. However, far from the minimum, the field behavior is dominated by the exponential factor so that it behaves similarly to an exponential potential, as introduced in [2]. At late times the field may get "stuck" in the local minimum where it can approximate the behavior of a cosmological constant. Since the field is dynamic, the energy density does not scale like a power law as it would for the other density components. Thus, we solve for the evolution of the field over cosmic history by simultaneously solving the Friedmann equation and the Klein-Gordon equation for scalar fields, the result of which is shown in Fig. 1.

3 Towards Resolving Cosmological Tensions

3.1 Mechanism for increasing H_0

In order to bring concordance between CMB and late-universe data one must take care not to disturb the angular scale of the sound horizon at recombination, θ_s^* since it is tightly constrained by Planck data [3]. Since

$$\theta_s^* = \frac{r_s^*}{D_M^*}$$

$$\text{where} \quad r_s^* = \int_{z_*}^{\infty} \frac{dz}{H(z)} c_s(z) \quad \text{and} \quad D_M^\star = \int_0^{z_*} \frac{dz}{H(z)}$$

is the comoving size of the sound horizon at recombination and the comoving angular diameter distance to the last-scattering surface respectively, an increased H_0 (at fixed ω_m) would decrease D_M^* and must therefore be compensated by a proportionate decrease in r_s^*.

The AS field can reduce the size of the sound horizon as it contributes an amount proportional to $\Omega_\phi \approx 4/\lambda^2$ (right panel in Fig. 1) to the total energy budget *prior* to recombination. Thus, if we keep ω_m fixed, the decrease in D_M^* must come from an increased $H(z \approx 0)$.

In order to approximate the requisite contribution from the field required to bring concordance with the SH0ES measurement, we note that the sound horizon decreases by an amount $\delta r_s^*/r_s \approx -4/(3\lambda^2)$ compared to the ΛCDM value (this would be $-2/\lambda^2$, but Ω_ϕ begins to decrease at the onset of matter-radiation equality which softens this response). We can then approximate that $\frac{\delta H_0}{H_0} \approx \frac{20}{3\lambda^2}$ so that, for a $\approx 7\%$ increase in H_0 one needs $\lambda \approx 10$ assuming we hold θ_s^* and ω_m fixed at the Planck calibrated ΛCDM values. Of course, this assumption is not true when exploring the full parameter space.

3.2 Mechanism for suppressing σ_8

The effective speed of sound for quintessence is $c_s^2 = 1$ (in the gauge co-moving with the field) which prevents the component from clustering on sub-horizon scales. In particular, even when $w_\phi \approx 0$, the entropy perturbations prevent gravitational collapse [4]. Intuitively, this suggests that one should expect some power suppression since there is now an additional contribution to the expansion rate but a negligible contribution to gravitational potentials. Mathematically, notice that, much after horizon crossing, the evolution of the matter contrast δ_m is given by

$$\delta_m'' + 2H\delta_m' = 4\pi \sum_i \rho_i \delta_i \tag{2}$$

(note the over-prime denotes derivative with respect to conformal time) where the scalar field contributes to the second term on the left-hand side, but does not contribute appreciably to the source term on the right-hand side compared to the contribution from matter. In particular, since Ω_ϕ begins to decrease at the onset of matter-radiation equality (see Fig.1), there is a scale dependent suppression of the density contrast. Modes that enter before matter-radiation equality experience the maximal suppression while modes that enter after asymptotically approach the ΛCDM solution. This effect is responsible for power suppression and leads to a decreased inference of the power spectrum normalization, σ_8.

4 Results

In order to obtain statistical constraints on the parameter space given the data, we vary the usual six cosmological parameters and additionally vary the quintessence parameter λ (in Eq. 1) so that the complete set of varied parameters is $\{\omega_b, \omega_{cdm}, \theta_s^*, n_s, A_s, \tau_{reio}, \lambda\}$. The other parameters appearing in Eq. 1 are of negligible cosmological significance: A plays the role of establishing a minimum such that for a given λ, a false vacuum exists if and only if $A < 1/\lambda^2$; B is completely degenerate with H_0, Ω_m^0, and λ; and the initial conditions for the field are set deep in the radiation-era where the Klein-Gordon equation admits an attractor. Finally, this leaves us with λ as the only outstanding parameter which we vary in the prior range $2 \leq \lambda \leq 1/\sqrt{A}$. The lower bound comes from the consideration that a tracking/scaling solution in the radiation era exists only for $\lambda \geq 2$ [5]. Note that larger values of λ drive the minimum to lower values of ϕ which in turn increases the probability for the scalar field to tunnel through the local minimum, leading to "cataclysmic" Coleman-De Luccia bubbles [6], thus we set $A = 0.0025$ so that $\lambda \leq 20$.

We use CLASS to solve the Einstein-Boltzmann equations and MontePython for parameter estimation. We plot the main parameters of interest for two choices of data sets in Fig. 2. One can immediately notice that, in both cases, H_0 and σ_8 increase and decrease by $\approx 1\sigma$ respectively. Perhaps strikingly, on the inclusion of SH0ES (dashed), the mechanism by which H_0 increases

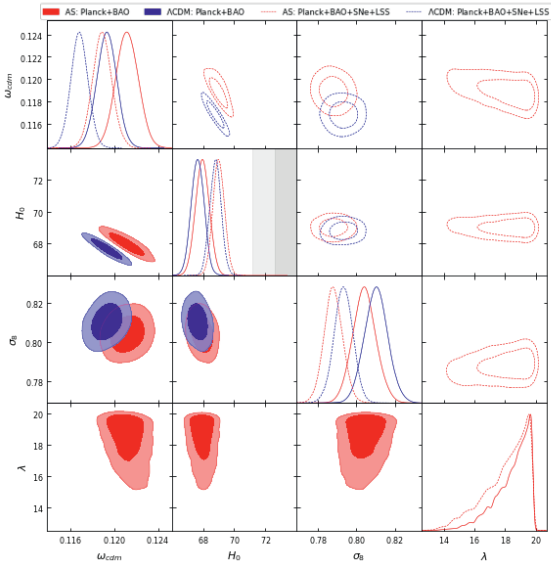

Figure 2 – Parameter inferences for two combinations of data. The lower triangle (solid) uses only `Planck` and `BOSS-BAO` data while the upper triangle (dashed) also includes `Pantheon`, `DES-KV` pior on S_8^7, and cepheid-calibrated supernovae measurement from `SH0ES-2019` (grey bands).

is the same as that in ΛCDM, namely by suppressing ω_{cdm}, as opposed to by increasing an early contribution from the scalar field (as indicated by almost no change in the posterior probability for λ). One might posit that this is due to changes in the damping scale (θ_D) induced by the inclusion of the scalar field. However, even when we vary the primordial Helium fraction Y_P (not shown), we see almost no change to the χ^2 budget. This is in stark contrast to an increased $N_{\rm eff}$ model where, not only does the inclusion of SH0ES favor an increased value of $N_{\rm eff}$, but that the χ^2 improves significantly (by ≈ -5) when one allows Y_P to vary freely. A closer analysis has led us to conclude that the strongest constraint comes from the radiation driving effect, which is also precisely the effect responsible for the increased inference of ω_{cdm} that has prevented the AS model from accomplishing the maximum possible increase in H_0 which one might have expected from the analysis in Section 3.1. Using Planck and BAO data, we find $\Delta\chi^2 \approx +6$, while for the more extensive data we find $\Delta\chi^2 \approx +1$, compared to the benchmark ΛCDM model.

References

1. A. Albrecht and C. Skordis, *Phys. Rev. Lett.* **84**, 2076 (2020).
2. B. Ratra and J. Peebles, *Phys. Rev.* D **37**, 3406 (1988).
3. L. Knox and M. Millea, *Phys. Rev.* D **101**, (2020).
4. C. Skordis and A. Albrecht, *Phys. Rev.* D **66**, (2002).
5. P. G. Ferriera and M. Joyce, *Phys. Rev.* D **68**, (1998).
6. J. Weller, *Particles, Strings, and Cosmology (PASCOS 99),* (2000).
7. T. Tröster *et al*, *Astronomy and Astrophysics* **633**, 1432-0746 (2020).

4.
21 cm

Current status and future of cosmology with 21cm Intensity Mapping

Réza Ansari
Université Paris-Saclay, CNRS/IN2P3, IJCLab, 91405 Orsay, France

21cm Intensity Mapping (IM) has been proposed about 15 years ago as a cost effective method to carry out cosmological surveys and to map the 3D distribution of matter in the universe, over a large range of post EoR redshifts, from z=0 to z=6. Since then a number of pathfinder instruments have been built, such as CHIME or Tianlai. Several other ones will be commissioned in the next few years (HIRAX, CHORD, BINGO), while even larger arrays, with several thousand antennae are being considered for the next generation experiments. We will briefly review the 21cm cosmology of the Epoch of Reionisation (EoR), and we will then focus on IM for late time cosmology. After presenting some of the promises of this technique to constrain the cosmological model, dark energy and inflation, we will review some of the instrumental and scientific challenges of IM surveys. The second part of the paper presents an overview of the ongoing and future experiments, as well as recent results by GBT, CHIME and Tianlai.

1 Introduction

Although the 21cm cosmology is mostly concerned with probing the dark ages and EoR, this paper is rather focused on late time cosmology, and mapping the cosmic matter distribution using the 21cm radio emission or absorption of neutral hydrogen gas (HI) through Intensity Mapping (IM). This technic refers to the detection of underlying structures formed by 21cm sources such as galaxies, without requiring detection of individual sources [1,2]. A brief overview of EoR science with 21cm is presented in this section, while the idea and instrumental concepts behind Intensity Mapping would be developed in the following sections.

Observations revealing the evolution of the universe during the dark ages and the reionisation era are crucial for understanding the formation of structures in the universe [3,4,5,6]. Dark ages refers to the period extending from Cosmic Microwave Background (CMB) last scattering era, at a redshift $z \sim 1100$ to the cosmic dawn, which corresponds to the birth of first stars and galaxies. The intense and energetic (UV, X) radiation from theses first sources initiated the process of ionising the neutral gas, marking the start of the Epoch of Reionisation (EoR). The 21cm hyperfine transition of atomic hydrogen (HI) is one the only spectral features that can be used to probe this era, as the universe contains no sources, but only gas, mostly hydrogen at high redshifts ($z \gtrsim 30$). The HI gas leaves an imprint on the cosmic background radiation (CMB) if the spin temperature T_s differs from the CMB temperature $T_{CMB}(z)$ at the corresponding redshift. The redshifted HIhyperfine transition, at a frequency of $\nu_{21}/(1+z)$ with $\nu_{21} \simeq 1420.4$MHz will appear as an emission, respectively an absorption feature, if the spin temperature $T_x(z)$ is higher, respectively lower, than $T_{CMB}(z)$. The history of the evolution of the spin temperature during the dark ages and EoR is rather complex [7]. T_s tracks at first T_{CMB}, then decouples around $z \gtrsim 150$ and decreases due to collision coupling with the gas kinetic temperature T_K. The $T_s \leftrightarrow T_{CMB}$ equilibrium is restored around $z \sim 50$, when the atomic collision rates becomes ineffective to maintain $T_s \leftrightarrow T_K$ coupling, due to gas dilution by the expansion. After the for-

mation of the first stars and galaxies, the spin temperatures gets coupled to the gas temperature again in the UV photon bath at $z \sim 30$, through the Wouthuysen-Field effect.

The measurement of the 21 cm emission temperature and its anisotropies as a function of redshift would therefore allow to precisely identify the different stages of the universe's evolution during the dark ages and EoR ($10 \lesssim z \lesssim 100$). In addition, the temperature anisotropies trace the distribution of matter in the linear regime over a broad range of wave modes (k-scales) at these redshifts, whereas non linearities affect a significant fraction of k-scales at later cosmological times ($z \sim 1$).

Although a number of dedicated instruments have been built over the last twenty years to observe the EoR 21cm signal, no undisputed observation has yet been reported. This is explained by the many challenges that needs to be overcome: the redshifted 21cm feature is located in the frequency range $10 - 50$MHz for redshifts $30 \lesssim z \lesssim 150$, which suffers from significant ionospheric absorption and diffraction as well as from major terrestrial, man-made disturbances (RFI). Moreover, the 21cm cosmological signal is very faint, in absolute terms, and completely buried in the foregrounds, specially the Galactic synchrotron and radio source emissions, which dominate this signal by 4 to 5 orders of magnitude. In addition, the reionisation history is very poorly constrained, making the experimental adventure quite risky, given the limited bandwidth that can be covered by any given instrument.

Some experiments, such as PAPER [8], SCI-HI [9] or EDGES [10] have targeted the global spectrum measurement and the detection of the distortions in the spectral shape of radio emission, due to EoR 21cm signal [11]. Although some authors have claimed a possible signal [12], the detection has not been confirmed. Other groups, have developed complex wide band interferometric instruments to detect the inhomogeneties of the cosmological 21cm signal and measure the associated power spectrum. LOFAR [13,14] and NenuFAR [15] have deployed antennae in Europe, LWA [16] is a large dipole array in New Mexico (USA), while MWA [17] or HERA [18,19] observe from Australia. Recent upper limits on the 21cm power spectrum from these experiments can be found in [20] for LOFAR, in [21] for MWA and in [22] for HERA. Detection of the 21cm EoR signal is also the main goal of the SKA-low instrument of the future SKA (Square Km Array) observatory [23].

An brief overview of post EoR ($z < 6$) 21cm Intensity mapping and its scientific promises and challenges is presented in section 2. The instrumental concepts suited for such surveys, as well as key technical issues are discussed in section 3. Ongoing and planned intensity mapping instruments and surveys and their latest results are presented in section 4. The last section, 5 gives an outlook and expectations for the near future.

2 21cm Intensity Mapping

The large scale distribution of matter in the universe is a powerful cosmological probe, used to reconstruct the universe expansion history, and to determine the statistical properties of the initial density fluctuations. Indeed, the quantum fluctuations, relics of the early universe inflationary phase are considered to be the seeds that generated the large structures, visible in the late universe, through the gravitational instability [24,25]. The LSS statistical properties, mostly encoded in the shape of the spatial correlation function $\xi(r)$ or the power spectrum $P(k)$, depends on the cosmological model and its parameters. The evolution of large structures with redshift, the growth rate of the structures in particular, is sensitive to changes in gravity [26], as well as to the neutrino masses, which, depending on their masses, partially erase small-scale structures [27]. The Baryon Acoustic Oscillations (BAO's) correspond to a preferred structure scale in the distribution of galaxies, originating from the baryon-photon plasma oscillations, prior to the decoupling. The BAO peaks, when observed at different redshifts, can be used as a standard ruler to reconstruct the cosmic expansion history, through the measurement of the Hubble parameter $H(z)$ and angular diameter distance $d_A(z)$ [28].

Historically, most cosmological surveys have been carried out using optical instruments through spectroscopic or photometric observations. Recent constraints on cosmological parameters derived from eBOSS and DES optical surveys can be found in [29] and [30]. However, mapping matter distribution in the universe in the radio wavelengths, through the observation of the redshifted 21 cm line of the atomic hydrogen (HI), is a complementary approach to optical surveys to constrain cosmology and dark energy. The 21 cm line is the only astrophysical spectral feature in the L band ($\sim$ GHz). It can therefore be used to determine unambiguously the redshift of an astrophysical object. Nevertheless, the detection of galaxies at 21cm needs a very large collecting area. The ALFALFA survey [31] carried out with the Arecibo antenna, one of the largest radio-telescopes in the world [a], with a primary reflector 300 m in diameter, detected objects up to a redshift of 0.2. SKA will be able to extend this limit and allow the observation of gas-rich galaxies up to $z \sim 0.5$.

Most of the cosmological information of large structures (LSS) is found at scales larger than a few Megaparsecs (Mpc). Therefore, the detection of individual galaxies is not mandatory for LSS studies. This is the essential idea behind the Intensity Mapping technique, which seeks to measure the aggregate 21 cm radiation of all the galaxies (a few hundred) contained in universe cells with a volume of a few hundred Mpc^3. A cosmological survey becomes then possible with more modest instruments [32,33,34,35], with a collection area of about few times 10^4m^2. However, the LSS cosmological signal has an average surface brightness of less than 1 mK, and is therefore totally overwhelmed by foreground emissions, mainly from the Milky Way synchroton emission and radio sources. These foreground emissions, with a temperature of $T_{\rm fgnd} \sim 2 - 5$K in the coldest parts of sky around 1 GHz, are in general about few thousand times brighter than the cosmological HI emission, while the instantaneous receiver noise is still about ten times larger with $T_{\rm sys} \sim 50$K. The reduction of fluctuations from instrumental noise ($T_{\rm sys}$) is achieved through long integration time, a few hours for each direction of the sky.

Extraction of the cosmological 21cm signal in the presence of these foregrounds is among the main IM scientific challenges. Several methods of separating the signal from the foreground emissions have been proposed which are all based on the smooth variation of the foreground brightness with frequency [35,36].

Since the early works on 21cm Intensity Mapping as a tool for cosmology , many authors have studied the science reach of such surveys, either generically [37,38], or targeting specific existing instruments such as FAST [39], or the SKA [40].

The white paper [41] present the science goals of an ambitious 21cm Intensity Mapping survey covering a broad redshift range, up to $z \sim 6$ with a very large dish array radio interferometer like PUMA [42]. Figure 1, adapted from [41], shows the precision that could be reached on the determination of the transverse and longitudinal BAO scales as a function of redshift, as well as for the structure growth rate $f\sigma_8$, assuming that the instrument can be built and operated, with map making and foreground subtractions reaching the projected performances. Thanks to the very large surveyed volume, such an IM experiment would significantly outperform surveys by the latest optical instruments (Rubin/LSST, DESI, WFIRST, Euclid). Radio observations can also be used to search for non-gaussianities and inflationary features in the reconstructed 3D LSS maps.

3 Instrumental concepts and challenges

As already mentioned in section 2, the relatively low radio brightness of HI clumps and galaxies limits the possibility of their detection to the vicinity, in cosmological sense, of our galaxy, with the available radio instruments. A galaxy with an HI mass of 10^{10}M$_\odot$, which is already a quite massive hydrogen cloud, would have a 21cm brightness $S_{21} \simeq 10\,\mu$Jy if located at a redshift

[a] The Arecibo 305 m telescope is being decommissioned, following damages to its structure `https://www.nsf.gov/news/news_summ.jsp?cntn_id=301674`

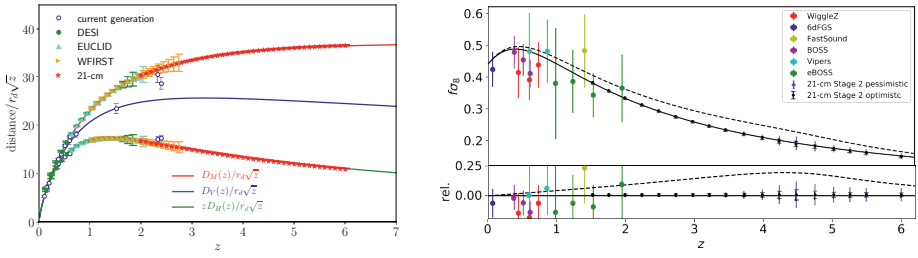

Figure 1 – Performance of a 21cm Intensity mapping survey with a Stage-II instrument, compared to the next optical surveys. Left: Expansion history reconstructed through different BAO distance scales measured as a function of redshift. Right: Statistical precision on the determination of the growth rate of structures. Figures adapted from reference [41].

$z = 1$. Its detection, with a reasonable integration time of a few hours will require more than 10^5m^2 of collecting area. Most of the cosmological information in the LSS is located at scales of a few arc-minutes or larger, as can be seen on figure 2, which shows the approximate level of the 21cm brightness temperature fluctuations power spectrum $P_{21}(k)$ for $z \sim 1$. The linear matter power spectrum has been converted into temperature, assuming an HIto baryon fraction $f_{H_I} \sim 1\%$, and using the following formulae, adapted from [4,35]:

$$P_{21}(k) \sim \left(\langle T_{21}\rangle\right)^2 \times P_{LSS}(k) \quad (1)$$

$$\langle T_{21}\rangle \simeq 0.042\text{mK}\,\frac{\Omega_{H_I}}{10^{-3}}\frac{H_0}{H(z)}(1+z)^2 \quad (2)$$

The cosmological information encoded in the LSS is statistical in nature, so a reasonably large volume of the universe needs to be surveyed to extract the information with low enough statistical errors. Instruments suitable for 21cm Intensity Mapping thus needs to have a large instantaneous field of view (FOV $\gtrsim 10 - 100\text{deg}^2$) and a large bandwith ($\Delta\nu \gtrsim 100$MHz), to be able to survey a large fraction of the sky with large integration time, over a significant redshift range.

Progress in the L-band analog electronics have made room temperature RF amplifiers quite competitive with low noise cryogenic electronic used in the large radio telescopes. Noise temperatures below $T_{noise} \lesssim 30$K can indeed now be reached by room temperature receivers. Large bandwidth interferometers with large number of feeds have become viable and cost effective, thanks to advances in digital electronic and computing (multi core CPU and GPU's), combined with progress in room temperature RF analog electronic.

Interferometers are most often used to reach high angular resolution, thanks to long baselines, but at the expense of a sparse sampling of the angular wave-mode or (u, v) plane. High resolution is not needed for LSS mapping for cosmological purposes, while high sensitivity is crucial, given the low signal strength. Although large dishes equipped with a multi-feed or phased array in their focal plane are a possible option, densely packed interferometric arrays, using rather small reflectors ($D \sim 5 - 10$m), operating in transit mode, are the type of instruments most widely considered for intensity mapping surveys. The small size of reflectors insures a large FOV ($\sim \left(\frac{\lambda}{D}\right)^2$ srad), and the dense packing concentrates the sensitivity in the $k_\perp$ range useful for LSS. Transit mode operation is well adapted for surveying large area of the sky, while reducing instrument complexity and cost. Initially, cylindrical reflectors, with their axis or the focal line oriented along the north-south direction were proposed [43], and implemented in the Pittsburgh CRT (Cylindrical Radio Telescope) prototype and then in CHIME, as well as in Tianlai. It was then realised that packed dish arrays might have some advantages, despite a smaller FOV and

z	$\delta\theta$ (arcmin)	d_{LOS} (Mpc)	H(z) (km/s/Mpc)	$a_\perp$ (Mpc)	$a_\parallel$ (Mpc)
0.5	13'	1950	90	7.2	1.3
1.0	17'	3530	120	17.3	1.8
1.5	21'	4660	160	28.5	2.2
2.0	26'	5310	200	39.	2.3
2.5	30'	5970	255	50.	2.5
3.0	34'	6500	308	63.	2.7

Table 1: Evolution of the transverse $a_\perp$ and the radial $a_\parallel$ resolutions of a radio array with $L = 100$m size, and 250kHz frequency resolution as a function of redshift, in the standard ΛCDM cosmology.

the need to change dish pointing in declination to cover a large enough sky area. PAON4 and Tianlai are early examples of dish based pathfinder instruments (see section 4).

Radio instruments are inherently diffraction limited with their angular resolution degrading at longer wavelengths, hence with redshift. The projected spatial resolution will in addition vary with redshift, depending on the cosmological distance scales, namely the line of sight distance $d_{LOS}(z)$ and Hubble parameter $H(z)$. Values of transverse and longitudinal spatial resolution of maps obtained with a radio array covering a $\sim 100 \times 100\text{m}^2$ area and with a 250kHz resolution are gathered in table 1. The approximate level of instrument noise projected on sky for a ~ 1600 element arrays, covering a $200 \times 200\text{m}^2$, surveying $\sim 5000\text{deg}^2$ over a year is shown in the figure 2, computed according to the scaling formula in [35]. One can see that the resolution, hence the projected noise level degrades quickly with increasing redshift. A few hundred element interferometer with a few thousands m^2 collecting area might be sufficient to detect the signal up to $z \lesssim 1$, while larger instruments, with 10^4 feeds and $\sim 10^5\text{m}^2$ are required to reach higher redshifts $z \sim 2 - 3$.

Reconstructing sky maps, from visibilities which are cross correlation signals measured by interferometers has been and is still a technical challenge and major efforts have been devoted to develop accurate and efficient map making methods and tools. The transit operation mode, with observations covering the full 24 hours of right ascensions, combined with the large covered sky area, has led to the development of mathematically rigorous and efficient methods to reconstruct sky maps from transit visibilities. These methods operate in the spherical harmonic (ℓ, m) domain, and take advantage of the full 24 hours coverage to decompose visibilities into m-modes. The huge matrix representing the linear relation between time dependent visibilities and the sky can be written as a block diagonal matrix in this representation, making the numerical problem tractable [44,45].

As stated in section 2 the 21cm signal is several orders of magnitude fainter than the broad band emissions from the Milky Way the te radio-sources. The foreground subtraction or component separation is a major difficulty in Intensity Mapping surveys, probably more challenging than in CMB experiments. The different approaches relie all on the foreground brightness varying smoothly with frequency, behaving as power laws, while the signal that follows the matter density fluctuations is structured along the frequency, corresponding to the radial direction. The inherent frequency dependence of the interferometer beam makes the foreground subtraction even more difficult. This is usually referred to as *mode mixing* as the angular modes probed by a given baseline changes with frequency.

21cm Intensity Mapping shares many technical aspects, map making and foreground subtraction in particular with the search for the 21cm signal from the EoR [46]. Although signal-foreground separation might be effective on a per visibility basis with filtering along the frequency axis [47,48] many authors have explored the methods where signal and foreground components are projected into different sub spaces or modes [44,49,45,50].

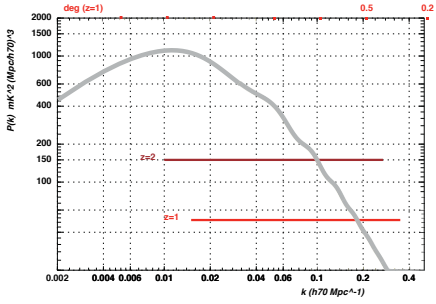

The power spectrum $P_{21}(k)$ in mK/(Mpc/h$_{70}$)^3 is plotted as a function of the comoving wavenumber k in $h_{70}\mathrm{Mpc}^{-1}$. The top scale shows the angular scales at $z \sim 1$ for the corresponding transverse $k_\perp$ wavemodes. The expected projected noise level, due to the instrument noise for $T_{\rm sys} \sim 50$K, in the white noise approximation, is also shown, at $z = 1$ and $z = 2$ for a survey of $\sim 5000\mathrm{deg}^2$, with an array of ~ 1600 dishes, covering $\sim 200 \times 200\mathrm{m}^2$. The noise level line extent shows the approximate accessible $k_\perp$ range.

Figure 2 – 21cm brightness temperature fluctuations power spectrum $P_{21}(k)$

4 Past, ongoing and future experiments

We review here some of the experimental and observational efforts initiated in the last decade to explore and possibly establish the faisability of observing large scale structures through 21cm intensity mapping. We start by mentionning some of the pioneering work performed using the GBT and Parkes radiotelescopes. We will then describe the dedicated pathfinder instruments, CHIME and Tianlai which have been specifically built to carry IM surveys, before presenting briefly few other projects, which are in the construction phase and will become operational in the coming years. Obviously, the list of projects mentioned here is incomplete.

The HI Parkes All Sky Survey (HIPASS) [51] was carried out from 1997 to 2001 with the 64 meter Parkes Australian telescope, equipped with the 21cm multi beam receiver [52]. It covers a large fraction of the southern, but also the northern sky, in the velocity range $-1280 < cz <$ 12700km/s, or $z \lesssim 0.042$. A positive cross-correlation of 21cm signal from HIPASS data cubes with galaxies from the 6dF [53] survey was reported in 2009 [54].

The fully steerable 100m diameter Green Bank Telescope (GBT) [b] has also been used to statistically detect the redshifted 21cm signal, in cross-correlation with optical surveys. Observations with the GBT have been carried out from 2010 to 2015, using the 680-920 MHz prime focus receiver covering the $0.6 \lesssim z \lesssim 1.0$ redshift range. A first cross-correlation detection from observation in DEEP2 fields [55] was reported in 2010 [56], confirmed with more data, using the WiggleZ [57] survey in 2013 [58]. The detection of the cosmological 21cm autocorrelation signal has also been claimed using the same data set [59]. More recently, using a subset of the GBT data, corresponding to about 100 hours of observations covering $\sim 100\mathrm{deg}^2$ and the SDSS-IV eBOSS and WiggleZ spectroscopic redshift catalogs, the HI gas fraction at redshift $z \sim 0.8$ has been measured [60], more precisely the product of hydrogren mass fraction, its bias and galaxy-hydrogen correlation coefficient ($\Omega_{H_I} b_{H_I} r_{H_I} \sim 0.35 - 0.6 \times 10^{-3}$ at $z \sim 0.8$).

Tianlai (Cosmic Sound in Chinese) is an international project led by NAOC, with US, French and Canadian contributions and is exploring 21cm Intensity Mapping. The collaboration operates two pathfinder instruments which have been built and installed in a radio quiet area in north-western China, a cylindrical reflectors (TCI) and a dish array interferometer (TDA). The observatory is located at (91°48′E, 44°09′N) and an altitude of $\sim$ 1500m, near Hongliuxia, about 500 km east of Urumqi, in the Xinjiang province. The feeds have been designed to cover a broad frequency range (400-1430 MHz), although the current digitisation and correlator electronic can only handle a narrower 100 MHz frequency interval. The frequency band is tunable by adjusting the local oscillator and changing the analog filters. All observations have been performed in the frequency band 700-800 MHz up to now.

[b] GBT: https://greenbankobservatory.org/

The TCI is composed of three cylinders, each 40 m long and 15 m wide. Only the central part of the focal line is currently instrumented with receivers. The three cylinders are equipped with a total of 96 dual polarisation feeds, representing 192 RF signals. The digital correlator computes 18528 visibilities from sampled signals, and channelised into 1024 frequency channels with 122kHz frequency resolution. Reference [61] present the basic system performance for the cylinder array.

The TDA is composed of 16 on-axis dishes, each 6 meter in diameter, arranged in a circular layout, with a central dish, surrounded by six dishes arranged as an hexagon, and then an outer ring with nine dishes. Although dishes are fully steerable, the array operates in transit mode, with all dishes fixed and pointed towards a given direction in the meridian plane. Each dish is equipped with a dual polarisation receiver, representing a total of 32 RF signals, sampled at 250 MSPS and 14 bits. A total of 528 visibilities (496 cross + 32 auto) are computed by an FPGA based correlator for 512 frequency channels with 244kHz resolution. A few thousand hours of observations have already been performed, with a significant fraction spent toward the NCP (North Celestial Pole). Indeed, one of the advantages of the dish arrays is their ability to be pointed toward a given declination band. By observing toward the NCP, it is possible to reach a high sensitivity over a small sky area. Detailed description of the Tianlai dish array and its performance, as well as preliminary results from deep observations toward the NCP can be found in reference [62].

Smaller instruments such as PAON4 [63] and BMX [64] have also been built to explore specific technical aspects of dish arrays operating in transit mode. PAON4 is a small, 4-dish test interferometer located at the Nançay radio observatory in France, operational since end of 2015. It consists in four D=5 m diameter dishes, equipped with dual linear polarisation feeds, arranged in a triangular layout with a fourth dish in the center. PAON4 is being upgraded and will serve as the qualification instrument for the new IDROGEN digitisation and processing electronic system. These FPGA (Field Programmable Gate Array) based boards exploits the White Rabbit technology [c] for precise clock synchronisation and can digitise L-band signals at the receivers, without frequency shifting. They can transfer waveform signals, or frequency components as digital streams over high throughput ($> 20Gb/s$) ethernet optical links.

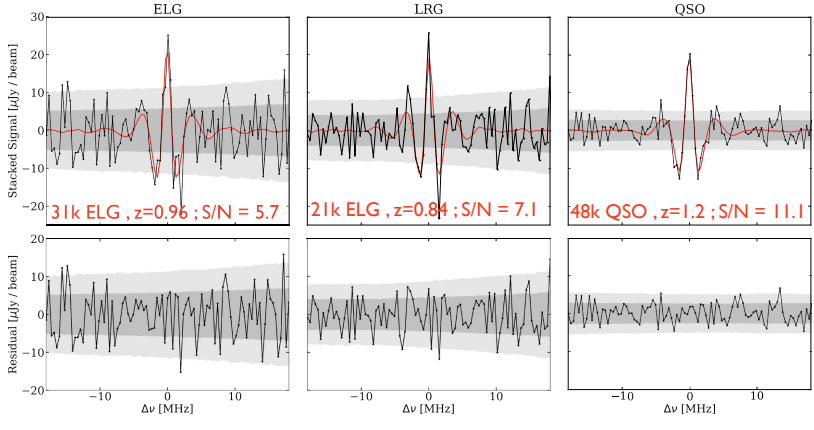

Figure 3 – Cross correlation of CHIME intensity maps with eBOSS galaxies and quasars. Top figures show the actual stacked signal in black, stacked on the positions of ELG's with mean redshift $\langle z \rangle = 0.96$ (left), LRG's with $\langle z \rangle = 0.84$ (center) and QSO with $\langle z \rangle = 1.2$ (right). The red curve corresponds to the best fit model and the bottom figures show the residuals, after best fit model subtraction. Adapted from [65]

[c] White Rabbit clock synchronisation over ethernet : https://white- rabbit.web.cern.ch

The Canadian Hydrogen Intensity Mapping Experiment (CHIME) [66] is a cylinder based interferometer designed and built for 21cm Intensity Mapping. It consists of four north-south oriented cylinderical reflectors, each 100m long and 20m wide, located at the DRAO observatory in Penticton, British Columbia (Canada). The instrument has a very broad bandwidth and covers the 400-800 MHz frequency range, corresponding to redshifts between 0.8 and 2.5. Each cylinder is fully instrumented and equipped with 256 dual polarisation feeds. The 2048 ($4 \times 2 \times 256$) analog signals are processed by an FX correlator. The F-engine uses FPGA custom designed electronics to perform digitisation and frequency decomposition into 1024 channels, each 390kHz wide. Correlations are computed for all N^2 feed pairs by the X-engine, which uses custom electronic for data exchange and 256 GPU nodes which perform the actual correlation computations. An overview of CHIME performance can be found in [67].

Thanks to their large FOV and bandwidth, Intensity Mapping instruments are also very efficient in detecting transient radio sources, such as FRB's (Fast Radio Bursts) [68] and pulsars. However, a specific backend is required to process the radio signals to search for fast transients. CHIME has proved to be a powerful radio burst and pulsar observation machine and has detected several hundred FRB's over a one year observation period [69].

Despite CHIME successful operation, efficient data processing and impressive performance, the detection of the 21cm cosmological signal appears more challenging than anticipated. However, CHIME has published very recently, in February 2022, [65] a sophisticated analysis showing convincing evidence for a correlation signal between CHIME intensity maps, and eBOSS [70] galaxies and quasars at redshifts $0.78 < z < 1.43$. Maps were reconstructed from over 100 nights of CHIME observations, then stacked on the angular and frequency positions of eBOSS galaxies and quasars, after filtering and foreground subtraction. Figure 4, adapted from [65], shows the stacked signals as a function of the frequency shift, for ELG's (Emission Line Galaxies), LRG's (Luminous Red Galaxies) and quasars (QSO), together with the best fit model.

BINGO (Baryon acoustic oscillations from Integrated Neutral Gas Observations) is a single dish instrument being built in Brazil [71]. It uses a off-axis $1600\text{m}^2, D \sim 50\text{m}$ primary reflector which illuminates a focal plane equipped with 28 horns through a secondary mirror. The whole optical setup is fixed and will observe a 15° wide declination band centered on $\delta = 15°$. The instrument covers the frequency range 980-1260 MHz corresponding to redshifts $0.13 < z < 0.45$.

HIRAX (Hydrogen Intensity and Real time Analysis eXperiment) [72] is a packed array interferometer using $D = 6\text{m}$ dishes and shares many technological components with CHIME. The 256 dish array, represents a total collecting area of $\sim 7200\text{m}^2$ being built. It will be located at the South African Radio Astronomy Observatory in the Karoo desert, a few kilometers away from the MeerKat site (The South African SKA precursor).

CHORD (Canadian Hydrogen Observatory and Radio transient Detector) [73] can be considered as a successor to CHIME, reusing many technologies developed for its predecessor, specially electronics and the FX correlator. But unlike CHIME, it will use 512 dishes, each 6m in diameter for the core array, representing a total collecting area of 14400m^2. The bandwidth will be slightly increased, covering the 300-1500 MHz band. Wide field of view outrigger stations located at large distances from the CHIME/CHORD instruments will also be built to enhance FRB localisation.

SKA, a very large general purpose interferometric radiotelescope, is being constructed by an international organisation [d]. A review of the cosmological surveys planned for SKA Phase-I, and their forecasted performance in the redshift range $0 < z < 3$ can be found in [74]. In addition to more traditional HI and continuum galaxy surveys at low redshifts $z < 0.35$, Intensity Mapping will enable to extend significantly the accessible redshift range, and even cover $3 < z < 6$ thanks to a deep survey over a 100deg^2 field. Finally, one can mention the PUMA white paper [42], which is a proposal for an ambitious close-packed interferometer array with 32000 dishes, covering the frequency range 200-1100 MHz ($0.3 < z < 6$), as a stage II intensity mapping instrument.

[d] SKA observatory: https://www.skaobservatory.org

5 Conclusions, discussion

21cm Intensity Mapping has emerged in the last decade as a novel, and possibly powerful method to map large scale structures at redshifts up to $z \sim 6$. Such surveys would be complementary to optical observations, and could be used to test and constrain the cosmological model, more specifically Dark Energy and Inflation. Densely packed interferometers with a large bandwidth of a few hundred MHz and large number of receivers (several hundreds to several thousands), observing in drift-scan or transit mode, without tracking, are the suitable instruments for such surveys. These instruments and projects share many technological issues, as well data analysis challenges, in particular calibration and foreground subtraction, with 21cm surveys for EoR, and more broadly, interferometers with large number of antennae. Few pathfinder and first stage instruments have been built to explore Intensity Mapping, and several others are planned or being constructed.

In the next few years, performance assessment and results from the ongoing and future IM experiments will shed light on some of the IM challenges. For example, it is important to show that it is possible to implement a cost effective design and construction process for a large number of antenna and receivers, as well as the associated electronics, while maintaining uniformity, construction quality and performance.

Precise array calibration is crucial to achieve large imaging dynamic range and to ensure foreground subtraction with the required precision. Among other aspects, it would be necessary to determine beam response for individual feeds, through a combination of electromagnetic simulations and on site beam measurements. Arrays with highly redundant baselines present many advantages for the calibration, whereas such arrays with many identical baselines, perform poorly in terms of mode mixing.

Structures in the instrumental frequency response, due to standing waves for example, should be minimized and precisely calibrated to be filtered out. Such frequency structures, if not corrected for, would indeed ruin the foreground subtraction. Another concern is the contribution of bright sources (sun, radiosources ...) through the far side lobes, which might be highly frequency dependent. It is also important to clarify the level of feed cross-couplings and correlated noise, which limits instrument sensitivity.

Faraday rotation causes linearly polarised sources to appear oscillating in frequency. The two linear polarisation measurements need to be combined during map making, to remove these oscillations, which in turn implies a good control of polarisation leakage and calibration. Also, some astrophysical effects such as self absorbed synchrotron might create higher order mode structures along the frequency axis, which would impact foreground subtraction.

Finally, I would like to mention that Line Intensity Mapping (LIM), using other atomic and molecular lines (CO, Carbon CII ...) [e] is also considered for astrophysics and cosmology surveys [75], although a discussion of LIM is well beyond the scope of this review.

Acknowledgments

I would like to thank my Tianlai and PAON4 collaborators, as well as CHIME colleagues, specially Olivier Perdrereau and Richard Shaw for valuable discussions.

References

1. Somnath Bharadwaj, Biman B. Nath, and Shiv K. Sethi. Using HI to Probe Large Scale Structures at z ~3. *Journal of Astrophysics and Astronomy*, 22:21, March 2001.
2. Richard A. Battye, Rod D. Davies, and Jochen Weller. Neutral hydrogen surveys for high-redshift galaxy clusters and protoclusters. MNRAS, 355(4):1339–1347, December 2004.

[e] Line Intensity Mapping : https://lambda.gsfc.nasa.gov/product/expt/lim_experiments.html

3. Steven R. Furlanetto, S. Peng Oh, and Frank H. Briggs. Cosmology at low frequencies: The 21 cm transition and the high-redshift Universe. Phys. Rep., 433(4-6):181–301, October 2006.
4. Jonathan R. Pritchard and Abraham Loeb. Evolution of the 21cm signal throughout cosmic history. Phys. Rev. D, 78(10):103511, November 2008.
5. Miguel F. Morales and J. Stuart B. Wyithe. Reionization and Cosmology with 21-cm Fluctuations. ARA&A, 48:127–171, Sep 2010.
6. Steven Furlanetto et al. Astro 2020 Science White Paper: Fundamental Cosmology in the Dark Ages with 21-cm Line Fluctuations. *arXiv:1903.06212*, 2019.
7. Jonathan R. Pritchard and Abraham Loeb. 21 cm cosmology in the 21st century. *Reports on Progress in Physics*, 75(8):086901, August 2012.
8. A. R. Parsons, D. C. Backer, G. S. Foster, et al. The Precision Array for Probing the Epoch of Re-ionization: Eight Station Results. AJ, 139:1468–1480, April 2010.
9. Tabitha C. Voytek, Aravind Natarajan, José Miguel Jáuregui García, Jeffrey B. Peterson, and Omar López-Cruz. Probing the Dark Ages at z ˜20: The SCI-HI 21 cm All-sky Spectrum Experiment. ApJ, 782(1):L9, February 2014.
10. Raul A. Monsalve, Alan E. E. Rogers, Judd D. Bowman, and Thomas J. Mozdzen. Calibration of the EDGES High-band Receiver to Observe the Global 21 cm Signature from the Epoch of Reionization. ApJ, 835(1):49, January 2017.
11. Adrian Liu, Jonathan R. Pritchard, Max Tegmark, and Abraham Loeb. Global 21 cm signal experiments: A designer's guide. Phys. Rev. D, 87(4):043002, February 2013.
12. Judd D. Bowman, Alan E. E. Rogers, Raul A. Monsalve, Thomas J. Mozdzen, and Nivedita Mahesh. An absorption profile centred at 78 megahertz in the sky-averaged spectrum. Nature, 555(7694):67–70, March 2018.
13. M. P. van Haarlem, M. W. Wise, A. W. Gunst, G. Heald, J. P. McKean, et al. LOFAR: The LOw-Frequency ARray. A&A, 556:A2, August 2013.
14. T. W. Shimwell, C. Tasse, M. J. Hardcastle, A. P. Mechev, W. L. Williams, P. N. Best, et al. The LOFAR Two-metre Sky Survey. II. First data release. A&A, 622:A1, February 2019.
15. Etienne Bonnassieux, Evangelia Tremou, Julien N. Girard, et al. Pilot Study and Early Results of the Cosmic Filaments and Magnetism Survey with Nenufar: The Coma Cluster Field. *Galaxies*, 9(4):105, November 2021.
16. Michael W. Eastwood, Marin M. Anderson, Ryan M. Monroe, et al. The Radio Sky at Meter Wavelengths: m-mode Analysis Imaging with the OVRO-LWA. AJ, 156(1):32, July 2018.
17. S. J. Tingay, R. Goeke, J. D. Bowman, D. Emrich, et al. The Murchison Widefield Array: The Square Kilometre Array Precursor at Low Radio Frequencies. PASA, 30:e007, January 2013.
18. J. C. Pober, A. Liu, J. S. Dillon, et al. What Next-generation 21 cm Power Spectrum Measurements can Teach us About the Epoch of Reionization. ApJ, 782:66, February 2014.
19. David R DeBoer, Aaron R Parsons, James E Aguirre, et al. Hydrogen epoch of reionization array (hera). *Publications of the Astronomical Society of the Pacific*, 129(974):045001, 2017.
20. F. G. Mertens, M. Mevius, L. V. E. Koopmans, A. R. Offringa, G. Mellema, S. Zaroubi, et al. Improved upper limits on the 21 cm signal power spectrum of neutral hydrogen at z $\approx$ 9.1 from LOFAR. MNRAS, 493(2):1662–1685, April 2020.
21. A. P. Beardsley, B. J. Hazelton, I. S. Sullivan, P. Carroll, N. Barry, M. Rahimi, et al. First Season MWA EoR Power spectrum Results at Redshift 7. ApJ, 833(1):102, December 2016.
22. Zara Abdurashidova, James E. Aguirre, Paul Alexander, Zaki S. et al. Ali, and HERA Collaboration. First Results from HERA Phase I: Upper Limits on the Epoch of Reionization 21 cm Power Spectrum. ApJ, 925(2):221, February 2022.
23. G. Mellema, L. Koopmans, H. Shukla, K. K. Datta, A. Mesinger, and S. Majumdar. HI tomographic imaging of the Cosmic Dawn and Epoch of Reionization with SKA. In *Advancing Astrophysics with the Square Kilometre Array (AASKA14)*, page 10, April 2015.
24. Andrew R. Liddle and David H. Lyth. *Cosmological Inflation and Large-Scale Structure*. 2000.
25. Christian Knobel. An Introduction into the Theory of Cosmological Structure Formation. *arXiv:1208.5931*, Aug 2012.
26. L. Amendola, M. Kunz, M. Motta, I. D. Saltas, and I. Sawicki. Observables and unobservables in dark energy cosmologies. Phys. Rev. D, 87(2):023501, January 2013.
27. K. N. Abazajian, K. Arnold, J. Austermann, et al. Neutrino physics from the cosmic microwave background and large scale structure. *Astroparticle Physics*, 63:66–80, Mar 2015.
28. Chris Blake and Karl Glazebrook. Probing Dark Energy Using Baryonic Oscillations in the Galaxy Power Spectrum as a Cosmological Ruler. ApJ, 594(2):665–673, Sep 2003.

29. Shadab Alam, Marie Aubert, Santiago Avila, et al. Completed SDSS-IV extended Baryon Oscillation Spectroscopic Survey: Cosmological implications from two decades of spectroscopic surveys at the Apache Point Observatory. Phys. Rev. D, 103(8):083533, April 2021.
30. T. M. C. Abbott, M. Aguena, A. Alarcon, et al. Dark Energy Survey Year 3 results: Cosmological constraints from galaxy clustering and weak lensing. Phys. Rev. D, 105(2):023520, January 2022.
31. Martha P. Haynes, Riccardo Giovanelli, Brian R. Kent, et al. The arecibo legacy fast alfa survey: The alfalfa extragalactic h i source catalog. *The Astrophysical Journal*, 861(1):49, Jul 2018.
32. Tzu-Ching Chang, Ue-Li Pen, Jeffrey B. Peterson, and Patrick McDonald. Baryon Acoustic Oscillation Intensity Mapping of Dark Energy. Phys. Rev. Lett., 100(9):091303, March 2008.
33. R. Ansari, J. . Le Goff, C. Magneville, et al. Reconstruction of HI power spectra with radio-interferometers to study dark energy. *ArXiv e-prints*, July 2008.
34. Hee-Jong Seo, Scott Dodelson, John Marriner, et al. A Ground-based 21 cm Baryon Acoustic Oscillation Survey. ApJ, 721(1):164–173, September 2010.
35. R. Ansari, J. E. Campagne, P. Colom, et al. 21 cm observation of large-scale structures at z ~1. Instrument sensitivity and foreground subtraction. A&A, 540:A129, April 2012.
36. L. Wolz, F. B. Abdalla, C. Blake, et al. The effect of foreground subtraction on cosmological measurements from intensity mapping. MNRAS, 441(4):3271–3283, July 2014.
37. Philip Bull, Pedro G. Ferreira, Prina Patel, and Mário G. Santos. Late-time Cosmology with 21 cm Intensity Mapping Experiments. ApJ, 803(1):21, April 2015.
38. Francisco Villaescusa-Navarro, Shy Genel, Emanuele Castorina, et al. Ingredients for 21 cm Intensity Mapping. ApJ, 866(2):135, October 2018.
39. George F. Smoot and Ivan Debono. 21 cm intensity mapping with the Five hundred metre Aperture Spherical Telescope. A&A, 597:A136, January 2017.
40. Marta Spinelli, Isabella P. Carucci, Steven Cunnington, Stuart E. Harper, Melis O. Irfan, José Fonseca, Alkistis Pourtsidou, and Laura Wolz. SKAO H I intensity mapping: blind foreground subtraction challenge. MNRAS, 509(2):2048–2074, January 2022.
41. Cosmic Visions 21 cm Collaboration, Réza Ansari, Evan J. Arena, Kevin Bandura, Philip Bull, et al. Inflation and Early Dark Energy with a Stage II Hydrogen Intensity Mapping Experiment. *arXiv e-prints*, page arXiv:1810.09572, Oct 2018.
42. Kevin Bandura, Emanuele Castorina, Liam Connor, et al. Packed Ultra-wideband Mapping Array (PUMA): A Radio Telescope for Cosmology and Transients. *arXiv:1907.12559*, Jul 2019.
43. Jeffrey B. Peterson, Kevin Bandura, and Ue Li Pen. The Hubble Sphere Hydrogen Survey. *arXiv e-prints*, pages astro–ph/0606104, June 2006.
44. J. Richard Shaw, Kris Sigurdson, Ue-Li Pen, et al. All-sky Interferometry with Spherical Harmonic Transit Telescopes. ApJ, 781(2):57, February 2014.
45. Jiao Zhang, Reza Ansari, Xuelei Chen, Jean-Eric Campagne, Christophe Magneville, and Fengquan Wu. Sky reconstruction from transit visibilities: PAON-4 and Tianlai dish array. MNRAS, 461(2):1950–1966, September 2016.
46. Joshua S. Dillon, Max Tegmark, Adrian Liu, et al. Mapmaking for precision 21 cm cosmology. Phys. Rev. D, 91(2):023002, January 2015.
47. Aaron R. Parsons, Jonathan C. Pober, James E. Aguirre, et al. A Per-baseline, Delay-spectrum Technique for Accessing the 21 cm Cosmic Reionization Signature. ApJ, 756(2):165, September 2012.
48. Miguel F. Morales, Bryna Hazelton, Ian Sullivan, and Adam Beardsley. Four Fundamental Foreground Power Spectrum Shapes for 21 cm Cosmology Observations. ApJ, 752(2):137, June 2012.
49. J. Richard Shaw, Kris Sigurdson, Michael Sitwell, et al. Coaxing cosmic 21 cm fluctuations from the polarized sky using m -mode analysis. Phys. Rev. D, 91(8):083514, April 2015.
50. Shifan Zuo, Xuelei Chen, Reza Ansari, and Youjun Lu. 21 cm Signal Recovery via Robust Principal Component Analysis. AJ, 157(1):4, January 2019.
51. M. J. Meyer, M. A. Zwaan, R. L. Webster, L. Staveley-Smith, et al. The HIPASS catalogue - I. Data presentation. MNRAS, 350(4):1195–1209, June 2004.
52. L. Staveley-Smith, W. E. Wilson, T. S. Bird, M. J. Disney, R. D. Ekers, and K. C. Freeman. The Parkes 21 CM multibeam receiver. *Publications Astronomical Society of Australia*, 13(3):7, 1996.
53. D. Heath Jones, Mike A. Read, Will Saunders, et al. The 6dF Galaxy Survey: final redshift release (DR3) and southern large-scale structures. MNRAS, 399(2):683–698, October 2009.
54. Ue-Li Pen, Lister Staveley-Smith, Jeffrey B. Peterson, and Tzu-Ching Chang. First detection of cosmic structure in the 21-cm intensity field. MNRAS, 394(1):L6–L10, March 2009.
55. Jeffrey A. Newman, Michael C. Cooper, Marc Davis, et al. The DEEP2 Galaxy Redshift Survey:

Design, Observations, Data Reduction, and Redshifts. ApJS, 208(1):5, September 2013.
56. Tzu-Ching Chang, Ue-Li Pen, Kevin Bandura, and Jeffrey B. Peterson. An intensity map of hydrogen 21-cm emission at redshift z˜0.8. Nature, 466(7305):463–465, July 2010.
57. Michael J. Drinkwater, Russell J. Jurek, Chris Blake, et al. The WiggleZ Dark Energy Survey: survey design and first data release. MNRAS, 401(3):1429–1452, January 2010.
58. K. W. Masui, E. R. Switzer, N. Banavar, K. Bandura, et al. Measurement of 21 cm Brightness Fluctuations at z ˜0.8 in Cross-correlation. ApJ, 763(1):L20, January 2013.
59. E. R. Switzer, K. W. Masui, K. Bandura, et al. Determination of z ˜0.8 neutral hydrogen fluctuations using the 21cm intensity mapping autocorrelation. MNRAS, 434:L46–L50, July 2013.
60. Laura Wolz, Alkistis Pourtsidou, Kiyoshi W. Masui, et al. H I constraints from the cross-correlation of eBOSS galaxies and Green Bank Telescope intensity maps. MNRAS, 510(3):3495–3511, March 2022.
61. JiXia Li, ShiFan Zuo, FengQuan Wu, et al. The Tianlai Cylinder Pathfinder array: System functions and basic performance analysis. *Science China Physics, Mechanics, and Astronomy*, 63(12):129862, September 2020.
62. Fengquan Wu, Jixia Li, Shifan Zuo, Xuelei Chen, et al. The Tianlai dish pathfinder array: design, operation, and performance of a prototype transit radio interferometer. MNRAS, 506(3):3455–3482, September 2021.
63. R. Ansari, J. E. Campagne, D. Charlet, et al. Design, operation and performance of the PAON4 prototype transit interferometer. MNRAS, 493(2):2965–2980, April 2020.
64. Paul O'Connor, Anže Slosar, Maile Harris, et al. The Baryon Mapping eXperiment: a 21cm intensity mapping pathfinder. In *SPIE Conference Series*, volume 11445, December 2020.
65. CHIME Collaboration, Mandana Amiri, Kevin Bandura, et al. Detection of Cosmological 21 cm Emission with the Canadian Hydrogen Intensity Mapping Experiment. February 2022.
66. Kevin Bandura, Graeme E. Addison, Mandana Amiri, J. Richard Bond, et al. Canadian Hydrogen Intensity Mapping Experiment (CHIME) pathfinder. In *Ground-based and Airborne Telescopes V*, volume 9145 of *SPIE Conf. Series*, page 914522, July 2014.
67. The CHIME Collaboration, Mandana Amiri, Kevin Bandura, Anja Boskovic, Tianyue Chen, et al. An Overview of CHIME, the Canadian Hydrogen Intensity Mapping Experiment. page arXiv:2201.07869, January 2022.
68. E. Petroff, J. W. T. Hessels, and D. R. Lorimer. Fast radio bursts. A&A Rev., 27(1):4, May 2019.
69. The CHIME/FRB Collaboration, :, Mandana Amiri, Bridget C. Andersen, Kevin Bandura, et al. The First CHIME/FRB Fast Radio Burst Catalog. page arXiv:2106.04352, June 2021.
70. Kyle S. Dawson, Jean-Paul Kneib, Will J. Percival, Shadab Alam, et al. The SDSS-IV Extended Baryon Oscillation Spectroscopic Survey: Overview and Early Data. AJ, 151(2):44, February 2016.
71. Carlos A. Wuensche, Thyrso Villela, Elcio Abdalla, et al. The BINGO Project II: Instrument Description. *arXiv e-prints*, page arXiv:2107.01634, July 2021.
72. Devin Crichton, Moumita Aich, et al. The Hydrogen Intensity and Real-time Analysis eXperiment: 256-Element Array Status and Overview. page arXiv:2109.13755, September 2021.
73. Keith Vanderlinde, Adrian Liu, Bryan Gaensler, Dick Bond, Gary Hinshaw, et al. The Canadian Hydrogen Observatory and Radio-transient Detector (CHORD). In *Canadian Long Range Plan for Astronomy and Astrophysics White Papers*, volume 2020, page 28, October 2019.
74. Square Kilometre Array Cosmology Science Working Group, David J. Bacon, Richard A. Battye, Philip Bull, et al. Cosmology with Phase 1 of the Square Kilometre Array Red Book 2018: Technical specifications and performance forecasts. PASA, 37:e007, March 2020.
75. Ely D. Kovetz, Marco P. Viero, Adam Lidz, Laura Newburgh, et al. Line-Intensity Mapping: 2017 Status Report. *arXiv e-prints*, page arXiv:1709.09066, September 2017.

Patchy Reionization: $\tau-$21 cm cross-correlation and $B-$mode contamination

Andrea Lapi
SISSA, Via Bonomea 265, 34136 Trieste, Italy

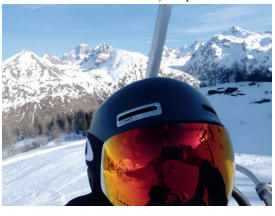

I discuss how patchy reionization can be probed via the cross-correlation between the optical depth for electron scattering τ as measured by CMB observations, and the 21 cm emission as measured from ground-based radio arrays. I also discuss the contamination of patchy reionization to the CMB $B-$mode polarization and the bias induced on the estimates of the scalar-to-tensor ratio.

1 Introduction

A few tenths billion years after the Big Bang (redshift $z \sim 10-20$) first galaxies and quasars light up and release into the interstellar and intergalactic medium huge amount of ionizing radiation. As illustrated in Fig. 1, ionization fronts and bubbles develop around these clustered sources, expand into the ambient medium, progressively overlap and eventually merge together, fully ionizing large portions of the Universe. This intrinsically patchy process, known as cosmic reionization, is completed at around $z \sim 6$.

2 $\tau-$21 cm cross-correlation

The ionized hydrogen fraction x_{HII} can be probed via the electron scattering optical depth

$$\tau(<z) = c\,\sigma_T\,\bar{n}_H \int_0^z \mathrm{d}z'\,\frac{(1+z')^2}{H(z')}\,f_e\,(1+\delta_b)\,x_{HII}(z') \tag{1}$$

as measured from CMB observations. The complementary neutral hydrogen fraction x_{HI} can be probed by the 21 cm emission from the hyperfine spin flip transition of the H atom, in terms of the 21 cm differential brightness temperature

$$\Delta T_{21} \approx 23\left(\frac{1+z}{8}\right)^{1/2}(1+\delta_b)\,x_{HI}\left(\frac{T_S - T_{CMB}}{T_S}\right)\,\mathrm{mK} \tag{2}$$

as measured from ground-based radio arrays. Patchy reionization induces spatial fluctuations in τ and ΔT_{21} along different lines of sight, that can be related as

$$\delta\tau \approx 0.0035\int \mathrm{d}z\,\left[(1+z)^{1/2}\,\delta_b - \frac{\delta[\Delta T_{21}(z)]}{8.8\,\mathrm{mK}}\right]\,. \tag{3}$$

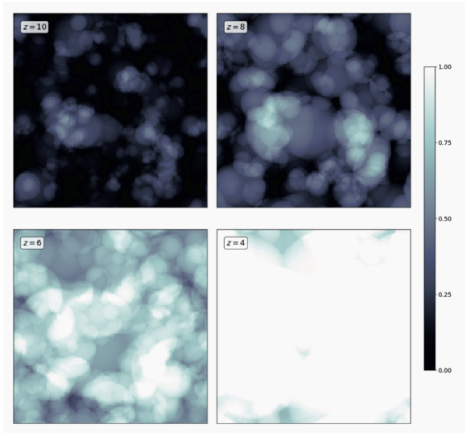

Figure 1 – Evolution of the ionization fraction (color-coded: darker color corresponds to more neutral, whiter to more ionized medium) according to a semi-empirical model of cosmic reionization.

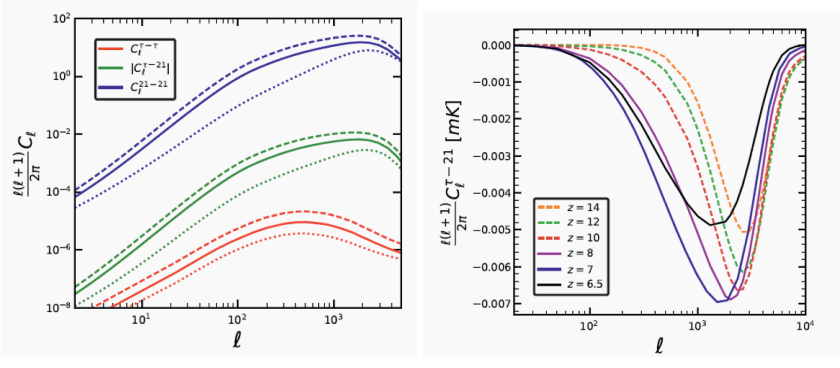

Figure 2 – Left: auto and cross-correlation power spectra at a reference redshift $z \approx 7$. Right: $\tau-21$ cross-correlation at different redshifts.

The $\tau-21$ cm cross-correlation power spectrum coefficients can be written as

$$C_\ell^{\tau 21} \approx T_0(z)\, \bar{n}_H\, \sigma_T\, f_e \int \frac{\mathrm{d}\chi}{a^2\, \chi^2}\, W(z,\chi)\, P\left(\chi, k = \frac{\ell}{\chi}\right) , \tag{4}$$

where P is the cross-spectrum; the window function W takes into account the narrow frequency band $\Delta\nu$ of ground-based radio arrays, which translates into a resolution in redshift or comoving distance $\Delta\chi \approx (\Delta\nu/0.1\,\mathrm{MHz})\,[(1+z)/10]^{1/2}$. Fig. 2 (left) shows the (absolute value of the) $\tau-21$ cross-correlation at a reference redshift $z \approx 7$, highlighting that it strikes an intermediate course between the τ and 21 cm autospectra. Fig. 2 (right) displays a tomographic view of the $\tau-21$ cross-correlation, which features an inverse bell shape. The minimum is deeper at the redshift where the Universe is 50% ionized. In addition, the location in scale (multipole) of the minimum and the width of the bell shape are strictly related to the typical size and spread of the ionizing bubble (typically lognormal) distribution. Thus tomographic measurements of the $\tau-21$ cross-correlation can yield relevant information on the physics of reionization sources.

This program struggles against the possibility to reconstruct the cross-correlation, taking into account instrumental noise and foregrounds. The signal-to-noise ratio for the cross-correlation

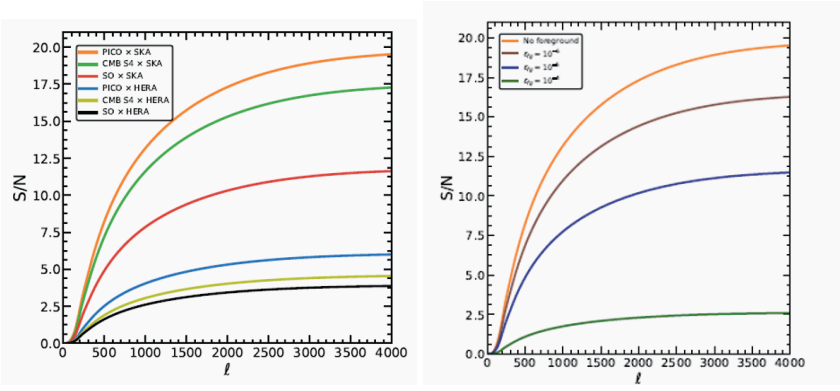

Figure 3 – Left: Signal-to-noise ratio for the reconstruction of the $\tau-21$ cross-correlation at a reference redshift $z \approx 7$ via combination of future CMB and 21 cm experiments. Right: effect of residual foreground contamination in 21 cm signal on the signal-to-noise ratio, for the reference PICO×SKA configuration.

can be computed as

$$\left(\frac{S}{N}\right)^2_z = f_{\rm sky} \sum_\ell (2\ell+1) \int_z {\rm d}z' \, \frac{|C_\ell^{\tau 21}(z')|^2}{(C_\ell^{\tau\tau} + N_\ell^{\tau\tau}) \times (C_\ell^{2121} + N_\ell^{2121})} \, . \tag{5}$$

Fig. 3 (left) shows the S/N expected for the reconstruction of the $\tau-21$ cross-correlation at a reference redshift $z \approx 7$ via combination of future CMB and 21 cm experiments, when only instrumental noise is included. The computed S/N are well above 5σ for almost all the combinations, with the best sensitivity achieved from PICO×SKA. For the latter configuration, Fig. 3 (right) shows the effect of residual foreground contamination in the 21 cm signal on the S/N. The analysis indicates that future 21 cm experiment should remove the foreground at the level of $> 5 \times 10^{-4}$ to detect the cross-correlation signal at a significance of 5σ.

3 Contamination to $B-$mode polarization

Patchy reionization can induce secondary $B-$mode polarization anisotropies in CMB radiation. The related power spectrum coefficients are written as

$$C_\ell^{BB} = C_\ell^{sca} + C_\ell^{scr} \, , \tag{6}$$

where the first term

$$C_\ell^{sca} \approx \frac{3\,\sigma_T^2\,\bar{n}_{p,0}^2}{100} \int {\rm d}\chi \, \frac{Q_{\rm rms}^2(\chi)}{a^4\,\chi^2} \, P_{x_e\,x_e}\left(k = \frac{\ell+1/2}{\chi}; \chi\right) \, e^{-2\,\bar{\tau}(\chi)} \tag{7}$$

is due to the Thomson scattering of the local CMB temperature quadrupole anisotropy off the inhomogeneous free electrons, while the second

$$C_\ell^{scr} \approx \frac{e^{-2\,\bar{\tau}}}{8\,\pi^2} \int {\rm d}^2\ell \, C_\ell^{EE(p)} \, C_\ell^{\tau\tau} \tag{8}$$

is due to the primary polarization being screened (i.e., scattered out of the line of sight) by the anisotropic optical depth. Fig. 4 (left) shows that patchy reionization induces a $B-$mode spectral shape similar to lensing $B-$modes, but with much lower amplitude. Patchy reionization

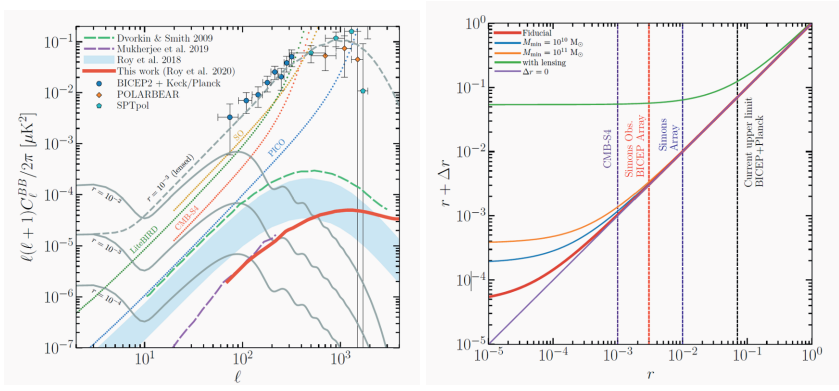

Figure 4 – Left: B-mode power spectrum, including the contamination induced by patchy reionization (thick red line). Right: bias on the scalar-to-tensor ratio r by patchy reionization (after 90% delensing).

has limited impact on $B-$mode searches for scalar-to-tensor ratio $r > 10^{-3}$, while it can be an issue if r approaches 10^{-4}. The related bias on the determination of r is given by

$$\Delta r = \frac{\sum_\ell C_\ell^{BB(sec)} C_\ell^{BB}(r=1)/\Delta C_\ell^2}{\sum_\ell [C_\ell^{BB}(r=1)]^2/\Delta C_\ell^2} \,. \tag{9}$$

Fig. 4 (right) illustrates that, after 90% delensing, patchy reionization can induce a $< 30\%$ bias on r for values $r > 10^{-3}$, while the bias increases up to 70% for $r \sim 10^{-4}$.

4 Summary

Reionization, being caused by the ionizing radiation emitted from clustered sources as primeval galaxies and quasars, is an intrinsically patchy process. Cross-correlation of CMB and 21cm can constitute a powerful probe of patchy reionization, if foregrounds are properly cleaned. In addition, patchy reionization induced $B-$mode signal could contaminate the primordial one for scalar-to-tensor ratio r smaller than 10^{-3}.

Acknowledgments

This presentation is based on the papers [1] and [2]. Most of the work has been carried out by Anirban Roy, my former Ph.D. student at SISSA (Italy) and now postdoc at Cornell (USA). I warmly thank D. Spergel and C. Baccigalupi for support and fruitful collaborations.

References

1. Roy, A., Kulkarni, G., Meerburg, P.D., Challinor, A., Baccigalupi, C., Lapi, A. , Haehnelt, M.G. 2021, JCAP, 1, 3
2. Roy, A., Lapi, A., Spergel, D., Basak, S., Baccigalupi, C. 2020, JCAP, 3, 62

Reionization constraints from HERA 21cm power spectrum limits

Stefan Heimersheim
Institute of Astronomy, University of Cambridge,
Madingley Road, Cambridge CB3 0HA, UK

I present our analysis of the 21cm power spectrum upper limits from the HERA radio interferometer, published in HERA Collaboration et al. 2022 [1]. We use the recent limits to constrain reionization and the properties of the IGM and galaxies in the early universe. I focus in particular on the possibility of a radio background in addition to the CMB (e.g. produced by early galaxies) which can lead to a stronger 21cm signal and is thus easier to constrain. I show what limits the HERA observations can put on these models and the IGM, and how this compares to existing constraints on the radio and X-ray background.

1 Introduction

Over the last decades we have explored both, the nearby Universe of quasars and galaxies, as well as the furthest edge of the observable Universe with the Cosmic Microwave Background. 21cm cosmology aims to fill the gap in between, probing the neutral hydrogen from Cosmic Dawn to the Epoch of Reionization, and now it is a focus of many instruments.

The key observational target is the signature of the 21cm hydrogen line seen against the background radiation. The line corresponds to the neutral-hydrogen hyperfine transition which can cause absorption or emission at the (redshifted) 1.42 GHz frequency. This deviation from the smooth spectrum of the background radiation can, in principle, be observed today. One of the telescopes aiming to detect the 21cm signal is the HERA radio interferometer in South Africa [2].

The strength of the 21cm signal is determined by the 21cm *brightness temperature,* T_{21}, which depends on the difference between the background radiation intensity (*radiation temperature,* T_{rad}) and the Hydrogen spin distribution (*spin temperature,* T_S), illustrated in Figure 1. The latter couples to the gas temperature T_K as soon as Ly-α photons are abundant (via the Wouthuysen-Field effect), which is usually the case for signals detectable by HERA. T_{21} is proportional to $(1 - T_{\text{rad}}/T_S)$, allowing for a positive signal (increase over the background by up to $\sim 30\,\text{mK}$), or a negative signal (absorbing a fraction of the background).

2 Methods

2.1 Data

The results presented here are based on the first public HERA data release [a], measurements taken with 39 science-quality antennas over 18 nights of observations. In particular we use the data originating from a low-foreground part of the sky (HERA *Field 1*).

A detailed description of the measurements and derived power spectra is provided in the HERA Upper Limits paper [3], but the key takeaway from the analysis is that the measurements constitute *upper limits* on the value of the cosmological 21cm power spectrum Δ^2_{21} as the observed values include non-cosmological "systematics" contributions. Marginalizing over possible systematic contributions we obtain a likelihood L_m for a given theoretical power spectrum Δ^2_{21} which is essentially a smoothed step function at the observed values.

2.2 Analysis

We model the 21cm power spectrum using a semi-numerical simulation most recently updated by Reis, Fialkov and Barkana [4]. The simulation covers a volume of 384 comoving Mpc side length with 3 comoving Mpc resolution and redshifts from Dark Ages ($z \sim 60$) to $z = 5$. We vary a number of parameters such as the minimum circular velocity V_c of star-forming halos and the fraction of collapsed gas forming stars f_*. Together these parameters determine the amount of stars and star forming halos, and thus scale the emission of radiation. Next we select the X-ray efficiency f_X and radio efficiency f_r relative to the present day population, and finally vary the amount of ionizing radiation emitted, mapping to a certain reionization optical depth τ.

To put constraints on these 5 parameters we need to vary all parameters at the same time, allowing us to derive marginalized 1D and 2D posteriors for every parameter and combination. For this we use a Markov Chain Monte Carlo (MCMC) method, specifically the ensemble sampler `emcee` [b]. To analyze and plot the resulting parameter samples we use the codes `anesthetic` [c] and `GetDist` [d]. In this process we use a neural network (emulator) to predict the power spectrum from the parameters. This essentially serves to interpolate between 10,000 existing simulation runs and significantly accelerates our analysis. This emulation introduces a relative error of about 20% but this is lower than the observational uncertainty of our data and has little effect on the likelihood. The full details of the simulation and analysis methods as well as all our results can be found in the HERA Astrophysical Constraints paper [1].

3 Results

We focus here on models which include the option for extra radio background sourced by early galaxies, and show what constraints the current HERA limits can provide on these models. Out of the 5 parameters we vary, only two have a significant effect on the posterior. The X-ray heating efficiency f_X and the radio efficiency f_r have large effects on the 21cm power spectrum as they determine the contrast between the gas temperature (heated by X-rays) and the background radiation (boosted by radio galaxies), and thus how large the 21cm signal and power spectrum can be (see Figure 1).

Figure 2 shows the posterior distribution of these two parameters, as well as their 2D posterior histogram. The 2D histogram clearly shows that most models with $f_X < 0.25$ and $f_r > 397$ (orange lines, approximately corresponding to the 95% confidence contours) are ruled out independently of the other parameters. This is corroborated by the 1D posteriors, indicating that values of $f_X < 0.25$ or $f_r > 397$ are disfavoured at 68% confidence level.

[a] `https://reionization.org/science/public-data-release-1/`
[b] `https://emcee.readthedocs.io/`
[c] `https://anesthetic.readthedocs.io/`
[d] `https://getdist.readthedocs.io/`

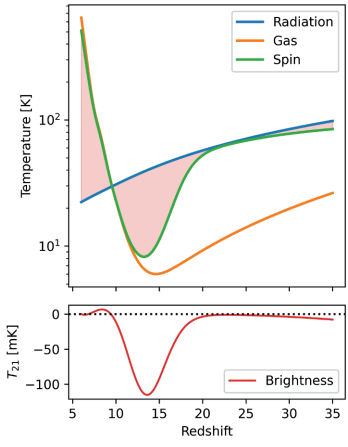

Figure 1: Radiation (blue), gas (orange) and spin (green) temperature evolution with redshift, illustrating the contrast (red area) that determines the 21cm brightness temperature (red line below).

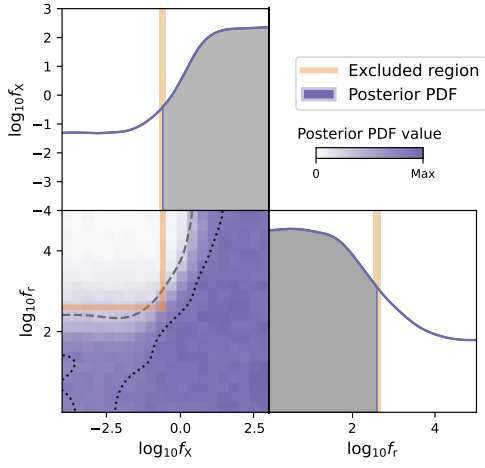

Figure 2: 1D and 2D marginalized posterior probability distributions for the two most relevant model parameters, f_X and f_r. The purple colour indicates the probability density, while the black lines show 68% and 95% 2D iso-probability contours.

To put these values into context we consider the level of radio and X-ray background observed today. The ARCADE2 experiment gives a limit on the radio background in excess of the CMB (approximately scales with $f_* \cdot f_r$), and the Chandra observations of unresolved X-ray background impose a bound on the amount of X-ray background produced (roughly proportional to $f_* \cdot f_X$). We impose these bounds as conservative constraints on our models, checking whether the models produce backgrounds exceeding these limits by redshift 8. Figure 3 (left) contains samples in this parameter space, showing a fraction of models excluded as they exceed the Chandra limit (marked with crosses), some models allowed by Chandra but exceeding ARCADE2/LWA measurements (empty circles), and the remaining parameter points as filled circles. We demonstrate which models can be constrained by HERA using the color scale, points in purple are compatible with HERA while points in orange are ruled out with a loglikelihood difference $\Delta \log L_m > 20$. HERA can clearly constrain a significant fraction of the models allowed by Chandra and ARCADE2/LWA, and complement these experiments.

In Figure 3 (right) we switch from model parameters to IGM properties and deliver a constraint on temperatures of the intergalactic gas $\bar{T}_K$ and the background radiation $\bar{T}_{\rm rad}$. Unlike in the case of model parameters, our priors here are not uniform so we show the prior distribution of temperatures in our model (orange) as well as the posterior (purple) after applying the HERA constraints. We see a clear bound on the ratio between radiation- and gas temperature; large ratios of $\log_{10}(\bar{T}_{\rm rad}/\bar{T}_K) > 1.1$ are ruled out at 95% confidence level.

Finally we briefly discuss standard models, without any radio background beyond the CMB, constrained by HERA together with complementary probes. In this case the strongest signals can be achieved with a cold IGM (little heating) and thus HERA mainly provides a lower limit on the the X-ray luminosity per star formation rate, constraining $L_{X<2\,\rm keV}/SFR$ to be in $[10^{40.2}, 10^{41.9}]$ at 68% confidence level. More details on this as well as further constraints can be found in the HERA paper [1].

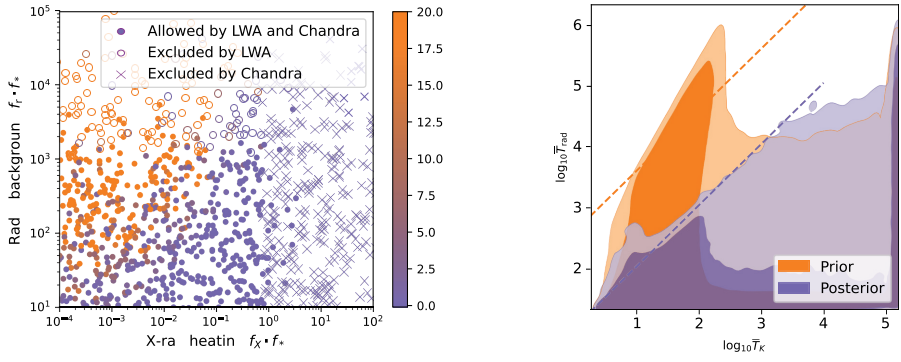

Figure 3: **Left:** Model parameter samples in $f_r \cdot f_* – f_X \cdot f_*$ space illustrating the LWA/ARCADE2 and Chandra constraints on parameter space. The colour indicates the HERA likelihood, showing models ruled out at $\gtrsim 4\sigma$ in orange. **Right:** Prior and posterior distribution of modelled radiation and gas temperatures at $z = 8$.

Acknowledgments

My presentation is based on work done together with the HERA Collaboration, summarized in a collaboration paper [1]. The work I focused on here would not have been possible without the support of the whole collaboration, especially my supervisor Anastasia Fialkov, and Steven R. Furlanetto who led the HERA Theory team. The additional results presented in my presentation are based on sections led by Jordan Mirocha, Julian B. Muñoz, Nicholas S. Kern, Steven G. Murray, and Yuxiang Qin. Beyond these headline names I want to explicitly thank everyone else who has contributed to the paper [e].

References

1. The HERA Collaboration, Astrophys. J. **924**, 51 (2022).
2. DeBoer et al., Publ. Astron. Soc. Pac. **129**, 045001 (2017)
3. The HERA Collaboration, Astrophys. J. **925**, 221 (2022).
4. Reis et al., Mon. Not. R. Astron. Soc. **506**, 5479 (2021)

[e] Zara Abdurashidova, James E. Aguirre, Paul Alexander, Zaki S. Ali, Yanga Balfour, Rennan Barkana, Adam P. Beardsley, Gianni Bernardi, Tashalee S. Billings, Judd D. Bowman, Richard F. Bradley, Philip Bull, Jacob Burba, Steve Carey, Chris L. Carilli, Carina Cheng, David R. DeBoer, Matt Dexter, Eloy de Lera Acedo, Joshua S. Dillon, John Ely, Aaron Ewall-Wice, Nicolas Fagnoni, Anastasia Fialkov, Randall Fritz, Steven R. Furlanetto, Kingsley Gale-Sides, Brian Glendenning, Deepthi Gorthi, Bradley Greig, Jasper Grobbelaar, Ziyaad Halday, Bryna J. Hazelton, Stefan Heimersheim, Jacqueline N. Hewitt, Jack Hickish, Daniel C. Jacobs, Austin Julius, Joshua Kerrigan, Piyanat Kittiwisit, Saul A. Kohn, Matthew Kolopanis, Adam Lanman, Paul La Plante, Telalo Lekalake, David Lewis, Adrian Liu, Yin-Zhe Ma, David MacMahon, Lourence Malan, Cresshim Malgas, Matthys Maree, Zachary E. Martinot, Eunice Matsetela, Andrei Mesinger, Mathakane Molewa, Miguel F. Morales, Tshegofalang Mosiane, Abraham R. Neben, Bojan Nikolic, Chuneeta D. Nunhokee, Aaron R. Parsons, Nipanjana Patra, Samantha Pieterse, Jonathan C. Pober, Nima Razavi-Ghods, Itamar Reis, Jon Ringuette, James Robnett, Kathryn Rosie, Mario G. Santos, Sudipta Sikder, Peter Sims, Craig Smith, Angelo Syce, and Nithyanandan Thyagarajan

Cosmology with the SKA Observatory

Stefano Camera
Dipartimento di Fisica, Università degli Studi di Torino, Via P. Giuria 1, 10125 Torino, Italy
INFN, Sezione di Torino, Via P. Giuria 1, 10125 Torino, Italy
INAF, Osservatorio Astrofisico di Torino, Strada Osservatorio 20, 10025 Pino Torinese, Italy
Department of Physics & Astronomy, University of the Western Cape, Cape Town 7535, South Africa

I shall review the most peculiar aspects of cosmology in the radio band, with a special focus on the SKA Observatory and its pathfinders and precursors. I shall present the main radio probes that can be exploited for late-time cosmology: neutral-hydrogen emission-line galaxy and continuum galaxy surveys, neutral hydrogen intensity mapping, and weak lensing cosmic shear at radio frequencies. Moreover, I shall also discuss the added value of multi-wavelength synergies, presenting some show-case example of the power of radio-optical cross-correlations to test the foundations of the concordance cosmological model, such as the nature of dark matter and dark energy, or tests of inflation and gravity.

Foreword

The author emphasises that the present text is a conference proceeding and, as such, is limited in scope and length. For this reason, it cannot be exhaustive and do justice to all the science cases related to cosmology with the SKA Observatory (SKAO). The reader is therefore referred to the most updated, official review in this respect: the *SKA Cosmology Red Book 2018*,[1] and references therein. It includes state-of-the-art technical specifications and performance forecasts that supersede the previous analyses performed in view of the international conference 'Advancing Astrophysics with the Square Kilometre Array', held in Sicily in June 2014.[2–10]

1 The SKA Observatory

The SKAO is an intergovernmental organisation officially born on 15th January 2021,[a] after an almost decade-long process started in October 2013 and that reached its latest stage after the SKA Convention was signed in Rome, Italy in March 2019. The original idea, however, dates back to more than twenty years earlier, when in September 1993 the International Union of

[a] http://skaobservatory.org/.

Radio Science established the Large Telescope Working Group to begin a worldwide effort to develop the scientific goals and technical specifications for a next generation radio observatory.

When finished by mid-2020s, the SKAO will be the largest scientific instrument ever built. It will be co-hosted by Australia and South Africa, the former housing its low-frequency instrument, comprising more than 100 000 antennas operating in the $[50, 350]$ MHz range, the latter siting its ~ 200 mid-frequency dishes, which will cover the $[0.35, 15]$ GHz frequency interval.

Goals of the SKAO are most varied, with cosmology being just one amongst others like cosmic dawn and the epoch of reionisation, galaxy evolution, pulsar science, cosmic magnetism, and the cradle of life.

2 SKA Cosmology

Drivers of the SKAO's efforts for cosmology are the main open questions in our current understanding of the Universe, namely the nature of dark matter and dark energy, the possibility of deviations from Einstein's general relativity on cosmological scales, and the early phase of cosmic inflation. These interrogatives will be tackled by exploiting a series of probes, which will be discussed in what follows, namely clustering of neutral hydrogen (HI) emission-line galaxies and continuum galaxies, HI intensity mapping, and weak lensing at radio wavelengths. For this, the following surveys are proposed: a wide Band-1 ($0.35 \leq z \leq 3$) survey over 20 000 deg^2 for continuum galaxies and HI intensity mapping; a medium-deep Band-2 ($0 \leq z \leq 0.5$) survey covering 5 000 deg^2 for HI-galaxies and weak lensing; and a deep ($3 < z < 6$) survey of 100 deg^2 sky coverage.

2.1 HI-line galaxies

Let me start this brief tour across radio-cosmology observables with the likely most well-known and well-studied probe of the late-time Universe, namely galaxy clustering. Galaxy clustering aims at reconstructing the properties of the cosmic large-scale structure (LSS) by means of galaxy positions as luminous tracers of the underlying dark matter distribution. If we focus on large enough scales, the density contrast of galaxy number counts in a given volume, Δ, is directly proportional to the matter density contrast, δ, with the constant of proportionality being the redshift-dependent and scale-independent (linear) galaxy bias, $b(z)$. This implies that measurements of the galaxy power spectrum can be related to the more fundamental matter power spectrum, thus allowing us to probe its dependence upon cosmological parameters and, consequently, constrain them within a given cosmological model.

In the case of the SKAO, the target galaxy sample will be emission-line galaxies in which the redshifted 21-cm emission line of HI is clearly detectable. Then, by inferring the three-dimensional position of the galaxies through their redshifts and angular locations in the sky, we can build boxes of galaxy overdensities centred in a given redshift and measure the galaxy power spectrum in a number of redshift bins. The main advantage of this approach is the possibility to reconstruct a three-dimensional map of galaxy positions with spectroscopic redshift accuracy; this is however also the reason of its main disadvantage, for the 21-cm emission line is very feeble and to resolve it a long exposure time is required, meaning that for a fixed time of observations on sky, only a small number of HI-line galaxies will be detected—compared to other emission-line galaxies.

Examples of HI-line galaxy surveys in the past include the HI Parkes All Sky Survey (HIPASS),[b] which detected about 4.5 thousand galaxies at a 5σ detection limit of 5.6 Jy km s^{-1} at 200 km s^{-1}, and the Arecibo Legacy Fast ALFA (ALFALFA) survey,[c] with more than 20 thousand galaxies at a 5σ detection limit of 0.72 Jy km s^{-1} at 200 km s^{-1}. Both surveys are, however,

[b] `https://astronomy.swin.edu.au/cosmos/h/HIPASS`.
[c] `http://egg.astro.cornell.edu/index.php/`.

at low redshift. On the contrary, a SKAO HI-line galaxy survey should be able to reach $z \sim 0.5$ with a volumetric galaxy number density of 0.5 to $1 \times 10^{-4}\,\mathrm{Mpc}^{-3}$.

As detailed in the corresponding section of the SKA Cosmology Red Book 2018 (and references therein),[1] HI-galaxy surveys conducted with the SKAO will include the canonical science cases for galaxy redshift surveys, i.e. measurements of baryon acoustic oscillations (BAO) and redshift-space distortions, as well as more recent techniques such as for the clustering properties of cosmic voids and cross-correlations with other cosmological and astrophysical probes, even including maps of the gamma-ray sky to probe the particle nature of dark matter, or gravitational-wave sources to scrutinise deviations from Einstein's general relativity.

However, besides the applications mentioned above, HI-line galaxy surveys with the SKAO will also allow us to conduct other, innovative research thanks to the peculiar nature of the radio signal. For instance, the intrinsic luminosity of a galaxy inferred from the 21-cm line width, combined with its measured redshift and inclination angle, gives access to the peculiar velocity of the galaxy in the line-of-sight direction. This way, a galaxy redshift survey effectively becomes a 'Tully-Fisher' survey, allowing for joint measurements of both the galaxy clustering power spectrum and the peculiar velocity power spectrum. By doing so, we can probe the underlying density field with two different tracers (density and peculiar velocities) at the same time, thus effectively performing multi-tracing.[11,12] Improvements on the estimation of the growth of structures with respect to density-only analyses are very promising; and all the more so at low redshift, where the most of the detected HI-galaxies will be, making this especially relevant in the context of the SKAO.

2.2 Continuum galaxies

Continuum galaxy surveys share with the HI-galaxy surveys described above the same target probe for cosmology, namely the distribution of galaxies as tracers of the matter density field. If HI galaxies are detected by identifying a specific emission line in their spectrum, in the case of galaxies observed in the radio continuum, the origin of the signal is the synchrotron radiation generated by charged particles within the galaxy. The main advantage of this technique is the strength of its signal compared to the need to resolve single emission lines, which allows for a large number of detected objects. On the other hand, the lack of spectral features in the synchrotron emission makes it almost impossible to disentangle the information about the total flux with that of the redshift of the source galaxy. This effectively collapses the three-dimensional reconstruction of the galaxies' positions onto a two-dimensional map on the sky. Despite this seeming disadvantage, continuum galaxy surveys have been profitably employed in cosmology. For instance, the first ever detection of the integrated Sachs-Wolfe (ISW) effect—a smoking gun for dark energy—was performed by cross-correlating anisotropies in the cosmic microwave background (CMB) temperature with galaxy over-density maps in the radio continuum.[13,14]

Nowadays, continuum galaxy surveys are beginning to rival optical surveys in terms of source density. This is because the synchrotron emission that dominates the extra-Galactic radio background at frequencies lower than 10 GHz comes from basically any galaxy with an ongoing star formation/accretion activity. Furthermore, the wide fraction of the sky surveyed by this kind of experiments extends to areas substantially larger than those covered by many of the forthcoming optical surveys, up to about $\simeq 30\,000\ \mathrm{deg}^2$. Among the most well-known examples of continuum galaxy surveys is certainly the NRAO VLA Sky Survey (NVSS),[15] which detected about two million galaxies over the entire Northern sky above $-40°$, with Stokes I-, U-, and Q-parameter maps, and FIRST (Faint Images of the Radio Sky at Twenty-Centimeters),[16] whose legacy is a catalogue of ~ 900 thousand galaxies over 10 000 sq. deg. NVSS is the very catalogue exploited to perform the aforementioned measurement of the ISW effect, whilst thanks to FIRST we had the first ever detection of weak gravitational lensing at radio wavelengths.[17]

As described in the SKA Cosmology Red Book 2018,[1] several applications are envisaged for a wide continuum galaxy survey with the SKAO. The obvious one is constraining cosmological

parameters via the ISW effect, for which forecasts show that a significant improvement over current constraints will be possible if some redshift information can be attached to the detected continuum galaxies. This could be done e.g. by cross-matching galaxies with optical surveys,[18] or by means of so-called 'clustering redshifts'.[19] Besides dark energy, the ISW effect will also be relevant to the aim of the amplitude of primordial non-Gaussianity, $f_{\rm NL}$, since a nonzero value of this parameter will impact the very largest scales where the ISW signal peaks.[20]

Finally, it is worth mentioning a couple of science cases that are peculiar to continuum galaxy surveys. The former exploits two facts: *i*) that galaxies detectable in the radio continuum pertain to different astrophysical populations, like star-forming galaxies and active galactic nuclei; and *ii*) that such populations preferentially form within dark matter haloes of given properties, e.g. a specific mass range.[21] Thanks to this, the multi-tracer technique can be employed,[11,12] allowing us to overcome the limitations of cosmic variance and to access thus the largest scales. By doing so, bounds on $f_{\rm NL}$ could in principle tighten by an order of magnitude, with the potential to rule out entire classes of inflationary scenarios.[22,23]

The latter science case focusses on testing one of the fundamental assumptions underlying our description of the Universe, that of homogeneity and isotropy. Thanks to the huge volume probed, continuum surveys have the potential to constrain the CMB dipole—i.e. the dipole associated with the proper motion of the Sun with respect to the CMB. Estimates of the radio dipole in the literature agree with the CMB dipole direction, but with an amplitude twice to five times larger than expected, and the reason for this is not understood.[24] Simulations matching expected SKAO performances show that the dipole due to LSS depends on the flux density threshold, providing an extra handle to disentangle it from the kinematic dipole.

2.3 HI intensity mapping

One of the most anticipated science cases for cosmology with the SKAO is certainly mapping the distribution of HI in the late, post-reionisation Universe ($z \lesssim 5$). This can be achieved by measuring the characteristic 21-cm transition of HI, resorting to a long-known astrophysical observable, dating back to the 1950s.[25] Since, after the end of reionisation, almost the entirety of HI resides inside galaxies, its distribution effectively acts as a tracer of the galaxy distribution and, as such, of the underlying cosmic LSS—a technique known as 'intensity mapping'.[26,27] However, due to the weakness of the signal it is necessary to integrate over large pixels on the sky to reach a desirable signal to noise, resulting into a poor angular resolution compared to (redshift and continuum) galaxy surveys. On the other hand, by mapping the HI brightness temperature at a given frequency, we automatically know the redshift that stretched the rest-frame 21-cm photon wavelength, thus obtaining exquisite resolution along the line-of-sight direction.

Despite such a premiss, mapping the distribution of HI on cosmic scales is technically extremely challenging, for reasons connected to both astrophysics and instrumentation. First of all, measurements are plagued by strongest astrophysical foregrounds, at levels three/four orders of magnitude louder than the cosmological signal, and their coupling with instrumental systematic effects further increases the complexity of data reduction.[28] As a consequence, detection of HI intensity mapping has hitherto only happened in cross-correlation with optical galaxy surveys, thanks to the fact that HI foregrounds and systematic effects do not correlate with maps of galaxy number count fluctuations. By now, a few detections in cross-correlation have been reported for single-dish experimental configurations—namely, where either the instrument is composed of single dish, or a number of dishes is employed at unison to reduce statistical noise. The first and the last of such detections made use of observations by the 100-metre diameter Green Bank Telescope (GBT), respectively resulting in a 4σ-evidence cross-correlation with the DEEP2 survey at $z \sim 0.8$,[29] and with two galaxy samples from the eBOSS survey over 100 sq. deg.[30] Otherwise, a recent measurement has been reported for interferometric observations by the Canadian Hydrogen Intensity Mapping Experiment (CHIME),[31] again in cross-correlation with eBOSS galaxy samples and quasars, with high to very high detection significance.

HI intensity mapping is by now recognised as an instrumental tool for contemporary cosmology, for it will allow us to track the growth of structures up to redshifts inaccessible to traditional galaxy surveys. Furthermore, it will be highly complementary to them, lending its exquisite redshift accuracy in exchange for its poor angular resolution—a trait clearly relevant for example to the purpose of measuring BAO.[32] In the SKA Comology Red Book 2018,[1] several applications of HI intensity mapping for astrophysics and cosmology are presented. From the point of view of our understanding of thermal history of the Universe, HI intensity mapping surveys with the SKAO at low and middle frequencies will allow us to pinpoint the evolution across redshift of the abundance of HI, $\Omega_{\rm HI}(z)$. This quantity is a fundamental ingredient in the modelling of HI clustering, and it is up to date extremely poorly constrained.

Besides that and other more traditional power spectrum analyses—like the aforementioned BAO, or measurements of the growth rate via redshift-space distortions—HI intensity mapping is envisaged as a means to access scales for the most part unreachable by galaxy surveys. As already mentioned, such ultra-large scales encode pristine information about the earliest phases of the Universe's evolution, allowing us to test inflationary models by constraining $f_{\rm NL}$.[33] But primordial non-Gaussianity is not the only way inflation can be thus constrained, for HI intensity mapping with the SKAO in auto- and cross-correlation with the CMB and other LSS probes has the potential to detect inflationary features in the primordial power spectrum. Moreover, relativistic effects in the clustering of tracers are strongest on those scales, meaning that if we measure them we shall have a further confirmation of the goodness of general relativity on scales where it has never been effectively tested.[34,35] And, last but not least, neutrinos and alternative dark matter candidates will also leave a detectable imprint on the distribution of HI on cosmic scales, giving us access to measure them with SKAO intensity mapping surveys.

2.4 Radio weak lensing

Gravitational lensing is a well-known effect predicted by general relativity.[36] Apart from rare observer-lens-source alignments giving rise to spectacular strongly lensed images, the vast majority of gravitational lensing effects fall within the category of 'weak' lensing, where image distortions are small perturbations. Nevertheless, weak lensing is a powerful tool for cosmology, since photons from all galaxies experience a large number of tiny scatters along their paths towards us due to their passing through the intervening LSS. As a result, all observed galaxy images are somewhat weakly lensed, the more so the farther away they are from us.

At linear order, weak lensing distortions to a source image can be decomposed into an overall magnification of its size—the convergence, κ—an area-conserving stretching of its shape—the complex spin-2 shear, γ—and a rigid revolving of its orientation—the rotation, ω. However, only the first two are sourced by scalar perturbations, the latter being to first order due to tensor perturbations only. Moreover, convergence is not easy to estimate, for we do not know the original size of a galaxy.[37] On the other hand, shear is a much clearer observable, since in the weak lensing regime the underlying LSS induces correlations in the orientation of galaxy images, which can be reconstructed by measuring galaxy ellipticities. For this reason, shear is the target of all purpose-built weak lensing surveys, such as the European Space Agency's *Euclid* satellite,[d] or the Vera C. Rubin Observatory.[e]

Weak lensing in the radio band shares many an aspect with its counterpart at optical/near-infrared wavelengths, for gravitational lensing is achromatic. However, it has also peculiarities that make the two probes highly complementary to each other. For a start, radio observations are not limited by dust obscuration, making radio lensing a stronger signal because galaxies detected in the radio continuum stretch deep in redshift—and, as mentioned, lensing is a cumulative effect. Moreover, most of the lensing signal comes from small scales, which at high redshift are less non-linear and thus modelled more robustly. Yet, small scales are also where shot noise

[d] `https://www.euclid-ec.org`.
[e] `https://www.lsst.org`.

dominates, and radio galaxy catalogues are sparser than optical ones. For this reason, besides the aforementioned single radio-only detection with FIRST,[17] measurements of radio weak lensing only happened in cross-correlation with either galaxies,[38] or optically measured lensed shapes.[39]

As detailed in the SKA Cosmology Red Book 2018,[1] applications of radio weak lensing mostly involve cross-correlations with optical shear surveys. By far, the main advantage of such synergic analyses is their potential to mitigate systematic effects known to plague cosmic shear studies. Consider that, on average, shear contributes to observed galaxy ellipticities by $\sim 1\%$. On top of this, the target sensitivity to dark energy parameters aimed at by oncoming shear surveys corresponds to a further 1%. Therefore, it is clear that data reduction pipelines need exceedingly good calibratio, not to induces biases in the estimation of cosmological parameters.

Performance is customarily parameterised in terms of additive and multiplicative bias for the reconstructed ellipticity, with both vanishing in the ideal scenario. Regarding the former, the value of radio-optical cross-correlation is readily apparent: observations in the two bands are performed via wholly different ways, reason for which additive bias in the observed shear will not correlate across wavelengths. Thus, the measured shear cross-power spectrum is devoid of additive-bias contamination. The situation is more subtle when it comes to multiplicative bias, for it does not drop in the cross-spectrum. Nonetheless, a joint radio-radio, optical-optical, and radio-optical analysis has the potential to self-calibrate, once multiplicative-bias nuisance parameters are properly included.

Finally, radio weak lensing also has the potential to alleviate the impact of intrinsic alignments, i.e. the observational contaminant due to galaxies formed within the same dark matter halo being preferentially aligned as a consequence of the processes that lead to their formation.[40] Indeed, radio observations can access information about the original integrated polarisation of a galaxy, or its resolved rotational velocity, two proxies of the unlensed orientation of the galaxy.

3 Cosmology with SKAO precursors and pathfinders

The great endeavour represented by the SKAO is going to be possible also thanks to the several precursor and pathfinder instruments currently paving the way. 'Precursors' like the South African MeerKAT and the Australian SKA Pathfinder (ASKAP) are located at SKAO sites, carrying out scientific studies related to future SKAO activities and helping the development/testing of new technologies. 'Pathfinders' are found all around the world, such as the Low Frequency Array (LOFAR), CHIME, or the Five-hundred-meter Aperture Spherical Telescope (FAST), and are also engaged in SKAO-related science and technology.

Many of these pathfinders and precursors are by now fully active and have already delivered their first results. For instance, measurements of the cross-correlation between the Rapid ASKAP Continuum Survey (RACS) and the CMB have been performed,[41] and science-verification data papers are oncoming for the Evolutionary Map of the Universe (EMU).[42,43] Regarding HI intensity mapping, a successful demonstration of single-dish intensity mapping calibration with an array of dishes was recently reported for MeerKAT.[44] Whereas an effort for radio weak lensing has been ongoing for some years with the upgraded Multi-Element Radio Linked Interferometer Network (*e*-MERLIN) .[45–47]

4 Conclusions

The invited contribution whose material sourced the present proceeding was aimed to be a general introduction to the SKAO's science cases for cosmology. It focussed on the main envisaged surveys, and related cosmological probes, as described in the reference text adopted, the SKA Cosmology Red Book 2018,[1] which the interested reader is encouraged to refer to for any detail.

Acknowledgments

The author acknowledges support from the 'Departments of Excellence 2018-2022' Grant (L. 232/2016) awarded by the Italian Ministry of University and Research (MUR).

References

1. Square Kilometre Array Cosmology Science Working Group, PASA **37**, e007 (2020).
2. R. Maartens, F. B. Abdalla, M. Jarvis, and M. G. Santos, PoS **AASKA14**, 016 (2015).
3. F. B. Abdalla, P. Bull, S. Camera, A. Benoit-Lévy, B. Joachimi, et al., PoS **AASKA14**, 017 (2015).
4. M. Jarvis, D. Bacon, C. Blake, M. Brown, S. Lindsay, A. Raccanelli, M. Santos, and D. J. Schwarz, PoS **AASKA14**, 018 (2015).
5. M. Santos, P. Bull, D. Alonso, S. Camera, P. Ferreira, et al., PoS **AASKA14**, 019 (2015).
6. M. Brown, D. Bacon, S. Camera, I. Harrison, B. Joachimi, et al., PoS **AASKA14**, 023 (2015).
7. P. Bull, S. Camera, A. Raccanelli, C. Blake, P. Ferreira, et al., PoS **AASKA14**, 024 (2015).
8. A. Raccanelli, P. Bull, S. Camera, C. Blake, P. Ferreira, et al., PoS **AASKA14**, 031 (2015).
9. S. Camera, A. Raccanelli, P. Bull, D. Bertacca, X. Chen, et al., PoS **AASKA14**, 025 (2015).
10. D. Bacon, S. Bridle, F. B. Abdalla, M. Brown, P. Bull, et al., PoS **AASKA14**, 145 (2015).
11. U. Seljak, PRL **102**, 021302 (2009).
12. P. McDonald and U. Seljak, JCAP **2009**, 007 (2009).
13. S. Boughn and R. Crittenden, Nature **427**, 45 (2004), ISSN 1476-4687.
14. S. Boughn and R. Crittenden, New Astronomy Reviews **49**, 75 (2005), ISSN 1387-6473.
15. J. J. Condon, W. D. Cotton, E. W. Greisen, Q. F. Yin, R. A. Perley, et al., AJ **115**, 1693 (1998).
16. R. H. Becker, R. L. White, and D. J. Helfand, ApJ **450**, 559 (1995).
17. T.-C. Chang, A. Refregier, and D. J. Helfand, ApJ **617**, 794 (2004).
18. S. Camera, M. G. Santos, D. J. Bacon, M. J. Jarvis, K. McAlpine, et al., MNRAS **427**, 2079 (2012).
19. B. Ménard, R. Scranton, S. Schmidt, C. Morrison, D. Jeong, et al., arXiv e-prints arXiv:1303.4722 (2013).
20. A. Raccanelli, O. Doré, D. J. Bacon, R. Maartens, M. G. Santos, et al., JCAP **2015**, 042 (2015).
21. R. J. Wilman, L. Miller, M. J. Jarvis, T. Mauch, F. Levrier, et al., MNRAS **388**, 1335 (2008).
22. Z. Gomes, S. Camera, M. J. Jarvis, C. Hale, and J. Fonseca, MNRAS **492**, 1513 (2020).
23. L. D. Ferramacho, M. G. Santos, M. J. Jarvis, and S. Camera, MNRAS **442**, 2511 (2014).
24. C. A. P. Bengaly, R. Maartens, and M. G. Santos, JCAP **2018**, 031 (2018).
25. J. H. Oort, F. J. Kerr, and G. Westerhout, MNRAS **118**, 379 (1958).
26. S. Bharadwaj, B. B. Nath, and S. K. Sethi, J. of Astrophysics and Astronomy **22**, 21 (2001).
27. R. A. Battye, R. D. Davies, and J. Weller, MNRAS **355**, 1339 (2004).
28. M. Spinelli, I. P. Carucci, S. Cunnington, S. E. Harper, M. O. Irfan, J. Fonseca, A. Pourtsidou, and L. Wolz, MNRAS **509**, 2048 (2022).
29. T.-C. Chang, U.-L. Pen, K. Bandura, and J. B. Peterson, Nature **466**, 463 (2010).
30. L. Wolz, A. Pourtsidou, K. W. Masui, T.-C. Chang, J. E. Bautista, et al., MNRAS **510**, 3495 (2022).
31. CHIME Collaboration, et al., arXiv e-prints arXiv:2202.01242 (2022).
32. A. Rubiola, S. Cunnington, and S. Camera, arXiv e-prints arXiv:2111.11347 (2021).

33. S. Camera, M. G. Santos, P. G. Ferreira, and L. Ferramacho, PRL **111**, 171302 (2013).
34. D. Alonso and P. G. Ferreira, PRD **92**, 063525 (2015)
35. J. Fonseca, S. Camera, M. G. Santos, and R. Maartens, ApJL **812**, L22 (2015).
36. M. Bartelmann and P. Schneider, Phys. Rep. **340**, 291 (2001).
37. J. Alsing, D. Kirk, A. Heavens, and A. H. Jaffe, MNRAS **452**, 1202 (2015).
38. C. Demetroullas and M. L. Brown, MNRAS **473**, 937 (2018).
39. C. Demetroullas and M. L. Brown, MNRAS **456**, 3100 (2016).
40. D. Kirk, M. L. Brown, H. Hoekstra, B. Joachimi, T. D. Kitching, et al., Space Science Reviews **193**, 139 (2015).
41. B. Bahr-Kalus, D. Parkinson, J. Asorey, S. Camera, C. Hale, and F. Qin, MNRAS (2022 in prep.).
42. R. P. Norris, J. Marvil, J. D. Collier, A. D. Kapińska, A. N. O'Brien, et al., PASA **38**.
43. K. Tanidis, J. Asorey, D. Parkinson, S. Camera, et al., MNRAS (2022 in prep.).
44. J. Wang, M. G. Santos, P. Bull, K. Grainge, S. Cunnington, et al., MNRAS **505**, 3698 (2021).
45. R. A. Battye, M. L. Brown, C. M. Casey, I. Harrison, N. J. Jackson, et al., MNRAS **495**, 1706 (2020).
46. S. M. Manning, C. M. Casey, C.-L. Hung, R. Battye, M. L. Brown, et al., MNRAS **495**, 1724 (2020).
47. I. Harrison, M. L. Brown, B. Tunbridge, D. B. Thomas, T. Hillier, et al., MNRAS **495**, 1737 (2020).

Chasing Neutral Hydrogen: an Intensity Mapping view of the large scale structure

Marta Spinelli
Institute for Particle Physics and Astrophysics, ETH Zürich,
Wolfgang Pauli Strasse 27,8093 Zürich, Switzerland

Radio telescopes such as MeerKAT, and in the future SKA, can map the spatial distribution of the post-reionization cosmic neutral hydrogen using Intensity Mapping techniques for the 21 cm line. These measurements can unveil the underlying large-scale structure of the Universe and contribute in a fundamental way to our understanding of structure growth. A key point is the subtraction of the bright foregrounds, orders of magnitude stronger than the 21cm signal. I briefly describe here the status of MeerKLASS, an Intensity Mapping survey with the MeerKAT telescope. Moreover, I report the results of an effort, led by the SKA Intensity Mapping Focus Group, to construct a realistic mock data cube with improved the sky model and instrument characterization, and to assess through simulations the performance of foreground cleaning methods.

1 Introduction

Over the next decades the telescope arrays of the SKA Observatory (SKAO) will observe of radio continuum emission and the 21-cm line emission from neutral hydrogen gas (HI) in order to test the standard cosmological model [1]. HI gas, as the first and most abundant element in the Universe, is an excellent tracer of the large-scale structure and its evolution. However, due to the weakness of its emission, detection is limited to very low redshift. Intensity Mapping (IM) is a relatively recent technique to circumvent this limitation by observing the integrated HI line emission from unresolved sources in large volume elements of the sky. HI IM surveys are very time-efficient compared to traditional galaxy surveys as the low spatial resolution and large redshift range allow the observation of cosmic volumes within relatively short telescope times. The resulting HI maps trace the largest scales of the matter distribution of the underlying dark matter field with excellent redshift resolution due to the telescope's fine frequency channelisation. For the SKA Observatory, the planned cosmological IM surveys will be conducted in the so-called single-dish mode: each dish operates as a single telescope, and maps are co-added [1]. IM surveys have been planned for the SKA precursor MeerKAT [10], and a Science Verification data campaign with this technique has already been successfully completed (and further telescope time is available). In section 2 the key result obtained by Wang et al.(2021) [2] will be briefly revised. The main obstacle for the detection of the HI signal comes from the presence

Table 1: Specifications of the MeerKAT Observations from Wang et al.(2021) [2].

Antennas	All 64 MeerKAT dishes
Observation mode	Single-dish
Polarisation	Linear (horiz. + vert.) feeds
System temperature	∼16 K
Frequency range	0.856-1.712 GHz
Frequency resolution	0.2 MHz
Number of channels	4096
Time resolution	2s
Exposure time	1.5hr x 7 scans
Target field	WiggleZ 11hr field ($10^\circ \times 30^\circ$)

of astrophysical foregrounds, orders of magnitude stronger than the HI signal. While the foregrounds, predominantly due to synchrotron and free-free emission at the relevant frequencies (around 1 GHz), have a known spatial distribution and frequency correlation, their convolution with instrumental systematics and other observational effects can render signal separation a very challenging task. The challenges of foreground removal will be addressed in section 3 where I will summarized the Blind Foreground Cleaning Challenge carried on by the SKA Intensity Mapping Focus Group (Spinelli et al. 2022 [3]) on a realistic, MeerKLASS-inspired, set of simulated single-dish observations.

2 MeerKAT Science Verification Data

As a first step towards demonstrating the feasibility of the single dish observing strategy, Wang et al.(2021) [2] have developed a calibration pipeline for dual-polarisation autocorrelation data from 64 MeerKAT dishes in the L-band (856 – 1712 MHz, 4096 channels), with 10.5 hours of data retained from six nights of observations. The pipeline includes a mulit-level RFI flagging, periodic noise diode injection to stabilize the gain drifts and an absolute calibration based on an assumed sky model. The specification for these observations are reported in table 1. Figure 1 shows, for a given frequency, the final recovered map of diffuse celestial emission and point sources over a $10^\circ \times 30^\circ$ patch of the sky overlapping with the WiggleZ 11hr field. The single per-dish reconstructed maps have a good level of consistency and results are in very good agreement with external datasets.

The map of figure 1, contains foreground at the Kelvin level. The target cosmic 21cm signal is expected to be instead around the mK. Similarly to the CMB case, the separation of the signal and the foregrounds needs to be properly achieved in order to exploit this type of observations for cosmology. This is work-in-.progress within the MeerKLASS collaboration and requires a careful cross-check with simulations which will be addressed in the next section. One useful strategy to mitigate the residual foreground and systematic level in the data after the cleaning process is to cross-correlate the cleaned maps with galaxy surveys in the same sky area. Cross-correlation with galaxy surveys has been proven successful for various IM experiments (see for example the recent results of Wolz et al. 2022 [12]). The cross-correlation between the MeerKLASS maps and WiggleZ is under study (Li et al. in prep).

3 The challenge of foreground removal

In recent years, many studies have addressed the separation of the HI signal from the foreground emission in the context of single-dish IM observations both with data and simulations. The foreground removal methods that have been proven to be the most powerful are Principal

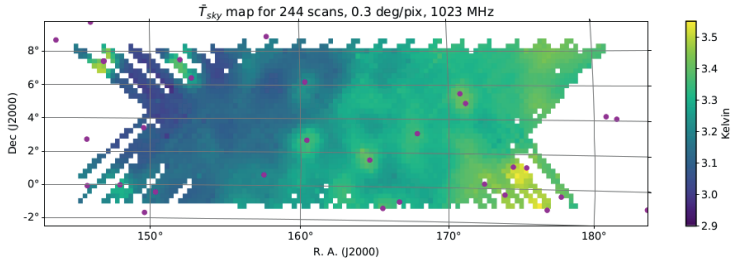

Figure 1 – The mean intensity maps at 1023 MHz from the combination of all scans after various rounds RFI subtraction. Magenta dots mark the positions of point sources with flux >1 Jy at 1.4 GHz, which were not included in the sky model used for calibration. The figure is taken from Wang et al.(2021) [2].

Component Analysis (PCA), Independent Component Analysis (ICA), and Generalised Morphological Component Analysis (GMCA). In addition, many studies set particular focus on the interaction between foreground removal and observational systematics such as primary beam effects [9], polarisation leakage [5,6], $1/f$ noise and radio frequency interference due to satellites [8].

Here I summarize the Foreground Cleaning Challenge we carried on constructing a realistic set of low-redshift HI IM simulations for a ~ 5000 deg^2 single-dish survey with MeerKAT or the SKAO-MID telescope. The simulations, covering the $950-1400$ MHz range, include a HI signal generated by combining a semi-analytical galaxy formation model with a cosmological halo simulation, and astrophysical foregrounds, generated using two alternative models: a Gaussian realisation of the foreground 2-point statistic and frequency scaling properties [11], and a more empirically informed one, based on the Planck Sky Model [7]. We simulated instrumental effects through a commonly used Gaussian beam and an Airy beam model that includes side-lobes [8,9]. We model a fixed-elevation scanning strategy resulting into a non-homogeneous noise level. The various setup combinations resulted in sixteen *dirty* data-cubes to be cleaned. These describes increasingly realistic scenarios which allow a gradual understanding of the role of individual observational features in the cleaning process.

Nine foreground cleaning pipelines joined this first Challenge, that was blinded: cleaning was attempted without prior knowledge of HI signal, foregrounds, beam model and noise level. Seven of the pipelines (versions of PCA [4], FastICA [6], and GMCA [5]) linearly decompose the given data-cube leveraging statistical properties of the foreground components such as non-Gaussianity or sparsity. The other two methods either impose the foreground smoothness in frequency (polynomial fitting) or make physical assumptions on the foreground properties (least-squares fitting). Testing many different methods on the same simulation allowed us to quantify their *relative* accuracy on cleaning. We devised a set of criteria to describe the quality of the cleaned residuals in terms of their angular and the line-of-sight power spectra and presented their relative performance using radar charts. An example of the results can be seen in figure 2. We find that methods based on statistical properties of the data outperforms the parametric ones, given the current knowledge of foregrounds at the relevant frequencies combined with the systematic effects. Moreover, we conclude that implementing the cleaning in parallel with more than one method is an excellent practice to unveil different data characteristics. For a more detailed discussion see Spinelli et al. 2022 [3].

This first Challenge was designed as the baseline case to test the ability to recover the HI cosmological signal, including realistic observational effects. These simulations lay the ground for developing more complex and detailed end-to-end simulations necessary to improve foreground cleaning pipelines leading to robust HI signal detection in the forthcoming MeerKAT/SKAO era.

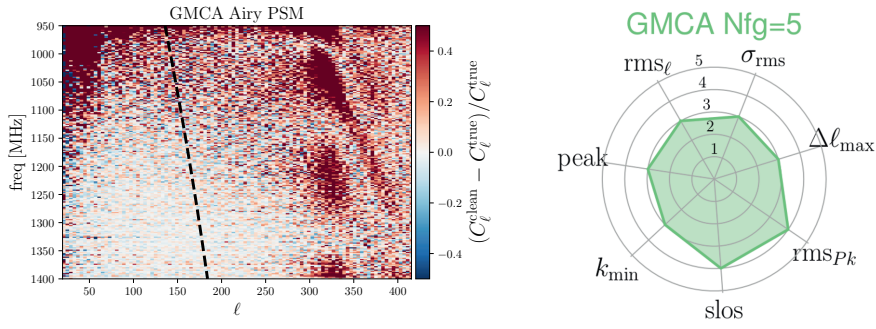

Figure 2 – *Left:* The estimator $(C_\ell^{\rm clean} - C_\ell^{\rm true})/C_\ell^{\rm true}$ for one of the cleaning methods (GMCA in this example), where $C_\ell^{\rm clean}$ is the angular power spectrum of the cleaned maps, while $C_\ell^{\rm true}$ is the angular power spectrum for the input cosmological signal and noise, as a function of frequency. For reference, the black dashed line traces the evolution with frequency of the angular scale of the FWHM of the telescope beam. *Right*: Example of radar charts showing the relative performance of the method in the left panel. For a given metric, we marked each method from 1 to 5, depending on the relative quality in the cleaning (1 =worst, 5 =best); hence, the bigger the area covered by the chart, the better the overall performance. Other results and a more detailed explanation on the metrics can be found in [3].

4 Conclusions

HI cosmology still have to prove its full potential but, in particular when the SKA Observatory will be operational, it will offer an incredible window into the evolution of the Universe. Crucially for this task, Intensity Mapping surveys are taking and analyzing data already, giving to the community the opportunity to discover and overcome the possible challenges. Observations from MeerKLASS Intensity Mapping survey with MeerKAT are under study, together with an effort in understanding the instrument and developing the analysis pipelines. It is therefore of paramount importance to develop ad-hoc simulations of both the HI signal and the foregrounds to fully prepare the ground for the SKAO era and its potential contribution to the knowledge of large-scale structures.

Acknowledgments

The results presented in this proceeding are based on the work of the MeerKLASS collaboration and the SKA Intensity Mapping Focus Group.

References

1. SKA Cosmology SWG, Pasa **37**, 007 (2020).
2. J. Wang et al., *MNRAS* **505**, 3 (2021).
3. M. Spinelli et al., *MNRAS* **509**, 2 (2022).
4. D. Alonso et al., *MNRAS* **447**, 1 (2015).
5. I. Carucci et al., *MNRAS* **499**, 1 (2020).
6. S. Cunnington et al., *MNRAS* **504**, 1 (2021).
7. J. Delabrouille et al., A&A **553**, A96 (2013)
8. S.E. Harper & C. Dickinson, , *MNRAS* **479**, 2 (2018).
9. S.D. Matshawule et al., *MNRAS* **506**, 4 (2021).
10. M.G. Santos et al., in *"MeerKAT Science: On the Pathway to the SKA"* (2016).
11. M.G. Santos, A. Cooray A., L. Knox, ApJ **625**, 575 (2005).
12. L. Wolz et al., *MNRAS* **510**, 3 (2022).

Time-redundant calibration of radio interferometers for HI intensity mapping

Tianyue Chen
Institute of Physics, Laboratory of Astrophysics, Ecole Polytechnique Fédérale de Lausanne (EPFL), Observatoire de Sauverny, 1290 Versoix, Switzerland

The 21cm intensity mapping is a promising new technique to map the large-scale-structures in the Universe at multiple redshifts. Due to the faintness of the 21cm signal, any systematic errors cannot only contaminate the signal, but also distort the spectral smoothness of the bright foregrounds, depressing the effective component separation. One such systematics for radio interferometry telescopes is the calibration errors in the individual receiver response, introducing receiver gain fluctuations in the data. In this work, we develop a novel calibration algorithm to calibrate a generic radio interferometer and correct for these gain fluctuations. The algorithm matches a given observation to a template constructed from the average of repeated observations. We apply the algorithm on the visibility data collected from the CHIME telescope, which successfully corrects sub-percent level gain fluctuations.

1 Introduction

The radio intensity mapping (IM) is a recent technique to measure large-scale-structures to probe the Universe evolution history. The concept of IM is to detect a single emission line, such as the HI line, from large scale fluctuations without resolving individual galaxies below the beam resolution [1]. The intensity maps provide angular diameter information from pixel-to-pixel fluctuations, as well as accurate redshift measurements from multiple fine frequency channels. Many intensity mapping experiments have been proposed, such as the Canadian Hydrogen Intensity Mapping Experiment (CHIME) [2] and the upcoming Square Kilometer Array (SKA) [3]. One of the main challenges for HI IM experiments is the effective removal of astrophysical foregrounds, which can be $\sim 10^5$ stronger than the HI signal. One relies on the smooth responses of foregrounds to the frequency to separate them from the frequency-independent HI signal [4]. However, instrumental systematics will distort the spectral smoothness of the foregrounds, undermining the component separation. In addition, systematics introduce an extra source of contamination and are often difficult to characterise due to their complexity [5]. Therefore, one must understand and mitigate residing instrumental systematics wherever possible. In this work, we focus on developing a novel algorithm to calibrate generic interferometric data and correct for calibration errors as one common types of systematics in radio interferometers.

2 Formalism

In an interferometer, the observed visibility, V_{ij}, from the antenna pair i and j is related to the true visibility $\widetilde{V}_{ij}$ through

$$V_{ij} = (1 + \Delta g_i + \Delta g_j^*)\widetilde{V}_{ij} + n_{ij}\,, \tag{1}$$

where n_{ij} is white noise in the data, $\Delta g_i, \Delta g_j << 1$ are the gain fluctuations of each receiver due to calibration errors. Assuming there exists a reference visibility $\overline{V}_{ij} \approx \widetilde{V}_{ij}$, one can deduce

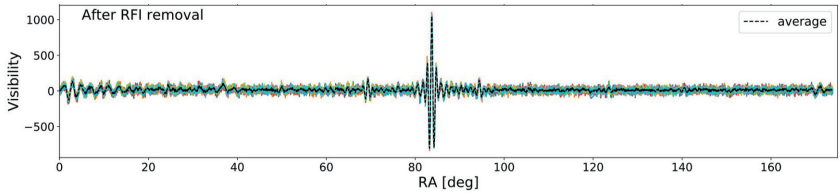

Figure 1 – An example visibility as a function of RA from 10 individual days (*colored*) and their averaged (*black*) observed by CHIME in Jan 2020.

the gain fluctuations and thus correct from the data to recover the true visibility given a known template and the observed visibility. This can be achieved through the minimum chi-square estimation, which is equivalent to solve

$$\sum_t \sum_{ij} [V_{ij} - (1 + \Delta g_i + \Delta g_j^*) \overline{V}_{ij}] \overline{V}_{ij}^+ = 0\,. \tag{2}$$

The advantage of the method is that the number of known parameters V_{ij}, $\overline{V}_{ij}$ is significantly larger than the number of unknown parameters Δg_i, since total number of visibilities from N receivers is $\frac{N(N+1)}{2}$. Equ. 2 thus becomes over-determined, allowing a precise solution of Δg_i. Since the visibilities and gain fluctuations are both complex numbers, we separately solve the amplitude and phase components of the gain fluctuations by writing $\Delta g_i = a_i + ib_i$. Including all antennas, we solve the a_i and b_i in the matrix format such that $\mathbf{M} \cdot \mathbf{A} = \mathbf{Y}$, where each element of $\mathbf{M}$ and $\mathbf{Y}$ is

$$m_{ij} = \begin{cases} \sum_{j=1}^n Re(D_{ij}) + Re(D_{ij}), & i = j \\ Re(D_{ij}), & i \neq j \end{cases}, \qquad y_i = \sum_{j=1}^n Re(C_{ij}) - \sum_{j=1}^n Re(D_{ij})\,. \tag{3}$$

$C_{ij} = \sum_t V_{ij} \overline{V}_{ij}^+$ is the cross-correlation between the provided template and the observed visibility, and $D_{ij} = \sum_t \overline{V}_{ij} \overline{V}_{ij}^+$ is the auto-product of the template itself. Similarly, the imaginary component becomes $\mathbf{M'} \cdot \mathbf{B} = \mathbf{Y'}$, where each element of $\mathbf{M'}$ and $\mathbf{Y'}$ is

$$m'_{ij} = \begin{cases} \sum_{j=1}^n Re(D_{ij}) - Re(D_{ij}), & i = j \\ -Re(D_{ij}), & i \neq j \end{cases}, \qquad y'_i = \sum_{j=1}^n Im(C_{ij})\,. \tag{4}$$

3 Data

We test our algorithm on 10 days of data observed by the CHIME telescope in Jan 2020. We select 12 hours of data centred at the Taurus A (TauA) transit located at 83° in right ascension (RA) and 22° in declination (DEC). The selected data expands between 0° and 175° in RA. The TauA transits around 10pm at the local time in Jan. Therefore, we have maximised the night time observation to minimise the Sun effect and the human interference in our data. The CHIME telescope consists of 4 cylinders, each with 256 dual polarisation antennas. We use 100 co-polarisation antennas for our analysis, with 25 equally spaced antennas per cylinder, forming 5050 visibilities in total. We choose one single frequency channel at 758.2 MHz for our analysis. Fig. 1 shows the visibility of an example baseline measured from individual days (*colored*) and their average (*black*) used as the template in our calibration. All data are RFI-excised and pre-calibrated by the standard point source calibration in order to satisfy the small perturbation assumption in Equ. 1. Indeed, the time-averaged template is moother and robuster against random fluctuations than individual days.

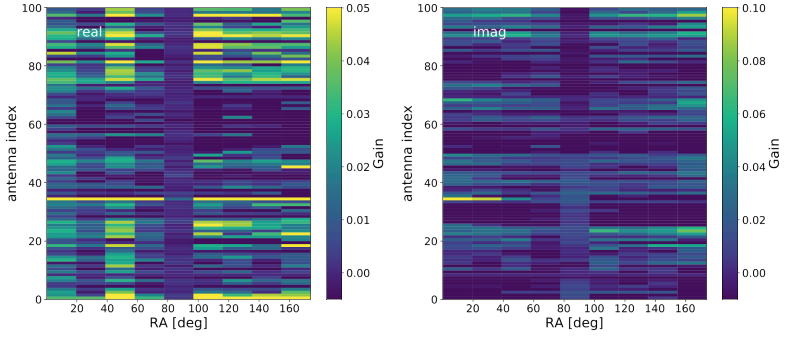

Figure 2 – The amplitude (*left*) and phase (*right*) of the detected gain fluctuations as a function of RA and antenna index.

4 Results

4.1 Day-averaged template calibration

We calibrate the 10 days of the data with their day-averaged template using our algorithm. We discard all auto-correlation baselines due to their outstanding noise level and low sensitivity. We also exclude all co-cylinder baselines which are known to be impacted by cross-talks between adjacent antennas. We derive the gain fluctuations using the formula in section 2 with an interval of 20° in RA, corresponding to a timescale of ~ 1.5 hours. Fig. 2 shows the amplitude (*left*) and phase (*right*) components of the gain fluctuations as a function of RA and antenna index. The on-transit region between 80° and 100° in RA has the minimum fluctuations shown as the dark vertical stripe in the middle of both panels. This is because the point source pre-calibration is most accurate at this region and thus has the least daily fluctuations. At off-transit regions, we detect a percent level gain fluctuation in both components on average. In addition, our algorithm is sensitive to systematics in the data, such as malfunctional antennas shown as bright horizontal stripes. The temperature variation also causes a physical shrinking or expansion of each cylinder. The resultant change of baseline distances is observed as a relative phase transition in the right panel of Fig. 2, where the phase fluctuations transit from negative (dark-colored) to positive (light-colored) vertically along the antennas for all four cylinders.

We calibrate each day of data using Equ. 1 with the derived gain fluctuations. In order to quantify the results of our calibration, we compute the relative residual power spectrum defined as

$$P_{ij} = \frac{\mathcal{F}^2(\delta^{\rm post}) - \mathcal{F}^2(\delta^{\rm pre})}{\mathcal{F}^2(\overline{V}_{ij})} \tag{5}$$

where for each antenna pair i and j, $\mathcal{F}^2(\delta^{\rm post})$ and $\mathcal{F}^2(\delta^{\rm pre})$ are the power spectra of the residual visibilities before ($\delta^{\rm pre}$) and after ($\delta^{\rm post}$) applying our calibration. Equ. 5 quantifies the fractional change in residual power when comparing a single day to the template with respect to the signal. A negative value indicates a less residual power after our calibration and thus an improvement compared with the point source pre-calibration. The median values of the residual spectra over days give -0.04% for the full RA range, -0.23% for pre-transit and -0.14% for post-transit. It confirms that our calibration is more important at off-transit regions as expected, and on average we correct sub-percent level gain fluctuations from the data, which can be crucial for detecting the 21cm signal giving the large foreground to signal ratio.

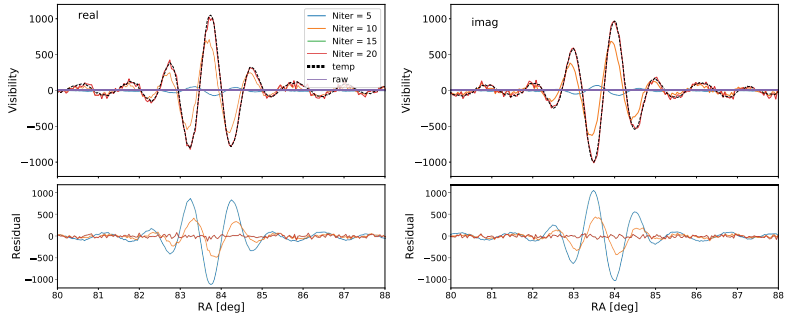

Figure 3 – *Upper*: The visibilities of the raw data, the template and the iteratively calibration data. *Lower*: The residuals between the calibrated data and the template. The visibilities shown here are from a typical day with a cross-cylinder baseline.

4.2 Iterative calibration of raw data

We also apply our algorithm on raw data without the point source pre-calibration in order to test if our algorithm is able to directly calibrate raw data given a template. In this case, we use the same template as above, but iteratively apply our algorithm to the raw data. As an example, for a typical day and a single baseline, Fig. 3 shows the visibilities (*upper*) and their residuals (*lower*) after different numbers of iterations in comparison with the template. It can be seen that the magnitude of raw data is significantly smaller compared with the template. By increasing the number of iterations, the difference gradually reduce until after 15 iterations where the calibrated visibilities converge with the template and no further improvement is obvious afterwards. We compare the calibrated visibilities in this case with the previous ones starting from pre-calibration. Through the relative residual power spectrum, the iterative calibration is highly consistent with the previous results with a difference as little as 0.01%. The results show that with a reasonable amount of iterations, our algorithm is able to directly calibrate raw data independent to the pre-calibration.

5 Conclusions

In this work, we develop the time-redundant calibration algorithm to calibrate radio interferometer data given a template derived from repetitive observations over days. Applied to the CHIME data, it is shown to have successfully corrected percent level gain fluctuations from individual days. Through iteration, the algorithm can directly calibrate raw data towards a given template, providing an independent and complementary approach to other existing calibration methods. The algorithm is applicable to a generic interferometry telescope such as the upcoming SKA telescope. It is particularly useful for 21cm surveys where any corrections of gain fluctuations is crucial for the signal detection given the large foreground to signal ratio.

References

1. R.A. Battye *et al*, *MNRAS* **355**, 1339 (2004).
2. CHIME collaboration, in prep. , (2022)
3. SKA Red Book, arXiv:1811.02743 , (2018)
4. R.J. Shaw, *Phys. Rev.* D **91**, 083514 (2015).
5. S.E. Harper *et al*, *MNRAS* **478**, 2416 (2018).

5.
CMB and Large Scale Structures

The Simons Observatory

Baptiste Jost, on behalf of the Simons Observatory collaboration
Université de Paris, CNRS, Astroparticule et Cosmologie,
75013 Paris, France

The Simons Observatory is a ground based CMB experiment being deployed in the Atacama desert in Chile and focusing on polarised signals. It is comprised of 3 small aperture telescopes and one large aperture telescope. It will observe the sky in 6 frequency bands from 27 to 280 GHz with more than 60,000 transition edge sensors in total in its nominal design. With unprecedented sensitivity SO will deliver novel and improved constraints on cosmological and astrophysical parameters probing physics from our Galaxy all the way to the early Universe. Here we review some of the Simons Observatory science goals, its design and some of the efforts made to understand and mitigate instrumental systematic effects to get the most pristine CMB polarisation signal as possible.

1 Introduction

The Simons Observatory (SO) is a ground based CMB experiment that is being deployed in the Atacama desert in Chile. It aims at observing the polarisation of the cosmic microwave background (CMB) and more generally the polarisation of the microwave sky with exquisite sensitivity to constrain cosmological and astrophysical parameters. SO has a wide range of scientific objectives covering a big part of the Universe's history from the very early Universe to present days. The international SO collaboration has more than 300 members from more than 10 countries and spanning over 40 institutions.

2 Science objectives

Figure 1 shows the broad science goals of SO, such as the measurement of primordial gravitational waves for primordial cosmology or the measurements of magnetic fields in the Galaxy for Galactic science.

Measuring the CMB primordial B-modes polarisation would be a hint for the cosmological era of inflation. The tensor-to-scalar ratio r that parametrises the CMB primordial B-modes amplitude is forecasted to be constrained with a precision of $\sigma(r = 0) = 3 \times 10^{-3}$ without delensing

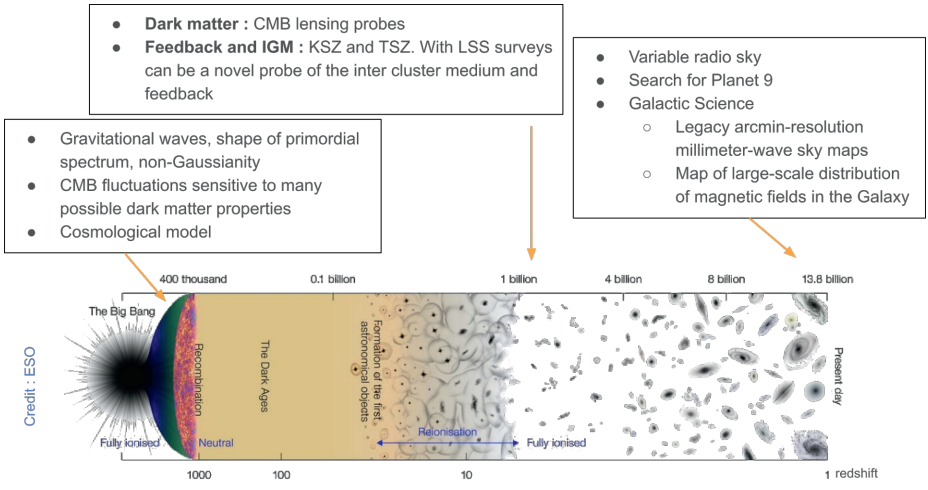

Figure 1 – Summary of some of the Simons Observatory science goals. Figure adapted from ESO.

by SO. With delensing this should be reduced by a factor $2^{1,7}$. SO's CMB polarisation measurements aims also at constraining the shape of the primordial spectrum and non-Gaussianity for instance. More broadly, measuring the CMB polarisation has the potential of constraining many cosmological probes such as dark matter properties or cosmic birefringence.

Further along the propagation of CMB photons other physical effects have an impact on the signal received. As reionisation occurs the neutral gas gets heated up and ionised. Similarly, galaxy clusters contain hot gas, this distorts the typical black body spectra of the CMB. Those spectral distortions are generated by an interaction of CMB photons on electrons in clusters; this effect is called the thermal Sunyaev–Zeldovich effect (tSZ) and the kinematic Sunyaev–Zeldovich effect (kSZ) and its characterisation is used to probe matter distribution and evolution in the Universe. For instance through excess of variance due to patchy reionisation, SO would be able to constrain the reionisation duration Δz with a precision of $\sigma(\Delta z) = 0.6$.
Matter on the line-of-sight (such as dark matter filaments or galaxy clusters) distorts CMB photons path and creates CMB lensing effects. It is a probe that can be used with temperature, E and B-modes anisotropies to estimate the number of relativistic species $N_{\rm eff}$. SO aims at constraining $N_{\rm eff}$ with a precision of $\sigma(N_{\rm eff}) = 0.07$. Lensing combined with BAO data from DESI also helps for the measurement of the neutrino mass Σm_ν. SO's precision on that measurement is planned to be $\sigma(\Sigma m_\nu) = 0.04$. Other synergies are planned using SO lensing and Rubin Observatory data to constrain the growth of structures as a function of redshift $\sigma_8(z)$, for instance with a redshift bin of $z = 1 - 2$ the projected precision is $\sigma(\sigma_8)/\sigma_8 = 0.015$. Other probes accessible with SZ effects, lensing and combination with LSS surveys are detailed in the SO forecast paper[1].

Finally SO will also observe signals from the local Universe that will help us understand some astrophysical effects. Indeed the legacy arc-min resolution maps of the millimetre-wave sky that SO will produce will open a new window on Galactic science. SO would for instance be able to create a map of large-scale distribution of magnetic fields in the Galaxy. There is also a case for the research of Planet 9 in the solar system using SO. And there are of course other science observables explored in the SO science goals and forecast paper[1] and the recent Galactic science paper[3].

3 Instrument design

These science goals drove the design of the SO instruments, some of the effects that need to be probed have an impact on large angular scales such as primordial gravitational waves, and other parameters such as σ_8 the amplitude of matter perturbation, need very high resolutions. To be able to probe both scales SO is deploying an array of 3 small aperture telescopes (SAT) that will observe the large scales (between $30 \leq \ell \leq 300$) of the CMB anisotropies and one large aperture telescope (LAT) for the small scales ($300 \leq \ell \leq 5000$). A rendering of both SAT and LAT are represented in Figure 2.

The science goals mentioned above and others discussed in the SO forecast paper[1] all require exquisite precision of CMB polarisation measurements. The design of the Simons Observatory aims at achieving this precision through several improvements with respect to the previous generation of CMB experiments. For instance SO will use state of the art dichroic bolometers (transition edge sensors) aiming to reach a baseline noise of ~ 2.6 μK-arcmin at 93 GHz for the SAT and ~ 8.0 μK-arcmin for the LAT. This type of detector being photon noise limited, SO will deploy over $60,000$ in the SO nominal design, a factor of a few above current observatories.

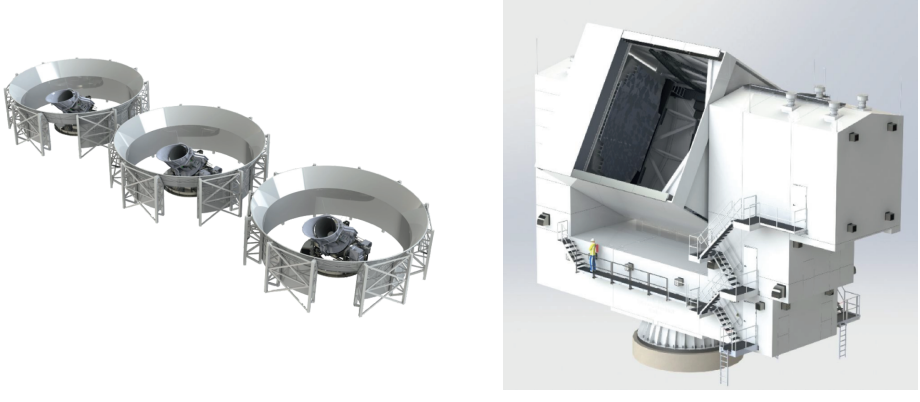

Figure 2 – The Small Aperture Telescopes (left), and the Large Aperture Telescope (right).

3.1 The three Small aperture telescopes (SAT)

The Simons Observatory will deploy an array of three small aperture telescopes that aim at observing the largest scale of the CMB polarisation anisotropies. The SATs are refractive telescopes with a 42 cm aperture. They will observe a $f_{sky} = 10\%$ patch, targeting low-foreground regions of the sky. The survey overlaps other CMB experiments coverage such as BICEP allowing for future cross-correlations. The SAT will have four focal planes. Through the use of dichroic TES each focal plane is sensitive to 2 frequencies, the planned SAT configuration is made of:

- 1 Low Frequencies (LF) focal plane observing at 27 and 39 GHz.
- 2 Mid Frequencies (MF) at 93 and 150 GHz.
- 1 High Frequencies (HF) at 225 and 280 GHz.

Where one of the MF focal plane will be replaced by the LF one during one year of observation to constrain synchrotron radiation in our patch while maximising the data in CMB dominated frequencies. Each MF and UHF focal plane has $10,000$ detectors allowing the SATs to have $30,000$ detectors observing the sky at any given time once the three SATs are deployed. The focal planes are cooled to 100 mK for the bolometers to be in their superconductive transition. The optics of the telescope are also cooled down between the $\sim$ 100 mK stage and the 50 K stage to limit the intrinsic emissions coming from the heat of the optical elements.

3.2 The Large Aperture Telescope (LAT)

The Simons Observatory's Large Aperture Telescope has a crossed dragone design with 2 mirrors[9]. The primary 6 meter diameter mirror will allow the LAT to produce an arcmin resolution map of the microwave sky. LAT's sky coverage will be $f_{sky} = 40\%$ and its survey will overlap with many others like Rubin Observatory, Euclid, DESI etc. As mentioned in section 2 this overlap allows for many synergies between SO and optical and spectroscopic surveys, such as the observation of large scale matter distribution. Future joint studies are planned such as the constraint of the growth of cosmic structures, baryonic feedback etc. Furthermore CMB observations and optical surveys use very different instrument design and observation techniques, so we will be able to cross correlate both data sets to mitigate possible systematic effects.
The LAT will observe in the same 6 frequency bands as the SATs and will use similar dichroic TES cooled down to 100 mK. Each focal plane observes in 2 frequencies and is embedded in an optics tube placed in the receiver. In its nominal design the LAT will have 7 optics tubes:

- 1 Low Frequencies (LF) focal plane observing at 27 and 39 GHz.
- 4 Mid Frequencies (MF) at 93 and 150 GHz.
- 2 High Frequencies (HF) at 225 and 280 GHz.

With this design the LAT will have more that $30,000$ detectors observing the sky. The receiver is able to host 13 optics tubes that will be deployed throughout the LAT's observation lifetime.

3.3 Systematic effects mitigation

Between the true CMB anisotropies signal and the retrieved power spectra used for cosmological parameter estimations, there are a lot of other signals, instrumental and data analysis effects that can bias our results. A lot of care is placed in the identification of those signals or effects and their mitigation. The methods used can be hardware or software-based and in general a mix of both is used to have the best result possible. Here we list some of those effects and the method used to mitigate them, this list is by no means exhaustive.
SO is a ground based telescope, this implies a variety of effects that are specific to ground experiments. For instance the ground itself, at $\sim$ 300 K will emit a signal that is possibly polarised by the instruments and their surroundings. To limit the ground pick-up that would particularly impact the large scale CMB signal, each SAT is surrounded by a ground shield (see left Figure 2) as well as a co-moving shield and a fore-baffle mounted on top of the receiver.

The atmospheric signal has to be mitigated as well. To do so the SAT are all equipped with a rotating half-wave plate (HWP). The latter is composed of layers of birefringent material that rotate the polarisation angle of the incoming light. The rotation of the HWP allows for a shift of characteristic frequency of the polarised CMB signal in frequency domain while the atmospheric noise is untouched resulting in a better signal to noise ratio and a mitigation of several systematic effects. The HWP is the first optical element in the optical chain of the SATs, reducing the possible I to P leakage coming from other optical elements. Furthermore the HWP

is part of the 50 K cryogenic stage which decreases the possible spurious emissions due to its thermal emission. To attenuate the vibration that the 2 Hz rotation of the HWP would induce and which could generate noise in the detectors, it is levitating using superconductor magnets. Another way atmospheric noise has been mitigated is in the choice of frequency bands. Indeed they correspond to bands where the atmosphere transmission is the best as shown on the right panel of Figure 3. It allows for a maximal amount of sky signal going through the atmosphere and lesser atmospheric contamination.

Calibration campaigns are also necessary to have the best understanding possible of the instrument (and to reduce its systematic effects). For instance the knowledge of the global polarisation angle of the telescope is necessary for the measurement of isotropic cosmic birefringence. Several methods are being explored for the SAT. For instance a rotating wire grid acting as a polariser will be deployed on top of the SAT aperture, allowing to measure the polarisation angle of the detectors with a forecasted precision between 0.2 to 1 degree[2]. Similarly another project plans to deploy a drone carrying a polarised source that has been calibrated in the lab and that would fly in the far field of the SATs. Here the aim is to compare between the emission of the polarised source and what is received by the telescope to fit for the polarisation angle of the detectors with a forecasted precision between 0.01 and 0.1 degree[2,8].

The major spurious contaminant for CMB polarisation analysis are the Galactic foregrounds. The 2 main signals are the synchrotron radiation and dust emissions. The synchrotron radiation is emitted by free electrons as they are being accelerated by the Galactic magnetic fields. The synchrotron signal tends to dominate at lower frequencies with respect to the peak of CMB emissions (see Figure 3 left). The other major foreground contaminant is thermal dust. In the interstellar-medium, dust grains get heated by nearby stars which results in an emission of microwave signal. And due to the asymmetry of the grains this emission is polarised. This emission dominates sky signals at high frequencies (with respect to the peak of CMB emission, see Figure 3 left). To characterise all those signals SO observes the sky in 6 frequencies from 27 to 280 GHz. The lowest frequency bands (27 and 39 GHz) help us characterise synchrotron radiation. Similarly, the highest frequency bands (225 and 280 GHz) are used to characterise the dust signal. Once those signals are understood in our sky patch, several methods are used to perform the separation between foreground and the CMB components. Those methods can be map-based or spectra based for instance. A data challenge that will result in a collaboration paper is in progress to compare the efficiency of the different pipelines for the estimation of r using realistic simulated SAT data and several foregrounds models varying in complexity.

This is only a glimpse of the complexity involved in the design of SO and analysis of its data. Many other effects need to be taken into account and are being dealt with by SO members dedicated to make sure SO will deliver state of the art cosmological data.

4 Conclusion

The Simons Observatory is being deployed in the Atacama desert in Chile at an altitude of $5,200$ meters. This is one of the driest places on Earth, limiting atmospheric effects as shown in Figure 3 (right). The site itself is near CLASS, ACT and the Simons Array and SO benefits from prior knowledge coming from those experiments. In that location almost 80% of the sky is accessible which allows SO's survey to overlap with other observations such as BICEP, Rubin Observatory, DESI and Euclid. To facilitate exchange SO is community oriented, maps will be regularly released, codes are shared (and already available [a]), notebooks and tutorials are available helping students or researcher wanting to use SO's data to learn.

[a] https://github.com/simonsobs

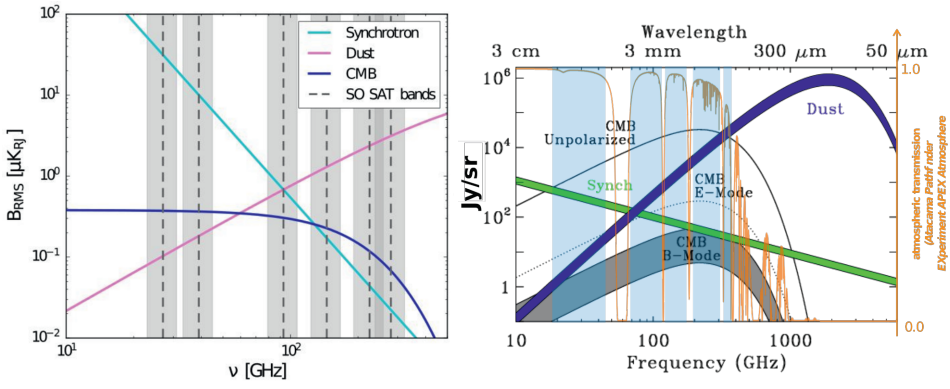

Figure 3 – SO frequency bands compared to sky components from[1] (left), and atmospheric transmission (right) adapted from[4].

Since the SO forecast paper[1] other papers have been released that go into more depths in some of the steps of the analysis. The SO Galactic Science paper[3] explore some of the astrophysical and Galactic observable achievable by SO.[7] explores delensing with SO and for instance its impact on r measurements.[5] validates the SO power spectrum estimation pipeline by comparing its results with fiducial Planck publications. Characterisation of the hardware involved in SO is also well underway, for example on the LAT receiver[10] or the SQUID multiplexing detectors[6]. The Simons Observatory has broad scientific goals with state of the art hardware and data analysis pipeline that will provide unprecedented data and understanding of the Universe. Observations will start soon so stay tuned for future exciting news!

The author presented this talk as a member of the Simons Observatory (SO) collaboration and requests that any references to the project be to the papers cited here.

References

1. Peter Ade et al. "The Simons Observatory: science goals and forecasts". In: *Journal of Cosmology and Astroparticle Physics* 2019.02 (Feb. 2019), pp. 056–056. DOI: 10.1088/1475-7516/2019/02/056. URL: https://doi.org/10.1088/1475-7516/2019/02/056.
2. Sean A. Bryan et al. "Development of calibration strategies for the Simons Observatory". In: *Millimeter, Submillimeter, and Far-Infrared Detectors and Instrumentation for Astronomy IX* (July 2018). Ed. by Jonas Zmuidzinas and Jian-Rong Gao. DOI: 10.1117/12.2313832. URL: http://dx.doi.org/10.1117/12.2313832.
3. Brandon S. Hensley et al. "The Simons Observatory: Galactic Science Goals and Forecasts". working paper or preprint. Nov. 2021. URL: https://hal.archives-ouvertes.fr/hal-03436792.
4. Alan Kogut et al. "The Primordial Inflation Explorer (PIXIE)". In: *Space Telescopes and Instrumentation 2016: Optical, Infrared, and Millimeter Wave*. Ed. by Howard A. MacEwen et al. Vol. 9904. International Society for Optics and Photonics. SPIE, 2016, pp. 331–353. DOI: 10.1117/12.2231090. URL: https://doi.org/10.1117/12.2231090.
5. Zack Li et al. "The Simons Observatory: a new open-source power spectrum pipeline applied to the Planck legacy data". In: (Dec. 2021). arXiv: 2112.13839 [astro-ph.CO].
6. Heather McCarrick et al. "The Simons Observatory Microwave SQUID Multiplexing Detector Module Design". In: *The Astrophysical Journal* 922.1 (Nov. 2021), p. 38. ISSN:

1538-4357. DOI: 10.3847/1538-4357/ac2232. URL: http://dx.doi.org/10.3847/1538-4357/ac2232.

7. Toshiya Namikawa et al. "Simons Observatory: Constraining inflationary gravitational waves with multitracer B-mode delensing". In: *Phys.Rev.D* 105.2 (2022), p. 023511. DOI: 10.1103/PhysRevD.105.023511. URL: https://hal.archives-ouvertes.fr/hal-03413907.

8. Federico Nati et al. "POLOCALC: A Novel Method to Measure the Absolute Polarization Orientation of the Cosmic Microwave Background". In: *Journal of Astronomical Instrumentation* 06.02 (May 2017), p. 1740008. ISSN: 2251-1725. DOI: 10.1142/s2251171717400086. URL: http://dx.doi.org/10.1142/S2251171717400086.

9. Michael D. Niemack. "Designs for a large-aperture telescope to map the CMB 10× faster". In: *Applied Optics* 55.7 (Feb. 2016), p. 1688. DOI: 10.1364/ao.55.001688. URL: https://doi.org/10.1364%2Fao.55.001688.

10. Ningfeng Zhu et al. "The Simons Observatory Large Aperture Telescope Receiver". In: *The Astrophysical Journal Supplement Series* 256.1 (Sept. 2021), p. 23. DOI: 10.3847/1538-4365/ac0db7. URL: https://doi.org/10.3847/1538-4365/ac0db7.

Distant foreground and the Hubble constant tension

V.N. Yershov
Moniteye U.K., 12 Ogle Street, London, W1W 6HU

It is possible to explain the discrepancy (tension) between the local measurement of the cosmological parameter H_0 (the Hubble constant) and its value derived from the *Planck*-mission measurements of the Cosmic Microwave Background (CMB) by considering contamination of the CMB by emission from some medium surrounding distant extragalactic sources (a distant foreground), such as extremely cold coarse-grain (grey) dust. As any other foreground, it would alter the CMB power spectrum and contribute to the dispersion of CMB temperature fluctuations. By generating random samples of CMB with different dispersions, we have checked that the increased dispersion leads to a smaller estimated value of H_0, the rest of the cosmological model parameters remaining fixed. This might explain the reduced value of the *Planck*-derived parameter H_0 with respect to the local measurements. The cold grey dust for some time has been suspected to populate intergalactic space and it is known to be almost undetectable, except for the effect of dimming remote extragalactic sources.

1 Introduction

The importance of the issue with the Hubble constant as measured by two different methods (the H_0 tension) can be appreciated from recent comprehensive reviews on the subject [1,2] and by the fact of special international conferences discussing exclusively this particular issue [a].

The *Planck* space observatory [3] revealed a statistically significant discrepancy between the cosmological parameter H_0 as calculated within the standard cosmological model by using the Cosmic Microwave Background (CMB) power spectrum, $H_0 = (67.37 \pm 0.54)\,\mathrm{km\,s^{-1}\,Mpc^{-1}}$, and the values of this parameter obtained by using other methods – mostly from direct local measurements [4]. One of these local measurements is based on optical and infrared (IR) observations of variable Cepheid stars, with the recent calculation of H_0 based on this method [5] being $H_0 = (73.48 \pm 1.66)\,\mathrm{km\,s^{-1}\,Mpc^{-1}}$. Both local and *Planck*-derived estimates of H_0 have passed a number of rigorous tests by considering many possible sources of systematic errors [6,7,8], but the discrepancy still remains.

Discussing the possible origin of this discrepancy, most authors and reviewers focus primarily on observational biases related to the method of standard-candles, Cepheids and type-Ia supernovae (SN), and on proposals going far beyond the standard cosmological and particle physics

[a] `https://www.eso.org/sci/meetings/2020/H0.html`

models. By contrast, possible biases intrinsic to the CMB are passed by almost without further thought.

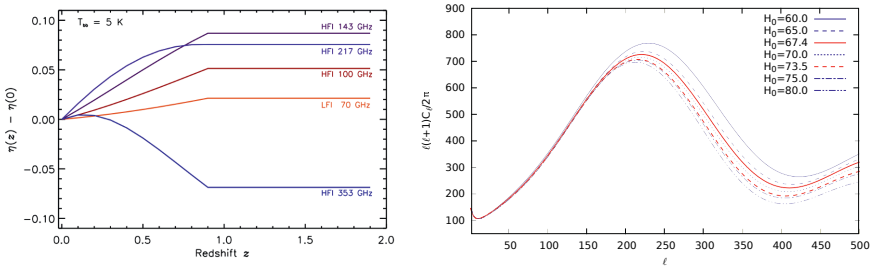

Figure 1 – *Left:* Redshift dependences of the blackbody radiation energy fraction $\eta(z)$ as observed in five *Planck* frequency bands for $T_{\rm bb} = 5\,{\rm K}$; the constant shifts of the curves with respect to each other have been normalised at $z = 0$ by subtracting from them their individual values $\eta(0)$; *Right:* CMB power spectra (in the standard normalised presentation) generated by using the code for anisotropies in the microwave background (CAMB tool) for seven different values of H_0.

2 Distant foreground

Various authors have reported that the contaminating emission from a medium around distant extragalactic sources should affect correlations between CMB and extragalactic cosmic structures traced by bright transient sources, like supernovae (SNe) or gamma-ray bursts. The signature of the distant foreground in the CMB, based on the WMAP and *Planck*-mission results and traced by SNe was previously reported by the author [9,10], who found a correlation between the SN redshifts, $z_{\rm SN}$, and CMB temperature fluctuations at the SNe locations, $T_{\rm SN}$.

By using different *Planck* frequency bands and computing the fractions $\eta_\nu(z)$ of blackbody radiation energy as observed in each frequency band ν for different redshifts z one can estimate the regression line slopes for these bands [11]. The functions $\eta_\nu(z)$ are shown in Fig. 1, as calculated for the blackbody temperature $T_{\rm bb} = 5\,{\rm K}$ and five of the *Planck* frequency bands $\nu = \{70, 100, 143, 217, 353\}$ GHz. Note that the temperature of the medium in thermal equilibrium with the CMB must exceed or be equal to 5 K for the redshifts $z > 0.835$, so for these redshifts the functions $\eta_\nu(z)$ appear horizontal.

We can calculate slopes ξ^c_ν of these functions for different $T_{\rm bb}$ and compare them with the observed slopes ξ^o_ν corresponding to different *Planck* frequency bands $\nu = \{70, 100, 143, 217, 353\}$ GHz which, according to our previous work [10], are the following: $\xi^o_{70} = 0.96 \pm 0.63$, $\xi^o_{143} = 1.09 \pm 0.31$, $\xi^o_{217} = 0.61 \pm 0.36$ and $\xi^o_{353} = -0.99 \pm 0.48$. The slope for the 100 GHz-band was used as a reference for normalisation, so $\xi^o_{100} = 1.00 \pm 0.39$.

The calculated slopes ξ^c_ν of these functions averaged between the temperatures $T_{\rm bb} = \{3, 4, 5, 6\}\,{\rm K}$ for each of the *Planck* frequency bands $\nu = \{70, 143, 217, 353\}$ GHz are $\xi^c_{70} = 0.45 \pm 0.03$, $\xi^c_{143} = 1.63 \pm 0.17$, $\xi^c_{217} = 0.73 \pm 0.74$ and $\xi^c_{353} = -1.48 \pm 0.43$ (again, the slope for the 100 GHz-band was used as a reference). They are within the 1-σ tolerance interval with respect to the above experimental values ξ^o_ν, which indicates that the temperature of the CMB-contaminating ingredient of the intergalactic medium is very low, likely to be between 3 K and 6 K. This can give clues as to the nature of the medium, which can be coarse-grain (grey) dust, and which for some time has been suspected to populate intergalactic space [12,13,14,15].

This "grey" dust leaves little or no imprint on the spectral energy distribution of background sources. However, it creates the long-known excess of radiation from some extragalactic objects in the far IR at $\lambda \approx 500\,\mu$m, which extends up to centimetre wavelengths and can interfere with the CMB radiation. Such a 500 μm radiation excess was confirmed and measured by the

Herschel space observatory [16]. In the 1990s, this excess was interpreted as an elevated spatial mass density of cold dust [17] with temperatures of 4 to 7 K. Here we confirm this interpretation from a completely different point of view.

3 CMB distrortion

The angular sizes of the observed regions with the 500 μm emission [16,18] range from 0.02° to 0.5°. So this emission would effectively distort the CMB power spectrum at the multipole moments $\ell \approx 360$ and higher, which would change the estimated parameter H_0. In order to quantify these changes we have used the code for anisotropies in the microwave background [19] (CAMB) which allows the extraction of different cosmological parameters from theoretical CMB power spectra generated by the same code. The calculated changes are shown on the right panel of Fig. 1 for the first trough of the CMB power spectrum, where its effect on the calculated parameter H_0 is quite strong.

In this code, the coefficients C_ℓ of the CMB power spectrum are calculated as sums of the integrals $a_{\ell m}$, $|m| \leq \ell$, which include temperature fluctuations $\Delta T(x, \phi)$ over the celestial sphere, where $x \in [-1, 1]$ is the cosine of the latitude and $\phi \in [0, 2\pi]$ is the longitude. Conversely, the functions $\Delta T(x, \phi)$ are calculated by summing up the integrals $a_{\ell m}$. For a given CMB power spectrum, we have calculated a set of corresponding values of $\Delta T(x, \phi)$ by using random $a_{\ell m}$ for $\ell = 0, 1, \ldots, \ell_{\mathtt{max}}$ with the restriction $\ell_{\mathtt{max}} = 500$. We have taken five equal-spaced values of H_0, namely, 60, 65, 70, 75 and 80 [km s^{-1} Mpc^{-1}] plus the values 67.4 [km s^{-1} Mpc^{-1}] (solid red curve on the right panel of Fig. 1) and 73.5 [km s^{-1} Mpc^{-1}] (dashed red curve on the same panel) corresponding, respectively, to the *Planck* result and to the local measurements of H_0.

Additionally, for checking the consistency of our calculations we have taken a few sets of normally distributed randomised values of $a^i_{\ell m}$, $i = 1, 2, \ldots, 5$, so that for each of the selected values of H_0, we have obtained five samples of $a^{H_0,i}_{\ell m}$ and, correspondingly, five samples of values $\Delta T^{H_0,i}$. For each of them, we have calculated the average of the CMB temperature fluctuations $\overline{\Delta T}$ and its standard deviation σ_T.

Here we are mainly interested in the way the values σ_T change when the parameter H_0 is varied. For each of these generated sequences, the trend of the calculated values σ_T was practically the same. Namely, when the dispersion of the CMB temperature fluctuations increases, the value of the estimated H_0 decreases, the difference between the two discussed H_0 values 73.5 and 67.4 [km s^{-1} Mpc^{-1}] being related to $\Delta\sigma_T = -0.60 \pm 0.04\,\mu$K. This value is the measure of CMB contamination by photons from the medium surrounding remote clumps of matter, and it can thus be used for estimating the amount of cold coarse-grain dust in the intergalactic medium.

4 Discussion

Between 2012 and 2019, new studies have appeared demonstrating that the dimming of the type-Ia supernovae was different in different directions [20,21,22,23,24,25,26]. Most of the authors of these studies interpret their results in terms of anisotropic acceleration of the Universe.

However, anisotropy of acceleration violates the main cosmological principle. Therefore, the grey-dust interpretation of the type-Ia supernovae anisotropic dimming becomes preferable: it would be much more logical to assume non-uniform distribution of dust rather than the Universe having different properties in different directions.

What might be the origin of this coarse-grain dust? Apart from the initial formation of dust particles within galaxies with their further transport into the intergalactic space, dust formation can also occur directly in the intergalactic medium [27]. The observational evidence for cold molecular clouds at the cooling flows in galaxy clusters and the presence of dust in these regions is widespread [28]. Besides this detectable dust clouds, there exists yet another possibility

of almost undetectable coarse-grain dust existing in the intergalactic space which, according to recent studies, should be seriously taken into consideration. Namely, these macroscopic dust particles can be formed by the process of hydrogen solidification under sufficiently low temperatures, e.g., when the CMB temperature gets below 10 K at $z < 2$, which was proposed in 1968 by F. Hoyle [29] and further discussed in the 1990s and early 2000s [30,31,32]. In the last decade, it was shown by experimental physicists that H_2 ice became stable in vacuum and do not sublime if it contains impurities [33,34,35] transported from galaxies into the intergalactic medium.

My conclusion is that the mechanism of contamination of CMB radiation by some distant foreground emission from cold dust can explain the discrepancy between the local measurements of H_0 and the *Planck*-derived value, without invoking unnecessary assumptions that violate the basic cosmological principles or break the standard cosmological and particle physics models.

References

1. Di Valentino E. *et al.*, Class. Quantum Grav. **38**, 153001 (2021)
2. Shah P., Lemos P., Lahav O., *Astron. Aph. Rev.* **29**, 9 (2021)
3. Planck Collaboration, *Astron. Aph.* **641**, A6 (2020)
4. Riess, A. G., Nat. Rev. Phys. **2**, 10 (2020)
5. Riess, A. G. *et al.*, *Aph. J.* **855**, 136 (2018)
6. Efstathiou G., *MNRAS* **440**, 1138 (2014)
7. Planck Collaboration, *Astron. Aph.* **607**, A95 (2017)
8. Follin, B., Knox, L., *MNRAS* **477**, 4534 (2018)
9. Yershov V.N., Orlov V.V., Raikov A.A., *MNRAS* **423**, 2147 (2012), arXiv:1205.5139
10. Yershov V.N., Orlov V.V., Raikov A.A., *MNRAS* **445**, 2440 (2014), arXiv:1410.5814
11. Yershov V.N. *et al.*, *MNRAS* **492**, 5052 (2020), arXiv:2001.09152
12. Eigenson M.S., *Astron. Zh.* **26**, 278 (1949)
13. Zwicky F., *Morphological Astronomy*, Springer-Verlag, Heidelberg (1957)
14. González, R.A. *et al.*, *Aph. J.* **506**, 152 (1998)
15. Alton, P.B., Bianchi, S., Davies, J., *Aph. Sp. Sci.* **276**, 949 (2001)
16. Galliano F. *et al.*, *Astron. Aph.* **536**, A88 (2011)
17. Reach W. T. *et al.*, *Aph. J.* **451**, 188 (1995)
18. Lisenfeld, U. *et al.*, *Astron. Aph.* **382**, 860 (2002)
19. Lewis A., *Phys. Rev.* D **87**, 103529 (2013)
20. Cai, R.-G., Tuo, Z.-L., 2012, *J. Cosmol. Astropart. Phys.* **02**, 004 (2012)
21. Cárdenas V. H., Bernal C., Bonilla A., *MNRAS* **433**, 3534 (2013)
22. Bernal C., Cárdenas V. H., Motta V., *Phys. Lett.* B **765**, 163 (2017)
23. Colin J., Mohayaee R., Rameez M., Sarkar S., *Astron. Aph.* **631**, L13 (2019)
24. Zhao D., Zhou Y., Chang Z., *MNRAS* **486**, 5679 (2019)
25. Rameez M., *Preprint* arXiv:1905.00221 (2019)
26. Luongo O. *et al.*, *Preprint* arXiv:2108.13228 (2021)
27. Fabian, A.C., Johnstone R.M., Daines S.J., *MNRAS* **271**, 737 (1994)
28. Russell H.R. *et al.*, *Aph. J.* **836**, 130 (2017)
29. Hoyle F., Wickramasinghe N.C., Reddish V.C., Nature **218**, 661 (1968)
30. Pfenniger D., Combes F., Martinet L., *Astron. Aph.* **285**, 79 (1994)
31. Wardle M. J., Walker M. A., *Aph. J.* **527**, L109 (1999)
32. Pfenniger D., Proc. IAU Symp. **220**, 241 (2004)
33. Schaefer J., Chem. Phys. **332**, 211 (2007)
34. Walker M. A., *MNRAS* **434**, 2814 (2013)
35. Kettwich S.C. *et al.*, *MNRAS* **450**, 1932 (2015)

Deriving the Hubble Constant using Planck and X-ray observations of galaxy clusters

F. De Luca, H. Bourdin, P. Mazzotta, F. Oppizzi
Dipartimento di Fisica, Università di Roma 'Tor Vergata',
Via della Ricerca Scientifica, 1, I-00133, Roma, Italy

In the last decades, several tensions in the concordance ΛCDM arose from different cosmological probes, such as the tension between the Hubble Constant derived from early Universe measurement of the Cosmic Microwave Background and studying the local Universe with cosmic distance ladder. In this work, we present a preliminary result of the Hubble Constant with a method independent from the early Universe measure and the local estimate from Chepeids and Supernovae using clusters of galaxies. We combine X-ray and millimetre observation of 118 galaxy clusters using XMM-*Newton* and *Planck* satellite data. For a ΛCDM model with $\Omega_m = 0.3$, $\Omega_\Lambda = 0.7$, we reduce the uncertainties of the method with respect to the previous estimates, with a preliminary value of $H_0 = 67 \pm 2 \mathrm{kms}^{-1}\mathrm{Mpc}^{-1}$.

1 Introduction

During the last decades, the cosmological model, with Cold Dark Matter and a cosmological constant associated with Dark Energy (ΛCDM), has been successfully proved by several cosmological studies. However, with the more accurate results we reach, several tensions between different cosmological probes emerge. That is the case of the Hubble Constant derived from the observation of Cosmic Microwave Background (CMB) by *Planck* Collaboration et al. (2020) [5] and the Riess et al. (2021) [6] measurement of H_0 using cosmic distance ladder (Cepheids plus supernovae). The two probes show a discrepancy, at a level of $\sim 4\sigma$, between the early Universe and the local estimate of H_0. The persistence of this tension after several years of refinements in the estimation of the uncertainties may be related to new physics that goes beyond the concordance ΛCDM cosmological model. In this scenario, independent constraints from the two previous probes, such as galaxy clusters studies, can help in mitigating the tension or give some hints for its solution. Considering all the structures that have formed across cosmic time, clusters of galaxies represent the largest gravitationally bound objects in the Universe. Clusters are mainly composed of Dark Matter (DM), which supplies the gravitational potential to keep bounded the baryonic matter: galaxies and a hot ionised intra-cluster medium (ICM). ICM and galaxies are almost in hydrostatic equilibrium within the DM potential well, with ICM heated up at high temperatures during the self-similar assembly of the clusters (see the work of Kravtsov et al. (2012) [4] for a more detailed description of the clusters formation and evolution). Therefore, ICM thermodynamical state must reflect the history of cluster evolution and, consequently, the cosmological framework from which clusters grow. Generally, cosmological information are extracted from the number density of clusters in the Universe, which depends on the estimation of the cluster masses. In this work, we follow another approach based on the work of Kozmanyan et al. (2019) [3].

2 Methodology

The method of Kozmanyan et al. (2019) [3] relies on the simple idea formerly proposed by Cavaliere et al. (1979) [7]. It is based on a distance-measuring technique that compares two observables of ICM to measure the angular distance of the clusters. ICM in galaxy clusters is responsible for the distortion, along the line of sight, of the CMB spectrum due to the interaction of the free electrons in the ICM and the CMB photons, known as the Sunyaev-Zeldovich (SZ) effect [8]. Moreover, ICM is observable in the X-ray bandwidth due to the bremsstrahlung emission from the same free electrons in the gas. These two observables prove the internal structure of clusters in different density regimes: bremsstrahlung emission is proportional to the integrated, along the line of sight ($dl = D_a d\theta$), density squared of the gas ($\Sigma_X \propto \int n_e^2 D_a d\theta$), while SZ depends only on the gas pressure, i.e. linearly by density ($y \propto \int n_e T_e D_a d\theta$).

Instead of extracting the cosmological information directly from the X-ray surface brightness (Σ_X) and the SZ signal (described in the non-relativistic regime by the comptonization parameter y), Kozmanyan et al. (2019) [3] method consists of studying cluster pressure profiles performing a joint X-ray and SZ analysis. In fact, all the thermodynamical properties of ICM extracted from the X-ray or SZ signal inherit the dependence of the angular diameter distance, i.e. of any cosmological information. In particular, they apply a parametric MCMC fit of the pressure profiles assuming the functional form proposed by Nagai et al. (2007) [9] and spherical symmetry. With this pressure profile and using the density profile template estimated from X-ray observation (considering the Vikhlinin et al. 2006 [10] models), they compare the projected temperature template with the observed spectroscopic X-ray one. In the ideal case, where all the assumptions in the cluster structure and the cosmological framework are well known, we do not expect any difference between the two profiles. However, in the more realistic case of interest, we can define a parameter, η_T, to consider any difference due to our incorrect knowledge of the cluster structure and the cosmology:

$$\eta_T = \left(\frac{\bar{D}_a}{D_a}\right)^{1/2} \left(\frac{2}{(2-Y_p)} \frac{1}{(2-\bar{n}_p/\bar{n}_e)}\right)^{1/2} \frac{C_\rho^{1/2}}{e_{LOS}^{1/2}} b_n, \tag{1}$$

where the first two parenthesis accounts for the cosmological model in use: D_a is the angular diameter distance, Y_p is the helium abundance, n_p/n_e is the fraction of protons with respect to electrons, and the other terms express departure from spherical symmetry, e_{LOS}, cluster clumpiness, C_ρ, and any other bias in the cluster modelling or fit with b_n. The barred terms in eq. 1 indicate the assumed values in the data analysis. Combining informed priors on the physics of the ICM obtained from hydrodynamical simulations and the observed measurement of η_T for 61 clusters, Kozmanyan et al. (2019) [3] derive finally an estimate for H_0 with a Bayesian approach, assuming the *Planck* Helium abundance for eq. 1. Reversely, if we assume the value of H_0 it is possible to constrain the Helium abundance, as done in Ettori et al. (2020) [11]. For this analysis, we assume the ΛCDM model with $\Omega_m = 0.3$, the *Planck* (2018) [5] (eq. 79b) primordial Helium abundance $Y_P^{BBN} = 0.243$, and $\Omega_\Lambda = 0.7$.

3 Dataset

We expand the preliminary work of Kozmanyan et al. (2019) [3] to the 118 galaxy clusters of the CHEX-MATE [1] sample. The CHEX-MATE project consists of a large, minimally unbiased, signal-to-noise limited sample of galaxy clusters detected by *Planck* via their SZ effect. Compared to Kozmanyan et al. (2019) [3], the sample is almost double in size with only 16 clusters in common. This sample aims to analyse both the most massive ($M_{500}{}^a > 7.25 \times 10^{14} M_\odot$, with $z < 0.6$) and

[a] The characteristic masses M_Δ of clusters are expressed in terms of overdensities, Δ, respect to the critical density of the Universe, $\rho_c(z)$, evaluated at the cluster redshift: $M_{500} = (4\pi/3)500\rho_c(z)R_{500}^3$.

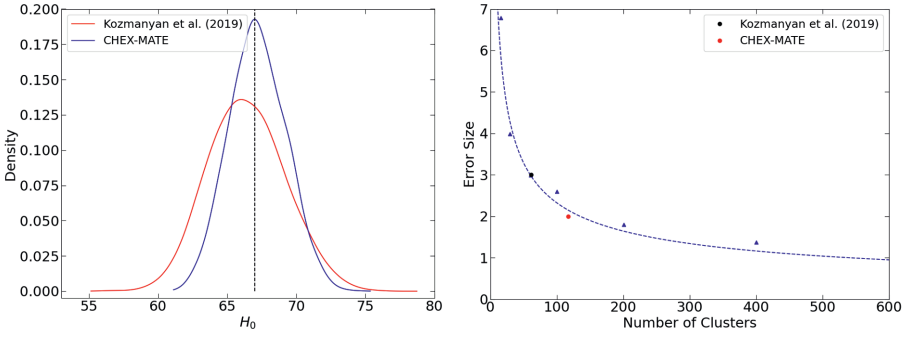

Figure 1 – Left panel: preliminary posterior distribution of H_0, compared with the Kozmanyan et al. (2019) [3] results. Vertical line show the best fit value for H_0. Right panel: forecast (in blue triangles) for the statistical uncertainties of the method when the sample size change. Black and red dots represent the uncertainties size measured in Kozmanyan et al. (2019) [3] and for this work, respectively.

the most recently formed ($0.05 < z < 0.2$ and $2 \times 10^{14} M_{\odot} < M_{500} < 9 \times 10^{14} M_{\odot}$) clusters in the Universe, to study cluster properties in the local volume and in the high mass regime.

We analyse the SZ and X-ray signals of the clusters following the technique developed by Bourdin et al. (2017) [2] for the *Planck* and XMM-*Newton* space telescopes data. In particular, we use the public data for the *Planck* High-Frequency Instrument (HFI) and the three EPIC cameras onboard the XMM-*Newton* telescope. This technique consists of a multi-component fit of the *Planck* HFI channels considering the contribution of the Galactic thermal dust, CMB primary anisotropies, and the cluster SZ signal. A further correction for the intra-cluster dust emission is also considered in the fit. For the X-ray analysis, we model the cluster emission with the APEC[b] spectral library, and we correct the spectra for the Galactic absorption of X-ray photons. In particular, we use the absorption cross-section of Verner et al. (1996) [12], the abundance table of Asplund et al. (2009) [13], and the Hydrogen column density derived from the HI4PI collaboration [14]. The X-ray cluster signal is separated from the background considering, in a parametric fit, the instrumental background, characterised by a quiescent particle background, and the contribution of the astrophysical background coming from the foreground emission of our Galaxy, the Cosmic X-ray Background as in Bourdin et al. (2017) [2].

For a more detailed description of the methods, we refer to Bourdin et al. (2017) [2] and Kozmanyan et al. (2019) [3] works.

4 Results

We show in the left panel of Fig. 4 the preliminary posterior distribution of the H_0, derived considering the η_T values of the clusters, compared with the precedent results of Kozmanyan et al. (2019) [3]. The best fit value is equal to $H_0 = 67 \pm 2 \mathrm{kms}^{-1}\mathrm{Mpc}^{-1}$ (with 68% error). The preliminary posterior distribution of H_0 derived from the CHEX-MATE sample is in agreement with the precedent estimation of Kozmanyan et al. (2019) [3], but with a more tight constraint due to the larger size of the cluster sample. In particular, the 68% confidence interval is $\sim 33\%$ lower than the precedent estimate. In fact, the clusters in this work are almost twice (118) the clusters in Kozmanyan et al. (2019) [3] work, with only 16 clusters in common. The improvement in the uncertainties agrees with the prevision of Kozmanyan et al. (2019) [3] shown in the right panel of Fig. 4. As a final consideration, we use to retrieve H_0 the same informed prior from hydrodynamical simulation of Kozmanyan et al. (2019) [3].

[b] http://www.atomdb.org/index.php

5 Conclusion

In this work, we present a preliminary estimation of the expansion rate of the Universe considering the new CHEX-MATE [1] galaxy cluster sample. To extract the cosmological information, we compare the thermodynamical profiles obtained from the X-ray and millimetre observations of XMM-*Newton* and *Planck* telescopes. In particular, we extract the SZ signal from the foreground and background components in the *Planck* data following the method described in Bourdin et al. (2017) [2].

From this fit, we estimate the cosmological information in interest considering the Kozmanyan et al. (2019) [3] method. In particular, we estimate the ratio η_T between the X-ray and SZ temperature profiles that inherit all the cosmological information. Finally, we combine, with a Bayesian approach, informed priors on the physics of the ICM obtained from hydrodynamical simulations with measurement uncertainties to separate the cosmological information from the cluster internal structure bias. Preliminary results are in agreement with the previous estimation of Kozmanyan et al. (2019) [3], but, most importantly, we stress the attention to the improvement in the uncertainties. This refinement is largely due to the larger sample employed in this work and is compatible with the prediction present in Kozmanyan et al. (2019) [3]. This result is promising in the context of the estimation of H_0, since it confirms the validity of galaxy clusters as cosmological probes independent from the early Universe CMB observation and the local estimate from Cepheids plus supernovae. Moreover, with larger samples, it should be possible to reduce further the uncertainties at a level comparable to other cosmological probes. Possible sources of systematics that may affect the estimate of H_0 are the X-ray temperature cross calibration (see also Wan et al. 2021 [15]), the assumptions of a specific Helium abundance, or the accuracy of simulation in describing real cluster structures. We are testing these systematics using different simulations and considering the extension of the analysis to a larger sample of clusters.

Acknowledgments

FDL, HB, PM, and FO acknowledge financial contribution from the contracts ASI-INAF Athena 2019-27-HH.0, "Attività di Studio per la comunità scientifica di Astrofisica delle Alte Energie e Fisica Astroparticellare" (Accordo Attuativo ASI-INAF n. 2017-14- H.0), from the European Union's Horizon 2020 Programme under the AHEAD2020 project (grant agreement n. 871158), support from INFN through the InDark initiative, and From "Tor Vergata" Grant "SUPERMASSIVE-Progetti Ricerca Scientifica di Ateneo 2021"

References

1. The CHEX-MATE Collaboration *et al*, A&A **650**, A104 (2021).
2. H. Bourdin *et al*, *APJ* **843**, 72 (2017).
3. A. Kozmanyan *et al*, A&A **621**, A34 (2019).
4. , A. V. Kravtsov and S. Borgani, *ARA&A* **50**, 53-409 (2012).
5. The Planck Collaboration *et al*, A&A **641**, A6 (2020).
6. A. G. Riess *et al*, Astrophys. J. Lett. **908**, L6 (2021).
7. A. Cavaliere *et al*, A&A **75**, 322-325 (1979).
8. , R. A. Sunyaev and Ya. B. Zeldovich, Comments on Astrophysics and Space Physics **4**, 173 (1972).
9. D. Nagai *et al*, *APJ* **668**, 1-14 (2007).
10. A. Vikhlinin *et al*, *APJ* **640**, 691-709 (2006).
11. E. Ettori *et al*, Astronomische Nachrichten **341**, 210-216 (2020).
12. D. A. Verner *et al*, *ApJS* **103**, 467 (1996).
13. M. Asplund *et al*, *ARA&A* **47**, 481-522 (2009).
14. The HI4PI Collaboration *et al*, A&A **594**, A116 (2016).
15. J. T. Wan *et al*, *MNRAS* **504**, 102-1076 (2021).

Cosmic voids and their imprint on the CMB lensing maps: from DES Year 1 to DES Year 3

P. E. Vielzeuf
Centre de Physique des Particules de Marseille (CPPM), 163, avenue de Luminy, 13288 Marseille, France

Correlation between the CMB radiation and large scale structure of our universe is probing the growth of structures in the low-redshift cosmic web and have recently been added as a new tool in our cosmological inference. In parallel, cosmic voids, due to their low dense environment sensible to gravity modification, are also raising interest to probe cosmology. The CMB lensing signal from cosmic voids and superclusters as been already observed using data from different experiments. I will present here the results from the the latest DESY3 catalogues (covering a surface of $\sim 5000 deg^2$ in the southern sky) super-structures correlated with the CMB-lensing radiation from the Planck satellite. This work being an extension of our previous measurement with the DESY1 catalogues ($\sim 1300 deg^2$). In there, using a staking methodology, we have measured the correlation signal between DESY3 observed super-structures (cosmic voids and super-cluster combined) and CMB lensing maps with a 10.3σ detection level. We then compare our measurement to the one of ΛCDM numerical simulations using the same methodology. We observe a 2σ deviation between the two signals suggesting an excess signal prediction in our ΛCDM fiducial recipe. Such deviation are also in agreement with our previous result from DESY1 and recent measurement from the DESI telescope.

1 Introduction

Cosmic voids are the largest under-dense structures in the low-redshift cosmic web, and have shown to be rich sources of cosmological information due to their low-density nature (*e.g.* their matter density profile, shape and redshift-dependent abundance contain information about the physics of dark matter and the growth rate of structure). On the other hand, similarly to the other structure at low redshift, cosmic voids will have an imprint on the observed radiation of the Cosmic Microwave Background (CMB) due to the alteration of the CMB radiation while crossing the underlying gravitational potential in their path toward us.

We present here the work of Vielzeuf *et al.*[1] and Kovács *et al.*[2] where cosmological imprint of cosmic voids identified in the Dark Energy Survey (DES) galaxy catalogues (after the first and the third years of observations) in the reconstructed lensing signal from the Planck satellite [4,5] has been estimated .

2 Data sets & methods

2.1 Dark Energy Survey data and Simulations

DES is a six-year photometric survey that covered approximately 5000 deg^2 of the sky area in the South Galactic Cap. Mounted on the Cerro Tololo Inter-American Observatory (CTIO) four metre Blanco telescope in Chile, the 570 megapixel Dark Energy Camera (DECam, Flaugher *et al.*[13]) images the field in *grizY* filters. In this work we have been using photometric redshift

galaxy catalogues from DES. In particular, we identified cosmic voids in the Luminous Red Galaxies from the DES observed catalogues selected by the RedMagiC algorithm (Rozo *et al.*[10]). RedMagic is meant to select high-resolution photometric redshift LRGs ($\sigma_z/(1+z) \sim 0.02$) with a constant co-moving space density.

The objective of this analysis was in the fist time to optimize the lensing imprint of cosmic voids in the CMB map detection and in a second time to compare the measured signal to the one estimated in simulated ΛCDM realization. For this purpose, we have been using the MICE (Marenostrum Institut de Ciencias de l'Espai) N-BODY light-cone (see Fosalba *et al.*[7] and Crocce *et al.*[8]) for which the CMB lensing potential map have been reconstructed using the "Onion Universe" methodology Fosalba *et al.*[6] The MICE simulation assumed a flat standard ΛCDM model with a cosmology based on the Five-Year Wilkinson Microwave Anisotropy Probe (WMAP) results [9].

2.2 Void finding

To identify cosmic voids in our different catalogues, we have used the void finder algorithm described in Sánchez *et al* [11]. This algorithm has shown to be in one hand adapted to be used in galaxy catalogues with photometric redshift uncertainties and on the other hand to be particularly adapted for lensing signal detection, due to the fact that the structure identified will be elongated along the line of sight. The finder is identifying the voids by i) dividing the galaxy sample in redshift slice of a given size in comoving distance, ii) computing the density field in each of the slices by counting the number of galaxies falling in each pixel of an Healpix map [14], iii)identifying the most underdense pixel and grow the void around it until the concentric external shell reaches the mean density of the given redshift slice. iv) following this procedure with the next most underdense pixels.

We identified voids using this algorithm both in MICE and DES catalogues (Y1 and Y3) and found good agreement in different voids parameters between the different catalogues.

2.3 Correlation methodology

The imprint of a single void in the CMB lensing signal is too noisy to be detected (see Krause *et al.*[12]), nevertheless it had been shown that by stacking the signal of different voids, one can increase the signal-to-noise of the measurement and reach detectable level. The stacking methodology consist in averaging re-scaled patches of the CMB lensing convergence map cut in alignment of our voids centers. The voids lensing profile can then be estimated by averaging the signal from the stacked image in all directions around the void center. Once the correlation signal have been measured, in order to estimate the concordance of our measurement to the ΛCDM simulated one, we defined an amplitude parameter as :

$$A_\kappa = \frac{\kappa_{DES}}{\kappa_{MICE}} \tag{1}$$

where κ_{DES} and κ_{MICE} are the corresponding stacked lensing signal in the DES observations and MICE simulations.

3 Results

3.1 DESY1

After the DES first year of observation, we applied the methodology presented here-above to the $1300 deg^2$ spanned by the Dark Energy Survey. The objective of this first analysis was to optimize our methodology in order to maximize our extracted correlation signal. Thus, we have tested our methodology varying different parameters :

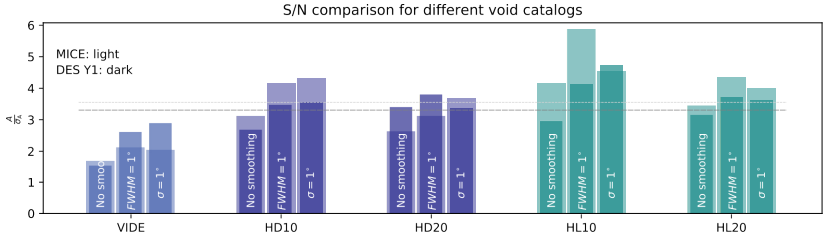

Figure 1 – Comparison of measurement significance in the form of A/σ_A. The conservative VIDE sample also provides useful consistency tests in agreement with our 2D analyses. The dashed horizontal lines mark the mean of the DES Y1 (dark) and the MICE (light) significances with values 3.31σ and 3.55σ, respectively.

- We tested different RedMagiC samples, the High luminosity (HL) and the High Density (HD) samples.
- We varied the smoothing parameter of the void finder and also used an alternative 3 dimensional void finder (VIDE [15]).
- We finally smoothed the CMB lensing map (in order to reduce the size of the small-scale fluctuations) using three different smoothing recipes : i) no smoothing, ii) Gaussian smoothing of $\sigma = 1°$, iii) Gaussian smoothing of $fwhm = 1°$.

Fig. 1 shows the different detection significances of the correlation signal obtained for the different void catalogues of MICE and DES and for all combinations of the different method parameters mentioned above. Overall, we robustly detected imprints at the 3σ significance level with most of our analysis choices, Using the 2D void catalogue with HL tracers and $10Mpc/h$ initial density smoothing (HL10), we reached $S/N \sim 5$ for given κ smoothing strategies.

3.2 DESY3

Applying now our fiducial methodology defined in the first year analysis, we used the observations of DES after 3 years (DESY3 $5000deg^2$). In the left panel of Fig.2 we show the stacked CMB convergence profile of the our cosmic voids identified in the MICE simulation (light blue) and in the DES observation (dark blue). The dashed grey line in the figure, correspond to the voids CMB lensing imprint in the alternative Websky simulation (see Kovács *et al.*[2] for more details). We report a detection of the CMB lensing signal by cosmic voids at the $S/N \sim 6.6\sigma$ level (8.4σ for super-clusters [a]). Moreover, as it can be seen on the figure, we reported a slightly lower lensing signal inside the voids ($R < R_v$) in the observed correlation compared to the simulated one. We measured a small $\sim 2\sigma$ weaker than expected signal from MICE (mostly originated in the centres of voids and superclusters). In addition to that, looking for the origins of the lower-than-expected κ imprints, we split the DES Y3 void and super-clusters catalogues roughly into halves, and measured the stacked κ imprints in the resulting subsets. The right panel of Fig.2 is showing the different A_κ values obtained for the different samples and sub-samples comparing as well with the recent measurement performed with the DESI experiment (Hang *et al.* [3]). We found that both voids and superclusters feature more discrepancy in the low-z part of the DES Y3 data at redshifts $0.15 < z < 0.55$, with $A_\kappa \sim 0.55 \pm 0.23$ and $A_\kappa \sim 0.70 \pm 0.15$, respectively. While the internal consistency of the supercluster sample is generally better, we also observed that deeper voids ($\delta_c < -0.6$ central under-density) imprint a lensing signal that is more anomalous with $A_\kappa \sim 0.56 \pm 0.14$. Similarly, larger voids ($Rv > 35h^{-1}Mpc$) also imprint a rather weak CMB κ signal with an $A_\kappa \sim 0.66 \pm 0.15$ amplitude.

[a] In the DESY3 analysis we also measured the CMB lensing imprint of over-densed regions identified by inverting our void identification methodology.

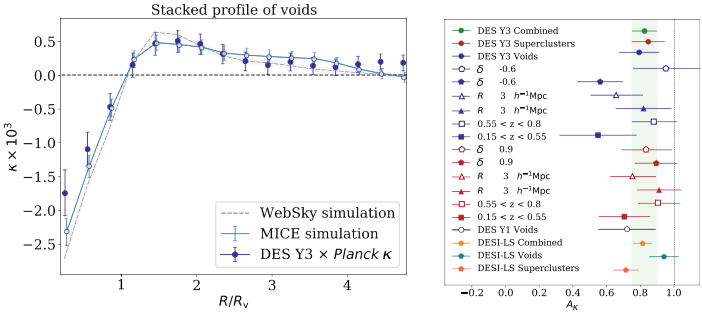

Figure 2 – *left panel:* Radial profiles measured from the stacked CMB κ images are shown for voids. *Right panel:* Void, supercluster, and combined constraints on the A_κ parameter, including the outcomes from the measurements using bins of central under-density, radius, and redshift. Moderately significant trends are seen for weaker signals from various subsets of the void data, while the superclusters bins are more consistent with each other. We also compare our DES Y3 results with the constraints from the DESI Legacy Survey, and from voids detected in the smaller DES Y1 data set

4 Conclusions

In this analysis we have studied the imprint of cosmic voids (and superclusters) in the CMB lensing convergence (κ) maps reconstructed from Planck observations. Using first the galaxy catalogues from DES first year of observation, we developed a methodology and optimized it in order to maximize our detection significance. We then used the Year 3 data set from DES to detect the lensing signal of both voids and super-clusters in the CMB maps. We then compared the DES Y3 observations to expectations from the MICE simulation. We determined that DES Y3 voids feature a highly significant ($S/N \sim 6.6$), albeit lower-than-expected, signal with $A_\kappa \sim 0.79 \pm 0.12$ amplitude, in comparison with the ΛCDM model implemented in the MICE simulation. Analysing DES Y3 superclusters, our detection significance reached the 8.4σ level, but again with a lower-than-expected $A_\kappa \sim 0.84 \pm 0.10$ amplitude. We found that these moderate $\sim 2\sigma$ deviations are mostly originated in the centres of voids and super-clusters ($R/Rv, sc < 1$).

References

1. Vielzeuf P., et al., *Mon. Not. R. Astron. Soc.* **500**, 464 (2021)
2. Kovács A., et al.,*arXiv e-prints* **arXiv:2203.11306**, (2022)
3. Hang Q., et al., *Mon. Not. R. Astron. Soc.* **507**, 510 (2021)
4. Planck Collaboration, *A. & A.* **641**, A8 (2020)
5. Planck Collaboration, *A. & A.* **594**, A15 (2016)
6. Fosalba P., et al., *Mon. Not. R. Astron. Soc.* **391**, 435 (2008)
7. Fosalba P., et al., *Mon. Not. R. Astron. Soc.* **448**, 2987 (2015)
8. Crocce M., et al.,*Mon. Not. R. Astron. Soc.* **453**, 1513 (2015)
9. Komatsu E., et al.,*Ast. J.* **180**, 330 (2009)
10. Rozo E., et al.,*Mon. Not. R. Astron. Soc.* **461**, 1431 (2016)
11. Sánchez C.,et al., *Mon. Not. R. Astron. Soc.* **465**, 746–759 (2017) .
12. Krause E., et al.,*Ast. J Lett.* **762**, L20 (2013)
13. Flaugher B., et al., *Ast. J.* **150**, 150 (2015)
14. Górski K. M., et al., *Ast. J.* **622**, 759 (2005)
15. Sutter P. M., et al., *Ast. & Comp.* **9**, 1-9 (2015)

Massive merging cluster PSZ2G091 as seen by the NIKA2 camera

E. Artis[1], R. Adam[2], P. Ade[3], H. Ajeddig[4], P. André[4], M. Arnaud[4], H. Aussel[4], I. Bartalucci[5], A. Beelen[6], A. Benoît[7], S. Berta[8], L. Bing[9], O. Bourrion[1], M. Calvo[7], A. Catalano[1], M. De Petris[10], F.-X. Désert[11], S. Doyle[3], E. F. C. Driessen[8], A. Ferragamo[10], A. Gomez[12], J. Goupy[7], C. Hanser[1], F. Kéruzoré[1], C. Kramer[13], B. Ladjelate[13], G. Lagache[9], S. Leclercq[8], J.-F. Lestrade[14], J.-F. Macías-Pérez[1], A. Maury[4], P. Mauskopf[3,20], F. Mayet[1], A. Monfardini[7], M. Muñoz-Echeverría[1], A. Paliwal[10], L. Perotto[1], G. Pisano[3], E. Pointecouteau[15], N. Ponthieu[11], G. W. Pratt[4], V. Revéret[4], A. J. Rigby[3], A. Ritacco[16,6], C. Romero[17], H. Roussel[18], F. Ruppin[19], K. Schuster[8], S. Shu[21], A. Sievers[13], C. Tucker[3], G. Yepes[22],

[1] *Univ. Grenoble Alpes, CNRS, LPSC-IN2P3, 53, avenue des Martyrs, 38000 Grenoble, France.*
[2] *LLR, CNRS, École Polytechnique, Institut Polytechnique de Paris, Palaiseau, France.*
[3] *School of Physics and Astronomy, Cardiff University, Queen's Buildings, The Parade, Cardiff, CF24 3AA, UK.*
[4] *AIM, CEA, CNRS, Université Paris-Saclay, Université Paris Diderot, Sorbonne Paris Cité, 91191 Gif-sur-Yvette, France.*
[5] *INAF, IASF-Milano, Via A. Corti 12, 20133 Milano, Italy.*
[6] *Institut d'Astrophysique Spatiale (IAS), CNRS, Université Paris Sud, Orsay, France.*
[7] *Institut Néel, CNRS, Université Grenoble Alpes, France.*
[8] *Institut de RadioAstronomie Millimétrique (IRAM), Grenoble, France.*
[9] *Aix Marseille Univ, CNRS, CNES, LAM, Marseille, France.*
[10] *Dipartimento di Fisica, Sapienza Università di Roma, Piazzale Aldo Moro 5, I-00185 Roma, Italy.*
[11] *Univ. Grenoble Alpes, CNRS, IPAG, 38000 Grenoble, France.*
[12] *Centro de Astrobiología (CSIC-INTA), Torrejón de Ardoz, 28850 Madrid, Spain.*
[13] *Instituto de Radioastronomía Milimétrica (IRAM), Granada, Spain.*
[14] *LERMA, Observatoire de Paris, PSL Research University, CNRS, Sorbonne Université, UPMC, 75014 Paris, France.*
[15] *Univ. de Toulouse, UPS-OMP, CNRS, IRAP, 31028 Toulouse, France.*
[16] *Laboratoire de Physique de l'École Normale Supérieure, ENS, PSL Research University, CNRS, Sorbonne Université, Université de Paris, 75005 Paris, France.*
[17] *Department of Physics and Astronomy, University of Pennsylvania, 209 South 33rd Street, Philadelphia, PA, 19104, USA.*
[18] *Institut d'Astrophysique de Paris, CNRS (UMR7095), 98 bis boulevard Arago, 75014 Paris, France.*
[19] *Univ. Lyon, Univ. Claude Bernard Lyon 1, CNRS/IN2P3, IP2I Lyon, F-69622, Villeurbanne, France.*
[20] *School of Earth and Space Exploration and Department of Physics, Arizona State University, Tempe, AZ 85287, USA.*
[21] *Caltech, Pasadena, CA 91125, USA.*
[22] *Departamento de Física Teórica and CIAFF, Facultad de Ciencias, Modulo 8, Universidad Autánoma de Madrid, 28049 Madrid, Spain.*

PSZ2 G091.83+26.11 is a galaxy cluster with $M_{500} = 7.43 \times 10^{14} M_{\odot}$ at $z = 0.822$ [1]. This object exhibits a complex morphology with a clear bimodality observed in X-rays. However, it was detected and analysed in the *Planck* sample as a single, spherical cluster following a universal profile [2]. This model can lead to miscalculations of thermodynamical quantities, like the pressure profile. As future multiwavelength cluster experiments will detect more and more objects at high redshifts, it is crucial to quantify this systematic effect. In this work, we use high-resolution observations of the NIKA2 camera [3,4,5,6] to integrate the morphological characteristics of the cluster in our modelling. This is achieved by fitting a two-halo model to the SZ image and then by reconstruction of the resulting projected pressure profile. We then compare these results with the spherical assumption.

1 Cosmological inference from cluster counts

The number of clusters per unit of mass and volume, modelled as the halo mass function [7], constitutes a robust cosmological probe [8]. However, the total mass of dark matter halos is not an observable quantity, and must be inferred from different physical phenomena [9], like the thermal Sunyaev-Zel'dovich effect [10] (tSZ). As a consequence, astrophysical systematic effects

Table 1: Characteristics of PSZ2 G091.83+26.11 [1]. $t_{\rm LPSZ}$ is the scheduled duration of the observations, while $t_{\rm obs}$ is the actual time during which the object has been observed.

z	M_{500}	θ_{500}	$t_{\rm obs}/t_{\rm LPSZ}$	tSZ decrement peak
0.822	$7.43 \times 10^{14} M_{\odot}$	2.2 arcmin	2.5h/2.5h=1	14.9σ

are biasing our measurements [11], and must be integrated in any cosmological analysis. Moreover, given the fact that the size of the catalogs will be increased by several orders of magnitude in the future, effects that are now neglected will play a crucial role [12,13].
The Large program SZ [14] of the NIKA2 experiment (LPSZ) aims at investigating these issues, taking advantage of the spatial resolution and FoV of the NIKA2 camera. Here, we focus on the impact of cluster morphology on the reconstruction of thermdynamical quantities.

2 The case of PSZ2G091

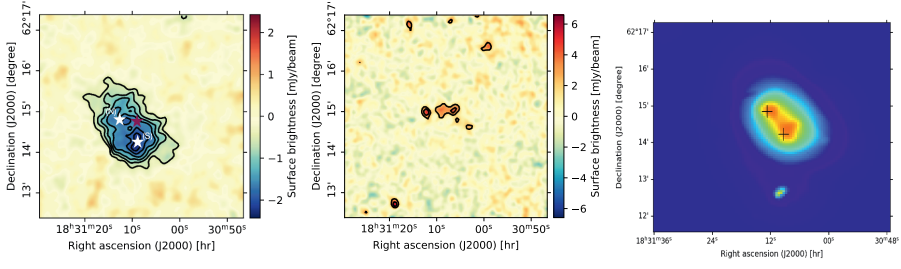

Figure 1: **Left**: Surface brightness map at 2 mm from NIKA2 observations. The black contours represent the SNR levels starting at 3σ increasing by 2σ at each step. The northern (N) and southern (S) X-ray peaks are shown as white stars, the X-ray centroid being in purple. **Middle**: Surface brightness at 1 mm. The signal exhibits several point sources, which are fitted in the analysis. **Right**: X-ray surface brightness of PSZ2G091 from *XMM-Newton*. The cluster exhibits two peaks at the position $(\alpha_{\rm N}, \delta_{\rm N}) = (277.80, 62.24)$, and $(\alpha_{\rm S}, \delta_{\rm S}) = (277.79, 62.237)$, shown with the black crosses.

As part of the LPSZ, PSZ2G091 was observed in October, 2017, with an average elevation of 58.5° and an average atmospheric opacity at 225 GHz of 0.243. These conditions are standard for observations at the IRAM 30 m telescope, at this season.
In figure 1, we show the results of the data reduction [3] at 1 and 2 mm. The cluster is clearly elongated in the NE-SW direction. There is a clear departure from sphericity, and a hint of bimodality later confirmed in the X-ray surface brightness map. The peaks in the X-ray map are in good agreement with the ones observed in the NIKA2 2 mm map. This would imply the presence of two well-defined sub-halos in the first stages of a major merger.

3 Imaging analysis

We first consider a single spherical halo centred on the X-ray centroid coordinates. A forward modelling approach is incorporated in an MCMC sampling framework to fit the parameters of the pressure profile, as well as the point sources, with the collaboration software `PANCO2` [15]. We use a power law model, where each of the 6 bins follows the identity

$$P(r) = P_i (r/r_i)^{-\alpha_i}. \quad (1)$$

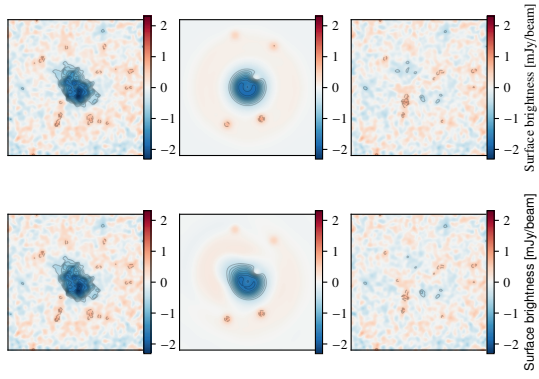

Figure 2: Single spherical model fit of the NIKA2 2 mm map for PSZ2G091 centered on the X-ray centroid coordinates (**top**), and 2-halo model (**bottom**). From **left** to **right**, we display the data, the model, with the point sources treated, and the residuals. The maps are given in a $5' \times 5'$ area, and for display purposes, each map is smoothed with a gaussian kernel. The contours are showing the SNR level sets, starting at 3σ and increasing with a step of 1σ.

The top row of figure 2 shows the results of the fitting procedure. The spherical symmetry clearly does not encapsulate the bimodal nature of the cluster. It is then required to improve our modelling.
Then, instead of considering a single pressure profile, we jointly fit two halos at the positions of the X-ray peaks. The results of the fits are shown on the bottom row of figure 2. It is clear that the two-halo model yields a more realistic representation of the dynamical state of the cluster. Additionally, the residuals are slightly improved in the region of the northern subhalo. Of course, due to the non-spherical nature of this cluster, it is not possible to consider a radial pressure profile. However, in section 4, we describe how we recover an average radial profile for the two-halo model.

4 Pressure profile reconstruction

Thermodynamical profiles are usually considered with the goal of reconstructing a mass profile, using the hydrostatic equilibrium assumption. This requires the presence of a 1D pressure profile, when we previously fitted a 2D map. Thus, we use the following procedure to recover an average 1D profile. With the assumption of the two sub-halos lying in the same plane perpendicular to the line of sight, we recover a mean radial pressure profile by integrating both the profiles in annuli centered around the X-ray centroid coordinates. The pressure in the i-th bin reads:

$$P_i = \left(\int_{r_i}^{r_{i+1}} (P_N(r) + P_S(r)) 2\pi r \mathrm{d}r \right) / \left(\pi (r_{i+1}^2 - r_i^2) \right), \tag{2}$$

where P_i is the value of the pressure, P_N and P_S are respectively the profiles of the northern and southern subhalos, r_i and r_{i+1} being the inner and outer radii of the annulus. This allows us to reconstruct the profile shown in figure 3, where we compare our reconstructed quantities with the universal profile [16] .

5 Conclusions

This analysis shows the challenges related to the complexity of cluster morphologies. In this work, we showed that for the case of the highly disturbed cluster PSZ2G091, taking into account

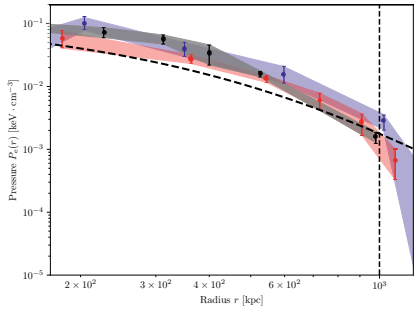

Figure 3: In red, composite pressure profile obtained by combining the northern (N) and southern (S) profiles, as described in equation 2. In blue, profile obtained with the single spherical model. In black, we represent the contours obtained from XMM X-ray data only, for the spherical case. The black dashed line represents the universal profile. The vertical dashed line represents the radius R_{500} obtained from X-ray data assuming spherical symmetry.

the merging state of the cluster yields results that are slightly different from the spherical profile. This is a promising result, as the pressure profile impacts the $Y_{500} - M$ relation. To complete this analysis, we plan to perform a full thermodynamical analysis of this cluster, recovering the 2D maps of physical quantities like the temperature and the entropy. This a precondition to assess the impact of the morphology of this cluster on its full mass reconstruction, and generally on cosmological inference using clusters.

Acknowledgments

We would like to thank the IRAM staff for their support during the campaigns. The NIKA2 dilution cryostat has been designed and built at the Institut Néel. In particular, we acknowledge the crucial contribution of the Cryogenics Group, and in particular Gregory Garde, Henri Rodenas, Jean-Paul Leggeri, Philippe Camus. This work has been partially funded by the Foundation Nanoscience Grenoble and the LabEx FOCUS ANR-11-LABX-0013. This work is supported by the French National Research Agency under the contracts "MKIDS", "NIKA" and ANR-15-CE31-0017 and in the framework of the "Investissements d'avenir" program (ANR-15-IDEX-02). This work has benefited from the support of the European Research Council Advanced Grant ORISTARS under the European Union's Seventh Framework Programme (Grant Agreement no. 291294). E. A. acknowledges funding from the French Programme d'investissements d'avenir through the Enigmass Labex. A. R. acknowledges financial support from the Italian Ministry of University and Research - Project Proposal CIR01_00010.

References

1. Planck Collaboration et al., A&A **594**, A27 (2016), 1502.01598
2. M. Arnaud et al., A&A **517**, A92 (2010), 0910.1234
3. L. Perotto et al., A&A **637**, A71 (2020), 1910.02038
4. R. Adam et al., A&A **609**, A115 (2018), 1707.00908
5. M. Calvo et al., Journal of Low Temperature Physics **184**, 816 (2016), 1601.02774
6. O. Bourrion et al., Journal of Instrumentation **11**, P11001 (2016), 1602.01288
7. W.H. Press, P. Schechter, ApJ **187**, 425 (1974)
8. S.W. Allen et al., ARA&A **49**, 409 (2011), 1103.4829
9. G.W. Pratt et al., Space Sci. Rev. **215**, 25 (2019), 1902.10837
10. R.A. Sunyaev, Y.B. Zeldovich, Ap&SS **7**, 3 (1970)
11. S. Bocquet et al. (2015), 1502.07357
12. E. Artis et al., A&A **649**, A47 (2021), 2101.02501
13. A. Fumagalli et al., A&A **652**, A21 (2021), 2102.08914
14. F. Mayet et al., EPJ Web of Conferences **228**, 00017 (2020), 1911.03145
15. F. Kéruzoré et al., EPJ Web of Conferences **257**, 00024 (2022), 2111.06493
16. Planck Collaboration et al., A&A **550**, A131 (2013), 1207.4061

CMB lensing measurements with the Atacama Cosmology Telescope: opportunities and challenges

Frank J. Qu
DAMTP, Centre for Mathematical Sciences, Wilberforce Road, Cambridge CB3 0WA, UK

For the first time, new observations with the Atacama Cosmology Telescope will allow CMB lensing power spectrum measurements to have higher precision than those attained by Planck. This high signal to noise lensing spectrum will translate into a few percent determination of σ_8 (providing a robust test of low amplitudes reported by galaxy lensing surveys) and will give one of the tightest constraints on the sum of neutrino masses. We present a detailed overview of our lensing pipeline with some preliminary results obtained using simulations together with our extensive null test suite to show that all relevant systematic are now well controlled. We highlight some of the challenges encountered with high-resolution ground-based challenges: extra-galactic foregrounds and noise modelling, as well as methods to solve them.

1 Introduction

The cosmic microwave background (CMB) encodes a wealth of information about our Universe. Measurements of variations of this radiation have enabled precise determination of the components of our Universe in terms of dark matter and dark energy. Furthermore, the CMB contains information regarding the distribution of mass (including dark matter and gas) as large scale structures of matter imprint new patterns in the CMB anisotropies via lensing. Cosmic microwave lensing is a phenomenon in which the light path from the primordial radiation of the Universe gets gravitationally deflected on arc-minute scales by structures of dark and baryonic matter as they travel toward us [1]. The net effect of many such deflections is a surface remapping of the CMB anisotropy pattern. The CMB is rather a unique probe to study weak lensing since the properties of the unlensed source plane is well understood as a Gaussian random field with a clearly defined angular power spectrum. This source is also well localised at redshift $z = 1100$ and is the furthest light source we can observe. Owing to this high redshift, CMB is sensitive to nearly all the mass fluctuation in our Universe, with most of the signal arising at high redshifts between $z = 0.5$ and $z = 3$, meaning that it can be modelled using linear physics without complications from non-linear evolution and baryonic feedback. CMB lensing measurements therefore can act as an important probe of cosmology.

In the last decade, CMB lensing experienced a fast transition from the first detection to the regime of precision measurements thanks to the advent of low noise, high-resolution CMB

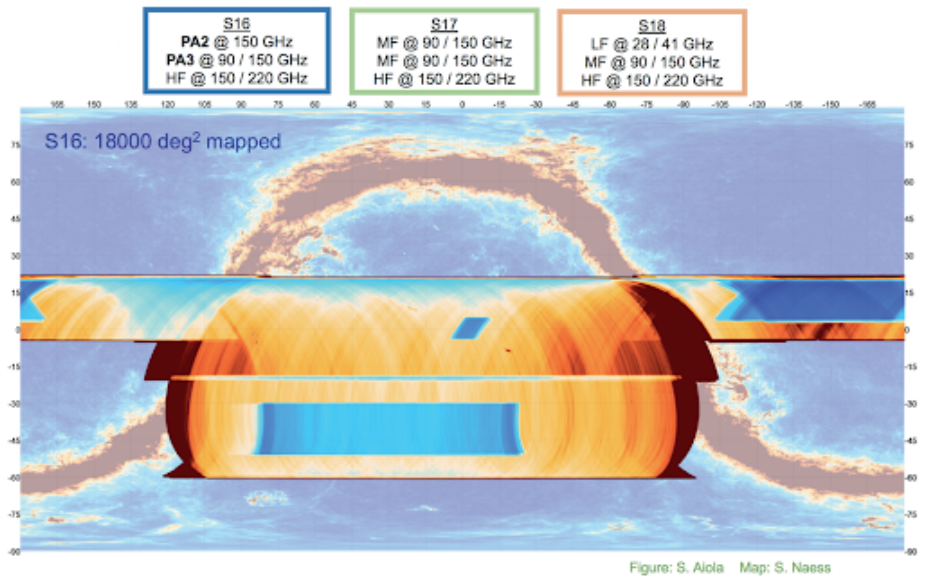

Figure 1 – Observational footprint of AdvACT. Color provides indication of depth

telescopes such as the Atacama Cosmology Telescope (ACT), the South Pole Telescope (SPT), and the Planck Satellite. Early evidence of lensing came from cross-correlation measurements made by WMAP [2], with the first direct detection made by the ACT team in 2011 [3]. Since then, lensing power spectrum measurements have been made by multiple groups. The Planck team had made the previous highest precision measurement of the lensing power spectrum[4], with a 40σ detection significance in their 2018 release.

The main goals of the lensing measurement with ACT are to present independent new measurements of the lensing power spectrum and to provide constraints on cosmological parameters. This will provide a powerful test of the Planck lensing measurements, which are generally in agreement with ΛCDM. In addition, several recent observations using low redshift probes like galaxy lensing and clustering are in mild tension with Planck's CMB and lensing constraints, reporting a lower amplitude on the matter density and fluctuations. Since CMB lensing is subjected to different systematic effects than the other weak lensing probes and is unaffected by problems like photo-z errors, shear uncertainties and intrinsic alignments, we expect our measurement to investigate this potential source of tension.

In this proceeding, we discuss in detail our lensing pipeline, highlighting in particular techniques employed to mitigate and control foreground contamination and noise modelling systematics.

2 Data Used

ACT is a six-meter aplanatic Gregorian telescope located in the Atacama Desert in Chile. The current receivers fitted to the telescope, the Advanced ACTPol (AdvACT) receiver are equipped with arrays of superconducting transition edge sensor bolometers, sensitive to both temperature and polarization at a frequency of 30, 40, 97,149 and 225 GHz.

We use data taken in season 6 covering over 12,000 square degrees, details of the footprint and scanning can be seen in Fig. 1. We combine the different coadded data maps $D_{A,f}$ with

arrays $A \in \{S16, S17, S18, S19\}$ and frequencies $f \in \{90\text{GHz}, 150\text{GHz}\}$ into a single CMB map M on which lensing reconstruction is carried out. The sky coverage and depth of observations enable ACT to reach noise levels smaller than Planck.

The combination of the maps is done in spherical harmonic space,

$$M_{\ell m} = B_{A_c,f_c}(\ell) \sum_{A,f} w_{A,f}(\ell) D_{A,f_{\ell m}} B^{-1}_{A,f}(\ell) \tag{1}$$

where the weights in harmonic space $w_{A,f}$ is given by the noise power spectra obtained from the beam deconvolved noise maps of the individual CMB maps.

$$w_{A,f} = \frac{N^{-1}_{A,f}(\ell) B^2_{A,f}(\ell)}{\sum_{(A,f)} N^{-1}_{A,f}(\ell) B^2_{A,f}(\ell)} \tag{2}$$

A deconvolution of the harmonic beams $B_{A,f}(\ell)$ is performed on each array and the resultant coadded map is convolved with the common beam B_{A_c,f_c}. The choice for this beam is arbitrary since it is deconvolved in the subsequent analysis.

The coadded Q and U maps are subsequently transformed to the $E-B$ basis using the pure EB method [5]. Resulting in the coadded CMB map M_X with $X \in T, E, B$. The same coadding operation is performed on simulations containing lensed CMB maps and noise maps. The resulting suite of coadded CMB simulations is used in the bias calculation part described in the subsequent part of the pipeline.

3 Lensing Pipeline

Lensing induces correlations between Fourier modes that are originally independent of each other and hence breaks the statistical isotropy of the original unlensed CMB temperature and polarization fields. One can think of its effect as a remapping of the temperature distribution of the unlensed CMB by the lensing deflection. The deflection field $\mathbf{d}$ is the gradient of the lensing potential ϕ which is the integrated measure of the gravitational potential along the unlensend line of sight. On the sphere, we can express this remapping as:

$$\Theta(\hat{\mathbf{n}}) = \widetilde{\Theta}[\hat{\mathbf{n}} + \nabla\phi(\hat{\mathbf{n}})] \tag{3}$$

where $\Theta(\hat{\mathbf{n}})$ is the unlensed CMB temperature along direction $\hat{\mathbf{n}}$ and $\Theta(\hat{\mathbf{n}})$ is the observed lensed temperature.

The lensing potential ϕ can be treated as a Gaussian random field characterised by the power spectrum $C_L^{\phi\phi}$ in harmonic space. Comparing the measured spectrum with the ones calculated using a given cosmology can be used to provide constraints on parameters. To have an intuitive understanding on the effect of lensing, we can Taylor expand Eq. 3:

$$\Theta(\hat{\mathbf{n}}) \approx \widetilde{\Theta}(\hat{\mathbf{n}}) + \nabla_i\phi(\hat{\mathbf{n}})\nabla^i\widetilde{\Theta}(\hat{\mathbf{n}}) + ... \tag{4}$$

from which we see that lensing introduces a dependence of the unlensed CMB temperature with its higher derivative terms, which leads to non-Gaussian effects, i.e a coupling previously independent harmonic modes in harmonic space and breaking the statistical isotropy.

An appropriate averaging over pairs of multipole moments, therefore, allows reconstruction of this lensing potential field. The so-called quadratic estimator achieves this:

$$\hat{\phi}_{LM} = A_L \int d\Omega Y^*_{LM}(\hat{\mathbf{n}}) \nabla^i [V(\hat{\mathbf{n}}) \nabla_i U(\hat{\mathbf{n}})] \tag{5}$$

Here A_L is the normalization and U and V are the Wiener and inverse variance filtered maps respectively:

$$V(\hat{n}) = \sum_{LM} \frac{1}{C_l^{\Theta\Theta} + N_l^{TT}} \Theta_{lm} Y_{lm}(\hat{\mathbf{n}}) \tag{6}$$

$$U(\hat{\mathbf{n}}) = \sum_{LM} \frac{C_L^{\Theta\Theta}}{C_l^{\Theta\Theta} + N_l^{TT}} \Theta_{lm} Y_{lm}(\hat{\mathbf{n}}) \tag{7}$$

Here Θ_{lm} are the beam deconvolved multipoles of the sky temperature. $C_l^{\Theta\Theta} + N_l^{TT}$, the total power spectrum for the measured temperature is composed of $C_l^{\Theta\Theta}$ being the lensed CMB power spectrum and N_l^{TT} is the power spectrum of the experimental noise. The estimator above correlates the inverse variance weighted temperature map $V(\hat{\mathbf{n}})$ with the gradient of the Wiener lensed field $U(\hat{\mathbf{n}})$. The inverse variance filter is in place to reduce the effects of Gaussian noise. Finally, the divergence in the estimator is used to extract the gradient part of the estimator. The curl part which is expected to be zero serves as a powerful null test to test for systematic effects.

One can then use the above estimator to measure a map of lensing potential from prepared CMB maps. We do this by combining the lensing field obtained from both temperature and polarization fields in a way to minimize reconstruction noise, such that the resulting reconstructed lensing potential is given by

$${}_1\hat{\phi}(\hat{\mathbf{n}}) = \mp \sum_{LM} (\hat{\phi}_{LM} \pm i\hat{c}_{LM})_{\pm 1} Y_{LM}(\hat{\mathbf{n}}) \tag{8}$$

This lensing field will be biased due to the existence of masks and anisotropic noise which will induce couplings between modes that mimic lensing. This meanfield bias can be calculated by averaging the reconstruction of the biased estimator over many simulations that have independent CMB and lensing potential realizations. The averaging will make sure that only the spurious, non-lensing couplings remain. Hence, an unbiased estimate of the lensing potential is given by:

$$\hat{\phi}_L^{XY} = \bar{\phi}_L^{XY} - \langle \bar{\phi}_L^{XY} \rangle \tag{9}$$

The naive lensing power spectrum obtained from the mean-field subtract lensing field $\hat{\phi}\hat{\phi}^*$ is also biased. There is a Gaussian disconnected bias N_0 which constitutes the bulk of the reconstruction noise[6]. Furthermore, there is the N_1 bias, which arises from the second-order contractions of two lensing potential fields in the measured four-point function[7]. Any additional non-idealities not captured at the map level must be simulated and included in a small Monte Carlo bias. A state of the art lensing power spectrum reconstruction encapsulates the above and can agree with a few percentage residual using theory only. This small residual, coming from high order and mask effects, constitute the Montecarlo bias.

Fig. 2 obtained using realistic AdvACT simulations shows that the reconstructed spectra agree well with the input theory spectrum. The residual bias to be simulated is only a few percent. Note that we have plotted the convergence power spectrum, which is related to the lensing power spectrum by:

$$C_L^{\kappa\kappa} = \frac{[L(L+1)]^2}{4} C_L^{\phi\phi} \tag{10}$$

4 Challenges for precision cosmology: Extragalactic foregrounds and noise mismodelling

CMB lensing, while being a cosmology probe that is clean and robust compared to galaxy weak lensing, still has two potential challenges that need to be resolved to obtain unbiased cosmological parameters. These are the presence of extra-galactic foregrounds and noise modelling.

4.1 Challenge 1: Contamination from extragalactic foregrounds

A major systematic dominating current and futuristic CMB lensing experiments are the presence of extra-galactic foregrounds. The observed millimetre sky also picks up the contaminated

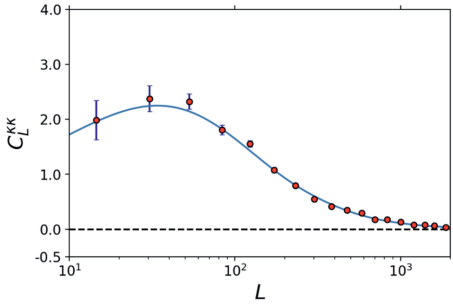

Figure 2 – Lensing convergence bandpowers obtained from simulation with realistic analysis errorbars. Overlaid on top of theory as predicted by ΛCDM.

contribution from the cosmic infrared background (CIB), the thermal and kinetic SZ effect and radio galaxy sources. The effects of these foregrounds on lensing are studied in detail in [8,9], for AdvACT level of sensitivity, if unmitigated, foregrounds can cause significant biases in the lensing power spectrum recovery and cosmological parameter estimation. Expressing the observed temperature field as $T = T_{\rm CMB} + f$ where $T_{\rm CMB}$ is the CMB signal of interest and f being the extragalactic foregrounds, one can characterise the bias to the quadratic estimator as follows:

$$\begin{aligned} C_L^{\phi\phi} &= \langle Q[T_{\rm CMB}, T_{\rm CMB}]Q[T_{\rm CMB}, T_{\rm CMB}]\rangle \\ &\quad + 2\langle Q[T_{\rm CMB}, T_{\rm CMB}]Q[f, f]\rangle + 4\langle Q[T_{\rm CMB}, f]Q[T_{\rm CMB}, f]\rangle + \langle Q[f, f]Q[f, f]\rangle \end{aligned} \tag{11}$$

Here Q represents the generic operation of taking the quadratic estimator of two CMB fields, the first term above is the lensing power spectrum of interest, while the rest of the terms are the bispectrum and trispectrum contributions of the foregrounds to the 4-point function. Failure to mitigate them can lead to biased lensing power spectrum recovery and biased cosmological parameter estimation.

A combination of strategies was developed in the pipeline to make sure foreground systematics are sub percentage, these mitigation strategies can be divided into three categories:

1. At the CMB map level, point sources and clusters were identified, masked and inpainted.
2. Geometric methods which either reconstruct the contribution of sources or clusters to the trispectrum and projects them off (bias hardening) or exploit that the symmetry properties of foregrounds are different than the lensing estimator (shear) to make lensing immune to foregrounds.
3. Multifrequency cleaning methods involving internal linear combinations ILC or symmetric multi-frequency cleaning by combining different frequency channels.

The above are all complemented with data based methods to show that the mitigation strategies applied on realistic simulations[10,11] agree well with the procedure applied on the data. This foreground pipeline will also play an important role in assessing the foreground levels of futuristic CMB missions like Simons Observatory where a large fraction of signal to noise still comes from the temperature channel where unfortunately foreground effects are more important.

4.2 Challenge 2: Challenge due to noise modelling

The lensing power spectrum recovery discussed above probes the 4-point connected function of the lensed CMB fields. The N_0 subtraction done was motivated by the fact that even in

the absence of lensing, chance correlations will result in Gaussian 4-point functions arising from contractions of pairs of CMB fields. The realisation dependent procedure introduced when subtracting this bias is arguably robust since it introduces data simulation combinations making the quadratic estimator robust to data and simulation mismatch to second order. This was demonstrated in past analyses [4,12,13].

However, we observed that for large sky ground-based surveys like AdvACT, this debiasing process is very challenging as indicated by simple failures in noise only null tests. Here we run the quadratic estimator on appropriately signal nulled maps such that the expected result should be zero but as indicated in green for Fig. 3, this is not the case. This null failure suggested that the simulations are missing something fundamental found in the data. We suspect that the atmosphere could be contributing to a trispectrum bias which is not accounted for in the simulations. We overcome this by introducing cross correlation-based quadratic estimator introduced in [14], which takes combinations of data realisations that have independent noise power to cancel the contribution from noise modelling or simulation of instrumental noise. Switching this more robust estimator shows how the noise only null tests go from failing to passing in the red bandpowers in Fig. 3.

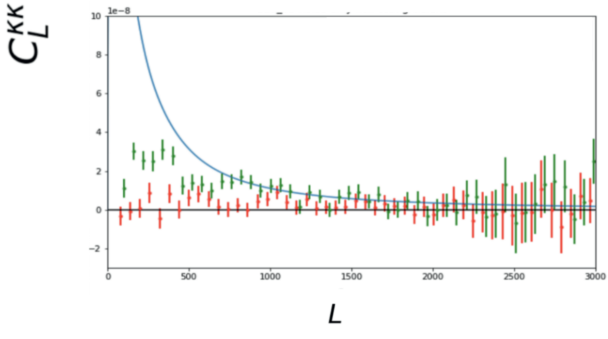

Figure 3 – Noise only null test using the standard quadratic estimator in green (failure) and the passing bandpowers using the cross correlation based estimator in red

5 Results

We expect to present foregrounds mitigated lensing power spectrum combining both the temperature and polarization channels as our baseline. This lensing spectrum is expected to reach sensitivities between $50 - 60\sigma$. The lensing power spectrum alone will be expected to provide strong constraints on the combination of $\sigma_8\Omega_m^{0.25}$ which are competitive with current galaxy lensing and clustering measurements, as can be seen in Fig. 5. In addition, combining with BAO enables breaking the degeneracy between H_0, Ω_m and σ_8 allowing percentage determination of σ_8.

This should allow AdvACT to shed some light on the hint of tension arising between the value of S_8 as measured by Planck and the relatively lower value observed by different low redshift probes such as galaxy lensing. One can see this hint of tension in Fig. 4. Note that the ACT-DR6 value shown here in red is for illustrative purposes only as the analysis is currently still blind. But the error bars shown here are indicative of the achievable precision.

In addition to the lensing power spectrum, we will also release a lensing map covering nearly 40% of the sky, this dark matter map will be signal dominated and correlated with many large scale galaxy surveys, making it ideal for cross-correlation science.

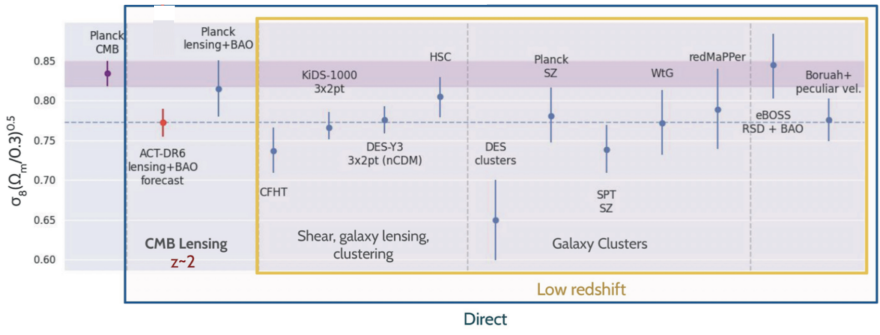

Figure 4 – Recompilation of S_8 measurements with direct low redshift probes such as galaxy lensing, clustering and BAO. Purple band indicates the value extrapolated by Planck CMB.

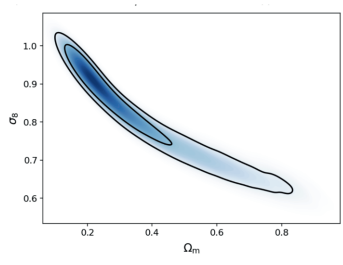

Figure 5 – Lensing only σ_8 measurements. Chains run with theoretical lensing bandpowers and realistic data covariance matrix

6 Conclusion

We presented in detail our lensing power spectrum pipeline, designed to analyse the new seasons of AdvACT data, covering nearly 12,000 square degrees of the sky. The large sky fraction means that sky curvature becomes important and the analysis is performed using spin spherical harmonics. The resulting lensing power spectrum is obtained by the optimal combination of temperature and polarization channels. We highlight two of the main challenges faced by large resolution ground surveys, namely the presence of extragalactic foregrounds and challenges in simulating noise. And demonstrate that these are under control using a large suite of null tests designed to identify systematic effects. The resultant lensing power spectrum will enable us to obtain strong constraints on the neutrino mass sum, as well as percentage measurements of σ_8, shedding some light on the hints of σ_8 tension between low and high redshift probes.

7 Acknowledgments

Frank J. Qu gratefully acknowledges support from Gonville and Caius travel scholarship and funding from DAMTP and the Cambridge Trust International Scholarship. The author also express gratitude to the organisers of the Rencontres de Moriond conference for organising a successful and smooth conference in pandemic times.

References

1. A Lewis and A Challinor. Weak gravitational lensing of the cmb. *Physics Reports*, 429(1):1–65, Jun 2006.
2. Kendrick M. Smith, Oliver Zahn, and Olivier Doré. Detection of gravitational lensing in the cosmic microwave background. *Physical Review D - Particles, Fields, Gravitation and Cosmology*, 76(4):1–27, 2007.
3. Sudeep Das and Blake D. et Al Sherwin. Detection of the power spectrum of cosmic microwave background lensing by the atacama cosmology telescope. *Physical Review Letters*, 107(2):9–11, 2011.
4. N. et Al Aghanim. Planck 2018 results: VIII. Gravitational lensing. *Astronomy and Astrophysics*, 641, 2020.
5. Kendrick M. Smith. Pseudo-c_ℓ estimators which do not mix e and b modesc estimators which do not mix e and b modes. *Physical Review D*, 74(8), Oct 2006.
6. Toshiya Namikawa, Duncan Hanson, and Ryuichi Takahashi. Bias-hardened CMB lensing. *Monthly Notices of the Royal Astronomical Society*, 431(1):609–620, 2013.
7. Michael Kesden, Asantha Cooray, and Marc Kamionkowski. Lensing reconstruction with CMB temperature and polarization. *Physical Review D - Particles, Fields, Gravitation and Cosmology*, 67(12):1–15, 2003.
8. Stephen J. Osborne, Duncan Hanson, and Olivier Doré. Extragalactic foreground contamination in temperature-based cmb lens reconstruction. *Journal of Cosmology and Astroparticle Physics*, 2014(03):024–024, Mar 2014.
9. A. Van Engelen, S. Bhattacharya, N. Sehgal, G. P. Holder, O. Zahn, and D. Nagai. CMB lensing power spectrum biases from galaxies and clusters using high-angular resolution temperature maps. *Astrophysical Journal*, 786(1):1–14, 2014.
10. Neelima Sehgal, Paul Bode, Sudeep Das, Carlos Hernandez-Monteagudo, Kevin Huffenberger, Yen-Ting Lin, Jeremiah P. Ostriker, and Hy Trac. Simulations of the microwave sky. *The Astrophysical Journal*, 709(2):920–936, Jan 2010.
11. George Stein, Marcelo A. Alvarez, J. Richard Bond, Alexander van Engelen, and Nicholas Battaglia. The Websky Extragalactic CMB Simulations. 600:0–37, 2020.
12. Blake D. Sherwin, Alexander van Engelen, Neelima Sehgal, Mathew Madhavacheril, Graeme E. Addison, Simone Aiola, Rupert Allison, Nicholas Battaglia, James A. Beall, Daniel T. Becker, J. Richard Bond, Erminia Calabrese, Rahul Datta, Mark J. Devlin, Rolando Dunner, Joanna Dunkley, Anna E. Fox, Patricio Gallardo, Mark Halpern, Matthew Hasselfield, Shawn Henderson, J. Colin Hill, Gene C. Hilton, Johannes Hubmayr, John P. Hughes, Adam D. Hincks, Renee Hlozek, Kevin M. Huffenberger, Brian Koopman, Arthur Kosowsky, Thibaut Louis, Loic Maurin, Jeff McMahon, Kavilan Moodley, Sigurd Naess, Federico Nati, Laura Newburgh, Michael D. Niemack, Lyman A. Page, Jonathan Sievers, David N. Spergel, Suzanne T. Staggs, Robert J. Thornton, Jeff Van Lanen, Eve Vavagiakis, and Edward J. Wollack. The Atacama Cosmology Telescope: Two-Season ACTPol Lensing Power Spectrum. pages 1–17, 2016.
13. P. A. R. Ade, Z. Ahmed, R. W. Aikin, K. D. Alexander, D. Barkats, S. J. Benton, C. A. Bischoff, J. J. Bock, R. Bowens-Rubin, J. A. Brevik, I. Buder, E. Bullock, V. Buza, J. Connors, B. P. Crill, L. Duband, C. Dvorkin, J. P. Filippini, S. Fliescher, J. Grayson, M. Halpern, S. Harrison, S. R. Hildebrandt, G. C. Hilton, H. Hui, K. D. Irwin, J. Kang, K. S. Karkare, E. Karpel, J. P. Kaufman, B. G. Keating, S. Kefeli, S. A. Kernasovskiy, J. M. Kovac, C. L. Kuo, E. M. Leitch, M. Lueker, K. G. Megerian, T. Namikawa, C. B. Netterfield, H. T. Nguyen, R. O'Brient, R. W. Ogburn IV, A. Orlando, C. Pryke, S. Richter, R. Schwarz, C. D. Sheehy, Z. K. Staniszewski, B. Steinbach, R. V. Sudiwala, G. P. Teply, K. L. Thompson, J. E. Tolan, C. Tucker, A. D. Turner, A. G. Vieregg, A. C. Weber, D. V. Wiebe, J. Willmert, C. L. Wong, W. L. K. Wu, and K. W. Yoon. Bicep2/keck arrayviii: Measurement of gravitational lensing from large-scaleb-mode polarization. *The Astrophysical Journal*, 833(2):228, Dec 2016.
14. Mathew S. Madhavacheril, Kendrick M. Smith, Blake D. Sherwin, and Sigurd Naess. CMB lensing power spectrum estimation without instrument noise bias. *Journal of Cosmology and Astroparticle Physics*, 2021(5):1–18, 2021.

Searching for accreting primordial black holes with CMB non-Gaussianity

Yacine Ali-Haïmoud
Center for Cosmology and Particle Physics, New York University, 726 Broadway, New York, USA

Primordial black holes (PBHs) could have been produced if the early Universe was sufficiently clumpy on small scales. They are therefore a potential window into cosmological initial conditions, as well as an interesting dark matter candidate. PBHs heavier than a solar mass or so can leave observable imprints in CMB anisotropies, through their accretion-induced energy injection, which modifies the ionization history. We point out that PBH accretion is expected to be highly inhomogeneous, as it is modulated by supersonic baryon-dark matter relative velocities. We compute the resulting inhomogeneities in the ionization history, and point out that they should leave significant non-Gaussian signatures in the CMB.

1 Motivations

The initial conditions of cosmological perturbations are well characterized on large scales, with comoving wavenumbers $k \sim \mathrm{Gpc}^{-1}$–Mpc^{-1}, which are probed by high-precision CMB-anisotropy measurements and large-scale structure surveys. CMB spectral distortions moreover set upper limits on initial perturbations on scales $k \sim 1 - 10^4$ Mpc^{-1}. On even smaller scales, initial conditions are mostly unconstrained, and could be probed by the observation of – or upper limits on – Primordial Black Holes (PBHs), which could moreover be (part of) the dark matter. It is thus interesting to devise sensitive observational tests of PBHs.

2 Review of CMB power spectra limits on accreting PBHs

CMB-anisotropy power spectra have been used to set constraints on the abundance of PBHs heavier than $\sim 1 M_\odot$. Here we summarize the basic physics [1]:

• PBHs accrete baryons. A simple estimate of the accretion rate $\dot{M}$ can be obtained from the Bondi-Hoyle expression

$$\dot{M} \sim \rho_b \frac{(GM)^2}{(c_s^2 + v_{\rm rel}^2)^{3/2}}, \tag{1}$$

where ρ_b is the baryon mass density, M is the black hole mass, c_s is the sound speed, and $v_{\rm rel}$ is the relative motion of the accreted gas at infinity.

• This accretion powers a luminosity $L = \epsilon \dot{M} c^2$. The radiative efficiency ϵ is strongly dependent

upon the geometry of the accretion flow. The lowest luminosity (leading to the most conservative limits) is obtained under the assumption of quasi-spherical accretion, and results from free-free emission of the accreted gas. It scales as $L \propto \dot{M}^2$.

• This luminosity leads to a volumetric energy injection rate $\dot{\rho}_{\rm inj} = n_{\rm pbh} L$, where $n_{\rm pbh}$ is the PBH number density.

• Part of this injected energy is *deposited* into the plasma, with volumetric rate $\dot{\rho}_{\rm dep}$. The deposition efficiency $\dot{\rho}_{\rm dep}/\dot{\rho}_{\rm inj}$ depends on the detailed channels of energy injection. In the case of free-free emission by accreting PBHs, we assume energy to be injected as a nearly flat photon spectrum, up to $\sim$ MeV energies.

• Part of this deposited energy goes into extra ionization of the plasma, thus modifies the evolution of the free-electron fraction x_e.

• CMB anisotropies are very sensitive to the ionization history. In particular, CMB power spectra are sensitive to its *spatial average* $\langle x_e \rangle$. To compute the latter, one uses the spatially-average PBH luminosity $\langle L \rangle$, obtained after averaging L over the distribution of relative velocities.

• With these ingredients, one can predict CMB power spectra as a function of PBH mass and abundance. By comparing these predictions to *Planck* data, one can then set upper limits on the abundance of PBHs.

3 Work in progress: non-Gaussian signatures of accreting PBHs

3.1 Basic idea and motivations

From the scalings given above, in the case of free-free emission, the luminosity of accreting PBHs scales approximately as $L \propto (c_s^2 + v_{\rm rel}^2)^{-3}$. Relative velocities between baryons and dark matter, whatever it is made of (as long as it has the same large-scale fluctuations as in standard ΛCDM), fluctuate on $\sim 10^2$ Mpc scales, with variance $\langle v_{\rm rel}^2 \rangle \sim 25 \times c_s^2$. Therefore, we expect the luminosity of accreting PBHs to be *highly* inhomogeneous. This is indeed shown in Fig. 1, where we see that the PBH luminosity is a highly non-Gaussian field, peaking in the small regions where local relative velocities are subsonic, and highly suppressed elsewhere.

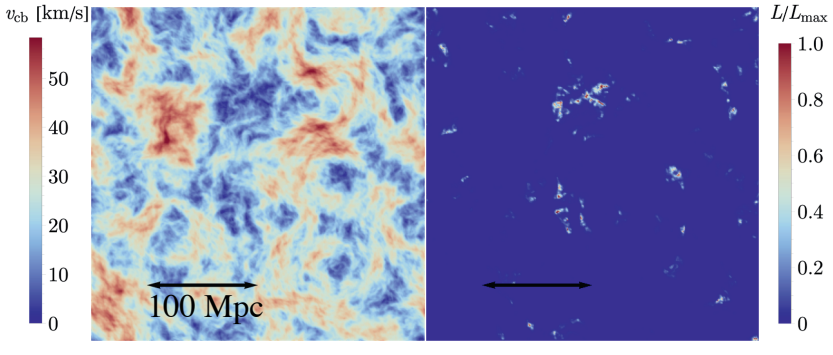

Figure 1 – The left panel shows a realization of the baryon-dark matter relative velocity field at recombination. The right panel shows the resulting fluctuations of PBH accretion luminosity. Figure credit: Julián Muñoz.

These spatial fluctuations of accretion luminosity (and thus energy injection) imply inhomogeneous energy deposition, and, ultimately, a spatially-varying free-electron fraction. This, in turn, sources *non-Gaussianities* in CMB anisotropies, even if initial conditions are Gaussian.

Let us now understand why this signal could be significant. Let us define by $\Delta x_e(t, \vec{x})$ the time- and spatially-dependent perturbation to the ionization history induced by accreting PBHs.

We split it into its spatial average and spatial fluctuations:

$$\Delta x_e(t,\vec{x}) = \langle \Delta x_e \rangle(t) + \delta x_e(t,\vec{x}). \tag{2}$$

The first piece arises from the spatially-averaged luminosity $\langle L \rangle$, and is used to compute the effect on CMB power spectra. Given that PBH luminosity has $\mathcal{O}(1)$ relative fluctuations, we expect that δx_e could be as large as $\langle \Delta x_e \rangle$, as long as the spatial fluctuations of energy injection are not washed out by the deposition process. For PBH abundance saturating CMB-anisotropy limits, $\langle \Delta x_e \rangle / x_e = \mathcal{O}(1\%)$. Therefore, we expect that $\delta x_e(t,\vec{x})/x_e$ could be as large as $\mathcal{O}(1\%)$.

Now, in the *standard* cosmological scenario, recombination is not perfectly homogeneous, and has spatial fluctuations at the level of $(\delta x_e/x_e)_{\rm std} \sim 10^{-4}$. Such small fluctuations are sufficient to generate non-Gaussianities that are just under the *Planck* detection threshold. We thus expect that non-Gaussianities sourced by accreting PBHs, whose abundance saturates CMB-power spectra limits, could lead to non-Gaussianity detectable with a signal-to-noise ratio of order 10^2. Put differently, *Planck* could be sensitive to a PBH abundance up to $\sim 10^2$ times smaller than current CMB upper limits, through CMB non-Gaussianities.

3.2 Preliminary results: perturbations to the ionization history

The first step in predicting the non-Gaussian signal is to evaluate $\delta x_e(t,\vec{x})$, the spatial fluctuations of the free-electron fraction. This calculation involves the following steps [2]:

• Evaluate the energy injection-to-deposition Green's function $G_{E_\gamma}(a_d, a_i, r)$, which depends on photon injection energy E_γ, and is defined explicitly through

$$a_d^3 \frac{\dot{\rho}_{\rm dep}}{H}\Big|_{a_d} = \int d\ln a_i \int \frac{d^3 r}{4\pi r^3} \int dE_\gamma \; G_{E_\gamma}(a_d, a_i, r) \; a_i^3 \frac{1}{H} \frac{d\dot{\rho}_{\rm inj}}{dE_\gamma}\Big|_{a_i}, \tag{3}$$

where $a_{i,d} \equiv (1+z_{i,d})^{-1}$ are the injection and deposition scale factors. We compute this Green's function with a radiative transport code, following photons through the expanding Universe as they photoionize hydrogen and helium atoms, and Compton-scatter off free and bound electrons. The code also accounts for the efficiency of energy deposition of secondary electrons, using highly accurate semi-analytic approximations. We show some values of the injection-to-deposition Green's function in Fig. 2, as well as its spatial average, which matches previous works.

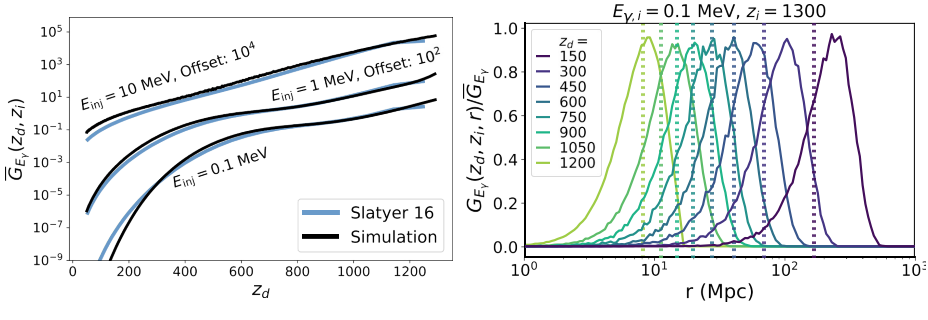

Figure 2 – Injection-to-deposition Green's function. *Left*: spatial average, for several injected photon energies, to compare with Slatyer (2016). *Right*: spatial variation, for injection of 0.1 MeV photons at $z_i = 1300$.

• Compute the energy deposition-to-ionization Green's function $G_{x_e}^{\rm dep}(a, a_{\rm dep})$, which is spatially local on the scales of interest, and defined as

$$\Delta x_e(z,\vec{r}) = \int d\ln a_d \; G_{x_e}^{\rm dep}(a, a_d) \; a_d^3 \frac{\dot{\rho}_{\rm dep}}{H E_I}\Big|_{a_d}, \tag{4}$$

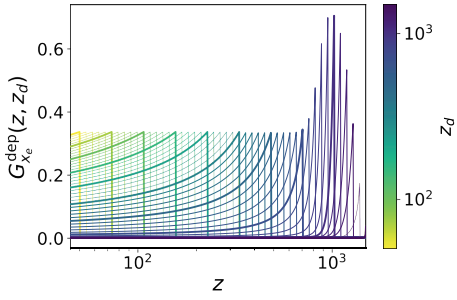

Figure 3 – Energy deposition to ionization Green's function, defined in Eq. (4).

where $E_I = 13.6$ eV is hydrogen's ionization energy. We compute $G^{\rm dep}_{x_e}(a, a_d)$ by linearizing the pertubed recombination equations [3] solved by HyRec-2 [4]. We show the result in Fig. 3.

• Convolve these two Green's functions with the spatially-fluctuating energy injected by accreting PBHs, to finally obtain the spatially fluctuating ionization fraction. We show this final result in Fig. 4. We see, from the left panel, that as anticipated, spatial fluctuations of the free-electron fraction have a characteristic amplitude of the same order as the mean change in x_e. From the right panel, we see that these perturbations peak at scales $k \sim 10^{-2} - 10^{-1}$ Mpc^{-1}, which correspond to scales probed by CMB anisotropies. These reuslts are promising and motivate investigating the non-Gaussian signal in detail, which is the subject of ongoing work.

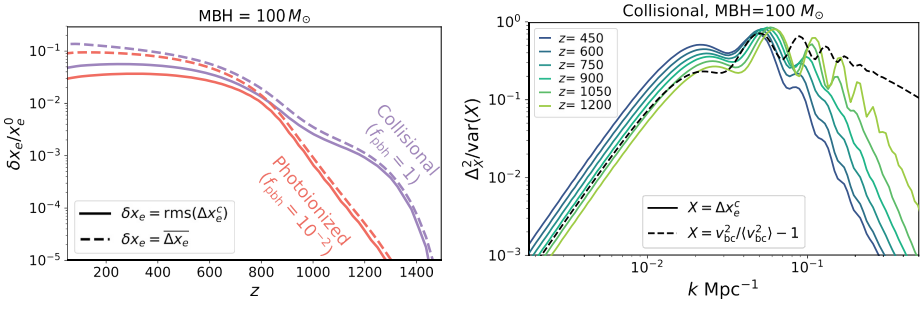

Figure 4 – *Left*: redshift evolution of the spatial average (dashed) and rms (solid) perturbation to the free-electron fraction due to accreting PBHs, in two accretion scenarios. *Right*: power spectrum of free-electron fluctuations, normalized by its overall variance.

Acknowledgments

YAH is supported by NSF grant No. 1820861 abd NASA grant No. 80NSSC20K0532.

References

1. Y. Ali-Haïmoud and M. Kamionkowski, *Phys. Rev.* D **95**, 043534 (2017)
2. T. W. Jensen and Y. Ali-Haïmoud, *Phys. Rev.* D **104**, 063534 (2021)
3. Y. Ali-Haïmoud and C. M. Hirata, *Phys. Rev.* D **83**, 043513 (2011)
4. N. Lee and Y. Ali-Haïmoud, *Phys. Rev.* D **102**, 083517 (2020)

Nonideal self-gravity and cosmology: the importance of correlations in the dynamics of the large-scale structures of the Universe

P. Tremblin
Maison de la Simulation, CEA, CNRS, Univ. Paris-Sud, UVSQ, Université Paris-Saclay, F-91191 Gif-sur-Yvette, France

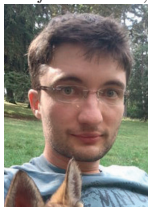

Inspired by the role of correlations in the statistical mechanics of nonideal self-interacting fluids, we suggest that unresolved sub-structures (i.e. correlations) have to be taken into account in the Virial theorem of self-gravitating astrophysical systems. We demonstrate that their omission leads to a missing mass problem by using the semi-analytic polytropic solutions of the Lane-Emden equation. This problem suggests to extend the Friedmann equations to the nonideal regime by taking into account correlations in the dynamics of the expansion. The increase of correlations induced by the formation of the large-scale structures could explain naturally the accelerated expansion of the Universe in such a paradigm.

1 The role of correlations in statistical mechanics

The statistical approach of the classical problem of a system of N-interacting particles (with $N \to \infty$) of mass m in a volume V, is based on the so-called BBGKY hierarchy [1,2]. In this hierarchy, the probability function to find one particle at $\vec{r}$ is defined by $P_1(\vec{r})$ while the probability to find one particle at $\vec{r}$ and another one at $\vec{r}'$ is given by $P_2(\vec{r},\vec{r}')$. These probabilities yield the definition of the radial distribution function as, for a homogeneous, isotropic fluid:

$$g(||\vec{r}-\vec{r}'||) = V^2 P_2(\vec{r},\vec{r}'), \tag{1}$$

or equivalently the correlation function, $\xi(||\vec{r}-\vec{r}'||)$:

$$\begin{aligned} \xi(||\vec{r}-\vec{r}'||) &= V^2(P_2(\vec{r},\vec{r}') - P_1(\vec{r})P_1(\vec{r}')) \\ &= g(||\vec{r}-\vec{r}'||) - 1. \end{aligned} \tag{2}$$

For an ideal fluid, in the absence of correlation, $P_2(\vec{r},\vec{r}') = P_1(\vec{r})P_1(\vec{r}')$, i.e. $\xi(||\vec{r}-\vec{r}'||) = 0$ and $g(||\vec{r}-\vec{r}'||) = 1$, $\forall(\vec{r},\vec{r}')$. In contrast, in the presence of correlations, $\xi(||\vec{r}-\vec{r}'||) \neq 0$ and $g(||\vec{r}-\vec{r}'||) \neq 1$. The presence of correlations yields a non-ideal contribution impacting all thermodynamic quantities in the fluid, including also interaction energies whose definition from the N-body dynamics is the sum over all distinct pairs of particles:

$$\langle H_{\rm int,Nbody}\rangle = \sum_{i<j} \phi(||\vec{r}_i - \vec{r}_j||), \tag{3}$$

which corresponds exactly to an integral over the two-point probability distribution function:

$$\langle H_{\rm int,Nbody}\rangle \approx \frac{N^2}{2}\iint_{V,V} P_2(\vec{r},\vec{r}')\phi(||\vec{r}-\vec{r}'||)dVdV', \tag{4}$$

with $\phi(r=||\vec{r}-\vec{r}'||)$ the pair potential.

2 The missing-mass problem induced by the omission of correlations

The Virial theorem in astrophysics is usually applied in a simplified way, ignoring correlations and sub-structures by using only the total mass M inside a given volume $V = 4\pi R^3/3$ with a gravitational interaction energy per unit mass proportional to $-GM/R$.

In order to show the importance of inhomogeneities in the virial theorem, we apply it as a simple semianalytical example to the case of a polytropic structure. In this case, we can explicitly compute $P_2(\vec{r},\vec{r}')$ by semianalytically computing an inhomogeneous density field and compare the result with a homogeneous assumption on the virial theorem. A polytropic stellar structure can be calculated by the Lane-Emden equation,

$$\frac{1}{z^2}\frac{d}{dz}\left(z^2\frac{dw}{dz}\right)+w^n=0, \tag{5}$$

with $\rho=\rho_c w^n$, $P=K\rho^\gamma$, $n=1/(\gamma-1)$ the polytropic index, $z=Ar$, and $A^2=(4\pi G/(n+1))\rho_c^{1-1/n}/K$. We choose a dimensionless unit system in which $\rho_c=K=G=1$. By solving the Lane-Emden equation for different polytropic indexes $n<5$, we can compute inhomogeneous density profiles that have a finite radius R (see the left panel of Fig. 1). For a polytrope, the following virial theorem (per unit mass) reads

$$\begin{array}{rl} H/M & = 2H_{\rm int}/M, \\ H & = \int_V \frac{\gamma}{\gamma-1}PdV, \\ M & = \int_V \rho dV, \end{array} \tag{6}$$

where H is the total enthalpy, M is the total mass, and $H_{\rm int}$ is the gravitational interaction energy with the zero of potential energy defined at the surface of the star. For a homogeneous density profile, with $\rho=M/(4\pi R^3/3)$, we obtain

$$\frac{H}{M}=\frac{GM}{5R}. \tag{7}$$

We now assume that an observer has only access to the total enthalpy, mass, and radius of different objects and does not know whether these objects have substructures. The naive assumption, as explained above, is to ignore the possible inhomogeneities and assume that the density is constant, $\rho=M/(4\pi R^3/3)$, hence using Eq. 7 for the virial equation. This assumption, however, is only correct for a polytropic index $n=0$. As shown in the right panel of Fig. 1, for profiles $n\neq 0$, the error on the total energy is significant and can be up to a factor 25 for $n=4$. Therefore, the assumption of a homogeneous profile within the structures will lead to a missing-mass problem. For a polytropic structure, however, we can calculate the inhomogeneous density profile semianalytically and thus calculate exactly the contribution of inhomogeneities to the total energy. We characterize this contribution by an inhomogeneous amplification factor $\alpha_{\rm ih}$, which can be calculated exactly,

$$\alpha_{\rm ih}=\frac{N^2\iint_{V,V}P_2(\vec{r},\vec{r}')\phi(|\vec{r}-\vec{r}'|)dVdV'}{N^2\iint_{V,V}1/(4\pi R^3/3)^2\phi(|\vec{r}-\vec{r}'|)dVdV'}, \tag{8}$$

with $V=4\pi R^3/3$. In our calculation, $N^2P_2(\vec{r},\vec{r}')=N^2P_1(\vec{r})P_1(\vec{r}')=\rho(\vec{r})\rho(\vec{r}')$ for the inhomogeneous structure at the numerator, while the homogeneous calculation corresponds to

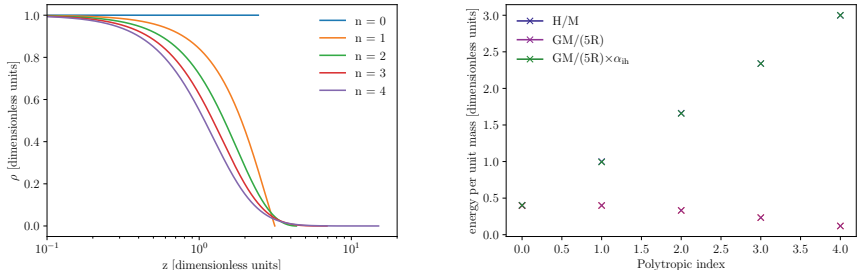

Figure 1 – Polytropic solutions. Left: Density profiles solutions to the Lane-Emden equation with different polytropic indexes n. Right: Total enthalpy per unit mass compared to gravitational interaction energy per unit mass assuming either a homogeneous density profile or accounting for inhomogeneities. Blue and green crosses are indistinguishable.

$N^2 P_2(\vec{r},\vec{r}') = N^2 P_1(\vec{r}) P_1(\vec{r}') = N^2/V^2$, with $P_1(\vec{r}) = 1/V$ at the denominator. We can now correct Eq. 7 to account for inhomogeneities,

$$\frac{H}{M} = \frac{GM}{5R}\alpha_{\rm ih}. \tag{9}$$

As shown in the bottom panel of Fig. 1, when this factor is taken into account, we exactly recover the correct enthalpy and the correct gravitational interaction energy for the different polytropic structures (the green and blue crosses in the figure are indistinguishable). This simple example demonstrates that it is mandatory to account for the contribution of substructures to correctly evaluate interaction energies in astrophysical structures.

3 The nonideal Friedmann equations

As suggested in Tremblin *et al.*[4], Einstein equations may not be suited for the study of correlated fluids for two reasons. First, the Newtonian limit gives back the Poisson equation that is a mean-field approximation ignoring the presence of correlations. Second, it can be explicitly shown that the equivalence principle for a fluid implicitly assumes the absence of correlations. We therefore propose to rely on the Newtonian demonstration of the Friedmann equations in order to get an intuition of how to design a nonideal version that takes into account correlations. Following Peacock[3], we assume an ensemble of particles of mass m in a volume V of radius R, whose fluid density is assumed to be homogeneous and isotropic at very large scales, but can be correlated at smaller scales, that is $P_1(\vec{r}) = 1/V$ but $P_2(\vec{r},\vec{r}') \neq P_1(\vec{r})P_1(\vec{r}')$. The total mechanical energy of this system under its N-body or fluid form is given by

$$E_m = \langle\, mv^2/2\rangle + \langle H_{\rm int,Nbody}\rangle. \tag{10}$$

Similarly to $\alpha_{\rm ih}$ in Sect. 2, we define $\alpha_{\rm ni}$ by

$$\alpha_{\rm ni} = \frac{\iint_{V,V} \phi(|\vec{r}-\vec{r}'|) P_2(\vec{r},\vec{r}') dV dV'}{\iint_{V,V} \phi(|\vec{r}-\vec{r}'|) P_1(\vec{r}) P_1(\vec{r}') dV dV'}. \tag{11}$$

The ideal (uncorrelated) fluid hypothesis corresponds to $\alpha_{\rm ni} = 1$. Eq. 10 can then be rewritten as

$$E_m \;=\; \langle\, mv^2/2\rangle + \alpha_{\rm ni}\langle H_{\rm int,ideal}\rangle. \tag{12}$$

Following Peacock[3], we take $\langle\ mv^2/2\rangle = M\dot{R}^2/2$ and $\langle H_{\rm int,ideal}\rangle = -GM^2/R$ and rewrite this equation as

$$E_m/M = \frac{\dot{R}^2}{2} - \frac{4\pi}{3}\alpha_{\rm ni} G\rho_m R^2. \tag{13}$$

Rearranging the different terms, we obtain

$$\frac{\dot{R}^2}{R^2} - \frac{2E_m/M}{R^2} = \frac{8\pi G}{3c^2}\alpha_{\rm ni}\rho_m c^2. \tag{14}$$

In the uncorrelated case, $\alpha_{\rm ni} = 1$, and with the substitutions $R \to a$ and $-E_m/M \to K$, we recognize the first Friedmann equation. Therefore, Eq. 14 indicates that correlations should be accounted for through a multiplicative factor $\alpha_{\rm ni}$ of the energy density for a proper nonideal generalization of the Friedmann equation (this could also be seen as a multiplicative factor of the gravitational constant). The last step in obtaining a nonideal first Friedmann equation is to take the thermodynamic limit in $\alpha_{\rm ni}$, $(N, V) \to \infty$ keeping $N/V = \rho$ constant. This can be done by introducing a near-field approximation on a scale λ_H, that is, by replacing ϕ by $\exp(-r/\lambda_H)\phi$ in Eq. 11, or equivalently, introducing a cutoff of the integrals at a radius $r_{\rm bound}$ of approximately λ_H. In the latter case, and assuming a large-scale flat, homogeneous, and isotropic Universe, we obtain the following first nonideal Friedmann equation:

$$H_{\rm ni}^2 = \frac{8\pi G}{3c^2}\alpha_{\rm ni}\rho_b, \quad \text{with} \quad \alpha_{\rm ni} = \frac{\int_0^{r_{\rm bound}} g(r) r dr}{\int_0^{r_{\rm bound}} r dr}. \tag{15}$$

We can now study the acceleration of the expansion. Because we can link the value of the Hubble parameter to the nonideal amplification induced by bound substructures, $\alpha_{\rm ni}$, it is natural to expect an acceleration of the expansion linked to an increase in the densities of these structures, due to the ongoing gravitational collapse. In order to get the second nonideal Friedmann equation, we use the first law of thermodynamics in an expanding universe with the derivation of the first Friedmann equation. The two nonideal Friedmann equations (for $K = 0$) in our formalism are given by

$$H_{\rm ni}^2 = \frac{8\pi G}{3c^2}\alpha_{\rm ni}\rho_b, \quad \text{and} \quad q_{\rm ni} = -1 - \frac{\dot{H}_{\rm ni}}{H_{\rm ni}^2} \approx \frac{1}{2} - \frac{\dot{\alpha_{\rm ni}}}{2H_{\rm ni}\alpha_{\rm ni}}. \tag{16}$$

It is then natural to obtain an acceleration of the expansion induced by the formation of the large scale structures of the Universe which naturally produces $\dot{\alpha}_{\rm ni} > 0$ with an increase of the absolute value of the gravitational interaction energy even if the mean density ρ_b is decreasing. Assuming the nonideal amplification factor $\alpha_{\rm ni}$ entirely explains the observed present-day expansion, that is, it varied from $\alpha_{\rm ni} = 1$ to $\alpha_{\rm ni} = \rho_c/\rho_b \approx 20$ over the age of the universe, $t_u \sim$14 Gyr, we can obtain an order-of-magnitude analytical expression,

$$q_{\rm ni} \approx \frac{1}{2} - \frac{\ln(\rho_c/\rho_b)}{2t_u H}, \tag{17}$$

which gives a deceleration parameter $q_{\rm ni} = -1.06$ that is compatible with the value based on type Ia supernovae $q = -1.0 \pm 0.4$ [5].

References

1. J. Yvon in *La théorie statistique des fluides et l'équation d'état*, ed. Actualités Scientifiques et Industrielles: Théories Mécaniques (Hermann & cie, 1935).
2. J. G. Kirkwood and E. M. Boggs, *J. Chem. Phys.* **10**, 394 (1942).
3. J. A. Peacock in *Cosmological Physics*, ed. Cambridge Astrophysics (Cambridge University Press, 1999).
4. P. Tremblin *et al.*, *A&A* **659**, A108 (2022).
5. A. G. Riess *et al.*, *AJ* **116**, 1009 (1998).

Relativistic effects: initial conditions for simulation of large-scale structure

T. Montandon
Department of Astrophysics, University of Vienna, Türkenschanzstraße 17, 1180 Vienna, Austria

One of the main challenges of cosmology is to understand the physics of the early universe. One way to probe this early period is the study of primordial non-Gaussianity (PNG) through the bispectrum of the matter distribution. The future large-scale structure (LSS) surveys are expected to provide a precise measurement of the distribution of matter in the late universe and therefore add more constraints on PNG. For this purpose, one needs to understand the full evolution of the perturbations beyond the linear theory since the LSS formation is a non-linear process. Among all the non-linearities generated, the relativistic effects (REs) are a well-known contaminant of the PNG. In this proceeding, I present the result of Adamek *et al.* [1]. I explain how we can simulate the large-scale structure of the universe with the N-body simulation "gevolution" by accounting for all the relevant second-order relativistic non-linearities.

1 Introduction

Inflation is the earliest period in the history of our universe corroborated by observations. The simple single-field models generate small adiabatic and quasi-Gaussian fluctuations [2]. A natural extension of the single-field model is to consider additional fields: this is the so-called multi-field inflation. The squeezed limit of the bispectrum is a powerful tool to constrain PNG. In particular, the detection of a squeezed limit signal with an amplitude $f_{\rm NL} \sim 0.1$ or larger would rule out all single-field inflation models [3].

The increasingly large number of precise galaxy surveys planned such as Euclid, the Vera Rubin Observatory or SPHEREx [4,5,6], opens the possibility of adding more constraints on the early universe physics [7]. The extraction of primordial physics from future data requires the greatest care, as galaxy clustering is a non-linear process. In particular, the modelization of the squeezed limit in the LSS is very challenging. Indeed, the squeezed limit involves both the large and the small scales where the physics are very different. On large scales, $k < 0.1\ h\mathrm{Mpc}^{-1}$, REs become important since we approach the cosmological horizon. On the small scales, $k > 0.1\ h\mathrm{Mpc}^{-1}$, the perturbation theory breaks down and numerical simulations are needed. Note also that the smallest scales enter the horizon at early time when radiation cannot be neglected.

The standard perturbation theory in the Newtonian limit has been deeply studied [8]. These standard results show that the CDM density grows like the scale factor a at first order and like a^2 at the second order. For this reason, for N-body simulation, it is enough to set first-order initial conditions at early enough time since the second-order contribution decays. The REs leading order is proportional to $\mathcal{H}^2/k^2$ where $\mathcal{H}$ is the Hubble factor defined w.r.t. the conformal time. When approaching the horizon, these corrections cannot be neglected anymore since $k \sim \mathcal{H}$. Many studies have been performed over the last 30 years to account for these effects up to second-order, see Villa *et al.* [9] for a complete review. One of the main conclusions of these works is that the dynamical REs are degenerated with PNG in the momentum space, i.e. they produce a signal in the squeezed limit of the bispectrum, as well as in the redshift

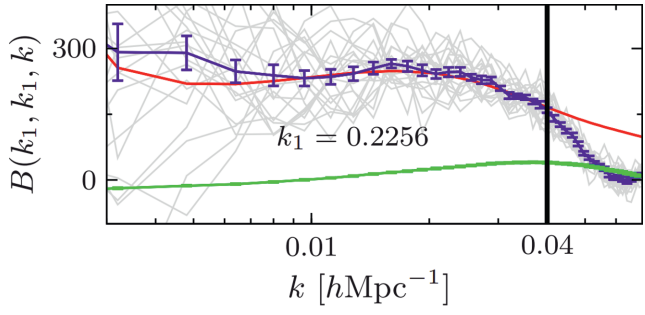

Figure 1 – Bispectrum of the CDM density bispectrum at redshift $z = 100$. The first two arguments are fixed to k_1 whose value in units of $h\,\mathrm{Mpc}^{-1}$ is indicated in the panel. The third argument varies on the x-axis. The squeezed limit is obtained by taking $k \ll k_1$. The red curve is the SONG bispectrum. The blue curve is the bispectrum of the RELIC realisations where we have subtracted the bispectrum of $10^2\delta^{(2)}$ plotted in green. The black vertical line indicates the cut-off scale.

space. Indeed, at second-order $a^2\mathcal{H}^2 \propto a$. This means that the REs cannot be neglected in the initial conditions of N-body simulation since they do not decay w.r.t. the linear solution. Therefore, it is crucial to estimate the amplitude of these systematic effects of the local PNG.

2 From Einstein-Boltzmann to N-body simulation

In this work, we use the standard *forward* approach to initialize a N-body simulation [10]. The basic forward approach consists on generating a Gaussian primordial curvature perturbation $\mathcal{R}(\mathbf{k})$ following the standard primordial power spectrum statistic. By using a first-order Einstein-Boltzmann code (we use CLASS [11] in our work), we can compute the first-order transfer function for the CDM density at the initial redshift of the simulation z: $T_\delta^{(1)}(z,k)$. Hence, the first-order CDM density field reads

$$\delta^{(1)}(z,\mathbf{k}) = T_\delta^{(1)}(z,k)\mathcal{R}(\mathbf{k})\,. \tag{1}$$

Numerical codes accounting for non-linear effects up to second order, including early radiation and REs, were first developed to compute the CMB intrinsic bispectrum [12,13,14]. The numeric code SONG [14] is the most efficient code solving the full Einstein-Boltzmann system up to second-order. Therefore, we use it to compute the second-order CDM transfer function $T_\delta^{(2)}(z,k_1,k_2,k_3)$ which can be used to evaluate the full second-order CDM density

$$\delta^{(2)}(z,\mathbf{k}) = \int \frac{d^3k_1}{(2\pi)^3} T_\delta^{(2)}(z,k_1,|\mathbf{k}-\mathbf{k}_1|,k)\mathcal{R}(\mathbf{k}_1)\mathcal{R}(\mathbf{k}-\mathbf{k}_1) \equiv \mathcal{I}_{TT}\,. \tag{2}$$

Based on this result, we developed the second-order initial conditions generator called RELIC [1]. In its most general configuration, RELIC is able to compute the integral Eq. 2. However, if we consider N modes, the computation of Eq. 2 scales like N^6 which makes it impossible for a reasonable large grid size (at least $N = 1024$). As explained in section 1, REs becomes important for scales of order $k \sim \mathcal{H}$, i.e. for the large scales. Hence, we introduce a cut-off scale k_Λ to split the k-range into *large scales* ($k < k_\Lambda$) and *small scales* ($k > k_\Lambda$). To properly account for REs, we evaluate the full integral 2 for the large scales. The time complexity of this computation is $N_\Lambda^3 N^3$, where N_Λ is the number of large modes. Since N_Λ can be keep small, the computation is manageable. For the small scales, we define the window function $W(k) = 1$ if $k < k_\Lambda$ and $W(k) = 0$ otherwise. Thus, the primordial curvature perturbation reads

$$\mathcal{R}(\mathbf{k}) = W(k)\mathcal{R}(\mathbf{k}) + (1 - W(k))\mathcal{R}(\mathbf{k}) = \mathcal{R}_L(\mathbf{k}) + \mathcal{R}_S(\mathbf{k})\,. \tag{3}$$

Introducing Eq. 3 into Eq. 2, we can re-write Eq. 2 into the sum of three different integrals:

$$\begin{aligned}\delta^{(2)}(\tau,\mathbf{k})|_{k>k_\Lambda} &= \int \frac{d^3k_1}{(2\pi)^3} T_z^{(2)}(\tau,k_1,|\mathbf{k}-\mathbf{k_1}|,k)\mathcal{R}_L(\mathbf{k_1})\mathcal{R}_L(\mathbf{k}-\mathbf{k_1}) \\ &\quad + \int \frac{d^3k_1}{(2\pi)^3} T_\delta^{(2)}(z,k_1,|\mathbf{k}-\mathbf{k_1}|,k)\mathcal{R}_S(\mathbf{k_1})\mathcal{R}_S(\mathbf{k}-\mathbf{k_1}) \\ &\quad + 2\int \frac{d^3k_1}{(2\pi)^3} T_\delta^{(2)}(z,k_1,|\mathbf{k}-\mathbf{k_1}|,k)\mathcal{R}_S(\mathbf{k_1})\mathcal{R}_L(\mathbf{k}-\mathbf{k_1}) \\ &\equiv \delta_{LL}^{(2)} + \delta_{SS}^{(2)} + 2\delta_{LS}^{(2)}\,.\end{aligned} \tag{4}$$

The first term in Eq. 4, $\mathcal{I}_{LL}$ accounts for the coupling between the large scales. Its time scaling is N_Λ^6. Since k_Λ can be keep small, this term can be computed. The second term, $\mathcal{I}_{SS}$, is a coupling between the small scales. This is the regime where Newtonian non-linearities dominates. If the initial conditions are set at early enough time, this term can be neglected since the Newtonian non-linearities grow like a^2. Note also that $\mathcal{I}_{SS}$ dominates the time complexity since it scales like N^6. The last term, $\mathcal{I}_{SL}$ is crucial for our purpose since it accounts for the coupling between the small and the large scale, i.e. it dominates the squeezed limit of the bispectrum. Fortunately, it scales like $N_\Lambda^3 N^3$ and can be computed. Our final approximation reads

$$\begin{aligned}\delta^{(2)}(\tau,\mathbf{k}) &= \delta_{TT}^{(2)} && \text{if } \mathrm{k} < \mathrm{k}_\Lambda\,, \\ &= \delta_{LL}^{(2)} + 2\delta_{LS}^{(2)} && \text{if } \mathrm{k} > \mathrm{k}_\Lambda\,.\end{aligned} \tag{5}$$

Thanks to this approximation, a ~ 1000 years computation in the most general case is reduced to 100 days which, with parallelization, can be done within a few hours. In Fig. 1, we show in blue the averaged bispectrum over 20 RELIC realisations where the second-order part has been boosted by a factor 100 ($\delta^{(1)} + 10^2\delta^{(2)}$). In green, the bispectrum of $10^2\delta^{(2)}$ which has been subtracted to obtain the blue curve. In red, we show the fiducial theoretical bispectrum obtained with SONG. As expected, RELIC is accurate as long as one of the considered scales is a large scales, i.e in the equilateral configuration if $k > k_\Lambda$ and in the squeezed limit, which corresponds to $k \ll k_1$.

3 Initialisation of particle in gevolution

We use the fully relativistic code gevolution [15]. To initialize the particles' positions and velocities, we need to compute the velocity and the potential. It can be shown that at second-order, for a CDM fluid, the velocity is potential [1]. The scalar Einstein equations have only one degree of freedom. Thus, by injecting the density, we can compute all the other potentials.

To find the initial position of the particles, one must find the displacement field ξ defined as

$$\mathbf{x}_p = \mathbf{x}_p^0 + \nabla\xi(\mathbf{x}_p^0)\,, \tag{6}$$

where $\mathbf{x}_p^0$ is the particles' positions on an homogeneous template and $\mathbf{x}_p$ are the initial positions. In its basic implementation, the code gevolution solves the discrete first-order equation

$$\rho(\mathbf{x}_g) = -\sum_{x_g'} \xi(\mathbf{x}_g') \sum_p \frac{m_p}{a^3} w_{\mathrm{grad}}(\mathbf{x}_g' - \mathbf{x}_p^0)\nabla\omega_{\mathrm{CIC}}(\mathbf{x}_g' - \mathbf{x}_p^0)\,, \tag{7}$$

where w_{CIC} and w_{grad} are the cloud-in-cell (CIC) and gradient kernels, $\mathbf{x}_g$ is the position on the grid and $\mathbf{x}_p$ the position of the particle p with mass m_p. Since Eq. 7 is a linear equation, even though the density $\rho(\mathbf{x}_g)$ is accurate at second-order, inverting Eq. 7 gives the first-order displacement field $\xi^{(1)}$. By using this displacement field, one can initialize the particles and re-project on the grid to verify that the density obtained $\hat{\rho}$ matches the input computed by RELIC ρ used in the left-hand side of Eq. 7. The re-projection procedure is fully non-linear, which means that $\hat{\rho}$ contains first-order terms, as well as quadratic terms such as $\xi^{(1)2}$. However, it does not contain the pure second order terms like $\xi^{(2)}$. Thus, the subtraction $\rho - \hat{\rho}$ kills the

first-order and first-order squared terms leaving only the pure linear second-order terms. Eq. 7 can be solved again, by replacing the left-hand side by $\rho - \hat{\rho}$, to find $\xi^{(2)}$. This method is iterative and works for any higher-order accuracy. The velocity and the gravitational potential can be interpolated at the initial positions of the particles.

Hence, we have initialized the particles of an N-body simulation by taking into account all the REs and radiation effects at second-order. Current studies are focusing on the evolution of these initial perturbations with gevolution.

4 Conclusion

With the increasingly large and precise number of LSS measurements, the relativistic effects may become a significant systematic effect in the squeezed limit of the matter bispectrum. Hence, it contaminates primordial non-Gaussianities. For this reason, it is crucial to model accurately these effects and take them into account in the theoretical interpretation of future measurements. In this proceeding, I have introduced the relativistic initial condition generator RELIC, that is able to generate initial conditions for simulation of the large-scale structure accurate at second-order for large scales and in the squeezed limit. It opens the possibility to account for all relativistic and radiation effects in the galaxy power spectrum and bispectrum modelization.

References

1. J. Adamek, J. Calles, T. Montandon, J. Noreña and C. Stahl, [arXiv:2110.11249 [astro-ph.CO]].
2. D. Baumann, doi:10.1142/9789814327183_0010 [arXiv:0907.5424 [hep-th]].
3. P. Creminelli and M. Zaldarriaga, JCAP **10** (2004), 006 doi:10.1088/1475-7516/2004/10/006 [arXiv:astro-ph/0407059 [astro-ph]].
4. L. Amendola, S. Appleby, A. Avgoustidis, D. Bacon, T. Baker, M. Baldi, N. Bartolo, A. Blanchard, C. Bonvin and S. Borgani, *et al.* Living Rev. Rel. **21** (2018) no.1, 2 doi:10.1007/s41114-017-0010-3 [arXiv:1606.00180 [astro-ph.CO]].
5. H. Zhan and J. A. Tyson, Rept. Prog. Phys. **81** (2018) no.6, 066901 doi:10.1088/1361-6633/aab1bd [arXiv:1707.06948 [astro-ph.CO]].
6. O. Doré, J. Bock, P. Capak, R. de Putter, T. Eifler, C. Hirata, P. Korngut, E. Krause, D. Masters and A. Raccanelli, *et al.* [arXiv:1412.4872 [astro-ph.CO]].
7. M. Biagetti, Galaxies **7** (2019) no.3, 71 doi:10.3390/galaxies7030071 [arXiv:1906.12244 [astro-ph.CO]].
8. F. Bernardeau, S. Colombi, E. Gaztanaga and R. Scoccimarro, Phys. Rept. **367** (2002), 1-248 doi:10.1016/S0370-1573(02)00135-7 [arXiv:astro-ph/0112551 [astro-ph]].
9. E. Villa, L. Verde and S. Matarrese, Class. Quant. Grav. **31** (2014) no.23, 234005 doi:10.1088/0264-9381/31/23/234005 [arXiv:1409.4738 [astro-ph.CO]].
10. R. E. Angulo and O. Hahn, doi:10.1007/s41115-021-00013-z [arXiv:2112.05165 [astro-ph.CO]].
11. D. Blas, J. Lesgourgues and T. Tram, JCAP **07** (2011), 034 doi:10.1088/1475-7516/2011/07/034 [arXiv:1104.2933 [astro-ph.CO]].
12. Z. Huang and F. Vernizzi, Phys. Rev. Lett. **110** (2013) no.10, 101303 doi:10.1103/PhysRevLett.110.101303 [arXiv:1212.3573 [astro-ph.CO]].
13. C. Pitrou, Gen. Rel. Grav. **41** (2009), 2587-2595 doi:10.1007/s10714-009-0782-1 [arXiv:0809.3245 [astro-ph]].
14. G. W. Pettinari, doi:10.1007/978-3-319-21882-3 [arXiv:1405.2280 [astro-ph.CO]].
15. J. Adamek, D. Daverio, R. Durrer and M. Kunz, JCAP **07** (2016), 053 doi:10.1088/1475-7516/2016/07/053 [arXiv:1604.06065 [astro-ph.CO]].

Precision cosmology from large-scale structure of the universe

A. Chudaykin
Department of Physics & Astronomy, McMaster University, 1280 Main Street West, Hamilton, ON L8S 4M1, Canada

Institute for Nuclear Research of the Russian Academy of Sciences, 60th October Anniversary Prospect, 7a, 117312 Moscow, Russia

Large scale structure of the Universe becomes a leading source of precision cosmological information. We present two particular tools that can be used in cosmological analyses of the redshift space galaxy clustering data: a new open-source code `CLASS-PT` and the theoretical error approach. `CLASS-PT` computes one-loop power auto- and cross-power spectra for matter fields and biased tracers in real and redshift spaces. We show that the code meets the precision standards set by the upcoming high-precision large-scale structure surveys. The theoretical error likelihood approach allows one to analyze galaxy clustering data without having to measure the scale cut $k_{\rm max}$. This approach takes into account that theoretical uncertainties affect parameter estimation gradually, which helps optimize data analysis and ensures that all available cosmological information is extracted.

1 Introduction

Large-scale structure (LSS) data becomes an increasingly important source of cosmological information. Very soon it will become competitive with the cosmic microwave background (CMB) data analysis [1]. In contrast with the CMB, the LSS data analysis is complicated by non-linear clustering which is very hard to predict analytically. This problem is resolved in the effective field theory of large-scale structure [2], and its various extensions, such as time-sliced perturbation theory [3], which allow one to systematically model various short-scale phenomena on mildly nonlinear scales.

In the first part of this note we present a new code `CLASS-PT` that embodies an end-to-end calculation of one-loop power spectra for matter field and bias tracers using the state-of-the-art perturbation theory approach [4]. Even though `CLASS-PT` is based on the well-known theoretical framework [5], it brings several novelties. First, it uses a new FFTLog method to efficiently compute convolution integrals [6]. Second, another crucial advantage of `CLASS-PT` is an accurate and efficient description of the BAO wiggles using the infrared (IR) resummation of long-wavelength contributions [7,8]. This is particularly important for data analysis, where the BAO encapsulate a significant portion of cosmological information.

In the second part, we introduce a novel data analysis technique based on the theoretical error covariance [9], which allows one to avoid uncertainties in the theoretical estimates of higher-order nonlinearities. We demonstrate that this approach yields unbiased constraints on all cosmological parameters. In addition, we also show that the theoretical error effectively optimizes the choice of $k_{\rm max}$ in realistic data analyses.

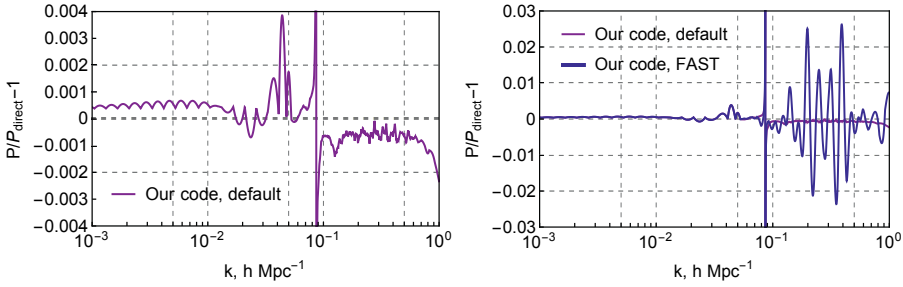

Figure 1 – Residuals between the one-loop correction to the matter power spectrum and its direct numerical evaluation for the default settings (left panel) and in the FAST mode (right panel).

2 CLASS-PT

Let us start with theoretical modeling of galaxy power spectrum in redshift space. The radial position of the galaxies in real surveys are distorted by the peculiar velocity field. It introduces so-called redshift-space distortions (RSD). We will work in the plane-parallel approximation, where the mapping between the redshift and real spaces is entirely parameterized by the cosine of the angle between the line-of-sight $\hat{\mathbf{z}}$ and the wavevector of a given Fourier mode $\mathbf{k}$, $\mu \equiv (\hat{\mathbf{z}}\cdot\mathbf{k})/k$. This setup allows one to express the one-loop redshift-space spectrum in the following simple form

$$\begin{aligned} P_{\rm gg,RSD}(z,k,\mu) =& Z_1^2(\mathbf{k})P_{\rm lin}(z,k) + 2\int_{\mathbf{q}} Z_2^2(\mathbf{q},\mathbf{k}-\mathbf{q})P_{\rm lin}(z,|\mathbf{k}-\mathbf{q}|)P_{\rm lin}(z,q) \\ &+ 6Z_1(\mathbf{k})P_{\rm lin}(z,k)\int_{\mathbf{q}} Z_3(\mathbf{q},-\mathbf{q},\mathbf{k})P_{\rm lin}(z,q) \\ &+ P_{\rm ctr,RSD}(z,k,\mu) + P_{\epsilon\epsilon,\rm RSD}(z,k,\mu)\,, \end{aligned} \tag{1}$$

where the redshift-space kernels can be found in [5]. $P_{\rm ctr,RSD}(z,k,\mu)$ represents counterterm contributions in redshift space which in the leading order can be written as follows

$$\begin{aligned} P_{\rm ctr,RSD,}(z,k,\mu) =& -2\tilde{c}_0(z)k^2P_{\rm lin}(z,k) - 2\tilde{c}_2(z)f(z)\mu^2k^2P_{\rm lin}(z,k) \\ &- 2\tilde{c}_4(z)f^2(z)\mu^4k^2P_{\rm lin}(z,k) - 2b_4(b_1+f\mu^2)^2k^4P_{\rm lin}(k)\,, \end{aligned} \tag{2}$$

$P_{\epsilon\epsilon,\rm RSD}(z,k,\mu)$ denotes the stochastic contribution which in the redshift space has the following structure

$$P_{\epsilon\epsilon,\rm RSD}(z,k,\mu) = P_{\rm shot}(z) + a_0(z)k^2 + a_2(z)\mu^2k^2\,, \tag{3}$$

where $P_{\rm shot}(z)$ describes a constant shot noise and the additional terms represent scale-dependent contrinutions to the monopole and the quanrupole moments of power spectrum.

The full angular dependence of the redshift-space power spectrum can be encoded in a number of multipoles using the following relation

$$P_{\rm gg,RSD}(z,k,\mu) = \sum_{\ell\ \rm even} \mathcal{L}_\ell(\mu)P_\ell(z,k)\,, \tag{4}$$

Explicit expressions for P_ℓ can be found in [4]. Let us briefly discuss the accuracy of calculations in `CLASS-PT`. In Fig. 1 we show the residuals between evaluation of the one-loop correction to the matter power spectrum with the FFTLog method and its direct numerical calculation for two different precision settings. In the default regime we implement the FFTLog method for the grid with $N_{\rm FFTLog} = 256$ harmonics. In the FAST mode we create a grid of lower dimension

Table 1: Performance of the code in the baseline and FAST precision modes. We show the execution time in [sec.] as follows: $t_{\rm full}(t_{\rm FFTLog})$, where $t_{\rm full}$ is the full evaluation time taken by the non-linear module, and $t_{\rm FFTLog}$ is the time elapsed during the matrix multiplication with FFTLog method.

Run	Real space	IR resum.	RSD	IR+RSD	IR+RSD+AP
Default mode					
Matter	0.036 (0.036)	0.175 (0.036)	0.375 (0.375)	0.75 (0.62)	0.76 (0.63)
Tracers	0.21 (0.21)	0.35 (0.21)	0.89 (0.89)	1.27 (1.12)	1.30 (1.14)
FAST mode					
Matter	6.3 (6.1) $\times 10^{-3}$	0.14 (0.0061)	0.063 (0.061)	0.22 (0.09)	0.22 (0.09)
Tracers	0.033 (0.034)	0.17 (0.034)	0.14 (0.14)	0.31 (0.18)	0.31 (0.18)

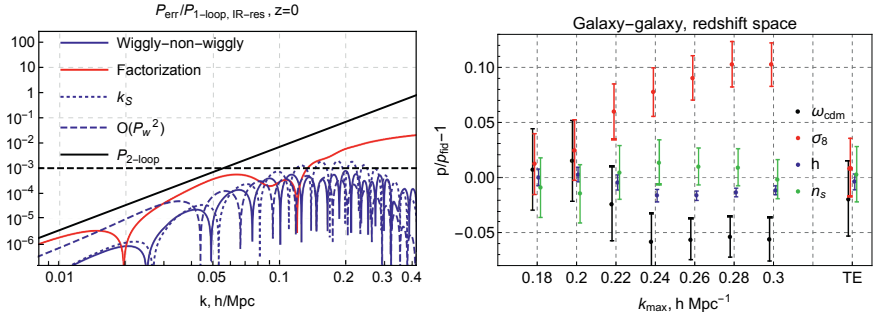

Figure 2 – *Left panel:* Error budget of various systematic effects relative to the two-loop contribution (black line) at $z = 0$. *Right panel:* Residuals in measurements of cosmological parameters from the redshift space galaxy multipoles of N-body data.

$N_{\rm FFTLog} = 128$ that significantly speeds up our calculations. We found that the default choice of $N_{\rm FFTLog} = 256$ provides $\sim 0.1\%$ accuracy which is sufficient for future galaxy surveys. The FAST mode has somewhat worse accuracy of the one-loop calculation, around $\sim 1\%$. Still, it translates to the $\mathcal{O}(0.1\%)$ accuracy on the *total* power spectrum. Therefore, the FAST mode is sufficient for the analysis of current LSS data.

Let us discuss the performance of `CLASS-PT`. Tab. 1 summarizes the run times for various tests in two regimes (default and FAST). Our results show that the galaxy power spectra in redshift space can be calculated over 1.3 seconds for high precision settings. In the FAST mode the execution time reduces to 0.3 seconds.

Finally, we discuss the systematic uncertainties associated with the implementation of IR resummation in the `CLASS-PT`. Detailed information about the implementation of IR resummation in `CLASS-PT` can be found in [4]. In the left panel of Fig. 2 we show the contributions of all these effect to the total error budget along with the two-loop correction at $z = 0$. Once can see that the errors caused by inaccuracies in IR resummation are always smaller than the two-loop contributions missed in our model. It means that the `CLASS-PT` provides a stable calculation of one-loop power spectrum up to next-to-leading order corrections. These corrections can be systematically taken into account within time-sliced perturbation theory.

3 Theoretical error approach

In this section we summarize the theoretical error approach [9,10]. We show how the theoretical error covariance can be included in the realistic data analysis.

1. Choose some fiducial cosmological model.

2. Select the fiducial data cut $k_{\rm max}^{\rm fid}$. This data cut should be reasonably small to make

theoretical error negligible.

3. Obtain the best-fit theoretical prediction $P^{\rm best-fit}(k)$ by fitting the data at $k^{\rm fid}_{\rm max}$ and by varying *only* nuisance parameters.

4. Take this best-fit theoretical curve and construct the theoretical envelope as $P_i^{\rm (TE)} = P_i^{\rm d} - P^{\rm best-fit}(k_i)$. The statistical scatter in the data vector $P_i^{\rm d}$ can be removed by fitting $P_i^{\rm (TE)}$ with a smooth polynomial.

5. Build up the TE likelihood using $P_i^{\rm (TE)}$

$$-2\ln\mathcal{L}(P(\vec{\theta})) = (C + C^{\rm (E)})^{-1}_{ij}(P(\vec{\theta}) + \bar{P}_i^{\rm (TE)} - P_i^{\rm d})(P(\vec{\theta}) + \bar{P}_i^{\rm (TE)} - P_j^{\rm d})\,, \qquad (5)$$

where $\vec{\theta}$ denotes the vector of cosmological parameters and

$$C^{\rm (E)}_{ij} = \bar{P}_i^{\rm (TE)}\bar{P}_j^{\rm (TE)} e^{-\frac{(k_i-k_j)^2}{2\Delta k^2}}\,, \quad \text{with} \quad \Delta k = 0.1\ h/\text{Mpc}. \qquad (6)$$

We demonstrate the application of this approach using a suite of LasDamas Oriana simulations. Further details can be found in [9].

We run several analyses with different $k_{\rm max}$ and compare these result with the TE approach. The marginalized constraints on cosmological parameters for the $k_{\rm max}$ and TE (rightmost point) analyses are shown in the right panel of Fig. 2. We found that the TE analysis yields unbiased cosmological constraints with errorbars that match those coming from a carefully chosen $k_{\rm max}$. Thus, the TE appraoch effectively optimizes the choice of the data cut.

4 Conclusion

In this work we presented a new module `CLASS-PT` that incorporates one-loop theory calculations. It contains all ingredients needed for direct application to real data. We also introduced a new approach based on the theoretical error covariance which allows one to avoid uncertainties in the theoretical estimates of higher-order nonlinearities. We showed that this approach yields unbiased estimates of cosmological parameters and effectively optimize the choice of $k_{\rm max}$.

Acknowledgments

We are grateful to Mikhail Ivanov, Oliver Philcox, and Marko Simonović for collaboration on the projects presented in this note.

References

1. A. Chudaykin and M. M. Ivanov, JCAP **11** (2019), 034, arXiv:1907.06666 [astro-ph.CO]
2. D. Baumann, *et al.* JCAP **07** (2012), 051, arXiv:1004.2488 [astro-ph.CO].
3. D. Blas, M. Garny, M. M. Ivanov and S. Sibiryakov, JCAP **07** (2016), 052, arXiv:1512.05807 [astro-ph.CO].
4. A. Chudaykin, M. M. Ivanov, O. H. E. Philcox and M. Simonović, *Phys. Rev.* D **102**, 6 (2020), arXiv:2004.10607 [astro-ph.CO].
5. M. M. Ivanov, M. Simonović and M. Zaldarriaga, JCAP **05** (2020), 042, arXiv:1909.05277 [astro-ph.CO].
6. M. Simonović, T. Baldauf, M. Zaldarriaga, J. J. Carrasco and J. A. Kollmeier, JCAP **04** (2018), 030, arXiv:1708.08130 [astro-ph.CO].
7. D. Blas, M. Garny, M. M. Ivanov and S. Sibiryakov, JCAP **07** (2016), 028, arXiv:1605.02149 [astro-ph.CO].
8. M. M. Ivanov and S. Sibiryakov, JCAP **07** (2018), 053 arXiv:1804.05080 [astro-ph.CO].
9. A. Chudaykin, M. M. Ivanov and M. Simonović, *Phys. Rev.* D **103**, 4 (2021), arXiv:2009.10724 [astro-ph.CO].
10. T. Baldauf, M. Mirbabayi, M. Simonović and M. Zaldarriaga, arXiv:1602.00674 [astro-ph.CO].

On the road to percent accuracy: the reaction way

Matteo Cataneo
Argelander-Institut für Astronomie, Auf dem Hügel 71, D-53121 Bonn, Germany

Taking advantage of the unprecedented statistical power of upcoming cosmic shear surveys will require exquisite knowledge of the matter power spectrum over a wide range of scales. Analytical methods can achieve such precision only up to quasi-linear scales. For smaller non-linear scales we must resort to N-body and hydrodynamical simulations, which despite recent technological advances and improved algorithms remain computationally expensive. Over the past decade machine learning and the advent of emulators have propelled our ability to hit the target accuracy with impressive computing efficiency. Yet, realistically these techniques will be able to produce high-precision non-linear matter power spectra only for a restricted sub-set of extensions to the "vanilla" ΛCDM cosmology. I will present a promising alternative to alleviate these shortcomings that draws strength from the combination of halo model, perturbation theory and emulators–the *reaction* framework. I will show how a power spectrum evolved in the standard cosmology can be readily adjusted to account for physics beyond ΛCDM, and discuss the accuracy of the reaction for well-known modifications to gravity, dark energy parametrizations and massive neutrino cosmologies.

1 Introduction

The last two decades have seen the rise of the Λ-Cold Dark Matter (ΛCDM) paradigm to Standard Model of Cosmology–a status granted for its ability to explain with only a handful of parameters a diverse array of observations tracing a staggering 13.8 billion years of cosmic evolution (for recent analyses see, e.g., Planck collaboration [1], eBOSS collaboration [2], DES [3] and KiDS [4] collaborations). The ever-increasing volume of data continues to challenge the ΛCDM model, and tantalizing tensions are now emerging between early- and late-time cosmological probes [5,6] potentially exposing cracks in the theory. When taken together with our largely phenomenological (rather than fundamental) understanding of the content of the Universe, this fact encourages the exploration of alternative models in an attempt to find (most likely, constrain) deviations from the standard picture.

Central to many cosmological analyses is the 2-point correlation function of the matter density field, or equivalently its Fourier transform, the matter power spectrum. In the era of Stage IV surveys, accurate predictions for this statistic down to small non-linear scales will be essential to derive tight as well as robust constraints on parameters informing us whether new physics is at work [7,8], be it yet unknown interactions, undetected particles or particle properties. As the clustering of matter can react quite dramatically to changes to General Relativity (GR), testing gravity on cosmological scales is high up on the agenda of all science collaborations [9,10,11,12]. Modelling the non-linear power spectrum in modified gravity scenarios is the focus of this talk, but I will also discuss how our framework can capture the impact of massive neutrinos–particularly relevant for its degeneracy with fifth force effects [13]–and evolving dark energy (i.e., $w \neq -1$).

2 Non-linear matter power spectrum predictions for ΛCDM extensions

N-body simulations are the gold standard for the study of non-linear structure formation, and they provide the means to directly estimate the statistical properties of the matter density field, including the power spectrum. On the flip side is their considerable computational cost. Unfortunately, the complexities of new physics in ΛCDM extensions only worsen this problem [14]. Methods to predict the non-linear power spectrum based on (semi-)analytical or machine learning approaches can provide a fast alternative to simulations, but their validity is restricted to particular domains (e.g., quasi-linear regime, certain class of cosmologies etc.)

By capitalizing on the strengths of well-established techniques (perturbation theory, halo model and emulators), the *reaction* method described below provides a framework for predicting the non-linear matter power spectrum of a broad class of cosmologies while meeting the accuracy requirements set by Stage IV surveys. Moreover, its small computation time is an especially attractive feature for likelihood analyses.

3 The Reaction framework

In this framework the non-linear matter power spectrum of our target cosmology (which we call the 'real' cosmology) can be obtained from that of a particular reference cosmology (the 'pseudo' cosmology) as [15]

$$P^{\rm real}(k,z) = \mathcal{R}(k,z) \times P^{\rm pseudo}(k,z)\,, \tag{1}$$

where $\mathcal{R}$ is a scale- and time-dependent quantity called *reaction*. The linear growth of the pseudo cosmology follows that of a flat and massless neutrino ΛCDM cosmology, with the important difference that the shape and amplitude of its linear power spectrum are specified by the real cosmology, i.e.

$$P_{\rm L}^{\rm pseudo}(k,z) = P_{\rm L}^{\rm real}(k,z)\,. \tag{2}$$

The reason for choosing the pseudo cosmology in such a way is twofold: (i) it ensures $\mathcal{R} \to 1$ on linear scales; (ii) since to a good approximation the spherical collapse threshold is only weakly dependent on cosmology, from the Press-Schechter formalism we expect the halo mass functions of the pseudo and real cosmology to be rather similar. We shall see that it is this similarity that enables us to predict the reaction with the required accuracy.

To take advantages of the complementarity between different techniques, we use flexible semi-analytical methods for the reaction together with an accurate simulation-based route for the pseudo cosmology non-linear power spectrum, so that errors in the predicted beyond-ΛCDM non-linear power spectrum will be mostly associated with inaccuracies in the reaction modelling. The challenge consists in computing the reaction at percent level for all wavenumbers $k \lesssim 10\,h/{\rm Mpc}$, and at the same time efficiently evaluate $P^{\rm pseudo}(k,z)$ for a broad class of linear power spectrum shapes.

3.1 Pseudo cosmology emulator

Thanks to the concept of pseudo cosmology the reaction framework can substantially reduce our reliance on beyond-ΛCDM simulations, therefore placing the construction of a wide scope emulator within the realm of possibility. The advantage is that the computing time for a pseudo cosmology simulation is similar to that for a ΛCDM run. However, compared to conventional emulators the pseudo cosmology emulator must capture a variety of linear power spectrum shapes that cannot be reproduced by the standard cosmological parameters. Giblin et al. (2019) [16] developed a proof-of-concept emulator precisely with this idea in mind. In addition to the five ΛCDM parameters they introduced a new set of effective parameters, $\Delta\alpha_{1-8}$, describing the ratio $S(k) \equiv P_{\rm L}^{\rm pseudo}(k)/P_{\rm L}^{\Lambda}(k)$ for a large class of cosmologies converging to ΛCDM on

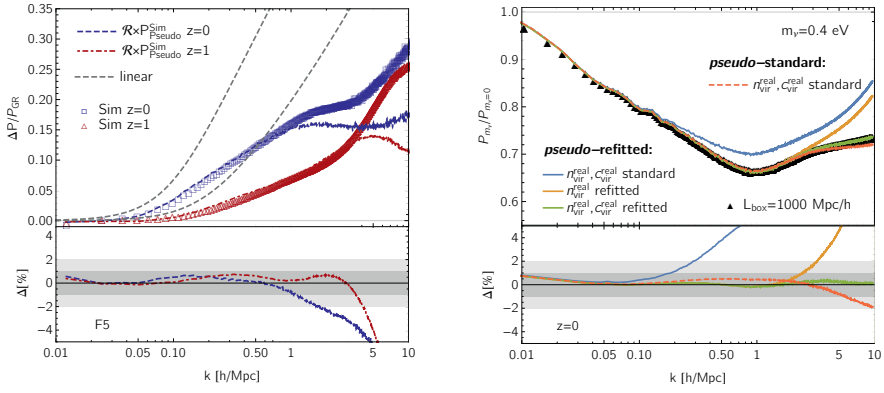

Figure 1 – *Left:* Matter power spectrum fractional enhancement in $f(R)$ gravity compared to GR. Symbols corresponds to the simulations and lines are our predictions based on the reaction. The dashed grey lines follow from linear theory calculations. The bottom panel shows that our predictions are within 1% of the simulations for $k \lesssim 1\,h$/Mpc. From Cataneo et al. (2019) [15]. *Right:* matter power spectrum ratio of a massive neutrino to a massless neutrino cosmology. The black triangles are simulation measurements. If the pseudo cosmology halo mass function and halo profiles extracted from the simulations are used to predict the reaction, we see that the inclusion of the corresponding measurements for the real cosmology brings the predictions in excellent agreement with the simulations (from blue to orange to green). From Cataneo et al. (2020) [18].

linear scales. By using Halofit as a proxy for the N-body simulations, they constructed a 13-dimensional Gaussian Process emulator trained on 500 parameter combinations distributed in a Latin Hypercube, and showed that this initial setup can already predict the pseudo non-linear power spectrum of their test cosmologies at 2% level.

3.2 The reaction

To model the reaction we resort to the halo model (HM) and standard perturbation theory (SPT). For modified gravity and dark energy cosmologies with a fraction, f_ν, of the total matter density (m) in massive neutrinos (ν) we have [17]

$$\mathcal{R}(k,z) \approx \frac{P^{\rm real}_{\rm HM}(k,z)}{P^{\rm pseudo}_{\rm HM}(k,z)} = \frac{(1-f_\nu)^2\,P^{\rm (cb)}_{\rm HM}(k,z) + 2f_\nu\,(1-f_\nu)\,P^{\rm (cb\nu)}_{\rm HM}(k,z) + f_\nu^2 P^{(\nu)}_{\rm L}(k,z)}{P^{\rm (m)}_{\rm L}(k,z) + P^{\rm pseudo}_{\rm 1h}(k,z)}\,, \quad (3)$$

with $P^{\rm (cb\nu)}_{\rm HM}(k,z)$ and $P^{\rm (cb)}_{\rm HM}(k,z)$ being, respectively, the cross power spectrum of the massive neutrinos and the CDM+baryons (cb), and the predicted halo model non-linear power spectrum for the CDM+baryons component. To lighten the notation the designation 'real' has been omitted for all terms in the numerator of Eq. 3. The expressions for the pseudo and real 1-halo terms follow the standard halo model prescription with halo mass functions and halo profiles adapted to the specific cosmologies. The left panel of Fig. 1 shows that when the halo profiles are not fully corrected for fifth force effects the reaction predictions can match well the simulation measurements up to $k \sim 1\,h$/Mpc. The right panel, instead, illustrates the strong connection enabled by the reaction framework between the halo properties (abundance and profiles) and the matter power spectrum: after calibrating the halo mass functions of the pseudo and real cosmologies with simulations, our power spectrum predictions can achieve sub-percent accuracy up to $k \sim 1\,h$/Mpc (orange line); including also information from the halo profiles improves the agreement with the simulations deep in the non-linear regime (green line).

Recently Bose et al. (2021) [17] have extended the reaction framework to include a class of interacting dark energy cosmologies, and packaged this formalism in `ReACT`, a publicly available C++ code and Python wrapper valuable for likelihood analyses of cosmic shear data [19].

4 Future directions

This research programme can be expanded in many ways: (*i*) the reaction framework uses the same halo mass function to predict both the matter power spectrum and the abundance of massive halos. This link has the potential to break parameter degeneracies in joint analyses of cosmic shear data and cluster number counts; (*ii*) our formalism is adaptable to a larger class of dark energy and modified gravity cosmologies falling under the umbrella of the Horndeski's theory. By generalizing the spherical collapse dynamics we will be able to capture the phenomenology of these models too. (*iii*) AGN feedback redistributes the gas content of massive halos ($M_{\rm h} \gtrsim 10^{13.5}\, M_\odot/h$) thus changing their overall density profiles. This effect can be readily incorporated into the reaction formalism, which together with multi-wavelength observations of groups and clusters of galaxies will put us in a better position to break degeneracies between astrophysical systematics and cosmology, currently a major limiting factor in cosmic shear analyses; (*iv*) the reaction framework enables the simultaneous treatment of various physics beyond the standard gravity-only paradigm, and thanks to the growing library of models implemented in `ReACT` it will be easier in the future to study the combined effect of exotic dark matter particles, new interactions, gravity beyond GR and astrophysics on the non-linear matter power spectrum; (*v*) finally, Cataneo et al. (2021) [20] found that for sufficiently large smoothing scales the real and pseudo modified gravity probability distribution functions of the matter density field are remarkably similar. This bodes well for potential applications of the reaction to higher-order statistics, e.g. the matter bispectrum, which will be essential to access the non-Gaussian information stored in the large-scale structure.

Acknowledgments

A big thanks to the organisers of the 56$^{\rm th}$ Rencontres de Moriond for giving us some relief from two years of virtual meetings with this fantastic in-person conference. The reaction framework rests on the amazing work of my collaborators, and to them goes my deepest gratitude. The author is supported by a Research Fellowship of the Alexander von Humboldt Foundation.

References

1. Planck collaboration, *Astronomy & Astrophysics* **641**, A6 (2020)
2. S. Alam *et al.*, *Phys. Rev.* D **103**, 083533 (2021)
3. DES collaboration, *Phys. Rev.* D **105**, 023520 (2022)
4. C. Heymans *et al.*, *Astronomy & Astrophysics* **646**, A140 (2021)
5. E. Di Valentino *et al.*, *Classical & Quantum Gravity* **38**, 153001 (2021)
6. E. Di Valentino *et al.*, *Astroparticle Physics* **131**, 102604 (2021)
7. C. Heymans & G.-B. Zhao, *Int. J. Mod. Phys. D* **27**, 1848005 (2018)
8. P. Taylor *et al.*, *Phys. Rev.* D **98**, 043532 (2018)
9. DES collaboration, *Phys. Rev.* D **99**, 123505 (2018)
10. T. Tröster *et al.*, *Astronomy & Astrophysics* **649**, A88 (2021)
11. L. Amendola *et al.*, *Living Reviews in Relativity* **21**, 2 (2018)
12. M. Ishak *et al.*, arXiv e-prints , arXiv:1905.09687 (2019)
13. M. Baldi *et al.*, *Mon. Notices Royal Astron. Soc.* **440**, 75 (2014)
14. C. Llinares, *Int. J. Mod. Phys. D* **27**, 1848003 (2018)
15. M. Cataneo *et al.*, *Mon. Notices Royal Astron. Soc.* **488**, 2121 (2019)
16. B. Giblin *et al.*, *Mon. Notices Royal Astron. Soc.* **490**, 4826 (2019)
17. B. Bose *et al.*, *Mon. Notices Royal Astron. Soc.* **508**, 2479 (2021)
18. M. Cataneo *et al.*, *Mon. Notices Royal Astron. Soc.* **491**, 3101 (2020)
19. B. Bose *et al.*, *Mon. Notices Royal Astron. Soc.* **498**, 4650 (2020)
20. M. Cataneo *et al.*, arXiv e-prints , arXiv:2109.02636 (2021)

Power Spectrum Accuracy in N-body simulations

Sara Maleubre [a]
Laboratoire de Physique Nucléaire et de Hautes Énergies, UPMC IN2P3 CNRS UMR 7585, Sorbonne Université, 4, place Jussieu, 75252 Paris Cedex 05, France
On behalf of
D. Eisenstein, L. Garrison and M. Joyce

We exploit a suite of large N-body simulations (up to N=4096^3), performed with Abacus, of scale-free models with a range of spectral indices n, to better understand and quantify convergence of the matter power spectrum. Using self-similarity to identify converged regions, we show that the maximal wavenumber resolved at a given level of accuracy increases monotonically as a function of time. At the 1% level it starts at early times from a fraction of k_Λ, the Nyquist wavenumber of the initial grid, and reaches at most, if the force softening is sufficiently small, $\sim 2-3k_\Lambda$ at the very latest times we evolve to. At the 5% level, accuracy extends up to wavenumbers of order $5k_\Lambda$ at late times. Expressed as a suitable function of the scale-factor, accuracy shows a very simple n-dependence, allowing an extrapolation to place conservative bounds on the accuracy of N-body simulations of non-scale free models like LCDM.

1 Introduction

The power spectrum (PS) is one of the most basic statistical tools employed to characterise clustering at large scales in cosmology. Building a precise theoretical framework for their calculation is crucial in order to fully exploit observational data coming from the next generation surveys, such as DESI, Vera C. Rubin Observatory LSST or Euclid, that will open a new window in the era of "precision cosmology". In this context the nonlinear regime of gravitational evolution is of particular importance, as it will be a key to distinguish among the plethora of exotic dark energy and modified gravity models, as well as tightly constraining the LCDM scenario.

Studies have estimated that to fully exploit the observed data, the matter PS in the range of scales ($0.1 \lesssim k/h\mathrm{Mpc}^{-1} \lesssim 10$) needs to be determined to a $1-2\%$ accuracy, depending on the specifications of the survey. Calculation of predictions at these scales rely entirely on numerical simulations that use the N-body method. One important and unresolved issue in this context is the accuracy limitations on such simulations arising from the fact that they approximate the evolution of the dark matter phase space distribution using a finite particle sampling, as well as a regularisation at small scales of the gravitational force. Despite the extensive use and spectacular development of N-body cosmological simulations over the last several decades, no clear consensus exists in the literature about how achieved accuracy, even for the PS, depends on the relevant parameters in an N-body simulation.

Frequently, convergence is probed by comparing between two or more codes to assess the accuracy of their results, but this establishes only a *relative convergence* that can give confidence in the accuracy of the clustering calculation but does not take into account the effects of discretiza-

[a] E-mail: sara.maleubre@lpnhe.in2p3.fr

tion and dependence on the N-body parameters. Alternatively, we propose a methodology based on Joyce (2020) [2], which uses the property of self-similarity of "scale-free" cosmological models to derive resolution limits to the PS with respect to particle density and gravitational softening.

2 Scale-Free cosmologies and Self Similarity

The value of scale-free models in the context of physical resolution of N-body simulations relies on the self-similarity of their evolution: *temporal evolution of clustering is equivalent to a well defined rescaling of the spatial coordinates.* This is the case because such models are characterised by just one length scale and one time scale: their initial (linear) PS of fluctuations is a simple power law $P(k) \propto k^n$, and the follow an Einstein-de-Sitter (EdS) expansion law $a \propto t^{2/3}$ (where a is the scale factor). The single length scale can thus be defined as the non-linearity scale R_{NL} given by

$$\sigma^2_{lin}(R_{NL}, a) = 1 \xrightarrow{\text{linear theory}} R_{NL} \propto a^{\frac{2}{3+n}} \tag{1}$$

where σ^2_{lin} is the variance of normalized linear mass fluctuations in a sphere, while the time scale is fixed by the normalization of the Hubble law (i.e. by the mean mass density combined with Newton's constant G).

For the case of statistics such as the PS which are a function of wavenumber k and time, it follows simply by dimensional analysis that a suitable dimensionless definition of the statistic f can be written as a function of $k\,R_{NL}(a')$ where a' is some reference scale-factor (left-hand side). As the reference scale-factor is itself arbitrary (because of the EdS expansion law) we can take $a' = a$ (right-hand side), and obtain:

$$f(k, a) = f(k\,R_{NL}(a'), a/a') = f_0(k\,R_{NL}(a))\,. \tag{2}$$

where f_0 is independent of time. For our study of the PS we use the canonical definition of the dimensionless PS, and thus self-similar behaviour corresponds to

$$\Delta^2(k, a) = \frac{k^3 P(k, a)}{2\pi^2} = \Delta^2_0(k\,R_{NL}(a))\,, \tag{3}$$

In N-body simulations of scale-free cosmologies, any deviations from this self-similar evolution can only be due to *unphysical scales*. Conversely results can represent the PS in the desired physical limit — which must be independent of these parameters — only to the extent that the rescaled dimensionless PS statistic becomes independent of time.

3 Numerical simulations

We have performed simulations using the Abacus N-body code [3]. It is designed for high-accuracy, high-performance cosmological N-body simulations, exploiting a high-order multipole method for the far-field force evaluation and GPU-accelerated pairwise evaluation for the near-field. The larger, $N = 4096^3$ simulations in this work were run as part of the AbacusSummit project [4] using the Summit supercomputer of the Oak Ridge Leadership Computing Facility.

We report results here based on the simulations listed in Table 1. We have simulated three different exponents for the PS ($n = -1.5, -2.0, -2.25$) in order to probe the range of exponents relevant to structure formation in a LCDM cosmology. The softening lengths have been chosen to include for each n a least one pair of simulations (with $N = 1024^3$) which differ only in this parameter (and for $n = -2.0$ a range of different softenings). Non-asterisk values of ϵ are fixed throughout the simulation in comoving units, while the ones with an asterisk are fixed in physical coordinates (i.e. $\epsilon/\Lambda \propto 1/a$) for $a > a_0$ and in comoving for $a < a_0$. In this study a_0 does not correspond to the scale factor today, but to the epoch at which fluctuations of peak-height $\nu \approx 3$ are expected to virialize in the spherical collapse model ($\sigma_{lin} \approx \delta_c/\nu$, with $\delta_c = 1.68$), and the first non-linear structures appear in the simulations.

Table 1: N-body simulations used for the analysis in this paper. From left to right we have: spectral index of the initial PS, number of particles, ratio of the effective Plummer force smoothing length ϵ to the initial grid spacing Λ at $a = a_0$.

n	N	ϵ/Λ	n	N	ϵ/Λ	n	N	ϵ/Λ
-1.5	4096^3	0.3*	-2.0	4096^3	0.3*	-2.25	4096^3	0.3*
-1.5	1024^3	0.3*	-2.0	1024^3	0.3*	-2.25	1024^3	0.3*
-1.5	1024^3	1/30	-2.0	1024^3	1/30	-2.25	1024^3	1/30
			-2.0	1024^3	1/60			
			-2.0	1024^3	1/15			

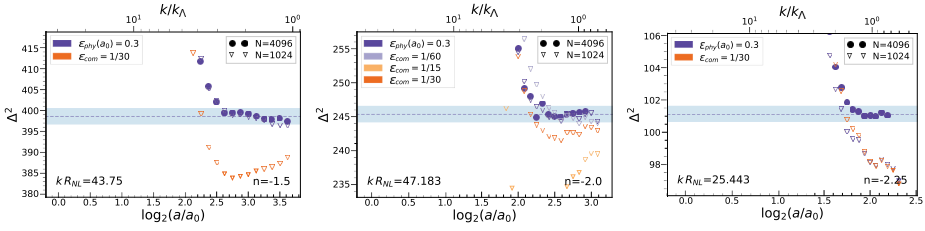

Figure 1 – Evolution of Δ^2 as a function of logarithmic scale factor $\log_2(a/a_0)$ (lower x-axis) and as a function of k/k_Λ (upper x-axis) for rescaled bins labelled by their kR_{NL} value. From left to right we have $n = -1.5$, $n = -2.0$ and $n = -2.25$. The horizontal dashed line marks our estimated converged value determined in the largest simulation, and the blue shaded region indicates that within $\pm 0.5\%$ of this value.

4 Results

The accuracy and extent of self-similarity, and how it is limited by the different unphysical simulation parameters, can be seen in Fig. 1. It shows the behaviour of Δ^2 at the non-linear regime for $n = -1.5$, $n = -2.0$ and $n = -2.25$. At these small scales the results are insensitive to box size, but do show dependence on the softening (except for $n = -2.25$ where box-size effects wipe out this behaviour). The simulations with proper softening and those with the smaller comoving softening show the widest and most coincident regions of self-similarity, while the simulations with larger comoving softening show a suppression of power relative to the self-similar value. Further the same $\epsilon = \Lambda/30$ comoving smoothing shows just marginal ($\sim 1\%$) deviation in the $n = -2.0$ simulation, but more significant ($\sim 3\%$) deviation for $n = -1.5$. Thus the limit on resolution at small scales at any time, corresponding to the largest k at which self-similarity may be attained, is determined by k_Λ alone (i.e. by the initial grid spacing, or mass resolution) provided the smoothing is chosen sufficiently small.

We can now determine the *estimated precision* of the PS at any scale and time, i.e. the difference between its measured value in a given simulation and the converged value for a given cosmology. Fig. 2 shows that *the precision of the measured PS at any given comoving k improves monotonically in time*. This reflects that the discretization on the lattice is the origin of imprecision (data is taken on a range of k/k_Λ unaffected by box-size effects and with an appropriate softening). It also illustrates the qualitative difference between the modes $k < k_\Lambda$ and $k > k_\Lambda$: the former are wavenumbers for which the PS is already resolved well in the initial conditions, and its behaviour depends on the exponent, as the mass variance of redder spectres dominates earlier over the effects of the lattice above k_Λ. For the latter the physical PS can only be resolved when the fluctuations from non-linear evolution dominate over the initial discreteness fluctuations at sub-grid scales. In addition, this regime seems *n-independent*, i.e. propagation of resolution migh be determined by the evolution of the comoving size of the first virialised structures.

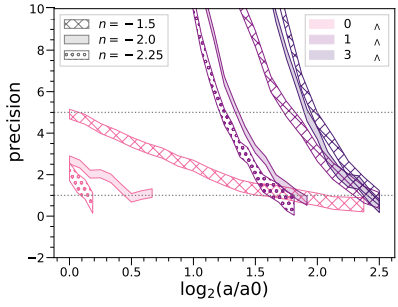

Figure 2 – Estimated precision of the PS (in $N = 4096$ simulations) relative to its true physical value as a function of time, for different selected comoving scales. Confidence intervals show the expected error in the converged value. The horizontal dotted lines correspond to 1% and 5%.

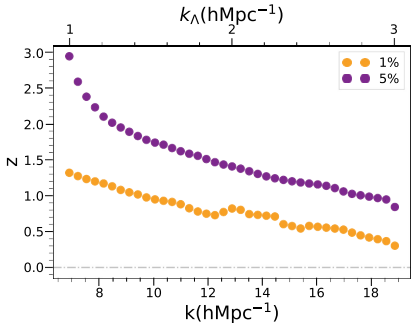

Figure 3 – Resolved k as a function of redshift for a fixed value of the mean interparticle spacing $\Lambda = 0.5h^{-1}$Mpc, using a standard LCDM cosmology ("Planck 2013" [5]). Orange points correspond to 1% precision, while purple points represent a 5%. We've added an axis for the k_Λ of the hypothetical LCDM simulation for an easier extrapolation with 2.

4.1 Resolution limits for non scale-free cosmologies

While our method is valid for scale-free cosmologies, our underlying motivation is to quantify the resolution in simulations of non scale-free cosmologies such as LCDM or variants of it. Such cosmologies are not very different from scale-free cosmologies for what concerns their non-linear evolution: their PS can be considered to be an adiabatic interpolation of power-law spectra, with the modified expansion rate due to dark energy only coming into play at very low redshift.

Using the definition of the linear variance, we can find a one-to-one relation between redshift in a ΛCDM simulation with a specific interparticle distance and our time variable $\log_2(a/a_0)$. In the limit in which accuracy is independent of the power index ($k > k_\Lambda$), we can carry over the results in Fig. 2 (modulo small possible corrections due to non-EdS evolution) to resolution as a function of scale and redshift. Fig. 3 shows, for a $\Lambda = 0.5h^{-1}$Mpc simulation of a standard "Planck13" [5] cosmology, the smallest scale which we will have access to as a function of redshift at a 1% and 5% precision.

Acknowledgments

This research used resources of the Oak Ridge Leadership Computing Facility at the Oak Ridge National Laboratory, which is supported by the Office of Science of the U.S. Department of Energy under Contract No. DE-AC05-00OR22725. The AbacusSummit simulations have been supported by OLCF projects AST135 and AST145, the latter through the Department of Energy ALCC program.

References

1. S. Maleubre, D. Eisenstein, L. Garrison, M. Joyce, *MNRAS* **512**, 1829 (2022)
2. M. Joyce, L. Garrison, D. Eisenstein, *MNRAS* **501**, 5051 (2020)
3. L. Garrison, D. Eisenstein, D. Ferrer, N. Maksimova, P. Pinto, *MNRAS* **508**, 575 (2021)
4. N. Maksimova, L. Garrison, D. Eisenstein, B. Hadzhiyska, S. Bose, T. Satterthwaite, *MNRAS* **508**, 4017 (2021)
5. Planck Collaboration et al., *A&A* **571**, A16 (2014)

The two-loop bispectrum in the effective theory of large-scale structure

Tobias Baldauf[1], Mathias Garny[2], Petter Taule[2] and Theo Steele[1]
[1] *Department of Applied Mathematics and Theoretical Physics, University of Cambridge, Wilberforce Road, CB3 0WA*
[2] *Physik Department T31, Technische Universität München, James-Franck-Straße 1, D-85748 Garching, Germany*

We study the bispectrum of large-scale structure in the EFTofLSS including corrections up to two-loop. We derive an analytic result for the double-hard limit of the two-loop correction, and show that the UV-sensitivity can be absorbed by the same four EFT operators that renormalize the one-loop bispectrum. For the single-hard region, we employ a simplified treatment, introducing one extra EFT parameter. We compare our results to N-body simulations, and show that going from one- to two-loop extends the wavenumber range with percent-level agreement from $k \simeq 0.08$ to $0.15\ h/\mathrm{Mpc}$.

1 Introduction

Current and near-future large-scale structure surveys are expected to return a wealth of information that may allow for testing deviations from ΛCDM as well as exploring alternative models. Given extended coverage of weakly non-linear scales, a lot of attention has been devoted to constructing a robust perturbative description. In Standard Perturbation Theory (SPT), dark matter is described as a perfect, pressureless fluid, modelled by the continuity and Euler equations assuming a vanishing velocity stress tensor. The non-linear equations are solved perturbatively in Eulerian space. However, higher order corrections do not lead to significant improvement on weakly non-linear scales, signalling the breakdown of perturbation theory. The issue is that the perfect fluid description is inaccurate on the scales of interest, and non-linear evolution on small scales produce a significant velocity dispersion that back-reacts on the observable scales via mode-coupling. This insight has over the last decade lead to the development of an effective field theory approach (EFTofLSS) that systematically captures the effect on small-scale physics onto larger, perturbative scales [1,2]. After coarse-graining the perturbation fields, the equations of motion contains an effective stress tensor that encapsulates the small-scale non-perturbative effects.

Complementary to the power spectrum, higher order statistics supplement information that can be instrumental in disentangling bias from fundamental physical parameters as well as providing consistency checks for the EFT parameters. In this work, we focus on the leading

non-gaussian statistic, the bispectrum, and compute for the first time the two-loop bispectrum in an EFT framework.

2 Effective field theory setup

The dynamical evolution of the coarse-grained density contrast δ and velocity divergence $\theta = \partial_i \mathbf{v}^i$ is in the EFT framework described by the continuity equation and a modified Euler equation,

$$\begin{aligned} \delta'(\mathbf{k}) + \theta(\mathbf{k}) &= -\int \mathrm{d}^3\mathbf{q}\, \alpha(\mathbf{q}, \mathbf{k}-\mathbf{q})\theta(\mathbf{q})\delta(\mathbf{k}-\mathbf{q})\,, \\ \theta'(\mathbf{k}) + \mathcal{H}\theta(\mathbf{k}) + \frac{3}{2}\Omega_{\mathrm{m}}\mathcal{H}^2\delta(\mathbf{k}) &= -\int \mathrm{d}^3\mathbf{q}\, \beta(\mathbf{q}, \mathbf{k}-\mathbf{q})\theta(\mathbf{q})\theta(\mathbf{k}-\mathbf{q}) - \tau_\theta(\mathbf{k})\,. \end{aligned} \tag{1}$$

We include only leading contributions in the gradient expansion to the effective stress tensor τ_θ and neglect stochastic contributions (proportional to k^4). In the basis we work with, the contributions to the effective stress tensors at first and second order in powers of the fields are

$$\begin{aligned} \tau_\theta|_1 &= -\gamma_1 \Delta\delta_1\,, \\ \tau_\theta|_2 &= -\gamma_1\Delta\delta_2 - e_1\Delta\delta_1^2 - e_2\Delta s^2 - e_3\partial_i\left[s^{ij}\partial_j\delta_1\right]\,, \end{aligned} \tag{2}$$

where δ_1, δ_2 are the first- and second order perturbation in the density contrast and s^{ij} is the tidal tensor. We have four free EFT parameters: $\{\gamma_1, e_1, e_2, e_3\}$. In principle one needs to write down EFT operators up to forth order in the fields to absorb UV-divergences of the two-loop bispectrum, however we will opt for a strategy where we do not need to know those higher-order operators explicitly.

The perturbative solution of the equations of motion (1) consists at one-loop of four loop-diagram contributions and two counterterms, of which the counterterms arises in the EFT due to the additional effective stress tensor in the equations. We can estimate the scaling of the UV-sensitivity of the four bare contributions by considering external wavenumbers scaling as $|\mathbf{k}_1| \sim |\mathbf{k}_2| \sim |\mathbf{k}_3| \sim k$ while letting the loop momentum $|\mathbf{q}|$ tend to infinity. The dominant UV-sensitivity has the form

$$k^2 P_{\mathrm{lin}}^2(k) \int^\Lambda \mathrm{d}q\, P_{\mathrm{lin}}(q) \equiv k^2 P_{\mathrm{lin}}^2(k)\sigma_d^2(\Lambda) \tag{3}$$

where we defined the displacement dispersion σ_d^2 and Λ is the cutoff. For general configurations of the external momenta k_1, k_2 and k_3, the limit has a complicated functional dependence on ratios k_i/k_j. Nevertheless, it can be shown that the shape dependence of the UV-limit exactly corresponds to that of the EFT operators defined in Eq. (2) [3,4,5]. Therefore, the contributions from the UV-region can be absorbed by the corresponding counterterms.

3 The two-loop bispectrum

To have an EFT description for the two-loop bispectrum, we need to assess the UV-sensitivity of the different loop contributions. At two-loop the UV-contributions can be divided into two categories: the *single-hard (h)* region in which one of the loop momenta becomes hard, $|\mathbf{q_1}| \to \infty$ (or equivalently $|\mathbf{q_2}| \to \infty$), and the *double-hard (hh)* region in which both loop momenta become large, $|\mathbf{q_1}|, |\mathbf{q_2}| \to \infty$.

3.1 Double-hard limit

The dominant contributions in the double-hard region have the form

$$k^2 P_{\mathrm{lin}}^2(k) \int^\Lambda \mathrm{d}\mathbf{q}_1 \mathrm{d}\mathbf{q}_2\, P_{\mathrm{lin}}(q_1) P_{\mathrm{lin}}(q_2)/q_1^2 \tag{4}$$

in an estimated parametric scaling. Therefore, one might suspect that the double-hard limit can be absorbed by the same counterterms as for the one-loop above. By computing the analytical limit of the F_6 kernel, we show that this is indeed the case: the shape dependence of the double-hard limit for general configurations of external momenta corresponds precisely to the four EFT operators defined above. We choose a renormalization scheme where we determine the EFT parameters by fitting the one-loop bispectrum to simulations, and remove the double-hard contribution from the two-loop correction. In other words we use the *subtracted* two-loop bispectrum defined as

$$B_{2\mathrm{L}}^{\mathrm{sub}}(k_1,k_2,k_3) = B_{2\mathrm{L}}(k_1,k_2,k_3) - B_{2\mathrm{L}}^{hh}(k_1,k_2,k_3). \tag{5}$$

3.2 Single-hard limit

To obtain a renormalized two-loop bispectrum we still need to consider the single-hard limit. In principle, one could take one-loop diagrams with an insertion of a one-loop EFT operator, however as this would be complicated to compute analytically, we opt for a numerical treatment. We follow the prescription used for the two-loop powerspectrum in Baldauf et. al. (2015) [6], and consider the limit

$$b_{2L}^{h}(k_1,k_2,k_3;\Lambda) \equiv \int_{|\mathbf{q}_2|<\Lambda} d^3\mathbf{q}_2\, d\Omega_{q_1} \left[\lim_{q_1\to\infty} q_1^2\, b_{2L}(k_1,k_2,k_3,\mathbf{q}_1,\mathbf{q}_2)\right] P_{\mathrm{lin}}(q_2)\,, \tag{6}$$

where b_{2L} consists of the two-loop integrand except for the factor $P_{\mathrm{lin}}(q_1)$. We can compute this integral numerically, fixing the magnitude of $\mathbf{q}_1$ to a large value $|\mathbf{q}_1| \gg \Lambda$. The single-hard limit contribution to the two-loop bispectrum is then

$$B_{2L}^{h}(k_1,k_2,k_3;\Lambda) = 8\pi\,\sigma_d^2(\Lambda) b_{2L}^{h}(k_1,k_2,k_3;\Lambda)\,, \tag{7}$$

We assume that we can renormalize the UV effectively by a shift in the value of the displacement dispersion $\sigma_d^2(\Lambda) \mapsto \sigma_d^2(\Lambda)+\gamma_2(\Lambda)$. Before writing down the corresponding counterterm, we note that part of the integral in Eq. (6) is degenerate with the double-hard contribution: For external wavenumbers much smaller than the cutoff, the integral covers a hard region $|\mathbf{q}_2| \gg |\mathbf{k}_{1,2,3}|$ which yields another contribution with a shape-dependence equal to that of the double-hard region. We choose to subtract this contribution, defining $b_{2L}^{h,\mathrm{sub}} \equiv b_{2L}^{h} - b_{2L}^{hh}$, therefore the counterterm becomes

$$B_{2L}^{\mathrm{ctr}}(k_1,k_2,k_3;\Lambda) \equiv \gamma_2(\Lambda)\, b_{2L}^{h,\mathrm{sub}}(k_1,k_2,k_3;\Lambda)\,. \tag{8}$$

In total, we have five EFT parameters at two-loop: $\{\gamma_1, e_1, e_2, e_3, \gamma_2\}$.

4 Numerics

To beat cosmic variance and allow for accurate calibrations of the EFT parameters from a modest simulation volume, we use the realization based calculation gridPT for the tree-level, one-loop, and subtracted two-loop contributions. The single-hard limit needed for the two-loop counterterm appears more complex to compute in gridPT, hence we compute it using Monte Carlo integration without specializing to a realization.

In addition to the four- and five-parameter models at one- and two-loop, respectively, we consider a simplified approach in which we assume that the operators in Eq. (2) enter in the same linear combination as the corresponding UV-contributions of SPT. Then the four parameters can be related, leaving one free parameter. This can (naively) be extended to two-loop by demanding $\gamma_2 = \gamma_1$.

The reduced χ^2 of the comparison with N-body simulations is shown in the left panel of Fig. 1. We take our full set of triangles with $|\mathbf{k}_{1,2,3}| < k_{\mathrm{max}}$ into account, which comprises 65 (369) triangles at $k_{\mathrm{max}} = 0.1$ (0.2) h/Mpc. The one-loop bispectrum remains in good fit with

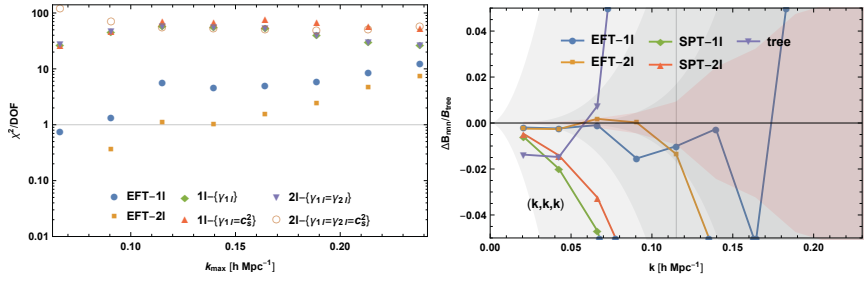

Figure 1 – *Left:* Reduced χ^2 for the EFT one- and two-loop bispectra relative to N-body simulation results, for a set of triangles with side lengths up to $k_{\rm max}$. In addition to the four- and five-parameter models, we show the χ^2 for simplified approaches with zero or one parameter (for the zero-parameter models, $\gamma_1 = c_s^2$ where c_s^2 is calibrated from the power spectrum). *Right:* The difference of the perturbative and the N-body result, normalized to the tree-level for a equilateral triangle configuration of side length k. The red shaded region indicates uncertainty from the N-body simulations, while the dark gray areas indicate expected theoretical uncertainty at tree-level, one-loop and two-loop, with increasing darkness, respectively.

the N-body result for wavenumbers up to about $k_{\rm max} \simeq 0.08\ h/{\rm Mpc}$, while adding the two-loop contribution extends the wavenumbers with 1σ agreement to $k_{\rm max} \simeq 0.15\ h/{\rm Mpc}$. It is also clear that the simple one-parameter schemes leads to significantly larger χ^2 than for the full parametrization. In the right panel, we display the difference of the perturbative bispectrum to the N-body result, normalized to the tree-level bispectrum, for an equilateral configuration and with a pivot scale of $k_{\rm max} = 0.115\ h/{\rm Mpc}$. The EFT clearly extends the agreement with N-body compared to SPT, and the remaining differences are compatible with expected theoretical uncertainty. Moreover, the two-loop correction improves the agreement compared to the one-loop result even at relatively small scales, where the uncertainties are small.

5 Conclusion

In this work we compute for the first time the two-loop bispectrum of large-scale structure in the EFTofLSS. We derive the analytic double-hard limit of the two-loop correction, showing that this contribution can be exactly absorbed by the four EFT operators known from the one-loop bispectrum. In addition we adopt a simplified treatment for the single-hard region, introducing one extra EFT parameter. We compare our results to N-body simulations, using gridPT in order to beat cosmic variance, and find that adding the two-loop contribution extends the range of wavenumbers with 1σ agreement from $k \simeq 0.08$ to $0.15\ h/{\rm Mpc}$.

Acknowledgments

MG and PT are supported by the DFG Collaborative Research Institution Neutrinos and Dark Matter in Astro- and Particle Physics (SFB 1258). TB is supported by the Stephen Hawking Advanced Fellowship at the Center for Theoretical Cosmology.

References

1. D. Baumann *et. al.* JCAP **07**, 051 (2012).
2. J. J. M. Carrasco *et. al.* JHEP **09**, 082 (2012).
3. T. Baldauf *et. al.* JCAP **05**, 007 (2015)
4. R. Angulo *et. al.* JCAP **10**, 039 (2015)
5. T. Baldauf *et. al. Phys. Rev.* D **104**, 12 (2021)
6. T. Baldauf *et. al. Phys. Rev.* D **92**, 12 (2015)

Do anthropic arguments really work?

D. Sorini
Institute for Astronomy, University of Edinburgh, Royal Observatory, Edinburgh EH9 3HJ, UK

The anthropic explanation for the peculiarly small observed value of the cosmological constant $\Lambda_{\rm obs}$ argues that this value promotes the formation of stars, planets, and ultimately of observers such as ourselves. I show that a recent analytic model of cosmic star formation predicts that although $\Lambda_{\rm obs}$ maximises the production of stars in the universe, the probability of generating observers peaks at $\sim 400 - 500\,\Lambda_{\rm obs}$. These preliminary results suggest that an immediate connection between star formation efficiency and observers' creation is not straightforward, and highlight the subtleties involved with the application of anthropic reasoning.

1 Fundamental problems of the ΛCDM paradigm

Although the ΛCDM paradigm has been remarkably successful at reproducing a plethora of observations, it is affected by fundamental and unsolved theoretical issues. Perhaps the biggest open question is the physical meaning of the cosmological constant Λ. The dominant view is that it is a manifestation of the energy of the quantum vacuum, but in this case the observed value $\Lambda_{\rm obs}$ is ~ 120 orders of magnitude smaller than the theoretical expectation [1]. There is still no consensus on a satisfactory explanation for the observed value of Λ from first principles.

Alternatively, one can adopt an anthropic approach, positing that we observe such peculiarly small but non-null value of Λ as a consequence of a selection effect: we are more likely to measure values that promote the creation of observers such as ourselves. As S. Weinberg noted in 1987 [2], if Λ were much larger than what we observe, then the accelerating expansion of the universe would occur at such early times that it would effectively prevent the formation of galaxies, stars, planets, and ultimately life (see also, e.g. [3,4]). Translating this argument to the Multiverse scenario predicted by some models of stochastic inflation, only the universes with a suitably small Λ would be populated with observers. But anthropic reasoning does not in itself require the physical existence of the Multiverse: one could still ask what values of Λ would promote observers' creation among a hypothetical ensemble of possible universes.

Making the minimal assumption that stars are necessary for producing observers, one can effectively consider star formation as a proxy for observers' creation. To test whether the anthropic approach can indeed explain the observed value of Λ, it is then necessary to understand how Λ impacts the total efficiency of star formation over the entire history of the universe. Re-

cently, this question was addressed by running suites of cosmological hydrodynamic simulations beyond redshift $z = 0$ [5,6], where Λ was increased up to $300\,\Lambda_{\rm obs}$ [7]. Although impressive, such simulations still face some important limitations. The parameter space is restricted to a few values of Λ due to the heavy computational cost. Furthermore, the latest cosmic time probed by simulations so far is $\sim 100\,$Gyr, but in principle one cannot exclude that there may be an important contribution to the global star formation history at even later times [8,9]. On the other hand, even though analytical models of cosmic star formation inevitably need to make some simplifying assumptions, they are not subject to the aforementioned restrictions. Therefore, they represent an attractive complementary approach for testing anthropic arguments.

Using the recent analytic model for cosmic star formation given by Sorini & Peacock (2021; hereafter, SP21) [9], I computed the total efficiency of star formation over the entire history of the universe, for a wide range of Λ. The preliminary results show that the efficiency is maximised when $\Lambda \approx \Lambda_{\rm obs}$. However, assuming a flat prior on Λ, the peak of observers' creation occurs in models with $\Lambda \sim 400 - 500\,\Lambda_{\rm obs}$. This shows that maximum stellar efficiency does not automatically correspond to maximum observers' creation, highlighting the subtleties involved with invoking anthropic reasoning.

2 Modelling past and future star formation in non-standard ΛCDM models

The SP21 analytical model of cosmic star formation allows a prediction of the star formation history in a flat ΛCDM model with any Λ, and for arbitrarily large cosmic times ($t \to \infty$). It is based on an extension of the formalism introduced by Hernquist & Springel (2003) [10], whereby the cosmic star formation rate density (CSFRD) is obtained as:

$$\dot{\rho}_*(z) = \bar{\rho}_0 \int s(M,\, z)\, \frac{dF(M,\, z)}{d\ln M}\, d\ln M, \tag{1}$$

where $\bar{\rho}_0$ is the comoving mean matter density of the universe, and $dF/d\ln M$ is the halo multiplicity function, with $F(M,\, z)$ being the collapse fraction in haloes with total mass $< M$. In the equation above, $s(M,\, z)$ is the star formation rate (SFR) within haloes of a fixed mass M, normalised by the total halo mass. Within the Hernquist-Springel formalism, $s(M,\, z)$ is set by whichever time scale is the shortest: an internal gas consumption time scale at high redshift, and the gas cooling time at low redshift [10].

SP21 extended this formalism in two main aspects. First, they included a model for supernovae-driven winds that can alter the baryon mass fraction within haloes. Second, they explicitly considered the impact of the collapse time of haloes on the gas cooling time scale. These extensions result in an improved match to observations of the CSFRD [11], which are reproduced within a factor of two over the redshift range $0 < z < 10$. More importantly, the model predicts a convergent time-integral of the CSFRD even for $t \to \infty$, and is therefore particularly well suited for testing anthropic arguments.

I thus adopt the SP21 model to compute the CSFRD for flat ΛCDM models, with $10^{-4} < \Lambda/\Lambda_{\rm obs} < 10^4$. Modifying the cosmological constant clearly changes $\Omega_{\rm m} = 1 - \Omega_\Lambda$, and hence the evolution of the Hubble constant $H(z)$. Subsequently, both the mean matter density and the halo multiplicity function in Eq. 1 are affected. Notably, altering Λ also impacts the normalised SFR $s(M,\, z)$. This happens because the amount of gas that undergoes cooling is determined by following the expansion of a cooling front from the centre of the halo outwards [10]. The extent of the cooling front depends on the virial radius, whose redshift evolution is in turn set by $H(z)$. As such, the cooling rate is sensitive to the cosmological model via the Hubble constant.

The total stellar mass that will ever be produced in a unit comoving volume $\rho_{*\,\rm tot}$ can be straightforwardly obtained by integrating the CSFRD in Eq. 1 from some initial time to $t \to \infty$. Equivalently, in terms of redshift:

$$\rho_{*\,\rm tot} = \int_{-1}^{z_{\rm in}} \frac{\dot{\rho}_*(z)}{(1+z)H(z)} dz. \tag{2}$$

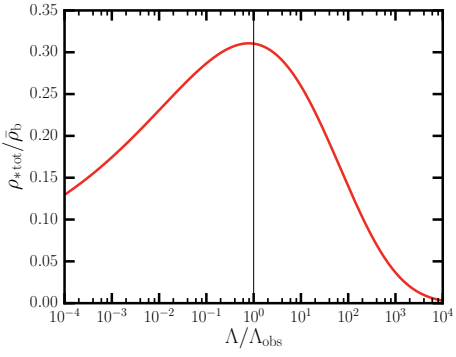

Figure 1 – Fraction of baryonic mass density converted into stars over the entire history of the universe, as a function of the cosmological constant Λ, predicted by the Sorini & Peacock (2021) model of cosmic star formation [9]. Such global stellar efficiency peaks around the observed value of Λ.

For $z_{\mathrm{in}} \gtrsim 20$ the resulting $\rho_{*\,\mathrm{tot}}$ is already well converged. Dividing $\rho_{*\,\mathrm{tot}}$ by the comoving baryonic mass density of the universe $\bar{\rho}_{\mathrm{b}}$, one obtains the total stellar efficiency of that universe.

Such total stellar efficiency is shown in Fig. 1, as a function of Λ. Quite curiously, the maximum efficiency is achieved around the observed value of Λ, which is marked in the plot with a vertical black line. However, it is noteworthy that the efficiency is not suddenly suppressed for $\Lambda > \Lambda_{\mathrm{obs}}$. Even for $\Lambda \sim 100\,\Lambda_{\mathrm{obs}}$, around $\sim 15\%$ of the baryonic mass in the universe is still converted into stars. To understand the implications of this result for anthropic arguments, we need to convert the stellar efficiency in Fig. 1 into a probability for the creation of observers in an ensemble of universes with different Λ.

3 Implications for anthropic arguments

To associate a probability of observers' creation to universes with different Λ, it is first necessary to assume a prior on Λ. I assume a flat prior, following S. Weinberg's argument that there is no compelling reason to prefer a small positive value of Λ to $\Lambda = 0$, therefore the distribution of Λ in the Multiverse should look approximately flat close to $\Lambda = 0$ [2].Secondly, one needs to connect the generation of observers to the star formation history. I will make the minimal assumption that the probability density of generating observers in a universe with cosmological constant Λ is simply proportional to the stellar efficiency shown in Fig. 1.

The resulting probability distribution is shown in Fig. 2. The peak occurs around $\sim 400 - 500\,\Lambda_{\mathrm{obs}}$ and not around Λ_{obs} as is the case for the stellar efficiency. This is a consequence of the flat prior on Λ, which gives more weight to larger values of Λ. This would not be the case if one assumed a different prior, such as a flat prior in $\log_{10}(\Lambda/\Lambda_{\mathrm{obs}})$. However, this choice would not allow for $\Lambda < 0$. Negative values of Λ are possible within the Multiverse ensemble predicted by the landscape of string theory, and I plan to extend my analysis to $\Lambda < 0$ in future work.

The preliminary results presented in this manuscript suggest that although Λ_{obs} maximises the stellar efficiency, observers' creation actually favours $\Lambda \approx 400 - 500\,\Lambda_{\mathrm{obs}}$. Instead, Λ_{obs} is not anthropically favoured, the probability that $\Lambda \leq \Lambda_{\mathrm{obs}}$ being $\sim 0.3\%$. This is even smaller than the $\sim 2\%$ probability found by Barnes et al. (2018) [7], adopting a mass-weighted probability measure. Nevertheless, the conclusion of this manuscript does not rule out anthropic arguments as a viable explanation for Λ_{obs}. Rather, this work highlights that maximum stellar efficiency does not necessarily imply maximum probability of observers' creation. When invoking anthropic reasoning, it is thus important to bear in mind the subtleties involved with the assumptions on the link between observers' creation and star formation, as well as on the prior on Λ.

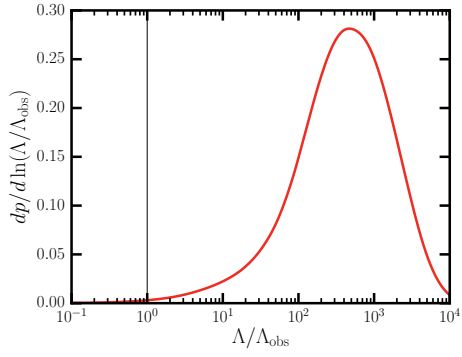

Figure 2 – Probability of generating observers vs. Λ, for a flat ΛCDM universe, assuming that it is proportional to the global stellar efficiency (Fig. 1), and imposing a flat prior on Λ. Values $\Lambda \leq \Lambda_{\rm obs}$ are disfavoured.

Acknowledgments

This work is done in collaboration with John A. Peacock and Lucas Lombriser. I acknowledge support from the European Research Council, under grant no. 670193, and the STFC consolidated grant no. RA5496.

References

1. Luke A. Barnes. The Fine-Tuning of the Universe for Life. *arXiv e-prints*, page arXiv:2110.07783, October 2021.
2. Steven Weinberg. Anthropic bound on the cosmological constant. Phys. Rev. Lett., 59(22):2607–2610, November 1987.
3. George Efstathiou. An anthropic argument for a cosmological constant. MNRAS, 274(4):L73–L76, June 1995.
4. J. A. Peacock. Testing anthropic predictions for Λ and the cosmic microwave background temperature. MNRAS, 379(3):1067–1074, August 2007.
5. Jaime Salcido, Richard G. Bower, Luke A. Barnes, Geraint F. Lewis, Pascal J. Elahi, Tom Theuns, Matthieu Schaller, Robert A. Crain, and Joop Schaye. The impact of dark energy on galaxy formation. What does the future of our Universe hold? MNRAS, 477(3):3744–3759, July 2018.
6. Boon Kiat Oh, John A. Peacock, Sadegh Khochfar, and Britton D. Smith. Evolving beyond z=0: insights about the future of stars and the intergalactic medium. MNRAS, 507(4):5432–5450, November 2021.
7. Luke A. Barnes, Pascal J. Elahi, Jaime Salcido, Richard G. Bower, Geraint F. Lewis, Tom Theuns, Matthieu Schaller, Robert A. Crain, and Joop Schaye. Galaxy formation efficiency and the multiverse explanation of the cosmological constant with EAGLE simulations. MNRAS, 477(3):3727–3743, July 2018.
8. Fred C. Adams and Gregory Laughlin. A dying universe: the long-term fate and evolutionof astrophysical objects. *Reviews of Modern Physics*, 69(2):337–372, April 1997.
9. Daniele Sorini and John A. Peacock. Extended Hernquist-Springel formalism for cosmic star formation. MNRAS, 508(4):5802–5824, December 2021.
10. L. Hernquist and V. Springel. An analytical model for the history of cosmic star formation. MNRAS, 341:1253–1267, June 2003.
11. Piero Madau and Mark Dickinson. Cosmic Star-Formation History. ARA&A, 52:415–486, August 2014.

Estimator for the anisotropic stress using relativistic effects in large-scale structure

Daniel Sobral Blanco
University of Geneva, Department of Theoretical Physics, 24, quai Ernest Ansermet 1211 Genève 4 Switzerland

The large-scale structure of the Universe is a rich source of information to test the consistency of General Relativity on cosmological scales. We briefly describe how the observed distributions of galaxies is affected by redshift-space distortions, but also by gravitational lensing and other relativistic effects. Then, we show how one of this relativistic effects, the gravitational redshift, can be used to build a model independent test that directly measures the anisotropic stress, i.e. the difference between the two gravitational potentials that describe spacetime fluctuations of the geometry.

1 Introduction

Testing the laws of gravity at cosmological scales is one of the main science drivers for the coming generation of large-scale structure surveys. At large scales and late times, our Universe can be consistently described by a set of four fields that quantify the deviations from an homogeneous and isotropic background: the two metric potentials, Φ and Ψ, describing the fluctuations in the geometry of the Universe, the matter density fluctuations, δ, and the galaxy peculiar velocity field, $\mathbf{V}$ [a]. Testing the laws of gravity requires then to test the relations between these four fields. This can be done by using the data obtained at galaxy surveys, which probe the late-time large scale structure of the Universe.

One of this test of gravity consists in measuring the ratio between the two metric potentials, characterized by the *anisotropic stress*, $\Phi = \eta\Psi$. ΛCDM and many dark energy models predict $\eta = 1$ but, generally, modified gravity models predict $\eta \neq 1$. However, the observables at late-times considered so far are sensitive to only three combinations of the four fields, namely δ, $\mathbf{V}$ and $(\Phi + \Psi)$. This means that current observations are not able to test all relations between the four fields. To overcome this problem, one usually has to assume that the continuity equation for dark matter holds: there is no exchange of energy between dark matter and dark energy; and that Euler equation also holds: dark matter follows geodesics. Using this, a measurement of $\mathbf{V}$ can be translated into a measurement of Ψ, which can then be compared to $(\Phi + \Psi)$ to test if the

[a] We use the metric convention $ds^2 = a^2(t)[-(1+2\Psi)dt^2 + (1-2\Phi)d\mathbf{x}^2]$ where t denotes conformal time.

two potentials are the same [1]. We argue that this procedure only provides an indirect test that fails to give a measurement of the anisotropic stress if any of the aforementioned assumptions is not valid [2].

In this talk, we give a gauge-independent observable for galaxy clustering at linear order in perturbation theory which include relativistic effects. These terms will become relevant for future generations of galaxy surveys. Given that the relativistic effects are sensitive to Ψ, it is thus possible to isolate and directly measure it in a model independent way. We finally show how we can build a new estimator for the anisotropic stress.

2 Galaxy number counts at linear order

Galaxy surveys probe the large-scale structure of the Universe at late-times. They provide us with maps of the sky in which the position of the galaxies can be parametrized in terms of redshift z and the direction of observation $\mathbf{n}$. We can then *count* the number of galaxies per pixel and measure the fluctuations between different pixels. Our observable is the *galaxy number counts*, defined as $\Delta(z,\mathbf{n}) = (N-\bar{N})/\bar{N}$, where N is the number of galaxies at the pixel $(z,\mathbf{n})$ and $\bar{N}$ the average number of galaxies per pixel. The question is now: how is Δ related to the initial perturbations, the theory of gravity and dark energy? In order to answer this question, we calculate the perturbed photon geodesics to infer the change in energy and the change in direction induced by the underlying structure, which induce distortions in the coordinate system of $(z,\mathbf{n})$. The final expression at linear order in perturbation theory reads [3,4,5]

$$\begin{aligned}
\Delta(z,\mathbf{n}) &= b\delta - \frac{1}{\mathcal{H}}\partial_r(\mathbf{V}\cdot\mathbf{n}) + (5s-2)\int_0^r dr' \frac{r-r'}{2rr'}\Delta_\Omega(\Phi+\Psi) \\
&+ \left(1-5s-\frac{\dot{\mathcal{H}}}{\mathcal{H}^2}+\frac{5s-2}{r\mathcal{H}}\right)\mathbf{V}\cdot\mathbf{n} + \frac{1}{\mathcal{H}}\dot{\mathbf{V}}\cdot\mathbf{n} + \frac{1}{\mathcal{H}}\partial_r\Psi \\
&+ \frac{2-5s}{r}\int_0^r dr'(\Phi+\Psi) + 3\mathcal{H}\nabla^{-2}(\nabla\mathbf{V}) + \Psi + (5s-2)\Phi \\
&+ \frac{1}{\mathcal{H}}\dot{\Phi} + \left(\frac{\dot{\mathcal{H}}}{\mathcal{H}^2}+\frac{2-5s}{r\mathcal{H}}+5s\right)\left[\Psi + \int_0^r dr'(\dot{\Phi}+\dot{\Psi})\right],
\end{aligned} \tag{1}$$

Where b is the galaxy bias, s is the magnification bias and $\mathcal{H} = aH$ is the comoving Hubble factor. The two first terms in the first line are the dark matter density perturbations and the *redshift-space distortions* [6,7 b], while the third term is the *weak-lensing* contribution. The latter is only relevant for very high redshifts and can be neglected for our purposes. The rest of the terms encode the *relativistic distortions*. The second line contain two Doppler effects and the *gravitational redshift* contribution, which is proportional to $\partial_r\Psi$ [c]. The latter can be isolated to provide a direct measurement of the metric potential Ψ [2]. The third and fourth lines are other relativistic distortions involving the scalar metric potentials.

3 Isolating Ψ in the correlation function

In practice, we do not measure the fluctuations in the number counts of galaxies per pixel individually. We study the correlation function between pairs of pixels and perform a multipole expansion. Using Eq.(1), the correlation function will be of the form

$$\begin{aligned}
\xi(z,d) &= \langle\Delta(\mathbf{x})\Delta(\mathbf{x}')\rangle \\
&= \langle\Delta_{st}(\mathbf{x})\Delta_{st}(\mathbf{x}')\rangle + \langle\Delta_{st}(\mathbf{x})\Delta_{rel}(\mathbf{x}')\rangle + \langle\Delta_{rel}(\mathbf{x})\Delta_{st}(\mathbf{x}')\rangle + \langle\Delta_{rel}(\mathbf{x})\Delta_{rel}(\mathbf{x}')\rangle,
\end{aligned} \tag{2}$$

[b] We call the combination of both as the *standard* terms, since they are the relevant contributions for current measurements of $\mathbf{V}$ and δ.

[c] Notice that we are not using Euler equation here. If we use it, the three terms in the second line combine to a single Doppler term. We want to keep the gravitational redshift explicit and the most general form of Δ.

where we wrote $\mathbf{x} = (z, \mathbf{n})$ for simplicity. The correlation function will only depend on the redshift z and the relative distance between the pixels, d. The last term is subdominant and can be neglected for our purposes. The relativistic corrections to the correlation function are thus encoded in the cross-correlation between *standard* and relativistic contributions to the number counts.

We now perform a multipole expansion in powers of the angle between the line of sight and the line joining the two pixels, denoted by β_{ij}. We perform the operation

$$\xi_l(z, d) = \sum_{ij} \Delta(\mathbf{x}_i)\Delta(\mathbf{x}_j)\, P_l(\cos\beta_{ij}), \tag{3}$$

where P_l are the Legendre polynomials and the sum runs over the pair of pixels. We find that $\langle \Delta_{st}(\mathbf{x})\Delta_{st}(\mathbf{x}')\rangle$ only contribute to the *even* multipoles ($l = 0,\ 2,\ 4$): we can combine the measurements of the monopole, quadrupole and hexadecapole to isolate δ and $\mathbf{V}$. This is what it has been done in current surveys [8]. The Doppler effects and the gravitational redshift contribute to the *dipole* ($l = 1$) and *octupole* ($l = 3$) alone, and therefore they break the symmetry of the correlation function [9]. However, this contributions are only non-zero when we correlate two populations of galaxies with different luminosities. We have to split our population of galaxies into two families, the *bright* and *faint* galaxies [d]. The other effects in Δ, the ones of the third and fourth line in Eq.(1), are independent on the direction $\mathbf{n}$ and thus contribute only to the monopole of the correlation function. They are subdominant with respect to the density perturbations and can be neglected [4,5]. Therefore, by correlating two populations of galaxies with different luminosities, we can combine the even and odd multipoles of the correlation function to isolate the gravitational redshift contribution [2,10].

4 Measuring the anisotropic stress

We have seen that the information about the distortions in the distribution of galaxies at large-scales is encoded in the multipoles of the correlation function. The different multipoles can be considered individual observables in its own right, since we can always fit the data to isolate them individually by weighting the correlation function with the correspondent Legendre polynomial (see Eq.(3)). The idea for the new test for the anisotropic stress is first to directly measure the dipole of the correlation function, and to combine it with the even multipoles to isolate Ψ.

In practice, the dipole of the correlation function contains the terms $\langle \delta V\rangle$, $\langle VV\rangle$, $\langle \delta\dot{V}\rangle$ and $\langle \delta\Psi\rangle$. The $\langle \delta V\rangle$ and $\langle VV\rangle$ correlations are removed by using the even multipoles. The $\langle \delta\dot{V}\rangle$ correlation can be inferred from redshift evolution of the multipoles. This is the price to pay given that we do not want to assume the validity of the Euler equation. Putting all this together, we are left with the correlation between the density perturbations and the gravitational potential, i.e. the observable $O^{\delta\Psi} \equiv (b_B - b_F)\langle \delta\Psi\rangle$ [2].

Finally, measuring the anisotropic stress require an observable sensitive to $(\Phi + \Psi)$. This can be provided by *galaxy-galaxy lensing*. Since $O^{\delta\Psi}$ is sensitive to the difference of the biases of bright and faint populations, we define a new observable that correlates the shapes of galaxies at high redshift (the lensed galaxies) with number counts of galaxies at low redshift (the lenses)

$$O^{\delta(\Phi+\Psi)} \equiv \langle \Delta_B\kappa\rangle - \langle \Delta_F\kappa\rangle \propto (b_B - b_F)\langle \delta(\Phi + \Psi)\rangle, \tag{4}$$

where κ is the magnification of the lensed galaxies. We could also use the shear instead. Therefore, the ratio between this observable and the dipole measurement can give an estimator for the anisotropic stress $\eta = \Phi/\Psi$,

$$O^{\eta} \equiv \frac{O^{\delta(\Phi+\Psi)}}{O^{\delta\Psi}} = \frac{(b_B - b_F)\langle \delta(\Phi + \Psi)\rangle}{(b_B - b_F)\langle \delta\Psi\rangle} \sim 1 + \eta. \tag{5}$$

[d] The choice is somewhat arbitrary, but the simplest case is to consider that half of our population has a luminosity above certain threshold (bright galaxies), while the other half has luminosity below the same luminosity threshold (faint galaxies).

Hence, the detection of any deviation from the value 2 in the observable O^{η} at any redshift will genuinely indicate the presence of an anisotropic stress. However, there is an important caveat here: we have implicitly assumed that the bias difference cancels. This means we need a survey which provides galaxy positions and shapes simultaneously, or the combination of two surveys that probe the same catalog of galaxies. While this is unlikely for the current and future (Euclid or SKA), we have found that there is no significant statistical difference if we measure $\langle \delta\Psi \rangle$ alone, which removes the need to define $O^{\delta(\Phi+\Psi)}$ as in Eq.(4) [10].

5 Conclusions & Outlook

Next generation of galaxy surveys will provide us with an enormous amount of data which can be used to test the laws of gravity on scales that are currently inaccesible. This opens the door to construct new observables which probe effects in the large-scale distribution of galaxies that are neglected in current analysis. On top of the density perturbations, redshift-space distortions and weak lensing, we have shown that the galaxy number counts at linear order in perturbation theory is also affected by relativistic distortions.

The relevant relativistic effects consist in two Doppler contributions and the gravitational redshift. They break the symmetry of the correlation function and contribute to the odd multipoles. In order to detect them, we must correlate galaxies with different luminosities. Given that each of the multipoles can be considered an individual observable, it is possible to combine even and odd multipoles to isolate the relativistic effects. This provides a direct measurement of $\langle \delta\Psi \rangle$, for which we expect an accuracy of $20-30\%$ in SKA at low redshift and large separations between galaxies [10]. Finally, the combination of this measurement with galaxy-galaxy lensing observations, which are sensitive to $\langle \delta(\Phi+\Psi) \rangle$, can be used to build an estimator for η [11]. This method is model independent, in the sense that it does not assume the validity of the Euler or continuity equations, and thus provides a genuine measurement of the anisotropic stress.

Acknowledgments

This project and the presence of the author at the conference has received funding from the European Research Council (ERC) under the European Union's Horizon 2020 research and innovation program (Grant agreement No. 863929; project title "Testing the law of gravity with novel large-scale structure observables"). We also acknowledge funding from the Swiss National Science Fundation (SNSF). The author also acknowledge the organization of the "56th Rencontres de Moriond" conference for the opportunity to present this work.

References

1. L. Amendola *et a.l.*, *Phys. Rev.* D **87**, 023501 (2013).
2. D. Sobral Blanco and C. Bonvin, *Phys. Rev.* D **104**, 063516 (2021)
3. C. Bonvin and R. Durrer, *Phys. Rev.* D **84**, 063505 (2011).
4. J. Yoo *et a.l.*, *Phys. Rev.* D **80**, 083514 (2010).
5. A. Challinor and A. Lewis *Phys. Rev.* D **84**, 043516 (2011).
6. N. Kaiser, *Mon. Not. Roy. Astron. Soc.* **227**, 1 (1984).
7. A. J. S. Hamilton in *Ringberg Workshop on Large Scale Structure, Ringberg, Germany, September 23-28, 1996*, (1997).
8. BOSS: Sapathy *et a.l.*, *Mon. Not. Roy. Astron. Soc.* **469**, 2 (2017).
9. C. Bonvin, L. Hui and E. Gaztañaga, *Phys. Rev.* D **89**, 083535 (2014).
10. D. Sobral Blanco and C. Bonvin, *in preparation.*
11. I. Tutusaus, D. Sobral Blanco and C. Bonvin *in preparation.*

6.
Posters

Polarization modulation from non-ideal HWP: QUBIC Technological Demonstrator calibration measurement and observation forecast

D'Alessandro G.
(Complete list of authors to be found at the end of the proceedings)
Università di Roma - La Sapienza, Roma, Italy,
INFN sezione di Roma, 00185 Roma, Italy

Systematic effects and foregrounds separation are two of the major challenges for the experiments approaching B-modes measurement. Since they aim to measure the polarization of cosmic microwave background, one of the biggest issues comes from the non-ideality of the polarimeter. The systematic effects induced by the instrument itself can be mitigated by a careful calibration phase both at the sub-system level and at the system level. QUBIC experiment will use a Stokes Polarimeter composed of a step-by-step rotating Half-wave plate and a fixed polarizer. We have performed dedicated calibration measurements at the sub-system level retrieving the frequency-dependent Mueller matrix of the HWP and we have measured the impact of the systematic effect at the system level. Then, with end-to-end simulation, the effect on the sky has been evaluated showing how the knowledge of the instrument, acquired in the calibration phase, is a good way to mitigate the systematic effects.

1 QUBIC Stokes polarimeter

The QUBIC polarimeter, described in D'Alessandro et al.[1], is composed of a polypropylene metamaterial HWP followed by a polarizer made of copper strips deposited on a mylar substrate. In the QUBIC-TD the HWP and the polarizer have a reduced diameter for the Full Instrument configuration, 180 mm and 370 mm respectively, Masi et al.[2]. The HWP and the polarizer have been characterized (sub-system level) with dedicated laboratory measurements by the Astronomy Instrumentation Group (AIG) in Cardiff by using a vector network analyzer (VNA). Then, using a fully polarized source in the QUBIC far field, we performed multifrequency measurements (system-level calibration). The spectral band has been measured with and without the polarimeter to evaluate the Efficient Mueller Matrix. Cross-polarization is $< 0.6\%$ at 150GHz. With this dedicated calibration, detailed forecasts about the effect on sky measurement are performed.

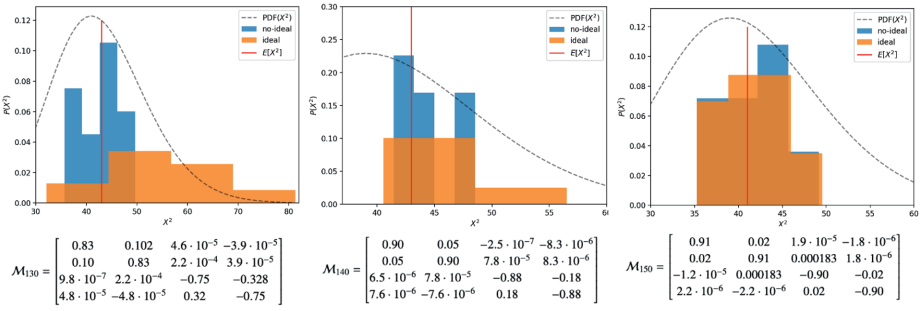

Figure 1 – χ^2 likelihood distribution fitting the measurement at 130 140 and 150 GHz with a real and ideal model of the HWP. The blue histogram is the results taking into account the real Mueller matrix and the orange one is obtained assuming the ideal one. The red vertical line is the expected value of the χ^2.

2 HWP Laboratory characterization

The Vector Network Analyzer illuminates the QUBIC-TD HWP with fully linearly polarized light at different frequencies. By measuring the transmitted intensity at different HWP rotation angles (0°, 45°, and 90° to the HWP C-axis) we can obtain the Jones matrix and then the Mueller matrix[3]. Knowing the instrument spectral response, see Torchinsky et al.[4] and the laboratory characterization of the HWP the efficient Muller matrix for QUBIC-TD is:

$$\mathcal{M}_{eff} = \begin{bmatrix} 0.91 & 0.02 & 3.8\cdot10-5 & 1.3\cdot10^{-6} \\ 0.02 & 0.91 & 1.6\cdot10^{-4} & -1.3\cdot10^{-6} \\ -3.3\cdot10^{-5} & 1.6\cdot10^{-4} & -0.90 & -0.02 \\ 3.2\cdot10^{-7} & -3.2\cdot10^{-7} & 0.02 & -0.90 \end{bmatrix} \quad (1)$$

3 System level calibration

Multifrequency measurements have been performed thanks to a fully polarized source in the instrument far field. Data has been fitted with the Stokes polarimeter ideal model and the QUBIC polarimeter real model including the efficient Mueller matrix. The χ^2-tests has been performed to test both models and the likelihood distribution is in Figure1

4 Systematic effect mitigation forecast

We have performed end-to-end simulations to see the effect of the systematic in real sky measurement. We assume to observe a sky patch: 20°x20° near the center of the galaxy (l=0,b=0). The HWP scanning step-by-step taking data only in its nominal positions: 0°-15°-30°-45°-60°-75°-90°. The input map has been retrieved with PySm and it is composed CMB radiation, intensity and polarization, and dust, intensity, and polarization as well. We assumed to observe the sky with the real instrument, and we reconstruct the sky both assuming to know the real Mueller matrix of the HWP and assuming an ideal case. The results is shown in Figure 2.

Acknowledgments

QUBIC is funded by the following agencies. France: ANR (Agence Nationale de la Recherche) 2012 and 2014, DIM-ACAV (Domaine d'Intérêt Majeur-Astronomie et Conditions d'Apparition de la Vie), CNRS/IN2P3 (Centre national de la recherche scientifique/Institut national de physique nucléaire et de physique des particules), CNRS/INSU (Centre national de la recherche

scientifique/Institut national et al de sciences de l'univers). Italy: CNR/PNRA (Consiglio Nazionale delle Ricerche/Programma Nazionale Ricerche in Antartide) until 2016, INFN (Istituto Nazionale di Fisica Nucleare) since 2017. Argentina: MINCyT (Ministerio de Ciencia, Tecnología e Innovación), CNEA (Comisión Nacional de Energía Atómica), CONICET (Consejo Nacional de Investigaciones Científicas y Técnicas).

D. Burke and J.D. Murphy acknowledge funding from the Irish Research Council under the Government of Ireland Postgraduate Scholarship Scheme. D. Gayer and S. Scully acknowledge funding from the National University of Ireland, Maynooth. D. Bennett acknowledges funding from Science Foundation Ireland.

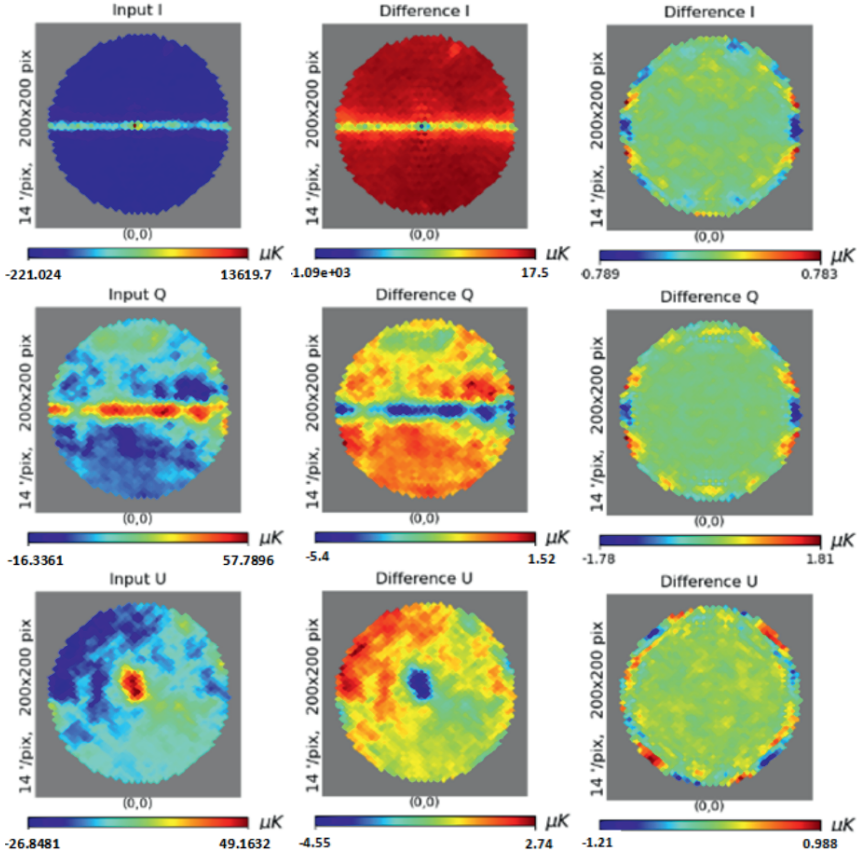

Figure 2 – End-to-end simulations result. The left column shows the input sky (CMB + dust, intensity, and polarization). The rows show the Stokes parameter I, Q, and U, respectively. The center and the right column are the differences between the input sky map and the reconstructed sky map. The sky is always observed with the real polarimeter but it is reconstructed with the ideal one (center column) and with the real one (right column). The plot shows that, by inserting the polarimeter calibration into the data analysis pipeline, the sky map is better retrieved.

References

1. G. D'Alessandro, L. Mele, F. Columbro, et al. QUBIC VI: cryogenic half wave platerotator, design and performances. *arXiv e-prints*, page arXiv:2008.10667, August 2020.
2. S. Masi et al. QUBIC V: Cryogenic system design and performance. *arXiv e-prints*, page arXiv:2008.10659, August 2020.
3. Sean A. Bryan, Thomas E. Montroy, and John E. Ruhl. Modeling dielectric half-wave plates for cosmic microwave background polarimetry using a mueller matrix formalism. *Appl. Opt.*, 49(32):6313–6323, Nov 2010.
4. S. A. Torchinsky et al. QUBIC III: Laboratory Characterization. *arXiv e-prints*, page arXiv:2008.10056, August 2020.

Full Authors List:

G. D'Alessandro[1,2], E.S. Battistelli[1,2], P. de Bernardis[1,2], F. Columbro[1,2], M. De Petris[1,2], M.M. Gamboa Lerena[24,33], L. Grandsire[3], J.-Ch. Hamilton[3], S. Marnieros[4], S. Masi[1,2], L. Mele[1,2], A. Mennella[5,6], L. Mousset[3], C. O'Sullivan[7], M. Piat[3], A. Tartari[9], S.A. Torchinsky[3,10], F. Voisin[3], M. Zannoni[11,12], P. Ade[8], J.G. Alberro[13], A. Almela[14], G. Amico[1], L.H. Arnaldi[15], D. Auguste[4], J. Aumont[16], S. Azzoni[17], S. Banfi[11,12], A. Baù[11,12], B. Bélier[18], D. Bennett[7], L. Bergé[4], J.-Ph. Bernard[16], M. Bersanelli[5,6], M.-A. Bigot-Sazy[3], J. Bonaparte[19], J. Bonis[4], E. Bunn[20], D. Burke[7], D. Buzi[1], F. Cavaliere[5,6], P. Chanial[3], C. Chapron[3], R. Charlassier[3], A.C. Cobos Cerutti[14], A. Coppolecchia[1,2], G. De Gasperis[21,22], M. De Leo[1,23], S. Dheilly[3], C. Duca[14], L. Dumoulin[4], A. Etchegoyen[14], A. Fasciszewski[19], L.P. Ferreyro[14], D. Fracchia[14], C. Franceschet[5,6], K.M. Ganga[3], B. García[14], M.E. García Redondo[14], M. Gaspard[4], D. Gayer[7], M. Gervasi[11,12], M. Giard[16], V. Gilles[1,25], Y. Giraud-Heraud[3], M. Gómez Berisso[15], M. González[15], M. Gradziel[7], M.R. Hampel[14], D. Harari[15], S. Henrot-Versillé[4], F. Incardona[5,6], E. Jules[4], J. Kaplan[3], C. Kristukat, L. Lamagna[1,2], S. Loucatos[3,27], T. Louis[4], B. Maffei[28], W. Marty[16], A. Mattei[2], A. May[25], M. McCulloch[25], D. Melo[14], L. Montier[16], L.M. Mundo[13], J.A. Murphy[7], J.D. Murphy[7], F. Nati[11,12], E. Olivieri[4], C. Oriol[4], A. Paiella[1,2], F. Pajot[16], A. Passerini[11,12], H. Pastoriza[15], A. Pelosi[2], C. Perbost[3], M. Perciballi[2], F. Pezzotta[5,6], F. Piacentini[1,2], L. Piccirillo[25], G. Pisano[8,1], M. Platino[14], G. Polenta[1,29], D. Prêle[3], G. Presta[1,2], R. Puddu[1,30], D. Rambaud[16], E. Rasztocky[31], P. Ringegni[13], G.E. Romero[31], J.M. Salum[14], A. Schillaci[1,32], C.G. Scóccola[24,33], S. Scully[7,34], S. Spinelli[11], G. Stankowiak[3], M. Stolpovskiy[3], A.D. Supanitsky[14], J.-P. Thermeau[3], P. Timbie[35], M. Tomasi[5,6], G. Tucker[36], C. Tucker[8], D. Viganò[5,6], N. Vittorio[21], F. Wicek[4], M. Wright[25], and A. Zullo[2]

[1]Università di Roma - La Sapienza, Roma, Italy,[2]INFN sezione di Roma, 00185 Roma, Italy,[3]Université de Paris, CNRS, Astroparticule et Cosmologie, F-75006 Paris, France,[4]Laboratoire de Physique des 2 Infinis Irène Joliot-Curie (CNRS-IN2P3, Université Paris-Saclay), France,[5]Università degli studi di Milano, Milano, Italy,[6]INFN sezione di Milano, 20133 Milano, Italy,[7]National University of Ireland, Maynooth, Ireland,[8]Cardiff University, UK,[9]INFN sezione di Pisa, 56127 Pisa, Italy,[10]Observatoire de Paris, Université Paris Science et Lettres, F-75014 Paris, France,[11]Università di Milano - Bicocca, Milano, Italy,[12]INFN sezione di Milano - Bicocca, 20216 Milano, Italy,[13]GEMA (Universidad Nacional de La Plata), Argentina,[14]Instituto de Tecnologías en Detección y Astropartículas (CNEA, CONICET, UNSAM), Argentina,[15]Centro Atómico Bariloche and Instituto Balseiro (CNEA), Argentina,[16]Institut de Recherche en Astrophysique et Planétologie, Toulouse (CNRS-INSU), France,[17]Department of Physics, University of Oxford, UK,[18]Centre de Nanosciences et de Nanotechnologies, Orsay, France,[19]Centro Atómico Constituyentes (CNEA), Argentina,[20]University of Richmond, Richmond, USA,[21]Università di Roma "Tor Vergata", Roma, Italy,[22]INFN sezione di Roma2, 00133 Roma, Italy,[23]University of Surrey, UK,[24]Facultad de Ciencias Astronómicas y Geofísicas (Universidad Nacional de La Plata), Argentina,[25]University of Manchester, UK,[26]Escuela de Ciencia y Tecnología (UNSAM) and Centro Atómico Constituyentes (CNEA), Argentina,[27]IRFU, CEA, Université Paris-Saclay, F-91191 Gif-sur-Yvette, France,[28]Institut d'Astrophysique Spatiale, Orsay (CNRS-INSU), France,[29]Italian Space Agency, Roma, Italy,[30]Pontificia Universidad Catolica de Chile, Chile,[31]Instituto Argentino de Radioastronomía (CONICET, CIC, UNLP), Argentina,[32]California Institute of Technology, USA,[33]CONICET, Argentina,[34]Institute of Technology, Carlow, Ireland,[35]University of Wisconsin, Madison, USA,[36]Brown University, Providence, USA

The Simons Observatory and new framework for constraining cosmic birefringence in the presence of systematics and galactic foregrounds

Baptiste Jost
Université de Paris, CNRS, Astroparticule et Cosmologie,
75013 Paris, France

Cosmic birefringence is a process that rotates the polarisation angle of CMB photons and that could be a hint for new physics. The measurement of isotropic birefringence is however degenerate with the polarisation angle of a CMB telescope's detectors. In this work I propose a method that combines parametric component separation and systematic effects correction with which we can robustly estimate birefringence angle in the presence of foregrounds and miscalibration angles. This work has been done in the context of Simons Observatory.

1 Introduction

Cosmic birefringence is a process that rotates the polarisation angle of CMB photons. It is a promising probe for physics beyond the standard model of cosmology, or axion dark matter search. In my work I focus on isotropic birefringence, however the possible signal of a non-zero isotropic cosmic birefringence is degenerate with the polarisation angle of the telescope and may suffer from astrophysical contamination and create spurious EB correlation that are critical in birefringence detection. Several methods have been proposed to circumvent this issue, Minami & Komatsu[1] propose to use foreground signals to calibrate the polarisation angle. Using Planck data, they showed hints of a non-zero cosmic birefringence angle $\beta_b = 0.35 \pm 0.14^{\circ}$[2] and further studies seem to go in the same way[3]. However this method assumes knowledge of the foregrounds EB power spectrum which is not well known yet. In particular the quoted result assumes no EB correlation, but recent work by Clark et al[4] shows that there are physical reasons to expect non-zero foreground EB correlation. In that context I work on a method to generalise component separation and to remove the dependence on foregrounds EB using calibration priors. In particular I work on the interplay between foreground cleaning, the correction of systematic effects and the estimation of the tensor-to-scalar ratio r and β_b.

2 Method and results

2.1 Generalised component separation

I generalised the parametric component separation method used in[5,6], the stiff scaling laws used in this method allow for shared information across frequency bands hence maximising the information obtained from priors and therefore getting a better estimation of systematic parameters. To lift the degeneracies between miscalibration angles and birefringence angle we use Gaussian priors given by calibration campaigns. In the first step we work in pixel space and the observed frequency maps d_p, are modeled as :

$$d_p = \boldsymbol{X}_p(\{\alpha_1, ..., \alpha_{n_f}\}).\boldsymbol{A}_p(\{\beta_{fg}\}).s_p + n_p \tag{1}$$

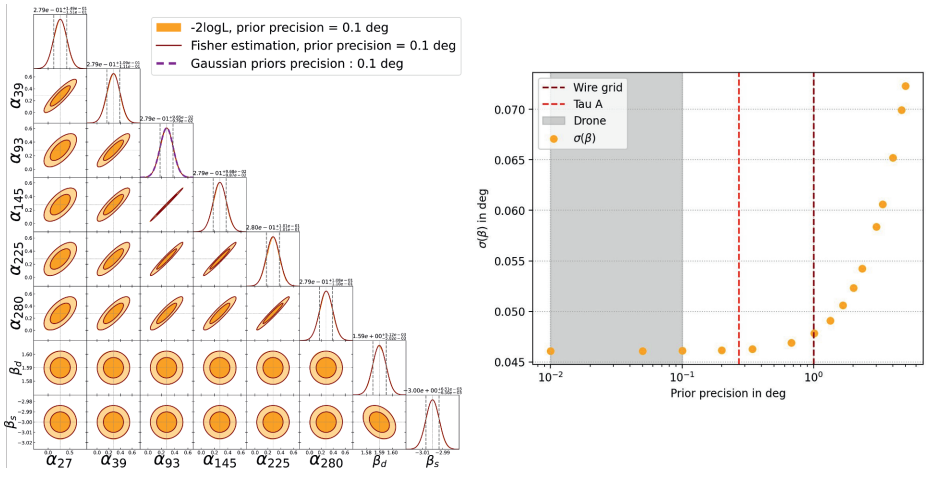

Figure 1 – Left : Spectral likelihood sampling with 0.1° prior at 93 GHz. Right: Evolution of the $\sigma(\beta_b)$ w.r.t. the precision of the Gaussian prior on the 93 GHz channel using SO SAT characteristics

Where $\boldsymbol{X}$ is a matrix encoding e.g. systematic effects such as the rotation induced by instrumental polarisation angles. $\boldsymbol{A}$ is the mixing matrix canonically used in the parametric component method and that links the different sky components to the observed frequency channels using the emission laws of the component involved. s_p is the vector with the true component maps (including the effect of birefringence), and n_p is the noise. We can then use the spectral likelihood method from[5] to fit for foreground parameters and miscalibration angles, allowing for the estimation of a CMB map that should be foreground cleaned and corrected for systematic effects. The sampling of the spectral likelihood is shown in Fig 1 left, where we used only one prior with a 0.1° precision on the 93 GHz channel. Here we can see that one prior is enough to estimate all miscalibration angles: this comes from the action of the mixing matrix $\boldsymbol{A}$ that relates observation across all frequency bands.

2.2 Cosmological likelihood

We then compute the power spectra of the CMB map and estimate cosmological parameters such as r and β_b. Generalising the residuals computation of[6] to include systematic parameters we are able to understand the impact of the generalised component separation on the estimation of cosmological parameters. Fig 1 (right) shows the evolution of $\sigma(\beta_b)$ with respect to the prior precision (with a prior on the 93 GHz channel). Those preliminary results seem to indicate that SO will get an improvement on birefringence estimation compared to previous results.

References

1. Minami, Y. et al. *PTEP* **2019**, *2019*, 083E02.
2. Minami, Y. et al. *Physical Review Letters* **2020**, *125*, DOI: 10.1103/physrevlett.125.221301.
3. Diego-Palazuelos, P. et al. *Physical Review Letters* **2022**, *128*, DOI: 10.1103/physrevlett.128.091302.
4. Clark, S. E. et al. *The Astrophysical Journal* **2021**, *919*, 53.
5. Stompor, R. et al. *Monthly Notices of the Royal Astronomical Society* **2008**, *392*, 216–232.
6. Stompor, R. et al. *Phys. Rev. D* **2016**, *94*, 083526.

Mitigation of systematic effects for high precision observation of CMB B modes with *LiteBIRD*

Clément Leloup on behalf of the *LiteBIRD* Collaboration
Université Paris Cité, Laboratoire Astroparticule et Cosmologie, Paris, France

LiteBIRD, the Lite (Light) satellite for the study of B-mode polarization and Inflation from cosmic background Radiation Detection, is a Japan-led international space mission whose goal is to open a new window on primordial physics via high precision measurement of the Cosmic Microwave Background (CMB) polarization. Its main scientific objective is to measure the inflationary tensor-to-scalar ratio r from a high precision observation of CMB B modes, with a total error of $\sigma(r) < 0.001$ assuming $r = 0$. A detection of the contribution from primordial gravitational waves in the spectrum of B modes would be strong evidence of new physics at energy scales far beyond our current understanding, and in particular of the hypothetical inflationary period. To reach such a high precision, *LiteBIRD* will have to achieve an extreme control of instrumental systematics, especially in the presence of foregrounds.

In a CMB experiment such as *LiteBIRD*, the systematic sources of uncertainty on the cosmological parameters come from the interplay between the lack of knowledge of Galactic foregrounds and the miscorrection of instrumental or environmental effects. Because they introduce residuals in the recovered CMB maps, they introduce a bias Δr on the measured value of r. Since the primary goal of the mission is to measure r, this bias will be the figure of merit for studies of systematic effects in *LiteBIRD*. Each systematic effect contributes to these residuals, with a power spectrum $C_\ell^{\rm sys}$. From this, we compute Δr as the maximum of the cosmological likelihood, assuming $r = 0$:

$$\ln\mathcal{L}(r) = -f_{\rm sky}\sum_\ell \frac{2\ell+1}{2}\left[\frac{C_\ell^{\rm obs}}{C_\ell^{\rm th}} + \ln\left(C_\ell^{\rm th}\right)\right] \tag{1}$$

where $f_{\rm sky}$ is the observed fraction of the sky, and $C_\ell^{\rm obs}$ and $C_\ell^{\rm th}$ are the observed and theoretical CMB B-mode power spectrum respectively, defined as:

$$C_\ell^{\rm obs} = C_\ell^{\rm sys} + C_\ell^{\rm lens} + N_\ell \qquad \text{and} \qquad C_\ell^{\rm th} = rC_\ell^{\rm prim} + C_\ell^{\rm lens} + N_\ell \tag{2}$$

Here, $C_\ell^{\rm prim}$ is the B modes power spectrum from primordial gravitational waves, $C_\ell^{\rm lens}$ is the power spectrum from lensing and N_ℓ is the power spectrum of the noise and statistical foreground residuals. The main sources of systematic uncertainties for *LiteBIRD* are shown in Table 1.

The total uncertainty on r is obtained by including all systematic effects and their correlations at once, as well as the effect of the noise and foreground statistical residuals. However, because there is a bias, the higher bound on r is overestimated. It is possible to reduce it by understanding where the bias comes from. Looking at the power spectrum of the combined systematic effects, we noticed that they are similar to the measured power spectrum of Galactic dust, from component separation. Therefore, we adopt a strategy of mitigation of the bias by

Table 1: Summary [1] of the main sources of systematic uncertainties for *LiteBIRD* along with their estimated Δr. They are divided into E type, for which Δr is evaluated from the current experimental set-up, and R type, for which Δr is chosen in order to meet the scientific goal and is translated into requirements on the instrument or on calibration performances.

Category	Systematic effect	Δr	Type
Beam	Far sidelobes	4.4×10^{-5}	R
	Near sidelobes	5.7×10^{-6}	R
	Main lobe	$< 10^{-6}$	E
	Ghost	5.7×10^{-6}	R
	Polarization and shape in band	$< 10^{-6}$	R
Cosmic ray	Cosmic-ray glitches	Noise	E
HWP	Instrumental polarization	$< 10^{-6}$	E
	Transparency in band	5.7×10^{-6}	R
	Polarization efficiency in band	5.7×10^{-6}	R
	Polarization angle in band	5.7×10^{-6}	R
Gain	Relative gain in time	5.7×10^{-6}	R
	Relative gain in detectors	5.7×10^{-6}	R
	Absolute gain	1.9×10^{-6}	E
Polarization angle	Absolute angle	9.1×10^{-6}	E
	Relative angle	5.7×10^{-6}	E
	HWP position	1.0×10^{-6}	E
	Time variation	$< 10^{-7}$	E
Pol. efficiency	Efficiency	5.6×10^{-6}	E
Pointing	Offset	5.7×10^{-6}	R
	Time variation	$< 10^{-6}$	E
	HWP wedge	5.7×10^{-6}	R
Bandpass	Bandpass efficiency	5.3×10^{-6}	R
Transfer function	Crosstalk	5.7×10^{-6}	R
	Detector time constant knowledge	5.7×10^{-6}	R

including an additional term in the theoretical power spectrum $C_\ell^{\rm th} = rC_\ell^{\rm prim} + C_\ell^{\rm lens} + N_\ell + \alpha M_\ell$, where M_ℓ is the Galactic dust power spectrum and α is an additional parameter to be marginalized over. Figure 1 shows the cosmological likelihood as a function of r without and with bias mitigation. After marginalization, we find a total uncertainty $\delta r = 1.0 \times 10^{-3}$ and no bias [1].

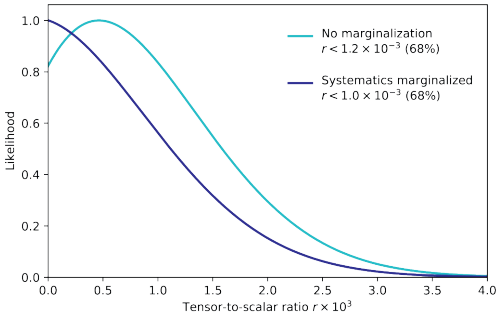

Figure 1 – Cosmological likelihood as a function of the tensor-to-scalar ratio [1]. The light blue line is obtained from equation 1 and the dark blue line is obtained after marginalization over α, assuming a centered gaussian distribution with $\sigma_\alpha = 10$.

Acknowledgements

LiteBIRD (phase A) activities are supported by the following funding agencies: ISAS/JAXA, MEXT, JSPS, KEK (Japan); CSA (Canada); CNES, CNRS, CEA (France); DFG (Germany); ASI, INFN, INAF (Italy); RCN (Norway); AEI (Spain); SNSA, SRC (Sweden); NASA, DOE (USA).

References

1. *LiteBIRD* Collaboration, *Probing Cosmic Inflation with the LiteBIRD Cosmic Microwave Background Polarization Survey*, submitted to PTEP, arXiv:2202.02773

Control of beam systematics and temperature-to-polarisation leakage: from BICEP/*Keck* demonstrated performance to forecasts for CMB-S4

Clara Vergès and the BICEP/*Keck* collaboration
Center for Astrophysics | Harvard & Smithsonian, Cambridge, MA 02138, USA

The BICEP/*Keck* series of experiments uses pair differencing to reconstruct the polarised CMB signal. One of the most important systematic effects to control is the differential beam response between orthogonally polarised detectors in the same pair, which leads to temperature-to-polarisation leakage. We use high-fidelity beam maps to estimate T→P leakage from undeprojected beam residuals in the BK data set. We build on this framework to investigate the impact of beam map noise properties, and forecast future beam mapping campaigns for the BICEP/*Keck* program, as well as for the upcoming CMB-S4 program, whose Small Aperture Telescopes will have a similar design to the most recent BICEP receivers.

1 T→P leakage bias on r using high-fidelity beam maps and specialised simulations

We have developed a specialised method to connect high-fidelity beam maps to the bias on the tensor-to-scalar ratio r from T→P leakage [1]:

1. Convolve measured beams with a CMB temperature-only map following actual scan trajectories, and the lowest-order beam difference modes to mirror the real CMB analysis and obtain a T→P leakage map template [2];

2. Take the cross-spectrum of this leakage template with real and simulated polarised CMB maps, as detailed in the legend of Figure 1;

3. Run our standard analysis pipeline over 499 simulations containing added T→P leakage template, to compute the bias $\Delta(r)$ and the uncertainty $\sigma(\Delta(r))$.

For BK18 [3], this leads to $\Delta(r) = 1.5 \pm 1.1 \times 10^{-3}$ - for comparison, the experiment's statistical uncertainty is $\sigma(r) = 9 \times 10^{-3}$. The uncertainty $\sigma(\Delta(r))$ is dominated by the polarised CMB map-depth, and not by noise in the beam maps. However, as sensitivity of future experiments improves, we need to better understand the relative importance of CMB map noise and beam map noise, and investigate how beam mapping can help reduce the uncertainty on T→P leakage.

2 Forecasting future beam mapping campaigns

In particular, one crucial question for future CMB polarisation experiments such as CMB-S4 is how deep do our beam maps need to be to constrain T→P leakage at the required sensitivity, and how much calibration data does this correspond to? The first step in answering this question is to understand how the number of beam maps taken during calibration affects the noise properties of the composite beam maps used for T→P leakage analysis, and how this translates in terms of $\sigma(\Delta(r))$.

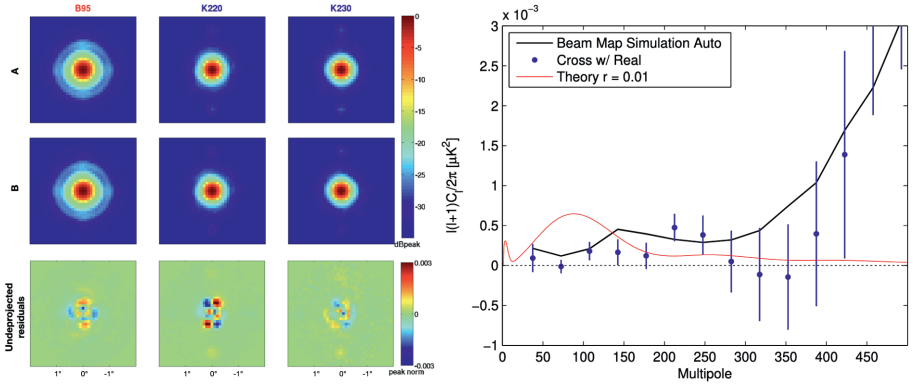

Figure 1 – *Left*: Band-averaged beams for BICEP3 and *Keck*. The top two panels show individual beams, and the bottom one shows the difference beams after deprojecting lowest-order differential modes. *Right*: Residual T→P leakage BB spectra for the BICEP3 receiver. The black line is obtained by feeding beam maps through a full simulation of the map-making process including deprojection of lowest-order modes. The blue points are the cross-correlation of the predicted leakage pattern with the real CMB maps (bias), and the blue error bars show the uncertainty on it.

We construct beam map noise estimates and incorporate them in the analysis pipeline as an additional source of uncertainty. We do this for an increasing number of beam maps N, corresponding to more time spent on the beam calibration process. We show that the noise in beam maps decreases as $1/\sqrt{N}$, and that uncertainty on leakage spectra and $\sigma(\Delta(r))$ also scales with noise in the beam maps, as summarised in Table 1.

Table 1: $\sigma(\Delta(r))$ as a function of the number of beam maps N

Number of beam maps N	10	20	40	60	80
$\sigma(\Delta(r)) \times 10^{-4}$	5.20	4.03	2.10	2.01	1.94

3 Conclusion & Perspectives

We have demonstrated a framework that ties T→P leakage estimate to uncertainties in beam map measurements. However, our current scaling of beam map noise only captures statistical noise, which in this study leads to lower $\sigma(\Delta(r))$ than in the BK18 case. This emphasizes the need for investigating systematic noise. Ultimately, once a better understanding of noise in beam maps can lead to a more confident detection of T→P leakage, we plan to include T→P leakage amplitude as an analysis parameter and marginalise over it.

References

1. The BICEP/*Keck* Collaboration, *ApJ* **884**, 114 (Oct. 2019).
2. T. St. Germaine and The BICEP/*Keck* Collaboration, SPIE Proceedings **11453**, 114532E (Dec. 2020).
3. The BICEP/*Keck* Collaboration, *Phys. Rev. Lett.* **127**, 151301 (Oct. 2021).

The CMB lensing imprint of cosmic voids

U. E. Demirbozan
Institut Fisica d'áltes Energies, Campus UAB, Facultat Ciencies Nord, 08193 Bellaterra, Barcelona, Spain

Cosmic voids gravitationally lens the cosmic microwave background (CMB). This weak lensing shows itself as negative convergence (kappa) κ imprint on the CMB lensing map. We use one of the largest available sky surveys (Dark Energy Survey Y3) and Planck 2018 CMB lensing map along with a simulated CMB lensing convergence map from the MICE N-body simulation to calibrate our detection. We stack void center positions on the CMB map and use a matched filtered approach (that has been used before for BOSS spectroscopic voids [1]) to further optimize our S/N. By using 2 different void types, we measure the lensing imprint of CMB by voids up to S/N =4.56 for DES Y3. We find that both types of voids show slightly weaker CMB lensing signal than ΛCDM expectations as calibrated by MICE N-body simulation. Our result is consistent with another DES Y3 study which uses another method (*Kovacs et al, in prep*) and also with DESI Imaging Survey DR8 study [2].

1 Introduction

The Dark Energy Survey (DES) is a five-year photometric survey that covers roughly ~ 5000 deg^2 of the South Galactic cap and recorded approximately 300 Million objects. We use DES Y1 and DES Y3 data in order to find voids within the galaxies and cross correlate with Planck CMB lensing map and DES mass maps. DES mass maps created DES weak lensing galaxy data set. The low density environment of cosmic voids makes them ideal to study nature of dark energy, neutrinos and modifications of gravity [4]. In addition to the weak gravitational lensing effect, they are also subject to gravitational redshift effect from the CMB called Integrated Sachs-Wolfe effect (ISW). Recently [3], reported an excess ISW effect coming from large voids as compared to ΛCDM simulations. In our study, we wanted to check if this excess also exists for CMB lensing around voids.

2 Results

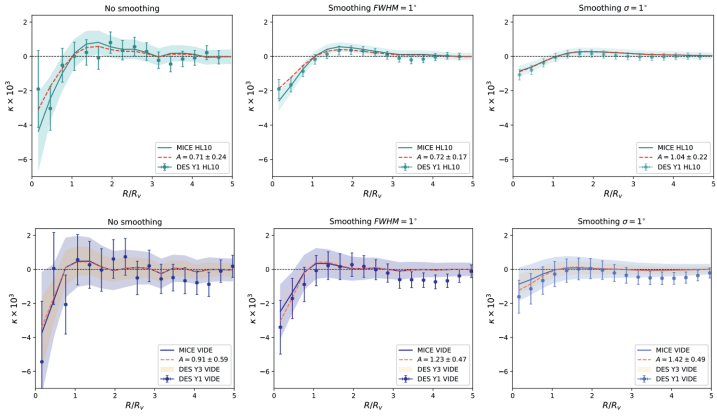

Figure 1 – The figures above taken from DES Y1 study [5] show the measured radial imprint from the stacked images of void locations with different Gaussian smoothing applied on the CMB lensing maps in the units of convergence (kappa).These are the first measurements hinting at CMB lensing signal may be slightly lower than ΛCDM expectation.

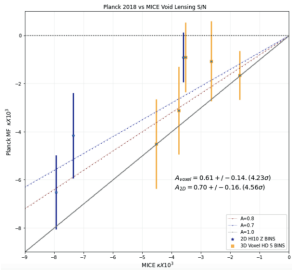

Figure 2 – The figure above shows 2D (blue) and 3D Voxel (orange) void types (*Demirbozan et al, in prep*) and their stacked central pixel value. The advantage of matched filter method is that it encodes all the lensing information to void central pixel. This matched filtered method has been used in [1] for the BOSS spectroscopic data to further optimize S/N. The 2D voids are binned tomographically based on their redshift (3 bins) and the 3D voids are binned (5 bins) based on a parameter consisting of radius and density. The joint fit results in 4.23σ for 3D Voxel voids and 4.56σ for 2D voids. It is clearly seen that almost all of the measured central pixel values are less than MICE expectation as they are above the A=1 amplitude linear amplitude line.

3 Conclusion

We can summarize our conclusion in following ways. Our observed Planck void lensing signal is slightly lower than ΛCDM expectations for DES Y3 data. Our results are also consistent with *Kovacs et al, in prep* which also uses DES Y3 data with another filtering method for the CMB lensing map (Gaussian). The weakness of Planck signal against ΛCDM expectation has also been mentioned in [2]. Further studies are needed to increase the precision of lensing S/N with larger surveys in order to better assess the weakness of Planck void lensing signal.

Acknowledgments

This project has received funding from the European Union's Horizon 2020 research and innovation programme under the Marie Skłodowska-Curie grant agreement No. 754558.

References

1. Raghunathan *et al*, *The Astrophysical Journal* **890**, 168 (2020).
2. Hang *et al*, *MNRAS* **507**, 510 (2021).
3. Kovacs *et al*, *MNRAS* **484**, 4 (2019).
4. Pisani *et al*, *Bulletin of the American Astronomical Society* **51**, 3 (2019).
5. Vielzeuf *et al*, *MNRAS* **50**, 464 (2021).

Theoretical and numerical aspects of CMB spectral distortions from non-thermal electromagnetic energy injections at high redshifts

Sandeep Kumar Acharya, Jens Chluba
Jodrell Bank Centre for Astrophysics, School of Physics and Astronomy, The University of Manchester Manchester, M139PL, UK

Cosmic Microwave Background (CMB) spectral distortions is one of the cleanest probe for electromagnetic energy injection scenarios in the pre-recombination universe. We carry out accurate thermalization computations, evolving the distorted CMB spectrum in a general, fully non-linear way, consistently accounting for the time-dependence of the injection process, modifications to the Hubble expansion rate and relativistic Compton scattering. Specifically, we study single energy injection and decaying particle scenarios, obtaining constraints on these cases. We show that for single energy cases, the constraints can differ significantly than that have been previously estimated.

1 Introduction

CMB spectrum is given by Planck spectrum to a very good approximation [1] with any deviation defined as CMB spectral distortion. Before recombination epoch ($z \gtrsim 10^3$), CMB photons and background electrons are tightly coupled. Energy injection to CMB heats the background electron which in turn boost the CMB photons from low frequency to high frequency creating y-distortion [2] at $z \lesssim 10^4$. For $z \lesssim 2 \times 10^6$, Compton scattering is the dominant exchange process between the photons and the electrons. At these redshifts, distorted CMB spectrum relaxes to Bose-Einstein distribution (μ-distortion)[3] as Compton scattering is photon number conserving. At $z \gtrsim 2 \times 10^6$, photon non-conserving processes such as Bremsstrahlung and Double Compton processes become efficient which thermalizes the distorted CMB spectrum to a Planckian spectrum.

2 Large energy release

In literature, it is usually assumed that the distortion on CMB is small ($<< 1$). We can then linearize the problem ignoring non-linear terms [4]. As an example, the Compton scattering of CMB photons with background electrons is given by Kompaneets equation [5],

$$\frac{dn}{d\tau} = \frac{\theta_e}{x^2}\frac{\partial}{\partial x} x^4 \left[\frac{\partial n}{\partial x} + \frac{T_z}{T_e} n(n+1)\right], \tag{1}$$

where n is the photon occupation number, τ is the optical depth, $x = \frac{h\nu}{k_B T_z}$ is the dimensionless frequency, k_B is the Boltzmann constant, T_z is the CMB temperature and T_e is the electron temperature. The occupation number is a superposition of background Planckian spectrum and the distortion i.e. $n = n_{pl} + \Delta n$. In the linearized approximation, we ignore $O(\Delta n)^2$ terms in the equation above. In our work [6], we solve for the evolution of distorted CMB spectrum using non-linear Kompaneets equations as well as the exact Boltzmann equation. In Fig. 1,

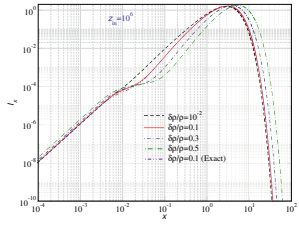

Figure 1 – Distorted CMB spectrum as a function of fractional energy release to CMB [6].

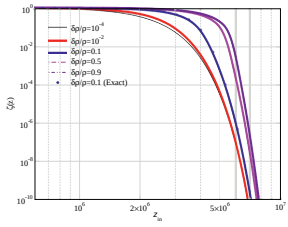

Figure 2 – Fraction of CMB distortion, surviving till today as a function of injection redshift.

we plot the total distorted CMB intensity as seen today for few one-time energy injection cases at $z = 10^6$. In Fig. 2, we plot the visibility function i.e. survival probability of distortion as a function of injection redshift. At $z \gtrsim 2 \times 10^6$, the visibility exponentially decay due to the increasing efficiency of photon non-conserving processes.

2.1 Constraints on energy injection from spectral distortions

Using the results of Sec. 2 and using the data [1], we obtain constraints on energy release cases. In Fig. 3, we plot the constraints for single energy cases while in Fig. 4, we do the same for decaying particle cases. For single energy cases, there are visible changes to the constraints at high redshifts compared to small distortions limit. This is expected as large energy injections is expected at higher redshifts. But for decaying cases, there are no visible changes as energy injection is over a broad redshift range which dilutes the amount of distortion present at a particular redshift.

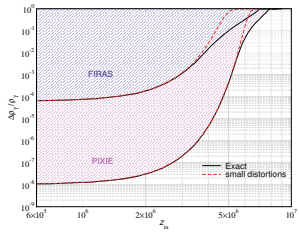

Figure 3 – Constraints on energy release for single energy release. We also show PIXIE [7] projections.

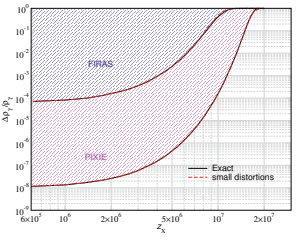

Figure 4 – Constraints on energy release as a function of lifetime of decaying particle.

Acknowledgments

This work was supported by the ERC Consolidator Grant CMBSPEC (No. 725456).

References

1. D.J. Fixsen *et al*, Astrophysical Journal **473**, 576 (1996).
2. Ya. B. Zeldovich and R. A. Sunyaev, Astrophysics and Space Science **4**, 301 (1969).
3. R. A. Sunyaev and Ya. B. Zeldovich, Astrophysics and Space Science **7**, 20 (1970).
4. J. Chluba, R. A. Sunyaev, Monthly Notices of the Royal Astronomical Society **419**, 1294 (2012).
5. A. S. Kompaneets, Soviet Journal of Experimental and Theoretical Physics **31**, 876 (1956).
6. S. K. Acharya and J. Chluba, arxiv:2112.06699 , (2021).
7. A. Kogut *et al*, Journal of Cosmology and Astroparticle physics **7**, 025 (2011).

CMB lensing power spectrum with next generation surveys

L. Legrand and J. Carron
Université de Genève, Département de Physique Théorique et CAP, 24 Quai Ansermet, CH-1211 Genève 4, Switzerland

We introduce a new estimator of the CMB lensing power spectrum, together with its likelihood, based on iterative lensing reconstruction. Despite the increased complexity of the lensing maps, this estimator shares similarities with the standard quadratic estimator. Most importantly, it is unbiased towards the assumptions done on the noise and cosmology for the lensing reconstruction. This new spectrum estimator can double the constraints on the lensing amplitude compared to the quadratic estimator, while keeping numerical cost under control and being robust to errors.

1 Iterative lensing spectrum estimator

Gravitational lensing of the CMB is a powerful probe of the growth of structures, and is expected to give tight constraints on the sum of neutrino masses. Current CMB experiments mostly rely on the well-known quadratic estimator (QE) to estimate the lensing potential. Next generation surveys, such as CMB-S4, will rely on a more efficient approach. Indeed, since the primordial B-mode signal is small, and if the foreground and noise levels are well below the lensing B-mode power of $\sim 5\mu$K-arcmin, one could reconstruct perfectly the lensing field from the observed polarisation maps. This can be achieved with a likelihood-based reconstruction[1]. An implementation of the maximum a posteriori (MAP) lensing reconstruction using an iterative delensing procedure was developed in [2]. In [3] we introduced a lensing spectrum estimator and its likelihood based on this MAP reconstruction. We summarize below our main results.

The lensing spectrum estimated with a QE [4] is a four-point function of the CMB maps. It contains the lensing spectrum $C_L^{\phi\phi}$ we want to measure, but also 'bias' terms, dominated by $N_L^{(0)}$ and $N_L^{(1)}$ which can be characterized analytically. This imply that one can debias this QE spectrum to get an estimate of the true lensing spectrum. In practice a standard cosmology analysis [5] uses a realisation dependant debiaser RD-$N_L^{(0)}$, robust to the assumptions made on the experimental noise and fiducial cosmology.

The lensing potential field reconstructed with an iterative MAP estimator[2] is a complex function of the CMB maps, and it is out of reach to track analytically the bias terms of its spectrum. In [3] we derive the $N_L^{(0)}$ and $N_L^{(1)}$ bias terms of the MAP lensing spectrum using the same expressions as for the QE, but replacing the fiducial CMB and lensing spectra with partially delensed spectra. These delensed spectra are obtained in an iterative procedure until convergence. We also introduce a RD-$N_L^{(0)}$ debiaser of the MAP estimate. Left panel of Fig.1 shows that we accurately estimate the bias terms of our MAP lensing spectrum. We see also that the MAP $N_L^{(0)}$ bias is lowered by a factor 2 compared to the QE, improving by the same amount the signal to noise ratio of the lensing spectrum amplitude.

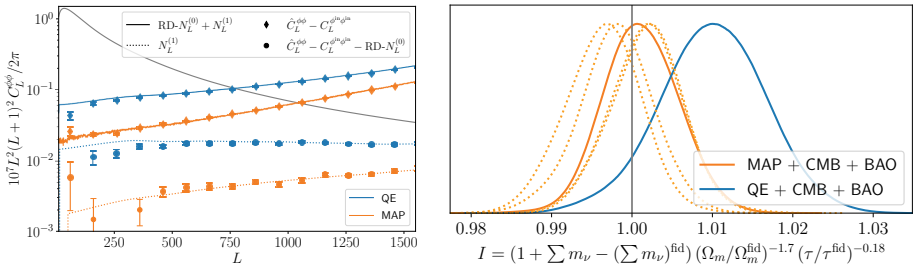

Figure 1 – *Left panel:* Diamonds show the estimated lensing spectra subtracted by the input spectrum (suppressing cosmic variance) for the QE and MAP estimators (resp. blue and orange), these should correspond to the sum of the RD-$N_L^{(0)}$ and $N_L^{(1)}$ biases, shown as solid lines. Circles show the estimated spectra subtracted by the input spectrum and by RD-$N_L^{(0)}$, which should be dominated by the $N_L^{(1)}$ bias shown as the dotted lines. The grey line shows the fiducial lensing spectrum. *Right panel:* Marginalized constraints on the derived parameter I for a CMB-S4 experiment combined with DESI-BAO. Constraint using a QE is shown in blue, while constraints with the MAP estimator are shown in orange. Dashed lines are four independent CMB realisations.

2 Lensing likelihood

We generate two datasets, each with a different cosmology, one being the fiducial cosmology used for the lensing reconstruction. We simulate a full-sky CMB-S4, and compute the QE and the MAP lensing fields. Our data-vectors are the pseudo spectrum debiased by RD-$N_L^{(0)}$ and $N_L^{(1)}$. We assume they follow a Gaussian likelihood, and we estimate their covariances from 1024 flat-sky simulations, rescaled to get a 40% sky fraction. We include the unlensed CMB and the DESI-BAO likelihoods, assuming all three likelihoods are independent. We sample the six standard ΛCDM parameters plus the sum of neutrino mass with a MCMC. For both datasets our MAP lensing spectrum likelihood is able to recover unbiased parameters estimates. It appears that the marginalised constraints on $\sum m_\nu$ with a MAP does not improve compared to a QE. This could be due to remaining degeneracies between parameters. We perform a principal component analysis of our chains on the parameters $\sum m_\nu, \Omega_{\rm m}$ and τ. We found that the combination shown in the right panel of Fig.1 gets a factor almost two reduction of the 1σ uncertainty from the QE to the MAP, reaching the statistical power of our new estimator.

To conclude, we introduced a new CMB lensing power spectrum estimator, robust towards the ingredients assumed for the lensing reconstruction. This opens the door to improved and unbiased constraints on key cosmological parameters, such as the sum of neutrino mass.

Acknowledgments

The authors acknowledge support from a SNSF Eccellenza Professorial Fellowship (No. 186879).

References

1. C. M. Hirata and U. Seljak, Phys. Rev. D **68** (2003), 083002
2. J. Carron and A. Lewis, Phys. Rev. D **96** (2017) no.6, 063510
3. L. Legrand and J. Carron, [arXiv:2112.05764 [astro-ph.CO]].
4. W. Hu and T. Okamoto, Astrophys. J. **574** (2002), 566-574
5. N. Aghanim *et al.* [Planck], Astron. Astrophys. **641** (2020), A8

Minkowski-Tensor-Based shape analysis methods on the sphere

C. Collischon[1], M. Klatt[2], C. Räth[3], M. Sasaki[1]
[1]*Dr. Karl Remeis-Sternwarte, FAU Erlangen-Nürnberg;* [2]*Institut für Theoretische Physik II, HHU Düsseldorf;* [3]*Deutsches Zentrum für Luft- und Raumfahrt (DLR)*

Recently, Minkowski Tensors (MT) have gained popularity for morphological analysis tasks. As opposed to the scalar Minkowski functionals (MF; in 2D given by area, perimeter and Euler characteristic), MT can characterize symmetry and orientation of a body. This has been used for a variety of tasks, e.g. to detect interstellar bubbles by tracing back the origins of filaments in HII-regions, or to search for alignment of structures in the CMB. I present a marching-square-based method for calculating MT and MF on the sphere for maps in the Healpix format. MT are calculated for a local neighborhood and can then be summed up/averaged over a larger region, using their additivity property. This provides the possibility of localized analyses looking for CMB anisotropies and non-Gaussianities at varying scales.

1 Background

Minkowski functionals (MF) and tensors (MT) are powerful and versatile shape descriptors. In 2D, the MF are up to prefactors given by area, perimeter, and Euler characteristic. Their tensorial counterparts can be defined the following way, using the position $\vec{r}$ and the normal vector $\vec{n}$:

Let K be a convex shape, then

$$W_0^{a,0}(K) := \int_K \vec{r}^{\,a}\,\mathrm{d}r \tag{1}$$

$$W_\nu^{a,b}(K) := \int_{\partial K} \vec{r}^{\,a} \otimes \vec{n}^{\,b}\,\lambda_\nu\,\mathrm{d}r \tag{2}$$

with $\nu \in \{1,\,2\}$, $\lambda_1 = 1$, $\lambda_2 = \kappa$ and $a, b \in \mathbb{N}_0$ and

$$(\vec{r}^{\,a} \otimes \vec{n}^{\,b})_{i_1 \ldots i_{a+b}} = \frac{1}{(a+b)!} \sum_{\sigma \in S_{a+b}} r_{i_{\sigma(1)}} \ldots r_{i_{\sigma(a)}} \cdot n_{i_{\sigma(a+1)}} \ldots n_{i_{\sigma(a+b)}}\,, \tag{3}$$

where S_n is the permutation group of n elements

They are additive $\left(W_i^{j,k}(K) + W_i^{j,k}(L) = W_i^{j,k}(K \cup L) - W_i^{j,k}(K \cap L)\right)$ for convex bodies K, L, which allows generalizations to certain non-convex shapes, including shapes defined by pixel images. For more properties, see e.g. Schröder-Turk et al. (2011)[1].

Hadwiger's theorem states that any additive, continuous, and translation invariant functional on convex bodies can be expressed as a linear combination of MF [2]. A similar theorem by Alesker states that the MT contain all additive morphological properties of a shape [3]. These definitions hold for the Euclidean plane; extension to the sphere is subject of current research.

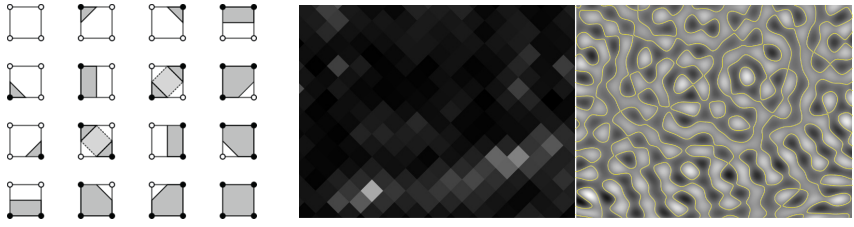

Figure 1 – Left: The 16 possible configurations of a marching square window. In the diagonal cases a choice must be made whether the shape should be connected. The exact corner position is interpolated. Center/right: Elongation as measured by the ratio of eigenvalues of $W_1^{0,2}$ (left) and the underlying Gaussian field with contours used for the Minkowski map (right).

2 Minkowski maps

Minkowski tensors can be calculated for pixel images with a range of grayscale values using a marching square technique. A 2x2 px-region is considered, where pixels above a chosen threshold are seen as part of the body. The 16 possible configurations of a 2x2 px-window are shown in Fig. 1. The desired MF/MT is calculated for the resulting simple shape in this window. To obtain the MF/MT of a larger region, the MF/MT of all contained marching squares are summed up, using the additivity property. The result of this can be displayed as a Minkowski map with each map pixel describing the shape of a local input image region, as shown in Fig. 1 (right).

3 Application

Raw MT need to be turned into scalars for visualization and analysis. This is possible in many ways using, e.g., eigenvalues, traces, or directions.

Shape properties can, e.g., be measured by the ratio of eigenvalues of $W_1^{0,2}$. This is shown in Fig. 1 (right), where parts of a Gaussian field that happen to have elongated structure can be seen as having a large ratio of eigenvalues. As opposed to previous MT/MF-analyses of the cosmic microwave background, which considered the whole sky at once (e.g. Joby et al. 2019 [4]), Minkowski maps enable localized search for anisotropies and non-Gaussianities. More generally, Minkowski maps have been successfully used to automatically detect bubble-like structures in the Magellanic Clouds [5].

References

1. G. E. Schröder-Turk, W. Mickel, S. C. Kapfer, M. A. Klatt, F. M. Schaller, M. J. F. Hoffmann, N. Kleppmann, P. Armstrong, A. Inayat, D. Hug, M. Reichelsdorfer, W. Peukert, W. Schwieger, and K. Mecke. Minkowski tensor shape analysis of cellular, granular and porous structures. *Advanced Materials*, 23(22-23):2535–2553, 2011.
2. H. Hadwiger. *Vorlesungen Über Inhalt, Oberfläche und Isoperimetrie*. Springer Berlin Heidelberg, 1957.
3. S. Alesker. Description of Continuous Isometry Covariant Valuations on Convex Sets. *Geometriae Dedicata*, 74(3):241–248, 1999.
4. P. K. Joby, Pravabati Chingangbam, Tuhin Ghosh, Vidhya Ganesan, and C. D. Ravikumar. Search for anomalous alignments of structures in Planck data using Minkowski Tensors. *Journal of Cosmology and Astroparticle Physics*, 2019(1):009, January 2019.
5. Caroline Collischon, Manami Sasaki, Klaus Mecke, Sean D. Points, and Michael A. Klatt. Tracking down the origin of superbubbles and supergiant shells in the Magellanic Clouds with Minkowski tensor analysis. *Astronomy & Astrophysics*, 653:A16, September 2021.

An emulator for the non-linear matter power spectrum in $f(R)$CDM cosmology

I. Sáez Casares & Y. Rasera
Laboratoire Univers et Théories, Université de Paris, Observatoire de Paris, Université PSL, CNRS, F-92190 Meudon, France

In order to probe modifications of gravity at cosmological scales one needs accurate theoretical predictions. N-body simulations are required to explore the non-linear regime of structure formation, which are very time consuming. In this work we build an emulator that performs an accurate and fast interpolation between the predictions of a given set of simulations in $f(R)$ modified gravity. We sample the 3D parameter space given by $\{\Omega_{\rm m}, \sigma_8, f_{R_0}\}$ with 110 points distributed in a Latin Hypercube. For each model we perform pairs of $f(R)$CDM and ΛCDM simulations covering an effective volume of $\left(560\,h^{-1}\mathrm{Mpc}\right)^3$ with a mass resolution of $\sim 2\cdot 10^{10} h^{-1} M_\odot$. We compute the matter power spectrum boost due to $f(R)$ gravity $B(k) = P_{f(R)}(k)/P_{\Lambda\mathrm{CDM}}(k)$ and build an emulator using a Gaussian Process Regression. The resulting emulator has an accuracy of 3% across the whole parameter space for scales $0.02\ h\mathrm{Mpc}^{-1} < k < 5\ h\mathrm{Mpc}^{-1}$ and $0 < z < 2$. Such an emulator could be used to probe $f(R)$ gravity with weak lensing analysis.

1 Introduction

In $f(R)$ gravity the Einstein-Hilbert action is modified by a new arbitrary function f depending on the Ricci scalar R

$$S_{\rm EH} = \frac{c^4}{16\pi G}\int \mathrm{d}^4x\sqrt{-g}\,[R + f(R)]\,. \tag{1}$$

This modification introduces a new dynamical scalar field in the theory $f_R = \mathrm{d}f/\mathrm{d}R$. Such field mediates an attractive fifth force between massive particles, which effectively enhances their gravitational interaction. In particular we use the Hu & Sawicki model [1]

$$f(R) = -m^2\frac{c_1\left(-R/m^2\right)^n}{c_2\left(R/m^2\right)^n + 1}. \tag{2}$$

This model is of cosmological interest since it is able to produce cosmic acceleration. It also exhibits the chameleon screening mechanism. The mass of a chameleon field increases with the environmental density. Therefore the range of the induced fifth force decreases in high density regions, effectively hiding or screening it. With this kind of model General Relativity is recovered at high densities, such as in the Solar system or in the early Universe.

We follow previous work [1] and fix m and c_1/c_2 in order to match the ΛCDM background expansion. The remaining free parameters n and $c_1/c_2^2 \sim f_{R_0}$ control the efficiency of the screening.

2 Simulations

We sample the parameter space given by $0.236 < \Omega_{\rm m} < 0.396$, $0.608 < \sigma_8 < 1.014$ and $-7 < \log_{10} f_{R_0} < -4$ using a Latin Hypercube Sampling with 90 training nodes and 20 validation nodes. We perform pairs of ΛCDM and $f(R)$ N-body simulations for each node with ECOSMOG[2], using an optimized solver[3]. This solver significantly accelerates the N-body simulations in $f(R)$ gravity, but is restricted to the particular case $n = 1$. For each node in the parameter space we produce 5 independent realisations, which combined cover an effective volume of $\left(560\,h^{-1}{\rm Mpc}\right)^3$ with a mass resolution of $\sim 2 \cdot 10^{10} h^{-1} M_\odot$.

3 The matter power spectrum boost

We focus on the matter power spectrum boost defined as

$$B(k) = P_{f(R)}/P_{\Lambda{\rm CDM}}. \tag{3}$$

It encodes the enhancement of the matter power spectrum due to $f(R)$ gravity with respect to ΛCDM. We have verified that this quantity is mostly independent of Ω_b, h and n_s. By taking the ratio of the power spectrum obtained in $f(R)$ and ΛCDM from the exact same initial conditions we obtain a significant cancelation of cosmic variance (resolution errors), which dominates the error budget at large (small) scales. With this method we are able to compute the power spectrum boost with an accuracy better than 2% across the whole parameter space and for $0.02\ h{\rm Mpc}^{-1} < k < 5\ h{\rm Mpc}^{-1}$ and $0 < z < 2$.

4 Emulation and validation

We interpolate between training nodes by combining a Principal Component Analysis (PCA) with a Gaussian Process Regression (GPR). The PCA is used to reduce the dimensionality of the data before performing the emulation with the GPR. We assess the accuracy of the interpolation using the validation nodes. Most predictions are accurate at the 1% level at all scales. In the worst cases emulation errors get as high as 2% at small scales.

We train an independent emulator for each output redshift of our simulation suite. With a linear interpolation between 19 redshift nodes we obtain predictions for any arbitrary redshift $0 < z < 2$ with the same accuracy.

5 Conclusion

We have built an emulator that predicts the amplification of the matter power spectrum due to $f(R)$ gravity. It is accurate at the 3% level for $0.02\ h{\rm Mpc}^{-1} < k < 5\ h{\rm Mpc}^{-1}$ and $0 < z < 2$. Such an emulator could be used to constrain $f(R)$ gravity with weak lensing analysis.

References

1. W. Hu and I. Sawicki, *Phys. Rev.* D **76**, 064004 (2007)
2. L. Baojiu *et al.*, *J. Cosmology Astropart. Phys.*, 1, 51 (2012)
3. S. Bose *et al.*, *J. Cosmology Astropart. Phys.*, 2, 50 (2017)

Calibration requirements for the width of redshift distribution for complex intrinsic alignment models

Silvan Fischbacher, Tomasz Kacprzak, et al.
Institute for Particle Physics and Astrophysics, ETH Zürich,
Wolfgang-Pauli-Strasse 27, CH-8093 Zürich, Switzerland

An accurate measurement of the redshift distribution is necessary to constrain cosmological parameters with weak lensing surveys. Surveys marginalize over redshift bin shifts to avoid biases in cosmological parameters, however, errors in the width of the redshift bins are typically not considered. We show that ignoring such errors in the analysis can lead to significant biases in the constraints of cosmological parameters, especially S_8. When adding complex intrinsic alignment models to the analysis, the interplay between intrinsic alignment and redshift estimation errors can even increase these biases. Adding the redshift bin width parameter as a nuisance parameter to the Bayesian analysis can reduce this bias, but not completely. Using multiple analyzes of mock observations, we compute requirements on the precision of the redshift bin mean and width for Stage III and upcoming Stage IV surveys.

1 Introduction & Methods

Modern weak lensing surveys need a precise measurement of the photometric redshift and an accurate intrinsic alignment modeling to get unbiased constraints on cosmological parameters. So far, surveys account for the errors in the photometric redshift by marginalizing over the parameter δ_z which corresponds to a shift of the whole redshift bin.

Additionally to δ_z, we account for errors in the redshift bin width characterized by σ_z (see Figure 1). We use a fast C_ℓ emulator to speed up the Bayesian inference of a mock observation. This way, we can bring a MCMC to convergence in a few seconds which enables us to analyze multiple mock observations and analyze the impact of specific errors. The best-fit is determined by maximizing the likelihood starting from the best sample of the MCMC. This method provides an accurate and unbiased estimate of the true maximum likelihood.

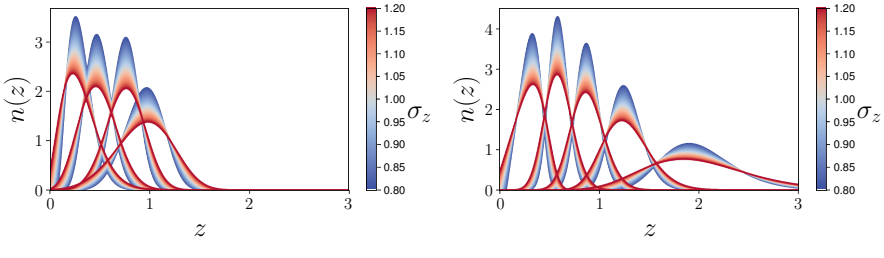

Figure 1: Impact of stretching parameter σ_z on redshift bins for Stage III (left) and Stage IV setup (right).

2 Impact of ignoring or including $n(z)$ shape errors

We find that errors in σ_z can significantly bias cosmological constraints when ignored in the analysis. A naive solution to avoid such biases is to include σ_z in the analysis similar to δ_z using Gaussian priors. This reduces the bias for the Stage IV but not for the Stage III setup. We have not enough constraining power on the redshift parameters due to the fewer high redshift galaxies in the Stage III setup and the posterior does not deviate from the prior.

3 Requirements

We analyze 1000 mock observations for varying setups. We sample δ_z and σ_z in the mock observations with varying prior width for each setup. These mock observations are then analyzed using priors on the redshift parameters corresponding to these prior widths. So we get 1000 posteriors for each setup. We repeat the steps above without varying the redshift errors in the mock observations to determine the noise contribution and to separate statistical and systematic errors. Finally, we compute the median S_8 bias of the best-fits and the highest density interval of the stacked posterior to get the uncertainty of S_8. The systematic bias (in terms of expected total uncertainty σ_{S_8}) and the uncertainty (as the fraction of systematic uncertainty over statistical uncertainty) for the Stage IV setup are shown in Figure 2.

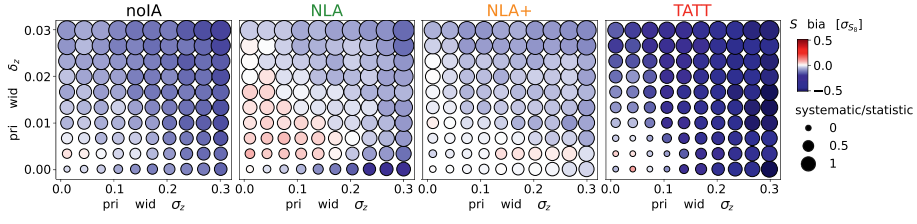

(a) Ignoring σ_z in the analysis

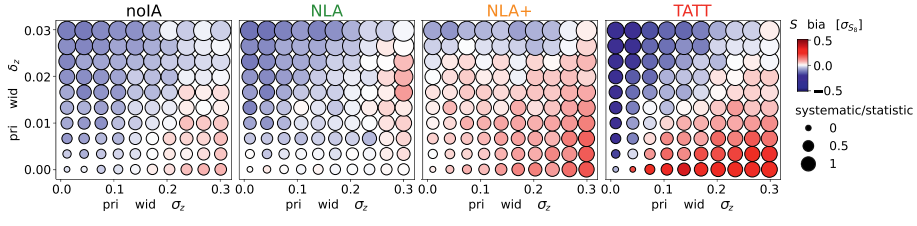

(b) Including σ_z in the analysis

Figure 2: Systematic bias and level of systematic uncertainty compared to the statistical uncertainty of the Stage IV setup.

4 Conclusion

Ignoring $n(z)$ shape errors such as σ_z can bias cosmological constraints. Marginalization over such errors can not significantly reduce these biases in current Stage III, but in upcoming Stage IV surveys. We suggest the above procedure for future surveys to determine the accuracy required in their redshift measurement to attain a given precision in cosmological constraints.

Does Planck actually "see" the Bunch-Davies state?

Benoit J. Richard in collaboration with
Rose Baunach, Nadia Bolis, R. Holman, Stacie Moltner
Minerva University, 1145 Market Street,
San Francisco, CA 94103, U.S.A.

We create a state in which the metric perturbations ζ are entangled with a spectator scalar field. The calculation of the corresponding primordial power spectrum $P_\zeta(k)$ then allows us to study the potential signatures our state may have on the temperature anisotropies C_l in the Cosmic Microwave Background (CMB). We observe intriguing variations with respect to the standard calculations of the same observables but involving the Bunch-Davies (BD) state. Furthermore, we address how an entire class of deviations from the Bunch-Davies state may be suitable candidates in inflationary theories. Finally, we discuss how the use of our entangled state may result in power spectra that are consistent with the Planck satellite data.

1 Introduction

The Bunch-Davies (BD) state is a natural candidate for the calculation of cosmological observables. One of its strengths is the fact that it approaches the Minkowski space vacuum state at infinitesimally early times and short distances. We cannot, however, rule out the eventuality of new physics occurring between very early times and the onset of inflation. At the center of this work is a specific deviation from the BD state resulting from the entanglement of the scalar metric perturbations ζ and a massive scalar field Σ. We address the legitimacy of such a state in addition to the impact of its use in the calculation of the primordial power spectrum $P_\zeta(k)$ and the temperature anisotropies C_l in the Cosmic Microwave Background (CMB).

2 Hamiltonian Density and Wavefunctional in the Schrödinger Picture

We construct a wavefunctional $\Psi[\zeta(\cdot), \Sigma(\cdot); \eta]$ corresponding to our state, η representing conformal time. We then investigate the evolution of $\Psi[\zeta(\cdot), \Sigma(\cdot); \eta]$ in the Schrödinger picture [1]. This allows us to compute cosmological observables in the form of expectation values of the relevant operators. Finally, we call upon the ADM formalism [3] to derive our action and ultimately the $\zeta - \Sigma$ Hamiltonian. Only terms up to quadratic order in the momentum space modes $\zeta_{\vec{k}}$ and $\chi_{\vec{k}}$ are kept. Not only is this sufficient for non-trivial entanglement to be generated, it permits us to construct a Gaussian state whose evolution can be easily followed.

3 Entangled Power Spectrum and CMB Temperature Anisotropies

Given our wavefunctional, we can compute the primordial power spectra for a set of parameter values $\{\mu,\ s_0,\ v_0\}$, the latter being the dimensionless mass, the dimensionless initial position in field space, and the dimensionless speed of our spectator field's zero mode. A more detailed exploration is presented in our paper [2].

In Figure 1, we present primordial power spectra and unlensed TT power spectra using the entangled state (in blue) we created for $\mu = 0.1$ and either a non-zero s_0 or a non-zero v_0. Note that the BD state equivalents (in red) are also presented for comparison. Focusing on the primordial power spectra, there are very noticeable features resulting from incorporating non-zero parameter values. For $v_0 \neq 0$, we observe undamped oscillations whose minima coincide with the BD power spectra values. Such drastic signatures, however, only translate to slight gains in power in the unlensed TT power spectra, especially in the first 3 peaks. Similar observations can be made for $s_0 \neq 0$. Furthermore, we have investigated a number of parameter values that give rise to TT power spectra indistinguishable from those generated from the BD state.

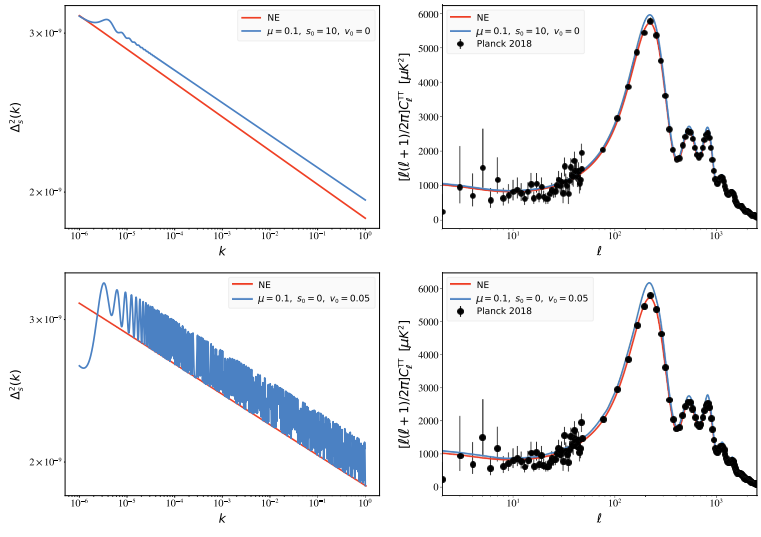

Figure 1 – The primordial power spectra (left column) and the unlensed TT power spectra (right column), in the case in which the spectator is a free massive scalar field with $\{\mu = 0.1, s_0 = 10, v_0 = 0\}$ (top row) or $\{\mu = 0.1, s_0 = 0, v_0 = 0.05\}$ (bottom row), are presented in blue. The non-entangled (NE) power spectra are displayed in red (all subfigures). The CMB data from Planck are shown in black (right column only).

4 Conclusions

Assuming the existence of a scalar field displaced from its minimum and/or with some initial velocity, we have shown that entangled Gaussian states may be easier to generate than previously thought. The premise itself is rather plausible, given how many extensions of the standard model include scalar fields. For ranges of parameter values, the CMB anisotropies obtained in our work are consistent with the Planck satellite data. Whether these parameter values can survive the scrutiny of a full parameter estimation probe is at the heart of current work with Andreas Albrecht, Arsalan Adil, Rose Baunach, Rich Holman, and Raquel H. Ribeiro.

References

1. A. Albrecht, N. Bolis and R. Holman, *JHEP* **11**, 093 (2014), [arXiv:1408.6859 [hep-th]].
2. R. Baunach, N. Bolis, R. Holman, S. Moltner and B. J. Richard, *JCAP* **07**, 050 (2021), [arXiv:2104.13410 [hep-th]].
3. R. L. Arnowitt, S. Deser and C. W. Misner, *Gen. Rel. Grav* **40**, 1997-2027 (2008), [arXiv:gr-qc/0405109 [gr-qc]].

Towards precision cluster cosmology with the Simons Observatory

I. Zubeldia
Jodrell Bank Centre for Astrophysics, University of Manchester, Oxford Road, Manchester M13 9PY, UK

The abundance of galaxy clusters across mass and redshift is a powerful cosmological probe [4]. CMB observations provide a unique window into the galaxy cluster population, allowing for cluster detection to high redshifts through the thermal Sunyaev-Zel'dovich (tSZ) effect, as demonstrated by *Planck*, ACT, and SPT. The upcoming Simons Observatory (SO) will lead to the detection of an order of magnitude more clusters than previous experiments, finding about 20 000 of them [2]. This will come with an unprecedented constraining potential, but for it to be realised, systematics will have to be understood more accurately than ever. In this poster, we present work carried out towards realising this potential. First, we introduce a new implementation of the multi-frequency matched filter cluster finding method, with which we are investigating several potential sources of systematics in cluster detection. It incorporates several novel features, notably, iterative noise estimation, which we show boosts the cluster detection SNRs and eliminates a bias due to noise covariance misestimation. In addition, we present a study of the matched filter optimisation bias, which will become a relevant effect in the context of SO.

1 Accurate cluster detection with the Simons Observatory: an iterative multi-frequency matched filter method

In CMB observations, clusters are typically detected with multi-frequency matched filters (MMFs), which search for clusters across sky location and cluster angular size [1]. MMFs have indeed been used in *Planck*, ACT, and SPT, and will also be used in SO. We have developed a new MMF implementation, which has some of the following key features:

- It returns as the main cluster observable the detection SNR, q; it also produces estimates of the clusters' central Compton-y parameter, angular size θ_{500}, and sky coordinates.
- It works with flat sky cut-outs following a HEALPix tessellation of the sky, guaranteeing that each point in the sky is covered only once.
- It properly accounts for mask coupling in the estimation of the noise covariance.
- It allows for iterative noise covariance estimation.

This MMF implementation has been tested extensively with realistic simulated observations including foregrounds.

Iterative noise covariance estimation is a key novel feature of our MMF implementation. In MMFs, the noise covariance is typically estimated from the data, taking it to be equal to the data covariance. This leads to an overestimation of the noise covariance, as the data also contains the signal that is being looked for, and hence to a loss of SNR, with fewer and less significant detections. In addition, the SNRs of the detections are biased low with respect to

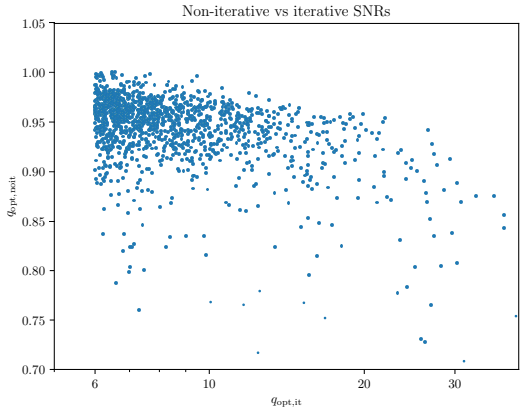

Figure 1 – Ratio of non-iterative SNRs $q_{\rm noit}$ to iterative SNRs for a *Planck*-like sample.

what would be predicted by the theory assuming the wrong covariance, which could potentially lead to biased cosmological constraints.

We have proposed and implemented an approach that prevents the SNR loss and the bias due to noise covariance overestimation: iterative noise estimation (Zubeldia et al., in prep.). In it, the noise covariance is re-estimated by masking high significance detections from the previous step, with a new catalogue then produced. This constitutes a robust, model-independent way of removing the contributions of the brightest clusters to the covariance, boosting the overall SNR. The impact of iterative noise estimation for a *Planck*-like sample is shown in Fig. 1.

2 Optimisation bias

When MMFs are used for cluster detection, clusters are identified as the peaks in the matched filter SNR distribution across sky location and cluster angular scale. These *optimal* SNRs are, by construction, larger than the SNRs at the true cluster parameter values, which is what can be predicted by the theory. This constitutes an 'optimisation bias', which we discuss extensively in[5], where we show that it can be approximated by $q_{\rm opt} \simeq (q_{\rm t}^2 + f)^{1/2}$, where $q_{\rm opt}$ is the detection SNR, $q_{\rm t}$ is the SNR at the true parameters, and f is the number of fitting parameters (typically three: two cluster coordinates and angular size). We find this bias to be negligible for *Planck*, but significant for SO.

References

1. J.-B. Melin, J. G. Bartlett, and J. Delabrouille. 2006, A&A, 517, A92.
2. Simons Observatory Collaboration. 2019, J. Cosmology Astropart. Phys., 2019, 056.
3. G. Stein et al. 2020, J. Cosmology Astropart. Phys., 2020, 012.
4. I. Zubeldia & A. Challinor. 2019, MNRAS, 489, 401
5. I. Zubeldia et al., 2021, MNRAS, 507, 4852

The reconstruction of the CMB lensing bispectrum

Alba Kalaja, Giorgio Orlando, P. D. Meerburg

Van Swinderen Institute for Particle Physics and Gravity, University of Groningen, Nijenborgh 4, 9747 AG Groningen, The Netherlands

Weak gravitational lensing is the leading non-linear effect on the cosmic microwave background (CMB) anisotropies due to the deflection of CMB photons by the intervening large-scale structure (LSS) of the Universe. The induced statistics of the signal can be used to reconstruct the lensing potential, making it a powerful tool to probe fundamental physics, such as neutrino masses and theories of modified gravity. In this work, we explore the three point function of the reconstructed lensing convergence, $\hat{\kappa}$. Next-generation CMB experiments will achieve the necessary sensitivity to detect the κ-bispectrum, which could break degeneracies between parameters. However, in the reconstruction process, additional noise biases that hinder the signal arise. Here, we compute the leading terms for the first time in the flat-sky limit and compare them to the bispectrum signal.

1 Introduction

Weak gravitational lensing of the CMB probes the growth of large-scale structure (LSS) on many scales ($0.1 < z < 5$), making it a powerful observable to constrain fundamental physics of late-time cosmology. The induced non-Gaussian signal can be used to reconstruct the projected gravitational potential at its origin, through the quadratic estimator [1]. This extra information has been used to constrain the dark energy equation of state and the sum of the neutrino masses. In addition, the cross-correlation between CMB lensing maps and other tracers, such as low-redshift galaxy surveys, not only circumvents the limit of cosmic variance, but also breaks degeneracies between cosmological parameters, such as galaxy bias and growth of LSS. So far, cosmological applications of CMB lensing rely on the assumption that the lensing potential is Gaussian. However, at late times, nonlinear clustering in the matter density fluctuations generates a matter bispectrum, which induces non-Gaussianity in the deflection of CMB photons. Ongoing and next-generation of CMB experiments might already be able to measure the κ-bispectrum, which encodes cosmological information that could further tighten the bounds on neutrino masses and dark energy models by up to $\sim 30\%$ when combined with the power spectrum [2].

2 Methodology and results

In the standard reconstruction procedure, that uses the Hu-Okamoto quadratic estimator

$$\hat{\kappa}(\boldsymbol{L}) = A^{\kappa}_{\boldsymbol{L}} \int \frac{\mathrm{d}^2\boldsymbol{l}_1}{(2\pi)^2} F(\boldsymbol{l}_1, \boldsymbol{l}_2)\, \widetilde{T}(\boldsymbol{l}_1)\widetilde{T}(\boldsymbol{l}_2)\,, \tag{1}$$

additional terms called noise biases arise from the six-point function of lensed CMB modes, similar to those in the power spectrum

$$\langle \hat{\kappa}(\boldsymbol{L}_1)\hat{\kappa}(\boldsymbol{L}_2)\hat{\kappa}(\boldsymbol{L}_3)\rangle = \; (2\pi)^2\delta(\boldsymbol{L}_{123})\Big[B_{\kappa}(\boldsymbol{L}_1, \boldsymbol{L}_2, \boldsymbol{L}_3) + N^{(0)}_{\mathrm{B}} + N^{(1)}_{\mathrm{B}} + N^{(3/2)}_{\mathrm{B}} + N^{(2)}_{\mathrm{B}}\Big]\,. \tag{2}$$

In this work, we estimate for the first time in the flat-sky approximation the magnitude of these terms with respect to the signal itself. Fig. 1 shows the numerical evaluation of the three main contributions – $N^{(0)}_{\mathrm{B}}$, $N^{(1)}_{\mathrm{B}}$ and $N^{(2)}_{\mathrm{B}}$ – in the equilateral slicing, compared to the κ-bispectrum computed using two different fitting formulas.

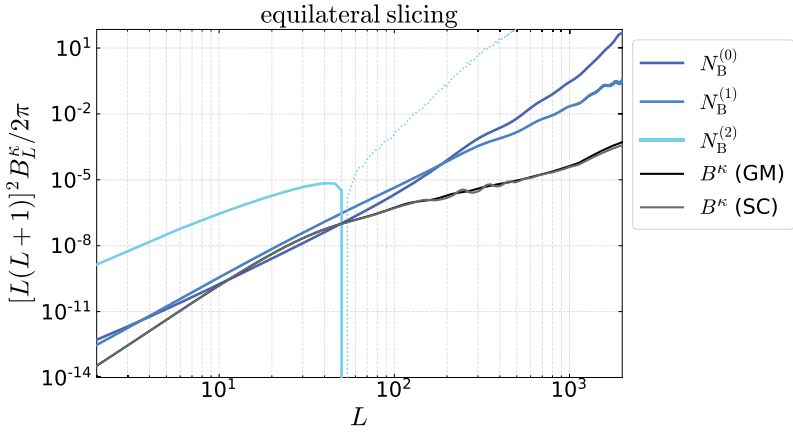

Figure 1 – Numerical evaluation of the bias noise terms. The dotted line represents negative values. The black and gray lines are the κ-bispectrum computed respectively with the Gil-Marín (GM) and Scoccimarro (SC) fitting formula.

3 Conclusions

Upcoming experiments will provide precise measurements of the CMB, unlocking the non-linear regime of matter distribution. In this context, the lensing bispectrum will represent a robust cosmological tool comparable to the lensing power spectrum. In this work, we have estimated the noise biases that arise in the reconstruction of the lensing convergence bispectrum. Our results will be critical for future attempts of reconstructing the lensing convergence bispectrum with real CMB data. These analysis and new results will be summarized in a forthcoming publication.

References

1. W. Hu and T. Okamoto, "Mass Reconstruction with Cosmic Microwave Background Polarization", *The Astrophysical Journal* **574**, 2 (2002).
2. T. Namikawa, "CMB Lensing Bispectrum from Nonlinear Growth of the Large Scale Structure," *Phys. Rev. D* **93**, no.12, 121301 (2016)

Cosmic rotation in solid inflation

Kenza Zeghari
Aix-Marseille University, Center of Theoretical Physics, Marseille, France

We study homogeneous cosmologies coupled to a matter source that has the field theoretical description of a solid. Models of solid inflation are known for being less efficient in diluting away anisotropy than standard inflation. Our study finds another potential feature of solid inflation, namely a "rotation" of the principal axes of the expansion. Due to the anisotropic stress generated by the solid, such a rotation is not just a gauge artifact but becomes a real dynamical quantity.

1 Introduction and broad motivations

I briefly report here on a recent work [1] about homogeneous cosmologies coupled to a matter source that has the field theoretical description of a solid. Among the broad motivations for this study is a better understanding of homogeneity and isotropy, the two great pillars of cosmology, in quantum gravity. On a Minkowski background, we know how to impose these symmetries, either at the classical level on a field configuration, $\phi(t, \vec{x}) = \phi(t)$, or at the quantum level on the wavefunctional, $\psi[\phi(R\vec{x}+\vec{a})] = \psi[\phi(\vec{x})]$. In the last equation R and a are a generic rotation and translation. However, in gravity, quantum states are given by $\psi[h_{ij}]$, with h_{ij} the spatial metric, and there is no background invariant way to define what it means to rotate or translate the metric field. It looks like we need a matter field to play the role of a "reference frame", in order to define these transformations. An example of such field is the solid.

Solids can drive a primordial inflationary phase (*solid inflation*) [2]. As opposed to standard inflation, as being less efficient in diluting away the primordial anisotropies [3]. While confirming this fact, our study recovers another potential feature of these models: rotation of the principal axes of expansion.

Now for the gravity part, keeping the gravitational field very general makes the quantum treatment difficult to handle. We use a class of spatially homogeneous models called Bianchi type I, allowing for a simple treatment as the space of all possible configurations for the metric field becomes finite: the so-called *mini-superspace* [4]. Even if this choice comes to a truncation of the field space, it may at least provide insights into the characterisation of "quantum isotropy".

2 Bianchi models and solids

Spatial homogeneity implies that spacetime consists of a family of space-like hyper-surfaces, defining an orthogonal "cosmic time":

$$ds^2 = -dt^2 + h_{ij}(t)dx^i dx^j \,, \tag{1}$$

This form of the metric is left invariant by a general linear coordinate transformation $GL(d)$ in the spatial part. A general parametrisation of the spatial metric (in $d = 2$) is given by:

$$h_{ij} = \begin{pmatrix} \cos\frac{\theta}{2} & \sin\frac{\theta}{2} \\ -\sin\frac{\theta}{2} & \cos\frac{\theta}{2} \end{pmatrix} \begin{pmatrix} A^2 e^{\xi} & 0 \\ 0 & A^2 e^{-\xi} \end{pmatrix} \begin{pmatrix} \cos\frac{\theta}{2} & -\sin\frac{\theta}{2} \\ \sin\frac{\theta}{2} & \cos\frac{\theta}{2} \end{pmatrix} , \tag{2}$$

with $A(t)$ the average scale factor, $\xi(t)$ and $\theta(t)$ parametrising resp. anisotropy and rotation. This form allows to identify the principal axes of expansion. In the absence of anisotropic stress, h_{ij} and its time derivative $\dot{h}_{ij}$ can be set to a stable diagonal form using the $GL(d)$ symmetry group, which makes of rotation a mare gauge artifact. But in the presence of anisotropic stress some of these symmetries are broken and rotation becomes "real".

Solids illustrate this point. The low energy effective description of a solid is made of scalar fields $\phi^I, I = 1, 2... \ d$ labeling the volume element of the medium. The dynamics is invariant under internal translations and rotations. The resulting most general Lagrangian for the solid is a general function of the following matrices,

$$L_{solid} = F([B], [B^2], ..., [B^d]) , \qquad [B] = Tr\ B^{IJ} , \qquad B^{IJ} \equiv \partial_\mu \phi^I \partial^\mu \phi^J , \tag{3}$$

In unitary gauge $B^{IJ} = h^{ij}$ and the action of the system in $2+1$ dimensions becomes

$$S = \int dt\, A^2 \Big[\frac{1}{N} \Big(-\frac{\dot{A}^2}{A^2} + \frac{\dot{\xi}^2}{4} + \frac{\dot{\theta}^2 \sinh^2 \xi}{4} \Big) - \ NF(A, \xi) \Big] . \tag{4}$$

Since the matter Lagrangian depends on ξ, it breaks the $GL(2)$ group down to $SO(2)$. It is now impossible to use the symmetry group to make the metric diagonal at all times. We specialize to the simplest model $F = [B]^\epsilon$ generating inflation with a constant slow-roll parameter ϵ in the isotropic limit, and couple it to the Bianchi type I model in 2+1 dimension.

3 Results and discussion

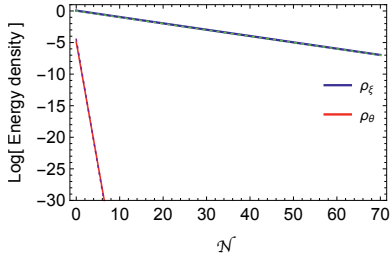

Figure 1 – The energy densities of the anisotropy ρ_ξ and the rotation ρ_θ with respect to the number of e-folds $\mathcal{N}$.

In the presence of anisotropy, the principal axes of expansion can be rotating. Such a rotation is not just a gauge artifact as in the case of Bianchi models alone or coupled to homogeneous scalar fields. Still, the effect is rapidly diluted away by the expansion, see Fig. 1.

In the future we aim to generalize the study to the 3+1 dimensional case, for which the corresponding unitary gauge action is considerably more involved and we expect new phenomena, such as the precession of the principal axes of expansion.

References

1. A. Nicolis, F. Piazza and K. Zeghari, arXiv:2204.04110 (2022).
2. S. Endlich, A. Nicolis and J. Wang, *JCAP* **10**, 011–011 (2013).
3. N. Bartolo, S. Matarrese, M. Peloso and A. Ricciardone, *JCAP* **08**, 022 (2013).
4. B. DeWitt, *Phys. Rev.* **160**, 1113–1148 (1967).

Penrose suggestion as to pre-Planck-era black holes showing up in present universe data sets discussed, with a possible candidate as to GW radiation which may provide initial CMBR data

A.W. Beckwith
College of Physics, Chongqing University Huxi Campus
No. 55 Daxuechen Nanlu, Shapingba District, Chongqing 401331 China

Our project has three parts. First, we examine the gist of the Penrose suggestion as to signals from a prior universe showing up in the CMBR. Second, we give a suggestion as to how supermassive black holes could be broken up as of a prior universe cycle by pre-big-bang conditions with, say, millions of pre-Planck black holes coming up out of a breakup of prior universe black holes. Three, we use a discussion of Bose–Einstein condensates set as gravitons composing the early-universe black holes. The BEC formulation gives a number N of gravitons, linked to entropy, per black hole, which could lead to contributions to the alleged CMBR signals.

1 Introduction

Beckwith [1] offers a well-crafted suggestion as to V. G. Gurzadyan and R. Penrose:

> The significance of individual low-variance circles in the true data has been disputed; yet a recent independent analysis has confirmed CCC's expectation that CMBR circles have a non-Gaussian temperature distribution. Here we examine concentric sets of low-variance circular rings in the WMAP data, finding a highly nonisotropic distribution.

There is initial inflationary expansion of the Universe, but the caveat is that matter–energy is sucked up in super-massive black holes. That is, rather than have a purported infinite expansion, and we see the following dynamic [1].

$$m \approx \frac{M_{\rm P}}{\sqrt{N_{\rm graviton}}} \tag{1}$$

$$M_{\rm BH} \approx \sqrt{N_{\rm graviton}} \cdot M_{\rm P} \tag{2}$$

$$R_{\rm BH} \approx \sqrt{N_{\rm graviton}} \cdot l_{\rm P} \tag{3}$$

$$S_{\rm BH} \approx k_B N_{\rm graviton} \tag{4}$$

$$T_{\rm BH} \approx \frac{T_{\rm P}}{\sqrt{N_{\rm graviton}}}. \tag{5}$$

Table 1: Scaling of mass of black holes, and their purported number, If CCC cosmology (Penrose) assumed for GW radiation release (may affect the CMBR)

End of prior universe time frame	Super massive end-of-time black hole 10^{41} to 10^{44} g.	10^6 to 10^9 of black holes, usually from centers of galaxies
Planck-era black-hole formation assuming merging of micro black-hole pairs	Micro black holes 10^{-5} to 10^{-4} g (approximately the Planck mass value).	10^{40} to 10^{45} black holes, assuming not too much destruction of matter–energy from pre-Planck to Planck conditions
Post-Planck-era black holes: Can use Eq. (6) to have 10^{10} gravitons/second released per black hole	Normal-sized black holes 10 g to 10^6 g	10^{20} to, at most, 10^{25} black holes with repeated black-hole pairs forming a single black hole multiple times.

Here, the first term, m, is the effective mass of a graviton. This is my take as to how to make all this mesh with special relativity.

2 Conclusion: Penrose Recycling of Energy in the Present Universe

Our preliminary supposition that Eq. (6) would be thermally based energy dumped into the space–time bubble assumed to be in [1,2].

$$E_{\text{universe}} = 10^{41} \times E_{\text{BEC–Graviton}} \approx 10^{41} \times \left(\frac{k_B T_{\text{BH}}}{2} \approx \frac{k_B \times 10^{-5} \times T_{\text{P}}}{2} \right) \tag{6}$$

This would be the thermal energy dumped in due to the use of Cyclic Conformal cosmology. Now use the following approximation of the universe, initially having the entropy of a black hole. That is, we are using Ng Infinite Quantum statistics, [1], while Area denotes the surface area of the regime of space–time.

$$S_{\text{universe}} \propto S_{\text{BH}} \simeq \frac{A}{4 l^2_{\text{Planck}}} \approx \frac{9 n_Q}{4} \approx n_{\text{graviton}}. \tag{7}$$

This way of noting entropy and the signals of the prior-universe black holes being generated secondarily is a surface area commensurate with the use of Eq. (6) for BEC condensation by gravitons for early universe black holes. This would show up in the CMBR [1].

References

1. A Beckwith, JHEPGC **7**, 1264 (2021).
2. A Beckwith, JHEPGC **7**, 559 (2021).

Arguments against the flatness problem

P. Helbig
Thomas-Mann-Str. 9, 63477 Maintal, Germany

Since I have been at most moderately successful in convincing the community of the lack of existence of the flatness problem, I highlight some similar claims from various authors better known than myself.

Here, I consider only ideal Friedmann–Robertson–Walker (FRW) models, because historically fine-tuning claims have been discussed within the context of those models, and the issues remain even in more-realistic models. I use notation such that $\Omega = \frac{8\pi G\rho}{3H^2}$ refers to the density of matter ('dust') and $\lambda = \frac{\Lambda}{3H^2}$ is the normalized cosmological constant (with dimension time^{-2} so that Λ has the same dimension as $G\rho$); the subscript 0 refers to the current value of a time-dependent parameter. $K = \Omega + \lambda - 1$ and $k = \mathrm{sign}(K)$. The two most common formulations of the flatness are referred to by Holman [1] as the *fine-tuning problem* ("there must be some reason why $\Omega = 1$ to very high precision in the early universe") and the *instability problem* ("even given that $\Omega = 1$ to very high precision in the early universe, if Ω is not exactly 1, then it would be unlikely to observe $\Omega \approx 1$").

The first argument in the literature against the flatness problem in FRW models appears to have been by Cho & Kantowski [2]. Putting "The Flatness Problem" in scare quotes makes their point already in the title. The last sentence of their abstract sums up their argument well: **"It is a distorted distribution of Ω values that sometimes misleads the casual observer to conclude that Ω must be exactly equal to 1."** Coles & Ellis [3] state clearly that **"*there is no flatness problem* in a purely classical cosmological model"** [emphasis in the original]. Kirchner & Ellis [4] also use Jaynes's principle to **"solve the flatness problem"** (direct quotation). Carroll [5], describing his work with collaborators [6,7,8], notes that **"flatness isn't a problem at all"**; **"[t]he flatness problem, meanwhile, turns out to be simply a misunderstanding"**; **"the flatness problem really isn't a problem at all; it was simply a mistake, brought about by considering an informal measure rather than one derived from the dynamics"**; **"The flatness problem, as conventionally understood, does not exist; it is an artifact of informally assuming a flat measure on the space of initial cosmological parameters"**; and **"is not intrinsic to the standard Big Bang model"**.

Rindler[9] points out that **"the so-called 'flatness problem'—the alleged improbability of finding the value of Ω_0 even within a factor of 10 of unity"** seems unproblematic for two reasons, first that **"at the big bang ($R = 0$), Ω always starts at one and then wanders away from that value unless $k = \Lambda = 0$"** (thus disputing the fine-tuning problem) and second that, in FRW models with $\lambda = 0$ and $\Omega > 1$, **"$\Omega < 10$ ... is true for fully 60 per cent of the entire time interval"**.

It appears that our Universe has a positive cosmological constant and will expand forever. For such models with $k = +1$, Lake[10] demonstrates that the instability argument does not hold because λ and Ω are large and the universe significantly non-flat only in the case that they are fine-tuned in the sense that $\alpha = k(27\Omega^2\lambda)/(4K^3) \approx 1$. Lake suggests that α, which has a fixed value throughout the life of the universe, is what should be used to characterize model universes. Adler & Overduin[11] discuss various definitions of 'nearly flat', using essentially using the same parameter as α used by Lake[10], and arriving at the same conclusion, namely that a significantly non-flat universe implies fine-tuning in α.

Arguments against the flatness problem and their history are discussed in much more detail by Helbig[12,13,14] and Holman[1]. See also Brawer[15] for an interesting historical perspective. The complete poster and some supplementary material can be found at `http://www.astro.multivax.de:8000/helbig/research/publications/info/moriond2022_1.html` .

This research has made use of NASA's Astrophysics Data System Bibliographic Services.

References

1. M. Holman, *Found. Phys.* **48**, 1617 (2018).
2. H. T. Cho and R. Kantowski, *Phys. Rev. D* **50**, 6144 (1994).
3. P. Coles and G. F. R. Ellis, *Is the Universe Open or Closed?* (Cambridge University Press, Cambridge, 1997).
4. U. Kirchner and G. F. R. Ellis, *Class. Quant. Grav.* **20**, 1199 (2003).
5. S. M. Carroll, arXiv:1406.3057 (2014).
6. S. M. Carroll and H. Tam. arXiv:1007.1417 (2010).
7. G. N. Remmen and S. M. Carroll, *Phys. Rev. D* **88**, 083518 (2013).
8. G. N. Remmen and S. M. Carroll, *Phys. Rev. D* **90**, 063517 (2014).
9. W. Rindler, *Relativity: Special, General, and Cosmological* (Oxford University Press, Oxford, 2001).
10. K. Lake. *Phys. Rev. Lett.* **94**, 201102 (2005).
11. R. J. Adler and J. M. Overduin. *Gen. Rel. Grav.* **37**, 1491 (2005).
12. P. Helbig, *MNRAS*, **421** 561 (2012).
13. P. Helbig, *MNRAS*, **495** 3571 (2020).
14. P. Helbig, *Eur. Phys. J. H* **46**, 10 (2021).
15. R. Brawer, *Inflationary cosmology and horizon and flatness problems: the mutual constitution of explanation and questions*, master's thesis (MIT, Boston, 1996), `http://hdl.handle.net/1721.1/38370`.

Conserved quantities in cosmology

P. Helbig
Thomas-Mann-Str. 9, 63477 Maintal, Germany

Lake pointed out that a certain combination, dubbed α, of Ω and λ is a constant of motion for evolutionary trajectories in the λ–Ω plane and used that to demonstrate the lack of a flatness problem for some cosmological models. I investigate other quantities which correspond to α and other constants of motion in the λ–Ω plane.

Here, I consider only ideal Friedmann–Robertson–Walker (FRW) models, because historically similar studies have been done within the context of those models and the basic concepts carry over into more-complicated models. I use notation such that $\Omega = \frac{8\pi G\rho}{3H^2}$ refers to the density of matter ('dust') and $\lambda = \frac{\Lambda}{3H^2}$ is the normalized cosmological constant (with dimension time^{-2} so that Λ has the same dimension as $G\rho$); the subscript 0 refers to the current value of a time-dependent parameter. $K = \Omega + \lambda - 1$, $k = \mathrm{sign}(K)$, and $\alpha = \frac{27k\Omega^2\lambda}{4K^3}$. The Hubble constant $H = \frac{\dot{R}}{R}$, where $R = \frac{c}{H\sqrt{|K|}}$. The deceleration parameter $q = -\frac{\ddot{R}}{RH^2} = \frac{\Omega}{2} - \lambda$.

In general, λ and Ω change with time. Thus, the evolution of cosmological models can be illustrated by trajectories in the λ–Ω plane [1]. Lake [2] pointed out that α is constant along a trajectory. What is the physical interpretation? The mass of (the dust in) a **closed universe** is $M = \rho V$; the volume $V = 2\pi^2 R^3$. From that, one can derive

$$\Lambda M^2 = \left(\frac{\pi^2 c^6}{4G^2}\right)\alpha \quad .$$

Thus, up to a constant, $\Lambda M^2 = \alpha$.

An obvious conserved quantity for cosmological models which have $q = 0$ at some time is the point of inflection in $R(t)$ which occurs when $\ddot{R} = 0$. At such a point, $q = \Omega/2 - \lambda = 0$ and hence $\Omega = 2\lambda$. Since $\rho \sim R^{-3}$ and $\lambda \sim R^0$, it follows that $(R_0/R_{\mathrm{infl}})^3 = \Omega_0/2\lambda_0$, which leads to

$$R_{\mathrm{infl}}^2\Lambda = c^2\sqrt[3]{\alpha} \quad .$$

In a universe which collapses in the future, $R_{\max}$ is obviously constant along a trajectory, and so could be interpreted as a constant of motion, though that is more interesting if expressed as a fundamental cosmological parameter. At $R = R_{\max}$, $\dot{R} = 0$, thus one can calculate the scale

factor (corresponding to the smallest value of R for which $\dot{R} = 0$) of the universe at maximum expansion for such models. That involves solving a cubic equation, and the actual expression depends on the model type. Although that solution depends on quantities such as $\Omega/(2\lambda)$ and $K/(3\lambda)$ (the square of the first divided by the cube of the second is, with the additional factor of sign(K), the definition of α), I am not aware of any simple expression relating α and $R_{\max}$, even though $R_{\max}$ is obviously constant along a trajectory. However, there are analytic solutions in special cases ($\lambda_0 = 0$, $\Omega_0 = 0$, $k = 0$). If $\Omega_0 = 0$ then $\alpha = 0$ and thus we cannot expect any constant of motion expressed in terms of physical quantities to involve α. It thus makes sense to express $R_{\max}$ (which exists in this case for $\lambda_0 < 0$) in terms of Λ by using the definition of λ to eliminate H_0 and λ_0, resulting in $R_{\max}^2 = (3c^2)/\Lambda$. If $k = 0$ and $\lambda_0 < 0$ then $\alpha = \infty$ since the radius of curvature is infinite. If we set $R_0 = c/H_0$, as is commonly done in such cases, then, *via* reasoning similar to that above, one obtains $R^6\Lambda^3 = 27c^6\Omega^2\lambda$ or, up to the constant c^6, $R^6\Lambda^3 = 4\alpha {K_0}^3$. Of course, that is rather meaningless since $\alpha K_0 = \infty * 0$ and results from using $R_0 = c/H_0$ instead of $R_0 = c/(H_0\sqrt{K_0})$. However, $R^6\Lambda^3 = 4\alpha$ is in some sense the limit for $K_0 \to 0$.

If $\Omega_0 > 1$ and $\lambda_0 = 0$ then $\alpha = 0$ and thus we cannot expect any constant of motion expressed in terms of physical quantities to involve α. It thus makes sense to express $R_{\max}$ in terms of M, since such models have $k = +1$ and hence a finite volume and finite mass. M is calculated above and $R_{\max} = (c/H_0)(\Omega/(\Omega - 1)^{\frac{1}{2}})$, thus $R = (4GM)/(3\pi c^2)$.

At $R = R_{\min}$, $\dot{R} = 0$, so one can calculate the scale factor (corresponding to the largest value of R for which $\dot{R} = 0$) of the universe at minimum contraction in the bounce models (which contract from ∞ before expanding) and the Eddington model (which expands from $R_0 > 0$ at $t = -\infty$). As with $R_{\max}$, there seems to be no simple relation between $R_{\min}$ and α, though for $\Omega_0 = 0$ one has $R_{\min}^2 = (3c^2)/\Lambda$.

For the the de Sitter model, which has $\lambda = 1$ always, in contrast to the other point-trajectory models (the Einstein–de Sitter model with $\lambda_0 = 0$ and $\Omega_0 = 1$ and (the relativistic equivalent of) the Milne model with $\lambda_0 = 0$ and $\Omega_0 = 0$), there is a set of models determined by Λ. $H = \sqrt{\Lambda/3}$ and is thus constant in time. H is thus the constant of motion in this model; the Hubble sphere—the sphere with radius c/H—is thus constant in time, which is not true in general. Also, the Hubble sphere is an event horizon [3]; in general the Hubble sphere is not associated with any type of horizon [4].

The static Einstein model [5] has $H = 0$ and hence λ and Ω are infinite. However, the relations discussed above hold when this model is seen as a limiting case.

The complete poster and some supplementary material can be found at `http://www.astro.multivax.de:8000/helbig/research/publications/info/moriond2022_2.html` .

References

1. R. Stabell and S. Refsdal, *MNRAS* **132**, 379 (1966).
2. K. Lake, *Phys. Rev. Lett.* **94**, 201102 (2005).
3. W. Rindler, *MNRAS* **116**, 662 (1956).
4. P. van Oirschot, J. Kwan, and G. F. Lewis, *MNRAS*, **404**, 1633 (2010).
5. A. Einstein, *Sitzungsb. Kön. Pr. Akad. Wiss.* **VI**, 142 (1917).

What it takes to measure Reionization with Fast Radio Bursts

Stefan Heimersheim
Institute of Astronomy, University of Cambridge,
Madingley Road, Cambridge CB3 0HA, UK

Fast Radio Bursts (FRBs) are recently discovered extra-galactic radio transients which are now used as novel cosmological probes. We show how the Bursts' Dispersion Measure can model-independently probe the history of Hydrogen reionization. Using a FlexKnot free-form parameterization to reconstruct the reionization history we predict an 11% accuracy constraint on the CMB optical depth, and 4% accuracy on the midpoint of reionization, to be achieved with 100 FRBs originating from redshifts $z > 5$.

1 Introduction

Fast Radio Bursts (FRBs) are short ($\sim$ 1 ms) bright bursts originating from outside of our galaxy. What makes FRBs an excellent cosmological probe is that the signal is dispersed by the free electrons in the Universe, most significantly the intergalactic medium (IGM) but also the Milky Way and host galaxy. Measuring this dispersion (DM) allows us to probe the integrated electron column density and thus probe distance or ionization state of the IGM.

The idea to constrain reionization, and in particular the CMB optical depth τ, with FRBs from high redshift ($z > 5$) has been proposed as early as 2016 [1] and has gained traction as thousands of FRBs have been discovered since. Even though no FRBs have been observed from the Epoch of Reionization, forecasts [2] expect $\sim$ 100 FRBs/day/sky from $z > 6$ to be observed with SKA.

2 Method

In our work [3] we address a problem of reionization constraints derived from FRBs, namely that the results are intrinsically sensitive to the shape of the reionization history $x_i(z)$. Because the dispersion measure gives an integral constraint on $x_i(z)$, conversion into the optical depth or ionized fraction depends on the model or parameterization assumed for $x_i(z)$. Besides pathological examples (e.g. sharp dips and peaks in the ionization history) this effect is relevant in practice – for example the commonly used *tanh* step function is an inadequate fit to the real ionization history and can deliver inaccurate results for realistic reionization scenarios.

Ideally we want to marginalize over all possible reionization histories i.e. derive constraints while averaging over all shapes, weighted by their likelihood. This is exactly what we propose to do with the "model-independent" FlexKnot method [4] – we parameterize $x_i(z)$ as an interpolation function between a (varying) number of interpolation knots, as shown in Figure 1 (left). This allows the algorithm to capture reionization histories of arbitrary complexity. We then marginalize over the number of knots by averaging all cases weighted by their Bayesian evidence as shown in Figure 1 (right). The evidence tends to fall when the number of knots exceeds the complexity warranted by the data, naturally creating an Occam's razor effect.

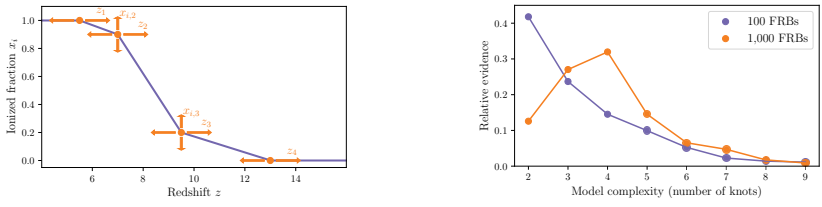

Figure 1 – **Left:** Illustration of the FlexKnot parameterization. **Right:** Evidence as function of knot number.

3 Results

Having sampled all parameters and reionization histories we can derive the Bayesian posterior distribution for $x_i(z)$ as shown in Figure 2 (left). The countours show the 68% and 95% confidence interval of x_i for every redshift z. The posterior provides tight constraints on $x_i(z)$ and agree well with the input fiducial history which was used to generate the data.

In addition we can constrain any derived quantity such as the midpoint of reionization (central blue lines) or the optical depth τ (Figure 2, right) by computing the quantity for every sampled history and then marginalizing over parameters. The expected midpoint constraints are competitive with current quasar constraints, and the optical depth measurement can improve current limits from the CMB. More details on both the method and results can be found in our paper [3].

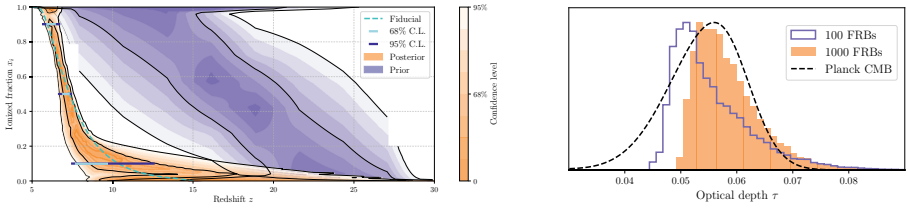

Figure 2 – **Left:** Constraints on reionization history for 1000 FRBs. **Right:** Posterior of optical depth τ.

References

1. Fialkov and Loeb, J. Cosmol. Astropart. Phys. **2016**, 004 (2016).
2. Hashimoto et al., Mon. Not. R. Astron. Soc. **497**, 4107-4116 (2020).
3. Heimersheim et al., arXiv:2107.14242
4. Millea and Bouchet, Astron. Astrophys. **617**, A96 (2018)

Measurement of telescope transmission using a Collimated Beam Projector

T. Souverin[1], J. Neveu[1,4], M. Betoule[1], S. Bongard[1], S. Brownsberger[2], J. Cohen Tanugi[3,7], S. Dagoret-Campagne[4], F. Feinstein[5], C. Juramy[1], L. Le Guillou[1], A. Le Van Suu[6], P. E. Blanc[6], F. Hazenberg[1], E. Nuss[3], B. Plez[3], E. Sepulveda[1], K. Sommer[3], C. Stubbs[2], N. Regnault[1], E. Urbach[2]
[1]*Sorbonne Université, CNRS, Université de Paris, LPNHE, 75252 Paris Cedex 05, France;* [2]*Department of Physics, Cambridge, Harvard University, MA 02138, USA;* [3]*LUPM, Université Montpellier & CNRS, F-34095 Montpellier, France;* [4]*Université Paris-Saclay, CNRS, IJCLab, 91405, Orsay, France;* [5]*CPPM, Université d'Aix-Marseille & CNRS, 163 av. de Luminy 13288 Marseille Cedex 09, France;* [6]*Observatoire de Haute-Provence, Université d'Aix-Marseille & CNRS, 04870 Saint Michel L'Observatoire, France;* [7]*LPC, IN2P3/CNRS, Université Clermont Auvergne, F-63000 Clermont-Ferrand, France*

The number of type Ia supernova observations will see a significant growth within the next decade, especially thanks to the Legacy Survey of Space and Time undertaken by the Vera Rubin Observatory in Chile. With this rise, the statistical uncertainties will decrease and the flux calibration will become the main uncertainty for the characterization of dark energy The uncertainty over the telescope transmission is a major systematic when measuring SNe Ia colors. Here we introduce the Collimated Beam Projector (CBP), a device that can measure the transmission of a telescope and its filters. Composed of a tunable monochromatic light source and optics to provide a parallel output beam this device is able to measure with high precision the filter transmissions. In the following, we will show how measuring precisely a telescope transmission can also improve the precision of the dark energy parameters. As an example, we will present the first results of the CBP in the context of the StarDice experiment.

1 Collimated Beam Projector

Type Ia supernovae (SNe Ia) are standard candles, a class of objects with predictable luminosity. By measuring the luminosity distance of SNe Ia at different redshifts, we can infer dark energy properties[1]. We obtain this distance by measuring the maximum amplitude of the SN Ia light curve, which is observed within different restfram telescope filters depending on its redshift. The knowledge of the relative transmission of the filters is thus necessary to account for the redshift effect on SNe Ia colors and therefore constrain the dark energy parameters.
The Collimated Beam Projector (CBP) is a device that measures the transmission of a telescope and its filters. It is composed of a tunable monochromatic laser (Ekspla NT252), that emits light within a range of [350 - 1100] nm, with a resolution of 1 nm and an accuracy of 1 Å. The light is injected with an optical fiber into an integrating sphere, whose output is a pinhole of variable size, producing a monochromatic, homogeneous and pointlike lightsource. The pinhole is set at the focal point of a 152mm Ritchey-Chrétien[a] mounted backwards, thus providing a parallel beam. A photodiode and a spectrograph monitor the surface brightness and wavelength of the light inside the sphere. The response of the CBP optical device $R_{\mathrm{CBP}}(\lambda)$ is measured by shooting directly into a flux calibrated solar cell [2], as the ratio of the charges detected in the solar cell over the charges detected the monitoring photodiode (fig.2).

[a]Ritchey-Chrétien Omegon Pro RC 154/1370

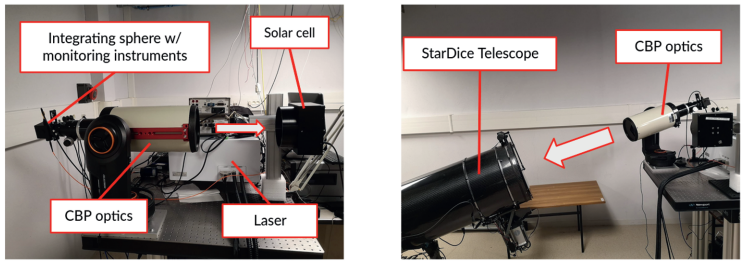

Figure 1 – Left : picture of the StarDice Telescope at LPNHE (Paris). Right : picture of the CBP device, pointing toward the StarDice telescope.

2 Telescope calibration

The goal is to measure the StarDice[3] telescope throughput $R_{\text{telescope}}(\lambda)$, which is a product of the telescope mirror reflectivities, the filter optical transmissions and the quantum efficiency of the CCD camera. To calibrate a telescope with the CBP, we shoot the parallel light beam into this instrument, and we measure the detected flux ϕ_{obs} on the CCD camera doing aperture photometry and dark subtraction. On the other hand we can monitor the emitted flux ϕ_{source} thanks to the CBP photodiode. The relation between these two values is:

$$\phi_{\text{obs}} = \phi_{\text{source}} \times R_{\text{CBP}}(\lambda) \times R_{\text{telescope}}(\lambda) \tag{1}$$

This measurement have been made at LPNHE, our best result so far is shown in figure 2. Systematic uncertainties are under investigation, but the precision should be around a few per mil.

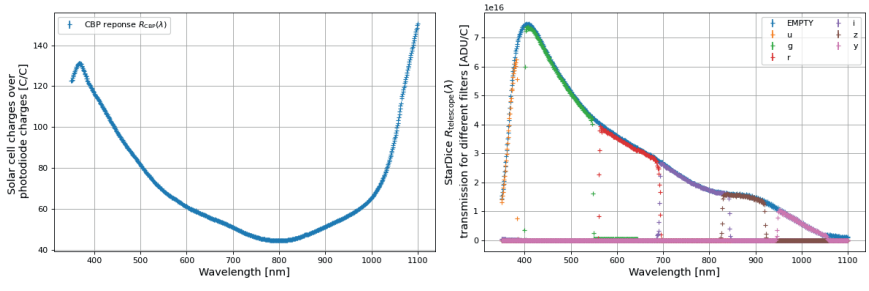

Figure 2 – Left: measurement of the response of the CBP optical device in a range of [350-1100] nm. Right: preliminary measurement of filter transmissions of the StarDice telescope obtained with the CBP.

The LSST telescope will increase significantly the number of SNe Ia observed. François Hazenberg[3] has shown in his thesis that this new dataset can improve the dark energy parameter constraint by a factor of 10, only if we know the filter transmissions of the LSST telescope with a precision greater than 0.1%. Thanks to the CBP, we demonstrated that we can reach such a precision on the StarDice filters, and our goal is to do likewise with LSST.

References

1. Betoule et al., Astronomy & Astrophysics **568**, A22 (2014)
2. Brownsberger et al., Journal of Astronomical Instrumentation **11**, 1 (2022)
3. Hazenberg, F. https://tel.ar-chives-ouvertes.fr/tel-02950846/document. (2020)

AutoMetaCal: self-calibration of shear biases with automatic differentiation

A. Z. Vitorelli[1], B. Remy[1], A. Guinot[2], F. Lanusse[1], T. C. Martins[3]
[1] *AIM, CEA, CNRS, Université Paris-Saclay, Université de Paris, F-91191 Gif-sur-Yvette, France*
[2] *Université de Paris, CNRS, Astroparticule et Cosmologie, F-75013 Paris, France*
[3] *Laboratório de Sistemas Complexos, Depto. de Engenharia Mecatrônica, Escola Politécnica da Universidade de São Paulo, São Paulo, Brazil*

We present a new implementation of metacalibration, the direct self-calibration of shear measurements, using automatic differentiation. We use TensorFlow to create this implementation and carry preliminary validation tests, that provides us with a working proof-of-concept. The source code is publicly available at https://github.com/CosmoStat/autometacal.

1 Shear Measurement Biases

Cosmic shear requires measurements that are as precise and unbiased as possible. A lot of effort has been taken by the community to study these biases. While many surveys use simulations to calibrate their measurements, METACALIBRATION [1,2] offers a data-driven framework to infer biases without simulations. This work aims to enhance METACALIBRATION by incorporating automatic differentiation and GPU computing.

2 Metacalibration

Shear measurements biases can be quantified linearly as $\langle \mathbf{e}_{\rm obs} \rangle = (1+m)\langle \mathbf{g} \rangle + c$, where c is additive bias (normally due PSF errors), and m is multiplicative bias, due to properties of the selection of galaxies, nonlinearity in measurements, and other effects.

In METACALIBRATION we the derivatives of measured ellipticities $\mathbf{e}$ with respect to an applied shear g as:

$$R = \frac{\mathrm{d}}{\mathrm{d}\mathbf{g}} \mathbf{e}(I'|g)\Big|_{\mathbf{g}=\mathbf{0}} , \tag{1}$$

The image $I'(\gamma)$ is generated by deconvolving the observed image by the observed PSF, applying shear γ and re-convolving with a synthetic PSF. This process degrades the image as explained in [1]. From eq. 1 we can calculate a first order correction to a shear estimator as $\langle \mathbf{g} \rangle \approx \langle R^{-1} \rangle \langle \mathbf{e}_{obs} \rangle$.

Normally, R is calculated by finite differences (FD), generating several I' with small shears on each component and calculating the difference in $\mathbf{e}$ that results. $\mathbf{e}_{obs}$ is measured on an image that has been processed in the same manner, but without shear.

3 Automatic differentiation

We use automatic differentiation (AD) to calculate R. AD works by creating a graph describing the end to end computation. The derivative is calculated by applying the chain rule of backwards.

Using AD, we aim to get more precise values for R and remove additional ellipticity measurements for each I' in FD, reducing computation time. And as no actual shear is applied to the image, some of the degradation previously mentioned may be mitigated.

4 Results

Our tests consisted in comparing with the NGMIX and comparing results between AD & FD. To perform these tests, we have generated simulated galaxies with GALSIM, using simple exponential profiles with a constant PSF.

Table 1: Residual multiplicative and additive bias for a set of 1000 very high snr simulated galaxy stamps.

NGMIX results: $R_{11} = 0.351126$			
m:	1.40164×10^{-4}	$\pm 3.17124 \times 10^{-4}$	(99.7% conf)
c:	7.39344×10^{-7}	$\pm 3.03715 \times 10^{-6}$	(99.7% conf)
AUTOMETACAL results: $R_{11} = 0.351128$			
m:	1.72179×10^{-4}	$\pm 3.29558 \times 10^{-4}$	(99.7% conf)
c:	4.41854×10^{-7}	$\pm 3.11028 \times 10^{-6}$	(99.7% conf)

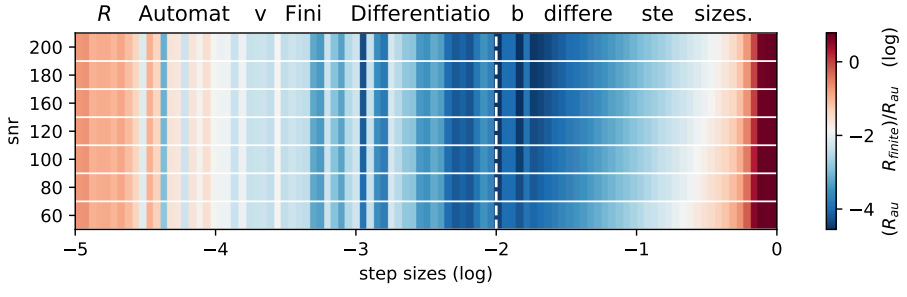

Figure 1 – Median relative differences between AD and FD computed R_{11} per galaxy across 1000 simulated galaxy images, using different signal to noise ratios (snr). The white dashed vertical line marks the common step size of 0.01 used in NGMIX.

Testing AUTOMETACAL against NGMIX we were able to validate numerically the metacalibration procedure, as shown in Table 1. On figure 1 use R_{11} to showcase the difference between AD and FD respective to step sizes. Both methods get closer results with decreasing step sizes upt to when numerical problems arise. We can also see that for higher S/N, we have generally smaller differences even for larger step sizes.

References

1. Huff, E. & Mandelbaum, R. Metacalibration: Direct Self-Calibration of Biases in Shear Measurement. *ArXiv.* **1702.026** (2017,2)
2. Sheldon, E. & Huff, E. Practical Weak-lensing Shear Measurement with Metacalibration. *The Astrophysical Journal.* **841**, 24 (2017,5), http://dx.doi.org/10.3847/1538-4357/aa704b

On bulk flow measurements with type Ia supernovae

M.Amenouche[1], P.Rosnet[1], M.Smith[2]
[1]Université Clermont Auvergne, CNRS/IN2P3, LPC, Clermont-Ferrand France
[2]Université de Lyon, Université Claude Bernard Lyon 1, CNRS/IN2P3, IP2I Lyon, F-69622, Villeurbanne, France.

The ΛCDM model has been validated by a wide range of cosmological observations but they all rely on one fundamental assumption : the Cosmological Principle. Measurements of bulk flow effects are thus a key test of the cosmological model. Type Ia Supernovae (SNeIa), as standard candles, are ideal probes of the matter distribution in the local Universe. The new low redshift ($z < 0.1$) dataset from the Zwicky Transient Facility (ZTF) constitutes a unique sample to investigate anisotropies in the Nearby Universe. Using realistic simulations, we show that ZTF will produce unbiased distance estimates of 1000 SNeIa up to 200 Mpc and with correctable biases for 3000 SNeIa to 400 Mpc. ZTF will constrain the bulk motion with precision of $< 200\ \mathrm{km\,s^{-1}}$ below $z < 0.08$, better than any previous constraints from SNeIa data.

1 Bulk flows in Cosmology

Bulk flows are average motion of matter in a region of space, relative to the Cosmic Microwave Background (CMB) frame. They are induced by peculiar velocities of galaxies and their motions can be predicted by the theory of structure formation. The amplitude of these motions are related to the growth of structure in the Universe. Bulk flow measurements are thus a key test of the ΛCDM model. With SNeIa as distances indicators, we can probe the matter distribution in the local Universe. The use of the redshift-distance relation of SNeIa to detect bulk flows has been limited by the number of SNeIa and their distribution in the sky. So far, bulk flows detection with SNeIa have led to multiple discrepant results[1]. A large, homogeneous and unbiased sample would highly contribute to resolve this tension.

2 The Zwicky Transient Facility data and simulations

With distance measurements to over 5000 SNeIa to redshift of 0.12 all across the northern sky (see Fig 2), ZTF provide a key datatset to measure anisotropies in the local universe. Yet to precisely measure cosmology, we need to understand what are the systematic errors and how they impact our measurements. To investigate how the observing pattern of ZTF will impact any measurement of bulk flows, we use simsurvey[2], that includes both the true observing strategy of ZTF and the best understanding of SNeIa to make realistic simulations. To validate the accuracy of simsurvey in reproducing the ZTF dataset, we simulated real ZTF discoveries from the ZTF Data Release 2 (DR2) using their observed properties as a ground truth. Using the SALT2 template[3], we simulate each event 10 times and compared the measured values to our predictions. Fig 1 shows an excellent agreement between our predictions and the observed values in both ZTF bands. When averaged over 100 events, we see no evidence of a bias in either transient brightness or signal-to-noise ratio across a wide range of flux. As a result, we

have shown that our simulations can accurately reproduce SNeIa light-curves data.

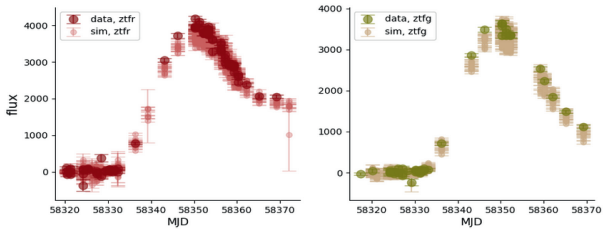

Figure 1 – DR2 and simulations of ZTF18ablqlzp SNIa at $z = 0.0413$, in r band (left) and g band (right). The simulations match the data after including the full selection function of the survey.

3 Results and conclusion

ZTF is a limited magnitude survey, at a fixed redshift, intrinsically faint objects will be preferentially lost. To understand this effect is key to ensure our distances are unbiased. Having shown that we can simulate individual ZTF SNeIa, we now study how the selection effects likely bias our final sample and distances. To do this, we simulate the entire ZTF survey including the photometric and spectroscopic selection efficiency as determined by the Bright Transient Survey[4]. Our results are shown in Fig 3. There is an excellent agreement between our simulated sample and that of the upcoming ZTF-DR2 cosmological sample. ZTF will produce a complete map of the Universe until $z = 0.05$, and be unbiased until $z = 0.08$. The final key step in our analysis is to study how these biases will affect bulk flow measurements. For that, we will inject realistic bulk flow velocity fields into our simulations and study how well they are recovered when the fulll ZTF observing pipeline is considered.

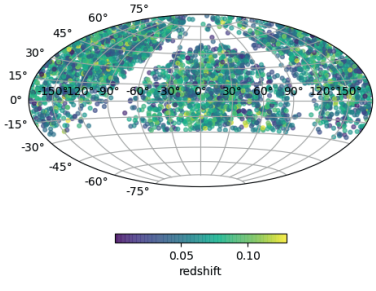

Figure 2 – Distribution of ZTF DR2 data in equatorial coordinates.

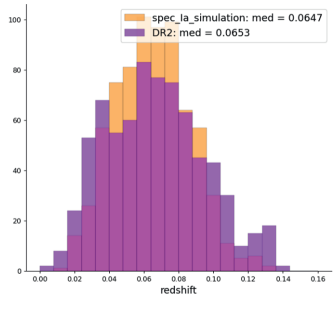

Figure 3 – Redshift distribution of ZTF DR2 and simulations with spectroscopic completeness.

References

1. G. J. Mathews et al, *ApJ* **827**, 60 (2016)
2. U. Feindt et al, *JCAP* **10**, 005 (2019).
3. J. Guy et al, *A&A* **466**, 1 (2007).
4. D. A. Perley et al, *ApJ* **904**, 35 (2020).

Forecasting the power of Higher Order Weak Lensing Statistics with automatically differentiable simulations

Denise Lanzieri[1], François Lanusse, Jean-Luc Starck, Chirag Modi, Ben Horowitz, Joachim Harnois-Déraps

1. AIM, CEA, CNRS, Université Paris Cité, Sorbonne Paris Cité, F-91191 Gif-sur-Yvette, France

In this work, we propose a methodology to investigate the relative constraining power of various higher−order (i.e. non−Gaussian) statistics in the analysis of weak gravitational lensing maps in an LSST setting. To achieve this goal, we implement fast lensing N−body simulations based on the TensorFlow framework for automatic differentiation. These simulations being based on differentiable physics, we can access derivatives of the resulting lensing summary statistics with respect to cosmological parameters, or any systematics included in the simulations, thus alleviating the need for finite differences in Fisher forecasts and enabling joint forecast over a large set of parameters. We show the potential of this methodology by applying it to two summary statistics: the *Starlet peak counts* and the *Starlet* l_{1norm}, finding that the starlet l_{1norm} outperforms the peak counts in terms of constraining power.

1 Introduction

The next generation of weak lensing surveys will provide large volumes of high quality data with unprecedented statistical power and great potential for new discoveries. It is known that existing analysis methods based on the two-point summary statistics do not capture the non-Gaussian information in the non-linear features of weak lensing data. Several alternative inference techniques have been proposed, but most of them require the computation of the gradient of the likelihood. Furthermore, it has been shown that even simulation-Based inference techniques can greatly benefit from differentiable simulation.[1] The goal of this work is to develop tools for building automatically differentiable lensing simulations, and, as a first application, we use this new methodology to investigate the constraining power of various map-based higher order statistics.

2 Methods

We build a set of N-body simulation based on the FlowPM code [2], a fast particle-mesh solver developed in Tensorflow. This kind of fast and low computational simulations, lack resolution on small scale and can't give accurate halo matter profiles or matter power spectrum. To recover this missing accuracy, we employ the PGD scheme[3], aimed to mimic the halo virialization lost in the low resolution simulations. By implementing ray-tracing in this framework, we are able to simulate lensing lightcones, and compute Higher Order lensing statistics on the resulting maps. We focus on two summary statistics: the peak counts and the l_{1norm}.

3 First application: Fisher forecasts

We apply our framework to reproduce the analysis choices of the LSST Y1 data. We simulate weak lensing convergence maps for a single source redshift z=1 and angular extend of 5°, based

on a 3D simulation with 128^3 particles in a box of side length 205 h^{-1}Mpc. The simulations are run with 4 time steps up to the redshift $z = 0.972$, and 11 time steps equally spaced in comoving distance of 205 h^{-1}Mpc up to the final redshift $z = 0.0$. We filter the simulated convergence maps with the Starlet transform, also called Isotropic Undecimated Wavelet Transform, which decomposes an image into a set of wavelet coefficients of different scales and a coarse resolution image. To construct a Fisher matrix, we assume a parameter-independent covariance matrix C_{ij} computed using 2000 independent simulations at the fiducial cosmology, and we compute by automatic differentiation the Jacobian of our output statistics with respect to input parameters. We use this Fisher matrix to estimate the information content extracted with the peak counts and $l_1$norm of the same Starlet transform scale at 4.7 arcmin. We show the increased information content of the l1norm statistic, that leads to tighter constraints for all the parameters, outperforming the peak counts.

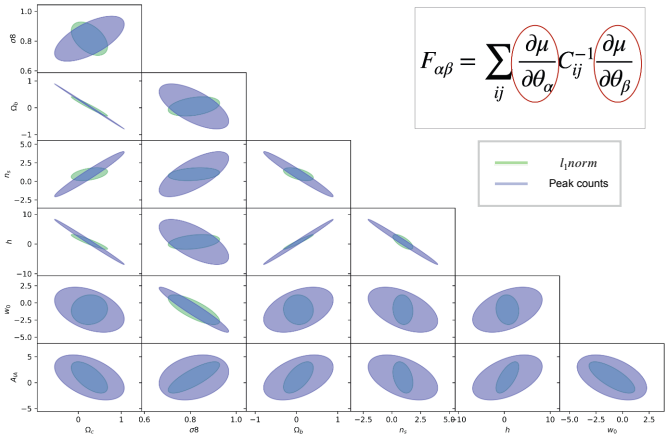

Figure 1 – Fisher constraints from peak counts and l1-norm, computed on a noisy Starlet filtered maps

Acknowledgments

We are grateful to the full DESC collaboration for their discussions and contributions. The presented work used computing resources provided by DESC at the the National Energy Research Scientific Computing Center, a DOE Office of Science User Facility supported by the Office of Science of the U.S. Department of Energy under Contract No. DEAC02-05CH11231;

References

1. T Lucas Makinen, Tom Charnock, Justin Alsing, and Benjamin D Wandelt. Lossless, scalable implicit likelihood inference for cosmological fields. *Journal of Cosmology and Astroparticle Physics*, 2021(11):049, 2021.
2. Chirag Modi, Francois Lanusse, and Uros Seljak. Flowpm: Distributed tensorflow implementation of the fastpm cosmological n-body solver. *arXiv preprint arXiv:2010.11847*, 2020.
3. Biwei Dai, Yu Feng, and Uroš Seljak. A gradient based method for modeling baryons and matter in halos of fast simulations. *Journal of Cosmology and Astroparticle Physics*, 2018(11):009–009, nov 2018.

A catalogue of cosmic filaments from SDSS data

J. Carrón Duque[1,2]
[1] *Dipartimento di Fisica, Università di Roma Tor Vergata, 00133, Roma, Italy*
[2] *INFN, Sezione di Roma 2, Università di Roma Tor Vergata, 00133 Roma, Italy*

A systematic detection of Cosmic Filaments can help studying the characteristics and evolution of the Cosmic Web. To this end, we produce a Cosmic Filament catalogue using the latest SDSS data, including QSO data up to $z = 2.2$. This catalogue, produced with an improvement upon the well–tested SCMS algorithm, has been explored and validated with different metrics. Here, we summarize the main aspects. The method and the catalogue are fully explained in Carrón Duque *et al* [1] and the catalogue is publicly available at javiercarron.com/catalogue.

1 Introduction

The distribution of matter in the Universe forms a structure called *Cosmic Web*. Galaxy Clusters are typically located on its nodes, while Cosmic Filaments are the 1–dimensional overdensities connecting the nodes; the rest of the space is mostly empty and receives the name of Cosmic Voids. The detection of Cosmic Filaments has attracted the attention of the community and several different methods to do it are present in the literature, with complementary strengths and weaknesses. However, these methods are rarely systematically applied to data to produce complete filament catalogues. By producing such a catalogue, we hope to ease their study.

2 Method and data

We improve upon a filament–finding algorithm called *Subspace Constrained Mean Shift* (SCMS), first applied in Cosmology by Chen *et al* [2,3]. This algorithm finds the 1–dimensional maxima of the density field, i.e., the Cosmic Filaments. This density field is estimated by smoothing a galaxy distribution with a Gaussian kernel; the choice of the kernel size significantly affects the results. The improvements we develop are mostly in two aspects:

- We use Machine Learning to reduce the importance of the kernel size. We estimate the density field at different sizes and combine all the relevant information through a Gradient Boosting algorithm. In this way, we have a single combined predictor of "filament–ness" for each point. This approach has the additional advantage of regularizing the results,

which allows this method to operate at higher redshift, where there are lower number of observed galaxies.
- We perform all the mathematical operations considering the spherical geometry of the sky, without a flat–sky approximation. This includes the computation of the gradient and the hessian. By doing this, we avoid possible artefacts, especially at higher latitude.

In order to estimate the density field, we use the Sloan Digital Sky Survey (SDSS) data [4], which currently provides the most large and complete spectroscopic galaxy catalogue. In particular, we use two of its surveys: BOSS and eBOSS.

3 The Catalogue

The Cosmic Filament catalogue is public and can be found at javiercarron.com/catalogue. The catalogue is divided on three blocks, depending on the data used. Block 1 uses BOSS (mainly LOWZ) data, with redshift between 0.05 and 0.45; only points within the LOWZ footprint are used, in both Galactic Hemispheres. Block 2 uses BOSS CMASS data, with redshift between 0.45 and 0.7, in both Galactic Hemispheres. Block 3 uses BOSS and eBOSS data (LRG and QSO), with redshift between 0.6 and 2.2; only points within the smaller eBOSS footprint are used, which lays in the North Galactic Hemisphere.

We remark that our method, boosted with Machine Learning, allows us to extract information of the Cosmic Web present in the QSO survey, more sparsly populated than other surveys.

We verify that the Cosmic Filaments in the catalogue are correlated with other observables, including independently detected Galaxy Clusters. We observe that Clusters are mostly located along the filaments, and especially at their intersections, as it is physically expected. We verified that galaxy number density is highly correlated to the Cosmic Web, as expected by construction.

4 Conclusion and future work

We hope that the elaboration of public catalogues of Cosmic Filaments, such as the one presented here, can help studying the characteristics of the Cosmic Web and its evolution. In particular, we are working on the extension and validation of their correlation with the Gravitational Lensing of the CMB and the Sunyaev–Zeldovich effect, which would allow the study of the structure of Cosmic Filaments. We also plan to use this methodology on N–body simulations to assess the viability of Cosmic Filaments as a cosmological probe; eventually, they could help studying the apparent tension between CMB Lensing observed in Cosmic Voids between simulations and data, as discussed in this conference by Vielzeuf [5] and by Demirbozan [5]. Finally, we believe that methods to reconstruct the Cosmic Web will be extremely valuable for upcoming galaxy surveys, like those expected from Euclid and LSST.

References

1. J. Carrón Duque, M. Migliaccio, D. Marinucci, and N. Vittorio, arXiv:2106.05253, *A&A* , in press (2022)
2. Y.-C. Chen, S. Ho, P.E. Freeman, *et al*, *MNRAS* **454**, 1140 (2015)
3. Y.-C. Chen, S. Ho, J. Brinkmann, *et al*, *MNRAS* **461**, 3896 (2016)
4. M.R. Blanton, M.A. Bershady, B. Abolfathi, *et al*, *AJ* **154**, 28 (2017)
5. P. Vielzeuf, A. Kovács, U. Demirbozan, *et al*, *MNRAS* **500**, 464 (2021)

The impact of neural architectures on the efficiency of cosmological simulation-based inference

Justine Zeghal, François Lanusse, Alexandre Boucaud, Eric Aubourg, Benjamin Remy, Denise Lanzieri
Université de Paris, CNRS, Astroparticule et Cosmologie, F-75013 Paris, France

Simulation-Based Inference (SBI), also known as Likelihood-free inference, is a promising framework that alleviates the need for analytic likelihoods to constrain cosmological parameters. Recent advances in SBI algorithms using neural density estimators have demonstrated an ability to achieve high-fidelity posteriors. These methods require a large number of simulations, and their applications can potentially be extremely time-consuming if cosmological simulations are involved. We present a dedicated approach to density estimation that allows us to incorporate the gradients of a simulator and reduces the number of simulations needed to achieve a given posterior estimation quality.

1 Simulation-Based Inference

SBI provides a framework to perform Bayesian inference without using an analytic likelihood. Given an observation x_0, a prior $p(\theta)$ for the model parameters θ, a simulator $x \sim p(x|\theta)$ to sample from the intractable likelihood and a density estimator q_ϕ, we estimate $p(\theta|x_0) \propto p(x_0|\theta)\, p(\theta)$ by evaluating $q_\phi(\theta|x = x_0)$. The SBI algorithm presented here works as follows:

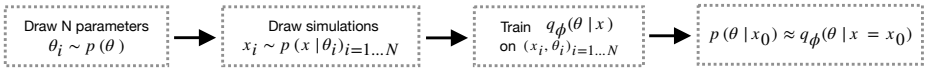

2 Extract additional information

Training a density estimator q_ϕ requires a large number of simulations and simulators are generally computationally expensive. This makes SBI difficult to use in domains such as cosmology. However, when the simulators are differentiable, one can extract for each simulation the gradient of joint log probability of the simulator with respect to input parameters. This gradient, also know as the *joint score*, provides significantly more information than the samples from the simulator, and can be used to help constrain the posterior density estimates obtained by SBI. In the following, we will note the joint score as: $\nabla_\theta \log p(\theta|x, z) = \nabla_\theta \log p(x|\theta, z) + \nabla_\theta \log p(\theta)$, where z are latent stochastic variables of the simulator.

3 Density estimators

To use both simulations and the joint posterior score, we define a specific density estimator $q_\phi(\theta|x)$. We focus on Normalizing Flows (NFs) (Rezende et al., 2015), a class of density estimators parametrised by neural networks that provide tractable density estimation. The key idea

of NFs is to transform a simple density distribution (e.g. a multivariate Normal distribution) through a series of bijective functions to reconstruct a complex target distribution.

To be trained using both simulations and gradients, a NF requires expressive derivatives. However, current C^∞ (infinitely differentiable) NFs such as those based on affine transformations lack expressivity to match the target distribution when taking their gradients with respect to θ. To overcome this issue, Köhler et al. (2021) propose a transformation based on a C^∞ diffeomorphism on $[0, 1]$

$$\begin{cases} x_{1:d} & = z_{1:d} \\ x_{d+1:D} & = \sigma_{(a,b,c)}(z_{d+1:D}) \end{cases}$$

with $\sigma(x) := c \cdot x + \frac{1-c}{1+\exp(-\rho(x))}$, $\rho(x) := a \cdot \left(\log\left(\frac{x}{1-x}\right) + b\right)$ and a, b, c learned using a neural network.

4 Results

We consider a toy cosmological SBI framework in which we are interested in approximating the posterior $p(\Omega_c, \sigma_8|x)$ from weak lensing shear maps. We start with a prior over the two cosmological parameters Ω_c and σ_8 and we consider a simple random Gaussian field simulator of a 10 by 10 degree weak lensing field at typical LSST (https://www.lsst.org) galaxy number density. The SBI algorithm works as follows

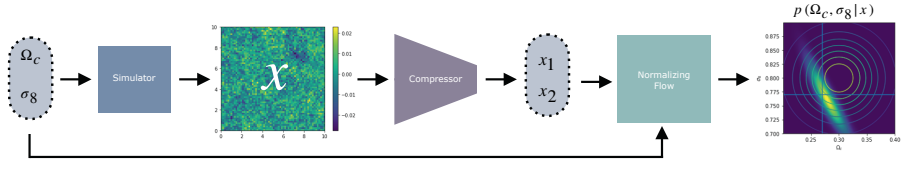

Figure 1 – **Diagram of the SBI toy cosmological experiment.** From a set of parameters $(\Omega_c, \sigma_8)_i$ we draw a shear map x_i . We use a convolutional neural network to compress this shear map into a set of summary statistics (x_1, x_2) . We train the NF on $((\Omega_c, \sigma_8)_i, (x_1, x_2)_i)_{i=1...N}$ using the two different losses: simulations only and simulations + gradients. The NF returns an approximate posterior $p(\Omega_c, \sigma_8|x_0) \approx q_\phi(\Omega_c, \sigma_8|x = x_0)$.

We demonstrate that using both simulations and gradients allow us to achieve a given posterior estimation quality with less simulations than traditional SBI methods.

References

1. Brehmer, J., Louppe, G., Pavez, J. & Cranmer, K. **Mining gold from implicit models to improve likelihood-free inference.** *Proceedings Of The National Academy Of Sciences.* **117**, 5242-5249 (2020,2), http://dx.doi.org/10.1073/pnas.1915980117. arXiv:1805.12244
2. Lueckmann, J., Boelts, J., Greenberg, D., Gonçalves, P. & Macke, J. Benchmarking **Simulation-Based Inference.** (2021). arXiv:2101.04653
3. Köhler, J., Krämer, A. & Noé, F. **Smooth Normalizing Flows.** (2021). arXiv:2110.00351
4. Rezende, D. & Mohamed, S. **Variational inference with normalizing flows.** *International Conference On Machine Learning.* pp. 1530-1538 (2015). arXiv:1505.05770

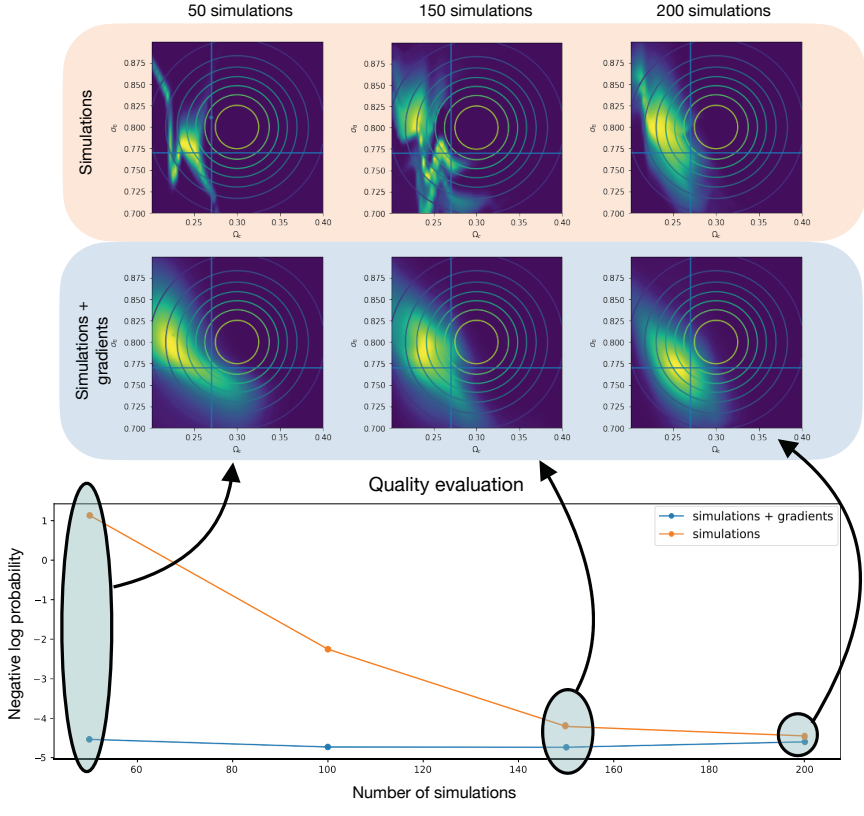

Figure 2 – **Posterior approximation performance as a function of the number of simulations, with (blue) and without (orange) the gradient loss.**
Top figure – illustration of the approximated posterior distribution $p(\Omega_c, \sigma_8|x_0)$ for 50, 150 and 200 simulations, when only simulations are used (first row) and when simulations and gradients are used (second row).
Bottom figure – evolution of the quality of the posterior approximation, measured by the negative log probability $-\mathbf{E}\left[\log q_\phi(\theta_0|x_0)\right]$ with θ_0 the "true" parameters that generated x_0. We show that the NF trained with the combination of simulations and gradients can approximate the posterior with less simulations.

Cosmology with the growth rate of structures using type Ia supernovae

B. Carreres, J. Bautista, D. Fouchez, F. Feinstein, B. Racine
CPPM, Aix-Marseille University, France

The growth rate of structures depends on gravity and dark energy. Until now, its measurement was made using galaxy surveys, but in the scope of new surveys like LSST and ZTF, type Ia supernovae could become new probes for it. Here we present our simulation work to prepare for this analysis.

1 The growth rate

The evolution of structures formed by matter is dictated by two main ingredients: the gravitational pull, responsible for making density perturbations growth, and the expansion of the Universe, which damps their growth. Velocity fields are linked to the growth rate which characterize the time rate of structures evolution and thus are great probes for gravity and dark energy.

2 Type Ia Supernovae as new growth rate probes

Until now, the growth rate of structures has been measured using galaxy surveys: either indirectly with the redshift space distortion (RSD) effect or directly from the peculiar velocities derived from Tully-Fisher or Fundamental plane distance estimates. The first method is limited by cosmic variance at low redshift and the second one use distance estimator ~ 5 times less precise than SN Ia [3].

SN Ia are standard candles. This allows the precise measurement of their distance. Combined with redshifts from spectroscopic galaxy surveys, they are competitive for a direct measurement of the growth rate. The next generation of survey like the **Zwicky Transient Facility** (ZTF), which is the first to survey the entire Northen sky to a redshift $z \sim 0.1$ with a high cadence or the **Legacy Survey of Space and Time** (LSST), that will scan the Southern sky up to a redshift $z \sim 0.8$, will provide several orders of magnitude more SN Ia than the present sample.

3 Host galaxy peculiar velocities measured from SNIa

We measure the peculiar velocities by using their contribution to the Hubble diagram residuals. As shown on figure 1 peculiar velocities (~ 300 km.s^{-1}) have two effects on the SN Ia Hubble diagram : a change in redshift ($\Delta z \sim 0.001$) due to Doppler effect and a modification of the apparent distance modulus ($\Delta\mu \sim 0.004$ mag) due to relativistic beaming.

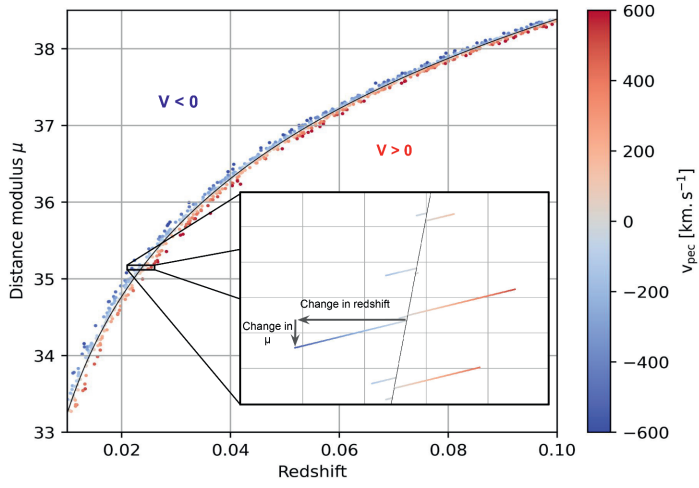

Figure 1 – Effect of peculiar velocities on the type Ia supernovae Hubble diagram

4 Analysis pipeline

The analysis of the growth rate can be affected by several biases, like the selection bias due to magnitude limited detection of SN Ia.

In order to study such biases and test the analysis, one key tool is using simulations of the SN survey. In this framework we have developed the SNsim[a] code to simulate supernovae with peculiar velocities. The analysis steps are the following: 1) take observation properties from the survey, and a velocity field from a N-body as input for the simulation, 2) generate SN Ia lightcurves using a SNIa model such as SALT2 [1], 3) add realistic selection functions of the survey, 4) fit the lightcurves and build a Hubble diagram, 5) use residuals to estimate the peculiar velocities [4], and 6) do summary statistics with the peculiar velocities in order to measure the growth rate of structures [5].

5 Conclusion

This pipeline is a useful tool to study biases due to selection effect and will be used to measure the growth rate of structure with ZTF and LSST data.

6 Acknowledgments

I would like to thank the Moriond organization team for the opportunity to present my work at this great conference.

References

1. J. Guy *et al.*, A&A **466**, (2007)
2. M. Betoule *et al.*, A&A **568**, (2014)
3. R. Graziani *et al.*, arXiv:2001.09095 (2020)
4. R. Watkins and H. A. Feldman MNRAS **450**, (2015)
5. C. Howlett *et al.* MNRAS **471**, (2017)

[a] https://github.com/bcarreres/snsim

How in situ atmospheric transmission can affect cosmological constraints from type Ia supernovae ?

Jérémy Neveu[1,2], Vincent Brémaud[1,2], Sébastien Bongard[1], Yannick Copin[3], Sylvie Dagoret-Campagne[2], Marc Moniez[2]

[1] *Sorbonne Université, CNRS, Université de Paris, LPNHE, 75252 Paris Cedex 05, France;* [2] *Université Paris-Saclay, CNRS, IJCLab, 91405, Orsay, France;* [3] *Univ Lyon, Univ Claude Bernard Lyon 1, CNRS/IN2P3, IP2I Lyon, UMR 5822, F-69622, Villeurbanne, France.*

The measurement of type Ia supernova colours in photometric surveys is the key to access to cosmological distances. But for future large surveys like the Large Survey of Space and Time undertaken by the Vera Rubin Observatory in Chile, the large statistical power of the promised catalogues will make the photometric calibration uncertainties dominant in the error budget and will limit our ability to use it for precision cosmology. The knowledge of the on-site atmospheric transmission on average for the full survey, or for season or each exposure can help reaching the sub-percent precision for magnitudes. We will show that measuring the local atmospheric transmission allows to correct the raw magnitudes to reduce the photometric systematic uncertainties. Then we will present how this strategy is implemented at the Rubin Observatory via the Auxiliary Telescope and its slitless spectrograph.

Cosmology measures and interprets the evolution of the whole universe. To probe its dynamic and understand the nature of dark energy, observers needs to compute distances at different epochs, from the light they received in telescopes. The evolution of cosmological distances with time tells how dark energy, dark matter and matter interacts and how they can be modelled.

Optical surveys use magnitude and colour comparisons to build a relative distance scale. For instance, type Ia supernovae (SNe Ia) revealed the presence of a dark energy component because they appeared fainter in the early universe than it was thought. More precisely, because SNIa colours redshift with universe expansion, high redshift supernovae were fainter in red bands than what can be inferred from low redshift supernovae observed in blue bands. This case underlines that colours need to be accurately calibrated in an optical survey to display the universe dynamics. Every chromatic effect that alter the astral light distort our dynamic perception of the universe expansion, like the galactic dust, the instrumental response or the local atmospheric conditions.

Let's take the example of the future Large Survey of Space and Time undertaken by the Vera Rubin Observatory in Chile (Cerro Pachon). This is a 10 year optical survey using 6 broad bandpass filters *ugrizy*, that will experience many different atmospheric conditions. The measured flux $\Phi_b^{\rm mes}$ in a band b and the corresponding magnitude $b^{\rm mes}$ are:

$$\Phi_b^{\rm mes} = \int_0^\infty S_*(\lambda) R_b(\lambda) T_{\rm atm}(\lambda|Z, t_{\rm exp}, \theta_a) \lambda {\rm d}\lambda / hc, \quad b^{\rm mes} = -2.5 \log_{10} [\Phi_b^{\rm mes}] + ZP \qquad (1)$$

with ZP is the reference zero point for the exposure, $S_*(\lambda)$ the source observer-frame SED, $R_b(\lambda)$ the LSST full instrumental response in band b and $T_{\rm atm}(\lambda|Z, t_{\rm exp}, \theta_a)$ the local atmospheric transmission at airmass Z, date $t_{\rm exp}$ depending on some parameters θ_a computed with Libradtran [1]. In this paper we only consider the Precipitable Water Vapor (PWV, in mm).

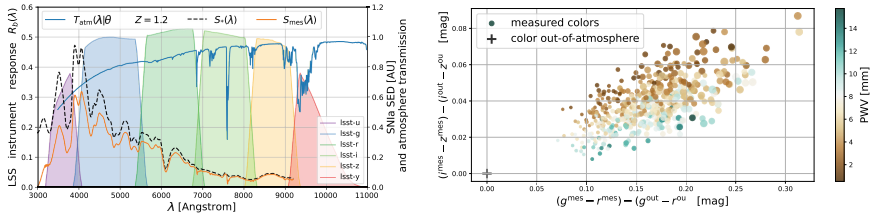

Figure 1 – *Left:* LSST instrumental response per filter, typical SNIa SED $S_\star(\lambda)$ at maximum, mean $T_{\rm atm}(\lambda)$ for LSST site. *Right:* bias and dispersion of colours due to airmass (point sizes) and PWV absorption (point colours) compared with out of atmosphere magnitude.

The impact of atmosphere on magnitude colours can be estimated by comparing magnitudes measured below atmosphere with magnitudes measured by the same instrument but out of atmosphere ($T_{\rm atm}(\lambda) = 1$). Seasonal effects can affect $i - z$ colour up to 40 mmag, if the observatory site alternates with dry and wet seasons (Figure 1). The PWV amplitude explored in Figure 1 is typical of the Rubin Observatory site according to the MERRA-2 database [2].

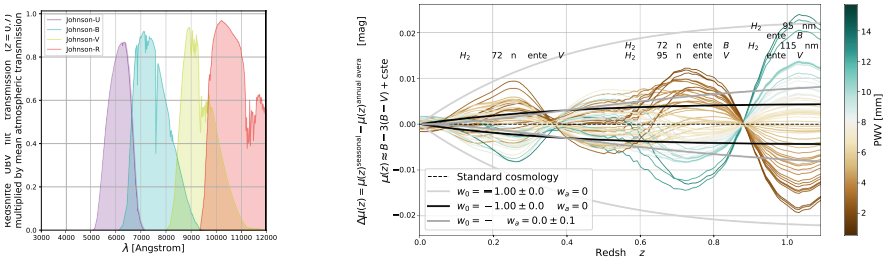

Figure 2 – *Left:* effective redshifted UBVR filter throughput with a mean atmospheric transmission ($z = 0.7$). *Right:* impact of PWV on SNIa distance moduli with respect to a mean distance moduli obtained with an effective annual average atmosphere, and comparison to cosmological signatures.

We simulated effective redshifted UBVR filter throughputs using different atmospheric conditions (Figure 2 left). Then we computed SNIa distance moduli $\mu(z) = B - 3(B - V)$ shifts around airmass 1.2 for different PWV values with the effective redshifted filters. Variations around the mean Hubble diagram up to 10 mmag are seen around redshift $z \approx 0.7$ depending on season humidity, whereas a 1% shift of w_0 from -1 leads to a 3 mmag offset at same redshift (Figure 2 right). This comparison helps setting requirements on the photometric calibration: to reach per-mille accuracy on the measurement of the dark energy equation of state parameter w_0 with SNe Ia, on-site PWV must be measured seasonally at a millimetre precision approximately.

The on-site PWV estimate can be performed using an auxiliary telescope equipped for spectrophotometry, like at the Rubin Observatory.Using a full forward modelling approach, the `Spectractor` software [3] can extract the atmospheric transmission from slitless spectrophotometer exposures with accuracy, according to tests on simulations and real data.

References

1. B. Mayer and A. Kylling, Atmospheric Chemistry and Physics **5**, 1855 (2005).
2. R. Gelaro *et al*, Journal of Climate **30**, 14 (2017).
3. J. Neveu *et al*, ASCL **2104.004**, (2021).

StarDICE : instrumental flux calibration with an artificial star for type Ia supernovae cosmology with the Legacy Survey of Space and Time

K. Sommer[1], E. Nuss[1], T. Souverin[2], J. Neveu[2,3], M. Betoule[2], S. Bongard[2], J. Cohen Tanugi[1,6], S. Dagoret-Campagne[3], F. Feinstein[4], C. Juramy[2], L. Le Guillou[2], A. Le Van Suu[5], P. E. Blanc[5], M. Moniez[3], F. Hazenberg[2], B. Plez[1], E. Sepulveda[2], N. Regnault[2]

[1] *LUPM, Université Montpellier & CNRS, F-34095 Montpellier, France;*
[2] *Sorbonne Université, CNRS, Université de Paris, LPNHE, 75252 Paris Cedex 05, France;*
[3] *Université Paris-Saclay, CNRS, IJCLab, 91405, Orsay, France;*
[4] *CPPM, Université d'Aix-Marseille & CNRS, 163 av. de Luminy 13288 Marseille Cedex 09, France;*
[5] *Observatoire de Haute-Provence, Université d'Aix-Marseille & CNRS, 04870 Saint Michel L'Observatoire, France;*
[6] *LPC, IN2P3/CNRS, Université Clermont Auvergne, F-63000 Clermont-Ferrand, France*

Measurements of luminosity distances using type 1a supernovae (SNe Ia) are essential to constrain the equation of state parameter ω [1,2,3]. Current measurements of SNe Ia are limited by the statistics and the underlying systematic errors [4]. The large number of detected SNe Ia with the upcoming Vera Rubin Observatory (VRO) will address the first issue [5]. In the Photometric Calibration Working Group of the Dark Energy Science Collaboration (DESC) of the Legacy Survey of Space and Time (LSST), we propose the StarDICE experiment which will put effort toward the reduction of systematic errors. StarDICE, is a metrology experiment installed at Observatoire de Haute-Provence (OHP) whose goal is to achieve millimagnitude calibration required to extract most of the statistical power of LSST. This implies knowing relative flux changes at $< 0.1\%$ on CALSPEC stars [6].

1 SNe Ia cosmology with Vera Rubin Observatory

The VRO, is an upcoming new generation multi-purpose telescope which will be part of Stage IV surveys. It consists of a 10-year complete southern-hemisphere photometric astronomical survey, known as LSST.

One of the main objective of LSST is the study of the dark sector of the Universe through the Rubin Observatory LSST Dark Energy Science Collaboration. The cadence of observations will allow transient detections such as type 1a supernovae, known to be excellent standard candles. If their intrinsic spectrum is known, their colors have the potential to accurately determine the distance of the source.

The LSST data will contain $\approx 50,000$ SNe Ia per year with high precision photometry for accurate light curve fitting at a mean redshift of $z \approx 0.5$ [5]. However, current measurements are limited by systematic effects including instrumental calibration. Millimagnitude calibration is necessary in order to benefit from the LSST statistical power and constrain ω_0 to ± 0.05, and ω_a to ± 0.10 within the redshift-dependent equation of state $\omega(z) = \omega_0 + \omega_a(\frac{z}{1+z})$ (see Fig. 1).

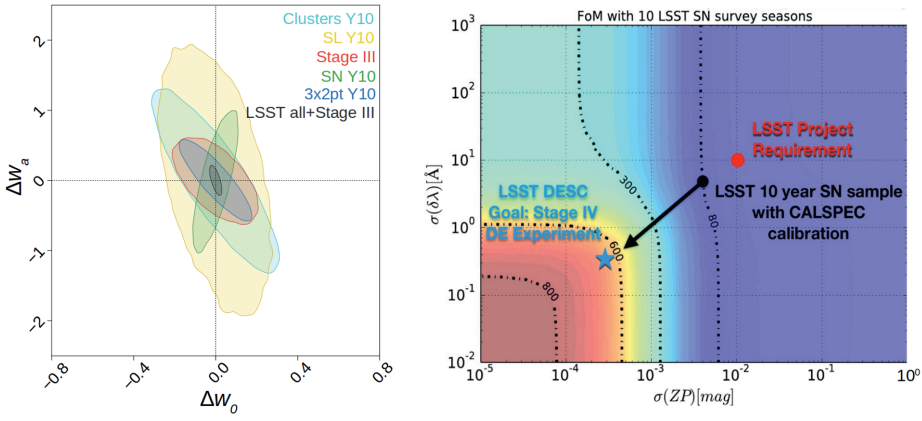

Figure 1 – Left : Dark energy forecasts for the precisions $\Delta\omega_0$ and $\Delta\omega_a$ which must be obtained with different probes combinations[7]. Right : Figure of Merit (FoM) for 10-year period of LSST SN survey, defined as the inverse of the area of the ellipse of the contour at 1σ of the uncertainties in the plane (ω_0, ω_a). Different calibration stages for LSST are represented. At 1% calibration the SNe Ia survey does not bring much to cosmology. 1 mmag precision is required to extract most of the statistical power of LSST [8].

2 The StarDICE experiment

The proposed strategy is the use of a stable calibrated light-source called the artificial star, as a flux standard to calibrate the flux response of a small aperture telescope. By knowing the calibrated flux of the NIST artificial star F_T^{LED}, we can correct the response of the instrumental chain:

$$\frac{F_M^{LED}(t,\lambda)}{F_M^{STAR}(t,\lambda)} = \frac{R(h,t,\lambda)}{R(H,t,\lambda)} \cdot \frac{F_T^{LED}(\lambda)}{F_T^{STAR}(\lambda)} \tag{1}$$

where R is the instrumental response with h the altitude of observation of the LED, H the altitude of observation of the star. F_T and F_M represent the theoretical and measured flux respectively. With enough observation data, we can fit F_T^{STAR} using a template to get the absolute flux of the CALSPEC star.

3 First results and prospects

The first version of the experiment designed to validate the concept has been installed and successfully tested at OHP by obtaining an average statistical flux uncertainty of 0.7% in each spectral band over 20 minutes of data acquisition [8] (see Fig. 2).

The target of 0.1% precision is within reach if we can accumulate between 50-100 visits of each star.

Following the proof of concept phase, design improvements have been made on every stage of the metrology chain (see Fig. 3).

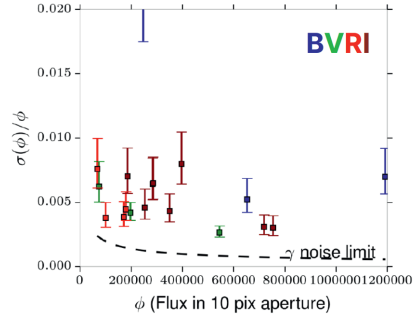

Figure 2 – Precision on CALSPEC star flux in BVRI bands for a 10 pixels aperture on multiple exposures.

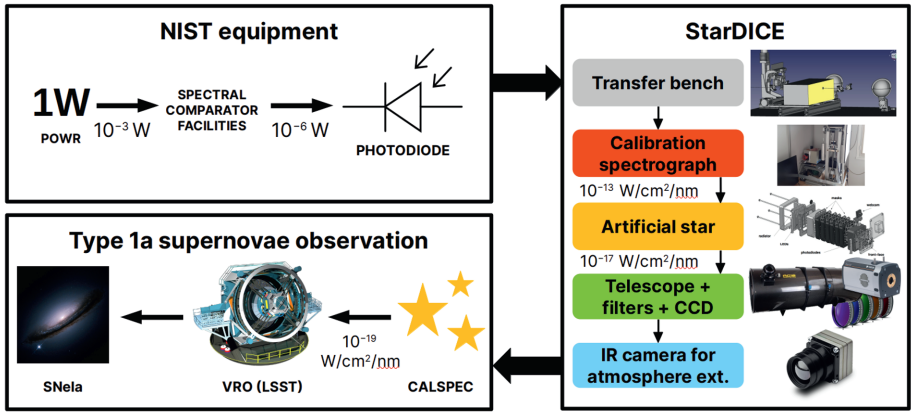

Figure 3 – Final metrology chain after design improvements. The NIST provides the artificial star. The StarDICE collaboration builds the dedicated bench transfer system to reach 10^{19} $W/cm^2/nm$ flux sensitivity.

StarDICE commissioning and first light after upgrade at OHP is expected to occur during the first semester of 2022.

References

1. Y. Gong *et al*, *Astroph. Journal* **709**, 1420 (2010).
2. M. Betoule *et al*, *Astro. and Astroph.* **568**, A22 (2014).
3. A. Goobar & B. Leibundgut, Annual Review of Nuclear and Particle Science **61**, 251 (2011).
4. A. Mitra & E. Linder, *Phys. Rev.* D **103**, 023524 (2021).
5. W. M. Wood-Vasey *et al*, LSST Sciencebook : Supernovae, 2011.
6. R. C. Bohlin *et al*, *Astroph. Journal* **147**, 127 (2014).
7. The LSST Dark Energy Science Collaboration, R. Mandelbaum, T. Eifler, *et al*, 2018.
8. F. Hazenberg, Calibration photométrique des supernovae de type Ia pour la caractérisation de l'énergie noire avec l'expérience StarDICE, PhD thesis, 2019.

New constraint on early dark energy from Planck and BOSS data using the profile likelihood [1]

Laura Herold, E. G. M. Ferreira, E. Komatsu
Max-Planck-Institut für Astrophysik, Karl-Schwarzschild-Str. 1, 85748 Garching, Germany

A dark energy-like component in the early universe, known as early dark energy (EDE), is a proposed solution to the Hubble tension. Currently, there is no consensus in the literature as to whether EDE can simultaneously solve the Hubble tension and provide an adequate fit to the data from the cosmic microwave background (CMB) and large-scale structure of the universe. In this work, we use the profile likelihood to understand the origin of different conclusions in the literature and to investigate whether the current constraints suffer from volume effects upon marginalization. We construct a confidence interval that is not subject to volume effects and find $f_{\rm EDE} = 0.072 \pm 0.036$ (68% C.L.).

1 Early Dark Energy meets Large Scale Structure

Early Dark Energy (EDE) is a proposed solution to the Hubble tension. EDE was shown to relieve the tension between the values of the Hubble constant H_0 inferred from the CMB data and baryon acoustic oscillation (BAO) and redshift-space distortion data from galaxy surveys, the Pantheon supernova sample, and the direct measurement by the SH0ES collaboration.[2,3] With this data set, $f_{\rm EDE} = 0.107^{+0.035}_{-0.030}$, where $f_{\rm EDE}$ is the maximum fraction of EDE, which gives $H_0 = 71.49 \pm 1.20\,$km/s/Mpc. However, it was pointed out that introducing EDE leads to an enhancement of the galaxy power spectrum at small scales[4]. Using the BOSS full-shape galaxy power spectrum, which is sensitive to this small-scale enhancement, combined with *Planck* CMB data, one finds that EDE is tightly constrained: $f_{\rm EDE} < 0.072$ at 95% C.L (with a mean of only $f_{\rm EDE} = 0.025^{+0.006}_{-0.025}$). [5,6] In this analysis all three EDE parameters are varied ("3-parameter model"): the maximum fraction of EDE $f_{\rm EDE}$, the redshift at which the EDE fraction is maximum z_c, and the initial value of the EDE field θ_i. It was argued that the reason for the small preferred value of $f_{\rm EDE}$ found in this analysis is due to volume effects upon marginalization.Volume effects can appear during the MCMC analysis due to the parameter structure of the EDE model: For $f_{\rm EDE} = 0$, the EDE model is degenerate with ΛCDM for any choice of θ_i and z_c. Therefore, the parameter volume for $f_{\rm EDE} = 0$ is larger than for every $f_{\rm EDE} > 0$. This can lead to a preference for $f_{\rm EDE} = 0$ in the marginalized posterior, affecting the inferred amount of EDE allowed by the data. [7] To avoid volume effects, it was proposed to

fix two EDE parameters $\{\theta_i, z_c\}$ ("1-parameter model") and find $f_{\rm EDE} = 0.072 \pm 0.034$ for the same data set. [3]. However, fixing some parameters of the model, as for the 1-parameter model, is an incomplete analysis; the results might depend on the particular choice of the parameters. In this work, we want to construct a confidence interval that is not subject to volume effects or a reduction of the EDE model by fixing two parameters.

2 Constraining Early Dark Energy using the profile likelihood

Comparison of the results obtained from Bayesian and frequentist analyses is useful for checking if priors or marginalization affect the results. A profile likelihood is a standard tool in frequentists' statistics, which by construction is not subject to prior or volume effects. To construct a profile likelihood, one fixes the parameter of interest, i.e. in our case $f_{\rm EDE}$, to different values and maximizes the likelihood $\mathcal{L}$ with respect to all the other parameters of the model. Figure 1 (left) shows the profile likelihood for $f_{\rm EDE}$ using the BOSS full-shape power spectrum and *Planck* CMB data. Using the Feldman–Cousins prescription[8] to determine the confidence interval, we find $f_{\rm EDE} = 0.072 \pm 0.036$ at 68% C.L. Our confidence interval differs from the full 3-parameter MCMC analysis[5] but is qualitatively similar to the result found within the 1-parameter model,[3] see Figure 1 (right). The confidence interval obtained with the profile likelihood is free from volume effects and does not depend on a specific choice of the other two EDE parameters $\{\theta_i, z_c\}$. We suggest that the profile likelihood is a powerful tool to understand whether EDE is a possible solution to the Hubble tension.

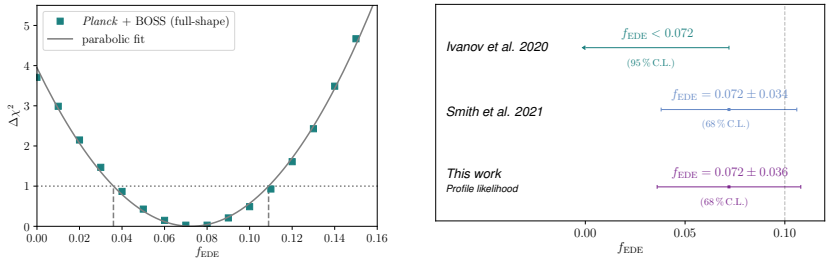

Figure 1 – *Left:* Profile likelihood of the fraction of EDE $f_{\rm EDE}$ from the *Planck* CMB and the BOSS full-shape galaxy clustering data. We show $\Delta\chi^2 = -2\ln(\mathcal{L}/\mathcal{L}_{\rm max})$, where $\mathcal{L}_{\rm max}$ is the maximum likelihood, (green markers) and a parabola fit (grey line). The confidence interval is constructed using the Feldman–Cousins prescription (vertical dashed lines). It is indistinguishable from the interval constructed from the intersection of the parabola with $\Delta\chi^2 = 1$ (horizontal dotted line, Neyman construction). *Right:* Comparison to different constraints in the literature.

References

1. L. Herold, E. G. M. Ferreira, E. Komatsu, *arXiv*:2112.12140 (2021).
2. V. Poulin, T. Smith, D. Grin, T. Karwal, M. Kamionkowski, *Phys.Rev.D* 98.083525 (2018).
3. T. Smith, V. Poulin, A. Mustafa, *Phys.Rev.D* 101.063523 (2020).
4. C. J. Hill, E. McDonough, M. W. Toomey, S. Alexander, *Phys.Rev.D* 102.043507 (2020).
5. M. Ivanov, E. McDonough, C. J. Hill, M. Simonović, M. W. Toomey, S. Alexander,M. Zaldarriaga, *Phys.Rev.D* 102.103502 (2020).
6. G. D'Amico, L. Senatore, P. Zhang, H. Zheng, *JCAP* 10.1088 (2021).
7. T. Smith, V. Poulin, J. L. Bernal, K. Boddy, M. Kamionkowski, R. Murgia, *Phys.Rev.D* 103.123542 (2021).
8. G. J. Feldman, R. D. Cousins *Phys.Rev.D* 57.3873 (1998).

Modeling of High Column Density Systems (HCDs) in the Lyman-α Forests

Ting Tan,[1], Jim Rich,[2] Jean-Marc Le-Goff,[2] and Christophe Balland[1]
[1] *Sorbonne Université, CNRS/IN2P3, LPNHE, 4 Place Jussieu, F-75252 Paris, France*
[2] *IRFU, CEA, Université Paris-Saclay, F91191 Gif-sur-Yvette, France*
Contact: ting.tan@lpnhe.in2p3.fr

The Dark Energy Spectroscopic Instrument is observing a large catalog of high redshift quasars, enabling a more precise measurement of the Baryon Acoustic Oscillation signal using quasars and Lyman-α forests. In our study, we focus on the modeling of High Column Density Systems, seen as strong absorption regions in the forests, which has a significant impact on the fitting of the Lyman-α correlation function.

1 Introduction

The Dark Energy Spectroscopic Instrument (DESI [a]) is an on-going stage-IV experiment, designed to obtain spectra of about a million Lyman-α quasars. This catalog is three times larger than the sixteenth data release (DR16 [1]) of the fourth generation of the Sloan Digital Sky Survey (SDSS-IV [10,3]), which contains $\sim 200,000$ Ly-α quasars with $z > 2.1$ from the completed extended Baryonic Oscillation Spectroscopic Survey (eBOSS [b] [4]). The Lyman-α forest is detected as the series of absorption lines in the quasar spectra, caused by the Lyman-alpha transitions of neutral hydrogen in the low-density, high-redshift intergalactic medium (IGM). It is a biased continuous tracer of the quasi-linear matter density field, and the auto (cross) correlation function of the forests (with quasars) have been used to detect the Baryon Acoustic Oscillation (BAO) signal [5]. In this work we studied the theoretical modeling of the High Column Density Systems (HCDs), one of the most important systematics in the Lyman-α analysis.

2 Modeling

The High Column Density Systems are categorized as HCDs or Damped Lyman-α Systems (DLAs) by the high NHI column density of the neutral hydrogen gas concentration along the line of sight: HCDs: $log(\mathrm{NHI/cm^{-2}}) >= 17$; DLAs: $log(\mathrm{NHI/cm^{-2}}) >= 20$. DLAs are detectable, seen as strong absorption regions in the Lyman-α forests, using machine learning algorithms [8]. We can therefore smooth the Lyman-α flux-fluctuation fields by masking out the detected DLAs, shown in Figure 1. However, the undetectable HCDs still have significant impact on the modeling of Lyman-α correlation function. The Fourier Transformation of the absorption profiles of those HCDs will induce a cut-off for the Lyman-α power spectrum at high $k_{||}$, and it affects the bias and redshift distortion parameters of Lyman-α tracers. The effective k-dependent bias is [7]:

$$b'_{\mathrm{Ly}\alpha} = b_{\mathrm{Ly}\alpha} + b_{\mathrm{HCD}} F_{\mathrm{HCD}}(k_{||}), \quad (1)$$

[a] https://www.desi.lbl.gov/
[b] https://www.sdss.org/surveys/eboss/

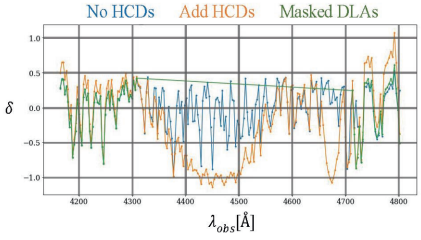

Figure 1 – flux-fluctuation fields of a Lyman-α forest. The blue curve shows the delta field without any HCDs, and the orange curve with HCDs inserted. We smooth the delta field by masking out the large DLAs, shown as the green curve.

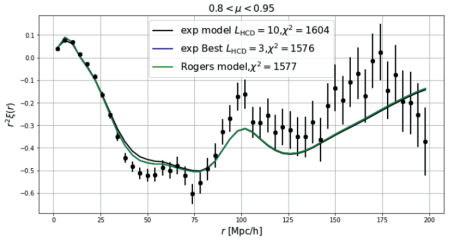

Figure 2 – BAO fitting for the Lyman-α auto-correlation function with different HCDs models, along the direction of $\mu = \frac{r_{||}}{r}$.

The $F_{\rm HCD}$ function can be modeled theoretically with the distribution of HCDs [9], assuming the HCDs parameterized with a voigt profile [6]:

$$F_{\rm HCD}^{\rm Rogers}(k_{||}) = \int \widetilde{(V-1)}(k_{||}, n) f(n) {\rm d}n, \tag{2}$$

However, the true HCDs distribution is unknown in the cosmology surveys. The expected distribution of HCDs gives an approximate form used in the eBOSS DR16 analysis [5]:

$$F_{\rm HCD}^{\rm exp}(k_{||}) = \exp\left(-L_{\rm HCD} * k_{||}\right), \tag{3}$$

The $L_{\rm HCD}$ is a free parameter characterizing the scale of HCDs effect, that is fixed to 10 in the DR16 analysis, while the best fitting for the Lyman-α auto-correlation function suggests $L_{\rm HCD} = 3$, as shown in Figure 2. The exp fitting function shows a good agreement with the Rogers model. However, none of these models give a good fitting for the region $25 < r < 80$, where HCDs play the most important role. This motivates us to search for a more accurate model, and understand better the physics of HCDs in the upcoming DESI analysis.

References

1. Ahumada, R., Prieto, C. A., Almeida, A., et al. 2020, The Astrophysical Journal Supplement Series, 249, 3
2. Arinyo-i Prats, A., Miralda-Escudé, J., Viel, M., & Cen, R. 2015, Journal of Cosmology and Astroparticle Physics, 2015, 017
3. Blanton, M. R., Bershady, M. A., Abolfathi, B., et al. 2017, The Astronomical Journal, 154, 28
4. Dawson, K. S., Kneib, J.-P., Percival, W. J., et al. 2016, The Astronomical Journal, 151, 44
5. du Mas des Bourboux, H., Rich, J., Font-Ribera, A., et al. 2020, The Astrophysical Journal, 901, 153
6. Di Rocco, H. O., & Cruzado, A. 2012, Acta Physica Polonica A, 122
7. Font-Ribera, A., & Miralda-Escudé, J. 2012, Journal of Cosmology and Astroparticle Physics, 2012, 028
8. Parks, D., Prochaska, J. X., Dong, S., & Cai, Z. 2018, Monthly Notices of the Royal Astronomical Society, 476, 1151
9. Rogers, K. K., Bird, S., Peiris, H. V., et al. 2018, Monthly Notices of the Royal Astronomical Society, 476, 3716
10. York, D. G., Adelman, J., Anderson Jr, J. E., et al. 2000, The Astronomical Journal, 120, 1579

Large Halo Sparsity, a Fast Detector and Chronometer for Galaxy Cluster Mergers

T.R.G. Richardson[1], P.-S. Corasaniti[1,2]
[1] *Laboratoire Univers et Théories, Observatoire de Paris, Université PSL, Université de Paris, CNRS, F-92190 Meudon, France*
[2] *Sorbonne Université, CNRS, UMR 7095, Institut d'Astrophysique de Paris, 98 bis bd Arago, 75014 Paris, France*

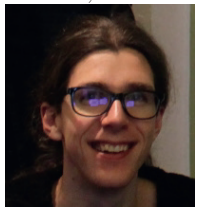

Galaxy clusters have proven themselves to be valuable probes of cosmology and astrophysics. However observing galaxy cluster merger events can give us additional insight on the properties of gas inside the intra-cluster medium, dark matter physics or the theory of gravitation, it is therefore of prime interest to devise a fast and reliable way of detecting which clusters have undergone recent mergers. Here we present a novel approach using halo sparsity and define thresholds $s^{th}_{200,500}(z)$ above which dark matter haloes can be considered as having undergone a recent major merger. We further expand this detection approach to estimate the approximate time at which the last major merger occurred. This work opens the way to detecting and timing major mergers in galaxy clusters solely through measurements of the their mass at different radii.

1 Introduction

Defined simply as the ratio of two masses measured at two overdensity contrasts, halo sparsity, $s_{\Delta_1,\Delta_2} = \frac{M_{\Delta_1}}{M_{\Delta_2}}$, gives access to the internal physics of dark matter haloes. Its strong correlation with known measurements of the dynamical state of a dark matter halo and the time since its last major merger, as seen in the MDPL2 gravity only simulation,[1] make it an ideal observable for galaxy clusters. The universal reaction to mergers seen in the NFW concentration in dynamically normalised time,[2,3]

$$T(a_{\rm LMM}|a) = \int_{t(a)}^{t(a_{\rm LMM})} \frac{dt'}{\tau_{\rm dyn}(t')} = \frac{\sqrt{2}}{\pi} \int_a^{a_{\rm LMM}} \frac{\sqrt{\Delta_{\rm vir}(a')}}{a'} da', \tag{1}$$

where $\Delta_{\rm vir}$ is the virial overdensity contrast, is reflected in halo sparsity as can be seen in the left panel of Fig. 1. This significantly alters the distribution of sparsities for haloes that have undergone a recent merger with respect to that of haloes with more quiescent histories as can be seen in the right panel of the same figure. This implies that high sparsities are indeed a sign of recent mergers.

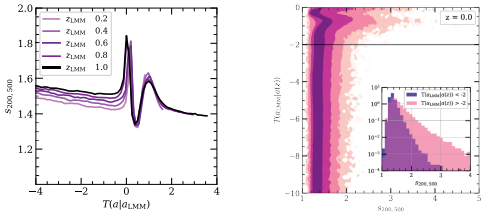

Figure 1 – *Left:* median sparsity response of haloes to major mergers in dynamical time units at various redshifts. *Right:* joint distribution of sparsities and dynamical times since the last major merger. *Right, inset:* marginalised sparsity distribution for recent, *pink*, and ancient mergers, *blue*.

2 Methods and Results

Within a frequentist framework, these observed differences in the distributions allow to statistically set up thresholds to detect recent mergers.[4] In the left panel of Fig. 2 these threshold sparsities are calculated for key $p-$values up to redshift $z = 2$. These can be used to rapidly detect mergers by checking if a cluster's sparsity is above a given threshold.

Extending to a Bayesian framework, it is possible to derive posterior distribution functions for the time at which the last major merger occurred using a single sparsity measurement, thus allowing one to recover a best estimate for this time and be informed on the dynamical state of the cluster. This framework can further be extended by adding additional sparsity measurements, increasing the robustness of the method.[4]

All of this analysis is implemented in the public Python package: LAMMAS [a] which also includes the calculation of $p-$values and handling of measurement uncertainty.

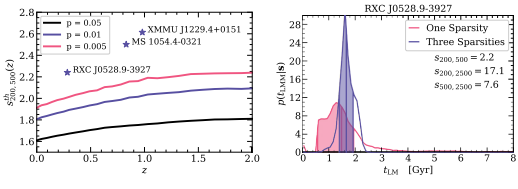

Figure 2 – *Left:* sparsity thresholds derived as a function of redshift with three clusters from the LC^2 – *single* catalogue [5] presenting high values of sparsity. *Right:* posterior distribution of the time since the last major merger occurred in the cluster RXC J0528.9-3927.

Acknowledgments

The CosmoSim database used in this paper is a service by the Leibniz-Institute for Astrophysics Potsdam (AIP). The MultiDark database was developed in cooperation with the Spanish MultiDark Consolider Project CSD2009-00064. The authors gratefully acknowledge the Gauss Centre for Supercomputing e.V. (www.gauss-centre.eu) and the Partnership for Advanced Supercomputing in Europe (PRACE, www.prace-ri.eu) for funding the MultiDark simulation project by providing computing time on the GCS Supercomputer SuperMUC at Leibniz Supercomputing Centre (LRZ, www.lrz.de).

References

1. Anatoly Klypin, Gustavo Yepes, Stefan Gottlöber, Francisco Prada, and Steffen Heß. MultiDark simulations: the story of dark matter halo concentrations and density profiles. MNRAS, 457(4):4340–4359, April 2016.
2. Kuan Wang, Yao-Yuan Mao, Andrew R. Zentner, Johannes U. Lange, Frank C. van den Bosch, and Risa H. Wechsler. Concentrations of dark haloes emerge from their merger histories. MNRAS, 498(3):4450–4464, November 2020.
3. Fangzhou Jiang and Frank C. van den Bosch. Statistics of dark matter substructure - I. Model and universal fitting functions. MNRAS, 458(3):2848–2869, May 2016.
4. T. R. G. Richardson and P. S. Corasaniti. Timing the last major merger of galaxy clusters with large halo sparsity. *arXiv e-prints*, page arXiv:2112.04926, December 2021.
5. Mauro Sereno. CoMaLit - III. Literature catalogues of weak lensing clusters of galaxies (LC^2). MNRAS, 450(4):3665–3674, July 2015.

[a] https://gitlab.obspm.fr/trichardson/lammas

Rapid simulations of halo and subhalo clustering

Pascale Berner[1,a], Alexandre Refregier[1], Raphael Sgier[1], Tomasz Kacprzak[1,2],
Luca Tortorelli[1,3], Pierluigi Monaco[4,5]
[1] *IPA, ETH Zurich,* [2] *Swiss Data Science Center, Paul Scherrer Institute,*
[3] *Ludwig-Maximilian-University Munich,* [4] *University of Trieste,* [5] *INAF, IFPU, INFN in Trieste*
[a] *pascale.berner@phys.ethz.ch*

We present our work on fast halo and subhalo clustering simulations based on PINOCCHIO. The subhalo progenitors are extracted from the merger history and the survival of subhalos is modelled. The spatial distribution of subhalos within their hosts is modelled using a number density profile. We compare our simulations with the halo finder Rockstar applied to the full N-body code GADGET-2.

1 Introduction

Forward modelling is a powerful method to simulate galaxy clustering without the need for an underlying complex model. Subhalo abundance matching allows us to model the relation between halos and galaxies with few free parameters. This approach requires fast cosmological simulations with a high resolution and large volume, to resolve small dark matter halos and subhalos associated to single galaxies.

2 Method

We start from a halo catalogue and the corresponding merger history from PINOCCHIO. For each halo, we extract the merging subhalos. The surviving subhalos are determined by estimating the merger time corresponding to the subhalo survival time. We assign the surviving subhalos the mass of the progenitor at merger. For the spatial distribution of subhalos we use a radial number density profile. Figure 1 shows our procedure.

3 Subhalo Survival Time

We introduce the following new fitting function for the merger time

$$\tau_{\rm merge} = 0.175\ \tau_{\rm dyn}\ \frac{(M_{\rm host}/m_{\rm sub})^{1.3}}{\ln(1+M_{\rm host}/m_{\rm sub})}\exp\left(1.9\eta\right)[\tfrac{1}{12}\log_{10}(m_{\rm sub})]^{(3.0+7.0\ z_{\rm obs})} \qquad (1)$$

where $\tau_{\rm dyn}$ is the dynamical time at the virial radius of the host, $M_{\rm host}$ is the host halo mass, $m_{\rm sub}$ is the subhalo mass at accretion, $z_{\rm obs}$ is the redshift of the host at observation and η is the orbital circularity that we draw from a distribution.
In simulations with a resolution leading to halos with masses above $5.7 \cdot 10^9$ $\mathrm{M}_\odot$/h, we find a number fraction of subhalos of 15-18% at $z \leq 1$ for our best fit of the subhalo survival time. The relation between halo and subhalo mass and the subhalo mass function of our model are similar to Rockstar run on GADGET-2.

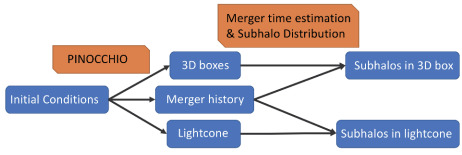

Figure 1 – Schematic of the method to generate halo-subhalo catalogues from the PINOCCHIO output, for both snapshots and lightcones.

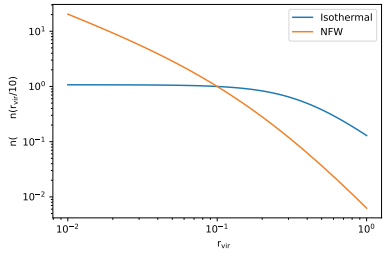

Figure 2 – The isothermal subhalo number density profile in blue and the NFW profile in orange.

4 Subhalo Distribution Functions

We compare an isothermal profile and an NFW profile (see Figure 2) for the radial distribution of subhalos within their hosts. The angular coordinates are drawn isotropically. The difference in the 3D two-point correlation function of subhalos is small at separations above 0.3 Mpc/h.

5 Halo and Subhalo Clustering

Using Corrfunc, we investigate the 3D two-point correlation functions of halos and subhalos of our model. By looking at halos and subhalos separately (Figure 3, for the mass bin $[10^{11}, 10^{12}]$ $M_\odot$/h), we see that the subhalo clustering is realistic and that the inclusion of subhalos is important for the small scale clustering. Considering different halo mass bins (Figure 4, mass bins given in $\log_{10}(M/(M_\odot/h))$, we see that the 2PCF of halos and subhalos together shows the correct mass dependence. Figures 3 and 4 are at redshift z = 0.5.

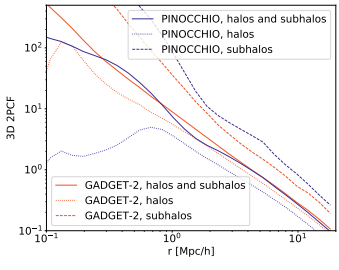

Figure 3 – 2PCF for halos and subhalos separetely.

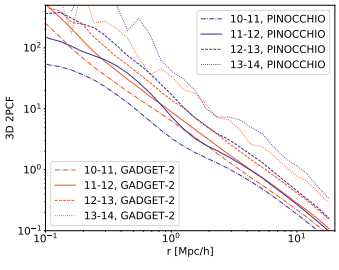

Figure 4 – Total 2PCF in different mass bins.

6 Conclusion and Outlook

We find that the subhalo statistics is realistic enough. For a box size of 200 Mpc/h and 1024^3 particles, we find a speed-up of ∼700 compared to a full N-body simulation with a halo finder. Our simulations are ready for further applications including subhalo abundance matching.

References

1. P. Berner *et al.*, submitted to *JCAP*, arXiv:2112.08389.

Authors Index

Authors Index

List of Participants

Family name	First name	Institution	Country	Email
Acharya	Sandeep Kumar	University of Manchester	UK	sandeep.acharya@manchester.ac.uk
Adil	Arsalan	UC, Davis	USA	aadil@ucdavis.edu
Ajani	Virginia	ETH Zurich	Switzerland	virginia.ajani@gmail.com
Ali-Haïmoud	Yacine	New York University	USA	yah2@nyu.edu
Amenouche	Melissa	CNRS/IN2P3/LPC - UCA	France	melissa.amenouche@clermont.in2p3.fr
Ansari	Reza	Univ. Paris Saclay / IJCLab	France	ansari@lal.in2p3.fr
Artis	Emmanuel	LPSC	France	emmanuel.artis@lpsc.in2p3.fr
Asorey	Jacobo	CIEMAT	Spain	jasorey@gmail.com
Astier	Pierre	LPNHE	France	pierre.astier@in2p3.fr
Avila	Santiago	UAM - Inst. Física Teórica - CSIC	Spain	santiago.avila@uam.es
Battye	Richard	JBCA/University of Manchester	UK	Richard.Battye@manchester.ac.uk
Bautista	Julian	CPPM - Aix-Marseille Uni.	France	bautista@cppm.in2p3.fr
Beckwith	Andrew	Chongqing University	China	rwill9955b@gmail.com
Belkner	Sebastian	University Geneve	Switzerland	sebastianbelkner@gmail.com
Berner	Pascale	ETH Zurich	Switzerland	bernerp@phys.ethz.ch
Biquard	Simon	APC	France	sbiquard@gmail.com
Biswas	Biswajit	APC	France	biswas@apc.in2p3.fr
Blanchard	Alain	IRAP	France	alain.blanchard@irap.omp.eu
Boucaud	Alexandre	APC	France	aboucaud@apc.in2p3.fr
Boyarsky	Alexey	Leiden University	Netherlands	boyarsky@mail.cern.ch
Braglia	Matteo	Inst. fisica teorica UAM-CSIC	Spain	matteo.braglia@csic.es
Brown	Kate	Newcastle University	UK	k.brown@newcastle.ac.uk
Camera	Stefano	University of Turin	Italy	stefano.camera@unito.it
Campeti	Paolo	MPI Astrophysics	Germany	pcampeti@mpa-garching.mpg.de
Carreres	Bastien	CPPM	France	carreres@cppm.in2p3.fr
Carron	Julien	Université de Genève	Switzerland	julien.carron@unige.ch
Carrón Duque	Javier	Roma Tor Vergata	Italy	javier.carron@roma2.infn.it
Casas	Santiago	RWTH Aachen University	Germany	casas@physik.rwth-aachen.de
Castello	Sveva	University of Geneva	Switzerland	Sveva.Castello@unige.ch
Cataneo	Matteo	Argelander-Inst. für Astronomie	Germany	mcataneo@uni-bonn.de
Chakraborti	Sreemanti	LAPTh, Annecy	France	chakraborti@lapth.cnrs.fr
Chaussidon	Edmond	CEA Saclay (IRFU)	France	edmond.chaussidon@cea.fr
Chen	Tianyue	EPFL	Switzerland	tianyue@mit.edu
Chluba	Jens	JBCA/University of Manchester	UK	jens.chluba@manchester.ac.uk
Chudaykin	Anton	McMaster University	Canada	chudayka@mcmaster.ca
Collischon	Caroline	Dr. Karl Remeis Sternwarte, FAU	Germany	caroline.collischon@fau.de
Coulton	William	CCA Flatiron Institute	USA	wcoulton@flatironinstitute.org
Cusin	Giulia	University of Geneva	Suisse	giugiuliacusin@gmail.com
D'Alessandro	Giuseppe	Sapienza University of Rome	Italy	giuseppe.dalessandro@roma1.infn.it
da Silveira Ferreira	Pedro	UFRJ	Brazil	pferreira@astro.ufrj.br
de Cabo Martin	Jaime	NCBJ	Poland	jaime.decabomartin@ncbj.gov.pl
de la Hoz	Elena	IF Cantabria (UC-CSIC)	Spain	delahoz@ifca.unican.es
De Luca	Federico	Roma Tor Vergata	Italy	federico.deluca@roma2.infn.it
de Mattia	Arnaud	IRFU, CEA, Uni. Paris-Saclay	France	arnaud.de-mattia@cea.fr
Demirbozan	Umut Emek	IFAE - UAB	SPAIN	umutdemirbozan@gmail.com
Diego-Palazuelos	Patricia	IF Cantabria (UC-CSIC)	Spain	diegop@ifca.unican.es
Dirian	Yves	IST Lisboa	Portugal	y.dirian@gmail.com
Dumarchez	Jacques	LPNHE	France	jacques.dumarchez@cern.ch
Facchinetti	Gaétan	Physique Th., ULB	Belgium	gaetan.facchinetti@umontpellier.fr
Fasiello	Matteo	IFT - UAM-CSIC, Madrid	Spain	matteorf@gmail.com
Feinstein	Fabrice	CPPM - Aix-Marseille Uni.	France	feinstein@cppm.in2p3.fr
Ferguson	Kyle	UCLA	USA	kferguson@physics.ucla.edu
Ferrer Ereza	Julia	Inst. Astrofísica Andalucía - CSIC	Spain	jferrer@iaa.es
Fischbacher	Silvan	ETH Zurich	Switzerland	silvanf@phys.ethz.ch
Flöss	Thomas	Van Swinderen & Kapteyn Inst.	Netherlands	tsfloss@gmail.com
Franco Abellán	Guillermo	LUPM	France	guillermo.franco-abellan@umontpellier.fr
Fumagalli	Alessandra	University of Trieste	Italy	alessandra.fumagalli@inaf.it
Giannini	Giulia	IFAE	Spain	ggiannini@ifae.es

Gouyou Beauchamps	Sylvain	CPPM	France	gouyou@cppm.in2p3.fr
Guinot	Axel	APC	France	guinot@apc.in2p3.fr
Heimersheim	Stefan	Inst. Astronomy, Uni. Cambridge	UK	heimersheim@ast.cam.ac.uk
Helbig	Phillip	IAGO - Uni. Liège	Belgium	helbig@astro.multivax.de
Herold	Laura	MPI Astrophysics	Germany	lherold@mpa-garching.mpg.de
Holman	Marc	Utrecht University	Netherlands	m.holman@uu.nl
Jost	Baptiste	APC	France	jost@apc.in2p3.fr
Kalaja	Alba	Van Swinderen, Uni. Groningen	Netherlands	a.kalaja@rug.nl
Kite	Thomas	JBCA/University of Manchester	UK	tomkite57@gmail.com
Kostyuk	Ivan	MPI Astrophysics	Germany	ivkos@mpa-garching.mpg.de
Kumar	Utkarsh	Ariel Univeristy	Israel	kumarutkarsh641@gmail.com
Lacroix	Leander	LPNHE	France	leander.lacroix@lpnhe.in2p3.fr
Lanusse	François	CNRS, UMR AIM	France	francois.lanusse@gmail.com
Lanzieri	Denise	CosmoStat, CEA Paris-Saclay	France	denise.lanzieri@cea.fr
Lapi	Andrea	SISSA	Italy	lapi@sissa.it
Lau	Kenny	The University of Minnesota	USA	kennylau@umn.edu
Lazeyras	Titouan	Milano Bicocca	Italy	titouan.lazeyras@hotmail.fr
Lee	Elizabeth	JBCA/University of Manchester	UK	elizabeth.g.lee0@gmail.com
Legrand	Louis	University of Geneva	Switzerland	louis.legrand@unige.ch
Leite Pimentel	Guilherme	Leiden University	Netherlands	glpimentel@gmail.com
Leloup	Clément	APC	France	leloup@apc.in2p3.fr
Lembo	Margherita	University of Sussex	UK	ml676@sussex.ac.uk
Lewandowski	Matthew	Northwestern University	USA	matthew.lewandowski@northwestern.edu
Lucca	Matteo	ULB	Belgium	mlucca@ulb.ac.be
Maleubre Molinero	Sara	LPNHE	France	sara.maleubre@lpnhe.in2p3.fr
Martinez-Gonzalez	Enrique	IF Cantabria (UC-CSIC)	Spain	martinez@ifca.unican.es
Martire	Felice Antonio	IF Cantabria (UC-CSIC)	Spain	martire@ifca.unican.es
Matalon	Ariel	LPNHE	France	amatalon@lpnhe.in2p3.fr
Mazzotta	Pasquale	Roma "Tor Vergata"	Italy	mazzotta@roma2.infn.it
McAllister	Liam	Cornell University	USA	mcallister@cornell.edu
Mena	Juan	CIEMAT	Spain	juanmena95@hotmail.es
Moniez	Marc	IJCLab-IN2P3	France	moniez@lal.in2p3.fr
Montandon	Thomas	APC	France	thomas.montandon@apc.in2p3.fr
Montier	Ludovic	IRAP	France	ludovic.montier@irap.omp.eu
Moradinezhad	Azadeh	University of Geneva	Switzerland	azadeh.moradinezhaddizgah@unige.ch
Morshed	Magdy	APC	France	morshed@apc.in2p3.fr
Moser	Beatrice	ETH Zurich	Switzerland	moserb@phys.ethz.ch
Mousset	Louise	IRAP	France	mousset@apc.in2p3.fr
Murray	Calum	CNRS – LPSC	France	calumhrmurray@gmail.com
Neveu	Jérémy	LPNHE	France	jeremy.neveu@universite-paris-saclay.fr
Nicolas	Nora	IP2I Lyon	France	n.nicolas@ip2i.in2p3.fr
Nistane	Viraj	University of Geneva	Switzerland	nato.viraj@gmail.com
Nuss	Eric	LUPM	France	eric.nuss@umontpellier.fr
Obata	Ippei	MPI Astrophysics	Germany	obata@mpa-garching.mpg.de
Padilla	Ivan	Johns Hopkins University	USA	padilla@jhu.edu
Pérez-Ràfols	Ignasi	IFAE - UAB	Spain	iperez@ifae.es
Piacentini	Francesco	Sapienza University of Rome	Italy	francesco.piacentini@roma1.infn.it
Piazza	Federico	CPT	France	fedosquare@gmail.com
Pierre	Marguerite	DAp - Cea Saclay	France	mpierre@cea.fr
Piga	Lorenzo	Università di Parma	Italy	lorenzo.piga@unipr.it
Pozsgay	Victor	Imperial College London	UK	v.pozsgay19@imperial.ac.uk
Qu	Frank J.	University of Cambridge	UK	jq247@cam.ac.uk
Racine	Benjamin	CPPM	France	racine@cppm.in2p3.fr
Ravoux	Corentin	CEA Saclay IRFU/DPhP	France	corentin.ravoux@cea.fr
Reeves	Alexander	ETH Zurich	Switzerland	areeves@phys.ethz.ch
Remy	Benjamin	CosmoStat, CEA Paris-Saclay	France	benjamin.remy@cea.fr
Renaux-Petel	Sébastien	IAP - CNRS	France	renaux@iap.fr
Ricci	Marina	LMU Munich	Germany	marina.ricci@lmu.de
Richard	Benoit	Minerva University	USA	brichard@minerva.edu

Richardson	Thomas	LUTH - Obs. de Paris | PSL	France	thomas.richardson@obspm.fr
Rizzieri	Arianna	APC	France	rizzieri@apc.in2p3.fr
Rossi	Graziano	Sejong University	South Korea	graziano@sejong.ac.kr
Rotti	Aditya	JBCA/University of Manchester	UK	aditya.rotti@manchester.ac.uk
Roucelle	Cécile	APC	France	roucelle@apc.in2p3.fr
Saadeh	Daniela	ICG, University of Portsmouth	UK	daniela.saadeh@port.ac.uk
Sáez Casares	Iñigo	LUTh, Observatoire de Paris	France	inigo.saez-casares@obspm.fr
Sánchez Cid	David	CIEMAT	Spain	davsan06@ucm.es
Santiago de Matos	Isabela	Uni. Federal do Rio de Janeiro	Brazil	isa@if.ufrj.br
Schmidt	Fabian	MPI Astrophysics	Germany	fabians@mpa-garching.mpg.de
Semenaite	Agne	MPI Extraterrestrial Physics	Germany	agne@mpe.mpg.de
Senatore	Leonardo	ETH Zurich	Switzerland	lsenatore@phys.ethz.ch
Smith	Mathew	IP2I Lyon	France	m.smith@ip2i.in2p3.fr
Sobral Blanco	Daniel	University of Geneva	Switzerland	daniel.sobralblanco@unige.ch
Sommer	Kélian	LUPM	France	kelian.sommer@umontpellier.fr
Sorini	Daniele	Inst. Astronomy, Uni. Edinburgh	UK	sorini@roe.ac.uk
Souverin	Thierry	LPNHE	France	thierry.souverin@lpnhe.in2p3.fr
Spinelli	Marta	ETH Zurich	Switzerland	mspinelli@phys.ethz.ch
Svalheim	Trygve Leithe	Inst. Theoretical Astrophysics	Norway	t.l.svalheim@astro.uio.no
Tan	Ting	LPNHE	France	ting.tan@lpnhe.in2p3.fr
Taule	Petter	Technical University of Munich	Germany	petter.taule@tum.de
Tremblin	Pascal	CEA Paris-Saclay	France	pascal.tremblin@cea.fr
Trombetta	Leonardo	CEICO / CAS	Czechia	trombetta@fzu.cz
Urban	Federico	CEICO / CAS	Czechia	federico.urban@fzu.cz
Vacher	Léo	IRAP	France	leo.vacher@irap.omp.eu
Van den Abeele	Enya	LPNHE	France	enya.vandenabeele@lpnhe.in2p3.fr
Vergès	Clara	Harvard CfA	USA	clara.verges@cfa.harvard.edu
Vernizzi	Filippo	Institut de Physique Théorique	France	filippo.vernizzi@ipht.fr
Vielzeuf	Pauline	CPPM	France	vielzeuf@cppm.in2p3.fr
Vikman	Alexander	CEICO / CAS	Czechia	vikman@fzu.cz
Wang	Pascal	CRAL, ENS de Lyon	France	pascal.wang@ens-lyon.fr
Werth	Denis	Sorbonne University / IAP	France	denis.werth@iap.fr
White	Simon	MPI Astrophysics	Germany	swhite@mpa-garching.mpg.de
Wilkins	Ashley	Newcastle University	UK	a.wilkins3@ncl.ac.uk
Winther	Hans	Inst. Th. Astrophysics, Uni. Oslo	Norway	hans.a.winther@gmail.com
Yèche	Christophe	CEA - Irfu	France	christophe.yeche@cea.fr
Yershov	Vladimir		UK	vyershov@moniteye.co.uk
Zamorano Vitorelli	André	CosmoStat, CEA Paris-Saclay	France	andre.zamoranovitorelli@cea.fr
Zeghal	Justine	APC	France	zeghal@apc.in2p3.fr
Zeghari	Kenza	CPT	France	kenza.zeghari@univ-amu.fr
Zubeldia	Iñigo	University of Manchester	UK	zubeldiainigo@gmail.com
Zürcher	Dominik	ETH Zurich	Switzerland	dominikz@phys.ethz.ch

Dépôt légal : octobre 2022
Achevé d'imprimer : octobre 2022
COPYMÉDIA
www.copy-media.net
1 bis avenue de Guitayne - 33610 CANÉJAN

Proceedings of the 56th Rencontres de Moriond